

**SHAKING TABLE TESTS ON THE RESPONSE OF
REINFORCED CONCRETE FRAMES WITH
NON-SEISMIC DETAILING**

by

SOHEIL YAVARI

A THESIS SUBMITTED IN PARTIAL FULFILMENT OF
THE REQUIREMENTS FOR THE DEGREE OF

DOCTOR OF PHILOSOPHY

in

THE FACULTY OF GRADUATE STUDIES
(Civil Engineering)

The University of British Columbia
(Vancouver)

February 2011

© Soheil Yavari, 2011

ABSTRACT

Reinforced concrete frames constructed before the introduction of modern seismic codes have performed poorly during past earthquakes. Such frames have primarily been designed for gravity load effects, leading to light transverse reinforcement in the columns, unconfined beam-column joints, and generally a lack of seismic details required for ductile post-yield behaviour. It has been demonstrated in literature that light transverse reinforcement in a column may result in shear and axial failure. Furthermore, lack of confinement may cause shear failure at joints. However, interaction of vulnerable components and their contribution to the collapse behaviour of existing reinforced concrete frames is not well understood. This research project was initiated to provide a better understanding of the factors contributing to collapse of the frames with non-seismic detailing.

In the experimental phase of this study, four 1:2.25 scale, two-bay-two-story specimens were designed with non-seismic details and tested on a shaking table. The target failure mode was intended to be damage leading to collapse that would enable examination of gravity load redistribution during the test. The tests provide unique benchmark data for both qualitative and quantitative assessment of the factors influencing the behaviour of reinforced concrete frames up to the point of collapse. Based on the results from the shaking table tests, this dissertation will evaluate the influence of axial load on shear and axial behaviour of non-ductile columns and the effects of unconfined joints on overall behaviour of a frame near the point of collapse.

The analytical phase of the research included evaluation of existing models for predicting shear and axial failure of non-ductile columns and collapse of frames. The currently available models for shear and axial failure of non-ductile columns are mainly drift-based. The results of the current study suggest that these models should be refined using the column ends

rotation demand. While results from comprehensive nonlinear models of the four specimens were compared with the test data, simplified models that can be easily employed in engineering practice for assessing existing frames were also evaluated. A refinement to provision from ASCE-41 on column effective stiffness was also proposed in this dissertation.

TABLE OF CONTENTS

| | |
|---|------------|
| ABSTRACT | ii |
| TABLE OF CONTENTS | iii |
| LIST OF TABLES | ix |
| LIST OF FIGURES | xi |
| ACKNOWLEDGMENTS | xxv |
| CHAPTER 1. INTRODUCTION | 1 |
| 1.1 Background | 1 |
| 1.2 Objectives and Scope | 3 |
| 1.3 Organization | 5 |
| CHAPTER 2. LITERATURE REVIEW | 8 |
| 2.1 Introduction | 8 |
| 2.2 Experimental Studies on Behaviour of Non-ductile Columns | 10 |
| 2.2.1 <i>Static and Pseudo-dynamic Experimental Tests</i> | 10 |
| 2.2.2 <i>Dynamic Experimental Tests</i> | 12 |
| 2.3 Modeling the Behaviour of Non-ductile Columns | 13 |
| 2.3.1 <i>Models for Drift at Shear Failure</i> | 13 |
| 2.3.2 <i>Models for Drift at Axial Failure</i> | 16 |
| 2.3.3 <i>Implementation of Shear and Axial Failure Models</i> | 19 |
| 2.4 Beam-column Joint with Non-seismic Detailing..... | 21 |
| 2.4.1 <i>Experimental Studies on Behaviour of Unconfined Joints</i> | 21 |
| 2.4.2 <i>Modeling the Behaviour of Unconfined Joints</i> | 23 |
| CHAPTER 3. DETAILS OF SPECIMENS AND TEST SETUP | 26 |
| 3.1 Introduction | 26 |
| 3.2 Specimen Description and Design..... | 26 |
| 3.3 Construction | 35 |

| | | |
|-------------------|--|------------|
| 3.4 | Test Setup | 37 |
| 3.4.1 | <i>Lateral Supporting System</i> | 38 |
| 3.4.2 | <i>Loading</i> | 39 |
| 3.4.2.1 | Gravity Load on Beams..... | 39 |
| 3.4.2.2 | Pre-stressed Axial Load on Columns | 40 |
| 3.4.2.3 | Inertial-mass System | 45 |
| 3.5 | Instrumentation..... | 49 |
| 3.6 | Ground Motion Selection | 50 |
| 3.7 | Experimental Program..... | 55 |
| CHAPTER 4. | EXPERIMENTAL TEST RESULTS | 57 |
| 4.1 | Introduction | 57 |
| 4.2 | Initial Vertical Load State | 59 |
| 4.3 | Fundamental Periods and Damping Ratios | 60 |
| 4.4 | Behaviour of Specimen MCFS..... | 61 |
| 4.5 | Behaviour of Specimen HCFS | 79 |
| 4.6 | Behaviour of Specimen MUF..... | 97 |
| 4.7 | Behaviour of Specimen MUFS | 116 |
| CHAPTER 5. | COMPARISON OF RESPONSE OF THE TEST SPECIMENS | 137 |
| 5.1 | INTRODUCTION | 137 |
| 5.2 | Comparison of Table Demands | 138 |
| 5.2.1 | <i>Comparison of Table Demands for Specimens MCFS and HCFS</i> | 138 |
| 5.2.2 | <i>Comparison of Table Demands for Specimen MCFS and MUF</i> | 141 |
| 5.2.3 | <i>Comparison of Table Demands for Specimen MCFS and MUFS</i> | 144 |
| 5.2.4 | <i>Comparison of Table Demands for Specimen MUF and MUFS</i> | 146 |
| 5.3 | Comparison of Failure Modes | 149 |
| 5.4 | Comparison of Test Data..... | 151 |
| 5.4.1 | <i>Floor Acceleration</i> | 152 |

| | | |
|--|--|------------|
| 5.4.2 | <i>Peak Inter-story Drift Demand</i> | 154 |
| 5.4.3 | <i>Backbone for Column Shear Hysteretic Response</i> | 155 |
| 5.5 | Effect of Axial Load on Key Parameters of Columns..... | 159 |
| 5.5.1 | <i>Story Drift Ratio at Maximum Recorded Shear Strength</i> | 159 |
| 5.5.2 | <i>Effect of Axial Load on Column Effective Stiffness</i> | 160 |
| 5.5.3 | <i>Effect of Axial Load on Column Secant Stiffness at Peak Shear</i> | 163 |
| 5.5.4 | <i>Effect of Axial Load on Slope of Column Vertical Displacement before and after Onset of Axial Failure</i> | 164 |
| 5.5.5 | <i>Effect of Axial Load on Story Drift Ratio at Onset of Axial Failure</i> | 166 |
| 5.5.6 | <i>Effect of Axial Load on Closeness of Drift Ratio at Onsets of Shear and Axial Failure</i> | 167 |
| 5.6 | Column Chord Rotation versus Drift Ratio..... | 168 |
| CHAPTER 6. ANALYSIS OF SHAKING TABLE TEST SPECIMENS | | 172 |
| 6.1 | Introduction | 172 |
| 6.2 | Description of the Analytical Models..... | 172 |
| 6.2.1 | <i>Footing and Beam Elements</i> | 173 |
| 6.2.2 | <i>Joint Elements</i> | 175 |
| 6.2.3 | <i>Column Elements</i> | 178 |
| 6.2.4 | <i>Modeling of Bar-slip for Beams and Columns</i> | 182 |
| 6.2.5 | <i>Load Model</i> | 183 |
| 6.2.6 | <i>Other Modeling Parameters</i> | 184 |
| 6.3 | Assessment of Analytical Models | 185 |
| 6.3.1 | <i>Static Pushover Analysis</i> | 186 |
| 6.3.2 | <i>Analytical Model of Specimen MCFS</i> | 191 |
| 6.3.2.1 | Comparison of Results for Test1 | 191 |
| 6.3.2.2 | Comparison of Results for Test2 | 197 |
| 6.3.3 | <i>Analytical Model of Specimen HCFS</i> | 202 |
| 6.3.3.1 | Comparison of Results for Test1 | 202 |
| 6.3.3.2 | Comparison of Results for Test2 | 208 |
| 6.3.4 | <i>Analytical Model of Specimen MUF</i> | 215 |

| | | |
|-------------------------|---|------------|
| 6.3.4.1 | Comparison of Results for Test1 | 215 |
| 6.3.4.2 | Comparison of Results for Test2 | 221 |
| 6.3.5 | <i>Analytical Model of Specimen MUFS</i> | 225 |
| 6.3.5.1 | Comparison of Results for Test1 | 225 |
| 6.3.5.2 | Comparison of Results for Test2 | 230 |
| CHAPTER 7. | SIMPLIFIED MODELING METHODS | 236 |
| 7.1 | Introduction | 236 |
| 7.2 | Analytical Model with Elastic Elements and no End-springs | 237 |
| 7.3 | Analytical Model with Nonlinear Column Elements and no End-springs | 238 |
| 7.4 | Analytical Model with Nonlinear Column Elements and Only Bar-slip End-spring | 241 |
| 7.5 | Evaluation of Capacity Backbone for Shear Hysteretic Response of Columns | 244 |
| 7.5.1 | <i>Effective Stiffness of Elastic Columns</i> | 245 |
| 7.5.2 | <i>Modeling Parameters for End Rotational Hinges</i> | 250 |
| 7.6 | Proposed Shear Capacity Backbone | 258 |
| 7.7 | Evaluation of Analytical Models with Elastic Columns and End Rotational Hinges | 260 |
| 7.7.1 | <i>Analytical Model with ASCE-41 Backbone</i> | 260 |
| 7.7.2 | <i>Analytical Model with Proposed Backbone</i> | 262 |
| CHAPTER 8. | CONCLUSIONS AND FUTURE WORK..... | 265 |
| 8.1 | Summary | 265 |
| 8.2 | Original Contributions from the Research..... | 267 |
| 8.3 | Conclusions | 270 |
| 8.3.1 | <i>Results from Experimental Tests</i> | 270 |
| 8.3.2 | <i>Results from Analytical Studies</i> | 271 |
| 8.4 | Future Research | 273 |
| REFERENCES | | 276 |

| | |
|---|------------|
| APPENDICES | 287 |
| Appendix A. Specimen Drawings and Material Properties | 287 |
| A.1. As-built Specimen Drawings and Specifications | 287 |
| A.2. Material Properties | 296 |
| A.2.1. Concrete Properties | 296 |
| A.2.2. Reinforcing Steel Properties..... | 299 |
| Appendix B. Instrumentation, Procedures, and Data Reduction..... | 305 |
| B.1. Introduction | 305 |
| B.2. Breakdown of Weights Connected to Specimens..... | 305 |
| B.3. Instrumentation..... | 306 |
| B.3.1. Force Transducers | 315 |
| B.3.2. Accelerometers | 315 |
| B.3.3. Displacement Measuring Instruments..... | 317 |
| B.3.4. Strain Gages..... | 317 |
| B.4. Data Reduction | 326 |
| B.5. Condition Assessment and Modeling Parameters for Existing Reinforced Concrete Columns Recommended by ASCE-41..... | 331 |
| Appendix C. Results of Test3 for Specimen MUF | 333 |

LIST OF TABLES

| | |
|--|-----|
| Table 3-1. Parameters and column material properties for the specimens | 32 |
| Table 3-2. Pre-stressing axial load on columns | 41 |
| Table 3-3. Chronology of dynamic tests for specimens | 56 |
| Table 4-1: Summary of frames modal properties | 61 |
| Table 4-2. Critical parameters for columns of specimen MCFS, Test1 | 65 |
| Table 4-3. Critical parameters for columns of specimen MCFS, Test2 | 66 |
| Table 4-4. Critical parameters for columns of specimen HCFS, Test1 | 84 |
| Table 4-5. Critical parameters for columns of specimen HCFS, Test2 | 84 |
| Table 4-6. Critical parameters for columns of specimen MUF, Test1. | 103 |
| Table 4-7. Critical parameters for columns of specimen MUF, Test2. | 104 |
| Table 4-8. Critical parameters for columns of specimen MUFS, Test1. | 122 |
| Table 4-9. Critical parameters for columns of specimen MUFS, Test2. | 122 |
| Table 6-1. Influence of joint rotation on lateral displacement of first story at $0.75V_{max}$, specimen MCFS..... | 190 |
| Table 6-2. Influence of joint rotation on lateral displacement of first story at $0.75V_{max}$, specimen MUFS..... | 190 |
| Table 7-1. Peak story drifts for models with different column effective stiffnesses (Specimen MCFS, Test1)..... | 247 |
| Table A-1. Average concrete compressive strengths..... | 296 |
| Table A-2. Concrete compressive strength test results for specimens MCFS and HCFS | 297 |
| Table A-3. Concrete compressive strength test results for specimens MUF and MUFS | 297 |
| Table A-4. Averages from column reinforcing steel coupon tests | 300 |
| Table A-5. Reinforcing steel properties for specimens MCFS and HCFS | 300 |
| Table A-6. Reinforcing steel properties for specimens MUF and MUFS | 300 |
| Table B-1. Weight of inertial-Mass wagons, connections, lead packet stacks on the beams, and specimen | 306 |
| Table B-2. Instrumentation list for specimen MCFS..... | 307 |
| Table B-3. Instrumentation list for specimen HCFS | 309 |
| Table B-4. Instrumentation list for specimen MUF | 311 |
| Table B-5. Instrumentation list for specimen MUFS..... | 313 |

| | |
|---|-----|
| Table B-6. Classification of columns for determination of modeling parameters | 331 |
| Table B-7. Modeling Parameters and numerical acceptance criteria for nonlinear procedures for reinforced concrete column (Table 6-8 ASCE-41) | 332 |

LIST OF FIGURES

| | |
|--|----|
| Figure 2-1. Shear failure defined by Elwood & Moehle drift-capacity model (Elwood & Moehle, 2005)..... | 15 |
| Figure 2-2. Comparison of Elwood & Moehle shear-drift model with test data (Elwood, 2002) | 16 |
| Figure 2-3. Axial failure defined by Elwood & Moehle drift-capacity model (Elwood & Moehle, 2005)..... | 18 |
| Figure 2-4. Shear and axial springs in series model (Elwood, 2002)..... | 19 |
| Figure 2-5. Shear spring model using LimitState Uniaxial material (Elwood, 2002)..... | 20 |
| Figure 2-6. Axial spring using LimitState Uniaxial material (Elwood, 2002)..... | 21 |
| Figure 2-7. Existing beam-column joints models (adopted from Celik and Ellingwood, 2008); (a) Alath and Kunnath (1995); (b) Biddah and Ghobarah (1999); (c) Yousseff and Ghobarah (2001), (d) Lowes and Altoontash (2003); (e) Altoontash (2004), and (f) Shin and LaFave (2004)..... | 25 |
| Figure 3-1. Naming convention for shaking table specimens..... | 27 |
| Figure 3-2. Shaking table test specimens..... | 30 |
| Figure 3-3. Cross-section and reinforcement details of test specimens..... | 34 |
| Figure 3-4. Specimen construction and casting steps; a) footing and columns bar cages; b) pouring concrete; c) finished footings; d) forms for first-story column and beams; e) bar cage for beam and slabs; f) bar cage for top column stubs..... | 36 |
| Figure 3-5. Locating the specimens on the shaking table..... | 37 |
| Figure 3-6. Lateral supporting system | 38 |
| Figure 3-7. Out-of-plane restraining system and catching beams during setup of testing apparatus | 39 |
| Figure 3-8. Pre-stressing system for adding axial load to columns | 42 |
| Figure 3-9. Fluctuation in applied axial load to columns during Test1 | 44 |
| Figure 3-10. Fluctuation in applied axial load to columns during Test2..... | 45 |
| Figure 3-11. Inertial-mass rolling system..... | 47 |
| Figure 3-12. Inertial-mass anti-rocking system | 47 |
| Figure 3-13. Inertial-mass lateral force transferring system..... | 48 |

| | |
|--|----|
| Figure 3-14. Input and recorded table acceleration, velocity, and displacement for specimen MCFS (Test1) | 52 |
| Figure 3-15. (a) Pseudo-acceleration and; (b) displacement response spectra for recorded table motions with 2% damping (Test1)..... | 53 |
| Figure 3-16. (a) Pseudo-acceleration and; (b) displacement response spectra for recorded table motions with 2% damping (Test2)..... | 54 |
| Figure 4-1. Definition of key parameters based on column shear-drift data envelope..... | 58 |
| Figure 4-2. First and Second mode shapes for the specimens | 61 |
| Figure 4-3. Comparison of spectral acceleration with 2% damping for Test1 and Test2 table motions, Specimen MCFS | 62 |
| Figure 4-4. Comparison of displacement response spectra with 2% damping for Test1 and Test2 table motions, Specimen MCFS..... | 62 |
| Figure 4-5. Shear and flexural cracks in columns of specimen MCFS, Test1; a) column A1 base; b) column B1 top; c) column B1 base; d) column C1 base..... | 63 |
| Figure 4-6. Failure mode of specimen MCFS | 64 |
| Figure 4-7. Failure of first-story columns of specimen MCFS in Test2..... | 64 |
| Figure 4-8. Story-level acceleration records for specimen MCFS, Test1 and Test2..... | 67 |
| Figure 4-9. Story-level drift response history for specimen MCFS, Test1 and Test2 | 69 |
| Figure 4-10. Minimum and maximum inter-story drift ratio profiles for specimen MCFS, Test1 and Test2 | 69 |
| Figure 4-11. First-story columns and frame base shear histories for specimen MCFS, Test1 and Test2..... | 70 |
| Figure 4-12. Story-level shear hysteretic response of specimen MCFS, Test1 and Test2 | 71 |
| Figure 4-13. Shear hysteretic response of specimen MCFS columns, Test1 and Test2..... | 72 |
| Figure 4-14. Axial load response history of first-story columns of specimen MCFS, Test1 and Test2..... | 74 |
| Figure 4-15. Axial load hysteretic response of first-story columns of specimen MCFS, Test1 and Test2..... | 75 |
| Figure 4-16. Vertical displacement ratio for columns of specimen MCFS, Test1 and Test2.... | 75 |
| Figure 4-17. Variation of axial load of specimen MCFS columns with vertical displacement, Test1 and Test2 | 76 |

| | |
|--|----|
| Figure 4-18. a) definition of chord rotation; b) first-story column chord rotations at base and top | 76 |
| Figure 4-19. Moment-chord rotation relationship at top of first-story columns of specimen MCFS, Test1 and Test2 | 78 |
| Figure 4-20. Moment hysteretic response of first-story columns of specimen MCFS at base, Test1 and Test2 | 78 |
| Figure 4-21. Comparison of spectral acceleration with 2% damping for Test1 and Test2 table motions, Specimen HCFS..... | 80 |
| Figure 4-22. Comparison of displacement response spectra with 2% damping for Test1 and Test2 table motions, Specimen HCFS | 80 |
| Figure 4-23. Shear and flexural cracks in columns of specimen HCFS after Test1; a) column A1; b) base of column B1; c) top of column B2; d) column C1..... | 81 |
| Figure 4-24. Cracks in beams after Test1; a) near joint C1; b) near joint A1 | 81 |
| Figure 4-25. Failure mode of specimen HCFS (sequence of failure shown by numbers)..... | 83 |
| Figure 4-26. Failure of columns of specimen HCFS, Test2; a) column A2; b) column B1; c) column C1 | 83 |
| Figure 4-27. Story-level acceleration records for specimen HCFS, Test1 and Test2..... | 86 |
| Figure 4-28. First-story acceleration records for specimen HCFS, Test1 and Test2, $32 < t < 36$ seconds | 86 |
| Figure 4-29. Story-level drift response history for specimen HCFS, Test1 and Test2..... | 87 |
| Figure 4-30. Minimum and maximum inter-story drift ratio profiles for specimen HCFS, Test1 and Test2..... | 88 |
| Figure 4-31. First-story columns and frame base shear histories for specimen HCFS, Test1 and Test2..... | 89 |
| Figure 4-32. Story-level shear hysteretic response of specimen HCFS, Test1 and Test2 | 90 |
| Figure 4-33. Shear hysteretic response of specimen HCFS columns, Test1 and Test2..... | 91 |
| Figure 4-34. Shear hysteretic response of specimen HCFS columns, Test1 and Test2, $32 < t < 36$ seconds | 92 |
| Figure 4-35. Axial load response history of first-story columns of specimen HCFS, Test1 and Test2..... | 93 |
| Figure 4-36. Axial load hysteretic response of first-story columns of specimen HCFS, Test1 and Test2 | 94 |

| | |
|---|-----|
| Figure 4-37. Variation of axial load of specimen HCFS columns with vertical displacement, Test1 and Test2 | 94 |
| Figure 4-38. Vertical displacement ratio for columns of specimen HCFS, Test1 and Test2 | 95 |
| Figure 4-39. Moment-chord rotation relationship at top of first-story columns of specimen HCFS, Test1 and Test2 | 96 |
| Figure 4-40. Moment hysteretic response of first-story columns of specimen HCFS at base, Test1 and Test2 | 96 |
| Figure 4-41. Comparison of spectral acceleration with 2% damping for Test1, Test2, and Test3 table motions, Specimen MUF | 98 |
| Figure 4-42. Comparison of displacement response spectra with 2% damping for Test1, Test2, and Test3 table motions, Specimen MUF | 98 |
| Figure 4-43. Damaged first-story joints of specimen MUF after Test1; a) joint A1; b) joint B1; c) joint C1 | 99 |
| Figure 4-44. Flexural cracks at the base of first-story columns of specimen MUF, Test1; a) column A1; b) column B1; c) column C1 | 99 |
| Figure 4-45. Damaged first-story joints of specimen MUF after Test2; a) joint A1; b) joint B1; c) joint C1 | 100 |
| Figure 4-46. Damaged first-story joints of specimen MUF after Test3; a) joint A1; b) joint B1; c) joint C1 | 101 |
| Figure 4-47. Failure mode of specimen MUF | 101 |
| Figure 4-48. a) direction of shear cracking in joint; b) state of joint after shear failure; c) shear-strain response of joint..... | 102 |
| Figure 4-49. a) direction of shear cracking in column; b) state of column after shear failure; c) shear-rotation response of column | 103 |
| Figure 4-50. Story-level acceleration records for specimen MUF, Test1 and Test2 | 106 |
| Figure 4-51. Story-level drift response history for specimen MUF, Test1 and Test2 | 107 |
| Figure 4-52. Minimum and maximum inter-story drift ratio profiles for specimen MUF, Test1 and Test2 | 107 |
| Figure 4-53. First-story columns and frame base shear histories for specimen MUF, Test1 and Test2 | 108 |
| Figure 4-54. Story-level shear hysteretic response of specimen MUF, Test1 and Test2 | 109 |
| Figure 4-55. Shear hysteretic response of specimen MUF columns, Test1 and Test2 | 110 |

| | |
|---|-----|
| Figure 4-56. Axial load hysteretic response of first-story columns of specimen MUF, Test1 and Test2..... | 110 |
| Figure 4-57. Axial load response history of first-story columns of specimen MUF, Test1 and Test2..... | 111 |
| Figure 4-58. Vertical displacement ratio for columns of specimen MUF, Test1 and Test2.... | 112 |
| Figure 4-59. Variation of axial load of specimen MUF columns with vertical displacement, Test1 and Test2..... | 112 |
| Figure 4-60. Moment-chord rotation relationship at top of first-story columns of specimen MUF, Test1 and Test2..... | 113 |
| Figure 4-61. Moment hysteretic response of first-story columns of specimen MUF, Test1 and Test2..... | 113 |
| Figure 4-62. Comparison of shear deformation at joint C1 of specimen MUF, recorded by diagonal instruments on exposed and transverse beam faces of the joint..... | 114 |
| Figure 4-63. Comparison of propagation of shear cracks to the top of column C1 of specimen MUF after Test3; a) exposed face; b) transverse beam face..... | 115 |
| Figure 4-64. Relation between shear force and shear deformation of joint C1 recorded at unconfined face of the joint for specimen MUF..... | 116 |
| Figure 4-65. Relation between first-story drift ratio and shear deformation of joint C1 recorded at unconfined face of the joint for specimen MUF..... | 116 |
| Figure 4-66. Comparison of spectral acceleration with 2% damping for Test1 and Test2 table motions, specimen MUFS..... | 117 |
| Figure 4-67. Comparison of displacement response spectra with 2% damping for Test1 and Test2 table motions, specimen MUFS..... | 118 |
| Figure 4-68. Damaged first-story joints of specimen MUFS after Test1; a) joint A1; b) joint B1; c) joint C1..... | 119 |
| Figure 4-69. Damage to the base of first-story columns of specimen MUFS during Test1; a) column A1; b) column B1; c) column C1..... | 119 |
| Figure 4-70. Damage to second-story columns of specimen MUFS during Test1; a) base of column A2; b) top of column B2; c) base of column C2..... | 119 |
| Figure 4-71. Failure mode of specimen MUFS..... | 121 |
| Figure 4-72. Damaged first-story joints of specimen MUFS after Test2; a) joint A1; b) joint B1; c) joint C1..... | 121 |

| | |
|---|-----|
| Figure 4-73. Damage to second-story columns of specimen MUFS after Test2; a) column A2; b) column B2; c) column C2..... | 121 |
| Figure 4-74. Story-level acceleration records for specimen MUFS, Test1 and Test2..... | 124 |
| Figure 4-75. Story-level drift response history for specimen MUFS, Test1 and Test2..... | 125 |
| Figure 4-76. Minimum and maximum inter-story drift ratio profiles for specimen MUFS, Test1 and Test2 | 125 |
| Figure 4-77. First-story columns and frame base shear histories for specimen MUFS, Test1 and Test2 | 126 |
| Figure 4-78. Story-level shear hysteretic response of specimen MUFS, Test1 and Test2 | 127 |
| Figure 4-79. Shear hysteretic response of specimen MUFS columns, Test1 and Test2..... | 129 |
| Figure 4-80. Axial load hysteretic response of first-story columns of specimen MUFS, Test1 and Test2 | 130 |
| Figure 4-81. Axial load response history of first-story columns of specimen MUFS, Test1 and Test2..... | 130 |
| Figure 4-82. Vertical displacement ratio for columns of specimen MUFS, Test1 and Test2 . | 131 |
| Figure 4-83. Variation of axial load of specimen MUFS columns with vertical displacement, Test1 and Test2 | 132 |
| Figure 4-84. Moment-chord rotation relationship at top of first-story columns of specimen MUF, Test1 and Test2 | 132 |
| Figure 4-85. Moment hysteretic response of first-story columns of specimen MUFS, Test1 and Test2..... | 133 |
| Figure 4-86. Moment-rotation hysteresis for column B1 of specimen MUFS, Test1 and Test2 | 133 |
| Figure 4-87. Comparison of shear deformation at joint C1 of specimen MUFS, recorded by diagonal instruments on east and west sides of the joint | 135 |
| Figure 4-88. Comparison of propagation of shear cracks to the top of column C1 of specimen MUFS after Test2; a) exposed face; b) transverse beam face | 135 |
| Figure 4-89. Relationship between shear force and shear deformation of joint C1 recorded at unconfined face of the joint for specimen MUFS..... | 136 |
| Figure 4-90. Relation between first-story drift ratio and shear deformation of joint C1 recorded at unconfined face of the joint for specimen MUFS..... | 136 |

| | |
|---|-----|
| Figure 5-1. Comparison of acceleration response history for specimens MCFS and HCFS at table and footing levels, Test1 | 139 |
| Figure 5-2. Comparison of spectral acceleration with 2% damping for specimens MCFS and HCFS, Test1 table motion..... | 139 |
| Figure 5-3. Comparison of acceleration response history for specimens MCFS and HCFS at table and footing levels, Test2 | 140 |
| Figure 5-4. Comparison of spectral acceleration with 2% damping for specimens MCFS and HCFS, Test2 table motion..... | 141 |
| Figure 5-5. Comparison of acceleration response history for specimens MCFS and MUF at table and footing levels, Test1 | 142 |
| Figure 5-6. Comparison of spectral acceleration with 2% damping for specimens MCFS and MUF, Test1 table motion..... | 142 |
| Figure 5-7. Comparison of acceleration response history for specimens MCFS and MUF at table and footing levels, Test2 | 143 |
| Figure 5-8. Comparison of spectral acceleration with 2% damping for specimens MCFS and MUF, Test2 table motion..... | 144 |
| Figure 5-9. Comparison of acceleration response history for specimens MCFS and MUFS at table and footing levels, Test1 | 144 |
| Figure 5-10. Comparison of spectral acceleration with 2% damping for specimens MCFS and MUFS, Test1 table motion..... | 145 |
| Figure 5-11. Comparison of acceleration response history for specimens MCFS and MUFS at table and footing levels, Test2 | 146 |
| Figure 5-12. Comparison of spectral acceleration with 2% damping for specimens MCFS and MUFS, Test2 table motion..... | 146 |
| Figure 5-13. Comparison of acceleration response history for specimens MUF and MUFS at table and footing levels, Test1 | 147 |
| Figure 5-14. Comparison of spectral acceleration with 2% damping for specimens MUF and MUFS, Test1 table motion..... | 147 |
| Figure 5-15. Comparison of acceleration response history for specimens MUF and MUFS at table and footing levels, Test2 | 148 |
| Figure 5-16. Comparison of spectral acceleration with 2% damping for specimens MUF and MUFS, Test2 table motion..... | 148 |

| | |
|---|-----|
| Figure 5-17. Comparison of failure modes during Test2; a) specimen MCFS; b) specimen HCFS..... | 149 |
| Figure 5-18. Comparison of failure modes in Test2; a) specimen MUF; b) specimen MUFS..... | 151 |
| Figure 5-19. Comparison of story-level acceleration records for specimens MCFS and HCFS, Test1..... | 152 |
| Figure 5-20. Comparison of story-level acceleration records for specimens MCFS and MUF, Test1..... | 153 |
| Figure 5-21. Comparison of story-level acceleration records for specimens MUF and MUFS, Test1..... | 154 |
| Figure 5-22. Peak story drift ratio profiles for Test1; a) negative direction; b) positive direction | 155 |
| Figure 5-23. Peak story drift ratio profiles for Test2; a) negative direction; b) positive direction | 155 |
| Figure 5-24. Comparison of shear strength backbone for first-story columns of specimens MCFS and HCFS; a) Test1; b) Test2..... | 156 |
| Figure 5-25. Comparison of shear strength backbone for first-story columns of specimens MCFS and MUF; a) Test1; b) Test2..... | 157 |
| Figure 5-26. Comparison of shear strength backbone for first-story columns of specimens MUF and MUFS; a) Test1; b) Test2..... | 158 |
| Figure 5-27. Influence of axial load on column drift ratio at the point of peak shear for first-story columns, a) Test1; b) Test2..... | 159 |
| Figure 5-28. Effect of axial load on effective stiffness; a) Test1; b) Test2 | 161 |
| Figure 5-29. Comparison of column EI_{eff}/EI_g with code suggested ratios for first-story columns; a) Test1; b) Test2..... | 162 |
| Figure 5-30. Comparison of calculated and measured effective stiffnesses in Test1; a) ASCE-41 model; b) Elwood & Eberhard model..... | 163 |
| Figure 5-31. Effect of axial load on column secant stiffness at peak shear for first-story columns; a) Test1; b) Test2..... | 164 |
| Figure 5-32. Schematic of slope of vertical displacement before and after axial failure | 165 |
| Figure 5-33. Influence of axial load on slopes “a” and “b” defined in Figure 5-32, Test2; a) pre-axial failure; b) post-axial failure | 165 |
| Figure 5-34. Effect of axial load on drift ratio at onset of axial failure | 167 |

| | |
|---|-----|
| Figure 5-35. Effect of axial load on distance between drift ratios at onsets of shear and axial failure | 168 |
| Figure 5-36. Comparison of column chord rotation with drift ratio at point of peak drift ratio for first-story columns in the positive direction of Test1; a) specimen MCFS; b) specimen HCFS; c) specimen MUF; d) specimen MUFS | 171 |
| Figure 6-1. Model of shaking table specimens MCFS and HCFS..... | 173 |
| Figure 6-2. Moment-curvature relationship for first-story beams. | 175 |
| Figure 6-3. The free-body diagram of the scissors model (Alath and Kunnath, 1995) | 176 |
| Figure 6-4. Comparison of drifts at onset of shear and axial failures, specimen MCFS and 2005 Test..... | 179 |
| Figure 6-5. Stress-strain relationships used in modeling; a) unconfined cover concrete with spalling; b) unconfined cover concrete, spalling ignored; c) confined concrete; d) Clough-type hysteretic steel model for column longitudinal reinforcement | 182 |
| Figure 6-6. Shear response of first-story columns of specimen MCFS, monotonic analysis under initial axial load | 187 |
| Figure 6-7. Shear response of first-story columns of specimen MCFS, monotonic analysis under peak axial load | 187 |
| Figure 6-8. Base shear response of specimen MCFS, monotonic analysis, Test1 and Test2.. | 188 |
| Figure 6-9. Components of drift ratio for column B1, monotonic analysis..... | 189 |
| Figure 6-10. Lateral deformation of frame with; a) flexible beams; b) rigid beams | 190 |
| Figure 6-11. Story and frame drift ratio histories (specimen MCFS, Test1)..... | 192 |
| Figure 6-12. First-story columns, second-story shear and frame base shear histories (specimen MCFS, Test1)..... | 193 |
| Figure 6-13. Shear hysteretic response of the columns (specimen MCFS, Test1)..... | 194 |
| Figure 6-14. Axial load history response of first-story columns (specimen MCFS, Test1).... | 195 |
| Figure 6-15. Axial load hysteretic response of first-story columns (specimen MCFS, Test1)196 | |
| Figure 6-16. Variation of axial load on first-story columns due to overturning (specimen MCFS, Test1)..... | 196 |
| Figure 6-17. Story and frame drift ratio histories (specimen MCFS, Test2)..... | 197 |
| Figure 6-18. First-story columns and frame base shear histories (specimen MCFS, Test2) ... | 198 |
| Figure 6-19. Shear hysteretic response of the columns (specimen MCFS, Test2)..... | 200 |
| Figure 6-20. Axial load history response of first-story columns (specimen MCFS, Test2).... | 201 |

| | |
|--|-----|
| Figure 6-21. Axial load hysteretic response of first-story columns (specimen MCFS, Test2) | 201 |
| Figure 6-22. Story and frame drift ratio histories (specimen HCFS, Test1) | 203 |
| Figure 6-23. First-story columns and frame base shear histories (specimen HCFS, Test1) | 204 |
| Figure 6-24. Comparison of shear hysteretic behaviour of column B1; a) limit curves were not shifted; b) limit curves were shifted by 0.3% | 205 |
| Figure 6-25. Shear hysteretic response of the columns (specimen HCFS, Test1) | 206 |
| Figure 6-26. Axial load history response of first-story columns (specimen HCFS, Test1) | 207 |
| Figure 6-27. Axial load hysteretic response of first-story columns (specimen HCFS, Test1) | 207 |
| Figure 6-28. Variation of axial load on first-story columns due to overturning (specimen HCFS, Test1) | 208 |
| Figure 6-29. Story and frame drift ratio histories (specimen HCFS, Test2) | 210 |
| Figure 6-30. First-story columns and frame base shear histories (specimen HCFS, Test2) | 211 |
| Figure 6-31. Shear hysteretic response of the columns (specimen HCFS, Test2) | 212 |
| Figure 6-32. Axial load history response of first-story columns (specimen HCFS, Test2) | 214 |
| Figure 6-33. Axial load hysteretic response of first-story columns (specimen HCFS, Test2) | 214 |
| Figure 6-34. Story and frame drift ratio histories (specimen MUF, Test1) | 216 |
| Figure 6-35. First-story columns and frame base shear histories (specimen MUF, Test1) | 217 |
| Figure 6-36. Shear hysteretic response of the columns (specimen MUF, Test1) | 219 |
| Figure 6-37. Axial load history response of first-story columns (specimen MUF, Test1) | 220 |
| Figure 6-38. Axial load hysteretic response of first-story columns (specimen MUF, Test1) | 220 |
| Figure 6-39. Story and frame drift ratio histories (specimen MUF, Test2) | 221 |
| Figure 6-40. First-story columns and frame base shear histories (specimen MUF, Test2) | 222 |
| Figure 6-41. Shear hysteretic response of the columns (specimen MUF, Test2) | 223 |
| Figure 6-42. Axial load history response of first-story columns (specimen MUF, Test2) | 224 |
| Figure 6-43. Axial load hysteretic response of first-story columns (specimen MUF, Test2) | 224 |
| Figure 6-44. Story and frame drift ratio histories (specimen MUFS, Test1) | 226 |
| Figure 6-45. First-story columns and frame base shear histories (specimen MUFS, Test1) | 227 |
| Figure 6-46. Shear hysteretic response of the columns (specimen MUFS, Test1) | 229 |
| Figure 6-47. Axial load hysteretic response of first-story columns (specimen MUFS, Test1) | 229 |
| Figure 6-48. Axial load history response of first-story columns (specimen MUFS, Test1) | 230 |
| Figure 6-49. Story and frame drift ratio histories (specimen MUFS, Test2) | 232 |
| Figure 6-50. First-story columns and frame base shear histories (specimen MUFS, Test2) | 233 |

| | |
|--|-----|
| Figure 6-51. Shear hysteretic response of the columns (specimen MUFS, Test2)..... | 234 |
| Figure 6-52. Axial load hysteretic response of first-story columns (specimen MUFS, Test2)..... | 234 |
| Figure 6-53. Axial load history response of first-story columns (specimen MUFS, Test2)..... | 235 |
| Figure 7-1. Comparison of drifts from nonlinear-inelastic and linear-elastic analyses, Test1 | 238 |
| Figure 7-2. First-story and frame drift ratio histories for the model with nonlinear columns and no end-springs (specimen MCFS, Test1)..... | 239 |
| Figure 7-3. Shear hysteretic response of the columns with no end-springs (specimen MCFS, Test1) | 240 |
| Figure 7-4. Shear hysteretic response of the columns with no end-springs (specimen MCFS, Test2) | 241 |
| Figure 7-5. First-story and frame drift ratio histories for the model with inelastic columns and only bar-slip springs (specimen MCFS, Test1) | 242 |
| Figure 7-6. Shear hysteretic response of the columns with only bar-slip springs (specimen MCFS, Test1)..... | 243 |
| Figure 7-7. Shear hysteretic response of the columns with only bar-slip springs (specimen MCFS, Test2)..... | 244 |
| Figure 7-8. Generalized components of force-deformation relations, ASCE-41 | 245 |
| Figure 7-9. Comparison of peak story drifts from models with different column effective stiffnesses (specimen MCFS) | 248 |
| Figure 7-10. Bilinear shear backbone for columns using effective stiffness from Model 3 (ASCE 41), (specimen MCFS, Test1) | 249 |
| Figure 7-11. Bilinear shear backbone for columns using effective stiffness from model 6, (specimen MCFS, Test1) | 249 |
| Figure 7-12. Calculated backbone A (specimen MCFS, Test1)..... | 253 |
| Figure 7-13. Calculated backbone A (specimen MCFS, Test2)..... | 254 |
| Figure 7-14. Calculated backbone B (specimen MCFS, Test1) | 255 |
| Figure 7-15. Calculated backbone B (specimen MCFS, Test2) | 256 |
| Figure 7-16. Calculated backbone C (specimen MCFS, Test1) | 256 |
| Figure 7-17. Calculate backbone using proposed model (specimen MCFS, Test1)..... | 259 |
| Figure 7-18. Calculate backbone using proposed model (specimen MCFS, Test2)..... | 259 |

| | |
|--|-----|
| Figure 7-19. Shear hysteretic response of analytical model using elastic columns with end lumped-plasticity, ASCE-41 backbone (specimen MCFS, Test1) | 261 |
| Figure 7-20. Shear hysteretic response of analytical model using elastic columns with end lumped-plasticity, ASCE-41 backbone (specimen MCFS, Test2) | 261 |
| Figure 7-21. Shear hysteretic response of proposed model using elastic columns with end lumped-plasticity (specimen MCFS, Test1) | 263 |
| Figure 7-22. Shear hysteretic response of proposed model using elastic columns with end lumped-plasticity (specimen MCFS, Test2) | 263 |
| Figure 8-1. Shaking table tests..... | 266 |
| Figure A-1. Specimens MCFS and HCFS | 288 |
| Figure A-2. Specimens MUF and MUFS | 289 |
| Figure A-3. Reinforcement layout (elevation), specimens MCFS and HCFS..... | 290 |
| Figure A-4. Reinforcement layout (elevation), specimens MUF. | 291 |
| Figure A-5. Reinforcement layout (elevation), specimen MUFS..... | 292 |
| Figure A-6. Reinforcement details of longitudinal and transverse beam | 293 |
| Figure A-7. Reinforcement details of columns and footings..... | 294 |
| Figure A-8. Beam stirrups, layout of weights on beams, and detail of connection of weights to beams | 295 |
| Figure A-9. Concrete stress-strain plots for three cylinders from footing concrete, specimens MUF and MUFS | 298 |
| Figure A-10. Concrete stress-strain plots for three cylinders from first-story concrete, specimens MUF and MUFS..... | 298 |
| Figure A-11. Concrete stress-strain plots for three cylinders from second-story concrete, specimens MUF and MUFS..... | 299 |
| Figure A-12. Reinforcing steel stress-strain plots for rebar #3, specimens MCFS and HCFS | 301 |
| Figure A-13. Reinforcing steel stress-strain plots for rebar #4, specimens MCFS and HCFS (dash-dotted curve ignored)..... | 301 |
| Figure A-14. Reinforcing steel stress-strain plots for rebar #5, specimens MCFS and HCFS (dash-dotted curve ignored)..... | 302 |
| Figure A-15. Reinforcing steel stress-strain plots for rebar #3, specimens MUF and MUFS. | 302 |
| Figure A-16. Reinforcing steel stress-strain plots for rebar #4, specimens MUF and MUFS. | 303 |

| | |
|--|-----|
| Figure A-17. Reinforcing steel stress-strain plots for rebar #5, specimens MUF and MUFS. | 303 |
| Figure A-18. Reinforcing steel stress-strain plots for transverse rebar 5mm, all specimens... | 304 |
| Figure B-1. Connection of load cells to footings and shaking table | 315 |
| Figure B-2. Location and name of accelerometers | 316 |
| Figure B-3. Elevation and side views of displacement measuring instruments | 318 |
| Figure B-4. Plan view of displacement measuring instruments | 319 |
| Figure B-5. Layout of local instrumentation for column B1 and Joint C1, specimens MCFS and HCFS..... | 320 |
| Figure B-6. Layout of local instrumentation for column B1 and Joint C1, specimens MUF and MUFS..... | 321 |
| Figure B-7. Location of strain gages, specimen MCFS..... | 322 |
| Figure B-8. Location of strain gages, specimen HCFS | 323 |
| Figure B-9. Location of strain gages, specimen MUF | 324 |
| Figure B-10. Location of strain gages, specimen MUFS..... | 325 |
| Figure B-11. Ratio of column shear to base shear for first-story columns of specimen MCFS | 328 |
| Figure B-12. Free-body diagram for first-story columns..... | 330 |
| Figure C-1. Story-level drift response history for specimen MUF, Test2 and Test3 | 333 |
| Figure C-2. Story-level acceleration records for specimen MUF, Test2 and Test3 | 334 |
| Figure C-3. First-story columns and frame base shear histories for specimen MUF, Test2 and Test3..... | 335 |
| Figure C-4. Story-level shear hysteretic response of specimen MUF, Test2 and Test3..... | 336 |
| Figure C-5. Shear hysteretic response of specimen MUF columns, Test2 and Test3 | 337 |
| Figure C-6. Axial load hysteretic response of first-story columns of specimen MUF, Test2 and Test3..... | 337 |
| Figure C-7. Axial load response history of first-story columns of specimen MUF, Test2 and Test3..... | 338 |
| Figure C-8. Vertical displacement of specimen MUF columns, Test2 and Test3 | 339 |
| Figure C-9. Variation of axial load of specimen MUF columns with vertical displacement ratio, Test2 and Test3..... | 339 |
| Figure C-10. Moment-chord rotation relationship at top of first-story columns of specimen MUF, Test2 and Test3 | 340 |

Figure C-11. Moment hysteretic response of first-story columns of specimen MUF, Test2 and Test3.....340

Figure C-12. Relation between shear force and shear deformation of joint C1 of specimen MUF, recorded at unconfined face of the joint, Test2 and Test3341

Figure C-13. Relation between shear deformation at joint C1, recorded at unconfined face and first-story drift of specimen MUF, Test2 and Test3341

ACKNOWLEDGMENTS

First and foremost, I would like to express my sincerest gratitude to my supervisor, Professor Kenneth Elwood, for his valuable guidance, continuing support, and encouragement during every stage of this research. I always enjoyed our friendly discussions and it has been a privilege for me to be his first PhD student and be a part of his research vision.

Special thanks to staff and faculty from the University of British Columbia, particularly professors Don Anderson, Carlos Ventura, Terje Haukaas, and Stephanie Chang who provided me with insightful feedback on this research. I am also grateful for valuable suggestions and recommendations from Professor Jack Moehle from the University of California, Berkeley.

This research has been partially funded by National Science and Engineering Research Council of Canada (NSERC), Canadian Seismic Research Network (CSRN), and NEES Grand Challenge project from USA. The experimental work described in this thesis was funded by National Center for Research on Earthquake Engineering (NCREE) in Taiwan. Their support is gratefully acknowledged.

I am especially thankful to Dr. Chiun-lin Wu from NCREE for providing me with the opportunity to conduct such a large scale experimental work. He also facilitated my several stays in Taiwan which I am deeply grateful for.

I also would like to extend my gratitude to Professor Shyh-Jiann Hwang from National Taiwan University as one of the key advisors for this collaborative study. His experience and knowledge were valuable assets for the project, while his kind hospitality made my stay in Taiwan a pleasant experience.

I should emphasize that the experimental tests would not be possible without the assistance of laboratory personnel and staff at NCREE. Their effort is much appreciated.

I am grateful to my friend Shih-han (Tracy) Lin from National Taiwan University (NTU) for his tireless assistance during the experimental phase of this research and drawing Figure 3-8 of Chapter 3. He also introduced me to Taiwanese culture and showed me the city of Taipei during my stay in Taiwan, a once in a life time experience. I am also thankful for assistance from my friend Beyhan Bayhan and the students from NTU who voluntarily helped me in setup the shaking table tests.

Special thanks to my dear friends Ramin, Maryam, Monir, Amin, and Ferdows who provided me with a pleasurable environment outside the university.

I extend my gratitude to my friends in Iran, US, and Canada for keeping me motivated during the course of this study. In particular, I would like to thank Mehrtash, Majid, Smitha, Yaqiong, Jose, Dominic, Tim, Mojtaba, Ehsan, Devin, and Alireza from the University of British Columbia for sharing my journey through the graduate studies.

I am eternally grateful to my parents. This degree and all my achievements would not be possible without their encouragements and continuous support. I dedicate this dissertation to them.

CHAPTER 1. INTRODUCTION

1.1 Background

One of the major structural engineering objectives is to avoid introducing earthquake-related collapse vulnerabilities in new constructions and to identify and retrofit those vulnerabilities in existing buildings. Many of existing reinforced concrete structures in Canada and worldwide do not satisfy the special seismic detailing requirements introduced in modern building codes. When such buildings are subjected to a strong earthquake, several inadequacies in their performance capabilities may become apparent and, in some cases, collapse may result. During an earthquake, lateral demands from ground shaking and vertical demands from gravity loads and overturning interact with the lateral and vertical capacity of the structural system. Collapse occurs when the lateral strength degrades due to lateral demands, followed by degradation of the vertical resistance below the level of the vertical demands on the structural system.

Due to architectural and functional constraints and lack of requirements in older building codes, most of the structures were designed and constructed with strong beams and weak columns before 1970s. In such buildings, columns and beam-column joints are more

vulnerable to damage than beams. The damage is commonly attributed to widely spaced and poorly anchored transverse reinforcement. Observations of damaged reinforced concrete building in the past earthquakes and experimental research have indicated that columns with light transverse reinforcement are vulnerable to shear failure and possibly reduction in axial load resistance during ground shaking. As the axial strength diminishes, the supported gravity must be transferred to adjacent elements which may spread the damage, leading to collapse of the structure.

There have been relatively few dynamic tests on behaviour of inadequately designed reinforced concrete frames in the literature, particularly tests up to the point of collapse. As a result of the relatively small data set, our understanding of component failure and collapse mechanisms is limited. This is confirmed by the fact that in contrast with the frequent collapse predictions based on current assessment procedures, post-earthquake reconnaissance studies show a relatively low rate of collapse amongst older concrete structures with non-seismic detailing even in major earthquakes (Otani, 1999). The observations suggest that current methods for assessing the collapse vulnerability of existing buildings are conservative and need refinement in order to identify the critical buildings that are most collapse-prone. Without refinement in current assessment procedures and identification of the most vulnerable buildings, rehabilitation of the very large inventory of existing buildings that are considered as collapse-prone is not feasible and cost-effective. This barrier leads to limited or no seismic rehabilitation and minor improvement in the seismic risk facing urban centers, nationally and internationally.

Current guidelines for evaluation of existing structures (ASCE, 2008) only consider the damage to individual components in assessment procedure up to the point of collapse.

Evidence from past earthquakes (Mitchell et al., 1995, Sezen et al., 2000, Doangün, 2004) reveal that components can experience significant damage, including column shear failures and loss of axial load capacity, without collapse of the building system, indicating that the entire system should be considered when evaluating the collapse limit state.

To achieve an improved assessment of the seismic response of existing reinforced concrete building frames, extensive research is required to develop practical analytical models for predicting failure of concrete elements and systems. Furthermore, experimental research is also required to validate the ability of such analytical models to capture the critical response characteristics of the structure. In an effort to address the issues discussed above, the scope and objectives of the current study will be defined in the next section.

1.2 Objectives and Scope

The overall objective of this research is to investigate, both experimentally and analytically, the dynamic behaviour of reinforced concrete frames with non-seismic details up to the point of collapse. In particular, the main focus of the study is to investigate the effects of structural framing on shear and axial failure of non-ductile columns, and conversely, the influence of column failure on collapse vulnerability of the frame. The impact of damage to beam-column joints on behaviour of concrete frames is also of interest in current study. Understanding these interactions is critical in assessing the collapse vulnerability of existing reinforced concrete structures.

To date, relatively few dynamic tests have been performed on frames with columns with light transverse reinforcement up to the point of collapse. Even those rare shaking table collapse tests have mostly focused on performance of one specific component (columns) and only considered relatively low gravity loads (Elwood, 2002, Ghannoum, 2007, Wu et al.

2009). Furthermore, all of these tests incorporated a combination of ductile and non-ductile columns which could influence the redistribution of loads near the point of shear and axial failure. To fill the gaps in knowledge, this study included designing and dynamic testing to collapse of four two-dimensional, two-bay-two-story, 1/2.25 scaled reinforced concrete frames. Three of the four frames contained columns with light transverse reinforcement. Proportions and reinforcement details allowed the columns to yield in flexure prior to shear strength degradation (commonly referred to as flexure-shear-critical columns) and ultimately reach axial failure. By applying high axial load on columns of one of the specimens, the effects of high axial load on shear and axial failure of non-ductile columns and collapse of the frames were investigated. The scope of this study did not include bi-directional loading or column lap-splice failures, but focused on shear failure leading to loss of axial load resistance of non-ductile columns due to unidirectional seismic loading.

Influence of joint failure on behaviour of the connecting columns and the overall frame response was also investigated. Nearly all of the observations on the behaviour of unconfined joints have been done through reversed-cyclic testing of joint sub-assembly (Beres et al., 1996, Walker, 2001, Alire, 2002, Pantelides et al., 2002). However, using shaking table, current research investigated the influence of unconfined joints on the collapse behaviour of frames by constructing and testing two of the four specimens with unconfined joints. One of the specimens was built with ductile columns to localize the damage only in the beam-column joints, for comparison purposes. Descriptions of the specimens will be discussed in detail in Chapter 3.

While providing benchmark data for validating analytical models, the tests particularly focused on two major issues:

- 1) Interaction of multiple vulnerable concrete components (i.e. columns, and beam-column joints) within a building frame as collapse is initiated.
- 2) Influence of high gravity loads on the collapse vulnerability of a structure.

Currently available analytical models for predicting the behaviour of frames were also evaluated in the course of this research. In particular, the models for predicting shear failure and axial load collapse of non-ductile columns were closely examined. Through comparison of the results from such analytical models with shaking table test data, the limitations, weaknesses, and strengths of the models were investigated. It is also of interest in the course of this research to evaluate simplified analytical models that can be employed in engineering practice and provide refinement to relevant provisions of current rehabilitation guidelines.

It should be noted that while the experimental phase of this research took place at National Center for Research on Earthquake Engineering (NCREE) in Taiwan, the conceptual and detailed design of the specimens and lateral supporting frame, test setup and design, instrumentation, data processing, and the comprehensive and simplified analyses discussed in this dissertation are amongst the contributions of the author. NCREE research staff and other collaborators provided valuable advice and assistance during the course of the experimental phase of the project.

1.3 Organization

This dissertation will describe and discuss the following: previous related research studies, test setup, response of the shaking table test specimens and comparison of the results, evaluation of available analytical models through a comparison with the shaking table test

results, and finally, comparison of results from simplified analyses with tests data. The dissertation has been organized as described below.

Chapter 2, "Literature Review," reviews previous research relevant to this study. Static and dynamic experimental tests conducted on non-ductile columns are presented along with analytical approaches used to model shear and axial failure for this type of column. While summary of previous experimental studies on unconfined joints are presented, currently available analytical models for beam-column joints are briefly discussed.

Chapter 3, "Details of Specimens and Test Setup," describes the design, construction, instrumentation, and preparation for shaking table testing of the specimens introduced in Section 1.2. A scaled ground motion record from the 1999 Chi-Chi earthquake is used as the input table motion. More details on the design, construction, and experimental setup are provided in Appendices A and B.

Chapter 4, "Experimental Test Results," presents and discusses the results from the shaking table tests. The specimens are subjected to sequential table motions with increasing peak amplitude. Failure modes for the specimens are identified and the results from the sequential tests are compared for each specimen. Response of the non-ductile columns and unconfined joints and the redistribution of loads during shear and axial failure are studied in this chapter, in detail.

Chapter 5, "Comparison of Response of the Test Specimens," compares the results from testing the four specimens described in Chapter 4. Effects of axial load on key parameters for columns including drift ratio, effective and secant stiffness, and slope of vertical deformation before and after axial failure are studied. Influence of joint failure on overall behaviour of the

frames is also explored by comparing the results from testing the two specimens with and without confined joints.

Chapter 6, "Analysis of Shaking Table Test Specimens," evaluates the accuracy of selected drift capacity models for shear and axial failure presented in Chapter 2 to represent the response of non-ductile columns during shear and axial failure. A relatively simple joint model described in Chapter 2 is also evaluated by comparison of test data with the results from an analytical model incorporating such a joint model.

Chapter 7, "Simplified Modeling Methods," evaluates the accuracy of simplified models commonly used in practice to predict the yield displacement, effective stiffness, and overall behaviour of one of the test frames. A backbone for simplified modeling of columns and refinement to the current rehabilitation standard (ASCE-41, 2008) are proposed in this chapter.

Finally, Chapter 8, "Conclusions and Future Work," summarizes the critical results from the report, highlights the contributions of this research endeavour, and provides recommendations for future research.

CHAPTER 2. LITERATURE REVIEW

2.1 Introduction

This chapter summarizes previous experimental and analytical studies that address the seismic performance of reinforced concrete frames that were designed without considering the significance of earthquake effects.

Reinforced concrete structures traditionally have been designed using provisions of older versions of ACI Standard 318 and the gravity load combination of $1.4DL + 1.7LL$, where DL and LL stand for dead and live loads, respectively. Little or no consideration for seismic resistance was taken into account in such design (Hoffmann et al., 1992). In one study, Beres *et al.* (1992) reviewed detailing manuals (ACI 315) and design codes (ACI 318) from past decades and identified the following typical problematic reinforcing details:

- 1) Longitudinal reinforcement ratio in columns was rarely more than 2%.
- 2) Only minimal transverse reinforcement was considered in columns to provide shear resistance and confinement.
- 3) Lapped splices of reinforcement were often placed just above the floor levels, the location that is vulnerable to plastic hinging.

- 4) Construction joints were usually located immediately below and above the beam-column joints.
- 5) Limited or no transverse reinforcement was considered within the beam-column joints.
- 6) Bottom reinforcement in the beams was terminated in the joints with a short embedment length.
- 7) Bending and shear capacity of columns were close to or less than those of the connecting beams, resulting in weak-column-strong-beam mechanism.

Extensive research has been done to address these issues, study the behaviour of elements with such properties, and offer retrofit solutions. Experimental evidence shows that many existing reinforced concrete columns are vulnerable to shear and axial failure after flexural yielding (Umemura and Endo, 1970, Wight and Sozen, 1973, Ohue et al., 1985, Sezen, 2002, Elwood, 2002, Ghannoum, 2007, Wu et al., 2009).

Several studies focused on behaviour of beam-column joints without seismic detailing, demonstrating the extensive shear damage or failure in the panel zone of such joints and significant damage to the connecting columns (Pessiki et al., 1990, Beres et al., 1992, 1996, Clyde et al., 2000, Pampanin et al., 2002).

A number of analytical models have been developed to simulate the behaviour of elements and degradation of shear and axial strength with increasing inelastic deformation of the members. The following sections present an overview of previous experimental and analytical research studies related to non-ductile behaviour of reinforced concrete columns and beam-column joints.

2.2 Experimental Studies on Behaviour of Non-ductile Columns

2.2.1 *Static and Pseudo-dynamic Experimental Tests*

Gilbertsen and Moehle (1980) studied the effects of variation in axial load on behaviour of non-ductile columns. Eight small-scale cantilever columns were subjected to constant and varying axial load proportional to cyclic lateral load. The results showed that the shear hysteretic responses of the columns were asymmetric about the axis of zero shear.

Kreger and Linbeck (1986) conducted experimental studies on three double-curvature specimens with various lateral and axial load, where two specimens were subjected to axial load proportional to the lateral loads and the third specimen was tested with separate axial and lateral loads. The results showed higher lateral stiffness with increasing axial load.

Lejano et al. (1992) tested three identical double-curvature columns subjected to cyclic lateral load, and constant and proportionally varying axial loads. Two of the specimens were tested under constant axial loads of $0.74A_gf'_c$ in compression and $0.26A_gf'_c$ in tension. For the third specimen, an initial gravity load of $0.25A_gf'_c$ was considered for the axial-lateral load relationship. The tensile axial load induced larger displacements and horizontal cracks, whereas the compressive axial load caused a brittle failure.

Pinho and Elnashai (2000) conducted a pseudo-dynamic test on a full-scale, four-story, three-bay reinforced concrete frame with light transverse reinforcement in the columns. Columns in the third story of the frame experienced brittle failure in shear and the test was terminated at that point.

Conducting cyclic tests on eight full-scale columns with constant axial load, Lynn (2001) compared the experimental data with the behaviour estimated by various evaluation

methods. It was observed that columns with inadequate shear resistance but with low axial load could sustain vertical loads after losing their lateral resistance.

Sezen (2002) tested four full-scale column specimens statically under unidirectional lateral load. Since the columns properties were identical, the test results demonstrated that the response of the columns significantly depended on the amount and history of axial and lateral loads. Specimens with low axial load lost most of their lateral strength at smaller displacements, whereas sustained axial load at larger displacement demands. It was observed that by increasing the axial load, lateral stiffness and strength increased at low displacements. However, the specimen experienced a sudden shear and axial failure.

Calvi et al. (2002) conducted a quasi-static cyclic test on a 2D frame with, three bays and three stories with non-seismic detailing. Beam-column joints had no transverse reinforcement. Damage concentrated in the exterior first-story joints, exhibiting brittle failure. Such behaviour reduced the rotational demand on exterior first-story columns, which increased the demands on the interior columns where joints showed limited cracking.

Pinto et al. (2002) performed pseudo-dynamic tests on two full-scale specimens with two bays by one-bay by four-story. Frames were constructed with smooth longitudinal bars, no joint reinforcement, and short lap splices at the column bases. The cause of collapse was longitudinal bar slippage in third-floor columns at a story drift ratio of 2.4%. It was concluded that using smooth bars with short lap splices makes this type of frame very vulnerable to seismic loading.

Lam et al. (2003) tested nine one-third scale reinforced concrete columns with low confinement. The transverse reinforcement for the specimens included ties with either 90° or

135° hooks. The tests results showed that the reinforcement with 90° hooks was less effective than transverse reinforcement with 135° hooks.

Ousalem et al. (2004) conducted two series of tests on scaled reinforced concrete columns. The first test series were performed with equal lateral loads for all specimens, but with different axial load histories. Columns in the second series had constant and equal axial loads with varying lateral load histories. Results showed that lateral deformation capacity and shear degradation for the columns were mainly influenced by the axial load history.

2.2.2 Dynamic Experimental Tests

Despite the numerous static and pseudo-dynamic tests conducted on non-ductile columns in the literature, very few dynamic tests were carried out on such columns up to the point of shear and axial failure.

Elwood (2002) tested two specimens on shaking table, where each specimen consisted of three columns connected by means of a rigid beam on top. The exterior columns were constructed with ductile detailing, whereas the center column was designed and constructed with light transverse reinforcement. While providing data on hysteretic response of the columns in shear, the test results demonstrated the redistribution of loads in a frame and degradation of axial load resistance after shear failure.

In 2005, Wu et al. (2009) conducted a shaking table test on a single-story frame with two ductile columns on one side and two non-ductile columns on the other side. The test results demonstrated that the variation of axial load, especially induced by overturning moment, and redistribution of load as collapse progresses, plays an important role in hysteretic characteristics of the column load-deformation response.

Shin (2007) performed twelve dynamic tests on planar, single-story, single-bay, one-third scale frames. The frames included either ductile, non-ductile, or a combination of one ductile column and one non-ductile column. Observed behaviour of the columns was significantly affected by column details, axial load, and input table motions.

Ghannoum (2007) tested a 2D, three-bay, three-story, one-third scale reinforced concrete frame on shaking table up to the point of collapse. While columns on two axes were constructed as ductile columns, specifications of the non-seismically detailed columns were selected to allow for yielding of the columns in flexure prior to initiation of shear strength degradation and ultimately axial failure. It was concluded that the rotational capacity of a non-ductile column before the onset of shear failure is related to transverse reinforcement, axial load and shear stress in the column. A shear failure model was introduced and verified with the test data.

2.3 Modeling the Behaviour of Non-ductile Columns

Some of the models that have been developed to estimate the lateral and axial behaviour of columns in reinforced concrete frames with non-seismically details are discussed in this section. Such models can be subdivided into two main categories: models that have been developed to predict the point of shear failure of non-ductile columns and capture the shear behaviour of the element before and after that point, and models that predict the axial behaviour of the columns beyond the onset of shear failure up to the point of axial failure.

2.3.1 Models for Drift at Shear Failure

Capturing the degradation of shear strength due to increasing inelastic deformations was the goal of several older models (Watanabe and Ichinose, 1992, Aschheim and Moehle, 1992,

Priestley et al., 1994, Sezen, 2002). Such shear-strength models are able to adequately estimate the shear strength for conventional strength-based design and assessment. However, they may not properly predict the deformation capacity given a shear force demand, the approach that is widely used in displacement-based design and assessment methods (ASCE, 2008). This can be explained by observing the shear-drift relationship of a flexural-shear-critical column, where the force demand remains relatively constant after flexural yielding, but the displacement demand is substantially increased. Consequently, the shear-strength models may not be appropriate for assessing the drift at shear failure and beyond.

The above-mentioned limitation resulted in need for development of displacement-based models for predicting the drift capacity of flexural-shear-critical columns, given a shear force demand. The model developed by Pujol et al. (1999) related drift at shear failure with aspect ratio of the column (a/d , where a is the column half span and d is the section depth from center of tension reinforcement to extreme compression fibre of the column), transverse reinforcement ratio and its yield stress, and column shear stress at shear failure. Poor agreement was observed between results from the model and the employed database, indicating that further refinements to the model were required.

Kato and Ohnishi (2002) proposed that the total drift ratio can be obtained from the sum of the drift ratio at yielding of longitudinal reinforcement and the calculated plastic drift ratio estimated based on axial load ratio, maximum edge strain in the core concrete, and the cross-section dimensions. In comparison with the other models discussed above, the calculated drift ratios at shear failure using Kato and Ohnishi's model demonstrated a better match with the test data from 50 laboratory tests on flexure-shear-critical columns described in the study by Sezen (2002). However, compatibility of the results is significantly dependent on accuracy of

estimation of the drift at yielding of the longitudinal reinforcement. Furthermore, it was observed that the model significantly overestimated the drift at shear failure for many of the columns with low axial loads.

Elwood and Moehle (2005) proposed an empirical model that relates the shear demand to the drift at shear failure (Δ_s/L) based on the transverse reinforcement, ρ'' , shear stress ratio ($\vartheta/\sqrt{f'_c}$), and axial load ratios ($P/A_g f'_c$). The afore-mentioned database of 50 flexure-shear-critical columns was employed for validation of the model. The point of shear failure in the model was determined by the intersection of shear-drift curve for the column and the limit surface defined by the drift capacity model (Figure 2-1). The proposed equation is:

$$\frac{\Delta_s}{L} = \frac{3}{100} + 4\rho'' - \frac{1}{40} \frac{\vartheta}{\sqrt{f'_c}} - \frac{1}{40} \frac{P}{A_g f'_c} \geq \frac{1}{100} \quad (2.1)$$

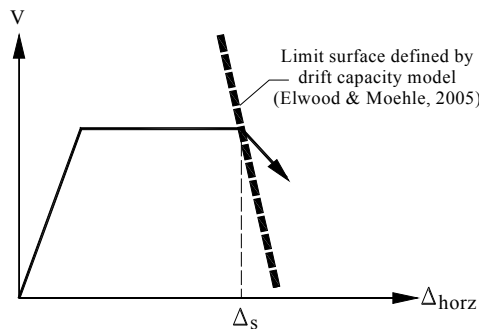


Figure 2-1. Shear failure defined by Elwood & Moehle drift-capacity model (Elwood & Moehle, 2005)

This model was used in simulating the shear behaviour of columns of the specimens studied in the current research, which are described in Chapters 3 and 4. Results of the modeling are discussed in detail in Chapters 6 and 7.

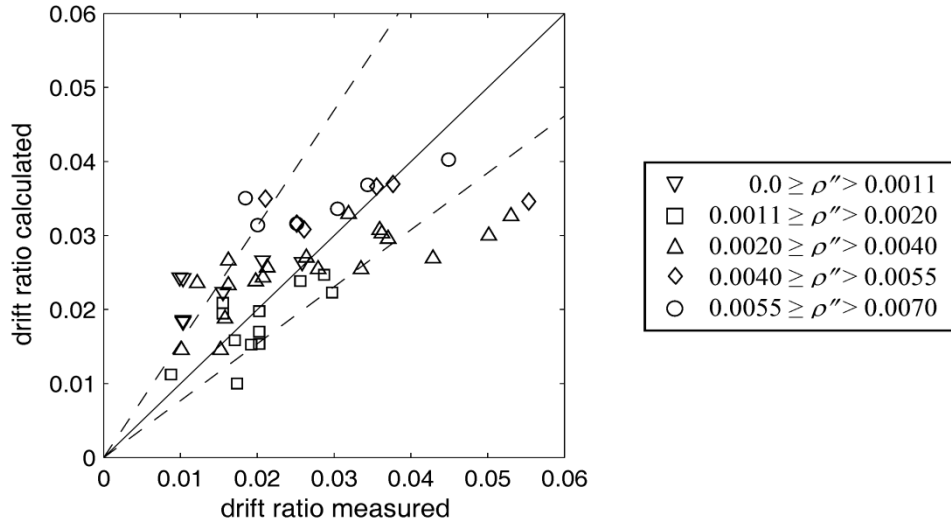


Figure 2-2. Comparison of Elwood & Moehle shear-drift model with test data (Elwood, 2002)

Ghannoum (2007) introduced a shear failure model which determines column rotations at onset of shear strength degradation for flexure-shear-critical columns. The model was based on a parametric regression analysis that was performed on a database of 56 column tests, demonstrating that the column rotational capacity prior to initiation of shear failure is correlated with transverse reinforcement spacing, compressive axial load, and shear stress. This model was not employed in the current study as it was not accompanied by a predictive model for axial failure. Furthermore, it was not implemented in OpenSees software (2009), the analysis platform that was used in the course of this research for simulation of the shaking table tests.

2.3.2 Models for Drift at Axial Failure

Previous experimental studies on collapse of non-ductile columns (Minowa et al., 1995, Lynn, 2001, Sezen, 2002, Elwood, 2002) have illustrated that the axial failure of such columns is mainly dependent on the axial stress, the amount and spacing of transverse reinforcement, and the drift demand. Other researchers have shown that axial failure occurs when the shear

resistance is significantly degraded (Yoshimura and Yamanaka, 2000, Yoshimura and Nakamura, 2002).

Based on results from five pseudo-dynamic tests in which shear damaged columns were returned to a plumb vertical position and loaded axially until vertical collapse, Tasai (2000) suggested that residual axial strength is decreased when maximum lateral drift demand and shear degradation are increased.

To date, a limited number of models (Elwood and Moehle, 2005, Mostafaei and Kabeyasawa, 2007) have been developed to estimate the axial-drift failure of non-ductile columns. The model employed in this study was developed by Elwood and Moehle (2005) using shear-friction models (Mattock and Hawkins, 1972, Mattock, 1988). The model was calibrated to test data from the 50-column database mentioned in Section 2.3.1. The relation for the drift ratio at axial failure can be presented as:

$$\frac{\Delta_a}{L} = 0.04 \frac{1 + (\tan(65^\circ))^2}{\tan(65^\circ) + P \left(\frac{s}{A_{st} f_{yt} d_c \tan(65^\circ)} \right)} \quad (2.2)$$

where P is the axial load, A_{st} is the transverse reinforcement area with yield strength f_{yt} and spacing s , and d_c is the depth of the column core between centerlines of the ties. In this equation, the angle of the shear failure surface from horizontal is assumed to be 65° . Similar to the shear-failure model described in previous section, the axial-drift model defines a limit surface at which axial failure is expected to occur, as shown in Figure 2-3. According to this model, columns with a low axial load or drift demand would not be expected to experience axial failure. Although such assumption is rational for most cases, the model may not detect axial failure in the situations where rotational demand on the column is more significant than drift demand.

Since the axial failure model was defined based on shear-friction models and the shear-friction model assumes that shear failure occurs before the axial failure, the model for axial failure must be used in conjunction with one of the shear failure models described in section 2.3.1.

Similar to the shear failure model, column behaviour after the onset of axial failure is not well understood; however, it is assumed that the axial load-horizontal deflection relation for the damaged column will remain on or below the limit surface after the failure is detected.

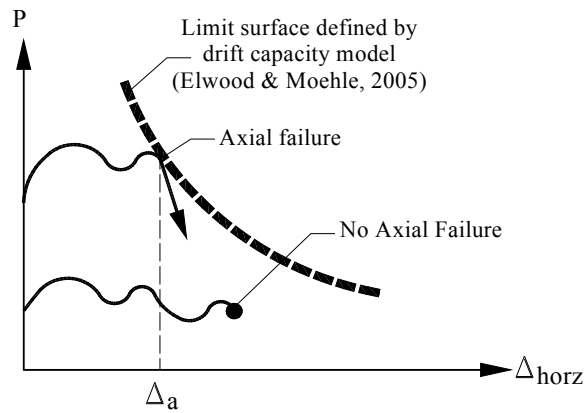


Figure 2-3. Axial failure defined by Elwood & Moehle drift-capacity model (Elwood & Moehle, 2005)

While the shear and axial models developed by Elwood and Moehle (2005) describe different phenomena, both models define a limit surface and change the hysteretic behaviour once the load-deformation relation for the column reaches the limit surface. This similarity allowed both failure models to be implemented in one *Uniaxial Material* model in OpenSees (Elwood, 2002) for structural analysis purposes.

2.3.3 Implementation of Shear and Axial Failure Models

Elwood (2002) implemented the shear and axial failure models (Equations 2.1 and 2.2) in OpenSEES as *LimitState Uniaxial* material, allowing for the complete simulation of behaviour of non-ductile column to collapse. The shear and axial failure models can be employed by adding zero-length springs in series with a beam-column element as illustrated in Figure 2-4.

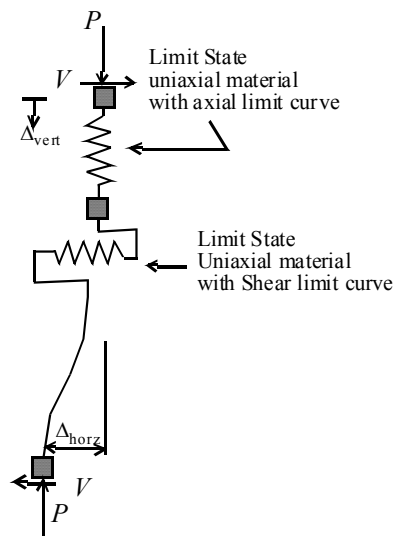


Figure 2-4. Shear and axial springs in series model (Elwood, 2002)

The properties of the springs are defined by the *LimitState Uniaxial* material with either shear or axial limit curve. The springs have different backbone curves before and after failures are detected by the drift capacity Equations 2.1 and 2.2. Prior to shear failure, the shear spring is linear-elastic with stiffness corresponding to the equivalent elastic shear stiffness of the column. Once the column element reaches the limit curve defined by Equation 2.1, the shear spring backbone curve is modified to a degrading hysteretic curve (Figure 2-5).

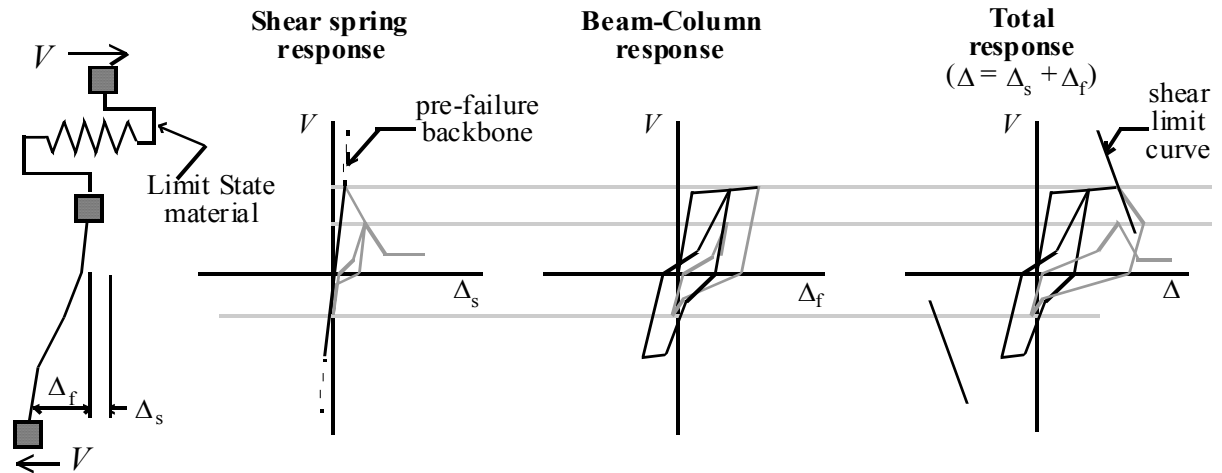


Figure 2-5. Shear spring model using LimitState Uniaxial material (Elwood, 2002)

Figure 2-6 shows the axial failure limit curve on plots of axial load versus vertical displacement of the column and total lateral drift. The shape of the limit curve is defined by $A_{st}f_yd_c/s$ which describes the strength of the transverse reinforcement. Similar to shear limit curve, the zero-length axial spring has a “rigid” backbone prior to reaching the axial load-drift limit curve (Figure 2-6). After axial failure occurs, the backbone will be redefined to include the degrading slope, K_{deg} , and the residual strength, P_{res} . Since the shear-friction model describes only compression failure, the backbone is only redefined for compressive axial loads (shown as positive).

The shear and axial models discussed in this section will be used throughout the analysis part of this research as they have been implemented in OpenSEES, providing a comprehensive basis for modeling the behaviour of non-ductile columns of the specimens described in Chapter 3.

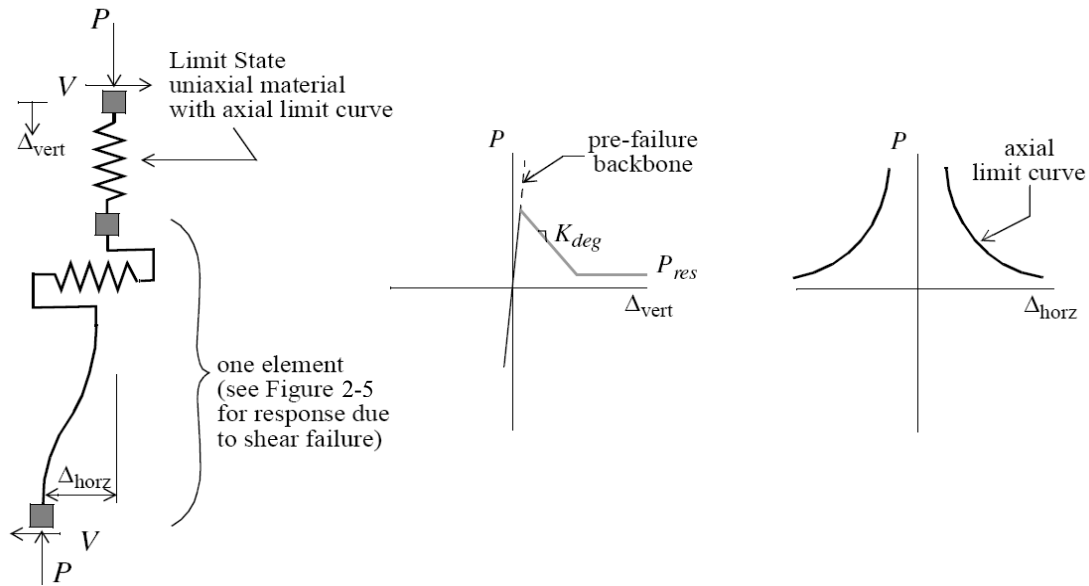


Figure 2-6. Axial spring using LimitState Uniaxial material (Elwood, 2002)

2.4 Beam-column Joint with Non-seismic Detailing

Older reinforced concrete buildings have several deficiencies including lack of transverse reinforcement at beam-column joints. Significant joint deterioration has been observed in structures containing joints with little or no transverse reinforcement during past earthquakes (Moehle and Mahin, 1991, Hall, 1995, Comartin, 1995, Sezen et al., 2000). This section describes some of the previous experimental and analytical studies on seismic performance of beam-column joints with non-seismic detailing which are commonly found in existing non-ductile buildings.

2.4.1 Experimental Studies on Behaviour of Unconfined Joints

Several experimental investigations on beam-column joint sub-assemblies have focused on factors influencing joint strength and deformation capacities. Townsend and Hanson (1977) tested 22 reinforced concrete beam-column T-shaped connections under column axial tension ($0.25A_gf'_c$), column axial compression ($0.15A_gf'_c$), and no column load. It was shown that

increasing column tension causes the moment capacity to decrease faster, representing a faster rate of concrete deterioration compared to specimens with zero load or compressive loads on the columns.

Based on test results from six exterior reinforced concrete beam-column sub-assemblages under cyclic loading, Ehsani and Wight (1985) suggested that in order to avoid the formation of plastic hinges in the joint, the flexural strength ratio for the sub-assemblages should be more than 1.4. The maximum joint shear stress in exterior connections should be limited to $12\sqrt{f'_c}$ (psi) to reduce excessive joint damage, column bar slippage, and beam bar pullout.

French and Moehle (1991) studied the effects of floor slabs on behaviour of beam-column-joints by testing a sub-assembly frame and observed a significant increase in beam ultimate moment strength when the slab was on the flexural tension side. Such increase in beam moment strength resulted in higher joint shear stress demands. Similar observations were reported by Cheung et al. (1991) and they also added that while slabs increased shear demands in the tested joints, the contribution to joint shear strength was minimal.

Bonacci and Pantazopoulou (1992) investigated the mechanics of beam-column joints in laterally loaded frames, showing that the shear strength of a joint depends on the usable compressive strength of concrete and joint shear strength is decreased with increasing column axial force. They also found that joint capacity can be limited by crushing along the principal diagonal or by yielding of vertical reinforcement after hoop yield. Through a parametric study on test results of 86 interior-joint connections with a wide range of axial loads, concrete strengths, and transverse reinforcement ratios, Bonacci and Pantazopoulou (1993) concluded

that the ratio of joint shear demand to capacity determines the likelihood of beam-column joint failure.

In an experimental study, Park (2002) tested a few beam-column joints, where no transverse reinforcement was considered in interior joints and very little transverse reinforcement was included in exterior joints. Inadequate seismic performance was observed for all the joints due to early concrete diagonal cracking, while exterior joints were found to have lower shear strength than interior joints.

In an experimental study, Pantelides et al. (2002) evaluated the seismic performance of six full-scale exterior beam-column joints with three different details of beam and beam-column joint reinforcement, where the two primary failure modes of bond-slip failure and joint shear failure were observed. They found that the joint strength coefficient, γ , changes with the variation of the column compressive axial load.

2.4.2 Modeling the Behaviour of Unconfined Joints

Hoffmann et al. (1992) studied the seismic performance of typical non-seismically detailed frames using finite element simulations. In these studies, the flexural capacities of beams and columns were implicitly modified to account for insufficient anchorage of beam bars and inadequate joint shear capacity.

Lumped-plasticity rotational hinge models have been proposed in several studies to directly model joint deformations (Alath and Kunnath, 1995, Biddah and Ghobarah, 1999, Youssef and Ghobarah, 2001, Walker, 2001, Lowes and Altoontash, 2003, Altoontash, 2004, Shin and Lafave, 2004). These models account for joint deformation by means of rotational springs placed at the ends of beam and column elements (Figure 2-7). Such models allow for separation of joint response from those of columns and beams and easier interpretation of the

results. However, some of the models are too complicated (e.g. Youssef and Ghobarah, 2001, Lowes and Altoontash, 2003) and may not be computationally efficient. On the other hand, the simpler models (e.g. Alath and Kunnath, 1995) do not account for variation of axial load.

Continuum finite element models that can be linked to beam-column elements through transition elements have also been proposed in literature (Fleury et al., 2000, Elmorsi et al., 2000). Such models were found to be computationally intensive and have not been tested for modeling of large frame-systems, especially at high deformation demands.

Although the model suggested by Alath and Kunnath (1995) may not capture the behaviour of the joints thoroughly, it was selected for modeling the unconfined joints in the current study due to its simplicity and practicality. The finite size of the joint panel is taken into account by introducing rigid links (see Figure 2-7a). Joint shear deformation is simulated by a rotational spring model with degrading hysteresis. Moment-rotation relationship for the joint panel zone is obtained using the joint shear stress-strain (see Section 6.2.2). The envelope to the shear stress-strain relationship is determined empirically, whereas the cyclic response is captured with a hysteretic model that is calibrated to experimental cyclic response. To implement the constitutive relationship for the panel zone in the analysis, a backbone curve based on previous experimental test data (Walker, 2001) was defined for the envelope and a pinched hysteresis model (*Pinching4* in OpenSees), proposed by Lowes and Altoontash (2003), was employed for the cyclic response.

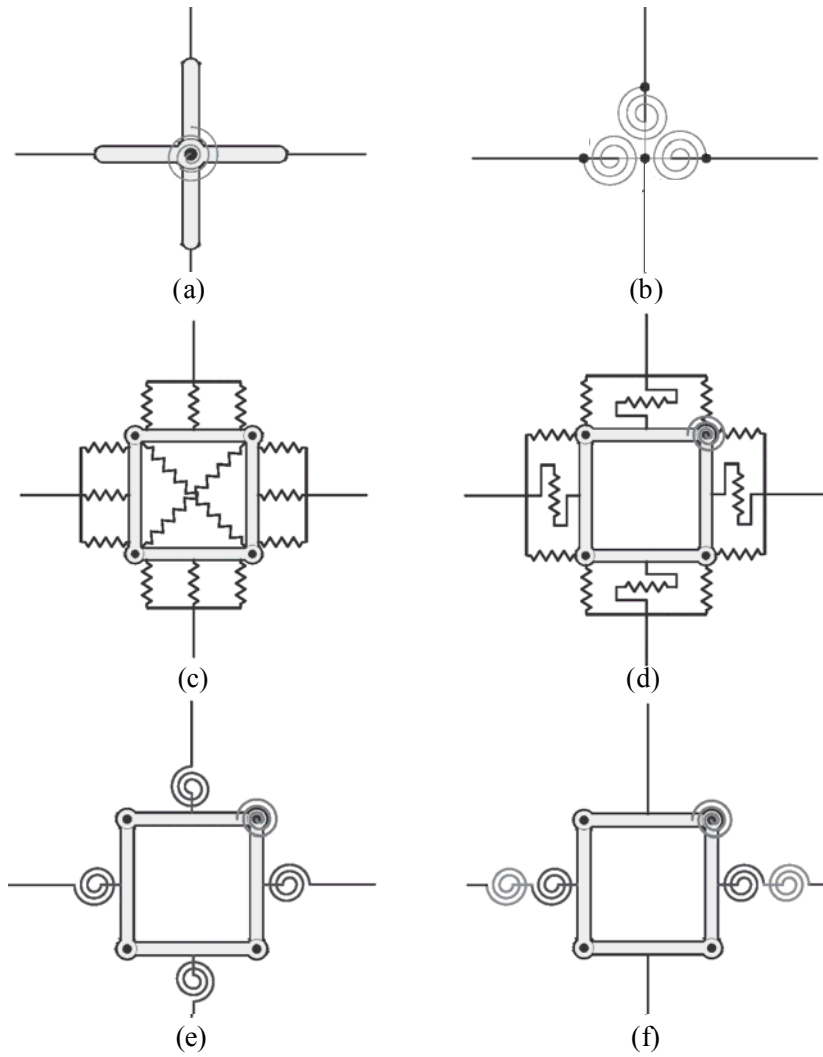


Figure 2-7. Existing beam-column joints models (adopted from Celik and Ellingwood, 2008); (a) Alath and Kunnath (1995); (b) Biddah and Ghobarah (1999); (c) Yousseff and Ghobarah (2001), (d) Lowes and Altoontash (2003); (e) Altoontash (2004), and (f) Shin and LaFave (2004).

CHAPTER 3. DETAILS OF SPECIMENS AND TEST SETUP

3.1 Introduction

This chapter presents details of the reinforced concrete specimens used in the experimental tests. The specimens were designed to observe the process of shear and axial failures in reinforced concrete frames. Presented is an overview of the design, construction, instrumentation, and testing of the reinforced concrete frame specimens. Details of the analytical model that was used during the design phase as an analysis tool to explore different design and test options are presented in Chapter 6.

3.2 Specimen Description and Design

To study the behaviour up to collapse of reinforced concrete frames with light transverse reinforcement, four two-bay and two-story frames were built and dynamically tested on a shaking table. Three frames contained non-seismically detailed columns whose proportions and reinforcement details allowed them to yield in flexure prior to shear strength degradation and ultimately reach axial collapse (these columns are commonly referred to as flexure-shear-

critical columns). The influence of unconfined joints on the collapse behaviour of the frame was also investigated. The geometries and details were selected to be representative of elements used in an existing six-story hospital building in Taiwan. The structure was designed in 1980's with non-seismic detailing. Final dimensions and reinforcement details of the frames were influenced by the following considerations: laboratory and shaking table limitations; replication and scaling of column details from the real building with non-seismic details; desired failure mode; available reinforcement; and cost. The target failure mode was intended to be damage leading to collapse that would enable examination of gravity load redistribution during the test. Figure 3-1 describes the four specimens.

| | |
|---|---|
| <p>Specimen MCFS: <u>M</u>oderate Axial Load <u>C</u>onfined Joints <u>F</u>lexure-<u>S</u>hear Columns</p> | <p>Specimen HCFS: <u>H</u>igh Axial Load <u>C</u>onfined Joints <u>F</u>lexure-<u>S</u>hear Columns</p> |
| <p>Specimen MUFS: <u>M</u>oderate Axial Load <u>U</u>nconfined Joints <u>F</u>lexure-<u>S</u>hear Columns</p> | <p>Specimen MUF: <u>M</u>oderate Axial Load <u>U</u>nconfined Joints <u>F</u>lexure Columns</p> |

Figure 3-1. Naming convention for shaking table specimens

Comparison of the results from specimens MCFS and HCFS will reveal the influence of axial load on shear and axial behaviour of flexure-shear-critical columns, while observations from MUF and MUFS will demonstrate the effects of unconfined joints on overall behaviour of the frame near the point of collapse and sequence of failure in the elements. Details of the specimens are described in the following section.

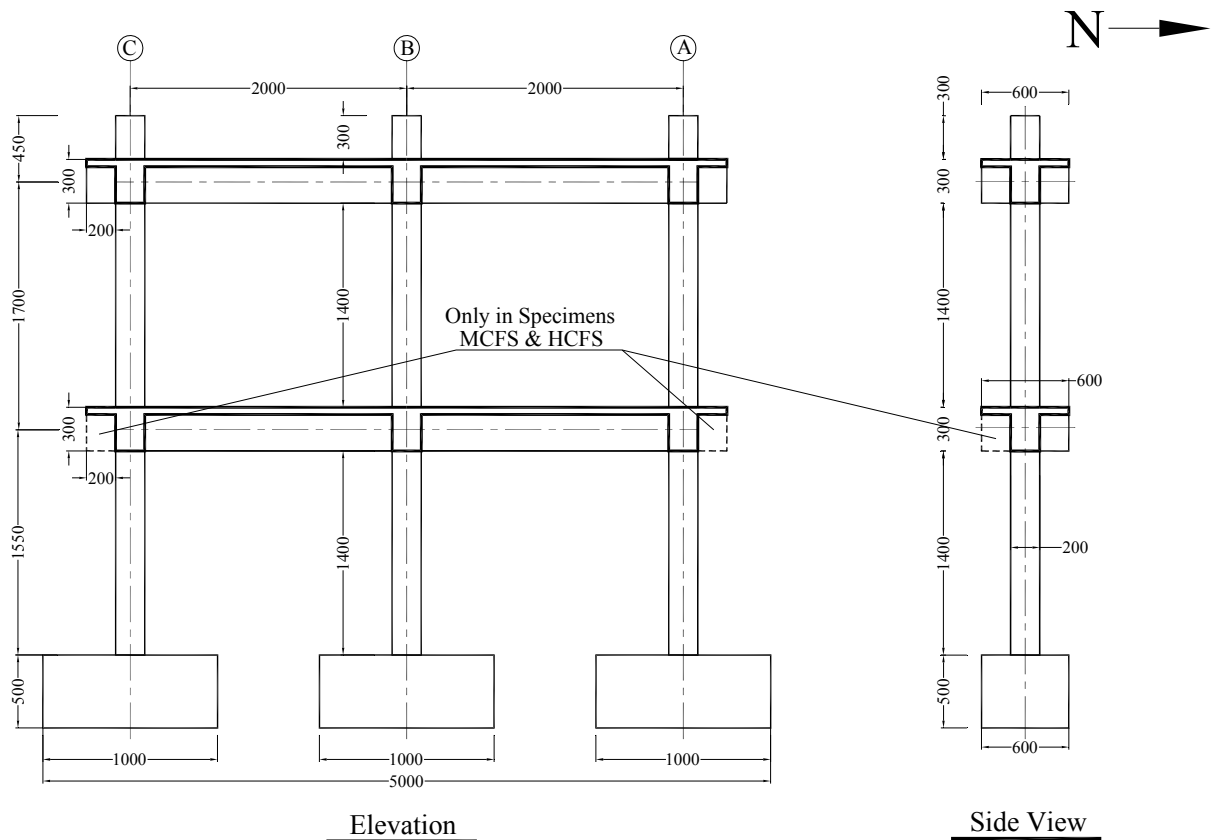
Since the scope of this study did not include bi-directional column loading, the test frames were preferred to be 2D rather than 3D. This choice resulted in considerable cost

savings and simplification in the experimental tests. The overall dimensions of the frames were limited by the shaking table size and capacity limits. Selecting the dimensions of the columns was considered a priority in designing the specimens, as the main goal of these experimental tests was to observe the behaviour of non-ductile columns and unconfined beam-column joints at the point of collapse. Given the complexity of the desired test frame behaviour and failure mechanisms, a detailed analytical model, rather than classical design methods, was used to select the test frame details. Considering the details of the full-scale columns in the existing hospital building (450 mm×450 mm columns with eight #7 longitudinal bars and #3@200mm transverse reinforcement), an extensive parametric study was performed to determine the optimal test frame final details. Effects of varying the following parameters were investigated: 1) number of bays in the test frames (which could directly influence the scaling factor for the structural elements due to the table dimensions); 2) dimensions of the columns; 3) number and size of the longitudinal and transverse reinforcement of the columns; 4) beams span, depth and height, and longitudinal and transverse reinforcement ratios; 5) number of stories in the frames; 6) concrete and steel material properties, and 7) ground motion input, selected to insure that the shaking table had sufficient capacity to fail the test specimen (see Section 3.6). This analytical exercise also served the purpose of evaluating the capability of current analytical models and methods within the analysis platform OpenSEES (McKenna et al., 2000) for modeling the behaviour of non-ductile reinforced concrete frames. Resulting test frame details and dimensions are presented here, while details of the analytical model used in the design process are presented later in Chapter 6.

Taking the construction and reinforcement limitations and results from the parametric analyses into account, 200mm×200mm was selected for the cross section of all columns; resulting in a scaling factor of 1/2.25 considering the full-scale columns of the prototype building. Due to the limited 5 meter length of the shaking table, the same scaling factor could not be used for the beams. To include two bays in each specimen, the beam spans had to be limited to two meters, while the span of the beams in the hospital building was five meters. In order to maintain the similarity between the specimens and the prototype building frame, the ratio of the story beam-to-column stiffness, representing the frame stiffness, was selected to be similar. Since the beam span was limited by the table dimensions, the beam depth was adjusted to achieve a target beam-to-column stiffness ratio of 1.7, similar to the prototype building. To account for the effects of slabs on the beam stiffness and joint demands, the beams were designed and constructed with a T-shape section. The thickness and width of the slabs were obtained by applying the 1/2.25 scaling factor to the thickness and effective width of the slabs using ACI code (ACI, 2008) of the prototype building. However, due to construction errors the slabs in specimens MUF and MUFS were constructed 10mm thicker than originally designed. Specifications and dimensions of the frames are shown in Figure 3-2.

Specimens MCFS and HCFS were designed with flexure-shear-critical columns and confined joints. In addition to transverse reinforcement in the joints, transverse beams with a length of 200mm, a width equal to the column width and height equal to the height of the longitudinal beam were used to provide confinement on all the vertical faces of the joints in both stories of these two specimens. Providing confinement in the joints forced the failure to happen in the columns. Sufficient confinement in the columns of specimen MUF ensured a flexural column response, while eliminating the confinement from the first-story joints was

expected to lead to a collapse mode dominated by joint failure. Constructing MUFS with no confinement in the first-story joints and light transverse reinforcement in the columns provided the opportunity to study the sequence of failure in a typical existing building frame with both unconfined joints and non-ductile columns. Discontinuity of the columns above the second floor made the joints susceptible to early failure; therefore, beam-column joints at second level were confined in all specimens.



Note: The height of beams was 310 mm for specimens MUF and MUFS

Figure 3-2. Shaking table test specimens

Table 3-1 provides a summary of parameters and material properties for the four test specimens. Eight deformed #4 bars (13 mm diameter) were selected for longitudinal reinforcement for all columns of all specimens. Column transverse reinforcement was designed as 5mm hoops (smooth bar) at 120 mm for specimens with flexure-shear-critical

columns (MCFS, HCFS, and MUFS), while the spacing was reduced to 40 mm for specimen MUF with ductile columns.

Beam transverse reinforcement (#3; 10 mm) with closed stirrups and 135° hooks provided sufficient shear strength to develop full flexural strength, while longitudinal reinforcement was chosen to create a weak-column-strong-beam mechanism typical of the older concrete construction. Longitudinal reinforcing bars #3 and #4 were selected for the beams in second floor, while #5 bars were chosen for the first-story beams. Lighter beam longitudinal reinforcement caused lower demands in the second-story beam-column joints which were intended to be protected from failure for all specimens. It should be noted that while no additional reinforcement was considered at first-story joints of specimens MUF and MUFS, the anchorage details of beam bar may differ from those used in older buildings. Neither beams nor columns had lap splices, thus removing splicing effects from the scope of this study. Cross-sectional dimensions and details of longitudinal and transverse reinforcement of the columns and beams are shown in Figure 3-3.

Concrete was chosen to be normal-weight density with a target cylinder compressive strength of 30 MPa in the design phase. Considering the properties of available steel rebar in Taiwan, reinforcing bars with specifications similar to ASTM A615 Grade 60 and yield strength of 440 MPa were selected. However, the material properties varied during the construction phase. The actual material properties for the specimen columns are presented in Table 3-1 and stress-strain relations for concrete and steel reinforcement for all structural members are shown in Appendix Section A.2.

Concrete-mix design for the prototype test frames was intended to be similar to that used in a full-scale model except the maximum nominal diameter of aggregate was limited to 15

mm. All the longitudinal reinforcing bars in the beams and columns, as well as transverse reinforcement in the beams, were deformed. Bar deformation helped in maintaining bond conditions similar to those in full-scale construction; although, considering the scaling of the elements, the bond may not scale perfectly. Due to limitation in material availability, transverse reinforcing bars were smooth wires of 5 mm diameters.

Table 3-1. Parameters and column material properties for the specimens

| | MCFS | HCFS | MUF | MUFS |
|---|-------------|-------------|------------|-------------|
| f'_c on Test Day (MPa) | 34.0 | 34.4 | 35.8 | 36.5 |
| Column Longitudinal Bars f_{yl} (MPa) | 439.0 | 439.0 | 467.0 | 467.0 |
| Column Transverse Bars f_{yt} (MPa) | 469.0 | 469.0 | 475.0 | 475.0 |
| Column Longitudinal Steel Ratio ρ_l (%) | 2.6% | 2.6% | 2.6% | 2.6% |
| Column Transverse Steel Ratio ρ'' (%) | 0.16% | 0.16% | 0.49% | 0.16% |
| Total Weight of Inertial-Mass System (kN) (see Section 3.4.2.3 for details) | 105.1 | 104.5 | 105.5 | 104.5 |

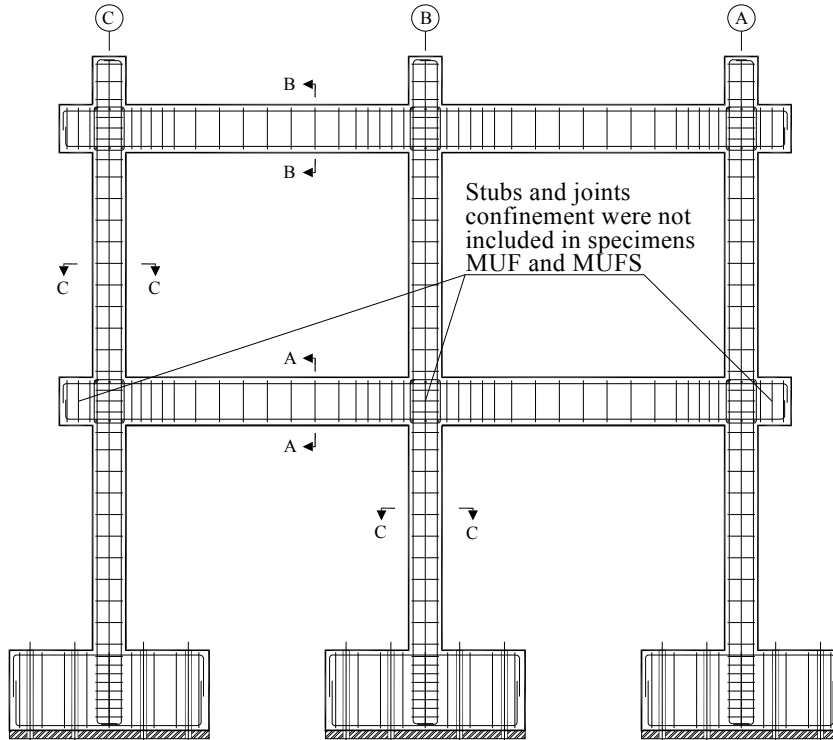
$\rho'' = A_{st}/bs$ where, A_{st} is the area of transverse reinforcement with spacing s , and b is the column width perpendicular to the direction of shaking

The expected failure mode of the columns was assessed using the ratio of the plastic shear demand on the columns (V_p) to the nominal shear strength (V_n) defined by ASCE-41 (ASCE, 2008). The plastic shear demand on the columns (V_p), was obtained by the section

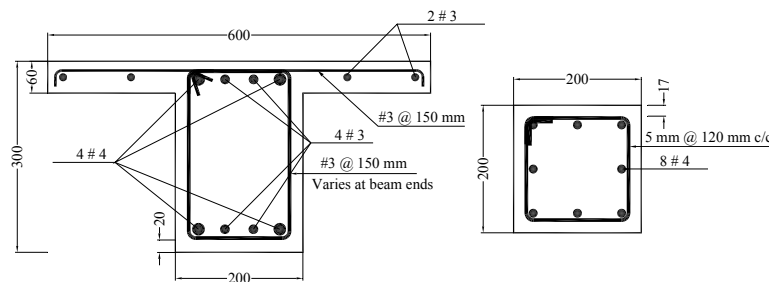
analysis of the columns using the software XTRACT (Imbsen, 2002). According to ASCE-41, the nominal shear strength (V_n) can be calculated from:

$$V_n = k(V_s + V_c) = k \frac{A_s f_y d}{s} + k \left(\frac{0.5 \sqrt{f'_c}}{a/d} \sqrt{1 + \frac{P_u}{0.5 \sqrt{f'_c} \cdot A_g}} \right) \cdot 0.8 A_g \quad (\text{MPa}) \quad (3.1)$$

where V_s and V_c are shear strengths provided by steel reinforcement and concrete, respectively. k is the factor to account for ductility-related strength degradation varying linearly between 1.0 for displacement ductility less than 2 and 0.7 for displacement ductility exceeding 6 (Sezen and Moehle, 2004). In order to obtain the initial shear strength at zero displacement ductility demand, k was considered as 1.0. In Equation 3.1, A_s is area of transverse steel, f_y is yield strength of transverse steel, d is effective section depth, s is tie spacing, f'_c is compressive strength of concrete (in MPa), a is the distance from maximum moment section to point of inflection, P_u is axial load (in N), and A_g is gross area of section (in mm²). For the design material properties and axial loads, the ratio V_p/V_n varied between 0.9 and 1.0 for the columns in specimens MCFS, HCFS, and MUFS, which complies with the ASCE-41 definition of flexural-shear-critical columns. V_p/V_n for the columns from the specimen MUF was 0.5, consistent with the ASCE-41 definition of flexure-critical columns. These ratios changed as the actual material properties were obtained after the completion of tests. The ratios for specimens MCFS, HCFS, and MUFS became slightly higher than 1.0, whereas the ratio for columns of specimen MUF remained lower than 0.6.

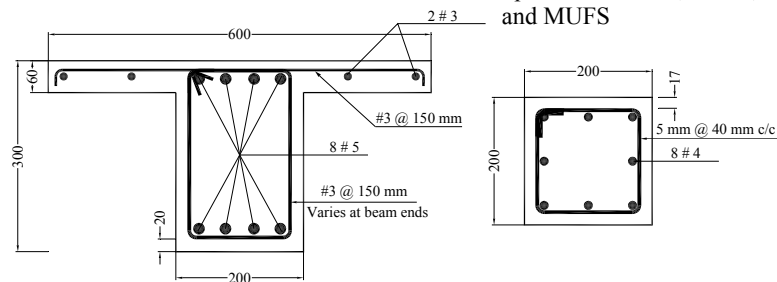


Reinforcement Layout



Beam Section B-B (Second Story)

**Column Section C-C
Specimens MCFS, HCFS,
and MUFS**



Beam Section A-A (First Story)

**Column Section C-C
Specimen MUF**

Note: Height of the beams and slabs were 310 mm and 70mm, respectively for specimens MUF and MUFS

Figure 3-3. Cross-section and reinforcement details of test specimens

Based on Figure 3-2, and for ease of reference throughout this study, elements of the specimens will be referred to using the following nomenclature: Columns will be referred to by their axis letter and story number; thus Column A1 is the first-story column at axis A (see Figure 3-2). Joints will follow a similar nomenclature with the number indicating the story number they are on; thus Joint A1 is the joint above Column A1. Beams will be referenced with four letters corresponding to the column axes that bound them; therefore Beam A1B1 is the first-story beam between columns A1 and B1.

3.3 Construction

The specimens were constructed in an upright position at a casting site adjacent to the testing laboratory. The column and beam reinforcing bars were instrumented by strain gages prior to the concrete pour (see Appendix Section B.3.4). The concrete formwork was constructed on-site. A special plastic formwork was used for the columns to provide smooth surfaces, while wooden formwork was utilized for the rest of the elements. Concrete was delivered to the site, where a slump test was performed to ensure the conformity with the specifications. The concrete pour was completed in four steps. Following the cast and curing the footing concrete, the first-story columns, longitudinal and transverse beams, beam stubs, and slabs were cast together. Same step was repeated for the second story, and then the column stubs (see Figure 3-2) were cast in the final step. Figure 3-4 shows the procedure of casting and construction of the frames.



(a)

(b)



(c)

(d)



(e)

(f)

Figure 3-4. Specimen construction and casting steps; a) footing and columns bar cages; b) pouring concrete; c) finished footings; d) forms for first-story column and beams; e) bar cage for beam and slabs; f) bar cage for top column stubs

3.4 Test Setup

Following concrete casting, the specimens were moved into the laboratory. Temporary X-shaped steel bracings were used to prevent cracking of columns and beams during the relocation of the specimens (Figure 3-5). Each Frame was lifted by crane onto the shaking table where it was bolted to six load cells (two per column), which were previously bolted to the shaking table through 50 mm-thick steel base plates. The arrangement of the holes on the shaking table did not match the needed locations for the load cells; therefore, the base plates were used to accommodate the misalignments. All bolts used for connecting the base plates to the shaking table and load cells were pre-stressed to maximize the friction between the surfaces. Vertical alignment of the specimens was very critical in the test setup; therefore, if necessary, thin steel shims were used between the table and the base plates to level the specimens. High-strength 30 mm diameter rods passing through 35 mm PVC pipes cast in the footings (see Figure 3-4b) were used to pre-stress the footings to the load cells.



Figure 3-5. Locating the specimens on the shaking table

3.4.1 Lateral Supporting System

Two steel frames were bolted to the shaking table on either side of the specimens (Figure 3-6). These frames were used to brace the specimen in the out-of-plane direction by means of frictionless rollers at each beam level, allowing free in-plane motion (both horizontal and vertical) of the frame. Two sets of rollers at mid span of the beams were adjusted to be firmly in contact with plates mounted on either side of the specimen beams.

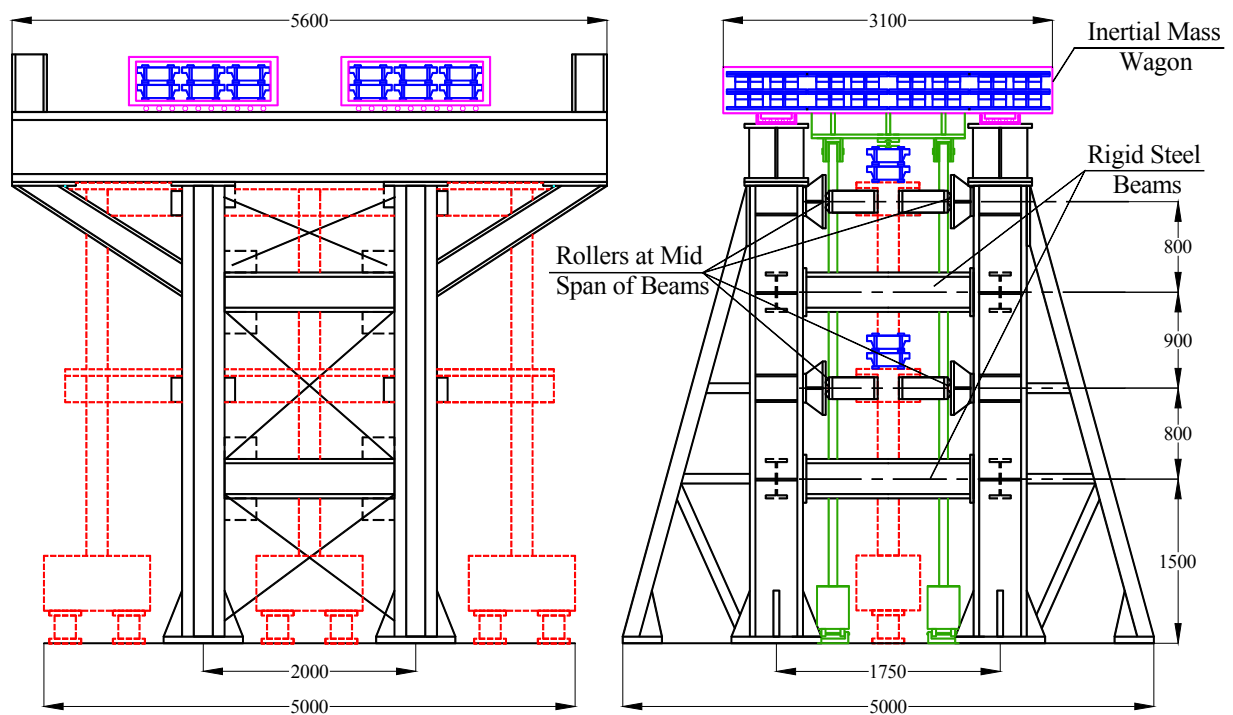


Figure 3-6. Lateral supporting system

Rigid transverse steel beams were connected to the supporting frame to catch the specimens after collapse and prevent any damage to the shaking table. Layers of rubber with total thickness of 300 mm were positioned on the top surface of the “catching beams” allowing the test specimens to fall by about 150 mm when collapse occurred, while absorbing the impact energy (Figure 3-7). However, the steel beams, columns, and connections were

designed for the forces induced by impact and a safety factor of two was considered during the design process of steel supporting frame.

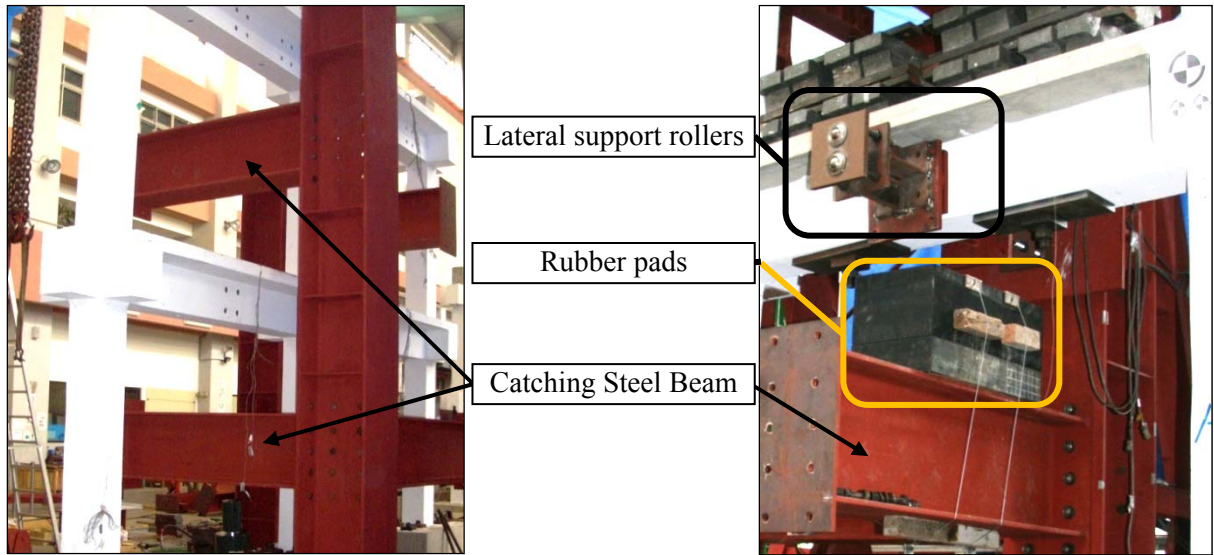


Figure 3-7. Out-of-plane restraining system and catching beams during setup of testing apparatus

3.4.2 Loading

Loading on the specimens can be categorized into three groups: 1) gravity load on beams 2) pre-stressed axial load on columns 3) inertial-mass system. Gravity load on the beams and the inertial-mass were applied using steel and lead weights, while the axial loads on the columns were achieved by means of hydraulic cylinders. The loading categories are described in detail in the following sections.

3.4.2.1 Gravity Load on Beams

The structure was intended to represent a hospital building with higher dead and live load demand than regular residential buildings. Gravity load on the beams was calculated by scaling the dead and live loads defined by the Building Technical Regulations of Taiwan (MOI, 2009) for such occupancy. Each beam was loaded with two sets of lead packets,

representing a distributed load with a total weight of 10 kN. Each set of lead packets consisted of two layers with four lead ignots in each layer (total of 16 lead ignots per beam). Lead-weights were pre-stressed onto the beams with contact points being one rubber shim and one steel shim per packet. The flexible rubber shims were used to reduce the stiffening effects of lead packets on beams, while steel shims in this arrangement provided the lateral load transfer between lead packets and concrete beams and were always placed towards the middle of the span where beam flexural deformations were smallest. Due to requirements for the connection of inertial-mass to the specimen (described in Section 3.4.2.3), layout of lead packets on second-story beams could not be similar to the first story. Therefore, fewer lead packets (total of 8 ignots per beam) with different arrangement were used on these beams, while steel sections were securely attached to the sides of the beams to compensate the lack of lead ignots on second story. Summary of the test frame weights can be found in Appendix Section B.2.

3.4.2.2 Pre-stressed Axial Load on Columns

As discussed in Sections 3.1 and 3.2, one goal of the study was to investigate the seismic behaviour of non-ductile frames under moderate and high axial loads. Due to capacity limits of the shaking table and safety concerns during collapse, the axial loads could not be achieved by adding significantly large weight on the columns, therefore, pre-stressing the columns by jacks was the only possible method for applying the axial loads. The middle columns of specimens MCFS, MUFS, and MUF were initially loaded with a moderate axial load (approximately $0.2A_gf'_c$), while the middle column of specimen HCFS was loaded with an axial load greater than the balance point load ($0.35A_gf'_c$). Considering the actual material properties of the column section (Table 3-1), such higher axial load is close to $0.31P_0 = 1.15P_b$, where P_0 is the concentric axial load capacity given by Eq. 3.2 and P_b is the balanced axial load.

$$P_0 = 0.85f'_c(A_g - A_{st}) + f_y A_{st} \quad (3.2)$$

where A_g is the gross area of the section, and A_{st} is the area of the longitudinal steel reinforcement. Note that $0.35P_0$ is used by Chapter 21 of ACI-318 as the limit above which gravity columns requiring seismic detailing and confinement similar to columns of a lateral force resisting system (ACI, 2008). The exterior columns of all frames were pre-stressed to carry approximately half of the axial loads applied to their corresponding middle columns. Table 3-2 shows the applied axial load on the columns of the specimens at the beginning of each test. The tensile force achievable using reasonably sized pneumatic jacks was considerably lower than the required axial force, thus pressure-controlled hydraulic jacks were employed to pre-stress the columns to the shaking table.

Table 3-2. Pre-stressing axial load on columns

| Specimen | Load Unit | Half-Yield Test | | | Test1 | | | Test2 | | |
|----------|--------------|-----------------|----------|----------|----------|----------|----------|----------|----------|----------|
| | | Column A | Column B | Column C | Column A | Column B | Column C | Column A | Column B | Column C |
| MCFS | (kN) | 126.7 | 243.4 | 130.3 | 126.5 | 243.3 | 130.4 | 127.2 | 244.0 | 131.2 |
| | $P/A_g f'_c$ | 0.09 | 0.18 | 0.10 | 0.09 | 0.18 | 0.10 | 0.09 | 0.18 | 0.10 |
| HCFS | (kN) | 243.1 | 483.1 | 241.2 | 242.0 | 483.1 | 240.6 | 237.2 | 478.87 | 239.1 |
| | $P/A_g f'_c$ | 0.18 | 0.35 | 0.18 | 0.18 | 0.35 | 0.17 | 0.17 | 0.35 | 0.17 |
| MUF | (kN) | 125.5 | 248.0 | 125.4 | 125.1 | 247.9 | 125.4 | 122.2 | 246.3 | 123.7 |
| | $P/A_g f'_c$ | 0.09 | 0.17 | 0.09 | 0.09 | 0.17 | 0.09 | 0.09 | 0.17 | 0.09 |
| MUFS | (kN) | 117.1 | 240.3 | 119.9 | 118.0 | 236.9 | 120.4 | 118.7 | 239.4 | 120.7 |
| | $P/A_g f'_c$ | 0.08 | 0.16 | 0.08 | 0.08 | 0.16 | 0.08 | 0.08 | 0.16 | 0.08 |

Figure 3-8 demonstrates the system used to maintain the axial load on the specimen columns. One jack was installed on each side of each column, while a transverse steel girder, placed on a pin at the top of the column, transferred the axial load to the column. A load cell,

located between the pin and the top of the column, was used to measure the applied axial load to the column. A clevis pin, aligned with the intended direction of shaking, was installed on each end of the girder. High-strength threaded rods attached the clevis pins to the hydraulic jacks which were secured to the shaking table through a second set of clevis pins. Pressure-regulating valves were used to ensure that the applied axial load would be approximately constant during the test. In spite of using accumulators and fast pressure relieving valves to passively control the axial load at the desired level, fluctuation in applied axial load was noticed during all tests.

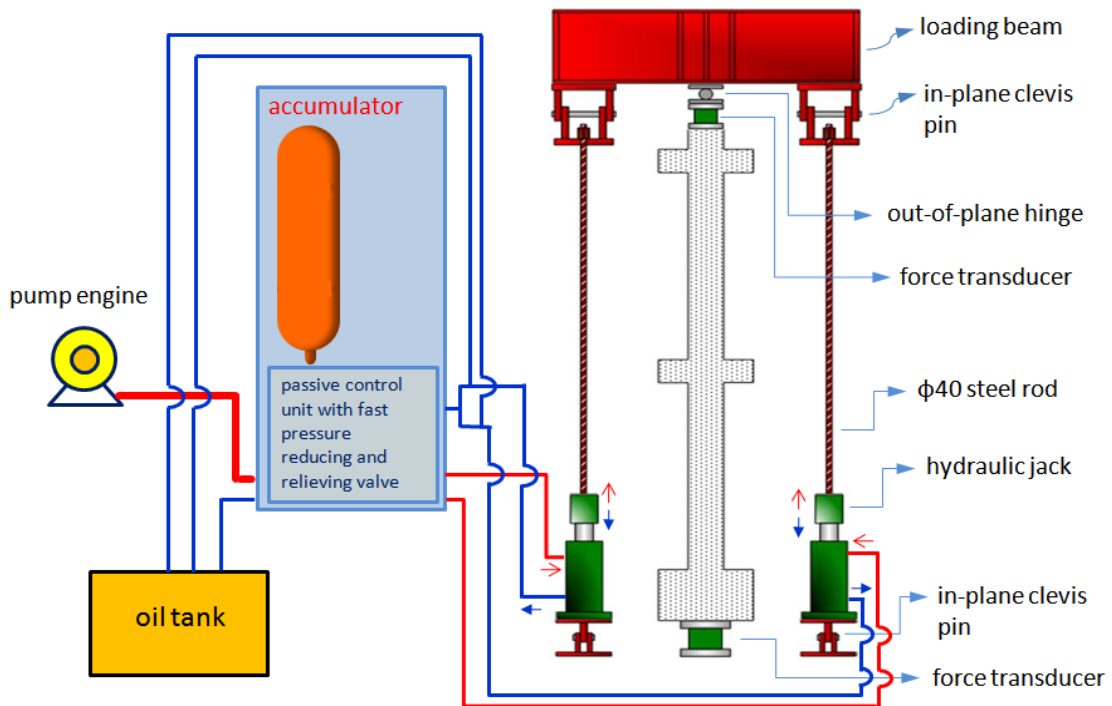


Figure 3-8. Pre-stressing system for adding axial load to columns

Figure 3-9 compares the variation of applied axial load on the columns of the frames during dynamic Test1 (see Section 3.7 for test name definitions). The peak fluctuation in applied axial load on columns remained similar for all tests (approximately 55 kN). The

maximum variation of 44% from the target load at peak demand was recorded for applied load on the exterior columns of specimens MCFS, MUF, and MUFS (with the initial axial load of approximately $0.1A_gf'_c$), whereas only 7% fluctuation was determined for the middle column of specimen HCFS with initial axial load of $0.35A_gf'_c$. Note that the aforementioned variations in applied load happened only in a relatively short period of time and for most of the duration of the tests, the fluctuation in applied load remained less than 15% and 2% for the moderate and high axial load, respectively. Similar rates of variation were observed during dynamic Test2 until the failure of columns in frames MCFS, HCFS and MUFS took place. As discussed in Chapter 4, column axial failure occurred very rapidly for all the specimens. Due to the sudden shortening of the column, there was a sudden drop in the axial load applied by the jacks at the instant of axial failure. The axial load was subsequently reapplied automatically by the pre-stressing system and, if possible, loads were redistributed to other columns. Frame MUF did not experience collapse during Test2 and consequently, the variation in axial load remained similar to Test1. Figure 3-10 demonstrates the variation of applied axial load on the columns of the frames during dynamic Test2. The data was cut off after collapse of the frame was detected (see Chapter 4 for details). Effects of the variation in applied axial load on the columns were considered in the analyses presented in Chapter 6. Note that this method of axial load application does not correctly account for P-delta effects, as the horizontal component of the applied axial load acts against the movement of the specimen; however, collapse of the frames was expected to be controlled by material degradation (shear and axial failure) rather than P-delta instability.

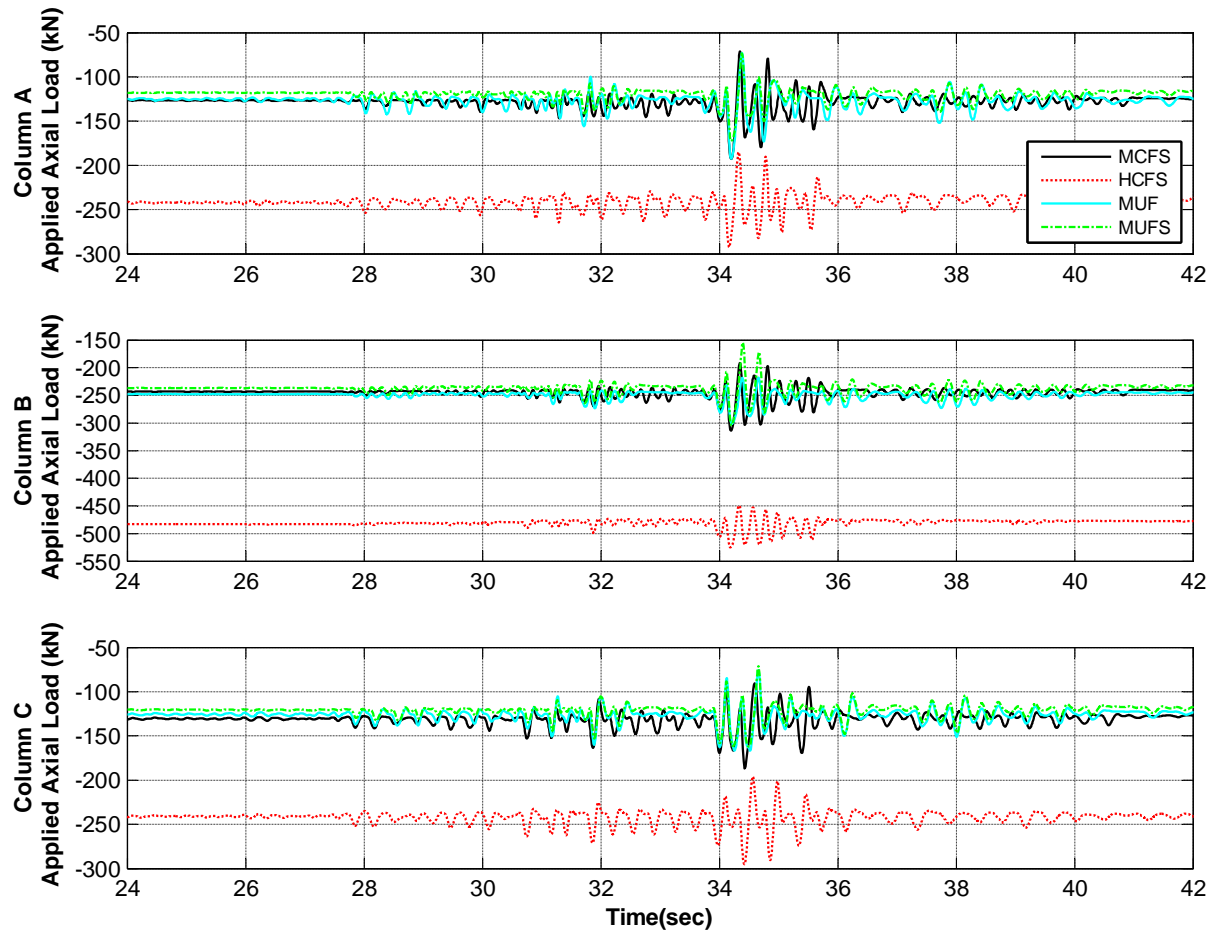


Figure 3-9. Fluctuation in applied axial load to columns during Test1

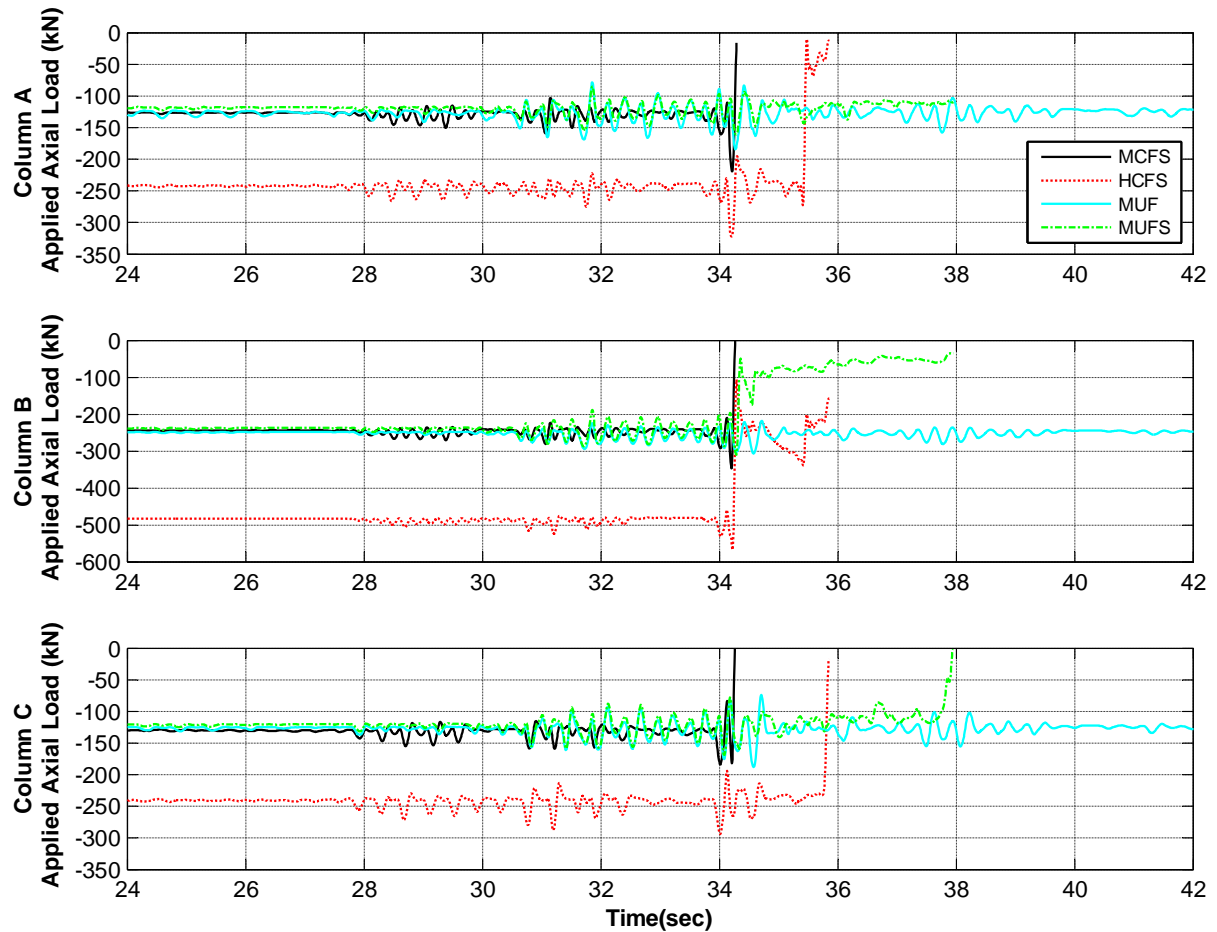


Figure 3-10. Fluctuation in applied axial load to columns during Test2

3.4.2.3 *Inertial-Mass System*

As mentioned earlier, each frame was assumed to be part of a six-story hospital building; however, only the first two stories of the frame were constructed due to the payload capacity and size of the shaking table, safety considerations during collapse tests, and the fact that damage is normally expected to be concentrated at the base of frame buildings. To account for the inertial forces from the upper stories, inertial-mass with a weight of approximately 100 kN was connected to the frame. The inertial-mass could be located on the shaking table or off the table. Each of these locations had advantages and disadvantages. For instance, selecting the off-table mass could simplify the test setup, lower the total weight on the table, and increase

the safety during the collapse tests. On the other hand, the drawbacks of an off-table mass included incorporating an asymmetric connection to the specimen, larger displacements that must be accommodated by the support system, and additional space required beside the shaking table. Examining pros and cons of each system, on-table inertial-mass was selected. In order to maintain the symmetry of the system, the inertial-mass consisted of two mass wagons, each located above the mid span of the second-story beams. The required weight for each wagon was achieved by the combination of the weight from steel plates used in the wagon, steel sections employed in the connections, and lead packets similar to those used for the gravity load on the beams. Break down of the weight of elements used for the inertial-mass system is shown in Table B-1 in Appendix Section B.2. Since the applied axial loads were provided by the hydraulic jacks, the connection of the inertial-mass to the frame should not transmit any gravity load to the specimens. Therefore, the steel out-of-plane supporting frame (see Figure 3-6) was employed to provide vertical support for the inertial-mass wagons using rollers mounted underneath the wagons. The top surface of the steel supporting girder and the rolling shafts of the vertical supports were machined to provide smooth contact surfaces with negligible friction. Side rollers in contact with the edges of the steel supporting beam were used to ensure any torsional movement of the inertial-mass wagons was restrained. Figure 3-11 demonstrates the details of the rolling supports and their connection to the wagons.

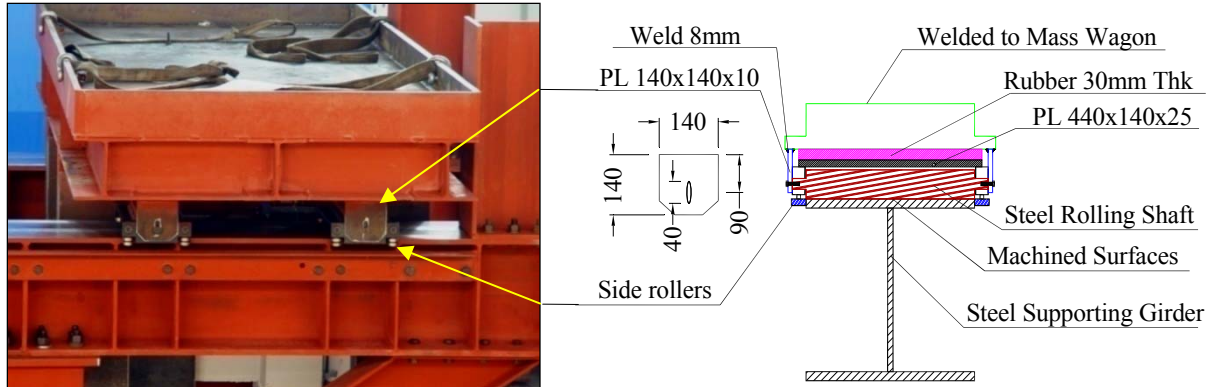


Figure 3-11. Inertial-mass rolling system

During an assessment test prior to the main tests described in this dissertation, it was observed that the inertial-mass wagons experienced rocking on the steel supporting beam. Therefore, an anti-rocking system (Figure 3-12) was designed to restrict rocking of the mass wagons; a machined-surface rolling shaft was placed underneath the steel girder at each corner of the mass-wagon and connected to the wagon through a perpendicular steel beam and two high-strength threaded rods. The high-strength rods were securely attached to the inertial-mass wagons to limit relative movement between the hanging beam and the wagons during testing.

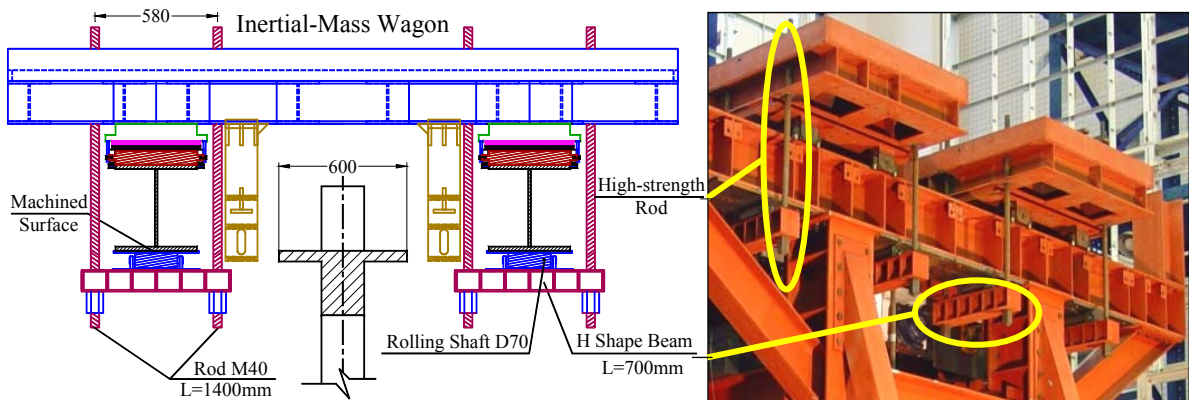


Figure 3-12. Inertial-mass anti-rocking system

The most challenging part of design was the connection of inertial-mass wagons to the specimen. The connection mechanism between the mass and the specimen should be designed

such that the inertial force could be transferred to the specimen, while the axial deformations of the columns were not restrained. Furthermore, the connection must allow for large vertical deformation of the frame at the point of collapse; otherwise, the downward force induced by sudden drop of the specimen could dislocate the wagons and cause significant damage to the shaking table. Connecting the inertial-mass wagons to second-story beams of the specimen could restrain the flexural deformation of the beams and impact the overall behaviour of the frame. Taking all aspects in consideration, the final design (Figure 3-13) consisted of a pin-ended rigid strut connecting the center column stub to the inertial-mass wagon by means of a perpendicular steel beam with slotted holes that allowed adjustment for imperfections in specimen geometry and vertical alignment. Rotation was allowed at two ends of the strut by using fish-eye hinges. A rectangular steel collar with 15mm thickness, enclosing the middle column-stub, was used to transfer the inertial force from the strut to the specimen. It was secured to the frame by bolting it to the second-story slab and using hydrostone (high strength non-shrink grout) to fill the gap between the inside surface of the collar and the column-stub.

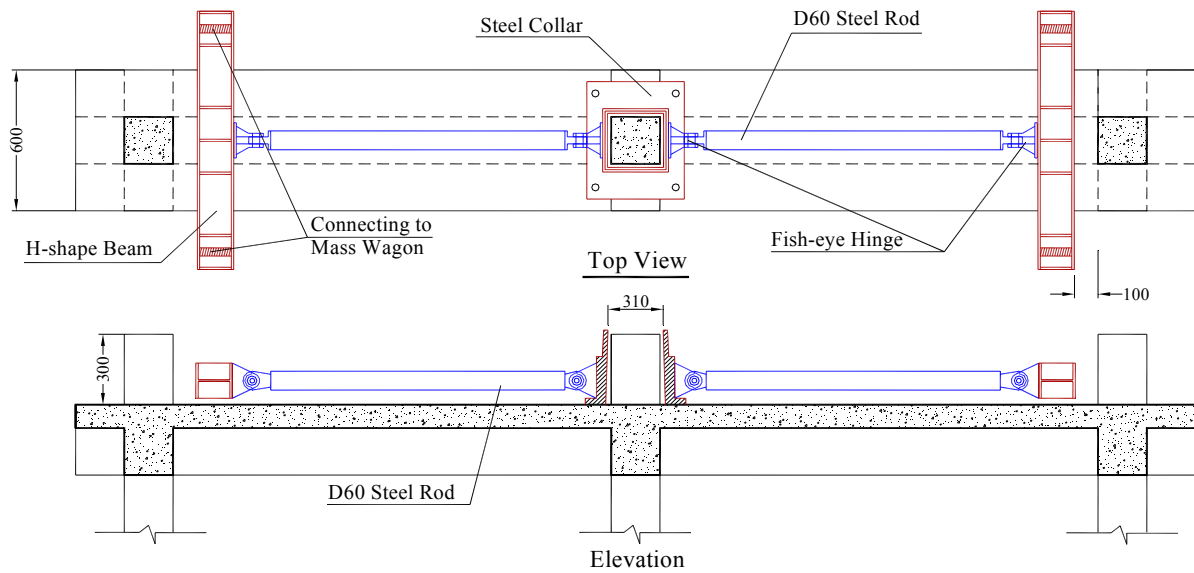


Figure 3-13. Inertial-mass lateral force transferring system

3.5 Instrumentation

Instrumentation used in the test experiments consisted of: 1) force transducers (load cells) to measure shear and axial forces at the base of the specimen footings, and applied axial load to the top of columns by means of pre-stressing system; 2) displacement transducers to measure global deformations of the specimens and local deformations of columns and joints; 3) accelerometers to measure horizontal and vertical accelerations at several points on the specimens; and 4) strain gauges to measure steel strain of longitudinal and transverse reinforcement in columns and beams. Details for all instruments can be found in Appendix Section B.3.

Each frame was attached to the shaking table through six load cells (two per column). These load cells were capable of reading axial force and shear parallel and perpendicular to the direction of motion. Due to significant shear and axial loads expected to be induced during the tests, load cells with high capacity (1000 kN for axial load and 500 kN for shear) were fabricated and pre-stressed to both shaking table and footings. Since the force transducers are very sensitive to the stiffness of the end conditions, steel plates, anchored to the footing during the construction phase, were used to provide an even and clean contact surface for the top plate of the load cells (Appendix Section B.3.1).

Twenty-one accelerometers were used to measure the vertical, longitudinal, and out-of-plane accelerations of the frame and inertial-mass. Accelerometers were mounted on the center column footing and all beam-column joints (on transverse beam face). Longitudinal accelerometers were also mounted on inertial-mass wagons to check that the wagons were moving with the second-story beams. The longitudinal accelerometers at each story level

provide data to check on the base shear measured by the force transducers. Details of location and direction of accelerometers are shown in Appendix Section B.3.2.

Displacement transducers, consisted of string potentiometers (string pots) and Novotechnik linear potentiometers, were used to measure the global vertical and horizontal displacement of the frame and inertial-mass, as well as the local deformations in plastic hinge zones of the first-story center column. Considering the severe damage to this column during the tests, the data from local displacement transducers are valid only before shear failure in Test2. Six Novotechnik potentiometers were mounted on the confined face of first-story exterior joint C1 of all the specimens, while additional potentiometers were mounted on the open face of exterior joints A1 and C1 of specimens MUF and MUFS to measure the shear deformations. This provides the opportunity to compare the shear deformations of the joint on the confined and unconfined faces of the beam-column-joints. More details on displacement transducers, locations and layout can be seen in Appendix Section B.3.3.

Strain gages were mounted on the longitudinal and transverse reinforcing bars in the column, beams, and joints. The strain gages were concentrated in plastic hinge zones of first-story columns and around the beam-column joints. The number of strain gages was increased for the exterior joints of specimen MUF and MUFS. More details and location of strain gages are provided in Appendix Section B.3.4.

3.6 Ground Motion Selection

Several factors were considered in selecting the ground motion record. First, the record needed to have enough intensity to fail the frames. Secondly, the study was not intended to include the effects of near fault ground motions; therefore, all considered ground motions were recorded at an average distance of 20-40 km from the fault. Thirdly, a relatively long-duration

ground motion was preferred as it would allow for observation of the interaction of structural elements, mechanics of failure, and redistribution of load while the specimen was still subjected to strong table shaking. Further restrictions were placed on selecting the ground motion by the capacity of the shaking table. The maximum allowable acceleration for the bare table was $\pm 2.0g$, while the maximum displacement of the table was limited to ± 200 mm. Considering the weight of the specimen and lead packets, steel supporting frame, the inertial-mass system, and the required equipments for pre-stressing the columns, the acceleration capacity of the table was reduced to $\pm 1.1g$. Various records from the 1999 Chi-Chi earthquake in Taiwan (Lee W.H.K., 2001) were explored using the test frame analytical model described in Chapter 6. Ultimately, the horizontal North-South component recorded at station TCU047 was selected for all tests. The station was located at $24.619^\circ N$, $120.939^\circ E$, in Da-Haes Elementary School, Miaoli County in Taiwan. The epicentral distance, R_{ep} , was 85.2km (closest distance to the rupture plane, R_{rup} , was 33.03km). Site soil condition was categorized under class C (very dense soil & soft rock, average shear velocity of the upper 30m soil deposit $V_s=360-760m/s$) with a PGA of 0.41g.

The original record was filtered and scaled to a nominal peak ground accelerations of 0.3g (Half-yield Test), 1.1g (Test1), and 1.35g (Test2) (test definitions and details are discussed in Section 3.7). As discussed earlier, the scale factor for the model was 1/2.25; therefore, the ground motion time-step was scaled by $1/\sqrt{2.25}$ to satisfy the similarity requirements. Figure 3-14 displays the input acceleration record, the achieved table motion, table velocity, and table displacement for specimen MCFS during Test1. Recorded acceleration at table- and story-levels for all the specimens are demonstrated in Chapter 4.

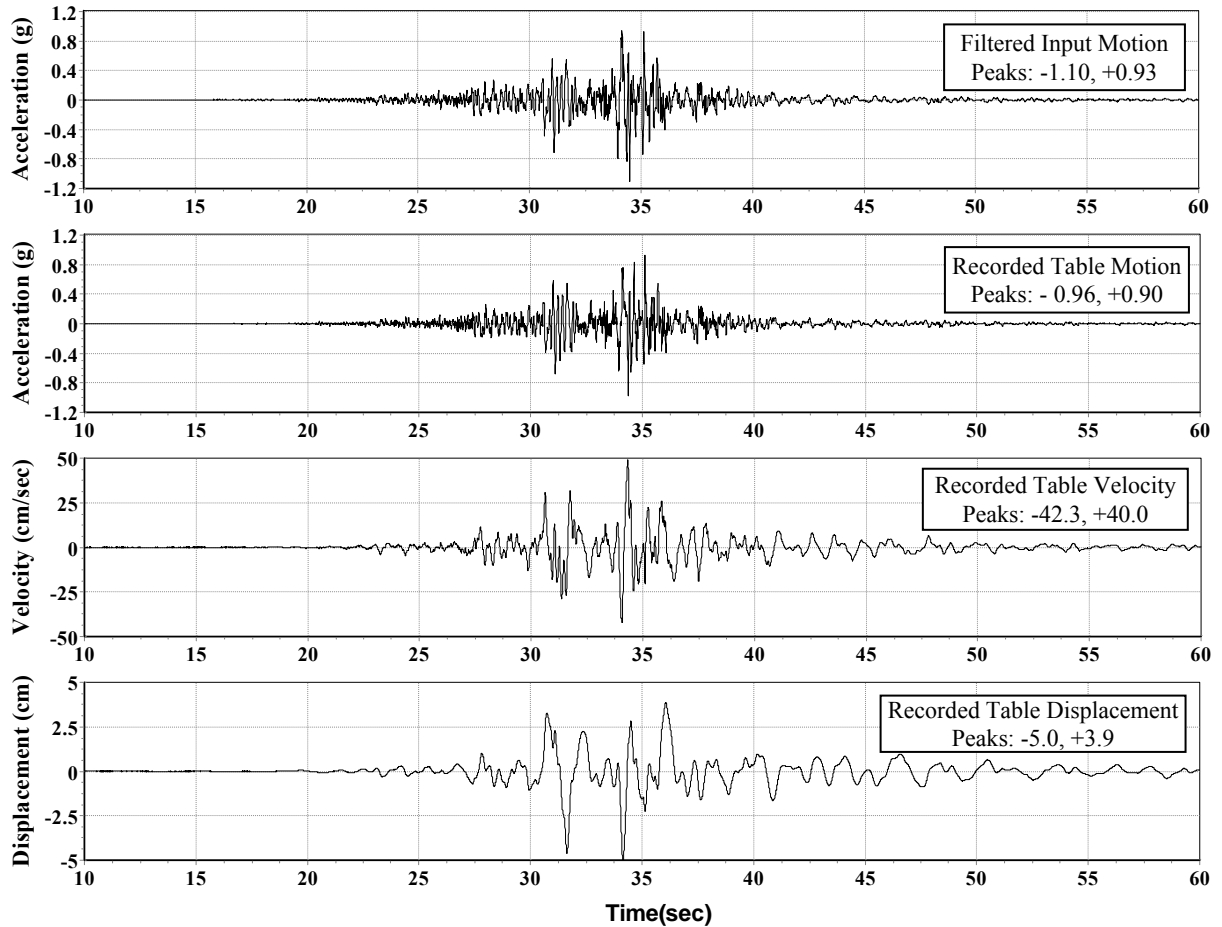


Figure 3-14. Input and recorded table acceleration, velocity, and displacement for specimen MCFS (Test1)

Figure 3-15 plots the displacement and pseudo-acceleration response spectra (2% damping) of the recorded table motions for the four specimens during Test1. Although the table control parameters and input motions were kept very similar making comparison of data from the four tests possible, it is observed that the achieved spectral accelerations for the tests were not equal, particularly around the peak spectral acceleration at a period of 0.2 seconds. On the other hand, fundamental period for the specimens was determined to be approximately 0.29 seconds (using the White-noise Test results; see Chapter 4) and Figure 3-15 shows that the spectral accelerations for all specimens were relatively close in the vicinity of such period (dashed line). Spectral accelerations and displacements also remained close for periods greater

than 0.29 seconds, an important observation as the periods of vibration for the specimens will increase as the specimens experience damage.

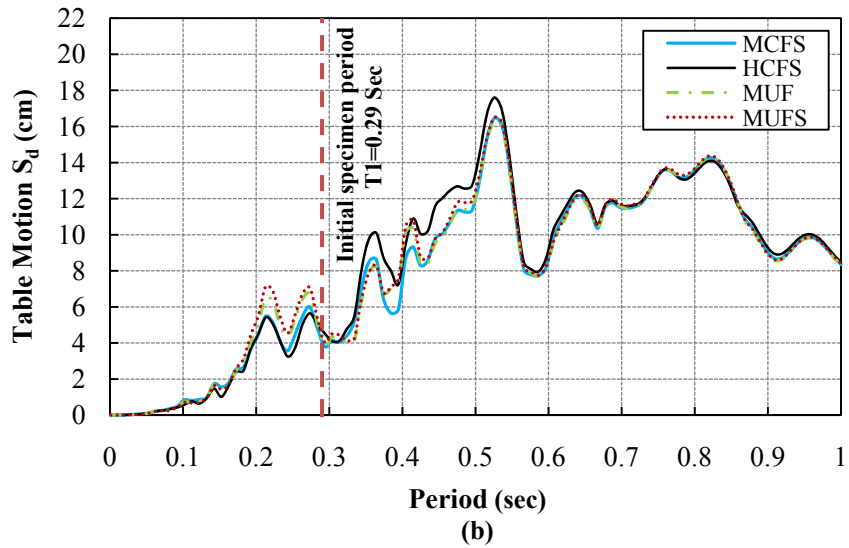
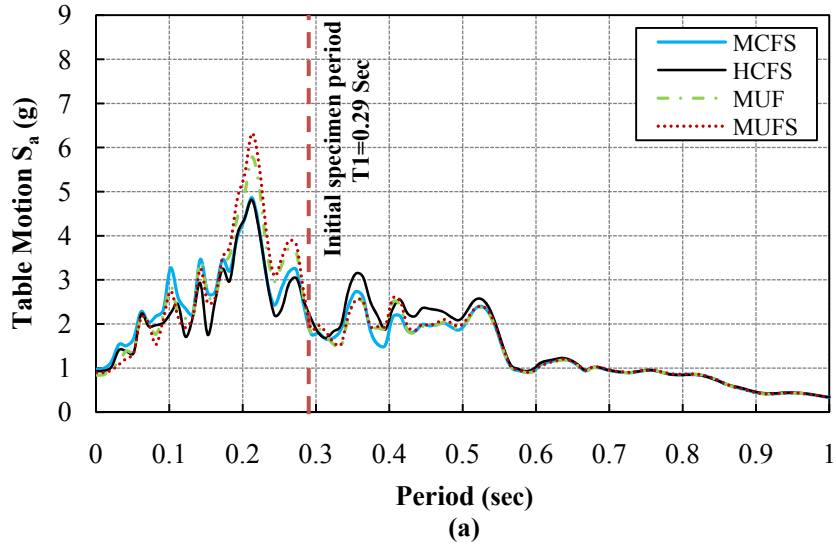


Figure 3-15. (a) Pseudo-acceleration and; (b) displacement response spectra for recorded table motions with 2% damping (Test1)

Figure 3-16 demonstrates the displacement and pseudo-acceleration response spectra (2% damping) of the recorded table motions for the specimens during Test2. Due to damage to the specimens during Test1 (see Chapter 4), natural periods for specimens MCFS and HCFS were lengthened to 0.36 seconds, whereas the periods for specimens MUF and MUFS were

lengthened to 0.46 seconds. Figure 3-16 reveals that while the spectral acceleration for specimen HCFS was about 10% lower than MCFS in the vicinity of the lengthened period of the specimens (dashed line), the spectral acceleration demand for specimen MUFS was only 4% higher than specimen MUF at the lengthened period of these two specimens (dotted line).

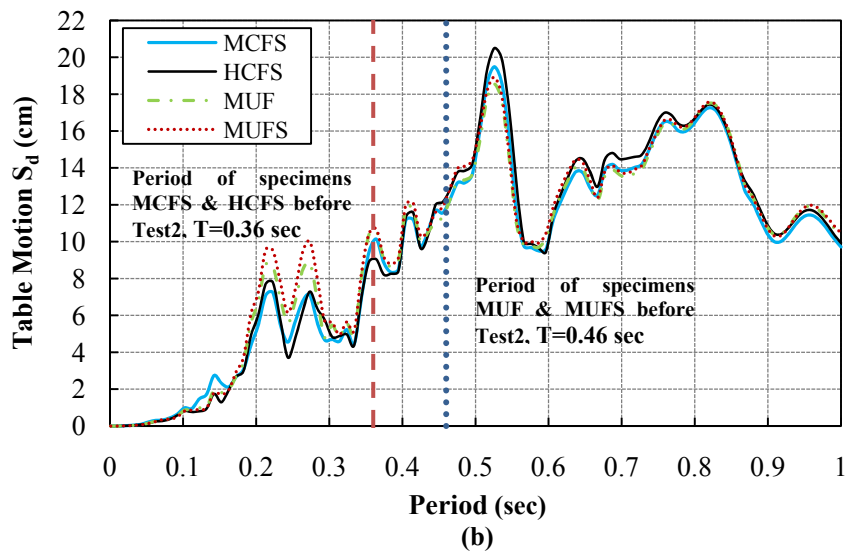
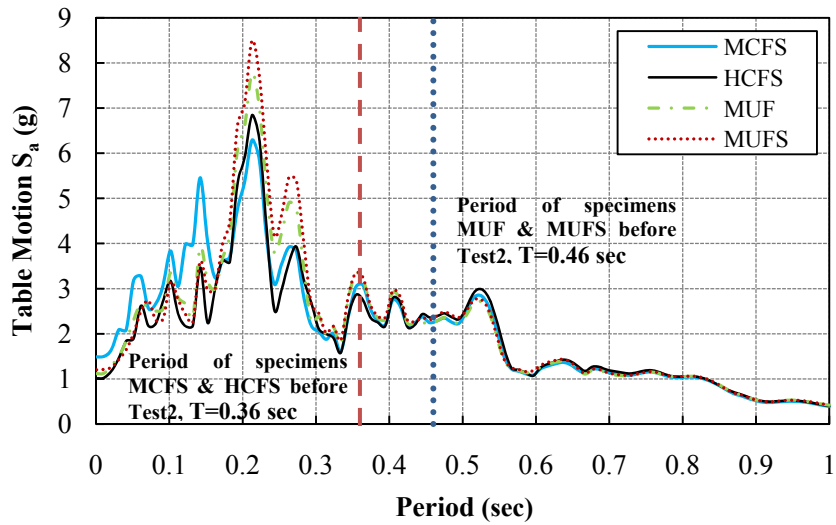


Figure 3-16. (a) Pseudo-acceleration and; (b) displacement response spectra for recorded table motions with 2% damping (Test2)

3.7 Experimental Program

Table 3-3 lists the chronology of the dynamic tests applied to the four specimens. Before applying the pre-stressing axial load to the columns, a low-amplitude white-noise with amplitude of 0.025g was conducted (herein referred to as “White-Noise L1 Test”). This test served as a check on all systems and instruments connected to the frame. Subsequent to pre-stressing the columns, another low-level white-noise test with amplitude of 0.025g was performed (herein referred to as “White-Noise L2 Test”). In order to obtain the natural periods and damping ratios of the frames, a white-noise test with amplitude of 0.1g was performed on the specimens (herein referred to as “White-Noise Test”). No damage (cracking) to the specimens occurred during this test. Following the White-Noise Test, a low-level dynamic test (herein referred to as “Half-yield Test”) was performed with an amplitude scaling factor of 0.75 from the original TCU047-NS ground motion. Similar to the White-Noise Test, no cracking due to Half-yield Test was observed for the specimens. Subsequently, all the specimens were subjected to the TCU047-NS motion scaled by a factor of 2.75 (herein referred to as “Test1”). Immediately after this test, another low level white-noise test with amplitude of 0.025g was imparted to the frames to assess the new “damaged” state dynamic properties (herein referred to as “White-Noise L3 Test”). In the end, a scaling factor of 3.38 was used to cause collapse or severe damage to the frames (herein referred to as “Test2”). All specimens except MUF experienced collapse at this level of table shaking. For specimen MUF, the input motion was scaled by a factor of 4.05 (Test3); however, this test did not prove sufficient to collapse the structure as the frame period had shifted significantly due to the damage it incurred in Test2. The intensity of the table motion could not be amplified due to the shaking table capacity limits.

Table 3-3. Chronology of dynamic tests for specimens

| Test Name | Table Motion | Table Motion Scaling Factor |
|-----------------------------|---------------------|------------------------------------|
| White-Noise L1 | - | N/A |
| White-Noise L2 | - | N/A |
| White Noise | - | N/A |
| Half-Yield | TCU047-NS | 0.75 |
| Test1 | TCU047-NS | 2.75 |
| White-Noise L3 [†] | - | N/A |
| Test2 | TCU047-NS | 3.38 |
| Test3 [§] | TCU047-NS | 4.05 |

[†] Not performed on specimen MCFS

[§] Only performed on specimen MUF

CHAPTER 4. EXPERIMENTAL TEST RESULTS

4.1 Introduction

This chapter presents the observations and results from dynamic tests performed on the four test frames (as enumerated in the previous chapter). Comparison of the behaviour of the specimens during the shaking table tests can be found in Chapter 5, while the results from the tests are compared with analytical models in Chapter 6. Filtering, synchronization, and procedures used to reduce the recorded data to the results presented here are summarized in Appendix Section B.4.

As discussed in Section 3.7, each specimen was tested under a sequence of table motions with increasing intensities. Since no visible cracks were found after the Half-Yield Test, for the sake of brevity, this chapter investigates only the behaviour of the specimens for Test1 and Test2 in which significant damage was observed. The specimens did not collapse during Test1, but, as described in detail below, all were to some extent damaged. As expected, columns of specimens MCFS and HCFS experienced flexural and shear cracks mainly in the first story, while Test1 damage was mostly concentrated at first-story joints of specimens MUF and MUFS. The specimens did not perform similarly during Test2 and the failure mode was

different for each frame. Only specimen MUF did not collapse during Test2. Frame MCFS collapsed due to shear and axial failure of all first-story columns. This was not observed for the other specimens, where a combination of plastic hinge development and damage to the structural elements caused the collapse of the specimen.

Initial vertical-load state of the test frames are described in Section 4.2 and the specimen dynamic properties at various damage stages as the frames were subjected to increasing levels of dynamic shaking are demonstrated in Section 4.3. Observations during testing the four specimens, global behaviour of the frames, and performance of the structural elements are discussed in detail in Sections 4.4 to 4.7. In each section, important data for the columns such as maximum experienced shear, V_{max} , corresponding story drift, $\delta_{V_{max}}$, and axial load, $P_{V_{max}}$, are summarized in tables for the positive and negative directions of each test. Based on the envelope of the test data, Figure 4-1 demonstrates such parameters, where k_{eff} is defined as the ratio of $0.75V_{max}$ and corresponding story drift. In Figure 4-1, $\delta_{80\%}$ is defined as the story drift at which the column shear is degraded by 20%. Naturally, $\delta_{80\%}$ may not be observed in the summary tables for columns with no or limited shear degradation.

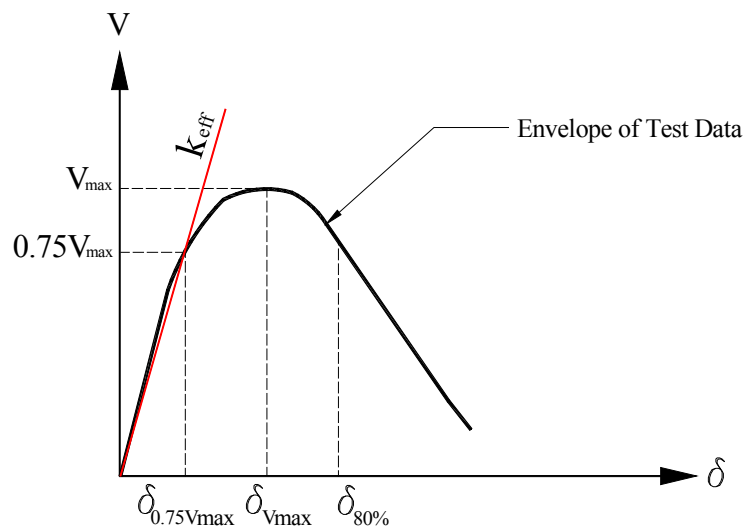


Figure 4-1. Definition of key parameters based on column shear-drift data envelope

The following definitions are used throughout this study:

- Initiation of column shear failure - the point where “notable” shear strength loss (defined here as 20% reduction in shear resistance) starts and large shear cracks are developed. In some cases, columns may experience axial failure prior to 20% reduction in shear resistance.
- Onset of column axial failure - the point at which the peak vertical displacement due to column lengthening is recorded followed by a sudden shortening of the column.
- Collapse of a specimen - the point where minimum axial load is recorded for the last column to experience axial failure. Specimen cannot stand the vertical demand at this point. Data is not shown beyond the point of specimen collapse.

It is noted that the data shown in this chapter are directly from the load and displacement readings during the tests (as described in Appendix B). The results have not been corrected for P-delta effects. Collapse of the frames was controlled by shear and axial column failure at low drifts (less than 2.5%) prior to dynamic instability due to P-delta effects and strength degradation. In order to provide similar grounds for comparison of the results, P-delta effects were also considered in the analytical simulations discussed in Chapters 6 and 7.

In the following sections, the positive direction for acceleration records is from South to North or from column axis C to column axis A (see Figure 3-2), while positive direction for shear and displacement are from North to South or from column axis A to column axis C.

4.2 Initial Vertical Load State

Ideally, measurements must be conducted before the dynamic tests to identify the pre-existing stresses/forces and strains/deformations due to gravity loading. For this purpose,

readings from load cells supporting the frames were taken at several intervals to monitor the change in loads on the specimens as they were being loaded. However, due to corrupted data recorded in a couple of intervals, the readings could not be used to assess the initial vertical forces in the frame. Furthermore, it was impractical to monitor the frame gravity-load deformations (which are very small) during the installation and loading process. Consequently, the frames initial forces and their corresponding deformations could only be estimated using an analytical model. The analytical model used for this task was the OpenSEES model described in Chapter 6, which was adjusted to match the actual frames material properties and loads. The initial readings from all the instruments were zeroed for the dynamic tests sequence, therefore, the analytically obtained initial values, were added to the measured values to account for the initial state of the specimens.

4.3 Fundamental Periods and Damping Ratios

Modal properties of the test frames were extracted from white-noise dynamic tests performed on undamaged specimens. Due to test setup and lab limitations, other methods, such as snap-back tests, were not feasible. The dynamic properties of the frames as obtained from all the corresponding tests are summarized in Table 4.1. It is noted that the “Initial State” in Table 4.1 refers to the status of the frames after applying the pre-stress axial load on the columns and before subjecting to ground motion records. This table contains the first two modal periods, frequencies, and the damping ratio of the frames. ARTeMIS Extractor (2010), an operational modal analysis software, was used to obtain the modal properties of the frames in the frequency domain, using peaks in the response Fourier Transformations or Transfer Functions. A white-noise test was not performed on specimen MCFS after Test1, therefore, lengthening of period for this specimen could not be calculated. Due to significant damage to

first-story joints during Test1, damping ratios for specimen MUF and MUFS could not be accurately extracted from the low-level white-noise test after Test1. Figure 4-2 demonstrates the first and second mode shapes for the specimens. Modal participating mass ratios for the first and second modes were obtained as 94% and 6%, respectively. This demonstrates that the behaviour of the specimens was mainly influenced by the first mode.

Table 4-1: Summary of frames modal properties

| Specimen | Mode No. | Initial State (White Noise1) | | | After Test1 (White Noise2) | | |
|----------|-----------------|------------------------------|----------------|-------------------|----------------------------|----------------|-------------------|
| | | Period (sec) | Frequency (Hz) | Damping Ratio (%) | Period (sec) | Frequency (Hz) | Damping Ratio (%) |
| MCFS | 1 st | 0.29 | 3.45 | 2.6 | - | - | - |
| | 2 nd | 0.08 | 12.50 | | - | - | |
| HCFS | 1 st | 0.28 | 3.57 | 2.9 | 0.36 | 2.78 | 11.4 |
| | 2 nd | 0.07 | 14.28 | | 0.09 | 11.11 | |
| MUF | 1 st | 0.29 | 3.45 | 3.2 | 0.46 | 2.18 | N/A * |
| | 2 nd | 0.07 | 14.28 | | 0.09 | 11.11 | |
| MUFS | 1 st | 0.29 | 3.45 | 3.1 | 0.46 | 2.18 | N/A * |
| | 2 nd | 0.07 | 14.28 | | 0.10 | 10.00 | |

* Damping ratios could not be extracted accurately.

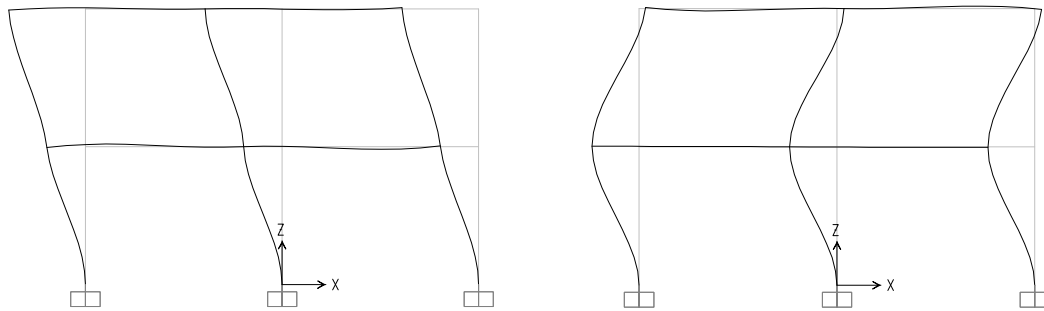


Figure 4-2. First and Second mode shapes for the specimens

4.4 Behaviour of Specimen MCFS

While subjected to moderate axial load, specimen MCFS with confined joints and non-ductile columns was considered as the benchmark for evaluation and comparing the behaviour of the four tested frames (see Chapter 5). Figure 4-3 compares the spectral accelerations for the table motions of Test1 and Test2, while displacement response spectra for the two tests are

compared in Figure 4-4. It is observed that the spectral acceleration demand was increased by 20% in the vicinity of the initial fundamental period of the frame (from 2.1g to 2.5g, dashed line). Due to lack of data records (see Section 4.3), the lengthened period of specimen MCFS after Test1 could not be obtained. However, similarity of the frame structural detailing with specimen HCFS suggests that the period of the damaged frame should be close to 0.36 seconds (see Table 4-1). At such period (dotted line), Figure 4-3 demonstrates a spectral acceleration demand of 3.1g for Test2, which is about 40% higher than Test1.

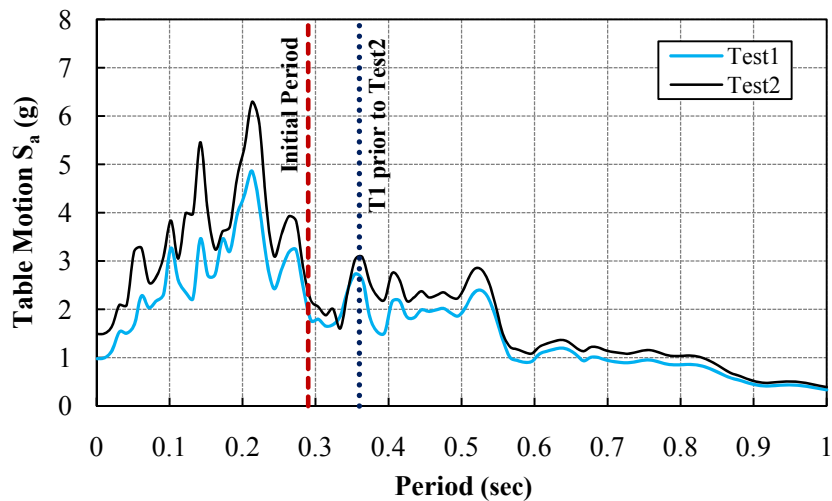


Figure 4-3. Comparison of spectral acceleration with 2% damping for Test1 and Test2 table motions, specimen MCFS

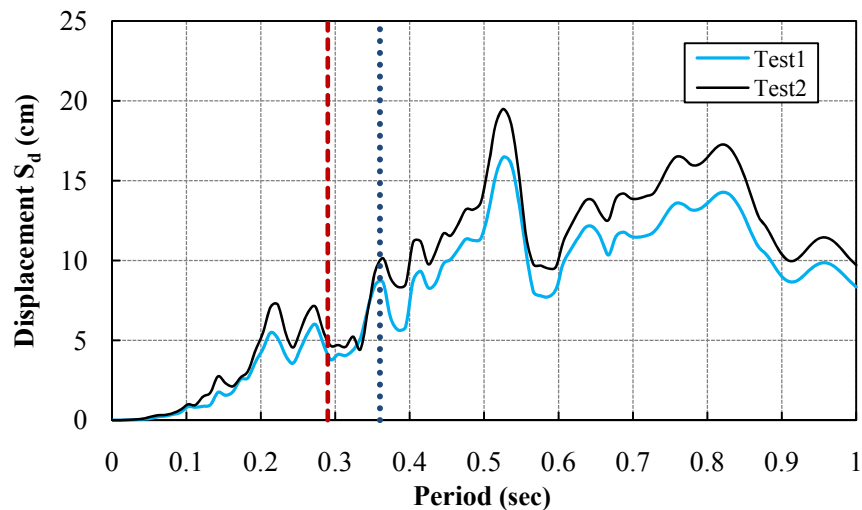


Figure 4-4. Comparison of displacement response spectra with 2% damping for Test1 and Test2 table motions, specimen MCFS

After Test 1, flexural cracks were seen in columns at both story levels, while shear cracks were mainly observed in column B1. None of the columns experienced severe shear damage, yet a few shear cracks with maximum width of 0.3 mm were observed at the top and bottom of Column B1 during Test1 (Figure 4-5). Maximum width for flexural cracks of columns A1 and C1 were observed as 0.15 mm and 0.2 mm, respectively.

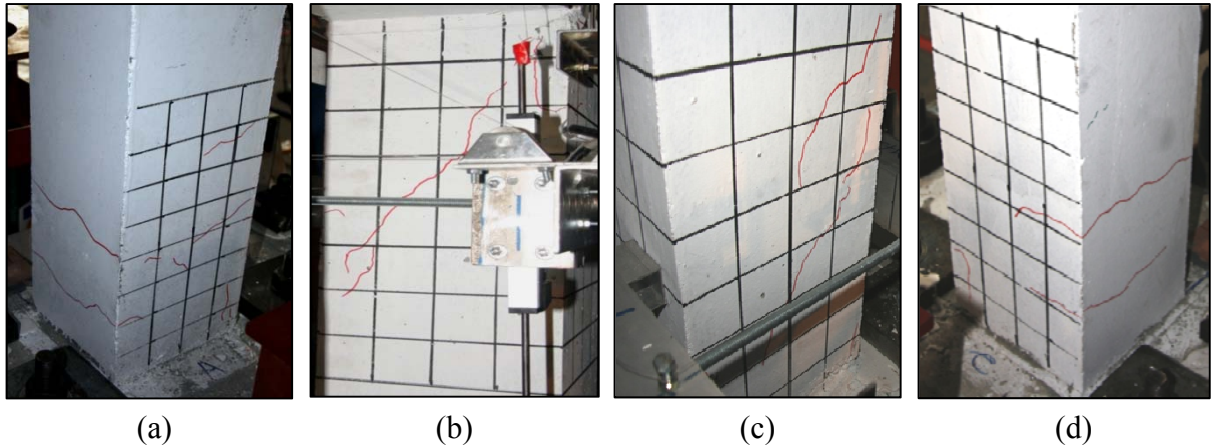


Figure 4-5. Shear and flexural cracks in columns of specimen MCFS, Test1; a) column A1 base; b) column B1 top; c) column B1 base; d) column C1 base.

Although specimen MCFS survived Test1, it collapsed at 34.30 seconds of Test2. The failure mode for specimen MCFS is shown in Figure 4-6, where the increasing demand in Test2, in addition to the damage caused by Test1, forced the frame to collapse by means of shear and axial failure of first-story columns at the base. As shown later in this section, by examining the maximum recorded shear, axial load, column vertical displacement, and corresponding drift ratios and occurrence time during Test2, it was observed that shear failure of column B1 occurred first, followed by axial failure of the column. Shear failure of column C1 took place later, followed by its axial failure. Finally, column A1 experienced shear failure leading to axial failure of the column and collapse of the frame.

The photographs in Figure 4-7 show the state of first-story columns after Test2. While bases of the columns were extensively damaged, only minor cracks were observed at top end of the columns. It was observed that the first two ties located within 300 mm of the column base were fractured, while the 90° hooks in the third layer opened. None of second-story columns experienced noticeable damage.

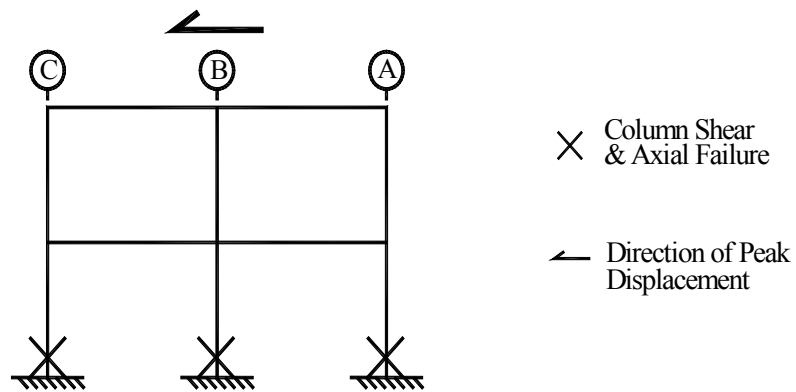


Figure 4-6. Failure mode of specimen MCFS

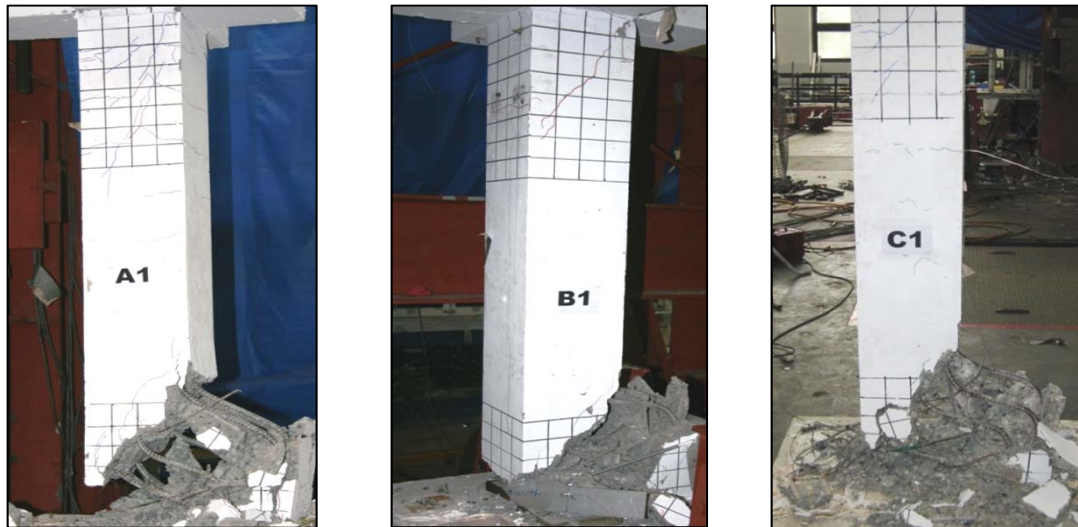


Figure 4-7. Failure of first-story columns of specimen MCFS in Test2

Maximum recorded shear for the columns and corresponding drifts, axial loads, and time steps in the positive and negative directions of Test1 and Test2 are shown in Table 4-2 and Table 4-3, respectively (see Figure 4-1 for details). These points will be discussed later in relation with the discussion on recorded data. Columns did not experience significant shear degradation during Test1; therefore, drift at 20% shear loss, $\delta_{80\%}$, could not be obtained. However, Table 4-3 demonstrates that all first-story columns experienced excessive shear degradation in the positive direction of Test2. It is observed that column B1 showed the highest effective stiffness, k_{eff} , while column A1 demonstrated the lowest during both tests. Comparison of effective stiffness of the columns during Test1 and Test2 shows about 40% reduction in k_{eff} resulted from shear and flexural cracking of the columns.

Table 4-2. Critical parameters for columns of specimen MCFS, Test1

| | A1 | B1 | C1 | A2 | B2 | C2 |
|--------------------------------|-----------|-----------|-----------|-----------|-----------|-----------|
| V_{max+} (kN) | 66.15 | 75.26 | 78.88 | 57.15 | 76.20 | 57.15 |
| δ_{Vmax+} (%) | 2.08 | 1.65 | 1.97 | 1.89 | 1.89 | 1.89 |
| P_{Vmax+} (kN) | -53.47 | -361.26 | -312.29 | -33.32 | -333.25 | -307.22 |
| t_{Vmax+} (sec) | 34.23 | 34.20 | 34.22 | 34.24 | 34.24 | 34.24 |
| δ_{80%+} (%) | - | - | - | - | - | - |
| V_{max-} (kN) | -64.32 | -79.93 | -61.93 | -56.60 | -75.47 | -56.60 |
| δ_{Vmax-} (%) | -1.95 | -1.95 | -2.04 | -1.30 | -1.29 | -1.30 |
| P_{Vmax-} (kN) | -311.34 | -344.72 | -48.08 | -296.46 | -329.27 | -48.06 |
| t_{Vmax-} (sec) | 34.45 | 34.45 | 34.46 | 34.43 | 34.43 | 34.43 |
| δ_{80%-} (%) | - | - | - | - | - | - |
| k_{eff} (kN/m) | 4043.2 | 6135.5 | 5490.1 | 3754.1 | 5006.2 | 3754.1 |

Table 4-3. Critical parameters for columns of specimen MCFS, Test2

| | A1 | B1 | C1 | A2 | B2 | C2 |
|--|-----------|-----------|-----------|-----------|-----------|-----------|
| V_{max+} (kN) | 65.73 | 79.49 | 87.24 | 68.08 | 90.77 | 68.08 |
| δ_{Vmax+} (%) | 2.60 | 1.89 | 2.16 | 2.39 | 2.39 | 2.39 |
| P_{Vmax+} (kN) | -93.92 | -377.27 | -350.99 | -78.47 | -250.20 | -318.96 |
| t_{Vmax+} (sec) | 34.23 | 34.20 | 34.21 | 34.23 | 34.23 | 34.23 |
| δ_{80%+} (%) | 4.01 | 2.35 | 2.73 | - | - | - |
| V_{max-} (kN) | -59.60 | -64.35 | -48.95 | -47.08 | -62.78 | -47.08 |
| δ_{Vmax-} (%) | -1.81 | -1.79 | -1.81 | -1.50 | -1.50 | -1.50 |
| P_{Vmax-} (kN) | -292.91 | -315.10 | -71.30 | -282.07 | -291.66 | -57.97 |
| t_{Vmax-} (sec) | 34.04 | 34.03 | 34.04 | 34.05 | 34.05 | 34.05 |
| δ_{80%-} (%) | - | - | - | - | - | - |
| k_{eff} (kN/m) | 2320.1 | 3923.2 | 3317.5 | 2197.5 | 2930.3 | 2197.5 |
| δ_{axial failure} (%) | 3.44 | 2.16 | 2.39 | - | - | - |
| t_{axial failure} (sec) | 34.25 | 34.21 | 34.22 | - | - | - |

Figure 4-8 plots the achieved table motion, as well as the longitudinal acceleration responses at footing and story levels. It is observed that the peak acceleration at table level was increased from Test1 to Test2 by 17% at 34.12 seconds, and a similar increase was recorded in acceleration at inertial-mass level, slightly later at 34.23 seconds. However, the maximum acceleration at second-story level is approximately the same for the two tests. Figure 4-8 demonstrates that the accelerometers at first-story level recorded a significant acceleration spike up to 2.45g at 34.20 seconds in Test2. This corresponds to the time at which column B1 failed in shear followed by shear failure of other first-story columns (see Table 4-3). It is also the time step in which the peak axial load was recorded for column B1. While acceleration phasing was similar for the two tests at the table and footing levels, Figure 4-8 shows a significant divergence in phasing of acceleration at story levels. Damage to the frame during Test1 increased the period of structure which affected the phasing of the frame response.

However, it is observed that the time at which the peak acceleration was recorded, remained the same for both tests in all story levels.

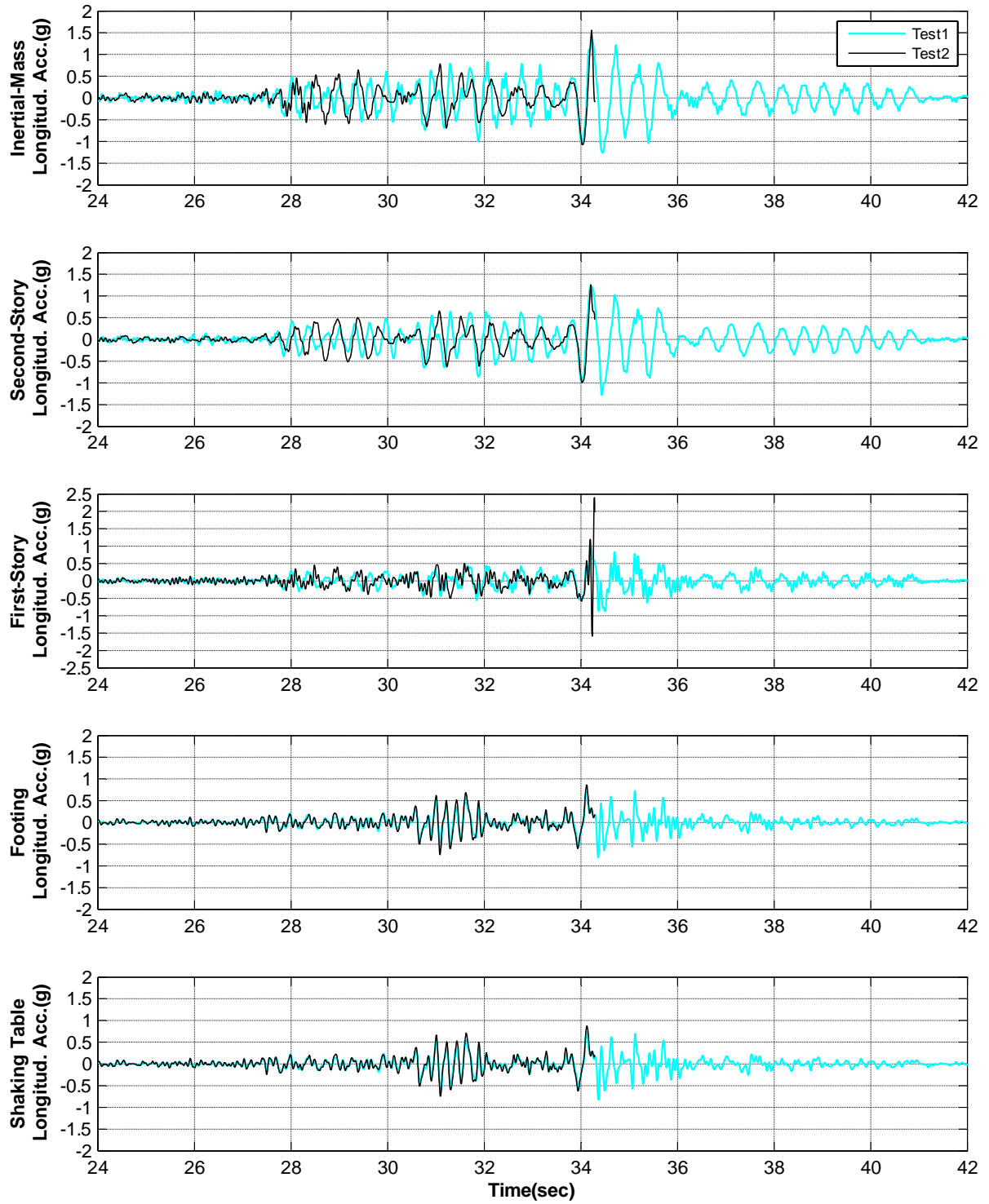


Figure 4-8. Story-level acceleration records for specimen MCFS, Test1 and Test2

Figure 4-9 plots inter-story drift ratio responses for the two story levels (i.e., differential movement between floors divided by the column clear height of 1.40 m), as well as the total drift ratio of the frame, which was obtained from dividing second-story lateral displacement by the height measured from top of the footing up to bottom of second-story beam (3.10 m for specimens MCFS and HCFS, and 3.11 m for specimens MUF and MUFS). It is observed that specimen MCFS experienced larger drifts in Test2, particularly in the time interval between 28 and 30 seconds. Figure 4-10 plots the minimum and maximum inter-story drift ratio profiles showing that the peak second-story drift remained smaller than the peak first-story drift in both tests. It is observed that the drift ratios in the positive and negative directions were nearly symmetric during Test1. On the other hand, damage to the frame in Test2, particularly in the positive direction, caused a concentration of deformations in the positive direction leading to collapse of the frame.

Figure 4-11 demonstrates the shear response histories of first-story columns as well as the base shear for Test1 and Test2. It is observed that except for the maximum peak shear and peaks in a time interval between 28.4 and 29.6 seconds, the peak column shear forces recorded during Test2 remained smaller than Test1. Shear demands were limited by yielding of first-story columns. After 34.05 seconds, similar shear values were observed for the two tests, until the maximum base shear of 223 kN was reached at 34.20 seconds. The specimen was not able to withstand the demands beyond this point in Test2 where shear failure of column B1 was initiated. Figure 4-12 plots the story shear hysteretic response of specimen MCFS for Test1 and Test2 and shows the softening of the frame stiffness due to damage sustained in Test1. Yielding of first-story columns during Test1 is observed at 0.9% drift ratio. Due to damage to

the columns during Test1, their initial stiffnesses in Test2 were lower than Test1 (see Table 4-3).

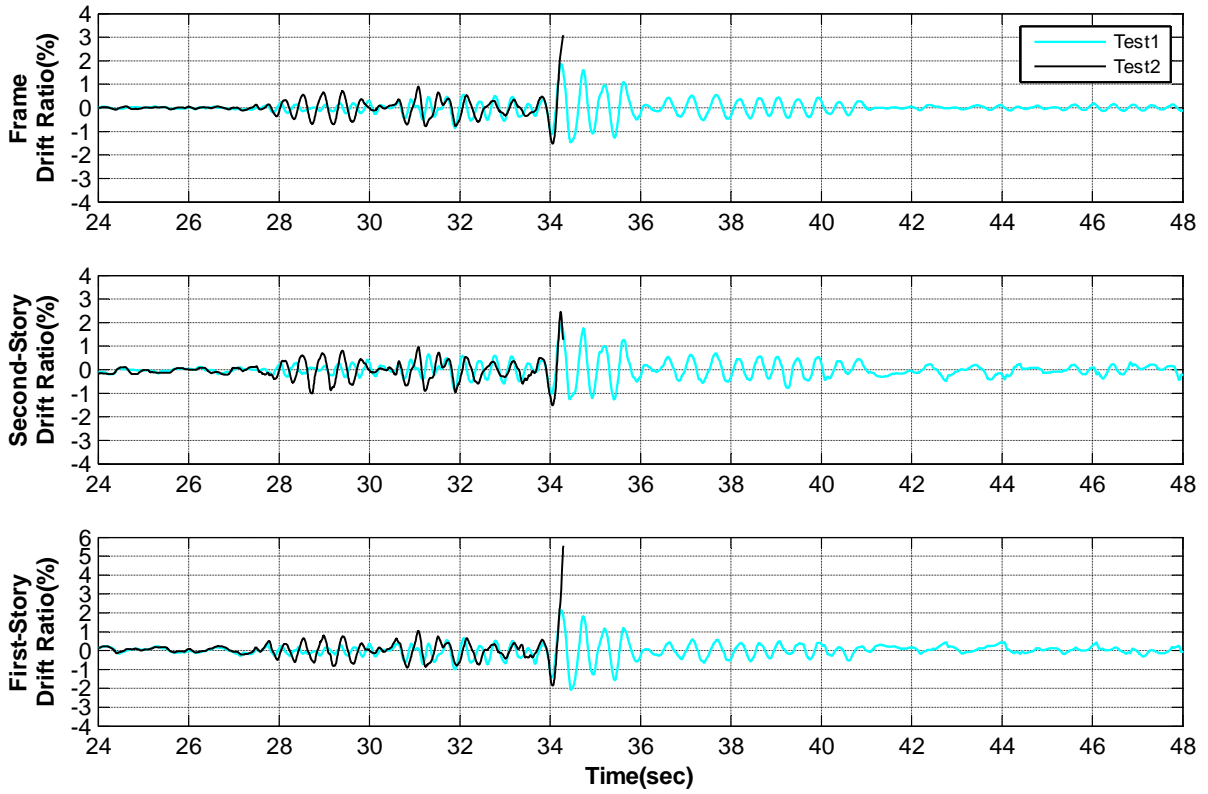


Figure 4-9. Story-level drift response history for specimen MCFS, Test1 and Test2

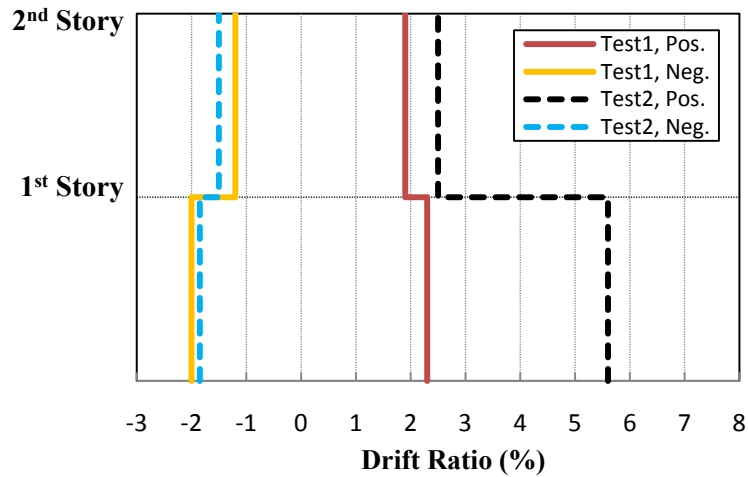


Figure 4-10. Minimum and maximum inter-story drift ratio profiles for specimen MCFS, Test1 and Test2

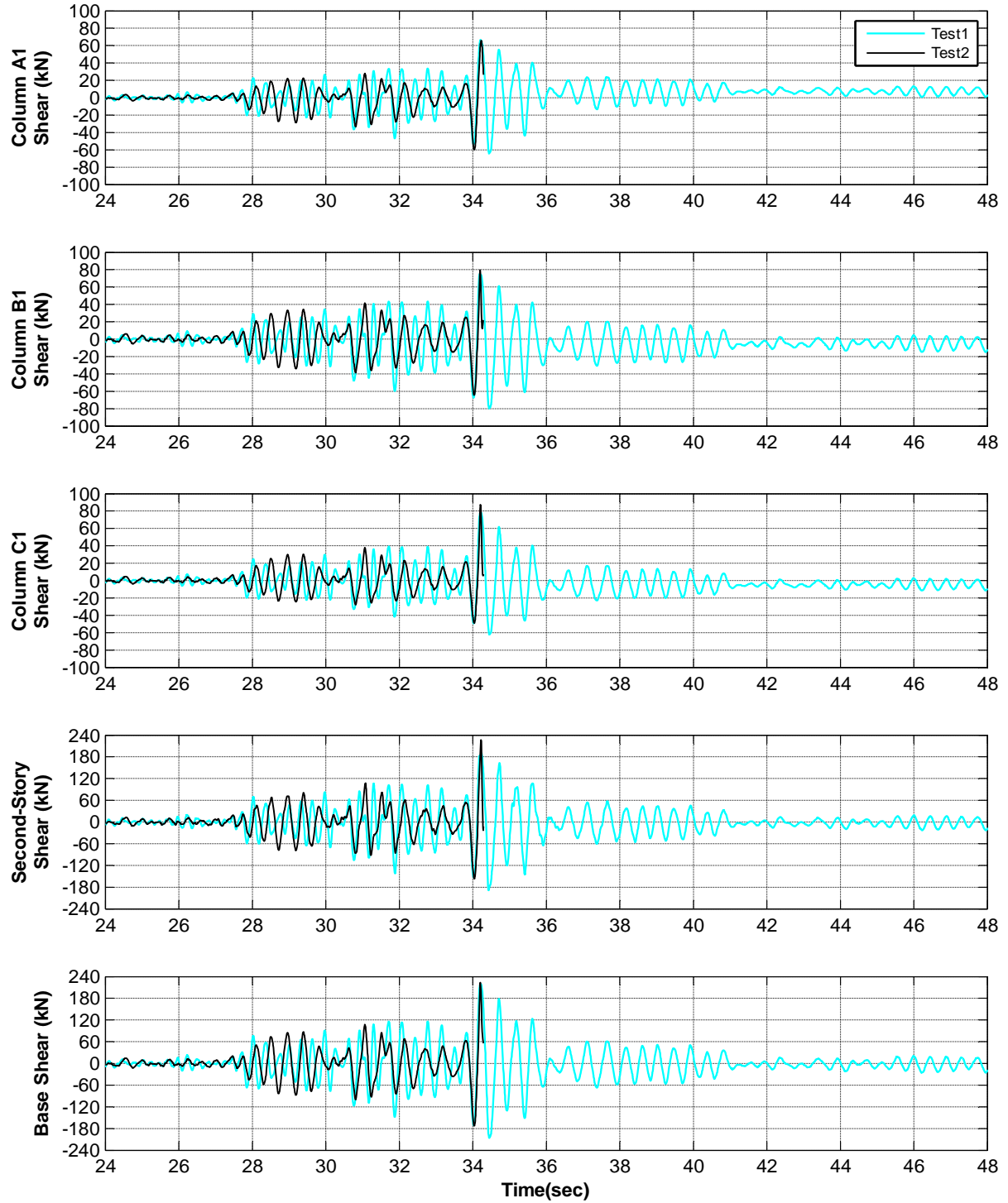


Figure 4-11. First-story columns and frame base shear histories for specimen MCFS, Test1 and Test2

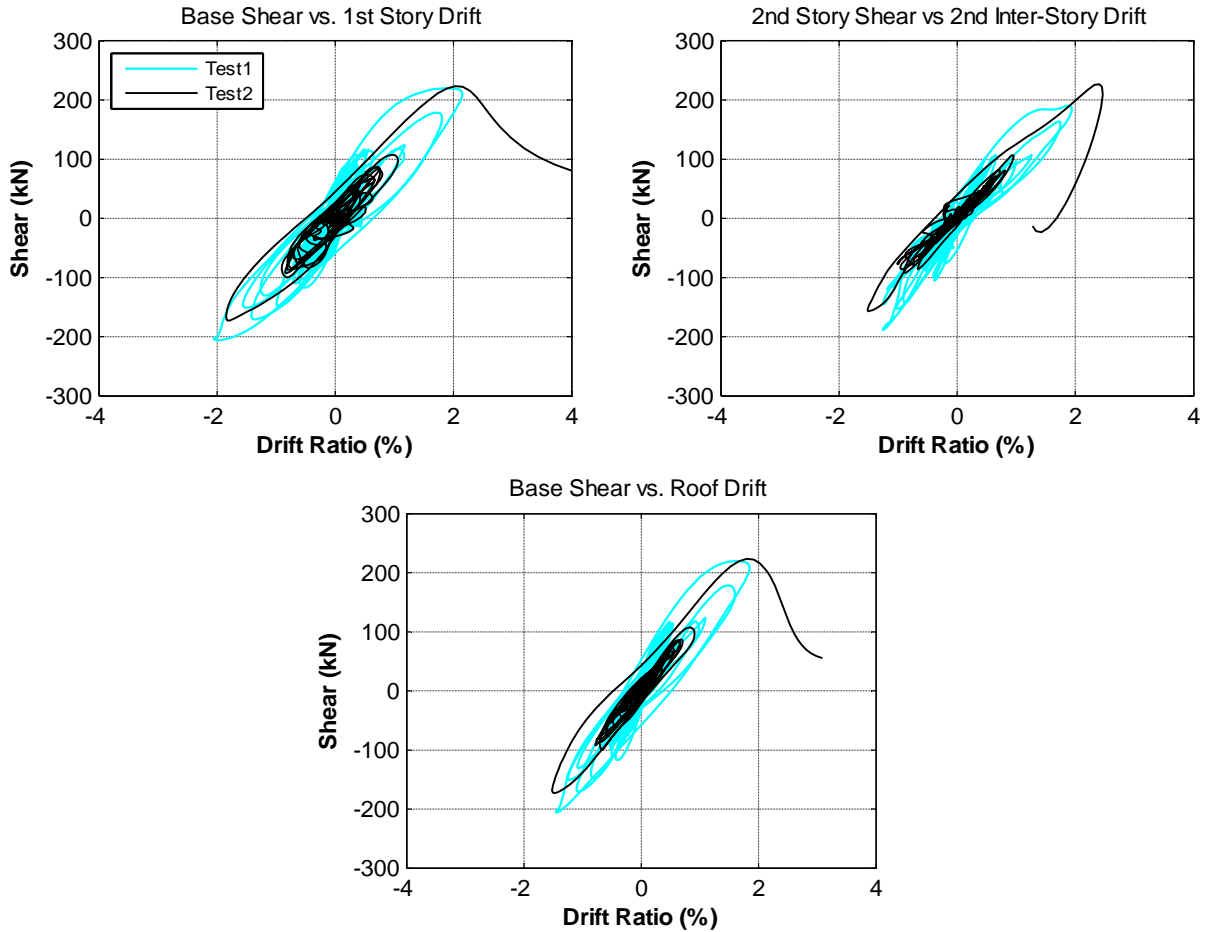


Figure 4-12. Story-level shear hysteretic response of specimen MCFS, Test1 and Test2

Observation of shear and axial load responses of the columns was one of the primary objectives of this experimental study. While Figure 4-13 plots the shear hysteretic response of the columns, Figure 4-14 to Figure 4-20 present other response quantities for the columns such as axial load and moments, in addition to the deformations measured by the instrumentation.

Figure 4-13 shows that shear strength degradation of first-story columns in Test2 started at 1.9% drift ratio for column B1, 2.2% for column C1, and 2.6% for column A1. This suggests that the center column (with axial load ratio of $P/A_g f'_c = 0.28$ at 1.9% drift ratio) experienced shear failure first, followed by exterior column C1 experiencing increased

compression ($P/A_g f'_c=0.26$) due to overturning, and finally column A1 with the lowest axial load ($P/A_g f'_c=0.08$) was the last to experience shear failure.

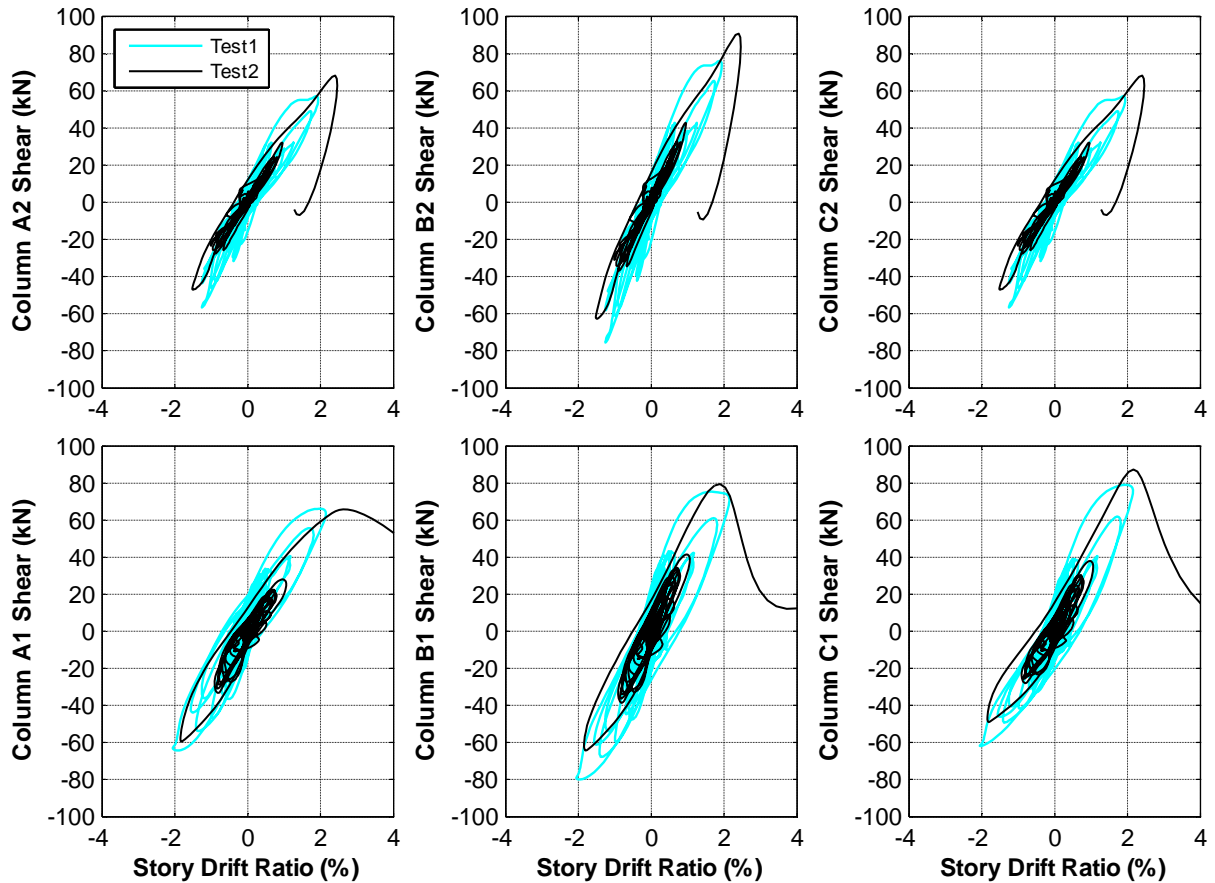


Figure 4-13. Shear hysteretic response of specimen MCFS columns, Test1 and Test2

Figure 4-14 and Figure 4-15 demonstrate the variation of axial load with time and hysteretic response of first-story columns during the two tests. As the direction of shaking reversed at 34.06 seconds of Test2, compression on column A1 decreased, while columns B1 and C1 started to pick up the load. The excessive load on the two columns at the peak table motion demand caused the axial failure of column B1 at 34.21 seconds, followed by axial failure of columns C1 and A1 at 34.22 and 34.25 seconds, respectively.

Maximum variation for axial load in column B1 was limited to 25% of the initial load in Test1 (95 kN at 34.2 seconds). However, the exterior columns A1 and C1 experienced much

larger variation in axial load resulting from overturning moment and fluctuation of applied pre-stress load. While the difference between maximum and initial axial load in column C1 was about 110% (173.7 kN at 34.2 seconds) during Test1, a maximum variation of 98% (160 kN) was recorded at 34.4 seconds for column A1.

While Figure 4-16 demonstrates the vertical displacement of the columns versus drift ratio during Test1 and Test2, Figure 4-17 plots the relationship between axial load and the vertical displacement of the first-story columns. The convex shape of the plots in Figure 4-16 is controlled by the lengthening and shortening of the column due to an increase in longitudinal strains over the length of the column resulting from flexural cracking. While the plot for the center column shows a nearly symmetric behaviour, effect of overturning moment can be observed by means of additional elongation or shortening of the exterior columns. A permanent elongation ratio of 0.02% (0.3 mm) was recorded for column B1 during Test1, whereas the ratio was limited to 0.01% (0.14 mm) for the exterior columns. As defined in Section 4.1, the initiation of axial failure is considered as the point at which the maximum vertical displacement is recorded. Figure 4-14 demonstrates that the axial failure of column B1 commenced at 2.03% drift ratio during Test2, while columns C1 and A1 failed at 2.39% and 3.44% drift ratios, respectively. These drift ratios and corresponding time instants were shown in Table 4-3, revealing the sequence of failure in first-story columns of specimen MCFS. Column B1 was the first column that experienced shear failure followed by axial failure. Shear and axial failure of column C1 took place later and at last, column A1 experienced shear failure leading to axial failure of the column and collapse of the frame.

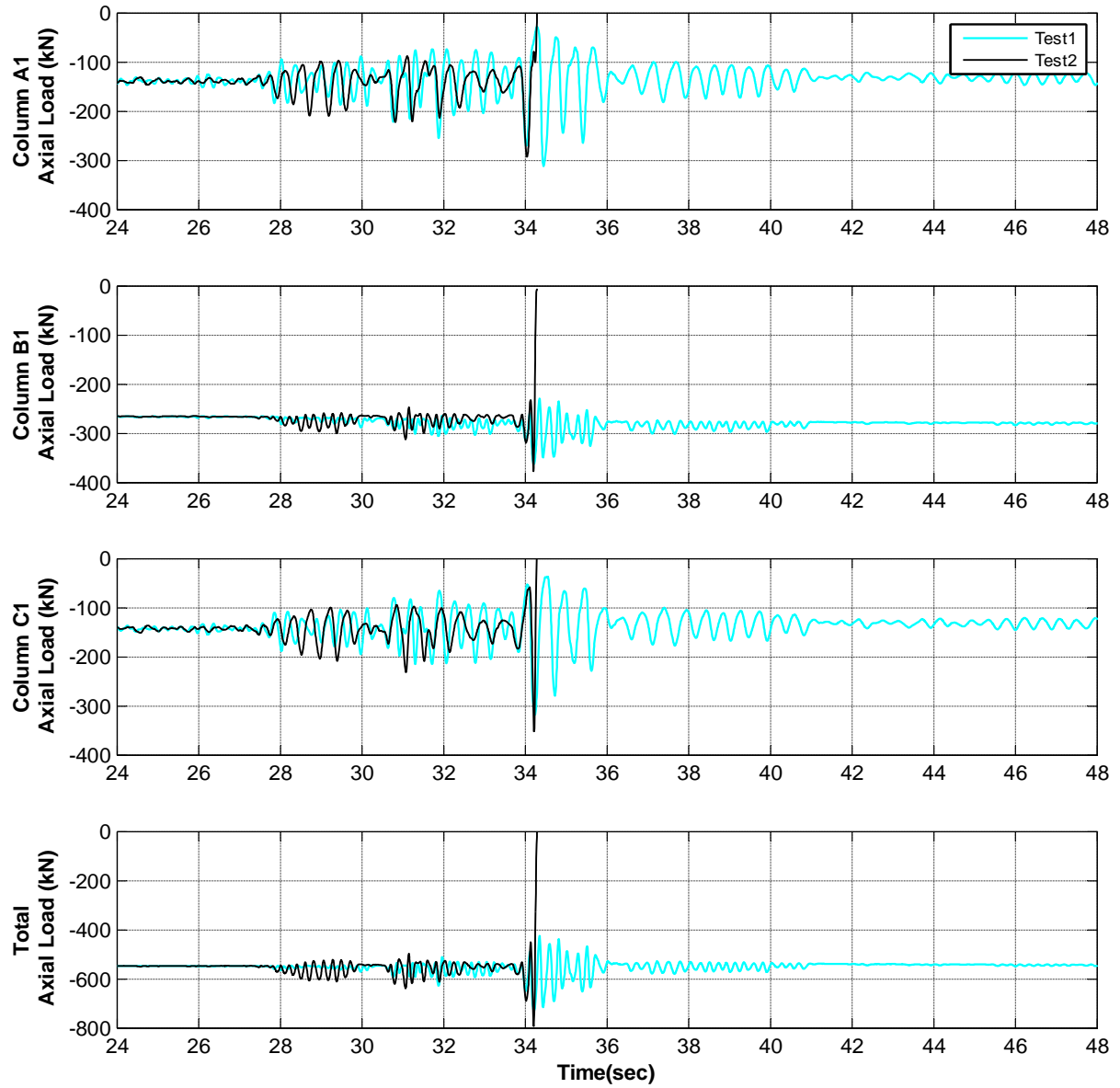


Figure 4-14. Axial load response history of first-story columns of specimen MCFS, Test1 and Test2

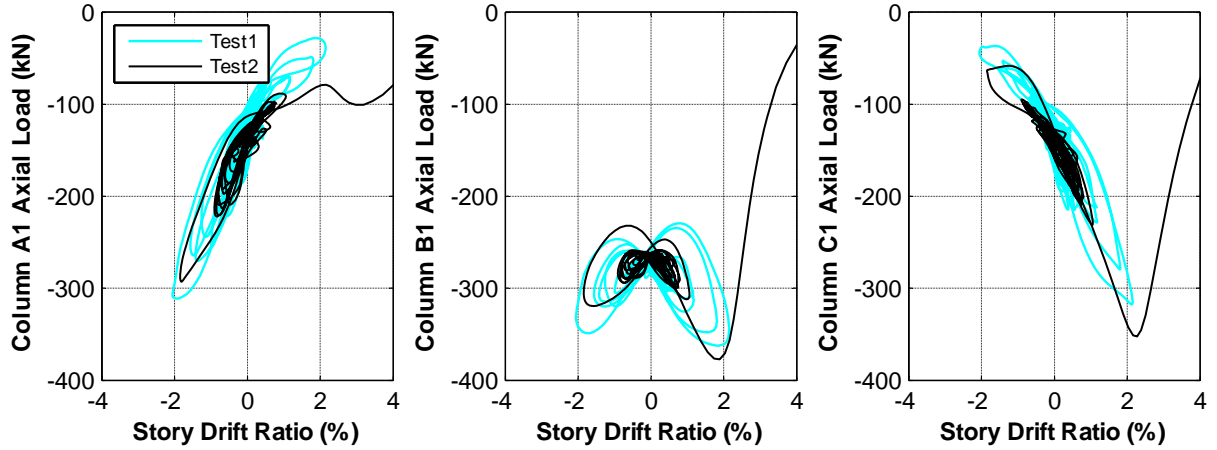


Figure 4-15. Axial load hysteretic response of first-story columns of specimen MCFS, Test1 and Test2

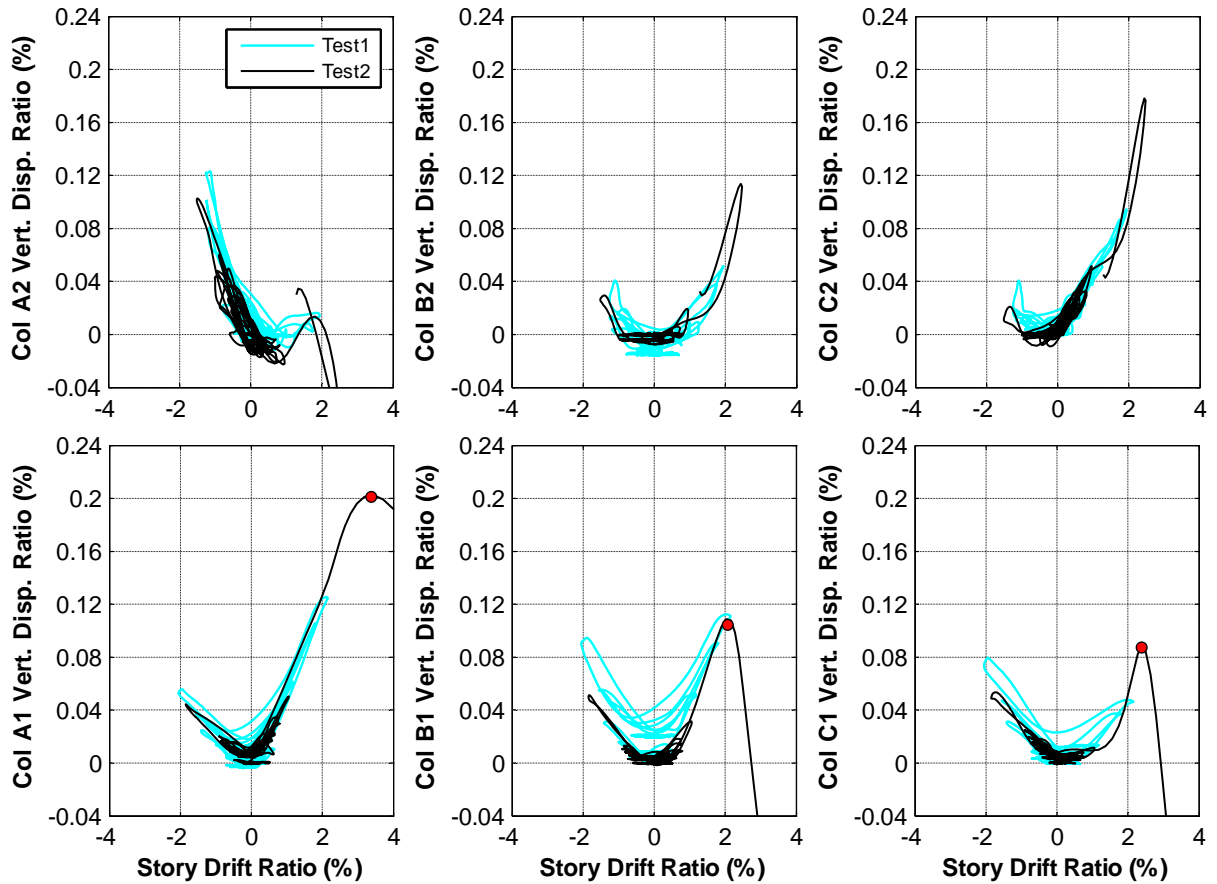


Figure 4-16. Vertical displacement ratio for columns of specimen MCFS, Test1 and Test2

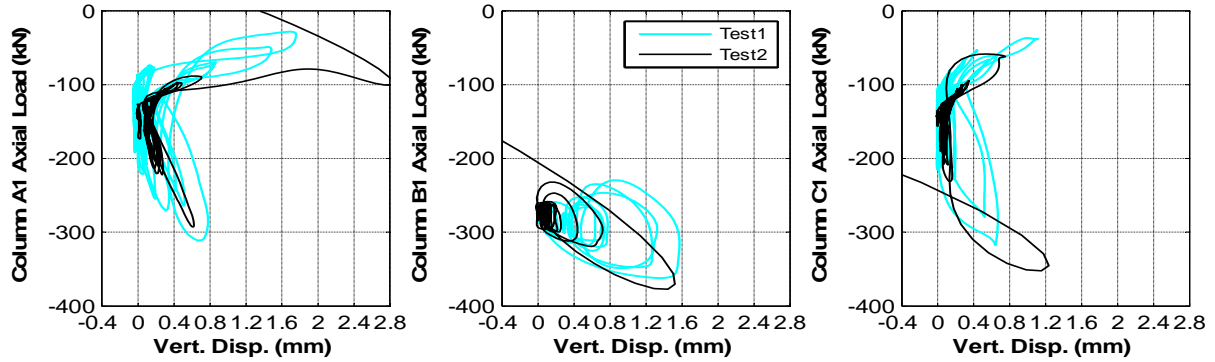


Figure 4-17. Variation of axial load of specimen MCFS columns with vertical displacement, Test1 and Test2

To account for the rotation of first-story joint blocks, column top chord rotation was used for the moment hysteretic response at the top of first-story columns. The chord rotation is defined as the angle between the chord connecting the column ends and the tangent at the member end (Figure 4-18a). Figure 4-18b illustrates that while the chord rotation at the base of a first-story column is equal to the story drift ratio, θ_{total} , the chord rotation at the top of the column should be considered as $\theta_{total} - \theta_j$, where θ_j is the rotation of the joint caused by the deformation of the connecting elements. Detail of measuring the joint rotation θ_j is shown in Appendix Section B.3.

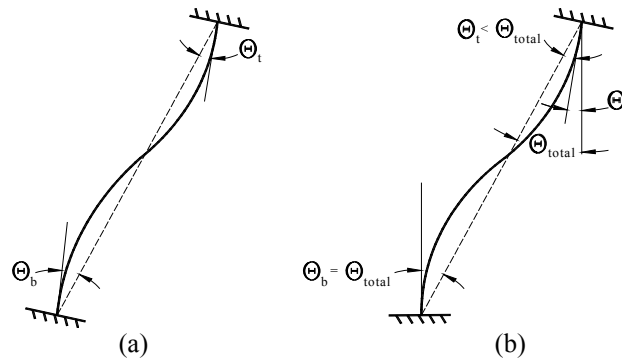


Figure 4-18. a) Definition of chord rotation; b) First-story column chord rotation at base and top

Contribution of deformation of first-story beams and columns in first-story drift ratio in elastic range, θ_{total} , can be obtained by calculating the relative stiffness ratio of those elements. While Equation 4.1 demonstrates the ratio of relative stiffness of elements at a connecting

joint, Equations 4.2 and 4.3 show the contribution of deformation of connecting columns and beams to the total inter-story drift ratio, respectively (Thermou and Panatazopoulou, 2011).

$$\lambda = \sum \left[\frac{EI_{beam}}{l_{beam}} \right] / \sum \left[\frac{EI_{col}}{l_{col}} \right] \quad (4.1)$$

$$\lambda_{col} = \lambda / (1 + \lambda) \quad (4.2)$$

$$\lambda_{beam} = 1 - \lambda_{col} \quad (4.3)$$

In the above-mentioned equations, EI_{beam} is the beam rigidity, EI_{col} is the column rigidity determined based on moment-curvature response at first yield, and l_{beam} and l_{col} are the beam and column spans, respectively. λ_{col} is the fraction of drift ratio due to column deformation and λ_{beam} is the portion of drift ratio due to beam deformation. Using the properties of first-story columns and beams, λ is calculated as 1.78 at first-story exterior joints of specimen MCFS, which results in a λ_{col} of 0.64 and a λ_{beam} of 0.36. On the other hand, due to significant rigidity of the footings, λ_{col} is equal to 1.0 at the column base. Subsequently, chord rotation at the top of first-story exterior columns can be estimated as $\theta_t = 0.64 \times (\Delta/h_c) < \theta_{total}$, whereas the column chord rotation at the base is $\theta_b = 1.0 \times (\Delta/h_c) = \theta_{total}$, where Δ is the story displacement and h_c is the height of the column. Comparison of θ_t and θ_b clearly shows a larger rotational demand at the column base, resulting in the expected failure of first-story columns at the base rather than the top. This is confirmed by observations from testing specimen MCFS where all first-story columns experienced shear and axial failure at the base. It should be noted that once either a beam or column has yielded, it accommodates more of the deformations and changes the rotation demands in all members. As it will be discussed in Section 5.6, column chord rotation can provide a better measurement of lateral demand on columns compared with story drift ratio. As mentioned earlier, chord rotation at the base of a first-story column is equal to inter-story drift ratio and larger than the chord rotation at the top-end. Note that chord rotations are

not available for the second story columns. To facilitate comparison with past testing and second story response, plots shown in this chapter will primarily use the column drift ratio.

Moment hysteretic response for the top and bottom ends of the first-story columns are shown in Figure 4-19 and Figure 4-20, respectively. Comparison of the figures reveals that the moments recorded for the top of first-story columns were not equal to the base moments. While the peak moments at the top of columns A1 and B1 were smaller than the corresponding moments at the base during Test1 (39% and 33%, respectively), top end of column C1 experienced 21% larger moment than the base. This suggests that the inflection points for columns A1 and B1 were moved toward the top, while the inflection point for column C1 was shifted toward the column base.

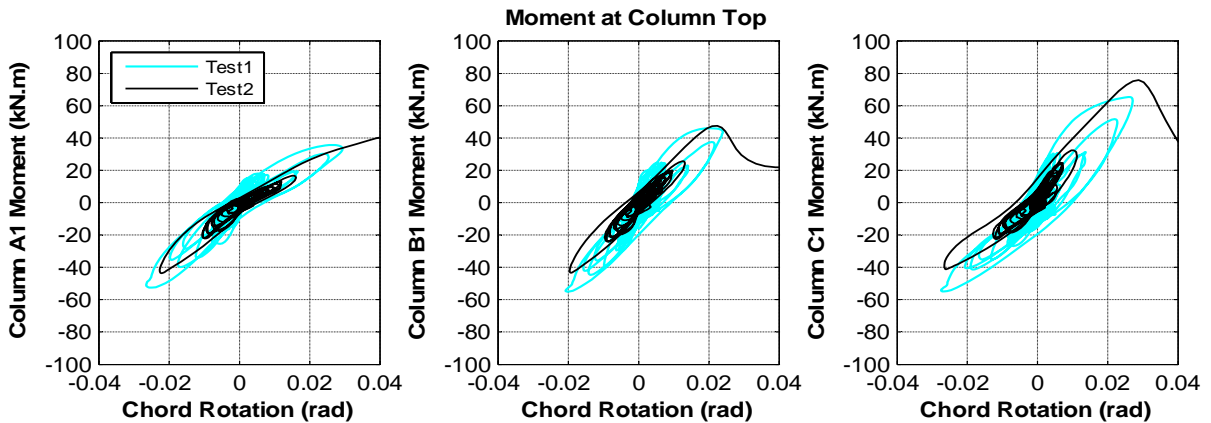


Figure 4-19. Moment-chord rotation relationship at top of first-story columns of specimen MCFS, Test1 and Test2

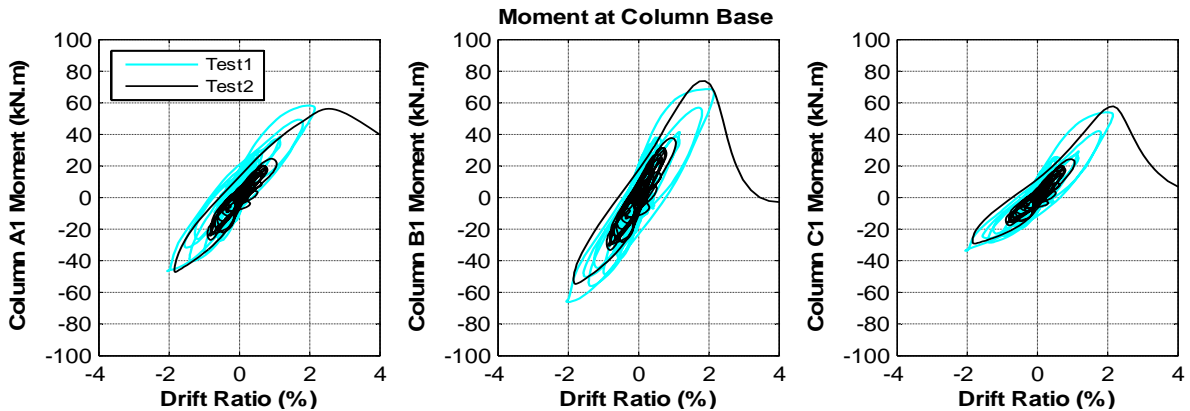


Figure 4-20. Moment hysteretic response of first-story columns of specimen MCFS at base, Test1 and Test2

In order to force the failure to happen only in the non-ductile columns of specimen MCFS, inelastic deformations were avoided at the joints by confining them thoroughly using transverse and end beam stubs, and additional hoops in the joint. To make certain that all possible deformations were captured, a complete set of instruments was used at joint C1 to measure any flexural and shear deformations of the joint (see Appendix Section B.3, for details of instrumentation). No shear or flexural crack was observed at the edges of the joints after Test1 or Test2, suggesting that the joints experienced very little local deformation during the tests. Data from the instrumentation of joint C1 also showed very limited deformations, with a maximum elastic shear deformation less than 0.001 rad recorded during Test2.

4.5 Behaviour of Specimen HCFS

Similar to specimen MCFS, confined joints and non-ductile columns were considered for test frame HCFS. The only difference was the applied axial load on the columns, where the pre-stressed axial load on the columns of specimen HCFS was almost twice the applied axial load for specimen MCFS (Table 3-2). This provides the opportunity to study the effect of high axial load on performance of non-ductile frames (see Chapter 5).

Figure 4-21 compares the spectral accelerations for Test1 and Test2 table motions, while Figure 4-22 plots the displacement response spectra for the two tests. It is observed that the spectral acceleration demand at the initial fundamental period of the specimen in Test1 (2.7g) was increased by 28% in Test2. As shown in Table 4-1, the natural period of the specimen was increased from 0.28 seconds (dashed line) to 0.36 seconds (dotted line) due to damage to the frame during Test1. Figure 4-21 demonstrates that the spectral acceleration demand at the new period for Test2 (2.8g) was only 4% higher than the observed spectral acceleration at the initial period for Test1.

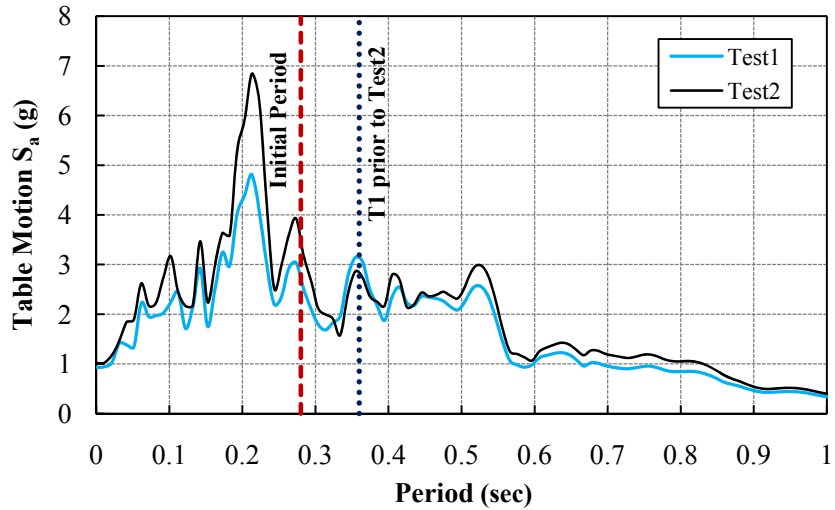


Figure 4-21. Comparison of spectral acceleration with 2% damping for Test1 and Test2 table motions, Specimen HCFS

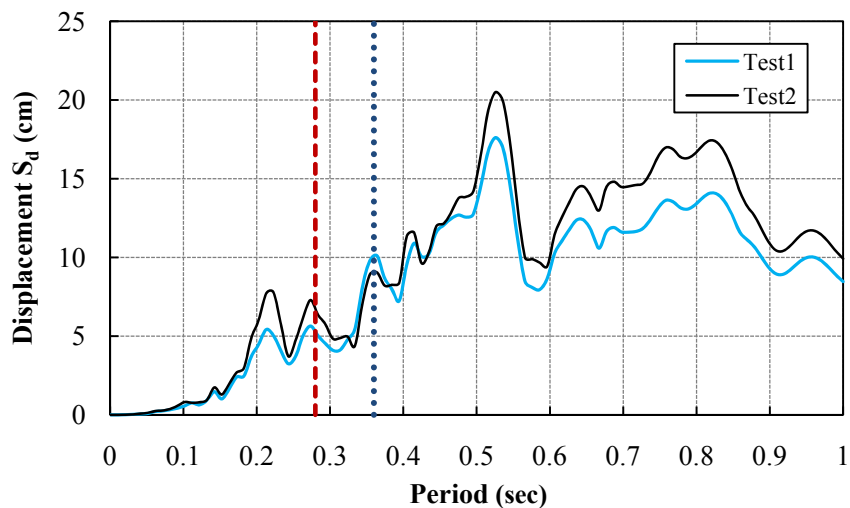


Figure 4-22. Comparison of displacement response spectra with 2% damping for Test1 and Test2 table motions, Specimen HCFS

Figure 4-23 shows the flexural and shear cracks in the columns of specimen HCFS after Test1. Note that all cracks on the exterior columns (except the crack at the top of column A1) occurred during the transportation phase (maximum width of 0.1 mm). Limited flexural cracks were seen at the top end of columns A1 and B2 after Test1 (maximum width of 0.1 mm). None of the columns experienced severe shear damage, yet few diagonal cracks with maximum

width of 0.3 mm were observed only at the base of Column B1 after Test1 (Figure 4-23b). While Figure 4-23b also demonstrates limited vertical bond cracks at the column base, no significant cracks were observed elsewhere.

Figure 4-24 demonstrates minor cracks in first-story beams near the exterior joints with maximum width of 0.1 mm. While beams in specimen MCFS remained uncracked during Test1, the beam cracking in specimen HCFS suggests slight beam yielding due to higher capacity of columns from higher axial loads.

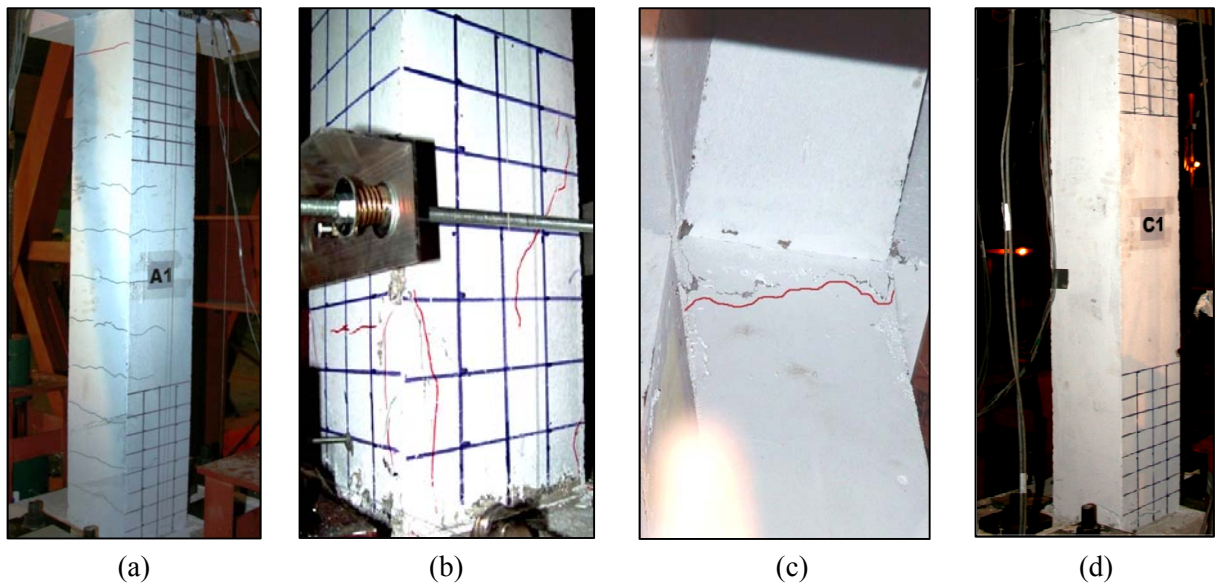


Figure 4-23. Shear and flexural cracks in columns of specimen HCFS after Test1; a) column A1; b) base of column B1; c) top of column B2; d) column C1



Figure 4-24. Cracks in beams after Test1; a) near joint C1; b) near joint A1

Failure mechanism of specimen HCFS was rather complicated due to the influence of high axial load on the columns. Unlike specimen MCFS, specimen HCFS suffered from damage in both levels, where collapse of the frame in Test2 resulted from failure of columns B1 and C1 in the first story, as well as column A2 in the second story. The failure mode for specimen HCFS during Test2 is shown in Figure 4-25. Due to the high axial loads imposed on column line B, axial failure of column B1 occurred right after shear failure and sudden shortening of the column was observed. Such rapid axial deformation in column B1 caused large flexural cracks in the connecting beams in the first story. Such nonlinear beam deformation accommodated the shortening of column B1 to some extents resulting in reduction of deformation demand on columns A1 and C1. Consequently, the first-story exterior columns survived to the next cycle, where redistribution of axial load from columns on line B, in addition to the local deformation at top of column A2, caused shear and axial failure of column A2. It should be noted that the local deformation at top of column A2 due to shortening of column B added to the deformation from lateral response, while the deformation at the top of column C2 due to shortening of column line B counterbalanced the deformation due to lateral response. Finally, axial failure of column C1 led to collapse of the frame. Employing the definition for axial failure described in Section 4.1, column B1 failed at 34.23 seconds, followed by failure of columns A2 and C1 at 35.41 and 35.76 seconds, respectively (Table 4-5). Figure 4-26 shows the state of these columns after Test2. Details of the steps that led to collapse of the frame will be discussed later in this section using the recorded data.

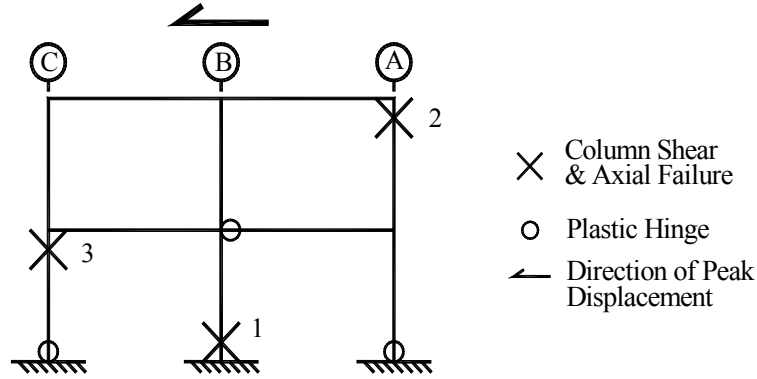


Figure 4-25. Failure mode of specimen HCFS (sequence of failure shown by numbers)

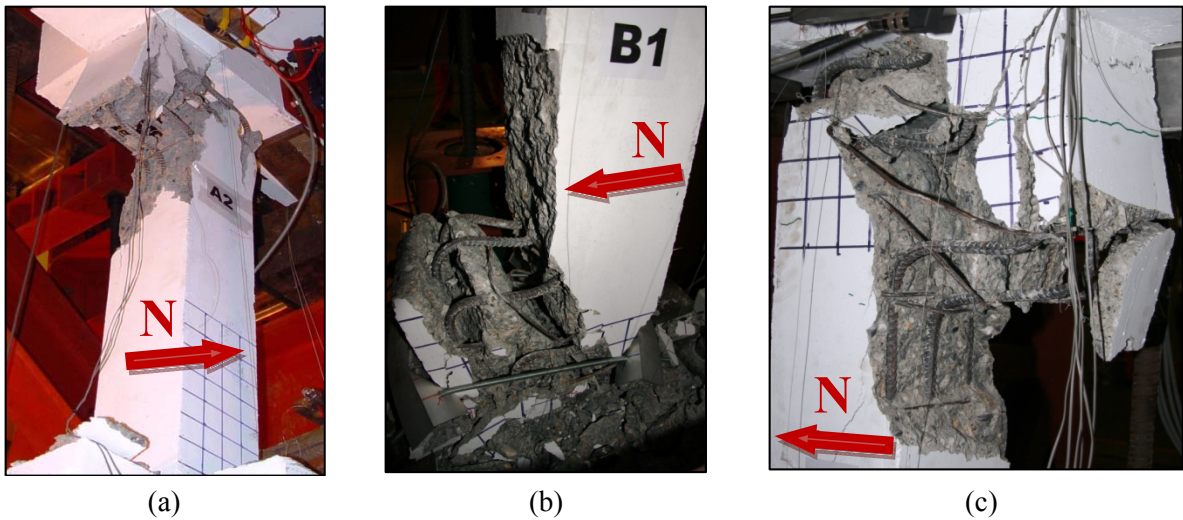


Figure 4-26. Failure of columns of specimen HCFS, Test2; a) column A2; b) column B1; c) column C1

Maximum recorded shear for the columns and corresponding drifts, axial loads, and time steps in the positive and negative directions of Test1 and Test2 are shown in Table 4-4 and Table 4-5, respectively (see Figure 4-1 for details). Since columns did not experience significant shear degradation during Test1, drift at 20% shear loss, $\delta_{80\%}$, was not reached during that test. On the other hand, Table 4-5 demonstrates that columns B1 and C1 experienced more than 20% shear strength loss in the positive direction of Test2.

Table 4-4. Critical parameters for columns of specimen HCFS, Test1

| | A1 | B1 | C1 | A2 | B2 | C2 |
|-------------------------|---------|---------|---------|---------|---------|---------|
| $V_{\max+}$ (kN) | 48.50 | 95.13 | 71.86 | 57.03 | 76.04 | 57.03 |
| $\delta_{V\max+}$ (%) | 1.68 | 1.76 | 1.68 | 1.78 | 1.78 | 1.78 |
| $P_{V\max+}$ (kN) | -155.08 | -551.96 | -414.35 | -131.70 | -531.78 | -408.16 |
| $t_{V\max+}$ (sec) | 34.18 | 34.19 | 34.18 | 34.20 | 34.20 | 34.20 |
| $\delta_{80\%+}$ (%) | - | - | - | - | - | - |
| $V_{\max-}$ (kN) | -75.95 | -69.47 | -68.36 | -57.39 | -76.52 | -57.39 |
| $\delta_{V\max-}$ (%) | -2.14 | -1.69 | -2.09 | -0.88 | -0.88 | -0.88 |
| $P_{V\max-}$ (kN) | -420.12 | -548.69 | -160.77 | -413.47 | -529.78 | -158.03 |
| $t_{V\max-}$ (sec) | 34.46 | 34.42 | 34.45 | 34.43 | 34.43 | 34.43 |
| $\delta_{80\%-}$ (%) | - | - | - | - | - | - |
| k_{eff} (kN/m) | 2822.3 | 6393.9 | 4634.2 | 4162.8 | 5550.6 | 4162.8 |

Table 4-5. Critical parameters for columns of specimen HCFS, Test2

| | A1 | B1 | C1 | A2 | B2 | C2 |
|-------------------------------------|---------|---------|---------|---------|---------|---------|
| $V_{\max+}$ (kN) | 58.28 | 86.46 | 81.59 | 60.12 | 80.17 | 60.12 |
| $\delta_{V\max+}$ (%) | 2.40 | 2.40 | 2.40 | 2.61 | 2.61 | 2.61 |
| $P_{V\max+}$ (kN) | -170.43 | -590.90 | -444.70 | -149.03 | -497.23 | -431.65 |
| $t_{V\max+}$ (sec) | 34.22 | 34.22 | 34.22 | 34.24 | 34.24 | 34.24 |
| $\delta_{80\%+}$ (%) | - | 2.73 | 3.56 | - | - | - |
| $V_{\max-}$ (kN) | -74.87 | -64.19 | -63.96 | -47.34 | -63.13 | -47.34 |
| $\delta_{V\max-}$ (%) | -1.66 | -1.54 | -2.46 | -1.34 | -1.34 | -1.34 |
| $P_{V\max-}$ (kN) | -464.01 | -544.84 | -281.93 | -399.97 | -523.61 | -168.19 |
| $t_{V\max-}$ (sec) | 34.52 | 34.04 | 34.59 | 34.04 | 34.04 | 34.04 |
| $\delta_{80\%-}$ (%) | - | - | - | - | - | - |
| k_{eff} (kN/m) | 2267.3 | 4260.5 | 2648.0 | 2847.3 | 3796.5 | 2847.3 |
| $\delta_{\text{axial failure}}$ (%) | - | 2.60 | 0.33 | 0.35 | - | - |
| $t_{\text{axial failure}}$ (sec) | - | 34.23 | 35.76 | 35.41 | - | - |

Figure 4-27 plots the recorded table motion and longitudinal acceleration response history at footing and story levels for Test1 and Test2. The peak acceleration of 0.91g was recorded for the first story at 34.2 seconds of Test1, whereas the second story experienced

higher peak acceleration of 1.4g at the same time. Figure 4-27 also demonstrates that the accelerometers at first-story level recorded a peak acceleration of 1.7g at 34.30 seconds of Test2, while the acceleration of the second story peaked earlier at 34.2 seconds. Acceleration phasing was similar for the two tests at table and footing levels. However, a significant divergence in phasing and amplitude is observed for acceleration records at story levels, where softening of the frame stiffness influenced the response.

As shown in Figure 4-27, two spikes were observed in the acceleration data recorded for first-story level at 34.30 and 35.48 seconds of Test2. To study this better, Figure 4-28 plots the acceleration records for the first story between 32.0 and 36.0 seconds. Diamond, star, and square markers in Figure 4-28 refer to onset of axial failure for columns B1, A2, and C1, respectively. These markers will be used throughout the section on specimen HCFS. It is observed that the first and second spikes were recorded 0.07 seconds after the initiation of axial failure of columns B1 and A2, respectively. This suggests that the columns did not suddenly lose all their axial load capacity after the onset of axial failure and there was a very small time gap between the initiation of axial failure and crushing of the column end.

Figure 4-29 compares the inter-story drift ratios that specimen HCFS experienced during Test1 and Test2, while Figure 4-30 demonstrates the minimum and maximum inter-story drift ratio profile for the specimen. It is observed that the specimen underwent much larger drifts during Test2, where the peak drift ratio for the first story (at 34.3 seconds) was twice the peak drift ratio recorded in Test1.

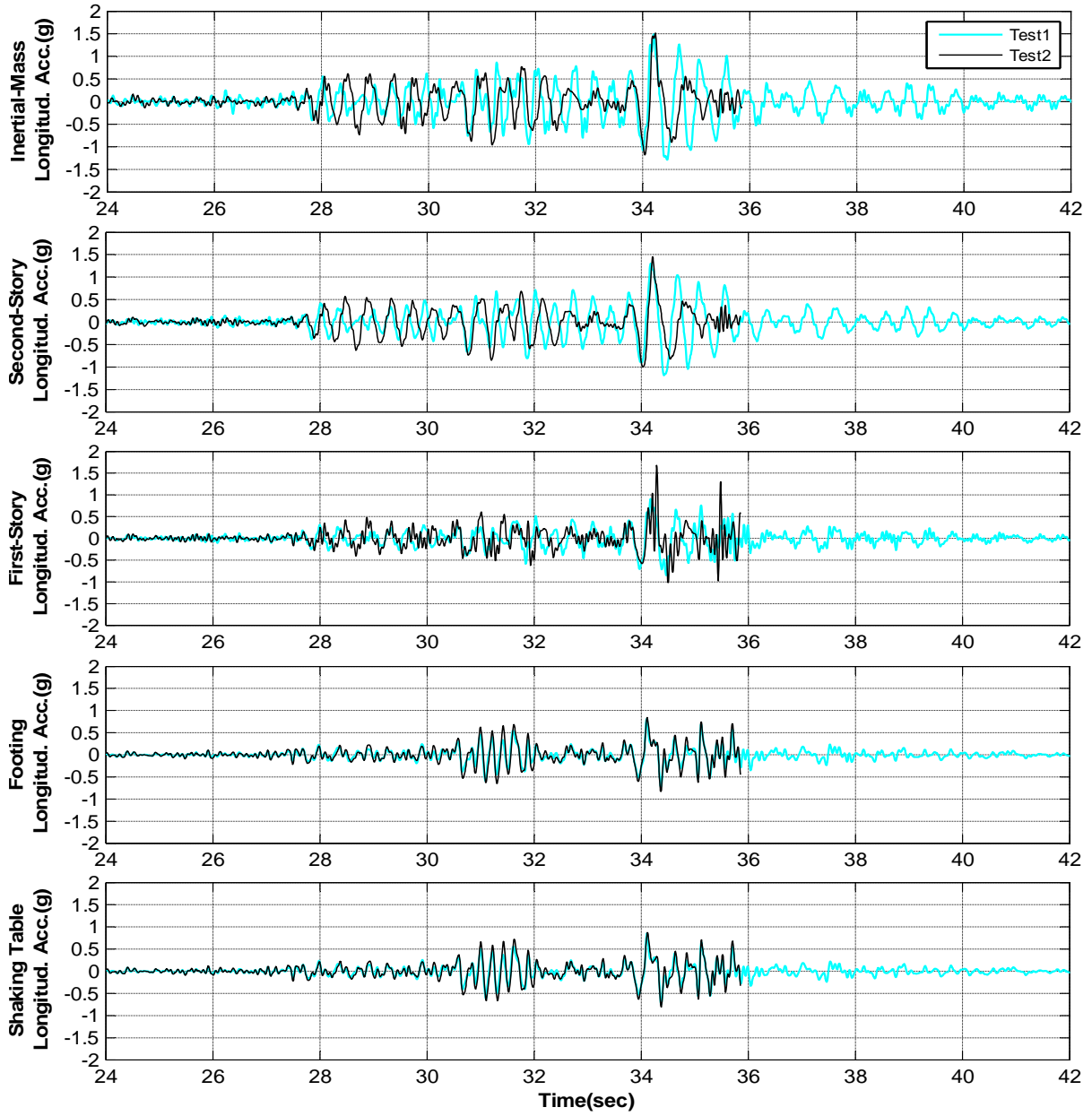


Figure 4-27. Story-level acceleration records for specimen HCFS, Test1 and Test2

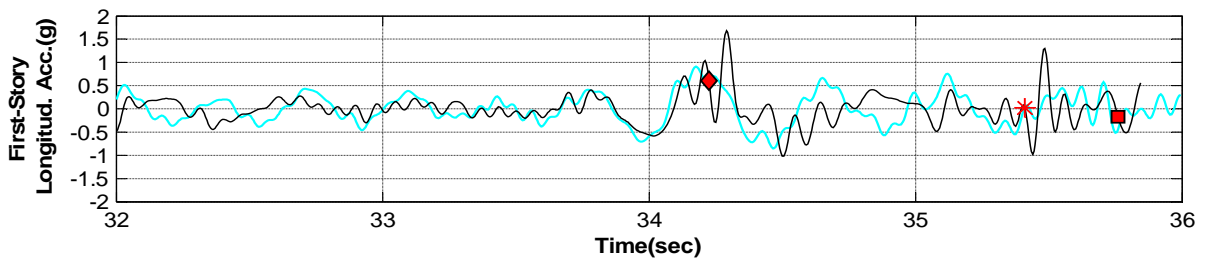


Figure 4-28. First-story acceleration records for specimen HCFS, Test1 and Test2, $32 < t < 36$ seconds

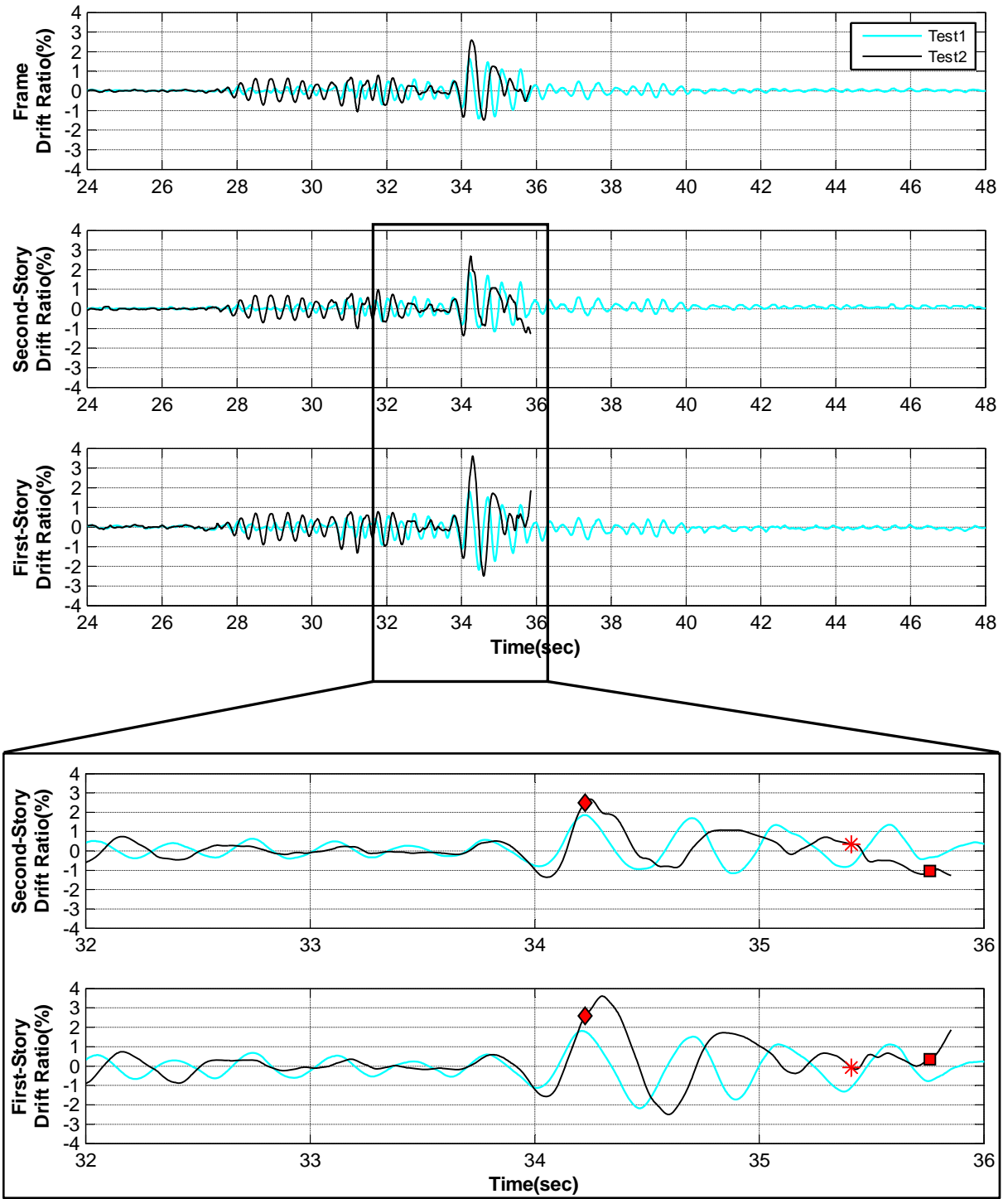


Figure 4-29. Story-level drift response history for specimen HCFS, Test1 and Test2

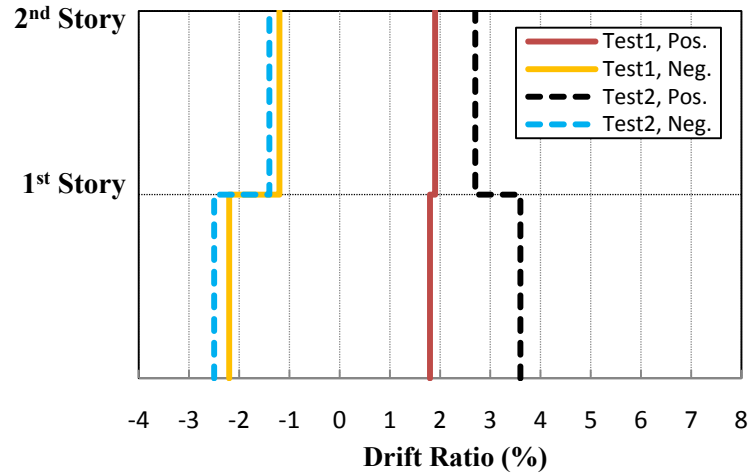


Figure 4-30. Minimum and maximum inter-story drift ratio profiles for specimen HCFS, Test1 and Test2

Figure 4-31 plots the shear response histories of the first-story columns and the frame base shear for Test1 and Test2. The maximum base shears of 216 kN at 34.15 seconds and 227 kN at 34.21 were recorded during Test1 and Test2, respectively. Shear degradation in column B1 and C1 started at 34.22 seconds of Test2, leading to axial failure of column B1.

Figure 4-32 compares the story shear hysteretic response of the frame for Test1 and Test2. While no significant shear degradation was observed during Test1, first-story shear resistance for Test2 noticeably degraded after a first-story drift ratio of 2.4%. This is the same drift ratio at which degradation of shear strength of column B1 was initiated.

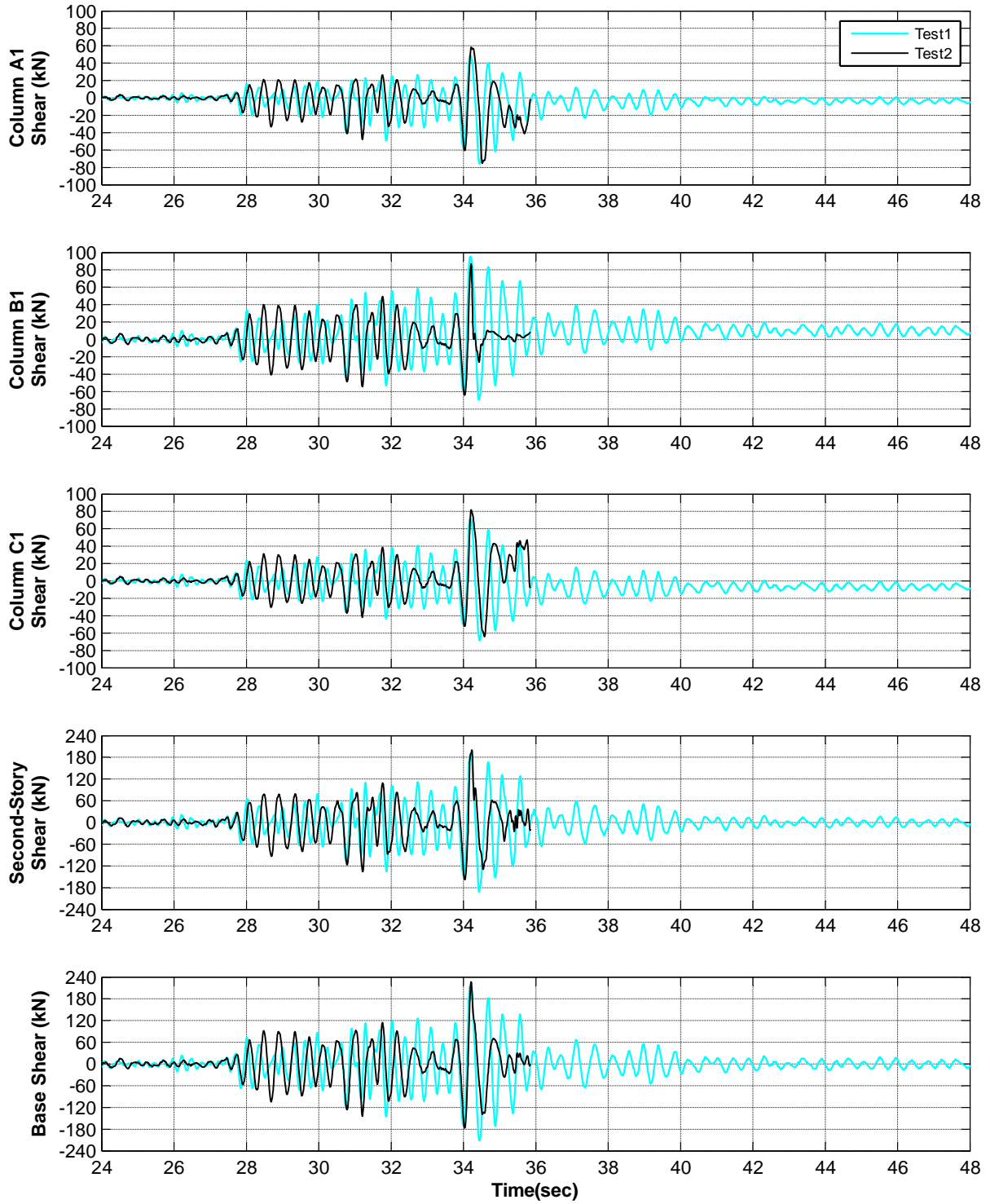


Figure 4-31. First-story columns and frame base shear histories for specimen HCFS, Test1 and Test2

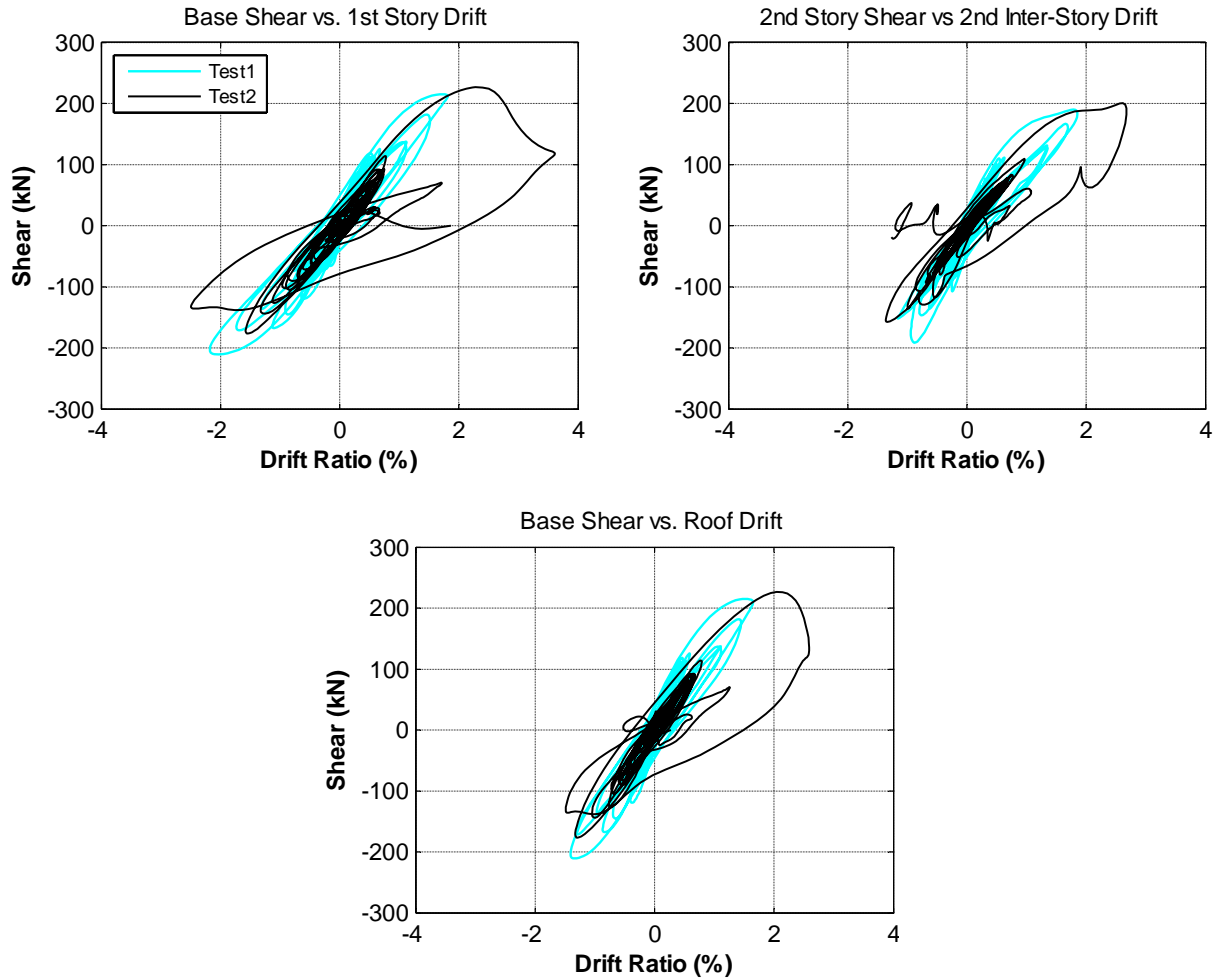


Figure 4-32. Story-level shear hysteretic response of specimen HCFS, Test1 and Test2

Figure 4-33 plots the shear hysteretic response of the columns during Test1 and Test2, while Figure 4-34 demonstrates only the cycles between 32.0 and 36.0 seconds of the tests. As discussed in Appendix Section B.4, shear response of second-story columns could not be captured directly using the instrumentation and therefore, Figure 4-33 and Figure 4-34 plot only an estimate of the shear hysteretic response of those columns. Figure 4-33 shows slight shear degradation for column B1 at 1.8% drift ratio in the negative direction of Test1 (marked by circle marker). The cracks shown in Figure 4-23b can be the source for such degradation. Figure 4-33 also reveals that while no significant loss of shear resistance was recorded for the

columns during Test1, column B1 experienced substantial shear degradation leading to shear failure after 2.4% drift ratio in Test2. Column C1 also suffered from shear degradation after 2.4% drift ratio in Test2, however, the column did not lose all shear resistance and withstood the lateral demand in that cycle. Although column A1 yielded during Test2, it did not fail during the test.

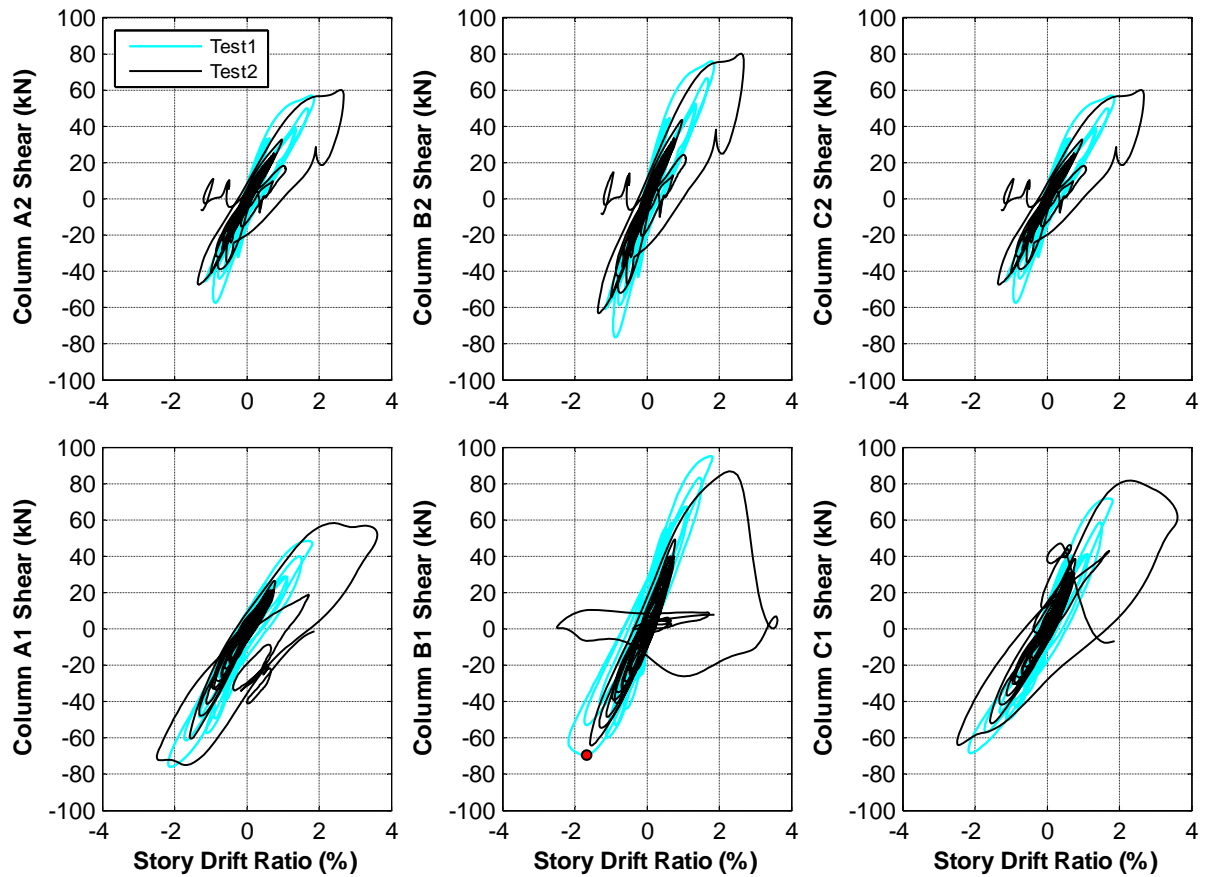


Figure 4-33. Shear hysteretic response of specimen HCFS columns, Test1 and Test2

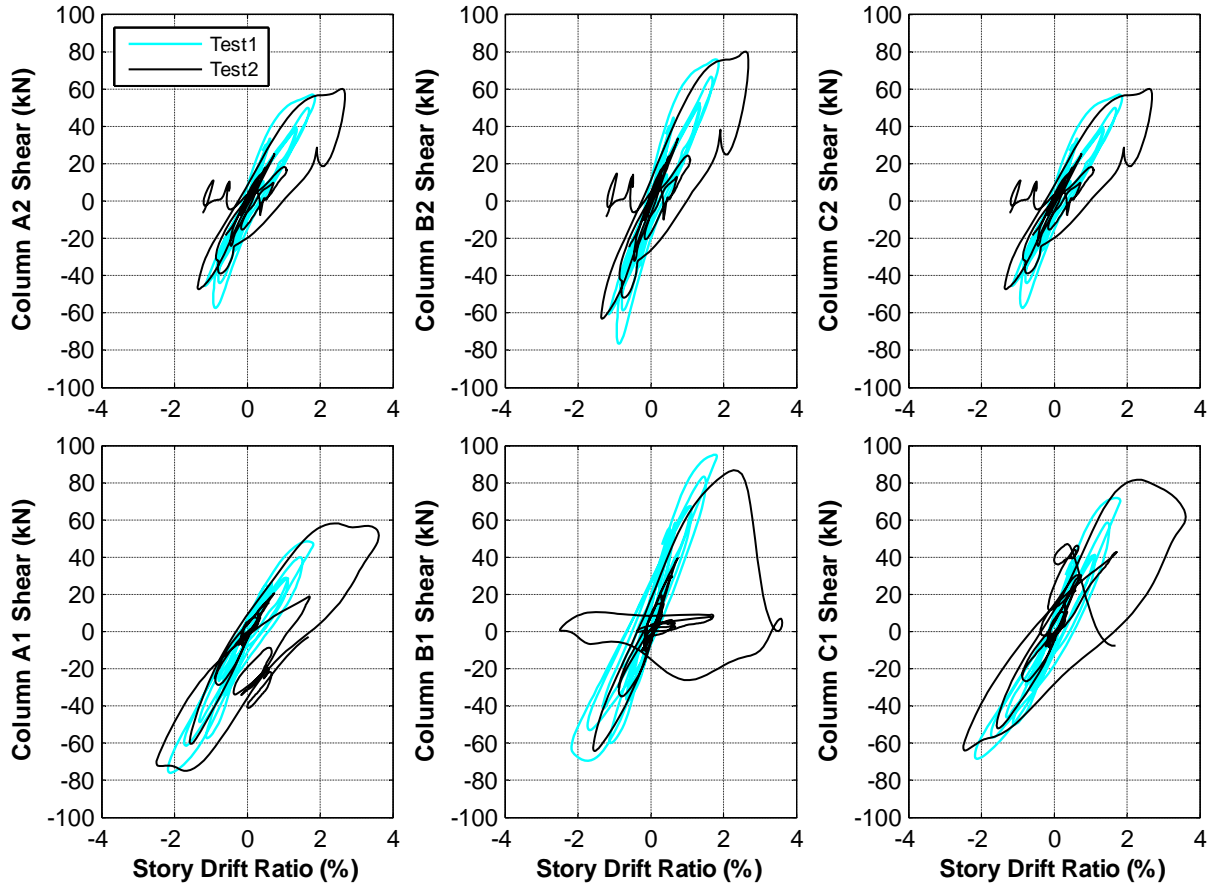


Figure 4-34. Shear hysteretic response of specimen HCFS columns, Test1 and Test2, $32 < t < 36$ seconds

Figure 4-35 and Figure 4-36 demonstrate the variation of axial load with time and hysteretic response of first-story columns during Test1 and Test2. Similar to Figure 4-28, diamond, star, and square markers in Figure 4-35 refer to onset of axial failure for columns B1, A2, and C1, respectively. It is observed that the maximum difference between peak and initial axial load in column B1 was only 10% of the initial during Test1 (53 kN at 34.2 seconds, Test1). However, due to effects of overturning moment, the difference between the maximum experienced and initial axial load was much larger for exterior columns A1 and C1. While the difference between the maximum and initial axial loads in column C1 during Test1 was about 38% (165.3 kN at 34.2 seconds), the maximum difference of 64% (170.2 kN) was recorded at

34.4 seconds for axial load in column A1. Figure 4-36 shows that while the sudden drop in axial load in column B1 started at 2.4% drift (shear failure of the column), rapid loss in axial loads of columns A1 and C1 occurred at -0.1% and 0.33% drift ratios, respectively. It should be noted that the point of sudden drop in axial load of column A1, shown in Figure 4-36, corresponds to loss of axial load capacity in column A2. However, axial failure of column A2 was recorded at 0.35% second-story drift ratio.

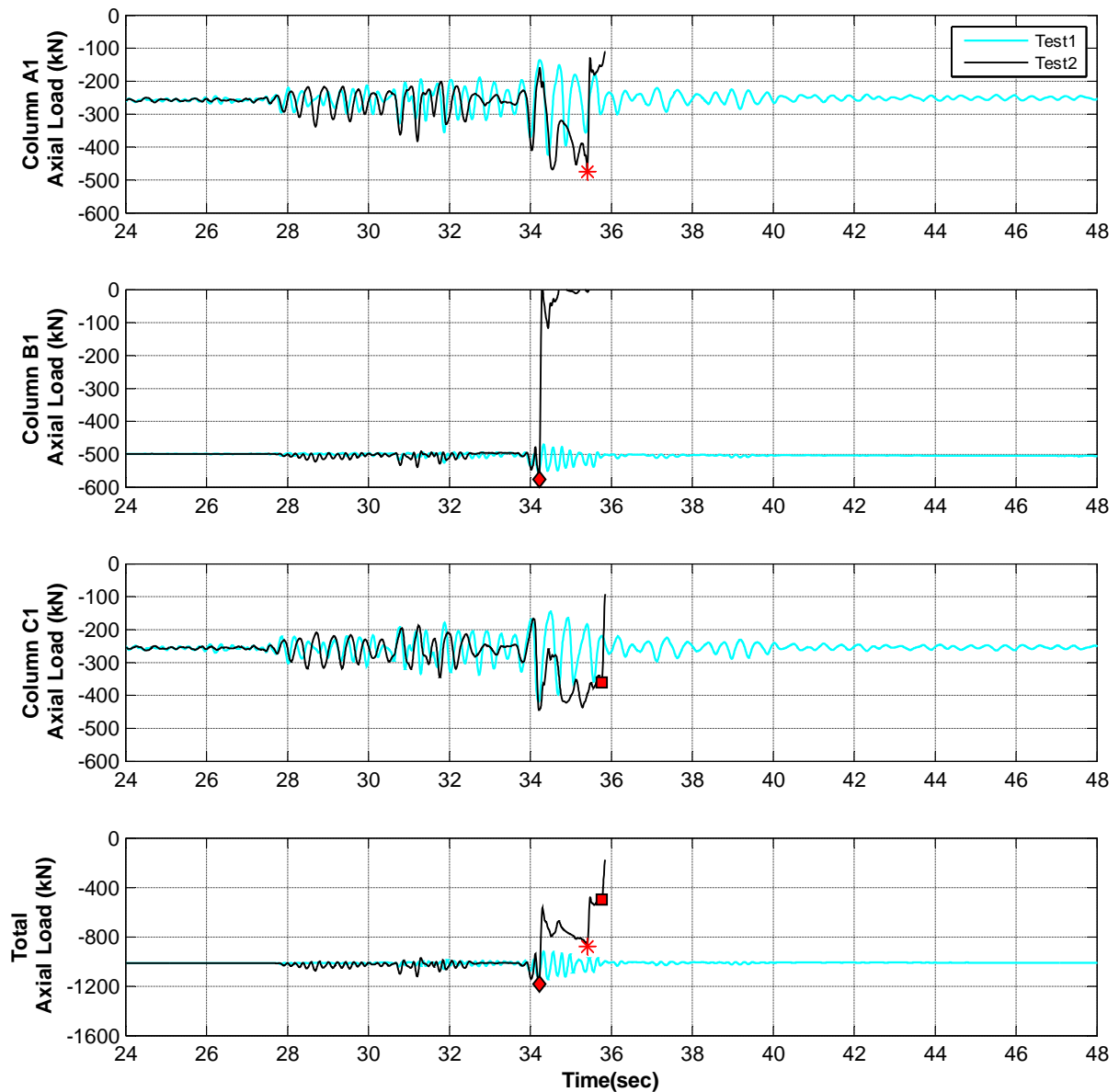


Figure 4-35. Axial load response history of first-story columns of specimen HCFS, Test1 and Test2

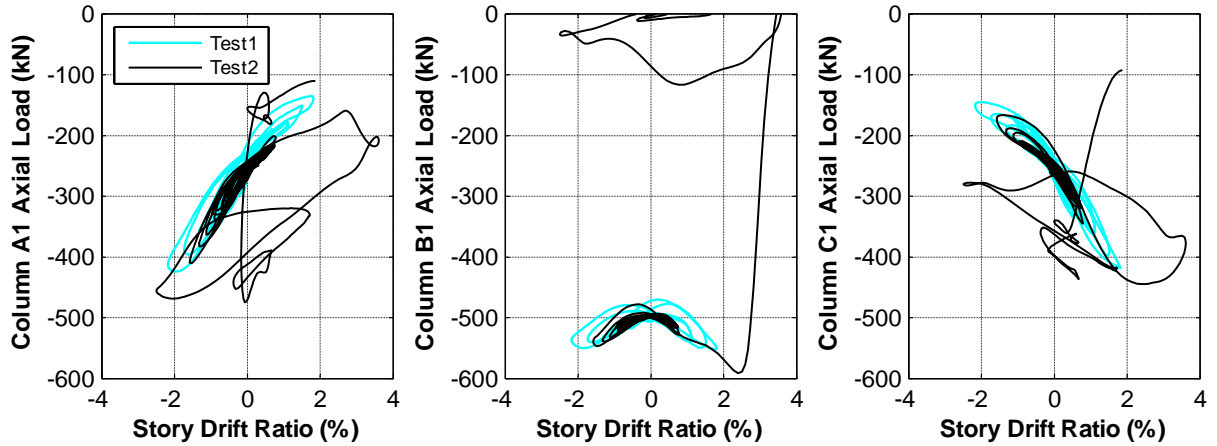


Figure 4-36. Axial load hysteretic response of first-story columns of specimen HCFS, Test1 and Test2

While Figure 4-37 demonstrates the relationship between axial load and the vertical displacement of first-story columns during Test1 and Test2, Figure 4-38 plots the vertical displacement ratio versus drift ratio for all the columns. Figure 4-38 shows that the lengthening of column B1 in the positive direction during Test2 was terminated at 2.6% drift ratio and 0.11% vertical displacement ratio due to initiation of axial failure after shear failure of the column at 2.4% drift ratio.

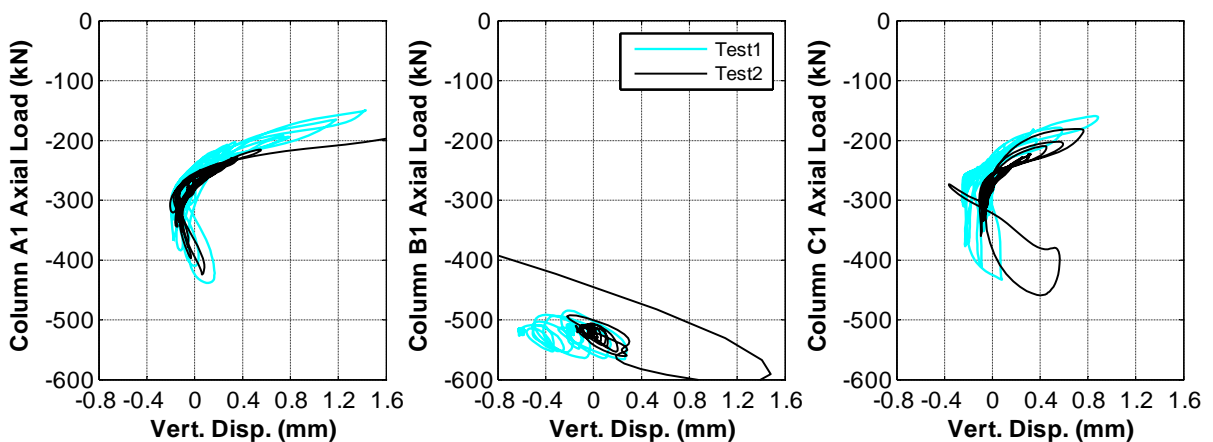


Figure 4-37. Variation of axial load of specimen HCFS columns with vertical displacement, Test1 and Test2

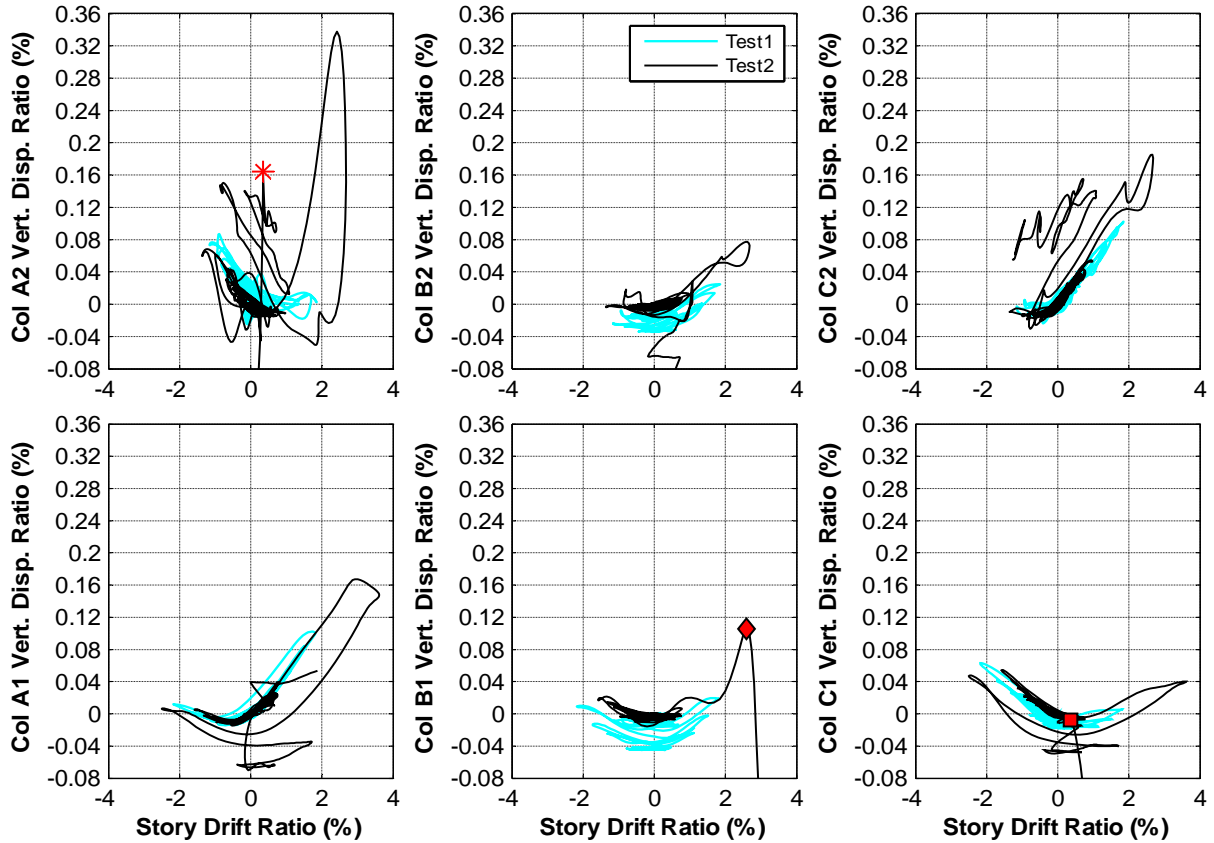


Figure 4-38. Vertical displacement ratio for columns of specimen HCFS, Test1 and Test2

Moment hysteretic response for the top and bottom ends of the first-story columns during Test1 and Test2 are shown in Figure 4-39 and Figure 4-40, respectively. To account for the elastic rotation of first-story joint blocks, column chord-rotation (see the definition in Section 4.4) was used for the moment hysteretic response of the top end of first-story columns (Figure 4-39). It is observed that the peak moments at the base of columns A1 and B1 were about 40% larger than the corresponding peak moments at columns top-end in Test1, thus, the inflection point of the columns were shifted toward the top when the moment peaked. In contrast, the peak moment at the top of column C1 was 15% larger than the bottom end-moment suggesting that the inflection point of the column was shifted toward the base when the moment peaked. While considerable difference between the top and bottom end-moments

was observed for the columns at the peaks, the average differences were calculated as 5.3 kN-m, 4.1 kN-m, and 1.9 kN-m for columns A1, B1, and C1, respectively. This suggests that except for the points of peak moment, the inflection points were not significantly shifted from the mid height of first-story columns. Similar observations were achieved for Test2.

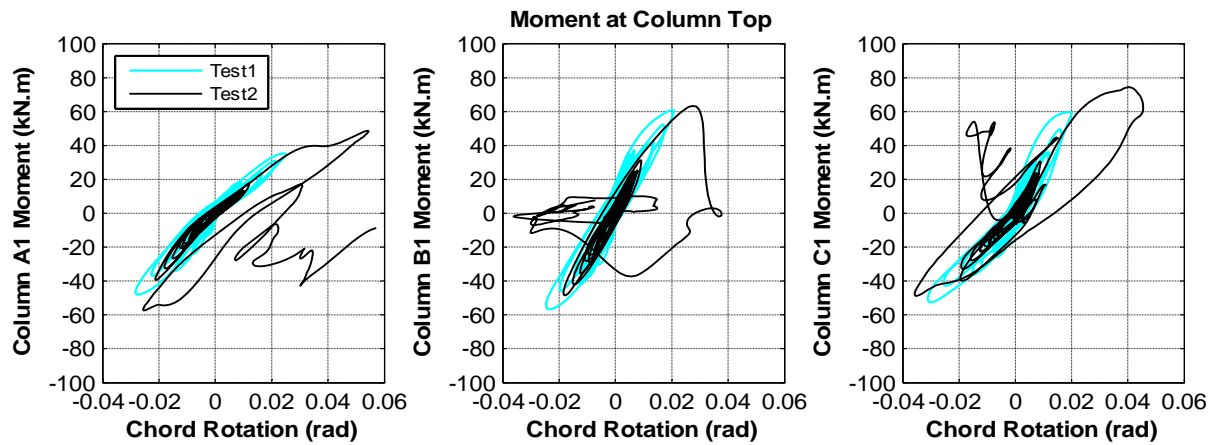


Figure 4-39. Moment-chord rotation relationship at top of first-story columns of specimen HCFS, Test1 and Test2

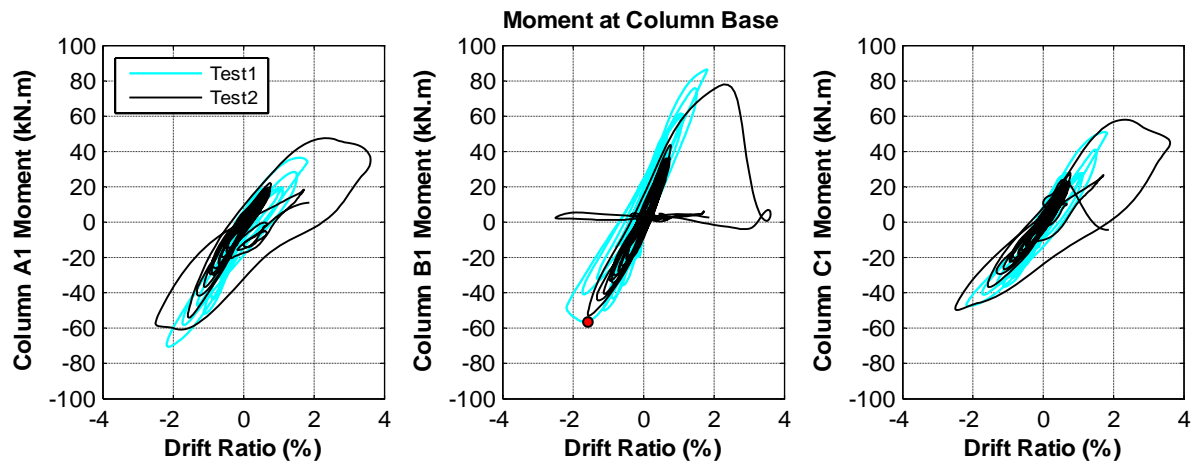


Figure 4-40. Moment hysteretic response of first-story columns of specimen HCFS at base, Test1 and Test2

4.6 Behaviour of Specimen MUF

As discussed in Section 3.2, details of specimen MUF were selected with the intention of forcing failure at the first-story joints. Typical of joint details from older reinforced concrete frames, all hoops were removed from the first story joints. In contrast to specimens MCFS and HCFS, end beam stubs were not included at the exterior joints in the first story, while transverse beams were limited to only one side of the frame at this story level (see Figure 3-2 and Figure 3-3). This exposed two faces of the exterior joints and one face of the interior joint, further decreasing the confinement of first-story joints. On the other hand, the second-story joints were properly confined (with hoops and beam stubs) as they were not intended to experience any damage during the tests to ensure no loss of support for the axial load pre-stress system. Additional column hoops, decreasing the spacing to 20% of the column width (40 mm), provided good confinement for the columns in both stories of the specimen.

Figure 4-41 compares the spectral table accelerations recorded during Test1, Test2, and Test3, while Figure 4-42 plots the displacement response spectra for the three tests. As shown in Table 4-1, period of the frame increased significantly due to damage to the joints during Test1. The spectral acceleration demand for Test2 (2.9g) was 30% higher than Test1 (2.2g) at the initial fundamental period of the specimen (0.29 seconds, dashed line in Figure 4-41), however the spectral acceleration increased by only 4% (2.3g) in the vicinity of the elongated period (0.46 sec, dotted line in Figure 4-41). Consequently, the specimen did not experience significantly higher demands during Test2. As discussed in Section 3.7, the input acceleration was subsequently amplified up to the shaking table limits for Test3. Figure 4-41 demonstrates that the spectral acceleration for Test3 (3.1g) was about 35% larger than Test2 at the period of the damaged frame (0.52 sec, dash-dotted line in Figure 4-41). However, the corresponding

spectral acceleration remained lower than the demand required to cause collapse of the specimen.

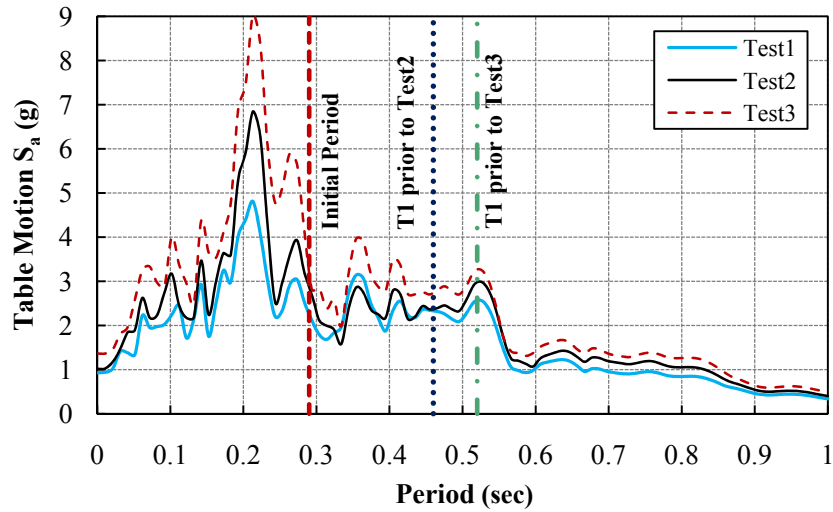


Figure 4-41. Comparison of spectral acceleration with 2% damping for Test1, Test2, and Test3 table motions, Specimen MUF

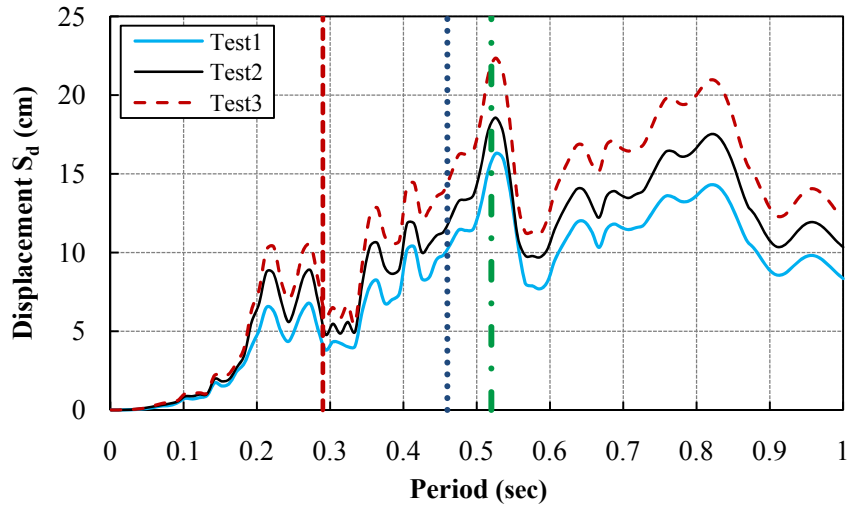


Figure 4-42. Comparison of displacement response spectra with 2% damping for Test1, Test2, and Test3 table motions, Specimen MUF

Figure 4-43 shows the damage to the first-story joints of specimen MUF after Test1, where the exterior joint A1 experienced the most damage. As discussed in Section 3.2, columns were designed and constructed weaker than the beams to provide the weak-column-

strong-beam mechanism common of many existing concrete frame buildings. As a result, it was observed that the joint cracks were extended into the columns rather than the beams. It was also observed that the transverse beams provided confinement to one side of the joints and therefore, joint cracking propagated mostly on the unconfined face of the joints.

Adequate transverse reinforcement prevented shear cracks in the columns, however, flexural cracks were observed at the base of first-story columns. While flexural cracking was not significant for the exterior columns, bottom end of column B1 suffered the most during Test1 (Figure 4-44).

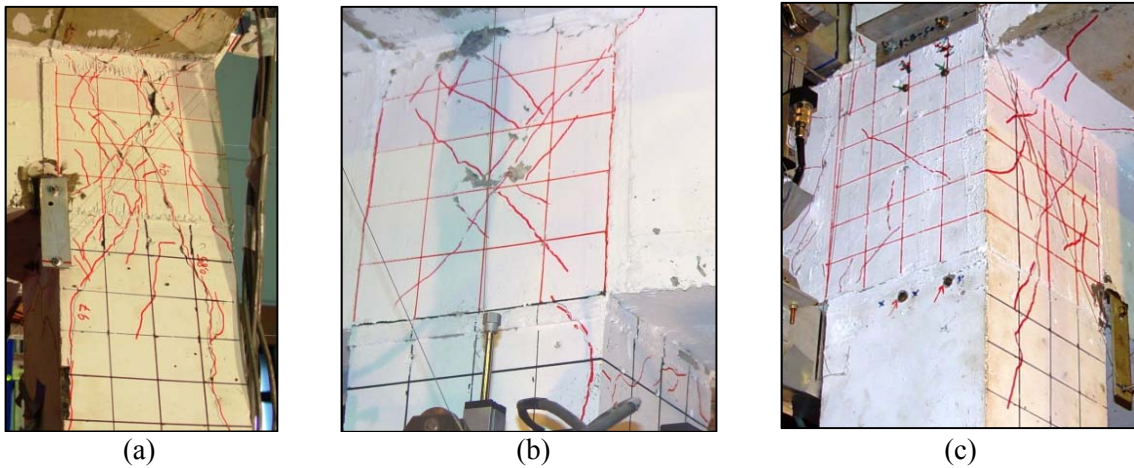


Figure 4-43. Damaged first-story joints of specimen MUF after Test1; a) joint A1; b) joint B1; c) joint C1

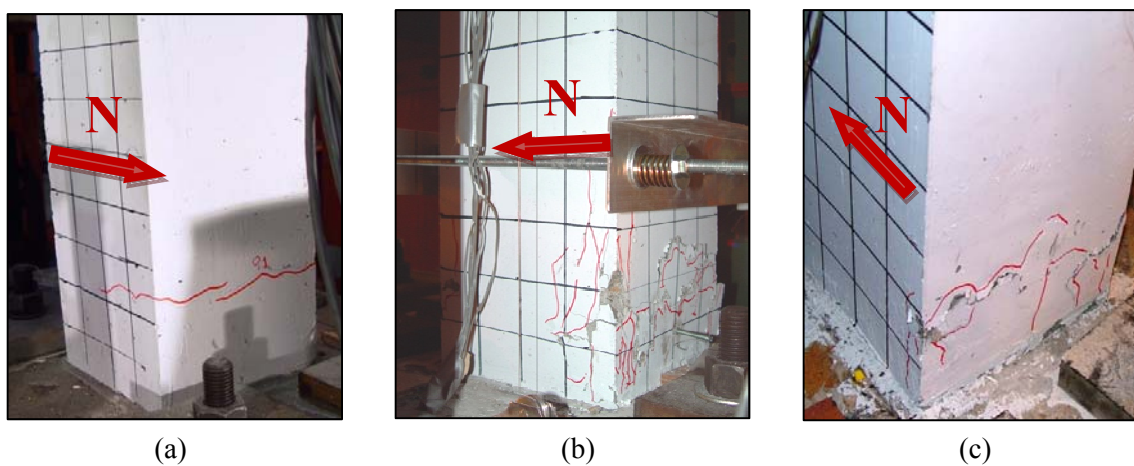


Figure 4-44. Flexural cracks at the base of first-story columns of specimen MUF, Test1; a) column A1; b) column B1; c) column C1

Specimen MUF was the only test frame amongst the four specimens that did not collapse during Test2, although all the first-story joints were severely damaged (Figure 4-45). Even the higher demands from Test3 did not cause collapse of specimen MUF, while increased damage to the joints (Figure 4-46). Cracks at first-story joints opened and closed during Test2 and Test3, localizing response through shear deformations at the joints. Therefore, these unconfined joints worked as a fuse and by accommodating much of the deformation demands, did not allow high shear forces to be developed in the first-story columns. Flexural cracks at the base of first-story columns increased in width during Test2 and Test3, suggesting the formation of plastic hinges at the base of first-story columns. Based on the observations from Test2 and Test3, the failure mode for specimen MUF can be considered as shown in Figure 4-47.

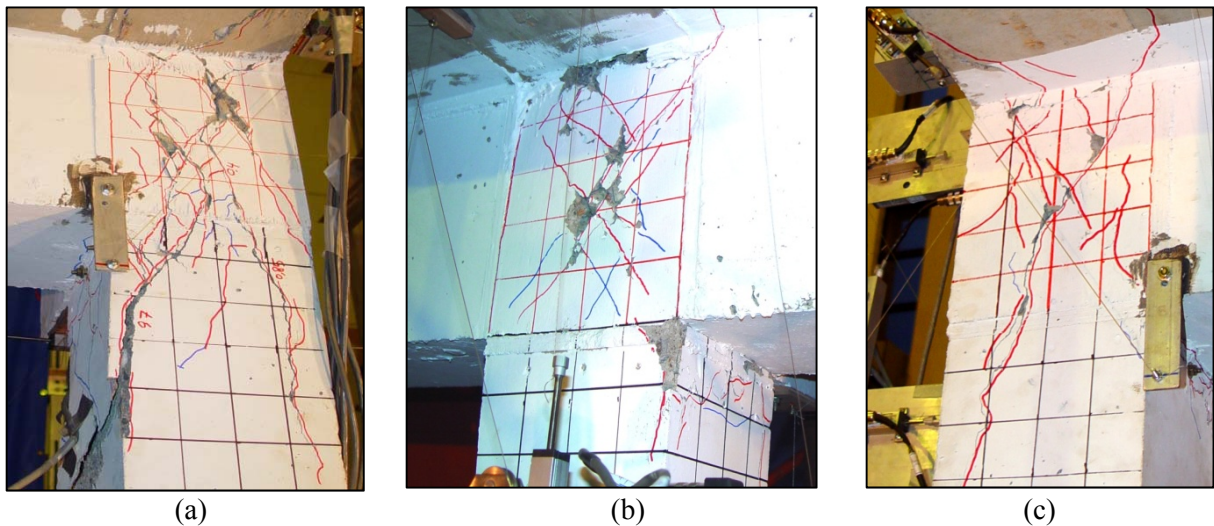


Figure 4-45. Damaged first-story joints of specimen MUF after Test2; a) joint A1; b) joint B1; c) joint C1

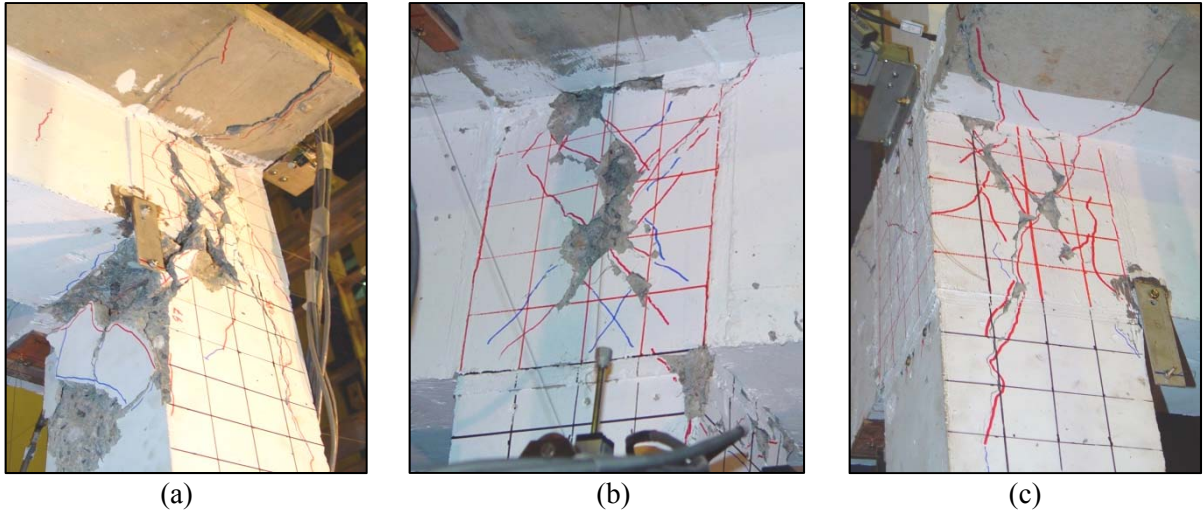


Figure 4-46. Damaged first-story joints of specimen MUF after Test3; a) joint A1; b) joint B1; c) joint C1

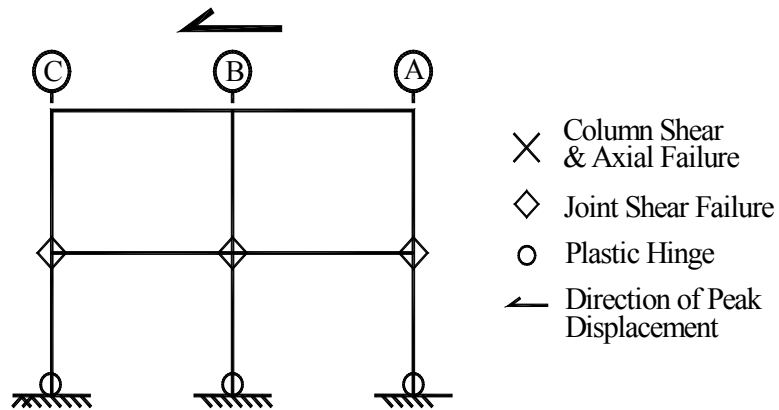


Figure 4-47. Failure mode of specimen MUF

The mechanism that led to joint failure is shown in Figure 4-48. Cracking occurs along the diagonal compression strut which connects the compression zones in the beam and top column to the compression zone in the bottom column. Note that after shear failure of the joint and degradation of shear resistance (Figure 4-48c), moments at the face of the joint will decrease as the joint begins to act like a “hinge”. The compression zones at the top and bottom of the joint therefore must shift toward the centerline of the column and axial loads must be

transferred across the diagonal shear cracks. It is observed that the direction of cracking, induced by internal forces, is such that the movement of upper stories tends to close the diagonal cracks and increase contact across the failure surface. This is in contrast with generation of shear cracks in a column, where after shear failure the contact across the failure surface is decreased due to opening of the diagonal cracks (Figure 4-49). Although only qualitative, Figure 4-48 and Figure 4-49 suggest that the likelihood of collapse of a frame due to failure of unconfined joints is lower than failure of non-ductile columns in the frame. It is noted that the observation is valid for the specimens studied here, while further studies are required to generalize this hypothesis.

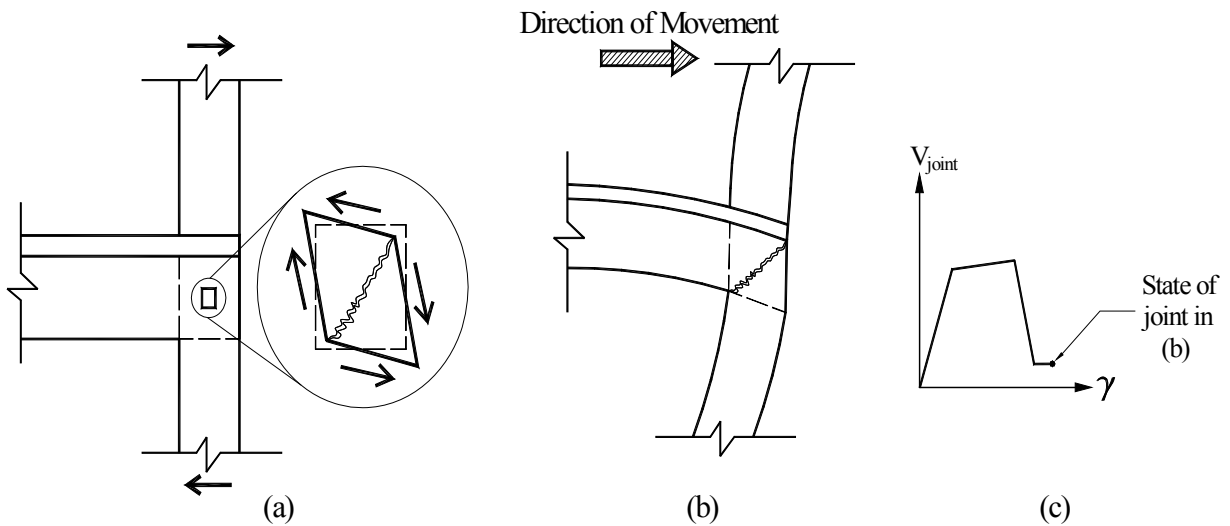


Figure 4-48. a) direction of shear cracking in joint; b) state of joint after shear failure; c) shear-strain response of joint

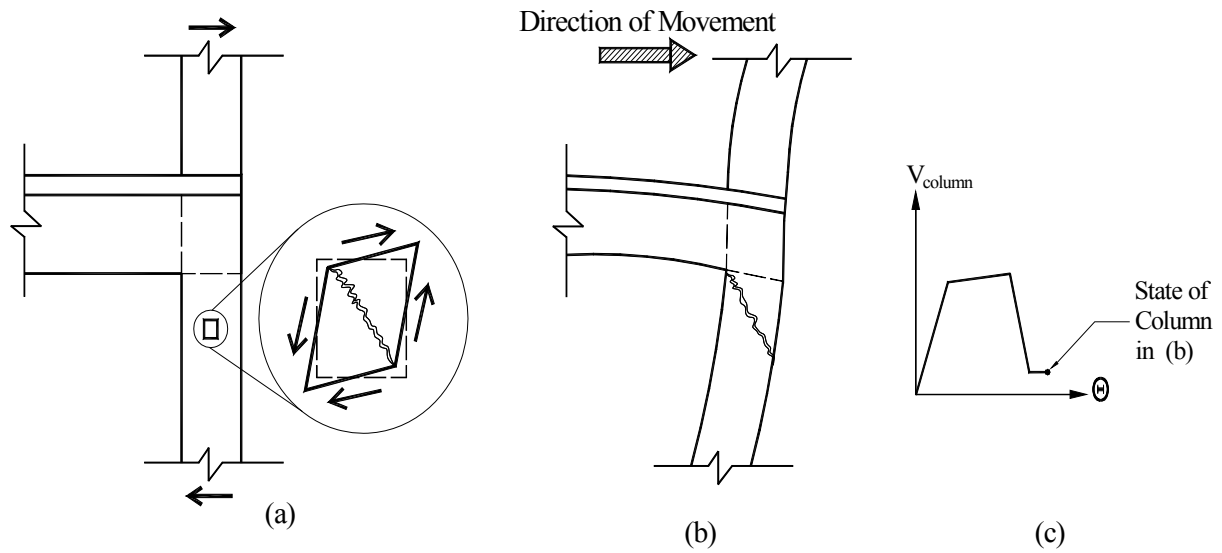


Figure 4-49. a) direction of shear cracking in column; b) state of column after shear failure; c) shear-rotation response of column

Maximum recorded shear for columns in the positive and negative directions and corresponding drifts, axial loads, and time steps during Test1 and Test2 are shown in Table 4-6 and Table 4-7, respectively (see Figure 4-1 for details). While maximum shear for first-story columns was recorded in different time steps of Test1 (Table 4-6), it is observed that the columns reached their peak shear at the same time during Test2.

Table 4-6. Critical parameters for columns of specimen MUF, Test1.

| | A1 | B1 | C1 | A2 | B2 | C2 |
|--------------------------|-----------|-----------|-----------|-----------|-----------|-----------|
| $V_{\max+}$ (kN) | 36.34 | 71.29 | 66.14 | 46.25 | 61.66 | 46.25 |
| $\delta_{V_{\max+}}$ (%) | 2.72 | 1.69 | 2.48 | 2.01 | 2.01 | 2.01 |
| $P_{V_{\max+}}$ (kN) | -78.88 | -314.45 | -323.53 | -82.87 | -295.01 | -300.05 |
| $t_{V_{\max+}}$ (sec) | 34.26 | 34.21 | 34.25 | 34.22 | 34.22 | 34.22 |
| $V_{\max-}$ (kN) | -56.38 | -68.19 | -45.46 | -44.17 | -58.89 | -44.17 |
| $\delta_{V_{\max-}}$ (%) | -1.95 | -1.86 | -1.96 | -1.66 | -1.66 | -1.66 |
| $P_{V_{\max-}}$ (kN) | -296.58 | -312.16 | -73.21 | -284.66 | -287.80 | -56.40 |
| $t_{V_{\max-}}$ (sec) | 34.54 | 34.53 | 34.53 | 34.55 | 34.55 | 34.55 |
| k_{eff} (kN/m) | 2673.02 | 6174.94 | 4356.73 | 2755.74 | 3674.46 | 2755.74 |

Table 4-7. Critical parameters for columns of specimen MUF, Test2.

| | A1 | B1 | C1 | A2 | B2 | C2 |
|--------------------------------|-----------|-----------|-----------|-----------|-----------|-----------|
| V_{max+} (kN) | 28.76 | 61.92 | 56.95 | 39.56 | 52.75 | 39.56 |
| δ_{Vmax+} (%) | 2.59 | 2.59 | 2.59 | 2.25 | 2.25 | 2.25 |
| P_{Vmax+} (kN) | -77.76 | -315.66 | -298.08 | -83.86 | -308.29 | -279.38 |
| t_{Vmax+} (sec) | 34.32 | 34.32 | 34.32 | 34.29 | 34.29 | 34.29 |
| V_{max-} (kN) | -46.15 | -66.66 | -47.21 | -43.61 | -58.15 | -43.61 |
| δ_{Vmax-} (%) | -2.50 | -2.40 | -2.50 | -2.09 | -2.09 | -2.09 |
| P_{Vmax-} (kN) | -280.59 | -364.39 | -78.40 | -273.94 | -336.28 | -57.91 |
| t_{Vmax-} (sec) | 34.59 | 34.58 | 34.59 | 34.61 | 34.61 | 34.61 |
| k_{eff} (kN/m) | 1169.03 | 2492.93 | 2033.48 | 1374.68 | 1696.93 | 1374.68 |

Figure 4-50 plots the recorded table motion and longitudinal acceleration response at footing and story levels for Test1 and Test2. As discussed earlier, the spectral acceleration demand from the two tests were relatively close and therefore, it is observed that the peak acceleration records in both tests were comparable. First story of the frame experienced peak accelerations of 0.81g and 0.9g in Test1 and Test2, respectively. The peak acceleration for second-story level was recorded as 1.05g during Test1, while it was decreased to 0.99g in Test2. Acceleration phasing was similar for the two tests at the table and footing levels, however, divergence in phasing is observed for the acceleration records above the base, particularly for the second story. Softening of the frame stiffness due to joint damage during Test1 significantly increased the natural period of the specimen and influenced the phasing of the response.

Figure 4-51 compares the story-level drift ratios for specimen MUF during Test1 and Test2, while Figure 4-52 demonstrates the minimum and maximum inter-story drift ratio profiles for the specimen. It is observed that the specimen experienced much larger drifts during Test2 up to 34 seconds. After 34 seconds, however, Figure 4-51 shows relatively close

amplitudes for the two tests for both story levels. Peak drift ratios during Test1 were recorded as 2.8% and 2.4% for the first and second stories, respectively. While the first story experienced a maximum drift ratio of 2.8% in the negative direction during Test2, the second story drifted up to 2.7% in the positive direction. As discussed earlier, damage to the unconfined joints at first-story level caused joint deformation that tended to make the story drift ratios similar.

Figure 4-53 plots shear response histories for the two stories and individual columns in the first story during Test1 and Test2, showing that the peak shear recorded for each column during the two tests remained relatively close. Figure 4-54 presents the shear hysteretic response of the frame stories during Test1 and Test2, which reveals the noticeable softening of lateral stiffness of the frame in both story levels. It is observed that stiffness softening occurred after 1% drift ratio at first-story level in the positive direction of Test1, where joint cracking was initiated. While damage to the base of the columns was not significant during Test1, development of cracks in the unconfined joints and propagation of cracks into the columns limited the shear demand on first-story columns and reduced their lateral stiffness.

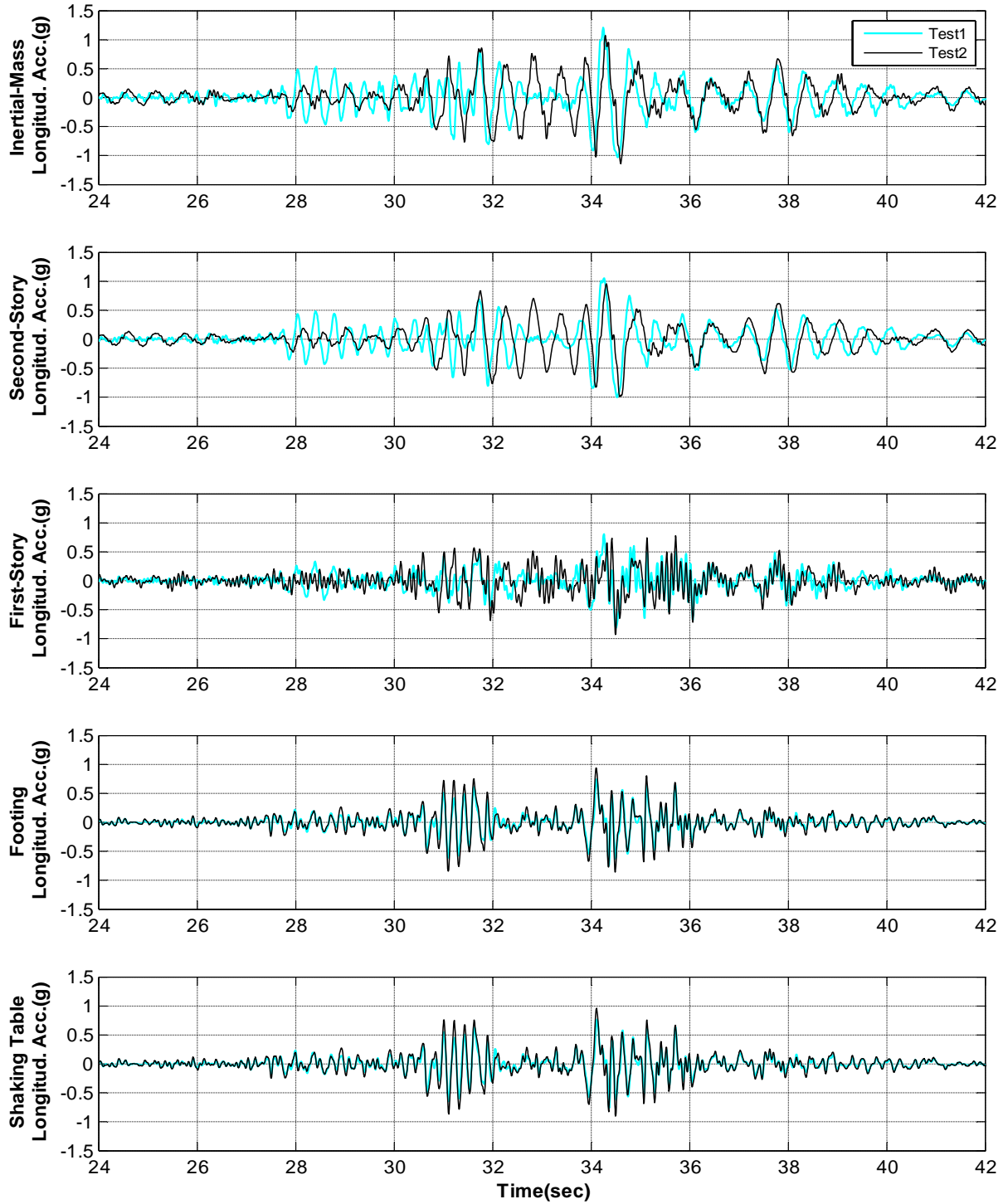


Figure 4-50. Story-level acceleration records for specimen MUF, Test1 and Test2

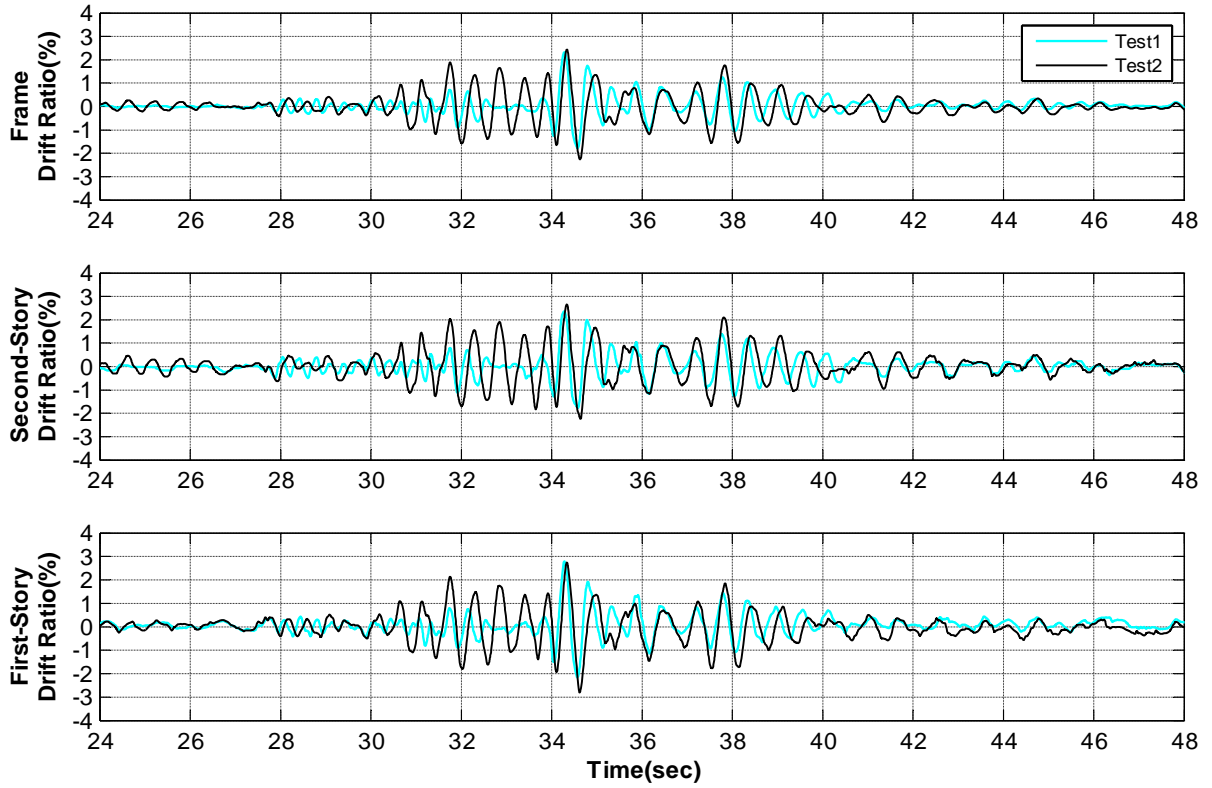


Figure 4-51. Story-level drift response history for specimen MUF, Test1 and Test2

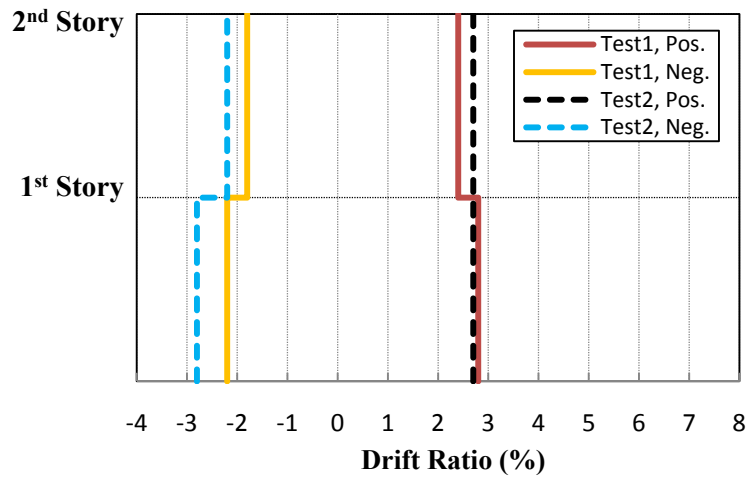


Figure 4-52. Minimum and maximum inter-story drift ratio profiles for specimen MUF, Test1 and Test2

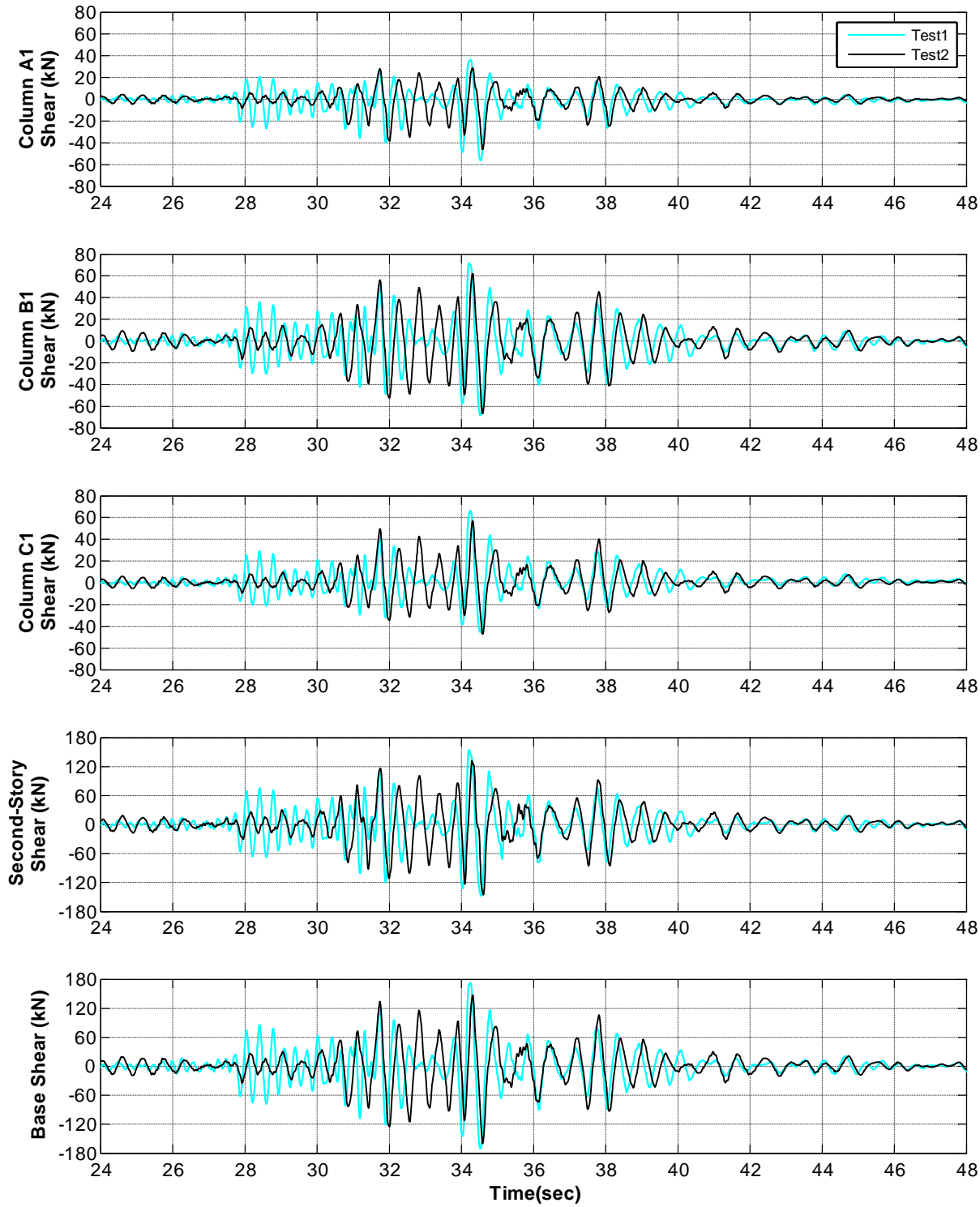


Figure 4-53. First-story columns and frame base shear histories for specimen MUF, Test1 and Test2

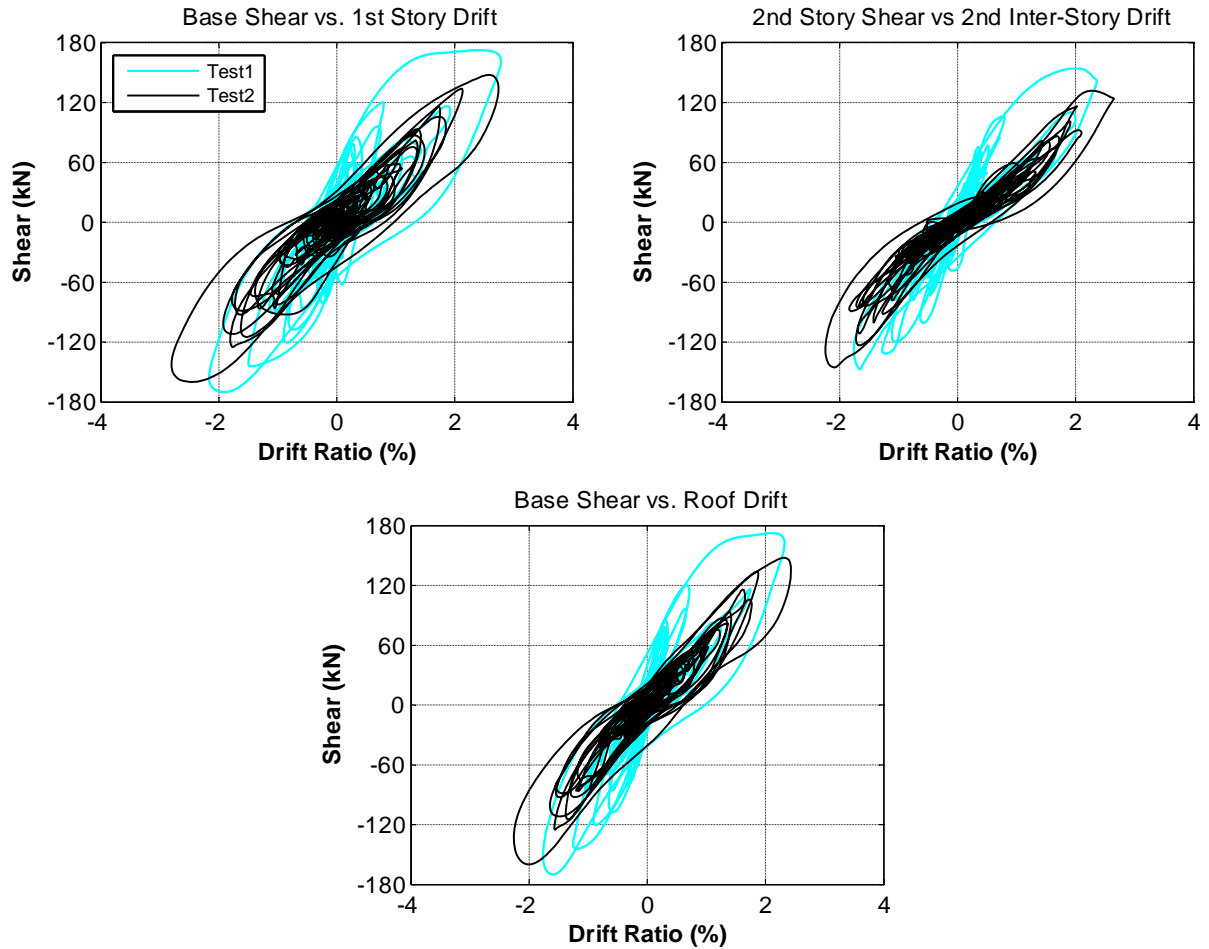


Figure 4-54. Story-level shear hysteretic response of specimen MUF, Test1 and Test2

Figure 4-55 compares the shear hysteretic response of the columns during Test1 and Test2. It is observed that the softening of stiffness was more evident for column A1, where the exterior joint A1 experienced more damage compared to the other joints during the two tests.

While Figure 4-56 plots the axial load hysteretic response of first-story columns, Figure 4-57 demonstrates the axial load response history of these columns. Variation in axial load during Test1 was noticeably less than Test2, particularly in time interval between 32 and 34 seconds.

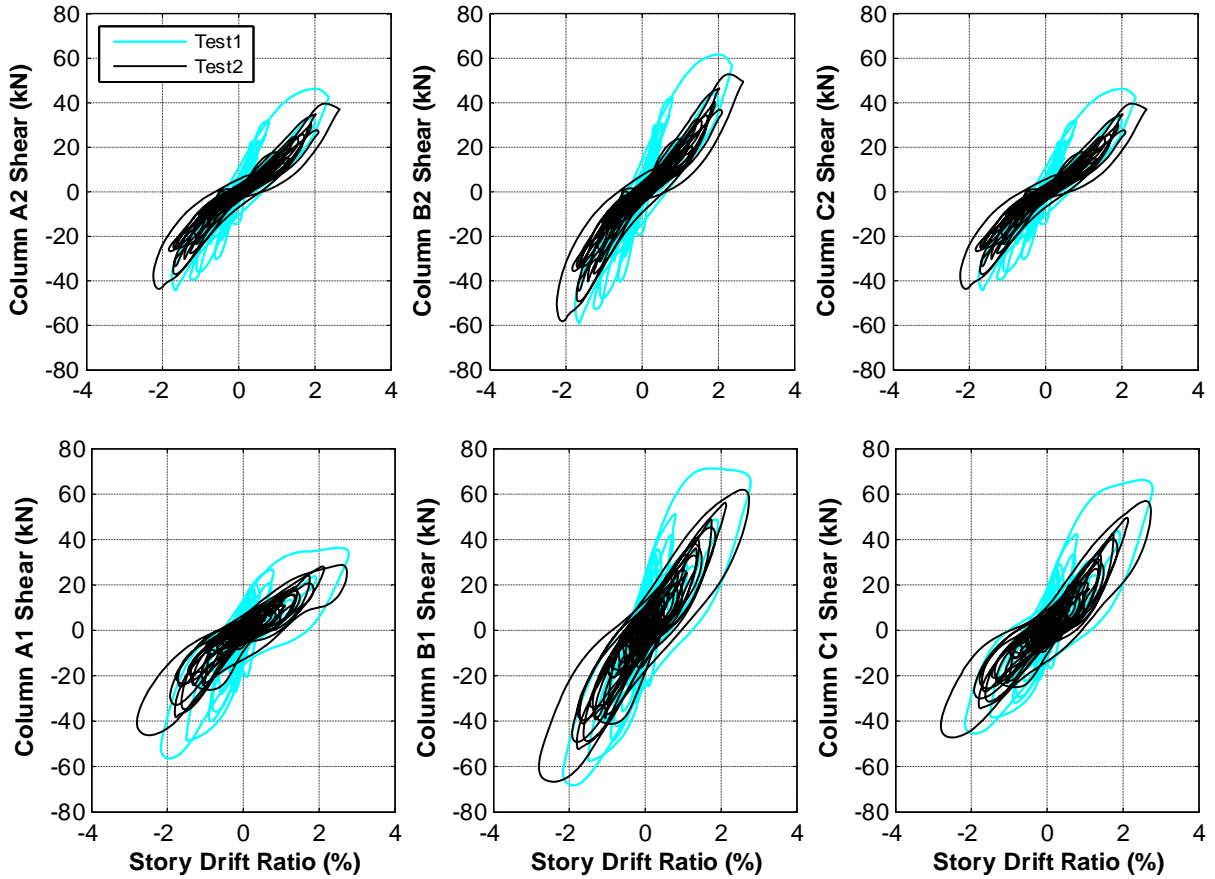


Figure 4-55. Shear hysteretic response of specimen MUF columns, Test1 and Test2

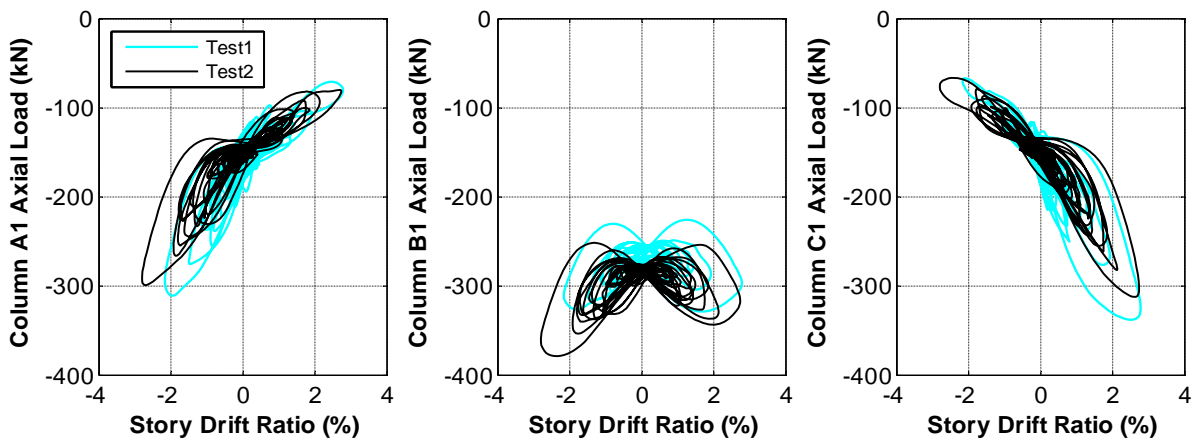


Figure 4-56. Axial load hysteretic response of first-story columns of specimen MUF, Test1 and Test2

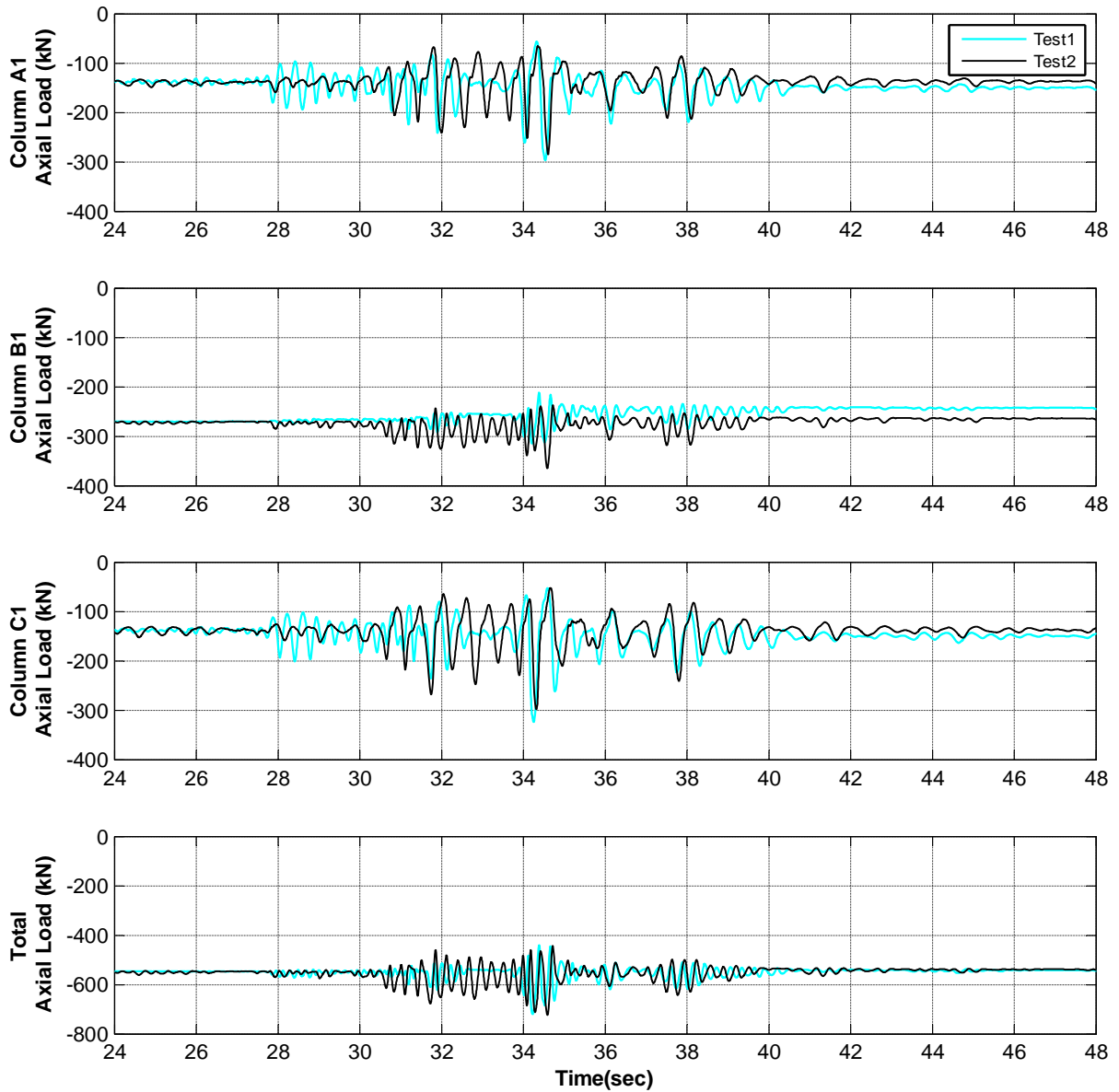


Figure 4-57. Axial load response history of first-story columns of specimen MUF, Test1 and Test2

Figure 4-58 plots the vertical displacement ratio versus story drift ratio for the columns during Test1 and Test2, while Figure 4-59 presents the relationship between axial load and vertical displacement of first-story columns. With a ratio greater than 0.12%, column A1 experienced the largest vertical displacement amongst the columns. The maximum vertical displacement for column A1 occurred at the time when the minimum axial load was recorded

for the column. Furthermore, joint A1 was damaged the most during the tests and consequently, releasing the restraints at the top end lowered the strains integrated over the height of the column.

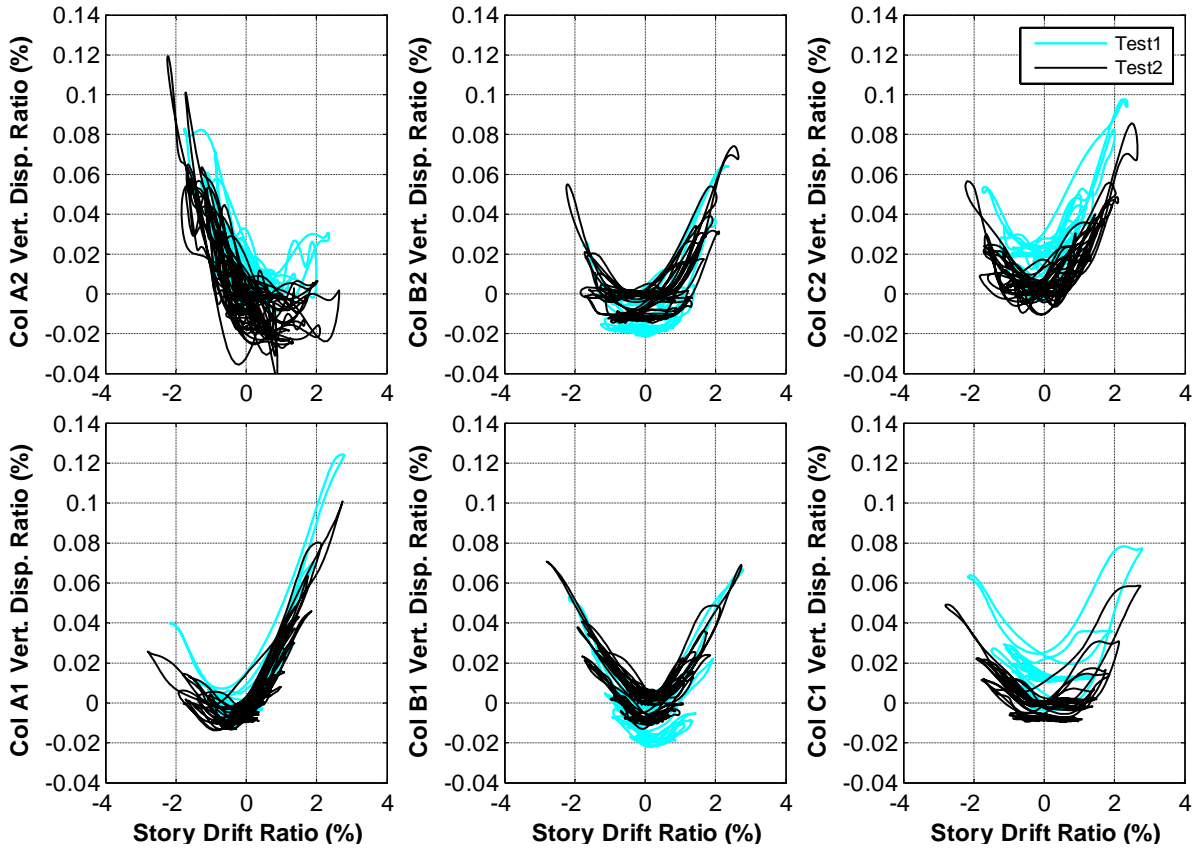


Figure 4-58. Vertical displacement ratio for columns of specimen MUF, Test1 and Test2

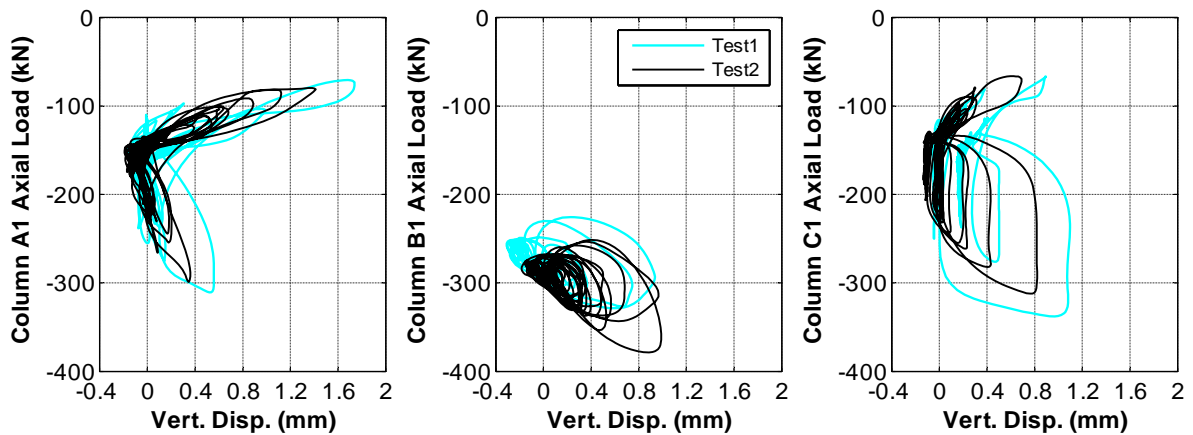


Figure 4-59. Variation of axial load of specimen MUF columns with vertical displacement, Test1 and Test2

Figure 4-60 and Figure 4-61 demonstrate the moment hysteretic response of first-story columns during Test1 and Test2 at the top and base of the columns, respectively. To account for the rotation of first-story joints, chord rotation at the top of columns (see the definition in Section 4.4), instead of story drift ratio, was used for Figure 4-60. It is observed that columns B1 and C1 were able to resist the moment demands at both ends. However, the moment hysteretic response of column A1 at the top-end demonstrates that a relatively small moment was transferred to the column due to shear failure and formation of a hinge at joint A1.

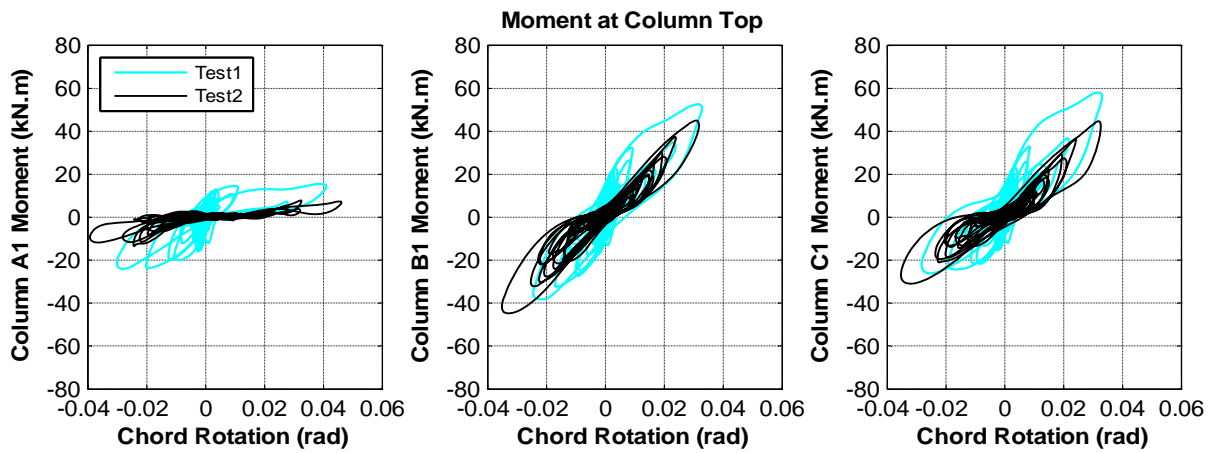


Figure 4-60. Moment-chord rotation relationship at top of first-story columns of specimen MUF, Test1 and Test2

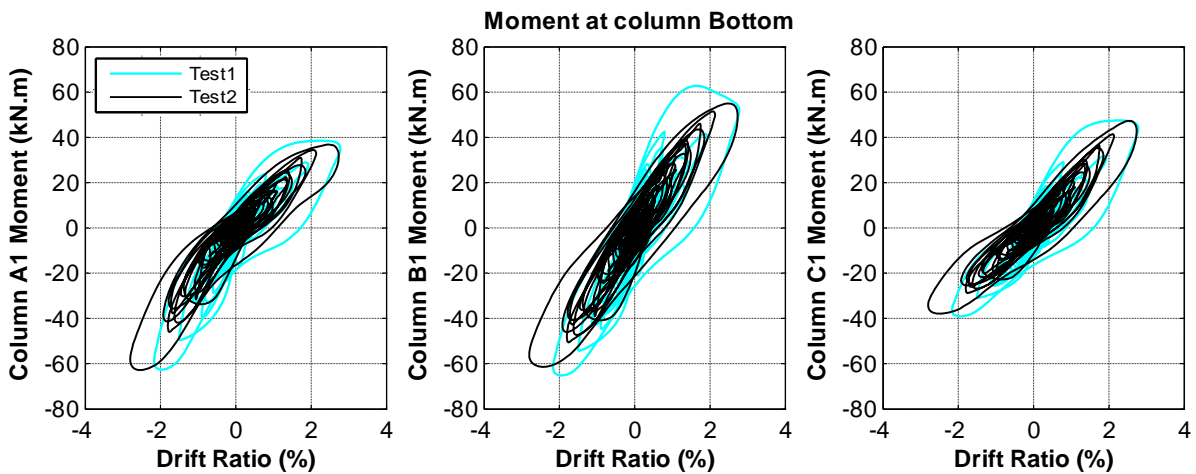


Figure 4-61. Moment hysteretic response of first-story columns of specimen MUF, Test1 and Test2

The main focus of testing specimen MUF was studying the behaviour of unconfined joints. Therefore, additional instruments were mounted on the exposed side of the exterior joints to measure their shear deformations during the tests. Details of such instrumentation are shown in Appendix Section B.3. Comparing the data from the instruments on both confined and unconfined surfaces of a joint reveals the effectiveness of transverse beams in restricting the development of shear cracks through the width of the joint in the direction of shaking. Figure 4-62 plots the shear deformations recorded for the transverse beam face (confined side) and the exposed face (unconfined side) of joint C1, during Test1 and Test2. It is observed that smaller shear deformations were recorded by the instruments on the confined side of joint C1, suggesting that the transverse beam restrained the development of shear cracks on the confined face. Photos in Figure 4-63 show the propagation of cracks into the column C1 for the two sides of the column after Test3, confirming the above conclusion.

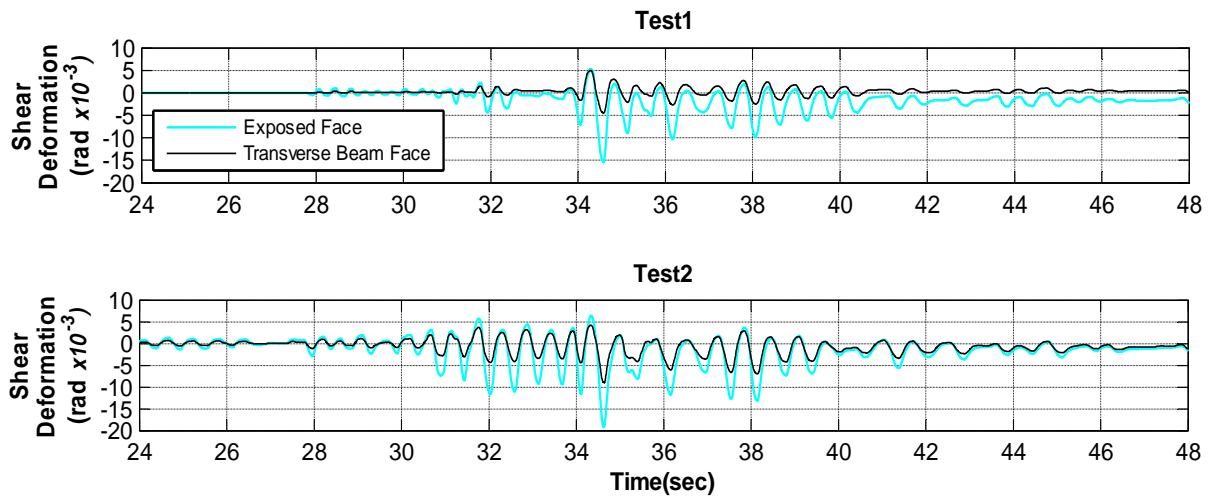


Figure 4-62. Comparison of shear deformation at joint C1 of specimen MUF, recorded by diagonal instruments on exposed and transverse beam faces of the joint

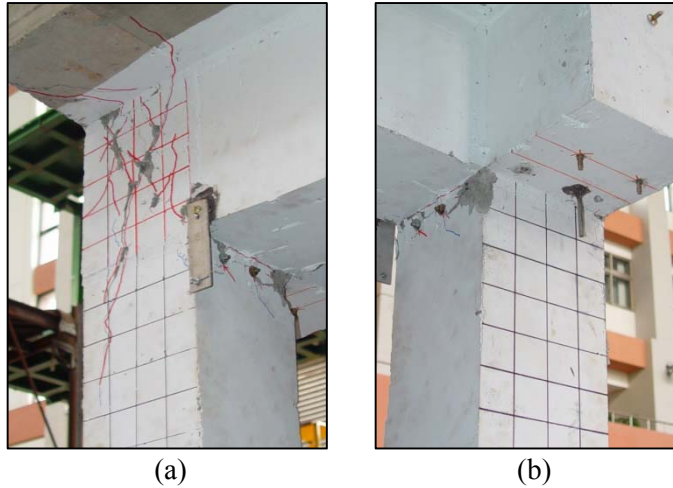


Figure 4-63. Comparison of propagation of shear cracks to the top of column C1 of specimen MUF after Test3; a) exposed face; b) transverse beam face

Figure 4-64 demonstrates the relationship of shear at the top of column C1 and the shear deformation recorded for the exposed face of the joint. Due to damage to the strain gages during the construction phase, strain and forces in the longitudinal bars of the connecting beam and consequently shear at joint C1 were not available. Therefore, shear at the top of columns were used in Figure 4-64. Joint C1 was initially able to withstand the shear demand. However, large shear cracks developed in the joint after a shear deformation of -0.004 rad during Test1, resulting in significant reduction in stiffness of the joint panel. As shown in Figure 4-65, this corresponds to 1.9% drift ratio in the positive direction of Test1.

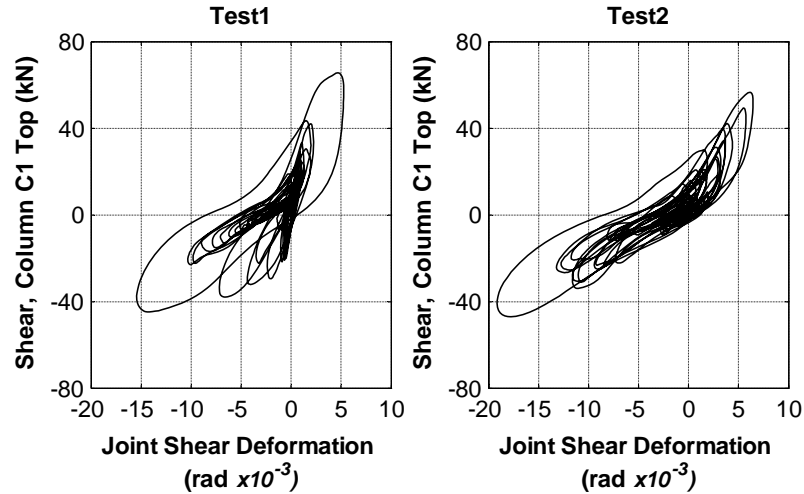


Figure 4-64. Relation between shear force and shear deformation of joint C1 recorded at unconfined face of the joint for specimen MUF

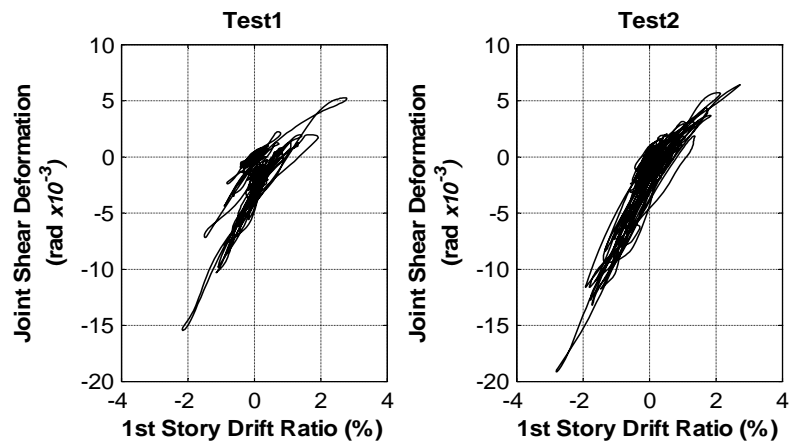


Figure 4-65. Relation between first-story drift ratio and shear deformation of joint C1 recorded at unconfined face of the joint for specimen MUF

4.7 Behaviour of Specimen MUFS

Amongst the four specimens, MUFS was composed of structural elements with details which most closely resembled the details expected in existing reinforced concrete frames. The columns had light transverse reinforcement (similar to MCFS and HCFS), while transverse reinforcement was omitted from the joints (similar to MUF). Consistent with specimen MUF,

transverse beams were limited to only one side of the frame at first-story level, whereas the second-story joints were properly confined as they were not intended to experience any damage during the tests.

Figure 4-66 compares the spectral table accelerations recorded during Test1 and Test2, while Figure 4-67 demonstrates the displacement response spectra for the two tests. As shown in Table 4-1, period of the frame was increased from 0.29 seconds (dashed line) to 0.46 seconds (dotted line) mainly due to joint damage during Test1. Although the spectral acceleration demand for Test2 was 45% higher than Test1 at the original period of the undamaged structure, the spectral acceleration in the vicinity of the new period was only 10% higher. Consequently, the specimen did not experience notably higher acceleration demands during Test2. However, significant damage to the joints led to reduction in the frame lateral load capacity in Test1, where failure of second-story columns in Test2 caused the collapse of the specimen.

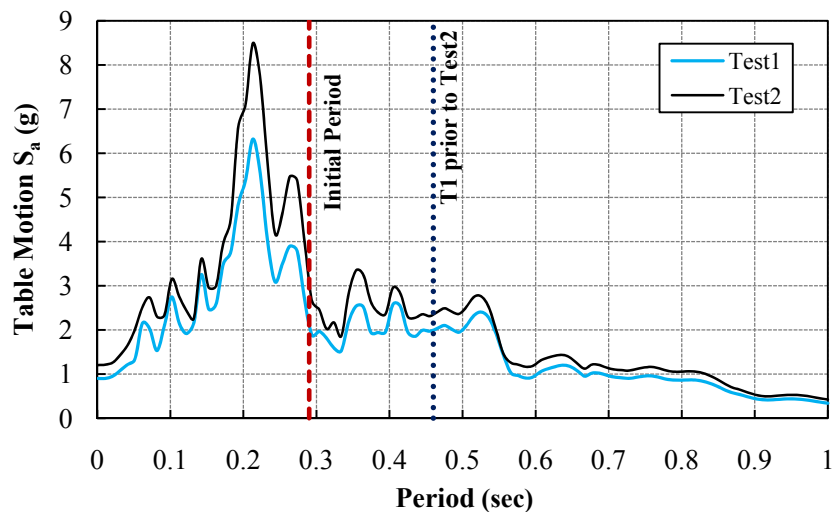


Figure 4-66. Comparison of spectral acceleration with 2% damping for Test1 and Test2 table motions, specimen MUFS

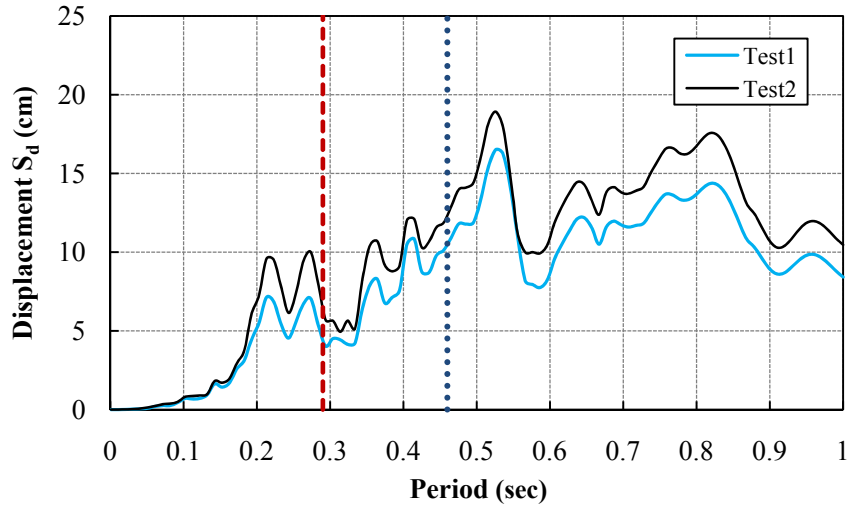


Figure 4-67. Comparison of displacement response spectra with 2% damping for Test1 and Test2 table motions, specimen MUFS

Figure 4-68 shows the damage to first-story joints of specimen MUFS during Test1. It is observed that the exterior joints experienced substantial damage, while interior joint B1 suffered only limited cracking. Since the columns were designed and constructed weaker than the beams, the cracks in the exterior joints extended into the columns rather than the beams. In contrast, relatively minor damage to joint B1 was localized in the joint and cracks did not propagate into column B1. Shear cracking was observed at the top of column B1 due to the low transverse reinforcement ratio used in this specimen (Figure 4-68b). Columns B1 and C1 experienced noticeable flexural and shear cracks at the base, whereas minor flexural cracks were observed at the base of column A1 (Figure 4-69).

While extensive cracking of exterior first-story joints were propagated into columns A1 and C1, Figure 4-70 demonstrates negligible cracks at the base of second-story columns after Test1, apparently due to the additional stiffness and strength provided by the slab. Shear and flexural cracks at the top end of column B2 are shown in Figure 4-70b.

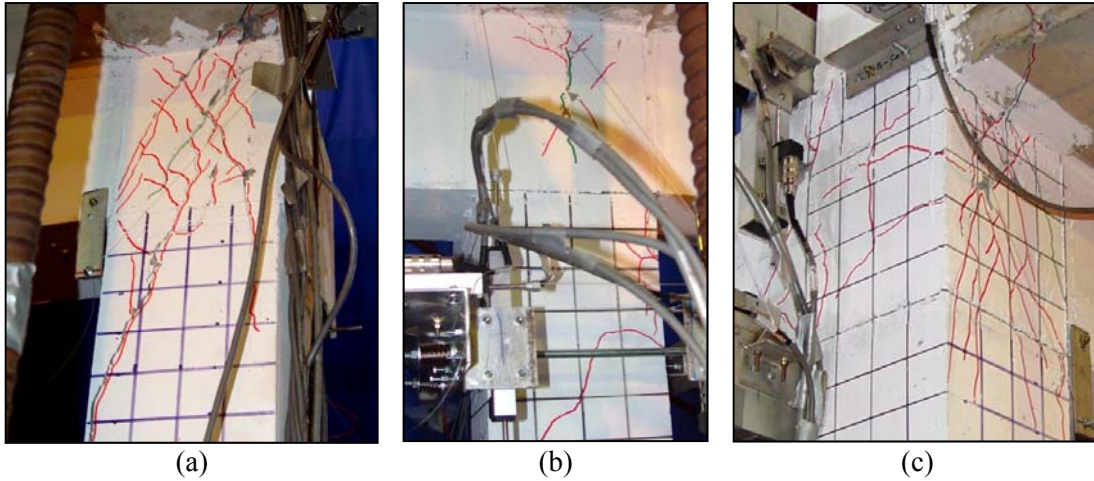


Figure 4-68. Damaged first-story joints of specimen MUFS after Test1; a) joint A1; b) joint B1; c) joint C1

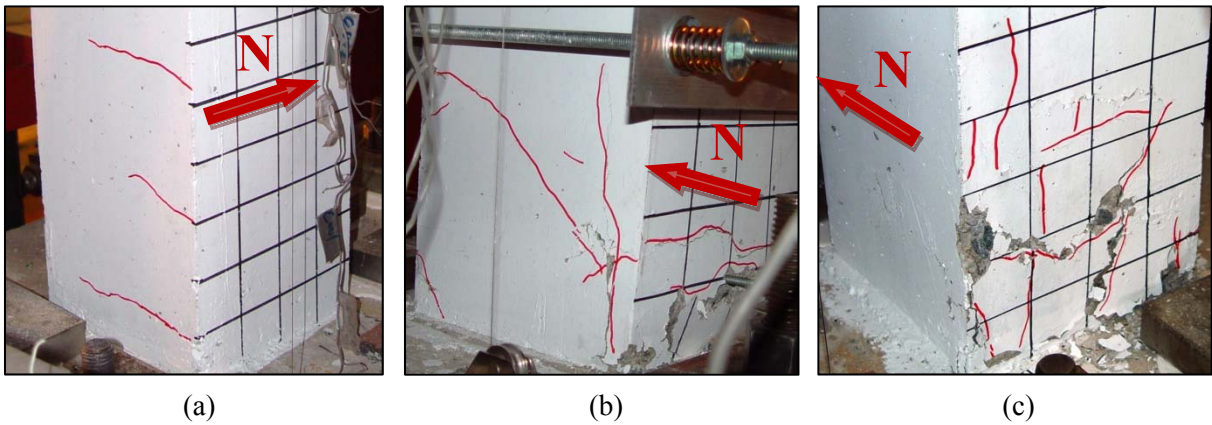


Figure 4-69. Damage to the base of first-story columns of specimen MUFS during Test1; a) column A1; b) column B1; c) column C1

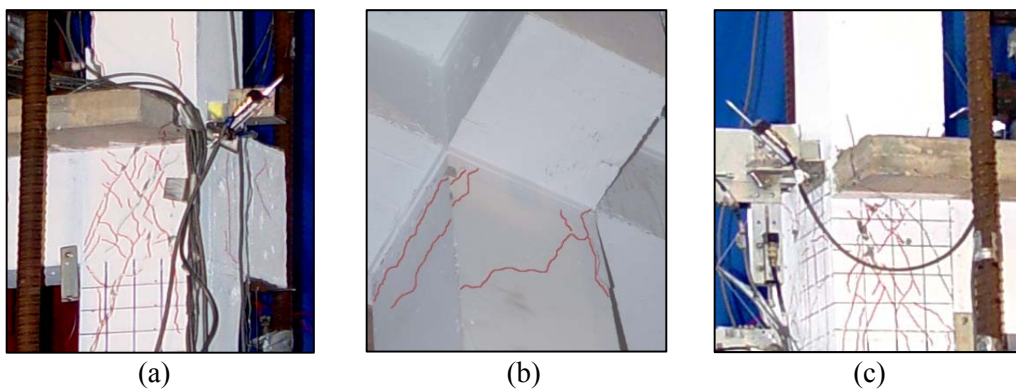


Figure 4-70. Damage to second-story columns of specimen MUFS during Test1; a) base of column A2; b) top of column B2; c) base of column C2

Although first-story joints and columns, particularly the exterior joints, were damaged during Test1, specimen MUFS survived the test demands. Similar mechanism that led to joint failure in specimen MUF (Figure 4-48) was observed for specimen MUFS. Cracks at first-story joints were opened and closed during Test2, localizing shear deformation at the joints. Therefore, the unconfined joints did not allow shear to be fully developed in first-story columns by accommodating much of the deformation demands. As discussed in Section 3.4.2.3, lateral force on the specimen resulted mainly from the inertial-mass system. Therefore, lateral and vertical demands in the second story were large enough to cause shear and axial failure of columns B2 and C2. Axial failure of columns B2 and C2 occurred at 34.29 and 37.66 seconds of Test2, respectively. Cracks at the base of first-story columns were intensified during Test2, allowing formation of plastic hinge at the base of these columns. Based on the observations from Test2, the failure mode for specimen MUFS is shown in Figure 4-71, where a combination of joint failure at first-story level and column failure in the second story caused collapse of the frame. While Figure 4-72 demonstrates the damaged first-story joints after Test2, Figure 4-73 shows the state of second-story columns after the test.

As shown in Figure 4-70, very limited cracks were observed in the first-story slab and base of second-story columns, suggesting that the undamaged portion of the joint at the slab depth (70 mm) provided a partially-fixed condition for the base of second-story columns. In contrast, damage to the joints, below the slabs, and propagation of cracks into the top end of first-story columns reduced the end-moment at the top of these columns. The rigid and well-confined joints at second-story level also provided a fixed-end condition at the top of the columns in the second floor, resulting in higher local deformation at column ends and more vulnerability to failure comparing to first-story columns.

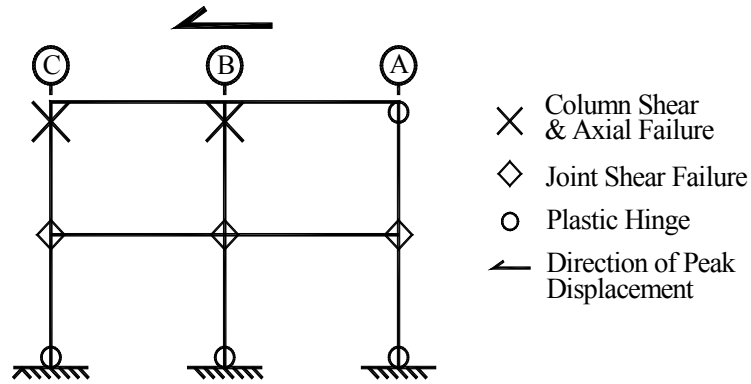


Figure 4-71. Failure mode of specimen MUFS

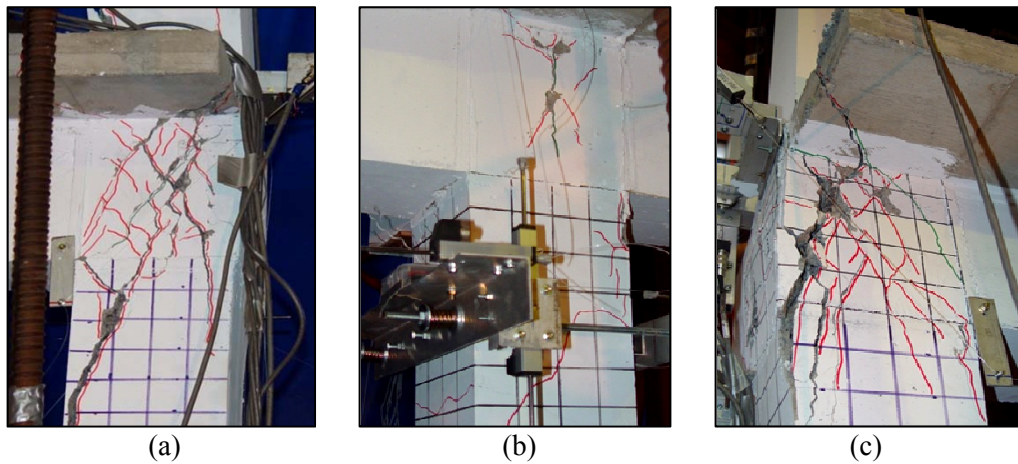


Figure 4-72. Damaged first-story joints of specimen MUFS after Test2; a) joint A1; b) joint B1; c) joint C1

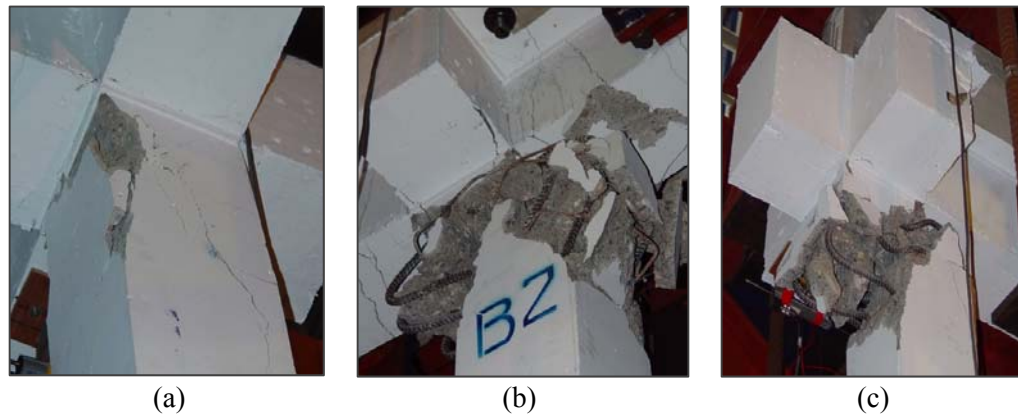


Figure 4-73. Damage to second-story columns of specimen MUFS after Test2; a) column A2; b) column B2; c) column C2

Maximum recorded shear for columns and corresponding drift, axial load, and time steps in the positive and negative directions of Test1 and Test2 are shown in Table 4-8 and Table

4-9, respectively (see Figure 4-1 for details). It is observed that while no severe shear strength degradation with more than 20% loss was recorded during Test1, columns in the second story of specimen MUFS experienced significant shear strength degradation in vicinity of 2.61% second-story drift ratio.

Table 4-8. Critical parameters for columns of specimen MUFS, Test1.

| | A1 | B1 | C1 | A2 | B2 | C2 |
|--------------------------------|-----------|-----------|-----------|-----------|-----------|-----------|
| V_{max+} (kN) | 52.74 | 68.12 | 67.12 | 50.93 | 67.91 | 50.93 |
| δ_{Vmax+} (%) | 2.70 | 1.78 | 2.01 | 2.01 | 2.01 | 2.01 |
| P_{Vmax+} (kN) | -54.69 | -348.50 | -293.11 | -48.37 | -329.27 | -282.87 |
| t_{Vmax+} (sec) | 34.24 | 34.20 | 34.21 | 34.21 | 34.21 | 34.21 |
| δ_{80%+} (%) | - | - | - | - | - | - |
| V_{max-} (kN) | -48.56 | -85.71 | -55.76 | -49.16 | -65.55 | -49.16 |
| δ_{Vmax-} (%) | -1.95 | -2.01 | -1.96 | -1.41 | -1.41 | -1.41 |
| P_{Vmax-} (kN) | -232.14 | -359.34 | -46.94 | -224.09 | -340.18 | -35.42 |
| t_{Vmax-} (sec) | 34.50 | 34.51 | 34.50 | 34.51 | 34.51 | 34.51 |
| δ_{80%-} (%) | - | - | - | - | - | - |
| k_{eff} (kN/m) | 3306.75 | 5213.38 | 4320.46 | 3099.24 | 4131.78 | 3099.24 |

Table 4-9. Critical parameters for columns of specimen MUFS, Test2.

| | A1 | B1 | C1 | A2 | B2 | C2 |
|--|-----------|-----------|-----------|-----------|-----------|-----------|
| V_{max+} (kN) | 32.13 | 57.06 | 54.68 | 38.65 | 51.53 | 38.65 |
| δ_{Vmax+} (%) | 2.17 | 2.52 | 2.49 | 2.26 | 2.26 | 2.26 |
| P_{Vmax+} (kN) | -91.02 | -271.71 | -276.13 | -77.13 | -300.45 | -264.61 |
| t_{Vmax+} (sec) | 31.72 | 34.31 | 34.30 | 34.29 | 34.28 | 34.29 |
| δ_{80%+} (%) | - | - | - | 2.61 | 2.60 | 2.61 |
| V_{max-} (kN) | -39.34 | -63.54 | -35.81 | -37.67 | -50.22 | -37.67 |
| δ_{Vmax-} (%) | -1.91 | -1.82 | -1.83 | -1.56 | -1.56 | -1.56 |
| P_{Vmax-} (kN) | -215.77 | -317.15 | -72.48 | -205.44 | -297.98 | -64.14 |
| t_{Vmax-} (sec) | 32.00 | 32.00 | 32.00 | 32.00 | 32.00 | 32.00 |
| δ_{80%-} (%) | - | - | - | - | - | - |
| k_{eff} (kN/m) | 1368.74 | 2092.71 | 1761.86 | 1785.76 | 2380.90 | 1785.76 |
| δ_{axial failure} (%) | - | - | - | - | 2.34 | 1.72 |
| t_{axial failure} (sec) | - | - | - | - | 34.29 | 37.66 |

Figure 4-74 plots the recorded table motion and longitudinal acceleration response at the footing and story levels for Test1 and Test2 revealing that the acceleration phasing above the base of the frame was not similar for the two tests, particularly between 32 and 34 seconds. Softening of the frame stiffness due to joint damage during Test1 significantly increased the natural period of the specimen and influenced the phasing of response.

Figure 4-75 compares the story-level drift ratios experienced by specimen MUFS during Test1 and Test2, whereas Figure 4-76 demonstrates the minimum and maximum inter-story drift ratio profiles recorded for the specimen. In contrast to Test1, Figure 4-75 shows that the specimen went through large drifts between 30 and 34 seconds of Test2. Figure 4-76 reveals that in contrast with Test1, the peak drift ratio in the second story was larger than the first story in Test2 due to shear and axial failure of column B2.

Figure 4-77 plots shear response histories for the two stories as well as first-story columns. It is observed that while the base shear reached the maximum of 189.6 kN during Test1 in the negative direction, the peak base shear was recorded as 143.7 kN in the positive direction of Test2. Comparison of shear response histories from the two tests reveals that the maximum shear responses in the story levels were closer in the positive direction than the negative direction. Figure 4-77 also demonstrates a more symmetric behaviour for column A1 than other first-story columns. Since joint A1 was damaged more during the tests, less shear was developed in column A1 and therefore, damage to the column remained minimal.

Figure 4-78 presents the shear hysteretic response of the frame stories during Test1 and Test2. Base shear degradation, marked by a square marker, started at positive 2.0% drift ratio (34.22 seconds). Slightly later, shear degradation in the second story was commenced at 2.1% second-story drift ratio (triangular marker). Degradation of base shear in the negative direction

was sharper and started at 34.5 seconds and 2.0% drift ratio (diamond marker), followed by a significant loss in stiffness of the frame.

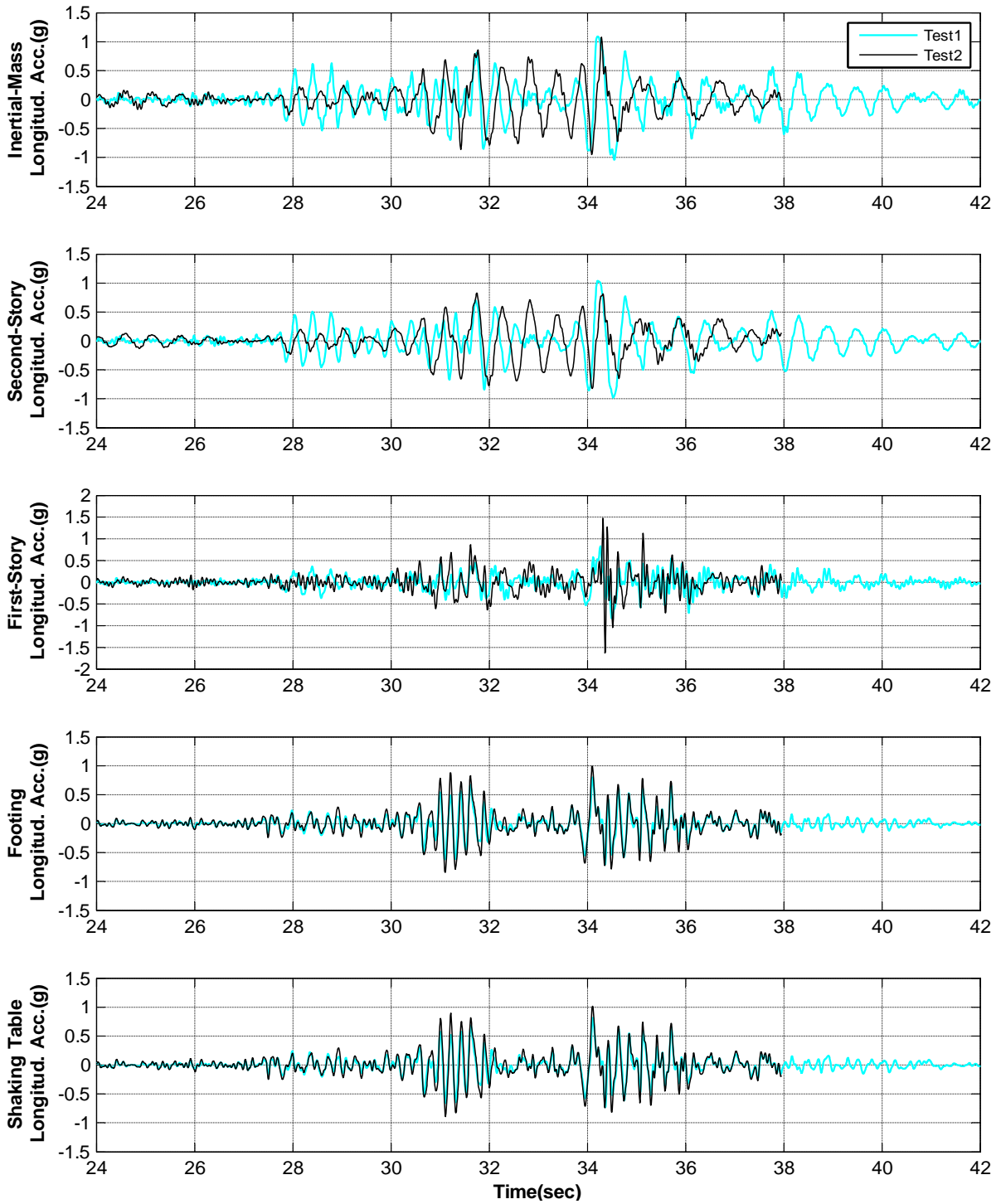


Figure 4-74. Story-level acceleration records for specimen MUFS, Test1 and Test2

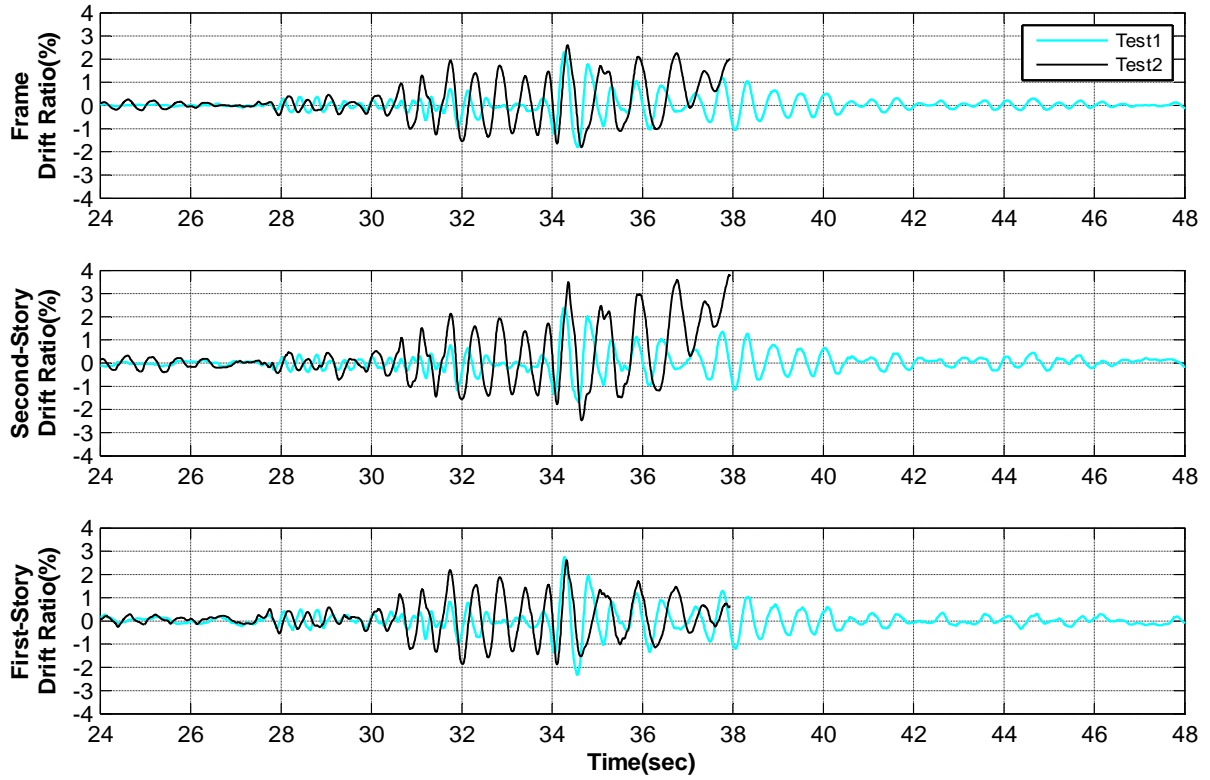


Figure 4-75. Story-level drift response history for specimen MUFS, Test1 and Test2

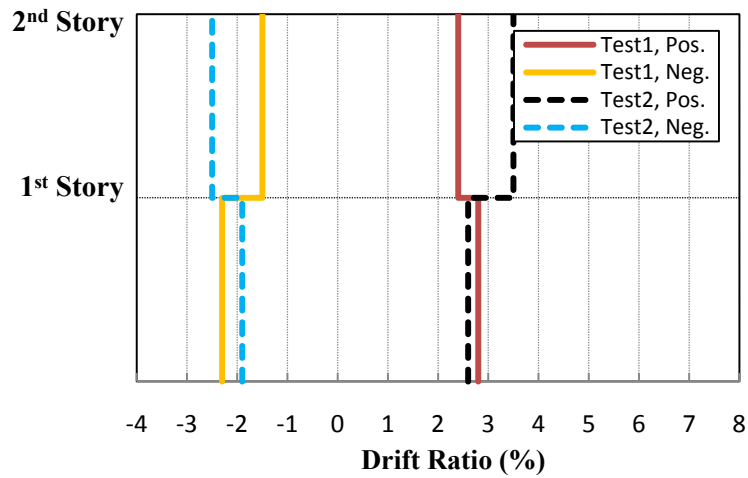


Figure 4-76. Minimum and maximum inter-story drift ratio profiles for specimen MUFS, Test1 and Test2

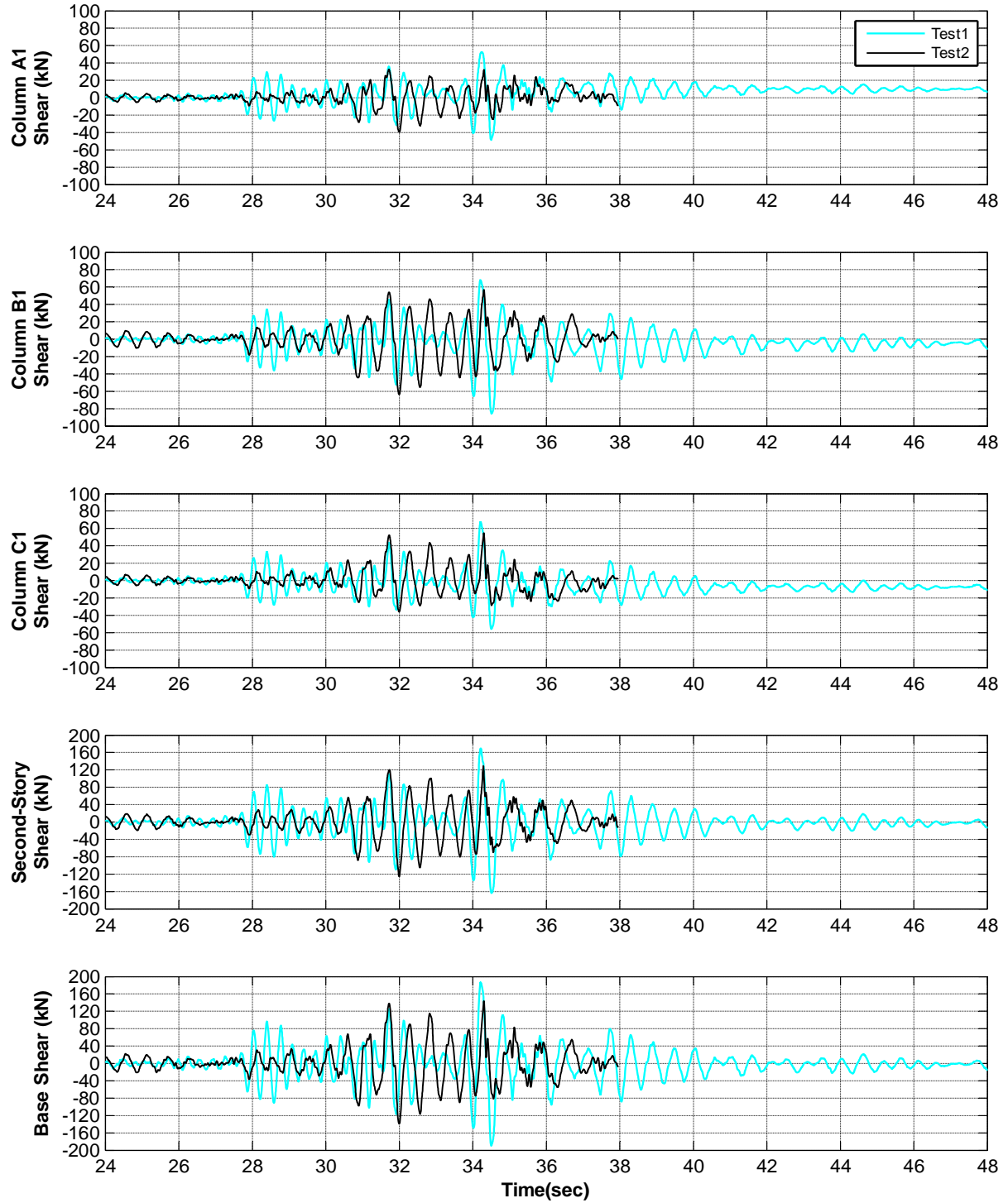


Figure 4-77. First-story columns and frame base shear histories for specimen MUFS, Test1 and Test2

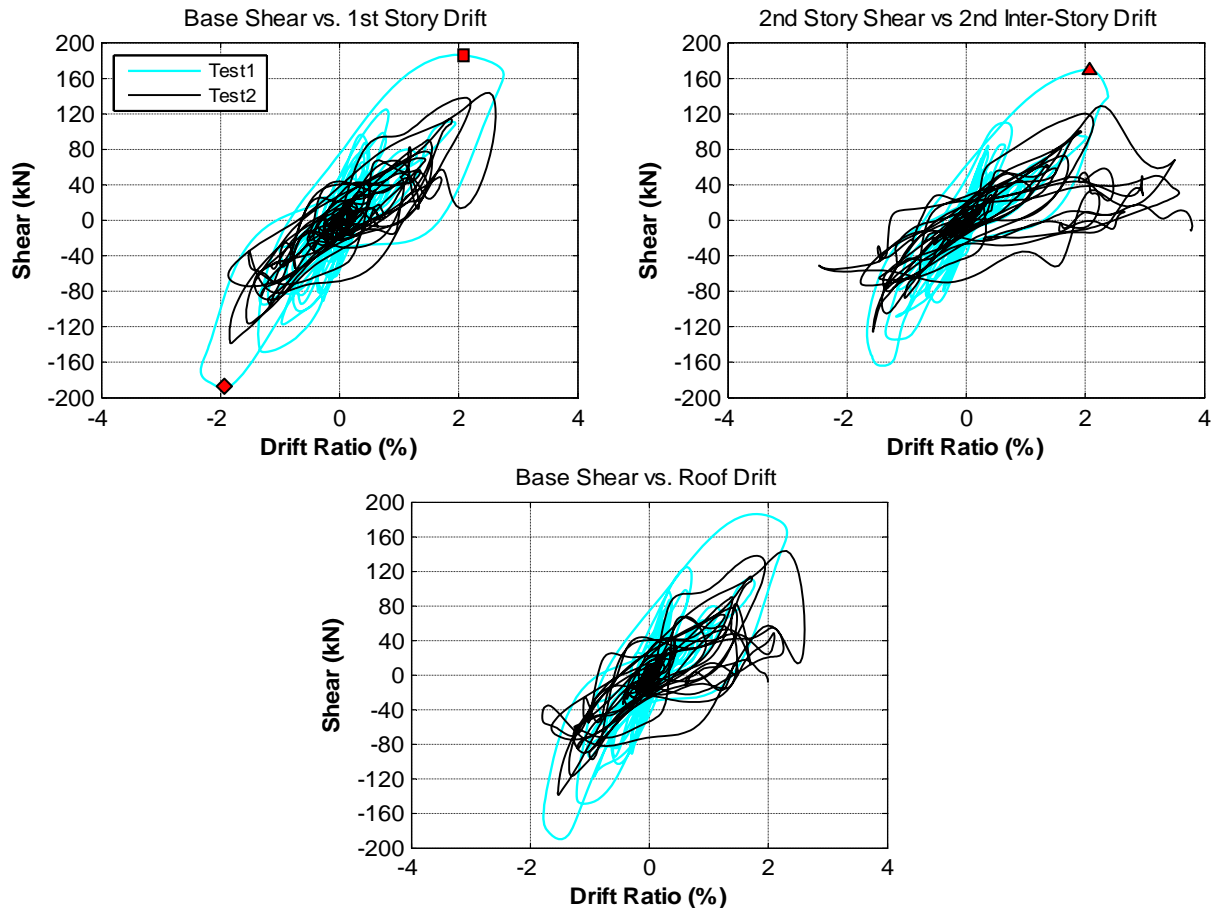


Figure 4-78. Story-level shear hysteretic response of specimen MUFS, Test1 and Test2

Figure 4-79 compares the shear hysteretic response of the columns for Test1 and Test2. Shear degradation for column B1 and C1, shown by square markers, commenced at 1.9% and 2.0% drift ratios in the positive direction of Test1, respectively. The degradation could be due to shear cracking in the columns, propagation of joint cracks into the columns, or combination of both. To identify the source of shear degradation for first-story columns, hysteretic response of those columns were closely examined. While joint A1 was damaged more than the two other joints during Test1, no sign of shear degradation was observed for the column in the positive direction. Therefore, it can be concluded that joint damage was not the source of shear strength degradation for columns B1 and C1 in the positive direction and as shown in Figure 4-69b and Figure 4-69c, damage to the base of these columns was the source of shear

strength degradation in that direction. On the other hand, as marked by diamond markers in Figure 4-79, shear degradation was observed for all the first-story columns (at -1.9% drift ratio for columns A1 and C1 and -2.0% drift ratio for column B1). As demonstrated in Figure 4-69a, the bottom-end of column A1 did not experience noticeable damage, whereas the column top-end was damaged due to propagation of cracks from joint A1 (Figure 4-68a). Therefore, it can be inferred that the source of shear degradation for column A1 in the negative direction (diamond marker) was joint damage, and similar conclusion can be reached for the other exterior column. Considering limited cracks in joint B1, Figure 4-68b and Figure 4-69b demonstrate shear cracks at both ends of column B1 which can be the source of shear strength degradation for the column in both directions.

Shear degradation for second-story columns during Test1 and Test2 could be caused by shear cracks at the top end of the columns. Onset of shear degradation for second-story columns was marked by triangular and circle markers for Test1 and Test2, respectively. As shown in Figure 4-70a and Figure 4-70c, joint cracks did not extend to the base of second-story columns, whereas Figure 4-70b demonstrates shear cracks at the top of column B2. Figure 4-79 demonstrates severe shear degradation for second-story columns during Test2. Since cracking in joint B1 remained similar in both tests, it can be concluded that the sharp shear degradation after the circle markers (2.3% drift ratio) was caused by damage to top-end of second-story columns. It is observed that the degradation for column B2 was the steepest, whereas shear degradation for column A2 was the least severe due to lower compression on the column resulted from overturning.

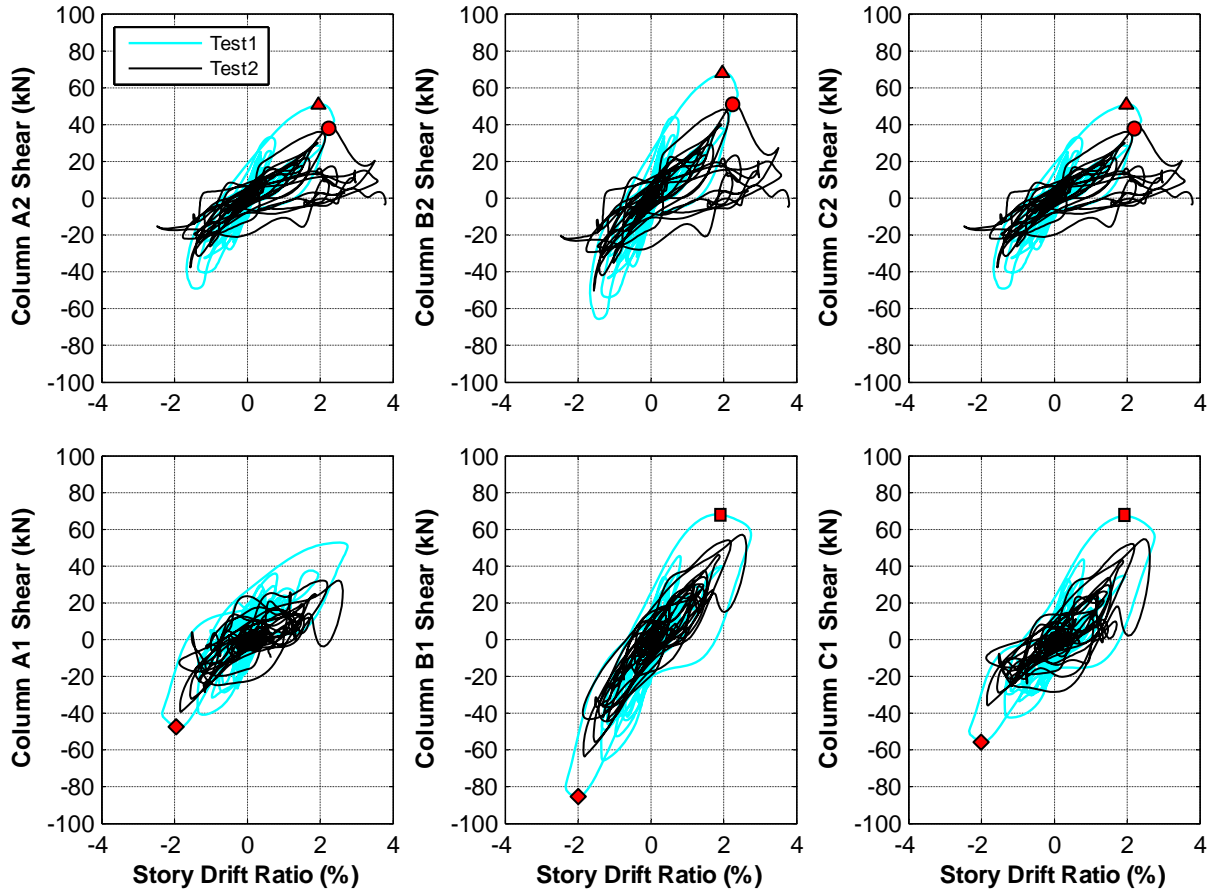


Figure 4-79. Shear hysteretic response of specimen MUFS columns, Test1 and Test2

Figure 4-80 plots the axial load hysteretic response of first-story columns, whereas Figure 4-81 demonstrates the axial load response history of these columns. Variation in axial load recorded for the columns during Test2 was larger than Test1, particularly for column B1. However, it is observed that the peak axial load for the exterior columns remained nearly similar during both tests. Figure 4-81 shows that following the failure of column B2 at 34.29 seconds (star marker), which released the load on column B1, the exterior columns started to pick up the load until the failure of column C2 at 37.66 seconds which released the load on column C1 (cross marker).

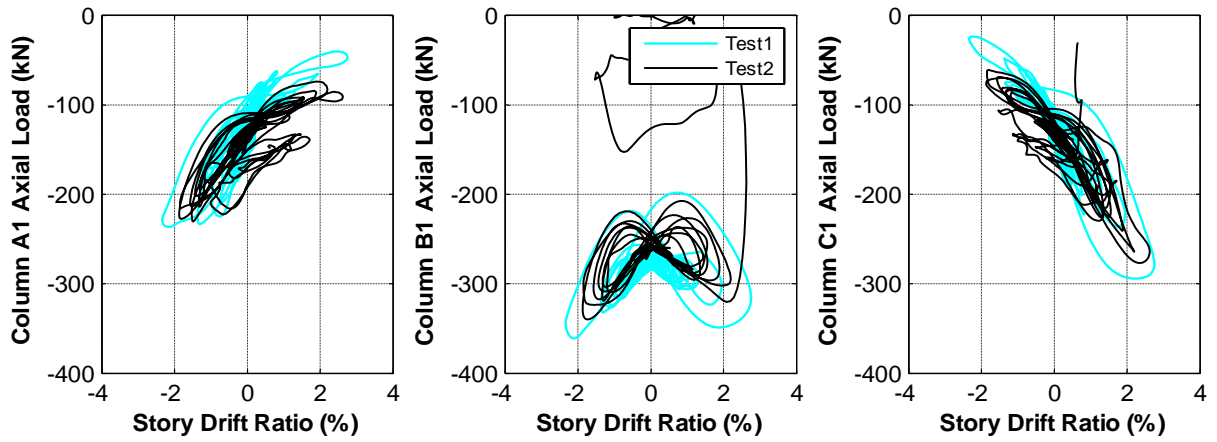


Figure 4-80. Axial load hysteretic response of first-story columns of specimen MUFS, Test1 and Test2

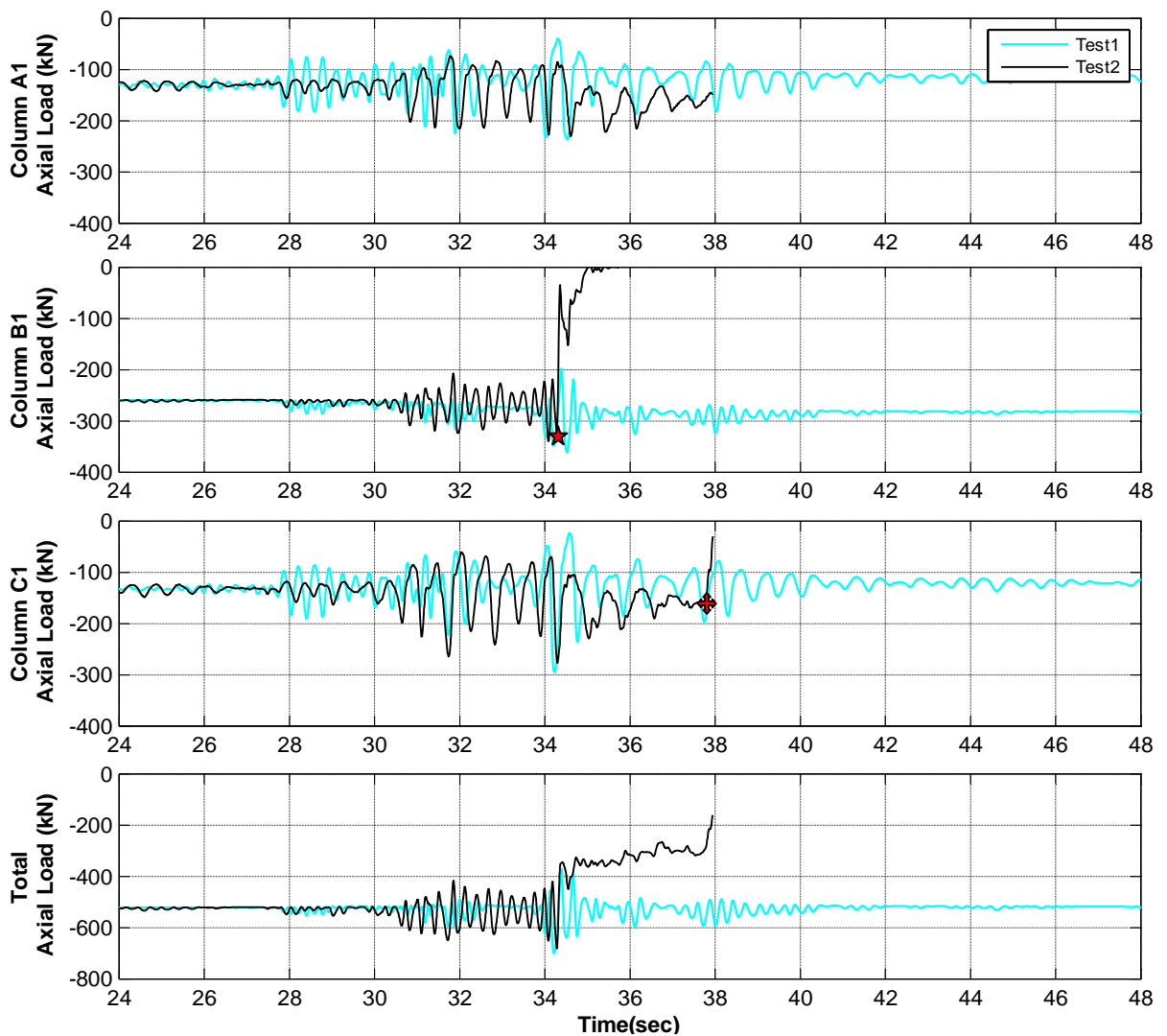


Figure 4-81. Axial load response history of first-story columns of specimen MUFS, Test1 and Test2

Figure 4-82 plots the vertical displacement ratio versus drift ratio of the columns during Test1 and Test2, while Figure 4-83 presents the relationship between axial load and vertical displacement of the first-story columns. With the maximum ratio of 0.21% during Test2, column A2 experienced the largest vertical displacement ratio amongst the columns. It should be noted that such large vertical displacement for column A2 was recorded before the failure of other columns. It is observed that the vertical displacement ratio for column B2 suddenly dropped at 0.12% vertical displacement ratio and 2.34% drift in Test2, which was the onset of axial failure of column B2. As mentioned earlier, the exterior columns started to pick up the load until axial failure of column C2 occurred at a lower vertical displacement ratio of 0.06% and 1.72% drift ratio.

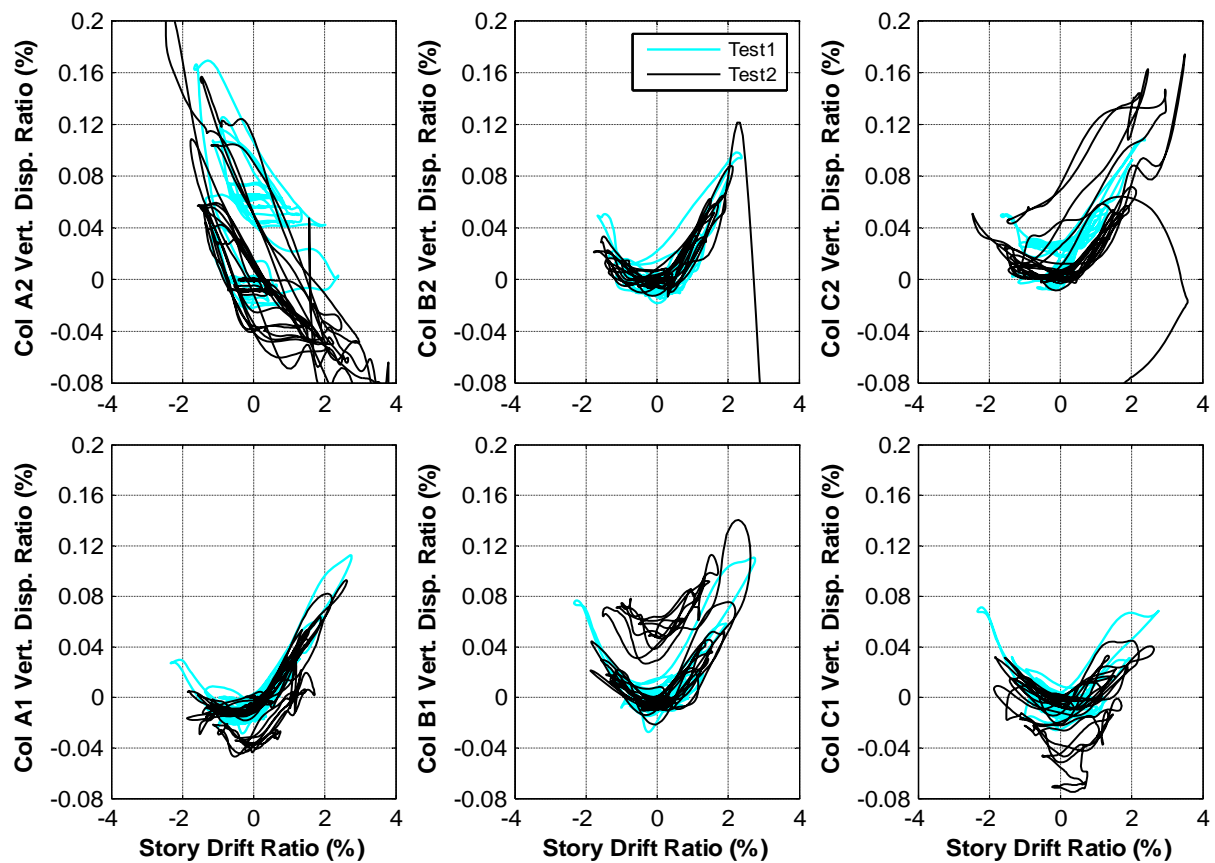


Figure 4-82. Vertical displacement ratio for columns of specimen MUFS, Test1 and Test2

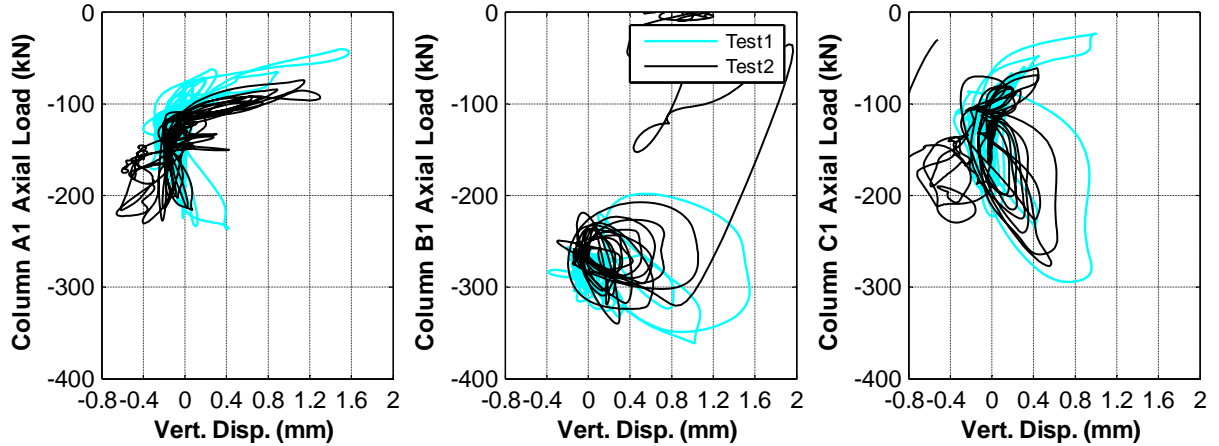


Figure 4-83. Variation of axial load of specimen MUFS columns with vertical displacement, Test1 and Test2

While Figure 4-84 plots moment versus chord rotation for the top-end of first-story columns during Test1 and Test2, Figure 4-85 compares the moment-drift hysteretic response of the columns at the base during the tests. It is observed that the hysteresis was very noisy for the column top (Figure 4-84). The source of such noise is unknown and therefore, the results should be interpreted with caution. Figure 4-85 shows that the end-moments for each column remained relatively similar during both tests.

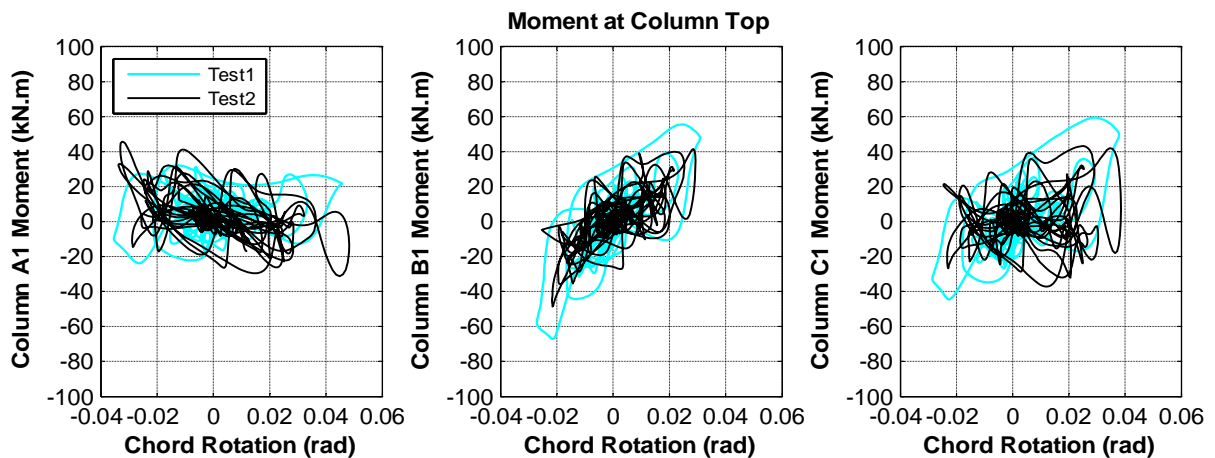


Figure 4-84. Moment-chord rotation relationship at top of first-story columns of specimen MUF, Test1 and Test2

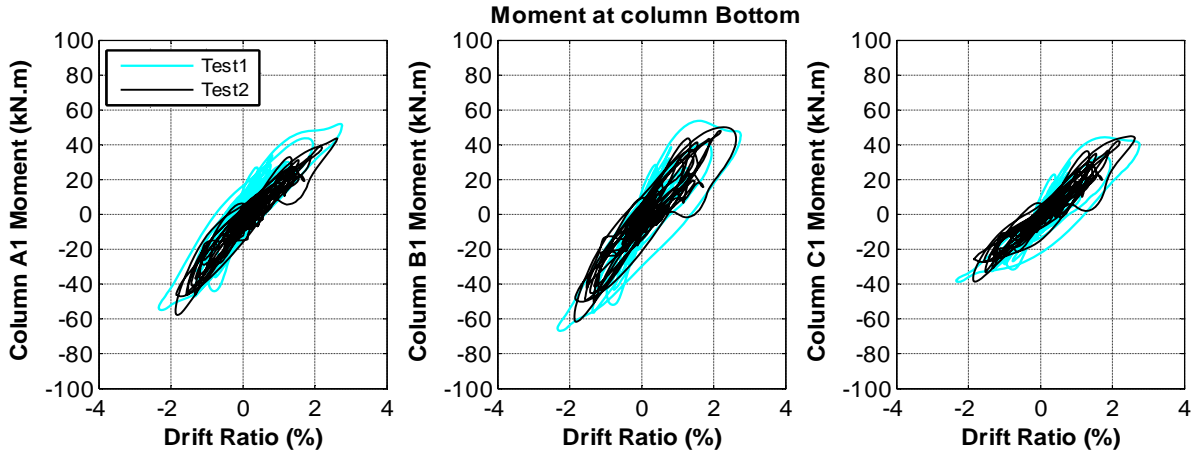


Figure 4-85. Moment hysteretic response of first-story columns of specimen MUFS, Test1 and Test2

Figure 4-86 plots the moment-rotation relationship for the plastic hinge zones at the top and bottom of column B1. Details of the local instrumentation for column B1 can be found in Appendix Section B.3. The rotational stiffness at the base of the column was reduced during Test1 at about 0.0014 rad (shown by triangular marker, $t = 28.4$ seconds). As an interpretation of damage to the column base, the moment-rotation hysteresis clearly showed the reduction of rotational stiffness, whereas the moment-drift hysteresis was not sensitive enough to capture the minor damage to the column bottom. This suggests that examining the rotation, rather than the drift, results in better prediction of damage to a column.

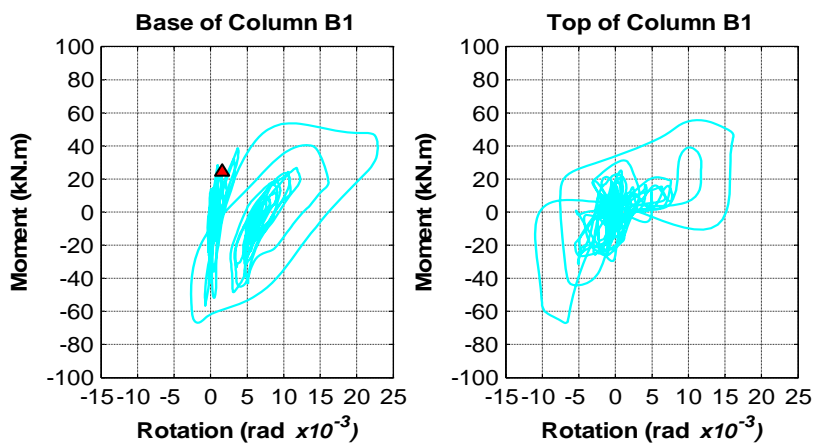


Figure 4-86. Moment-rotation hysteresis for column B1 of specimen MUFS, Test1 and Test2

Similar to specimen MUF, additional instruments were used to measure the diagonal deformation of the exterior joints on their exposed face located on the east side of the frame (see Appendix Section B.3). Comparison of shear deformations recorded for both confined (transverse beam face) and unconfined (exposed) surfaces of joint C1 (Figure 4-87) reveals that the out-of-plane beam significantly restricted the development of shear cracks through the width of the joint in the direction of shaking. It is observed that the largest shear deformation on the transverse beam face of the joint was recorded as 0.005 rad during Test1, whereas the maximum deformation on the exposed surface was 0.019 rad. Similar observation is attained for Test2, where maximum shear deformations of 0.006 rad and 0.016 rad were recorded for the transverse beam and exposed faces of the joint, respectively. Photos in Figure 4-88 compare the propagation of cracks into column C1 for the two faces and confirm the mentioned observations.

Figure 4-89 demonstrates the relationship of shear at the top end of column C1 and the shear deformation recorded for the exposed face of the joint. The joint was initially able to withstand the shear demand. However, due to development of shear cracks, a significant reduction in stiffness of the joint panel was observed after a joint deformation of -0.0025 rad in Test1. As shown in Figure 4-90, such deformation corresponded to a first-story drift ratio of 0.4% in the negative direction of the test. Although joint C1 presented a softer behaviour during Test2, it was able to resist the shear demand until the failure of the columns in the second story occurred.

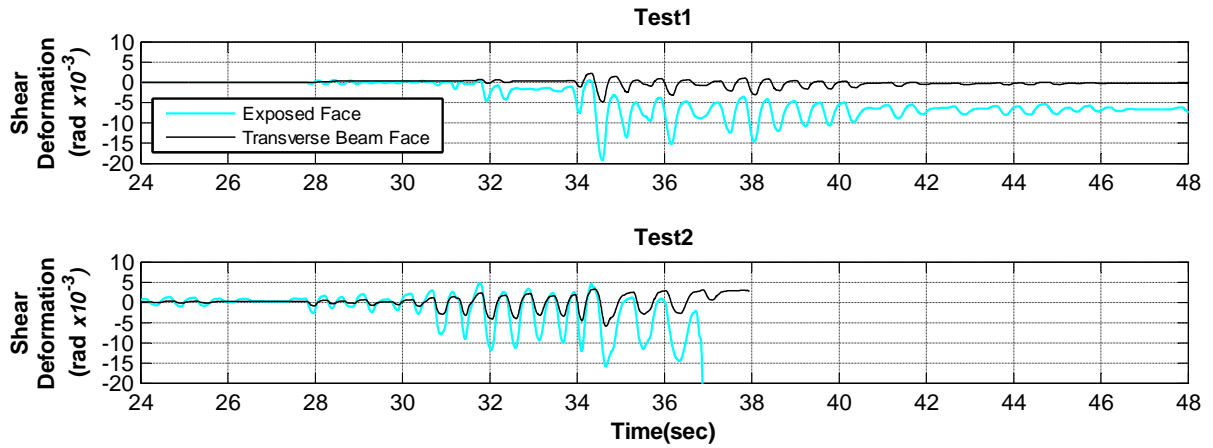


Figure 4-87. Comparison of shear deformation at joint C1 of specimen MUFS, recorded by diagonal instruments on east and west sides of the joint

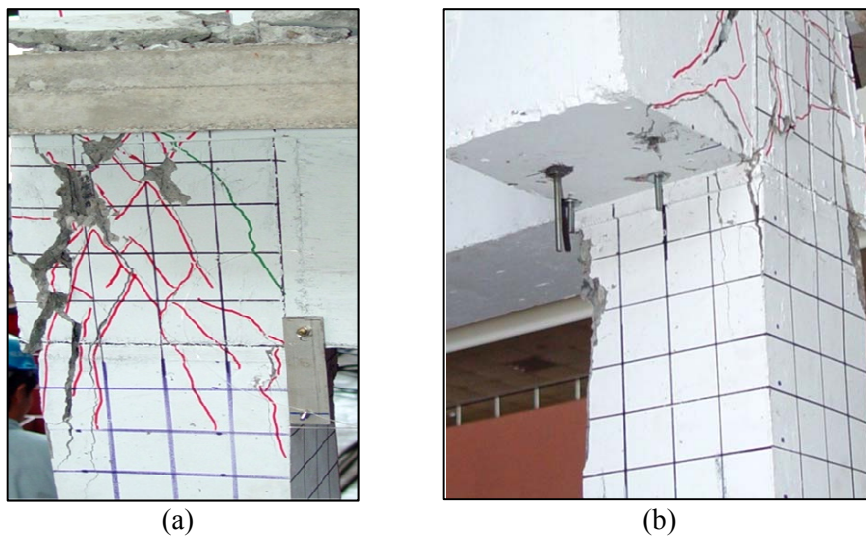


Figure 4-88. Comparison of propagation of shear cracks to the top of column C1 of specimen MUFS after Test2; a) exposed face; b) transverse beam face

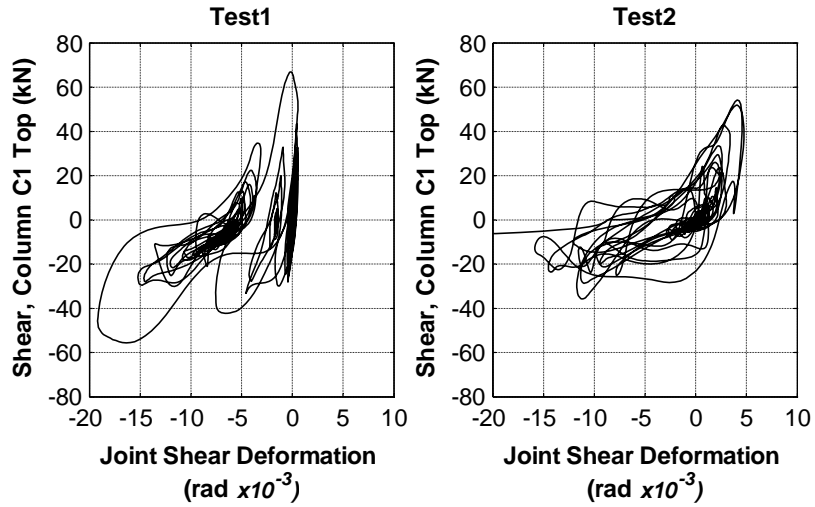


Figure 4-89. Relationship between shear force and shear deformation of joint C1 recorded at unconfined face of the joint for specimen MUFS

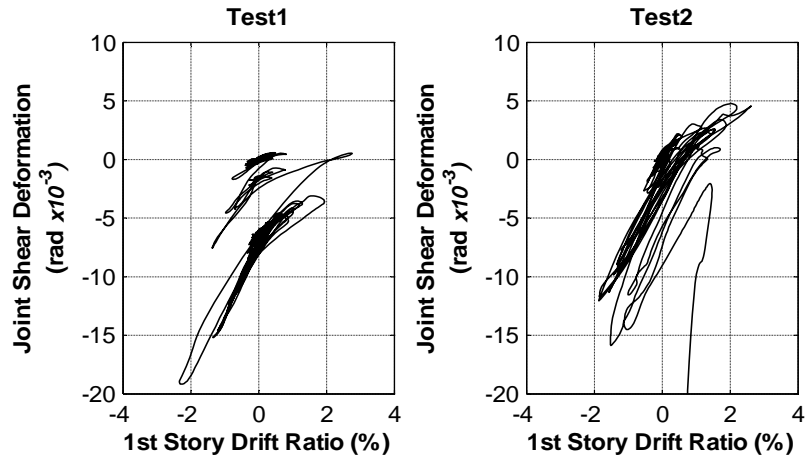


Figure 4-90. Relation between first-story drift ratio and shear deformation of joint C1 recorded at unconfined face of the joint for specimen MUFS

CHAPTER 5. COMPARISON OF RESPONSE OF THE TEST SPECIMENS

5.1 Introduction

This chapter will compare and discuss the results from testing the four specimens described in Chapter 4. The table demands for the test frames during Test1 and Test2 are compared in Section 5.2. Similarity of lateral demands and comparability of material properties and frame geometries allowed for a valid comparison of the test results. While failure modes of the specimens are discussed and compared in Section 5.3, test results including acceleration recorded at story levels, peak drift demands, and shear backbone for first-story columns of the specimens are compared in Section 5.4. Effects of higher axial load on key parameters for columns including drift ratio, effective and secant stiffness, and slope of vertical deformation before and after axial failure are studied in Section 5.5. Finally, advantages of column chord rotation over drift ratio for characterizing column deformation demands are discussed in Section 5.6.

5.2 Comparison of Table Demands

In order to study the influence of one parameter (e.g. axial load) on behaviour of structural elements during different tests, it is important to keep the other influential parameters (e.g. table demands) similar. In this section, acceleration at table level and spectral acceleration demands for the specimens are compared during Test1 and Test2. To allow for better comparison, table demands for only two specimens are shown in each figure. Considering specimen MCFS as the benchmark test, input demands for other specimens during Test1 and Test2 are compared with this specimen in Sections 5.2.1 to 5.2.4.

5.2.1 Comparison of Table Demands for Specimens MCFS and HCFS

As discussed in Chapter 4, the main difference between specimens MCFS and HCFS was the applied axial load, where columns of specimen HCFS carried almost twice the axial load as columns of specimen MCFS (see Table 3-2). Comparison of recorded table motion and acceleration response recorded at the footing and story levels of specimens MCFS and HCFS during Test1 demonstrates that the table- and footing-level acceleration records remained very similar for both specimens (Figure 5-1).

The spectral accelerations recorded for specimen MCFS and HCFS during Test1 are compared in Figure 5-2. As discussed in Section 4.3, the fundamental period of specimen HCFS (0.28 sec) was slightly shorter than specimen MCFS (0.29 sec). It is observed that while the spectral acceleration for specimen HCFS remained smaller than specimen MCFS for periods smaller than 0.27 seconds, the spectral acceleration for specimen HCFS became larger than specimen MCFS right before the fundamental period of specimen HCFS. Figure 5-2

demonstrates that the spectral acceleration demand for specimen HCFS was about 14% higher than MCFS at the fundamental periods of the frames.

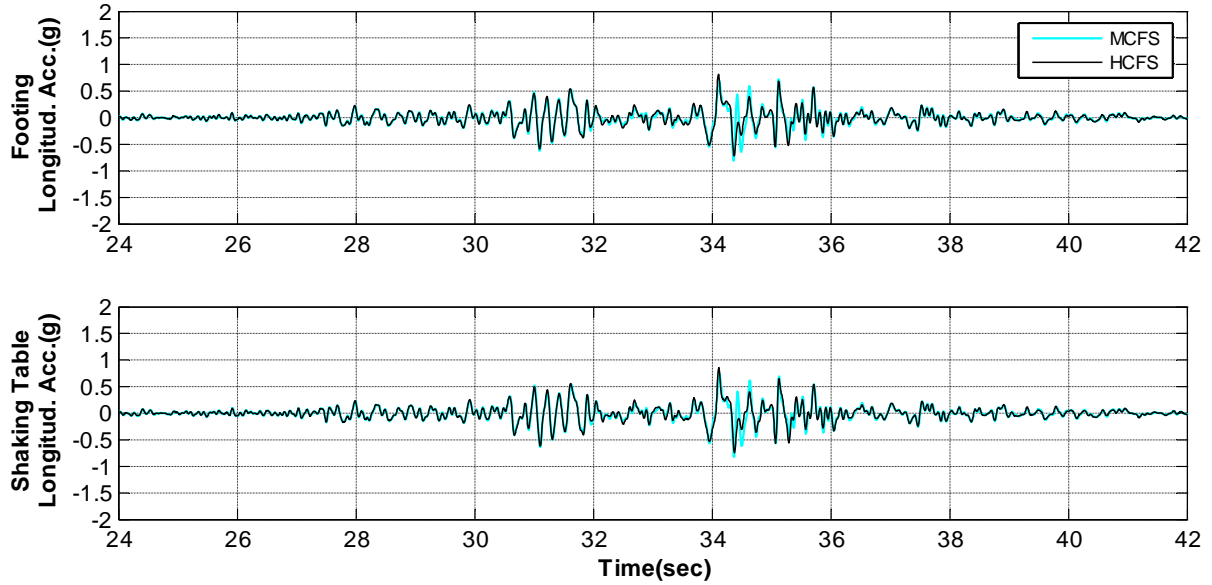


Figure 5-1. Comparison of acceleration response history for specimens MCFS and HCFS at table and footing levels, Test1

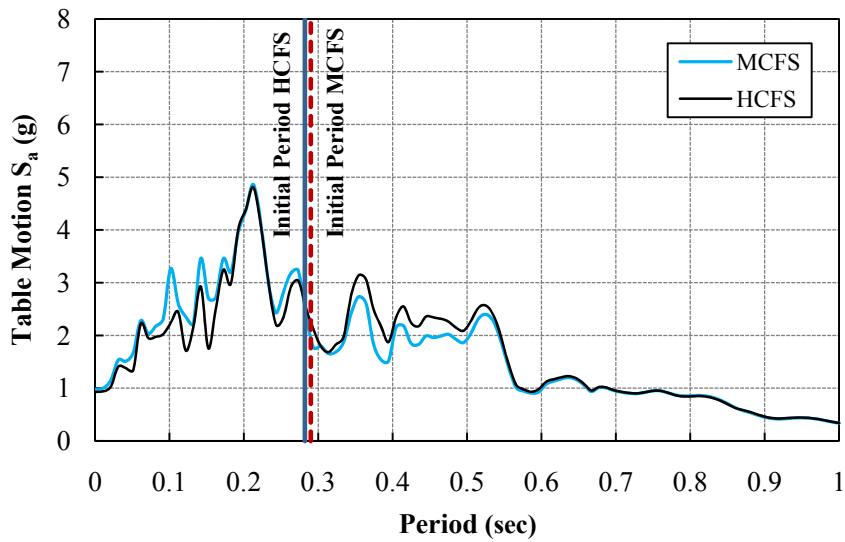


Figure 5-2. Comparison of spectral acceleration with 2% damping for specimens MCFS and HCFS, Test1 table motion

Figure 5-3 plots the recorded table motion and longitudinal acceleration response at the footing level for specimens MCFS and HCFS during Test2, where the acceleration at the table and footing levels remained identical for both specimens up to the point of collapse of specimen MCFS. (Note that data in Figure 5-3, and subsequent figures for the collapse tests, were terminated at the time of specimen collapse). It is observed that specimen HCFS survived longer than specimen MCFS before collapse. While test frame MCFS collapsed at 34.30 seconds (circle marker), collapse of specimen HCFS was recorded at 35.85 seconds.

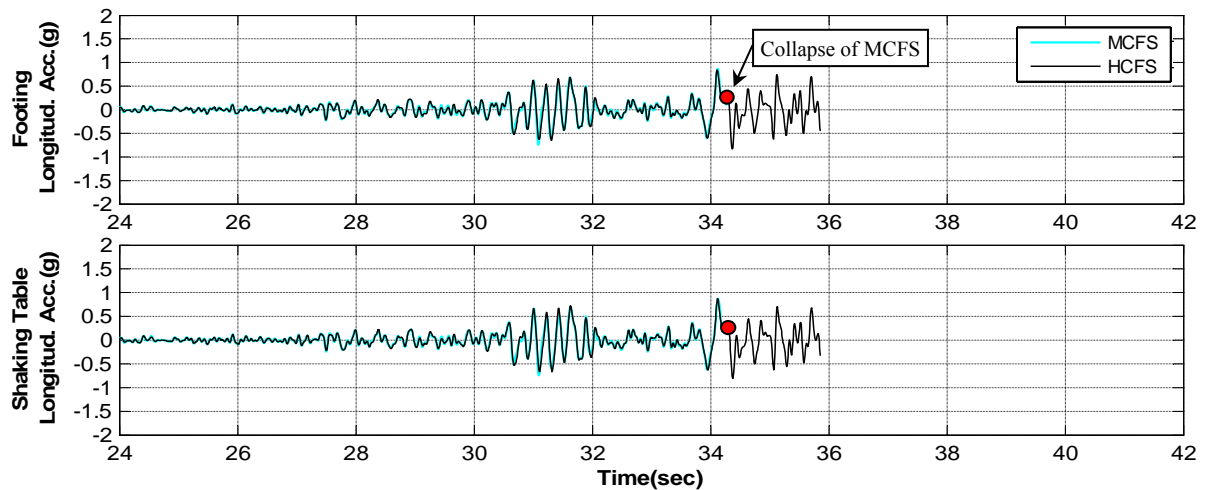


Figure 5-3. Comparison of acceleration response history for specimens MCFS and HCFS at table and footing levels, Test2

Figure 5-4 compares the spectral accelerations recorded for specimen MCFS and HCFS during Test2. As discussed in Chapter 4, the natural period of the specimens lengthened to 0.36 seconds due to damages to the frames during Test1. Figure 5-4 demonstrates that unlike the spectral accelerations at the original periods of the frames, the spectral acceleration for specimen HCFS became smaller than specimen MCFS at the lengthened period. Figure 5-4 shows that the spectral acceleration demand for specimen HCFS was about 8% lower than MCFS in the vicinity of the lengthened period of the frames (dashed line).

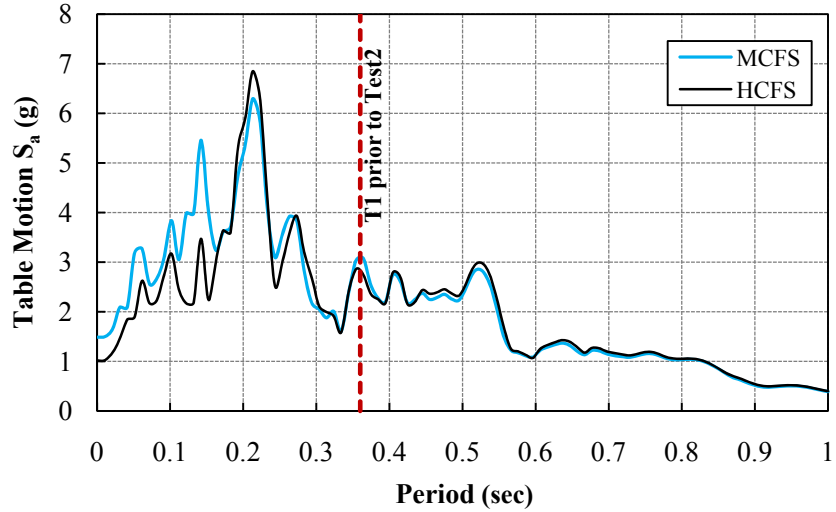


Figure 5-4. Comparison of spectral acceleration with 2% damping for specimens MCFS and HCFS, Test2 table motion

5.2.2 Comparison of Table Demands for Specimen MCFS and MUF

As discussed in previous chapter, specimen MCFS was built with non-ductile columns and confined joints, whereas specimen MUF was constructed with ductile columns and unconfined joints. Applied axial loads on the columns of the two specimens were similar (Table 3-2).

Comparison of recorded table motion and longitudinal acceleration response at the footing level for specimens MCFS and MUF during Test1 (Figure 5-5) demonstrates that the table and footing level accelerations recorded for the specimens remained very similar during the test. Figure 5-6 compares the spectral accelerations recorded for specimen MCFS and MUF during Test1, showing that spectral acceleration demand for specimen MUF was only 2% higher than specimen MCFS at the fundamental period of the two frames (0.29 seconds, dashed line).

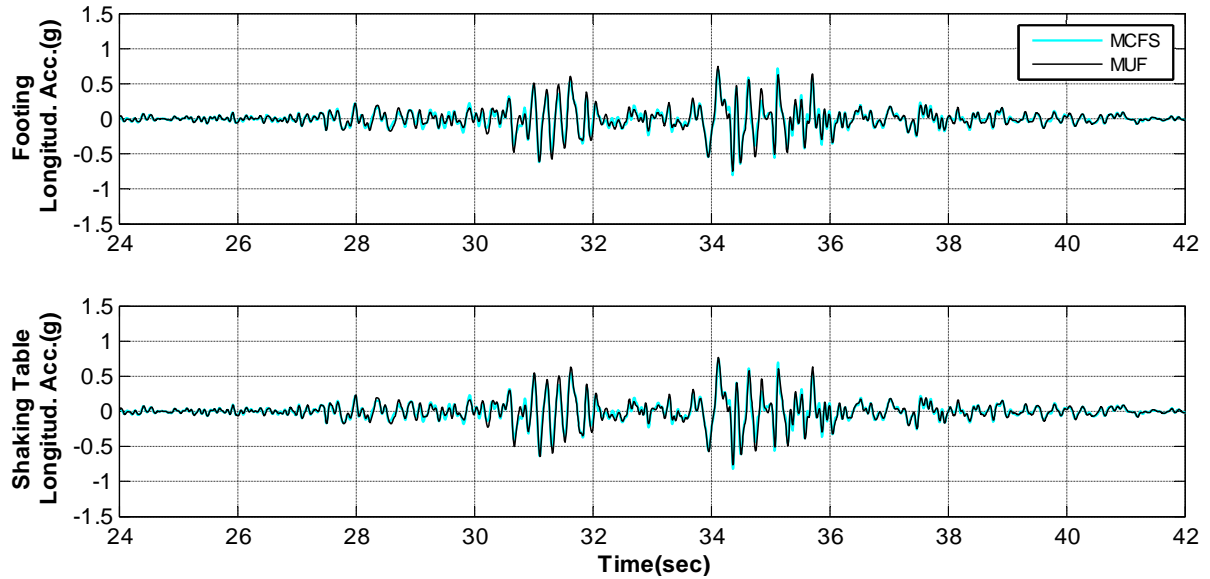


Figure 5-5. Comparison of acceleration response history for specimens MCFS and MUF at table and footing levels, Test1

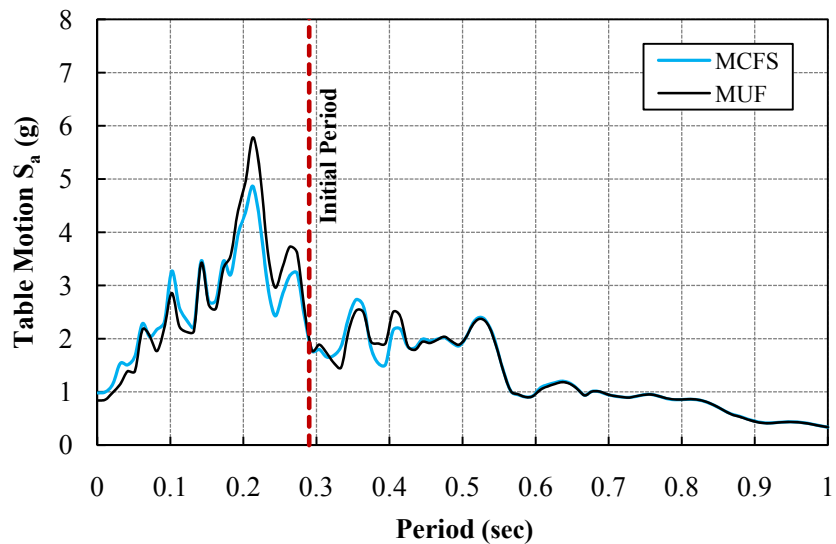


Figure 5-6. Comparison of spectral acceleration with 2% damping for specimens MCFS and MUF, Test1 table motion

The recorded table motion and longitudinal acceleration response at the footing level for specimens MCFS and MUF during Test2 are compared in Figure 5-7. It is observed that the table and footing level accelerations remained similar for the two specimens up to the point of failure of specimen MCFS at 34.30 seconds (circle marker). Although larger peaks were

recorded for specimen MUF between 30.8 and 32.0 seconds of the test, the peak recorded acceleration remained very close for the two specimens.

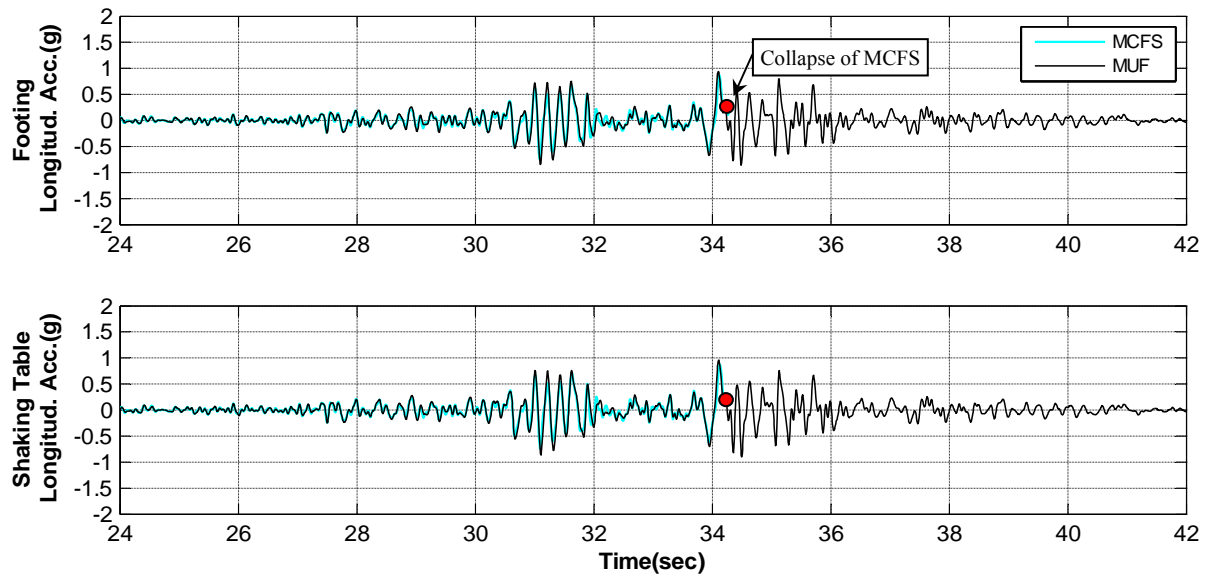


Figure 5-7. Comparison of acceleration response history for specimens MCFS and MUF at table and footing levels, Test2

Figure 5-8 compares the spectral accelerations recorded for specimens MCFS and MUF during Test2. As shown in previous chapter, the natural period of specimen MCFS lengthened from 0.29 seconds to 0.36 seconds (dashed line), whereas the period of test frame MUF increased from 0.29 seconds to 0.46 seconds (dotted line), where the larger increase in the frame period resulted from the additional damage to the unconfined beam-column joints in specimen MUF. Figure 5-8 demonstrates that the spectral acceleration demand for specimen MCFS at 0.36 seconds was about 3.1g, whereas the acceleration demand for specimen MUF at 0.46 seconds was only 2.3g.

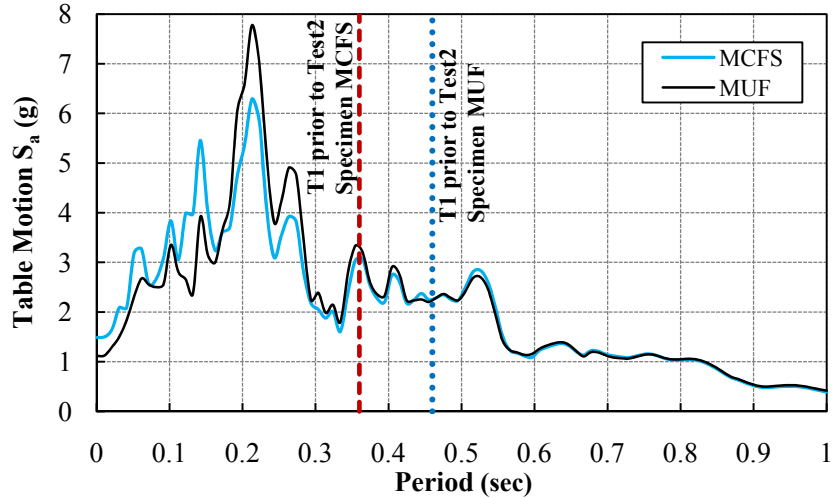


Figure 5-8. Comparison of spectral acceleration with 2% damping for specimens MCFS and MUF, Test2 table motion

5.2.3 Comparison of Table Demands for Specimen MCFS and MUFS

While the recorded table motion and longitudinal acceleration response at the footing level during Test1 for specimens MCFS and MUFS are compared in Figure 5-9, Figure 5-10 compares the spectral acceleration records for specimen MCFS and MUFS during Test1, demonstrating that the spectral acceleration demand for specimen MUFS was about 9% higher than MCFS at the initial fundamental period of the frames (0.29 sec, dashed line).

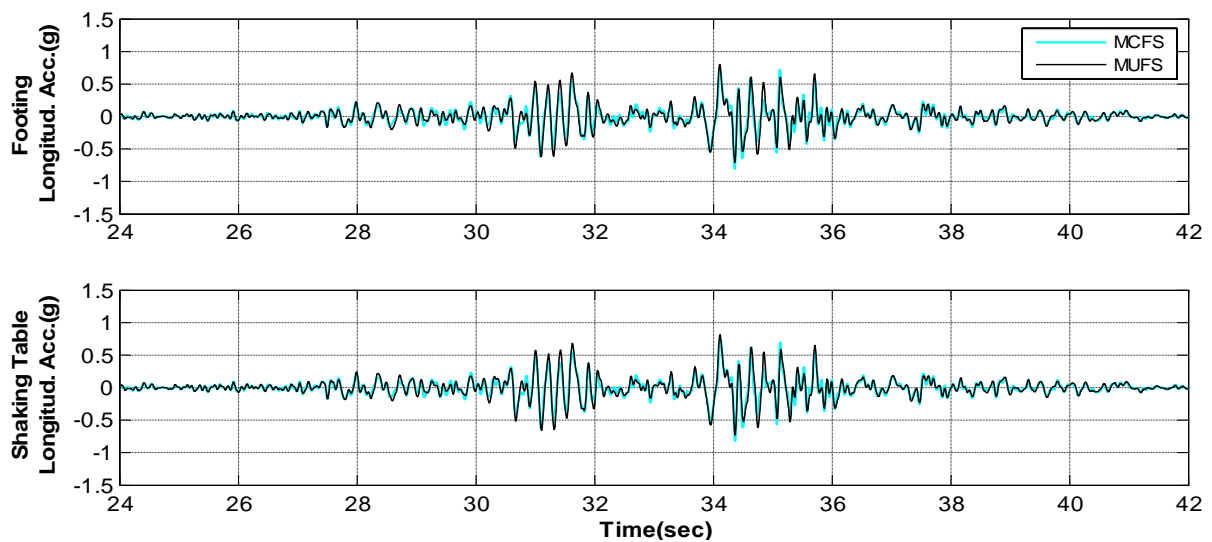


Figure 5-9. Comparison of acceleration response history for specimens MCFS and MUFS at table and footing levels, Test1

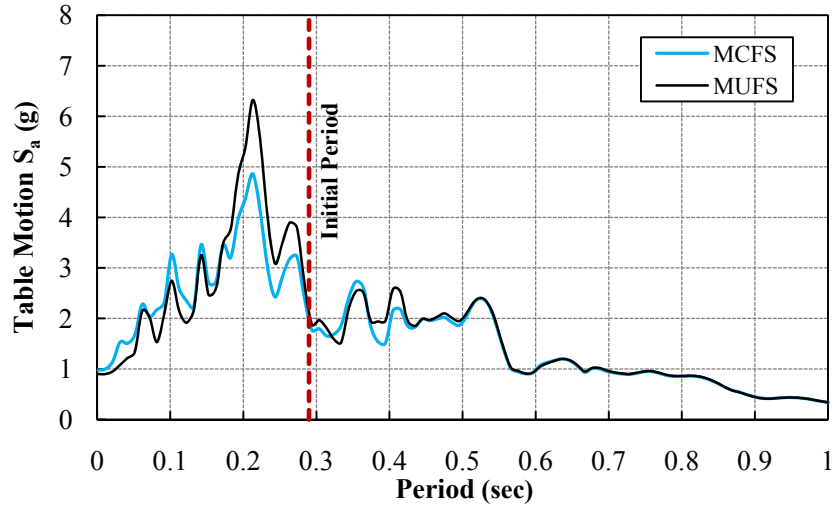


Figure 5-10. Comparison of spectral acceleration with 2% damping for specimens MCFS and MUFS, Test1 table motion

Figure 5-11 compares the recorded table motion and longitudinal acceleration response at the footing level for the above-mentioned specimens during Test2. Acceleration records remained very similar for the two specimens at the table and footing levels except for the time between 30.7 and 32.0 seconds, where larger acceleration peaks were observed for specimen MUFS. The peak acceleration recorded for specimen MCFS was 12% lower than the other specimen. While collapse of specimen MCFS occurred at 34.30 seconds (circle marker), specimen MUFS collapsed later at 37.95 seconds of Test2.

Despite differences in the acceleration histories, Figure 5-12 compares the spectral accelerations recorded for specimen MCFS and MUFS during Test2 and shows a close agreement for the spectral acceleration of the two specimens. As discussed in Chapter 4, natural period of specimen MCFS was lengthened from 0.29 seconds to 0.36 seconds (dashed line), whereas the period of test frame MUFS was lengthened from 0.29 seconds to 0.46 seconds (dotted line) due to severe damage to first-story joints. As shown in Figure 5-12, the spectral acceleration demand for specimen MCFS at 0.36 seconds was 3.1g, whereas the demand for specimen MUFS at 0.46 seconds was 2.4g.

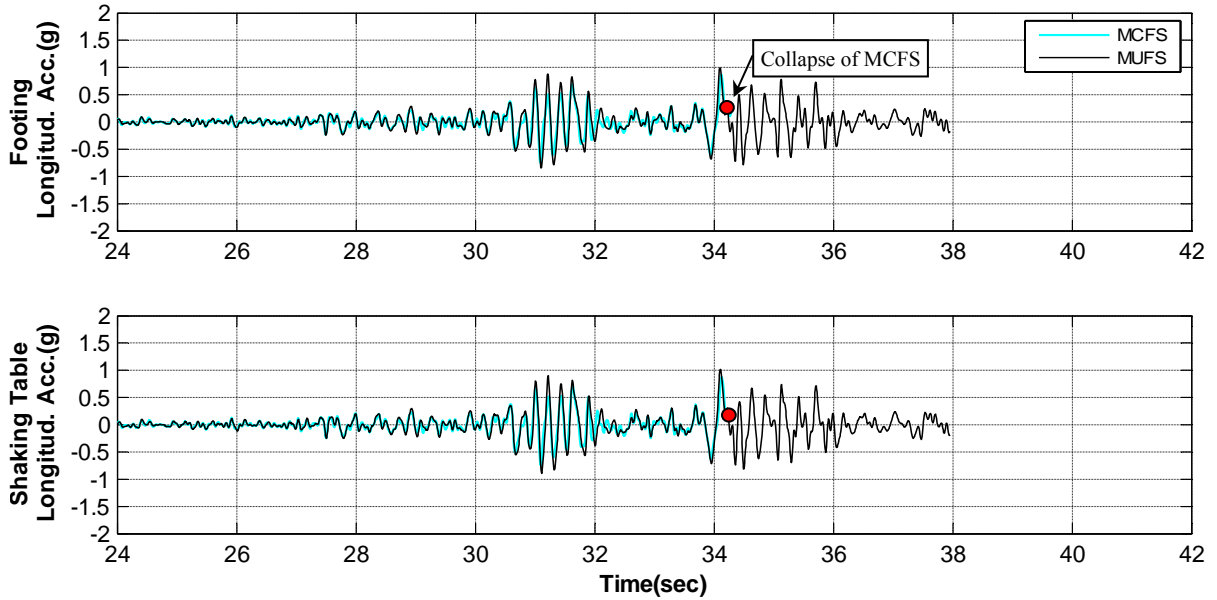


Figure 5-11. Comparison of acceleration response history for specimens MCFS and MUFS at table and footing levels, Test2

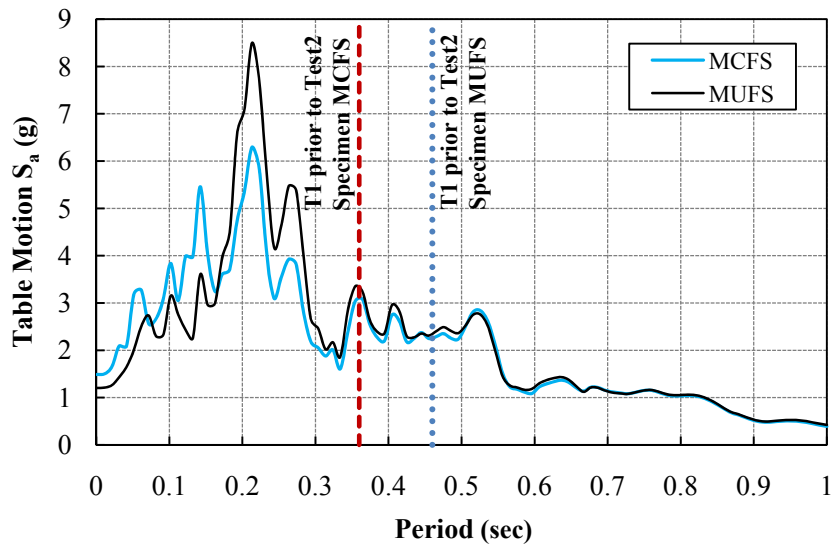


Figure 5-12. Comparison of spectral acceleration with 2% damping for specimens MCFS and MUFS, Test2 table motion

5.2.4 Comparison of Table Demands for Specimen MUF and MUFS

Comparison of the recorded table motion and longitudinal acceleration response at the footing level during Test1 for specimens MUF and MUFS (Figure 5-13) shows that the

acceleration remained almost identical for the two specimens throughout the test. Figure 5-14 compares the spectral accelerations recorded for the two specimens during Test1. Very similar spectral acceleration demands were observed for the two specimens at the fundamental period of the frames (0.29 sec, dashed line).

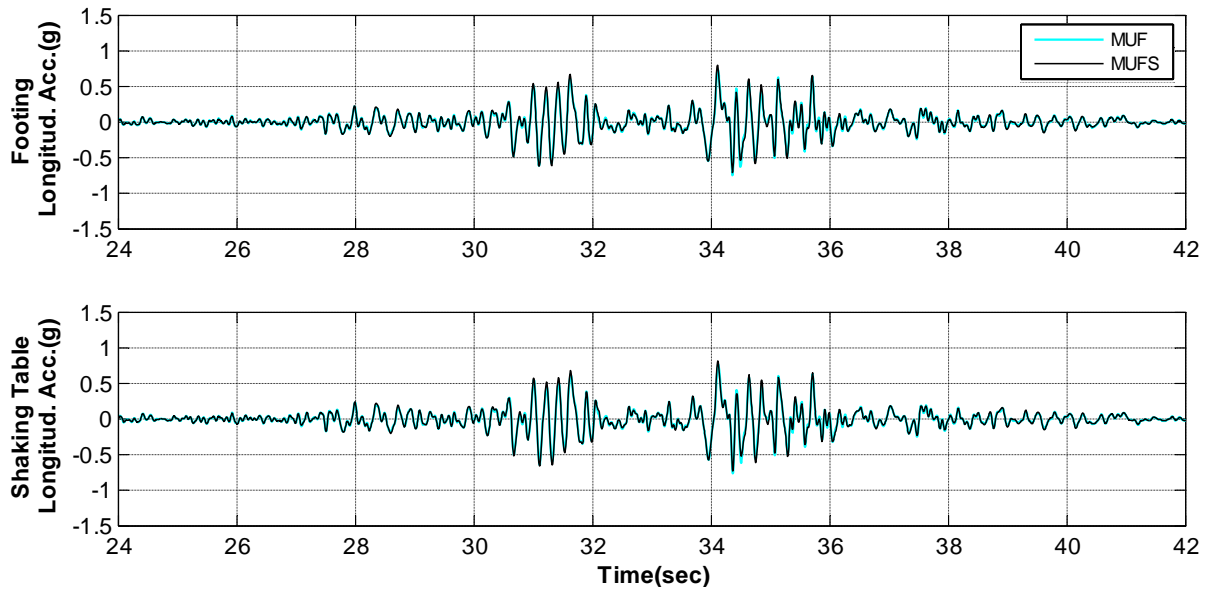


Figure 5-13. Comparison of acceleration response history for specimens MUF and MUFS at table and footing levels, Test1

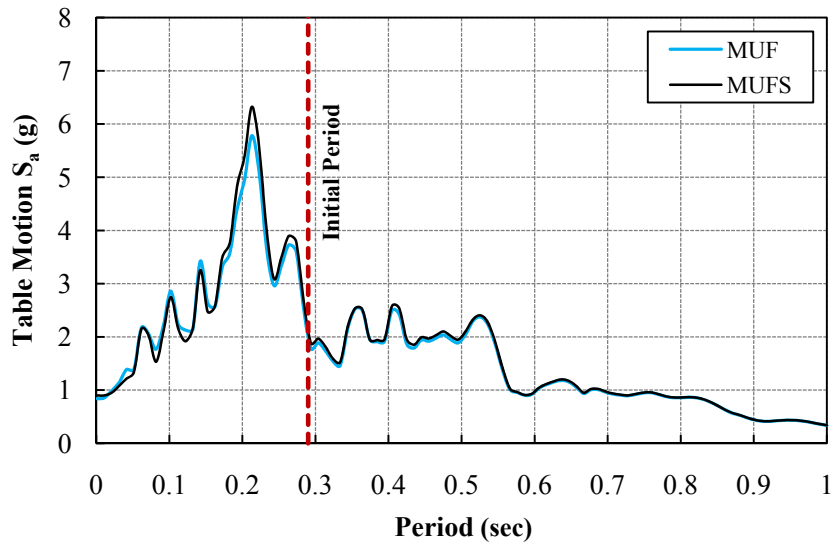


Figure 5-14. Comparison of spectral acceleration with 2% damping for specimens MUF and MUFS, Test1 table motion

While Figure 5-15 compares the recorded table motion and longitudinal acceleration response at footing level during Test2 for specimens MUF and MUFS, Figure 5-16 compares the spectral accelerations recorded for the two specimens. Acceleration records remained almost equal at the table and footing levels before collapse of specimen MUFS. Figure 5-16 shows that the spectral acceleration demand for specimen MUFS was only 4% higher than specimen MUF at the lengthened period of the two frames (0.46 sec, dashed line).

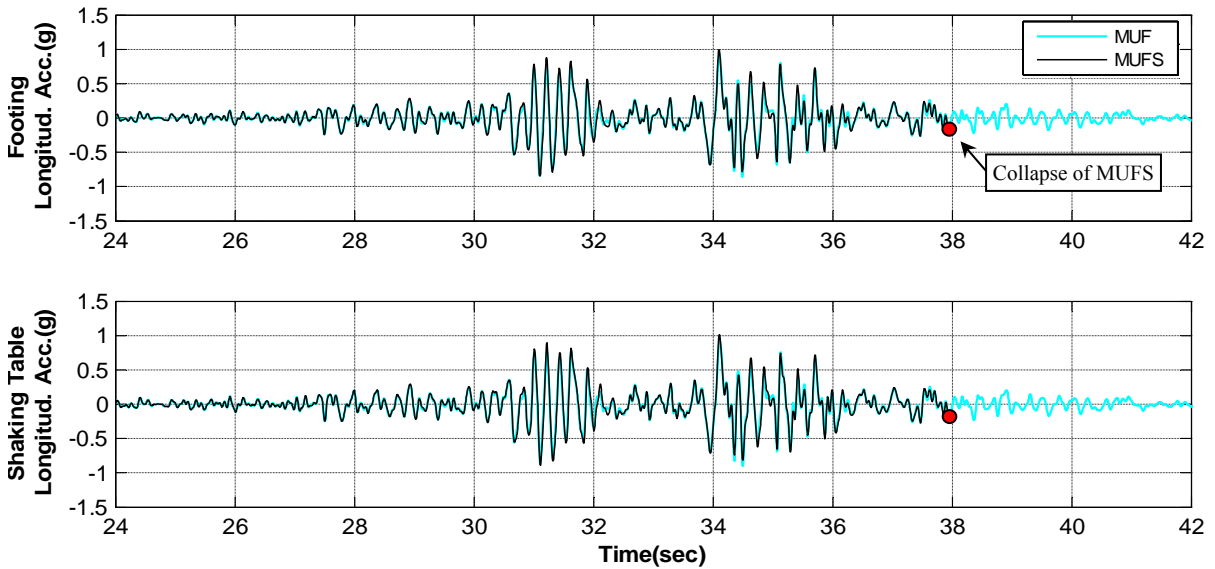


Figure 5-15. Comparison of acceleration response history for specimens MUF and MUFS at table and footing levels, Test2

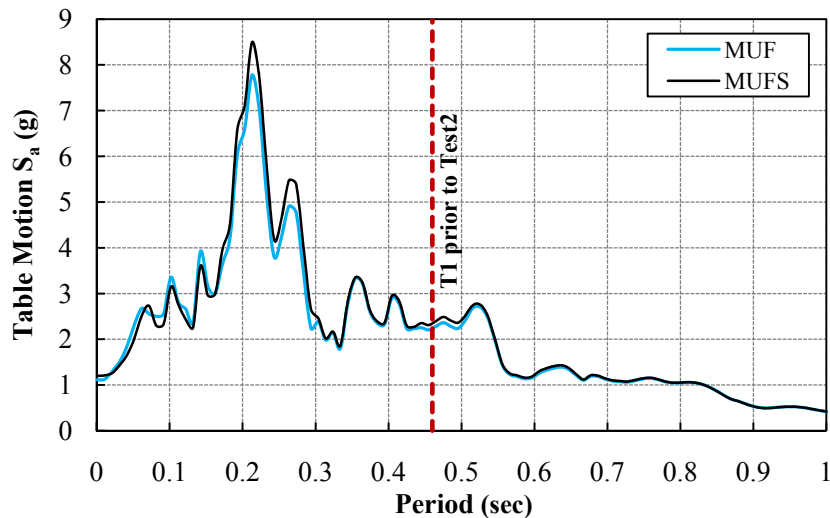


Figure 5-16. Comparison of spectral acceleration with 2% damping for specimens MUF and MUFS, Test2 table motion

Comparison of acceleration response histories and spectral acceleration demands for the specimens during the shaking table tests, shown in Sections 5.2.1 to 5.2.4, demonstrates that the table motion demands were relatively similar for all the specimens. This provides strong grounds for comparison of the test results from the four specimens.

5.3 Comparison of Failure Modes

Although the lateral demands, material properties, and global geometry of the specimens were reasonably similar, collapse of the specimens occurred differently due to axial load demands and detailing of columns and joints. While specimen MCFS collapsed due to shear and axial failure of all of first-story columns at the base, combination of column shear and axial failure and formation of plastic hinges caused the collapse of specimen HCFS. Photos in Figure 5-17 show the failure modes of frames MCFS and HCFS in Test2. No sign of plastic hinging was observed in specimen MCFS, whereas the inset of Figure 5-17b shows severe cracking of the beam suggesting that a plastic hinge was formed in the beam at the face of joint B1 of specimen HCFS.



Figure 5-17. Comparison of failure modes during Test2; a) specimen MCFS; b) specimen HCFS

Comparison of axial load in column B1 of specimens MCFS and HCFS demonstrates that the axial load at the point of shear failure of column B1 of specimen HCFS was 1.6 times the axial load in the corresponding column of specimen MCFS. Due to such excessive axial load in the center column of specimen HCFS, axial failure of column B1 occurred immediately after shear failure and sudden shortening of the column was observed. Due to the higher axial loads in the columns of specimen HCFS, the beam to column strength ratio at the exterior joints was lower for specimen HCFS compared with specimen MCFS. Consequently, additional beam deformations, at the drift at which column B1 failed, caused additional flexural cracking in first-story beams. Such beam deformation means that the exterior columns did not need to experience as much deformation (chord rotation) to achieve the total drift demand. This drop in local deformations of exterior first-story columns protected them enough to allow the columns to survive to the next cycle. Redistributed axial load from the center column, in addition to local deformation at the top of column A2, caused the shear and axial failure of column A2. Finally, the entire vertical load was redistributed from the failed columns on axes A and B to column C1, leading to shear and axial failure of the column and collapse of the frame. In contrast, lower axial load in column B1 of specimen MCFS allowed it to deform more gradually and therefore, load was distributed better to the exterior columns without damaging the beams. Consequently, column C1 failed under higher axial load due to overturning moment in the positive direction and redistributed load from column B1. Finally, shear and axial failure of column A1 caused the collapse of the frame.

As discussed in Chapter 4, all first-story joints in specimens MUF and MUFS experienced shear failure. Nevertheless, joint failure did not cause the collapse of the frames. While specimen MUF did not collapse even during Test3 with the highest table motion

amplitude (Figure 5-18a), shear and axial failure of second-story columns of specimen MUFS resulted in collapse of the specimen (Figure 5-18b). Therefore, comparison of failure modes for the two specimens suggests that the likelihood of collapse of a frame due to failure of unconfined joints is lower than collapse due to failure of non-ductile columns. Mechanism that led to collapse of specimen MUFS was described in Section 4.7.

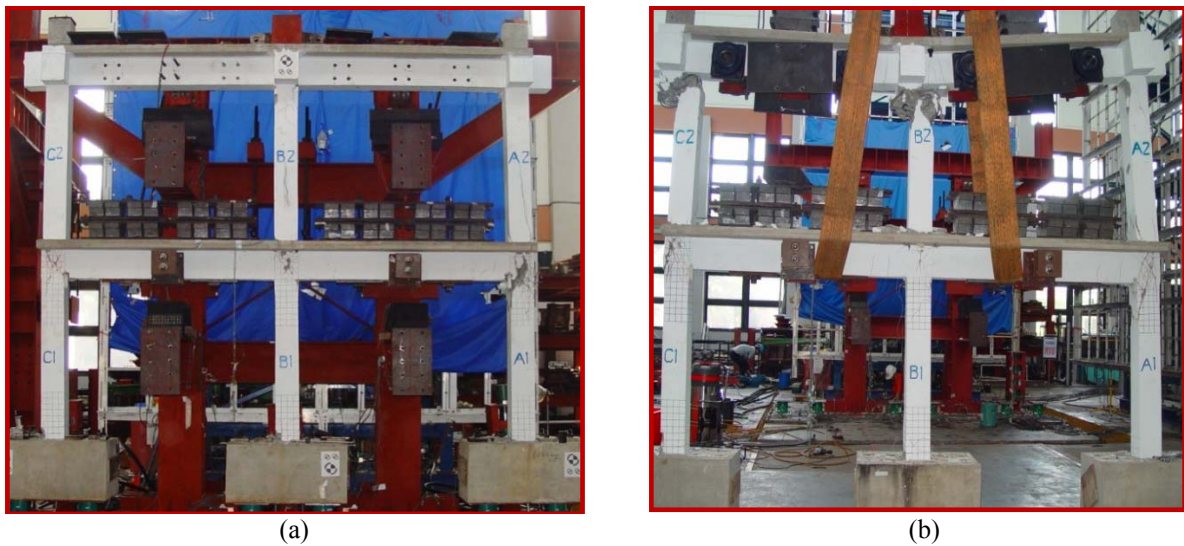


Figure 5-18. Comparison of failure modes in Test2; a) specimen MUF; b) specimen MUFS

5.4 Comparison of Test Data

In this section, the following important parameters of the four specimens are compared for Test1 and Test2:

- 1) Floor acceleration
- 2) Peak inter-story drift demand
- 3) Backbone for shear hysteretic response of first-story columns

5.4.1 Floor Acceleration

Figure 5-19 compares the acceleration response histories for specimen MCFS and HCFS during Test1. In contrast to very similar acceleration response histories recorded at table level, it is observed that the cycles peaked earlier for the stories of specimen HCFS. Given the similarity of material properties and table demands for the two specimens, differences in behaviour of the test frames can be attributed to the difference in applied axial load on the frames (see Table 3-2). While the peak acceleration for specimen HCFS was smaller than MCFS in the first story by 11%, the peak acceleration recorded for the second story of HCFS was larger by 6%, demonstrating that the upper stories of specimen HCFS experienced higher acceleration during Test1. Comparison of acceleration response histories for the two specimens during Test2 also shows that the acceleration in the stories of specimens MCFS and HCFS were not the same due to differences in the damage patterns and columns axial load.

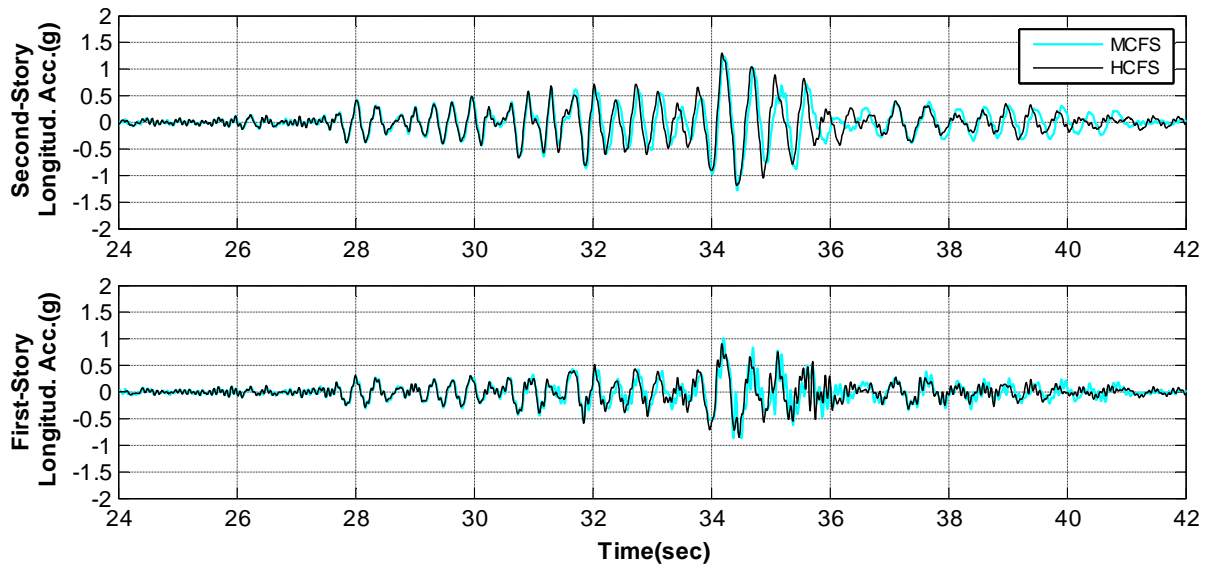


Figure 5-19. Comparison of story-level acceleration records for specimens MCFS and HCFS, Test1

Although applied axial load on columns of specimens MCFS and MUF and their table demands were relatively similar, amplitude and phasing of recorded floor accelerations were

very different (Figure 5-20), potentially due to damage to different structural elements for the two specimens (columns for specimen MCFS and joints for specimen MUF). Divergence in acceleration was initiated at 28.1 seconds, where acceleration peaks remained considerably larger in upper levels of specimen MUF until 28.9 seconds. The maximum recorded floor acceleration of specimen MUF were lower, where its first and seconds stories experienced 33% and 21% lower acceleration than the corresponding stories of specimen MCFS, respectively. Similar observations were made for recorded floor accelerations for specimens MCFS and MUFS.

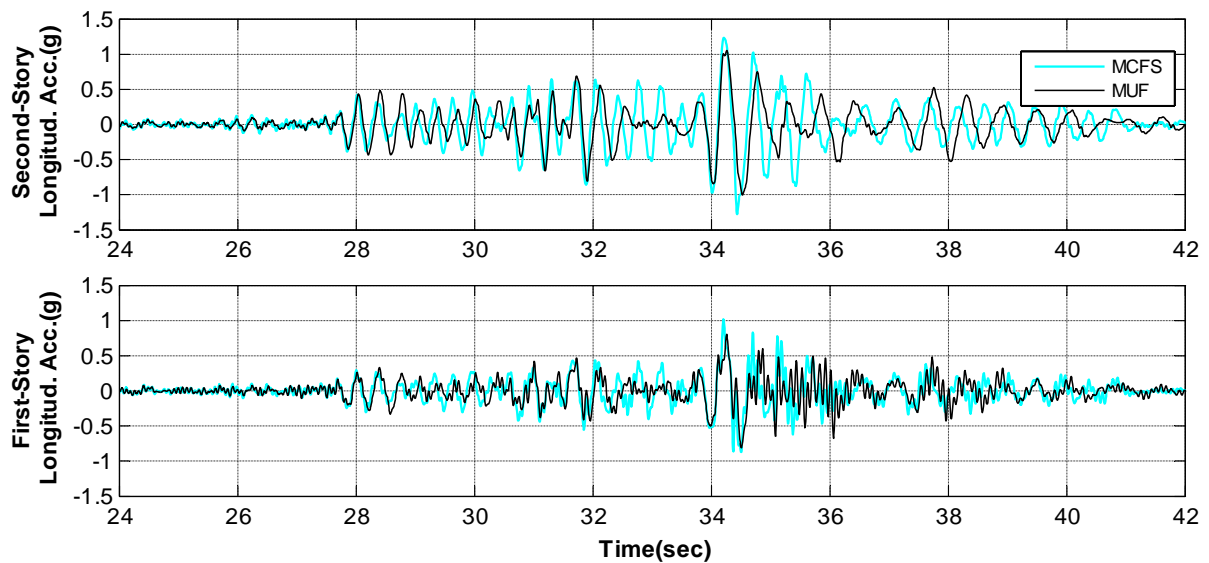


Figure 5-20. Comparison of story-level acceleration records for specimens MCFS and MUF, Test1

Although the transverse reinforcement ratios for the columns were different for specimens MUF and MUFS, the acceleration records in the first and second stories of the two specimens were almost identical during Test1 due to their identical geometries and gravity and lateral load demands (Figure 5-21). Only minor differences were observed for first-story accelerations recorded between 34.6 to 35.1 seconds. The acceleration records remained very similar during Test2 up to the point of shear failure of column B2 of specimen MUFS.

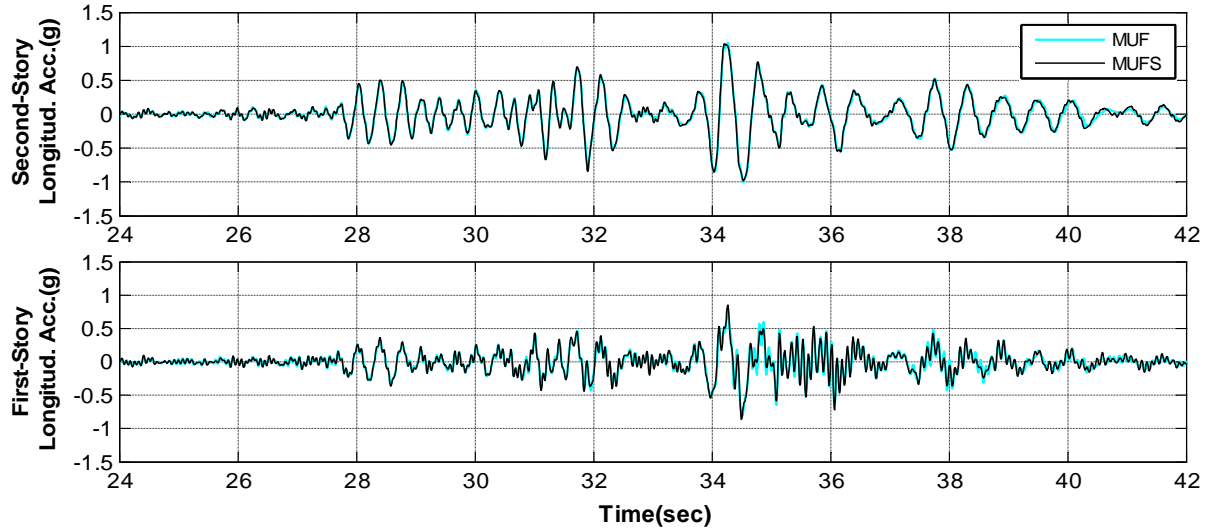


Figure 5-21. Comparison of story-level acceleration records for specimens MUF and MUFS, Test1

5.4.2 Peak Inter-story Drift Demand

Figure 5-22 and Figure 5-23 demonstrate the peak story drift ratio profiles recorded for the specimens during Test1 and Test2, respectively. It is observed that the peak drift ratios recorded for the specimens with unconfined joints (specimens MUF and MUFS), were larger in both directions of Test1 (Figure 5-22). Shear damage to first-story joints of these specimens during Test1 contributed in larger peak drift ratios.

Sequential shear and axial failure of all first-story columns of specimen MCFS caused collapse of the test frame in the positive direction during Test2, making the peak story drift ratio for specimen MCFS the largest amongst the specimens (Figure 5-23b). Large peak drift ratios were observed in the second stories of specimens MUF and MUFS, in both directions. Figure 5-23 also shows that specimen MUFS was the only specimen that experienced larger peak drift ratio in the second story than the first story. As discussed in chapter 4, collapse of specimen MUFS occurred due to shear and axial failure of second-story columns in Test2. Therefore, failure of such columns, in addition to damage to first-story joints in Test1, contributed in larger recorded peak story drift ratio for the second story of specimen MUFS.

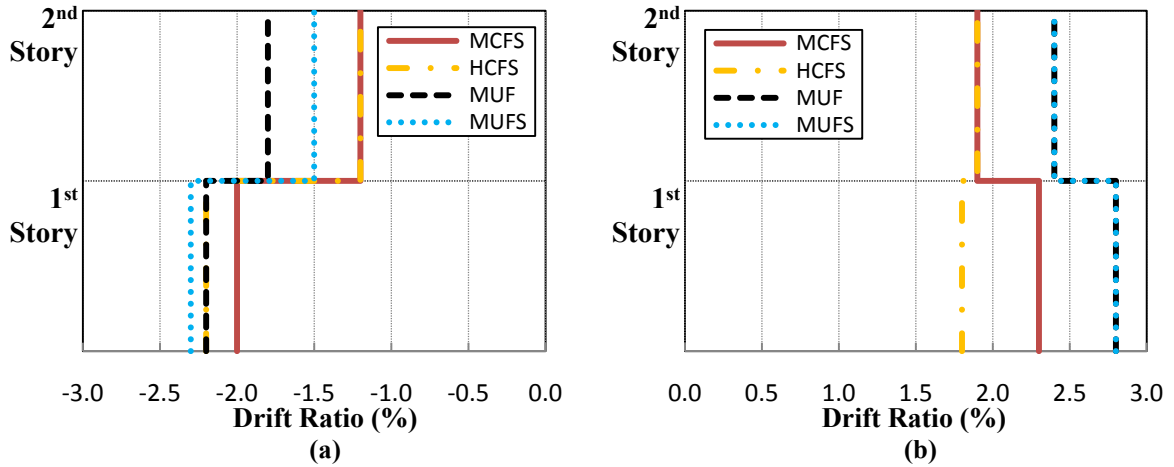


Figure 5-22. Peak story drift ratio profiles for Test1; a) negative direction; b) positive direction

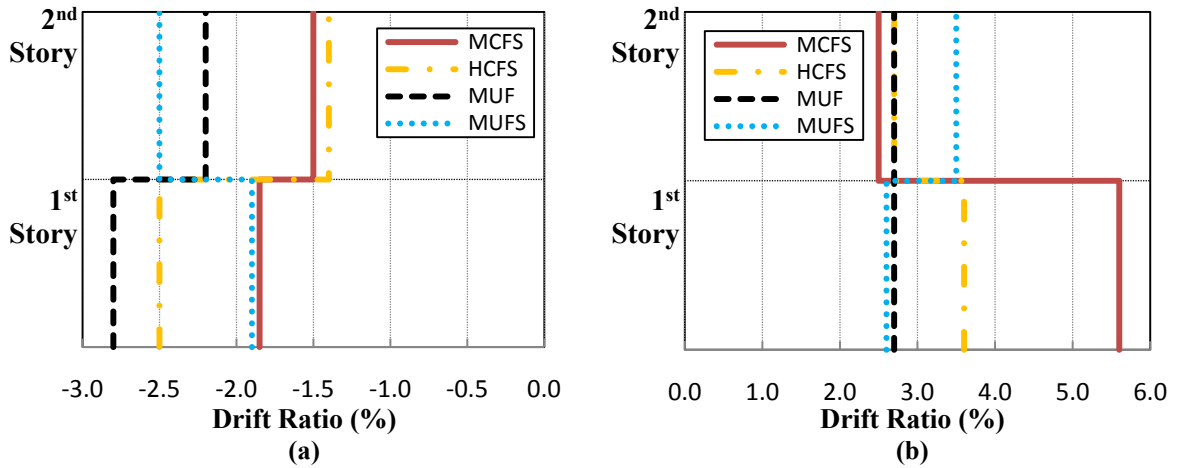


Figure 5-23. Peak story drift ratio profiles for Test2; a) negative direction; b) positive direction

5.4.3 Backbone for Column Shear Hysteretic Response

In this section, backbones for shear hysteretic response of first-story columns of the specimens are compared. The tri-linear backbone for the column shear hysteresis was obtained using the story drift ratio at $0.75V_{max}$, story drift ratio at V_{max} , and maximum story drift ratio (V_{max} = maximum recorded column shear). It should be noted that the story drift ratios used for the backbones shown in this section include deformations due to flexibility of the joints.

Figure 5-24 compares the backbones for shear hysteretic response of first-story columns of specimens MCFS and HCFS during Test1 and Test2. It is observed that the effective stiffnesses (up to $0.75V_{max}$), as well as stiffnesses of the second branch of backbones for corresponding columns from the two specimens remained relatively similar in Test1. However, Figure 5-24b shows that the degradation of shear resistance was more severe during Test2 for column B1 of specimen HCFS, potentially due to the higher axial load.

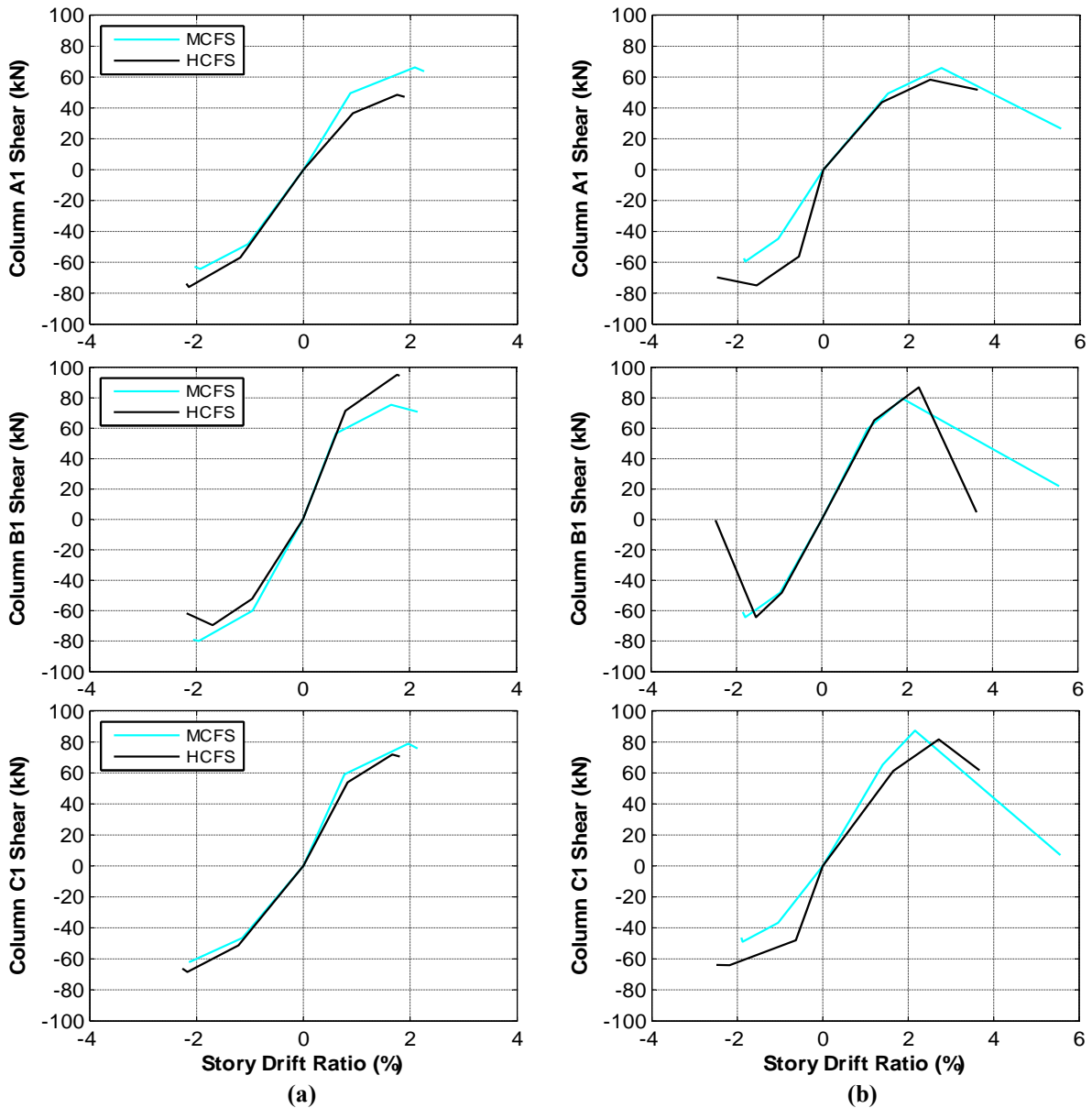


Figure 5-24. Comparison of shear strength backbone for first-story columns of specimens MCFS and HCFS; a) Test1; b) Test2

Comparison of shear backbones for first-story columns of specimens MCFS and MUF is shown in Figure 5-25. Not only the effective stiffness, but also the stiffnesses of the second branch of the backbones were lower, particularly for the exterior columns of specimen MUF during Test1. Although the MUF specimen did not collapse in Test1, the stiffnesses were reduced even more during Test2. It is observed that shear in the columns of specimen MUF remained lower in both tests, confirming that shear could not be fully developed in first-story columns of this specimen due to damage to the connecting beam-column joints.

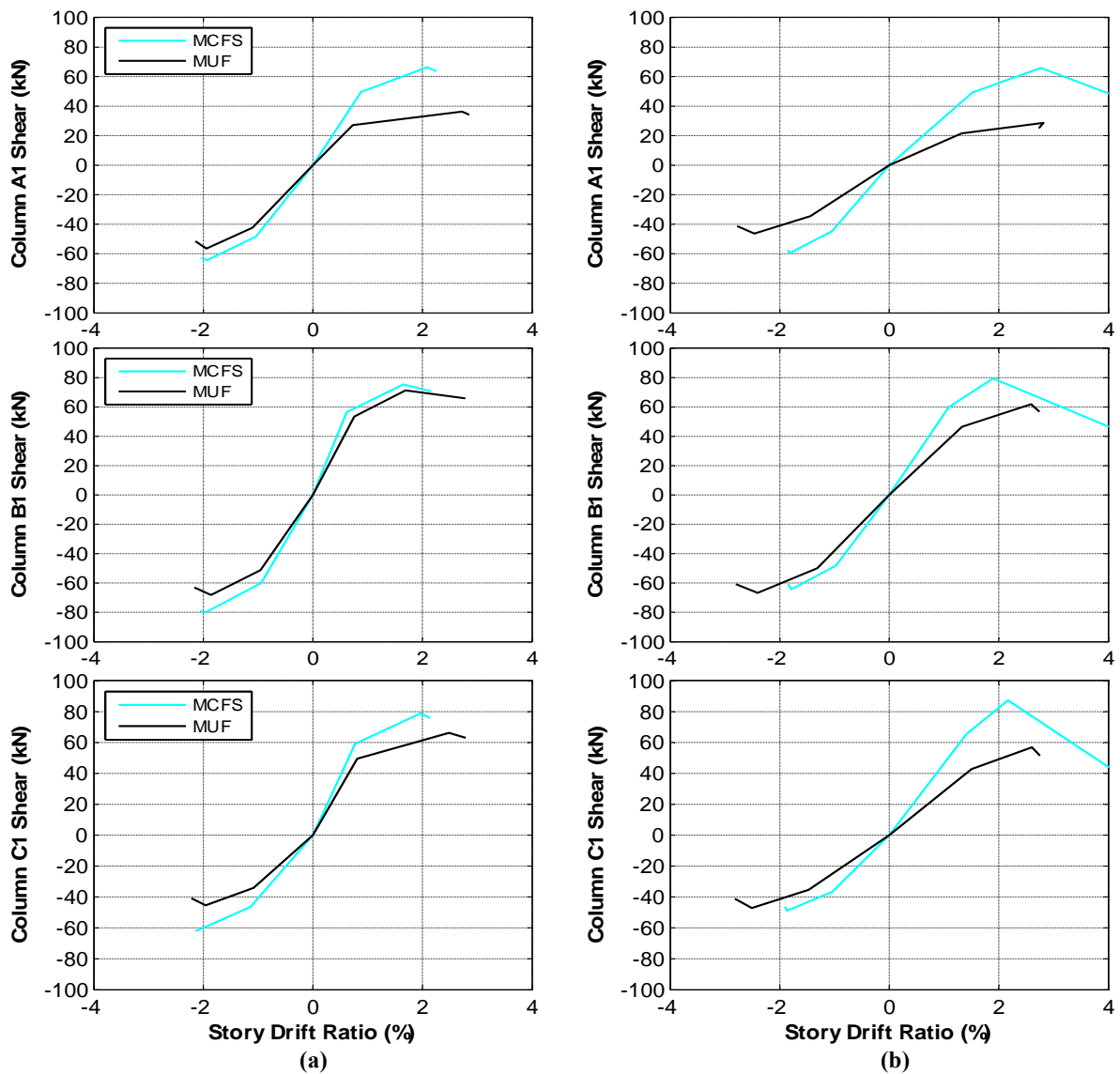


Figure 5-25. Comparison of shear strength backbone for first-story columns of specimens MCFS and MUF; a) Test1; b) Test2

Backbones for shear hysteretic response of first-story columns of specimens MUF and MUFS during Test1 and Test2 are compared in Figure 5-26. With the exception for column A1 during Test1, effective stiffness and other branches of the backbones for the corresponding columns from the two specimens remained relatively similar during Test1 and Test2. As shear hysteretic response of first-story columns were influenced by the shear damage of first-story joints, such similarities suggest that the damage to first-story joints of the two specimens were comparable and significantly influenced the stiffness of the frames.

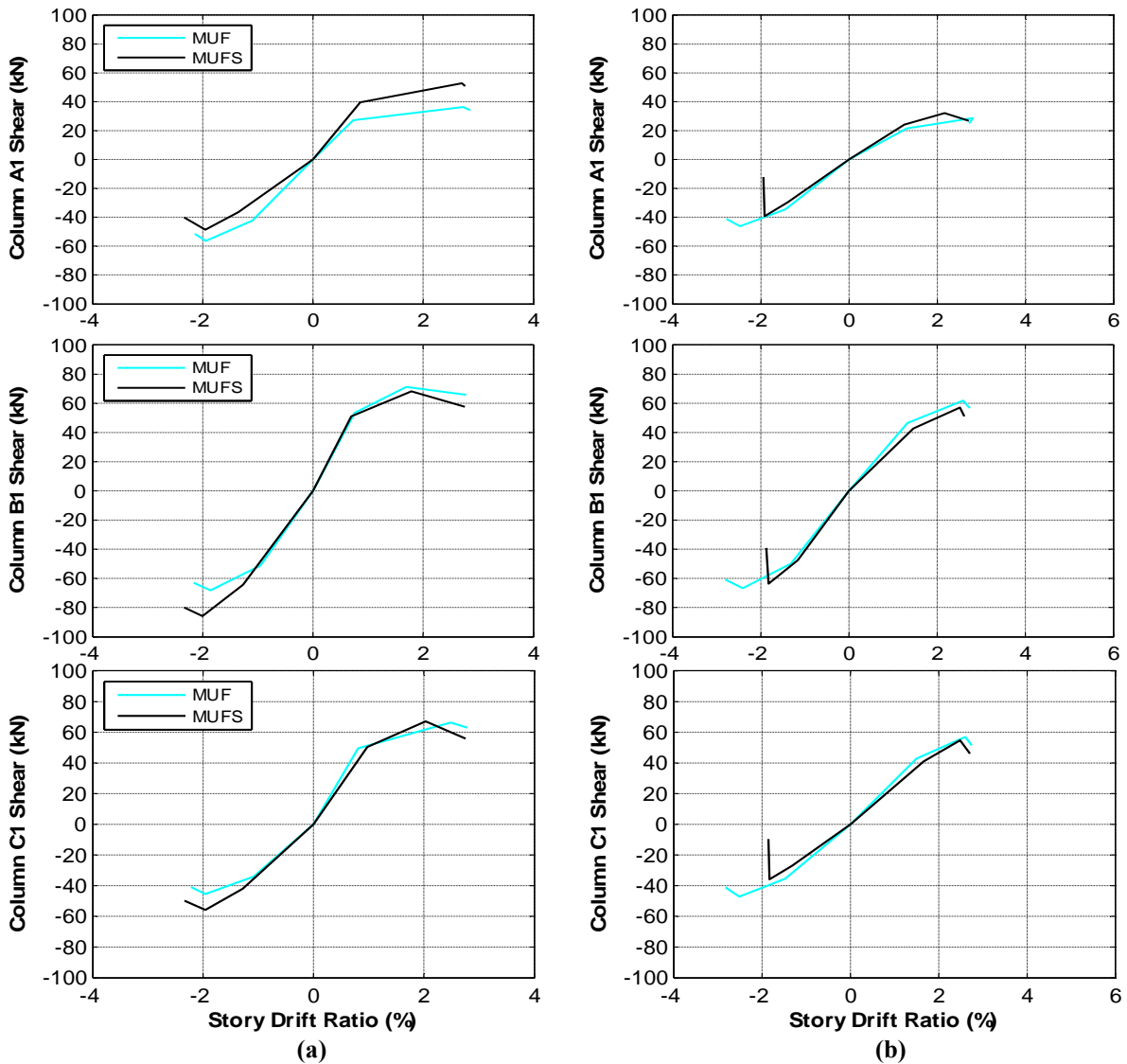


Figure 5-26. Comparison of shear strength backbone for first-story columns of specimens MUF and MUFS; a) Test1; b) Test2

5.5 Effect of Axial Load on Key Parameters of Columns

Influence of axial load on drift ratio demands, effective and secant stiffnesses, response of columns before and after axial failure, and differences between drifts at shear and axial failure of columns are studied in this section.

5.5.1 Story Drift Ratio at Maximum Recorded Shear Strength

Figure 5-27 demonstrates inter-story drift ratio recorded at the point of maximum shear versus corresponding axial load for first-story columns of the four specimens. It is observed that the trend of drift ratios decreased for higher axial loads during both tests. However, as the columns were damaged during Test2, the influence of axial load on the drift ratios was reduced (Figure 5-27b).

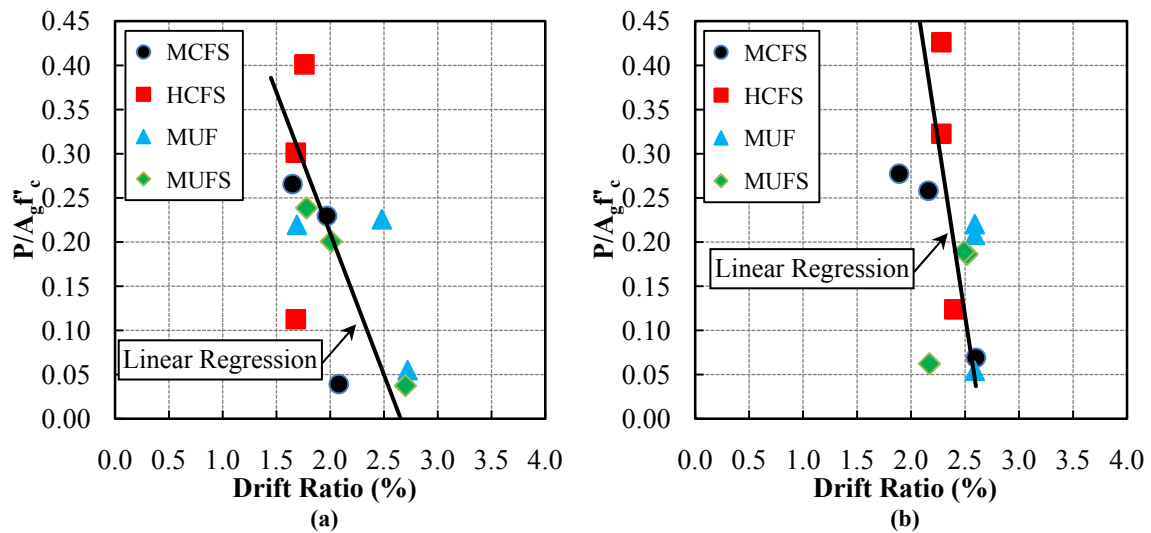


Figure 5-27. Influence of axial load on column drift ratio at the point of peak shear for first-story columns, a) Test1; b) Test2

5.5.2 Effect of Axial Load on Column Effective Stiffness

As defined in Chapter 4, the effective stiffness was obtained as the ratio of $0.75V_{max}$ and the corresponding drift ratio. Since the drift ratio is influenced by the flexibility of the frame, this effective stiffness is expected to be lower than that for the column alone. Results from the analytical models for the studied specimens but with rigid beams and joints (representing columns with fixed-ends condition) are compared with the results from the models with the actual stiffness of the beams (representing columns with end rotation) in Chapter 6. As it is demonstrated in Section 6.3.2.1, the contribution of beam flexibility and joint rotation in lateral displacement of first-story columns are less than 5% and 15% for the middle and exterior columns, respectively. It is observed that the influence of frame flexibility on drift of center column was not significant and therefore, using story drift ratio instead of column drift ratio for calculating the effective stiffness of that column is a reasonable assumption. However, such assumption may not be as valid for the exterior columns and the results should be interpreted with caution. Values for the middle column of the specimens are distinguished with hollow markers in Figure 5-28 to Figure 5-31. A detailed discussion on effective stiffness of columns in reinforced concrete frames can be found in Chapter 7 (Section 7.5.1).

Figure 5-28 demonstrates the influence of axial load on effective stiffness of the columns. Although the calculated stiffness for the columns for Test2, (Figure 5-28b), does not represent the actual effective stiffness of the undamaged specimen, it still demonstrates the frame resistance to lateral demands during Test2. While effective stiffnesses of the columns were increased due to higher axial load, comparison of Figure 5-28a and Figure 5-28b demonstrates that the sensitivity of stiffness to axial load is reduced when the columns and joints are damaged.

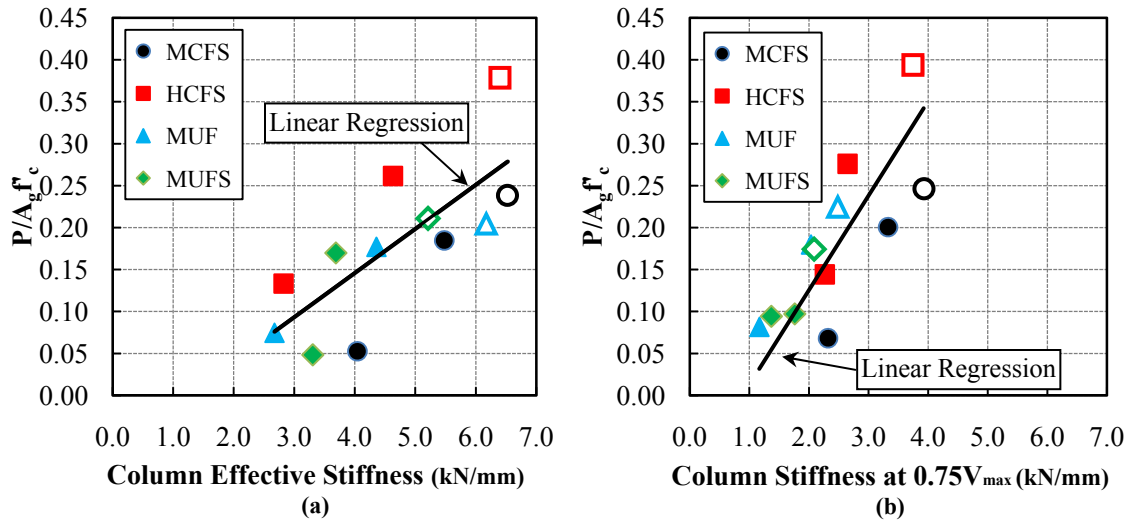


Figure 5-28. Effect of axial load on effective stiffness; a) Test1; b) Test2

Figure 5-29 compares the effective stiffnesses for first-story columns, EI_{eff} , expressed as a fraction of the gross-section stiffness, EI_g , with suggested values from ACI318-08 (ACI, 2008) and ASCE41 (ASCE, 2008). ACI 318-08 provides three options for estimating member stiffnesses: (a) $0.5EI_g$ for all members; (b) $0.35EI_g$ for flexural members with $P < 0.1A_g f'_c$ and $0.7EI_g$ for compression members with $P \geq 0.1A_g f'_c$; or (c) as determined by “a more detailed analysis considering the reduced stiffness of all members under the loading conditions”. Figure 5-29 compares options (a) and (b) with the measured effective stiffnesses of first-story columns of the four specimens. It is observed that option (a) overestimates the effective stiffness of the columns, particularly those with lower axial loads. Option (b) also overestimates the stiffness for the columns, especially for the columns with higher axial load. The figure also includes the evaluation of the effective stiffness model suggested by ASCE-41. According to ASCE-41, the effective stiffness of a column should be obtained from:

$$0.3 \leq \frac{EI_{eff}}{EI_g} = 0.2 + \frac{P}{A_g f'_c} \leq 0.7 \quad (5.1)$$

where P is the axial load due to design gravity load (positive in compression), A_g is gross cross-sectional area of the column, and f'_c is the compressive strength of concrete. Although Equation 5.1 provides a better estimate of the measured effective stiffness, Figure 5-29 demonstrates that even the model from ASCE-41 overestimates the effective stiffnesses of first-story columns of the four specimens.

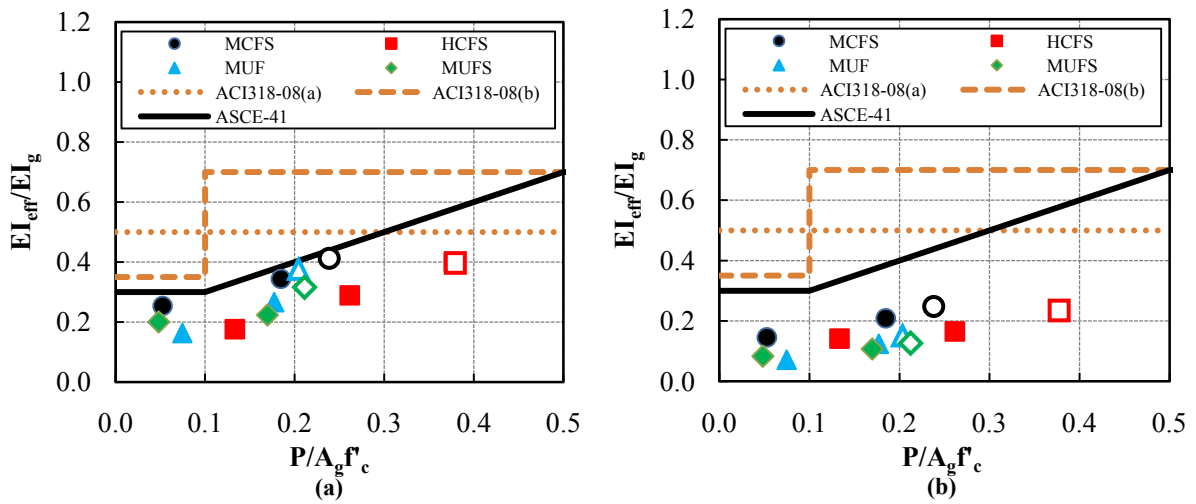


Figure 5-29. Comparison of column EI_{eff}/EI_g with code suggested ratios for first-story columns; a) Test1; b) Test2

Elwood and Eberhard (2009), suggested a more detailed equation that includes the influence of longitudinal bar size, column aspect ratio and axial load on column stiffness:

$$0.2 \leq \frac{EI_{eff}}{EI_g} = \frac{0.45 + 2.5P/A_g f'_c}{1 + 110 \left(\frac{d_b}{D}\right) \left(\frac{D}{a}\right)} \leq 1.0 \quad (5.2)$$

where d_b is the nominal diameter of longitudinal bars, D is the diameter of circular column, or column depth in direction of loading, and a is the shear span of the column. Other parameters have the same definition as Equation 5.1. Figure 5-30 compares the effective stiffnesses

calculated using Equations 5.1 and 5.2 with measured effective stiffnesses during Test1. While effective stiffnesses were significantly overestimated by Equation 5.1, particularly for lower axial loads (Figure 5-30a), Equation 5.2 better estimated the effective stiffness for the columns (Figure 5-30b).

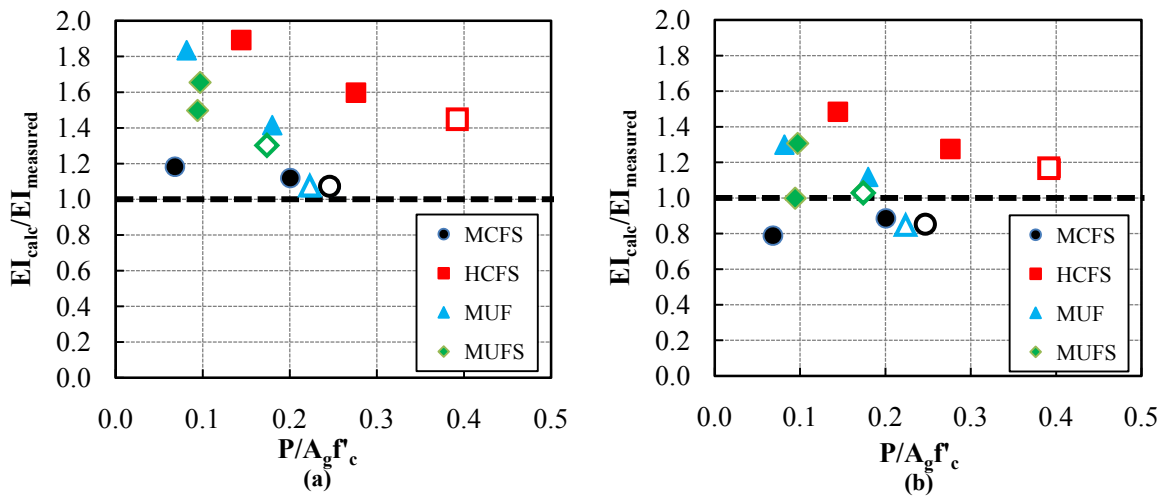


Figure 5-30. Comparison of calculated and measured effective stiffnesses in Test1; a) ASCE-41 model; b) Elwood & Eberhard model

5.5.3 Effect of Axial Load on Column Secant Stiffness at Peak Shear

While initial and effective stiffness can be adopted for the serviceability limit state for a column, secant stiffness at the point of maximum shear or maximum displacement can be selected for the ultimate limit state (Priestley et al., 2007). Figure 5-31 compares the secant stiffness at the peak recorded shear for the columns in the positive direction of Test1 and Test2, showing that the higher axial load increased the secant stiffness at the point of maximum shear. Although the test frames were damaged during Test1, comparison of Figure 5-31a and Figure 5-31b reveals that the trends of increasing secant stiffness with axial load remained very similar for the two tests. It should be noted that the selected point (peak shear)

was the onset of shear failure for first-story columns of specimen MCFS and HCFS during Test2.

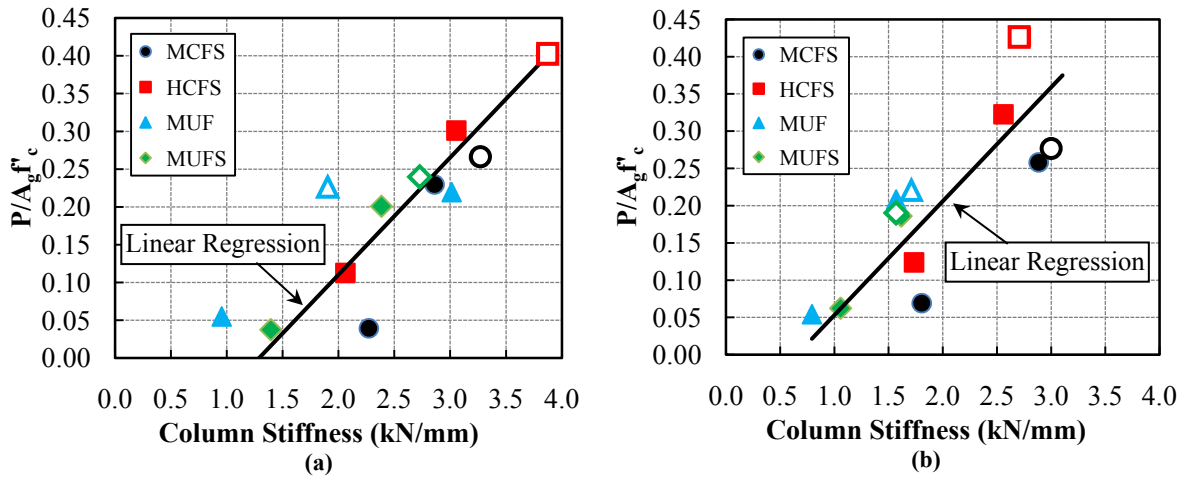


Figure 5-31. Effect of axial load on column secant stiffness at peak shear for first-story columns; a) Test1; b) Test2

5.5.4 Effect of Axial Load on Slope of Column Vertical Displacement before and after Onset of Axial Failure

The effect of axial load on vertical displacement of columns before and after the onset of axial failure is studied in this section. Figure 5-32 shows a schematic of column hysteretic response before and after onset of axial failure, comparing the horizontal and vertical displacement of a column. As demonstrated in Figure 5-32, the slopes before and after the onset of axial failure are denoted as “*a*” and “*b*”, respectively. Figure 5-33 compares the effect of axial load on slopes *a* and *b*, demonstrating that both slopes became steeper for the columns under higher axial loads. However, comparison of Figure 5-33a and Figure 5-33b reveals that the influence of axial load on slope *b* was more significant than slope *a*. Figure 5-33 also demonstrates that the degradation of axial load resistance after the onset of axial failure was more severe for the columns with higher axial load. Based on this observation, it can be reasonably assumed that all the axial load will be lost instantly once axial failure is initiated

for columns with high axial load (e.g. $0.5A_g f'_c$). Such assumption will make the modeling of response after onset of axial failure easier as there will be no need to define a relationship path for axial load and drift. It should be noted that very sudden loss of axial load can result in dynamic amplification of gravity load during load distribution and must be taken into account in modeling process (Matthews, 2007).

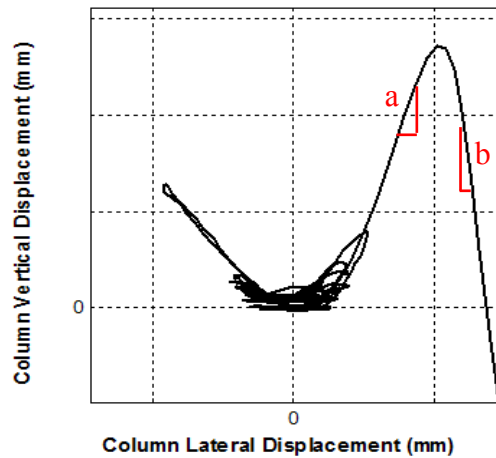


Figure 5-32. Schematic of slope of vertical displacement before and after axial failure

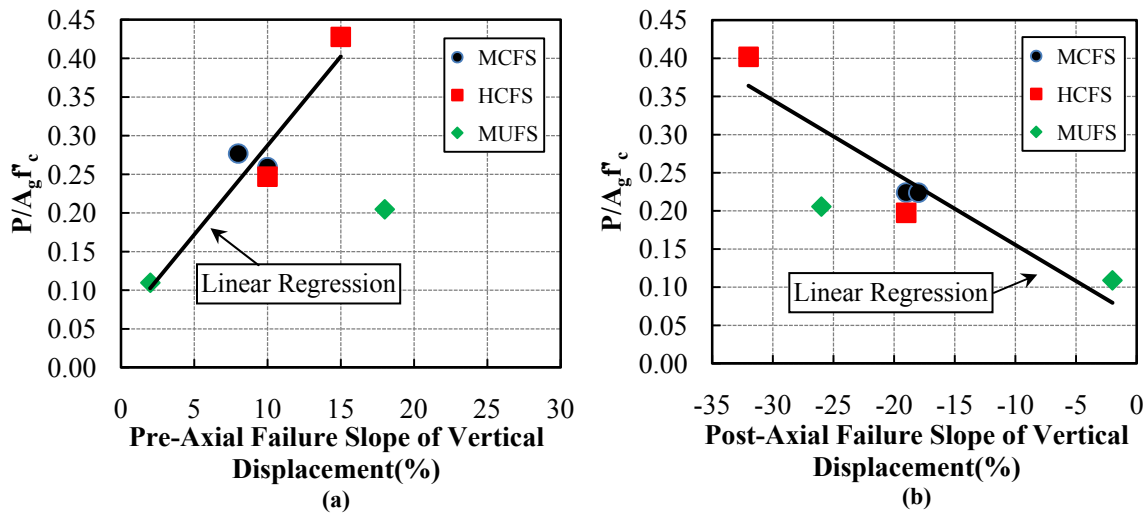


Figure 5-33. Influence of axial load on slopes “a” and “b” defined in Figure 5-32, Test2; a) pre-axial failure; b) post-axial failure

5.5.5 Effect of Axial Load on Story Drift Ratio at Onset of Axial Failure

Figure 5-34 compares the drift ratios at point of axial failure for the columns that failed in Test2. The drift ratios for these columns were also compared with the calculated drift ratios using the axial capacity model (Equation 2.2). It is observed that there is a significant difference between the curve suggested by Equation 2.2 and the drift ratio at the onset of axial failure for columns A2 and C1 of specimen HCFS. As discussed in Section 4.5, column A2 of specimen HCFS experienced shear and axial failure due to excessive local rotation demand at the top of the column. Therefore, the drift-based model from Equation 2.2 could not capture the point of axial failure of the column. Failure of column C1, on the other hand, resulted from large axial load redistributed from columns on axes A and B and instability of the frame after axial failure of two columns in the three-column frame. It is also observed that Equation 2.2 could not predict the point of axial failure of columns A1 from specimen MCFS and column C2 from specimen MUFS. Similar to column C1 of specimen HCFS, these columns were the last columns in their specimens that experienced axial failure before collapse of the frame and therefore, their drift ratios at axial failure were influenced by the instability of the system and may not be suitable for evaluation of the axial capacity model.

It is observed that the model adequately predicted the drift ratios for axial failure of columns with lower axial load. However, the drift ratio for axial failure of column B1 of specimen HCFS, with higher axial load, was noticeably under-estimated. The slope of the curve should be adjusted to better fit the points for higher axial load. As discussed in Section 2.3.2, Equation 2.2 was developed based on static tests of single columns. Additional data points from dynamic tests are required to properly evaluate the model for predicting the onset of axial failure for columns and particularly columns with higher axial loads.

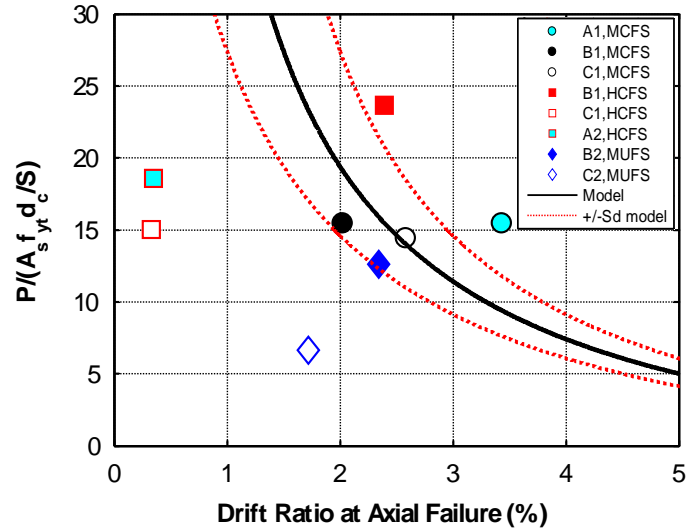


Figure 5-34. Effect of axial load on drift ratio at onset of axial failure

5.5.6 Effect of Axial Load on Closeness of Drift Ratio at Onsets of Shear and Axial Failure

The difference between the drift ratios at the points of shear and axial failure of a column depends on several factors including transverse reinforcement ratio, material properties, axial load, etc. In this section, effect of axial load on proximity of the onsets of shear and axial failure for non-ductile columns is studied. Figure 5-35 compares the drift ratios at the onsets of shear and axial failure for column B1 of specimens MCFS and HCFS. Column B1 was the first column in both specimens that failed under lateral and axial demand in the same cycle. Failure of other columns in the aforementioned specimens as well as test frame MUFS occurred either due to local rotation demands or concentration of load on the column right before the frame collapse and therefore, were not selected for this comparison. As the axial loads on center column of specimens MCFS and HCFS were relatively high (greater than $0.25A_g f_c'$), drift ratios from another shaking table test, done in National Center for Research on Earthquake Engineering (NCREE) in 2005 are included in Figure 5-35. Details and results from this test can be found in the companion papers by Wu et al. (2009) and Yavari et al.

(2009). Material properties and transverse reinforcement of the selected column from the 2005 Test was comparable to column B1 of specimen MCFS and HCFS. Figure 5-35 demonstrates that for higher axial loads, the drift ratios at the onsets of shear and axial failure became closer together. This has particular importance in developing analytical models for predicting the points of shear and axial failure and building collapse. Such models must precisely predict the onsets of shear and axial failure for a column with high axial load, otherwise, the behaviour of the column may not be captured correctly (See Figure 6-24 for sensitivity of the analysis results to changes in the point of shear failure).

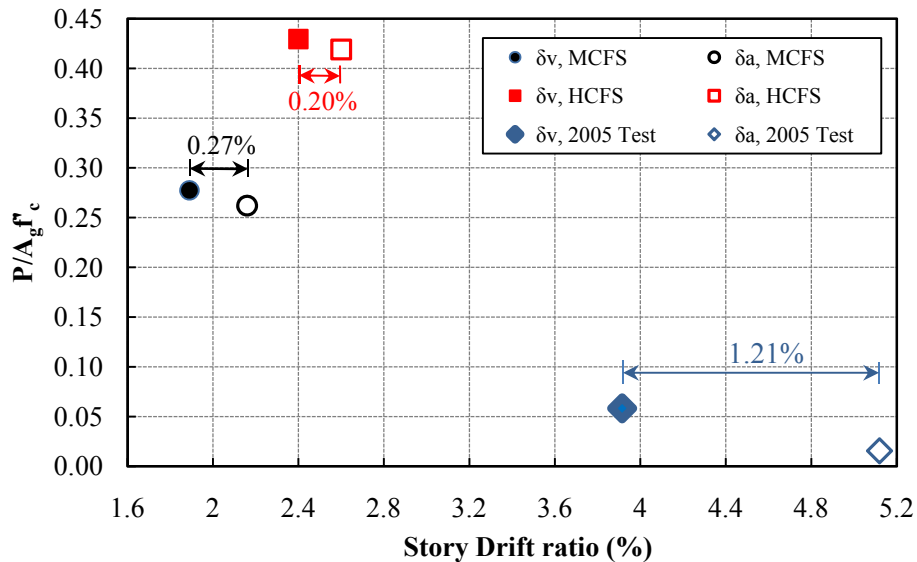


Figure 5-35. Effect of axial load on distance between drift ratios at onsets of shear and axial failure

5.6 Column Chord Rotation versus Drift Ratio

As shown in Chapter 4, inelastic deformation demands can be different at opposite ends of a column due to different boundary conditions and loadings. Story drift ratio is widely used in practice representing the lateral deformation demands on columns and many of the models

previously derived [Pujol et al. (1999); Kato and Ohnishi (2002); Elwood and Moehle (2005)] relate lateral drift ratio at shear and axial failure to various parameters. These models were derived empirically from reversed-cyclic tests of columns mostly with fixed-fixed end conditions. However, due to flexibility of the beams and rotation of beam-column joints in a real frame building, story drift ratio includes the deformation demands on the connecting joint in addition to the deformation demands on the column. An alternative approach is to employ plastic rotations at the column ends instead of drift ratio, the same approach taken by ASCE-41 (2008). Since measuring the plastic end rotations was extremely difficult during the shaking table tests, column chord rotation was selected for this study instead. Chord rotation for top-end of each of first-story columns was obtained by adjusting the drift ratio using the rotation of the connecting joint, measured by means of additional string potentiometers (see Appendix Section B.3 for details of instrumentation). Definition of chord rotation was shown in Figure 4-18 in Section 4.4. Figure 5-36 compares the chord rotation at top-end and drift ratio for first-story columns at the point of maximum story drift ratio in the positive direction of Test1. It is observed that while the drift ratios remained relatively similar for the columns of each specimen, the recorded chord rotations at top-end were different for the columns of each test frame. Comparison of Figure 5-36a and Figure 5-36b demonstrates that the trends for peak drift ratios of first-story columns of specimens MCFS and HCFS remained comparable. Similarly, the trends for top-end chord rotation of the corresponding columns from these two specimens were almost equal (slope of 10-12%). It is observed that most of the columns with higher axial load had higher chord rotation compared to the other columns in the same frame; however, such conclusion could not be generalized to columns from different specimens.

Comparison of Figure 5-36a with Figure 5-36c and Figure 5-36d demonstrates that the trends for top-end chord rotation of columns from specimens MUF and MUFS were considerably flatter than specimen MCFS. However, such difference was not observed in the trends for their drift ratios. Since the unconfined joints of specimens MUF and MUFS were damaged before reaching the peak first-story drift ratio, the difference between chord rotations and drift ratios became more noticeable due to the high contribution of joint rotations to the measured drift ratios. It is also observed that for specimens MUF and MUFS that the difference between top-end chord rotation and drift ratio for columns with lower axial load was larger than that for columns with higher axial loads. Nevertheless, influence of the location of the column and its connecting joint must also be taken into account. While the center column of all the specimens experienced the highest axial load, the rotation of the center joint was the lowest due to symmetry and balance of the connecting elements deformations. Therefore, the top-end chord rotation for the center joint was closer to drift ratio comparing to the exterior joints of the specimens.

While chord rotation becomes equal to drift ratio for columns with fixed-fixed end condition, the above discussion on Figure 5-36 suggests that column chord rotation may be a better parameter compared to story drift ratio for assessing the lateral demand on columns of a moment frame. It is essential to use chord rotation for measuring the lateral demands on columns in the frames with unconfined joints and this becomes even more critical for the columns with lower axial load.

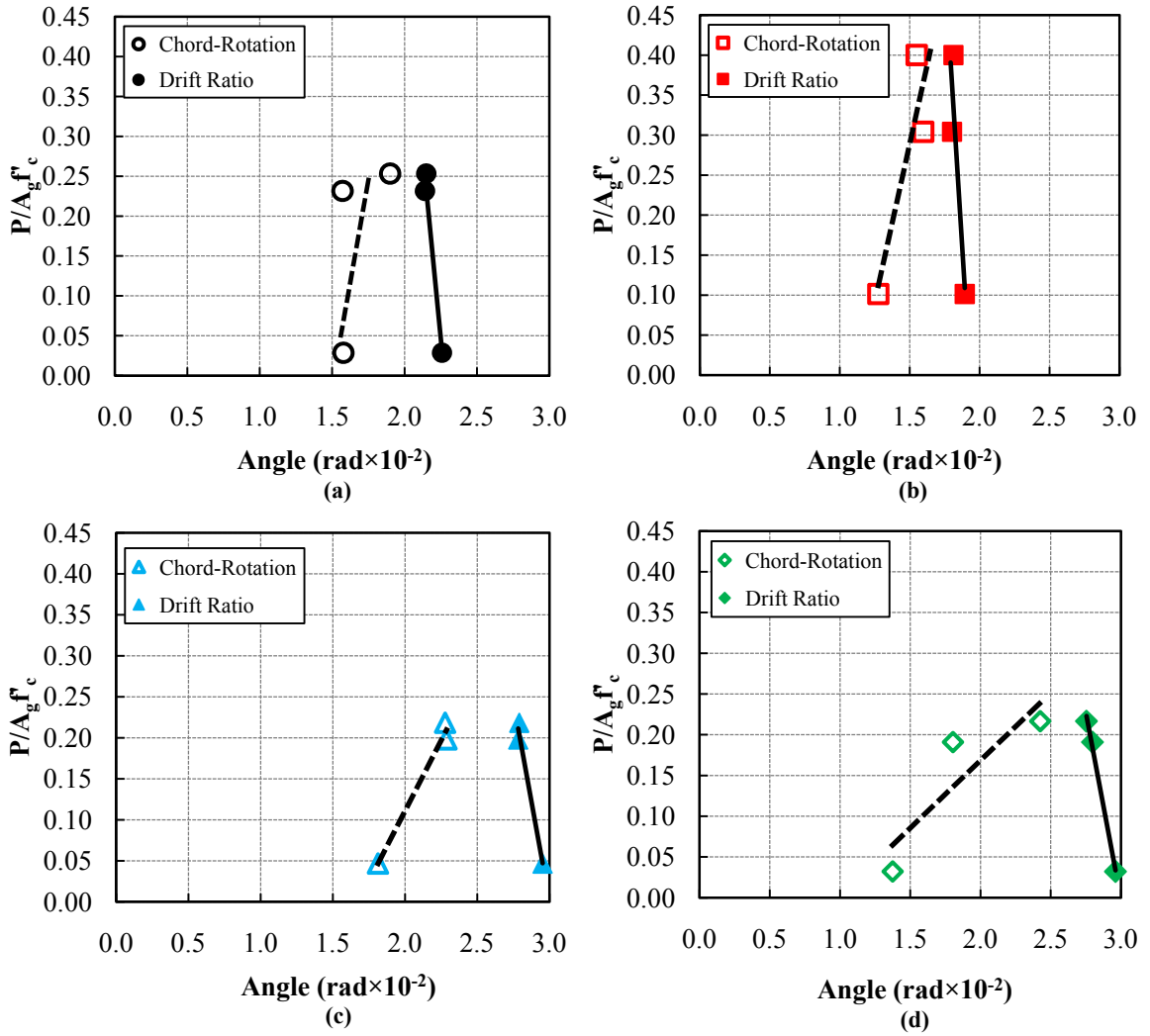


Figure 5-36. Comparison of column chord rotation with drift ratio at point of peak drift ratio for first-story columns in the positive direction of Test1; a) specimen MCFS; b) specimen HCFS; c) specimen MUF; d) specimen MUFS

CHAPTER 6. ANALYSIS OF SHAKING TABLE TEST SPECIMENS

6.1 Introduction

This Chapter describes analytical models for the shaking table test specimens developed using OpenSEES, a finite-element analysis platform designed for earthquake engineering simulation (OpenSEES, 2009). The models presented herein will attempt to reproduce the observed response of the shaking table tests described in Chapters 3 and 4. The goal is to evaluate the ability of the models to simulate the hysteretic behaviour of the specimen components and to estimate the vertical and lateral deformation of the elements. The models are also assessed for their ability to capture the initiation of shear and axial-strength degradation of the structural members and failure mode of the test frames.

6.2 Description of the Analytical Models

This section describes the analytical models for the test frame components, loading, and other modeling parameters. The analytical models described in this section are relatively complex models with nonlinear fibre elements to represent the columns and springs-in-series

at the ends of columns and beams simulating bar-slip, shear, and axial strength degradation for non-ductile columns of specimens MCFS, HCFS, and MUFS, and joint rotation for unconfined joints of specimens MUF and MUFS. Figure 6-1 shows the layout of the nodes and elements for the models. Comparison of the results from the analyses and data from the shaking table tests reveals the level of accuracy of simulating the behaviour of the frames using such detailed models. Less sophisticated models are described in Chapter 7, showing the advantages and limitations of such models in assessing the behaviour of non-ductile concrete frames.

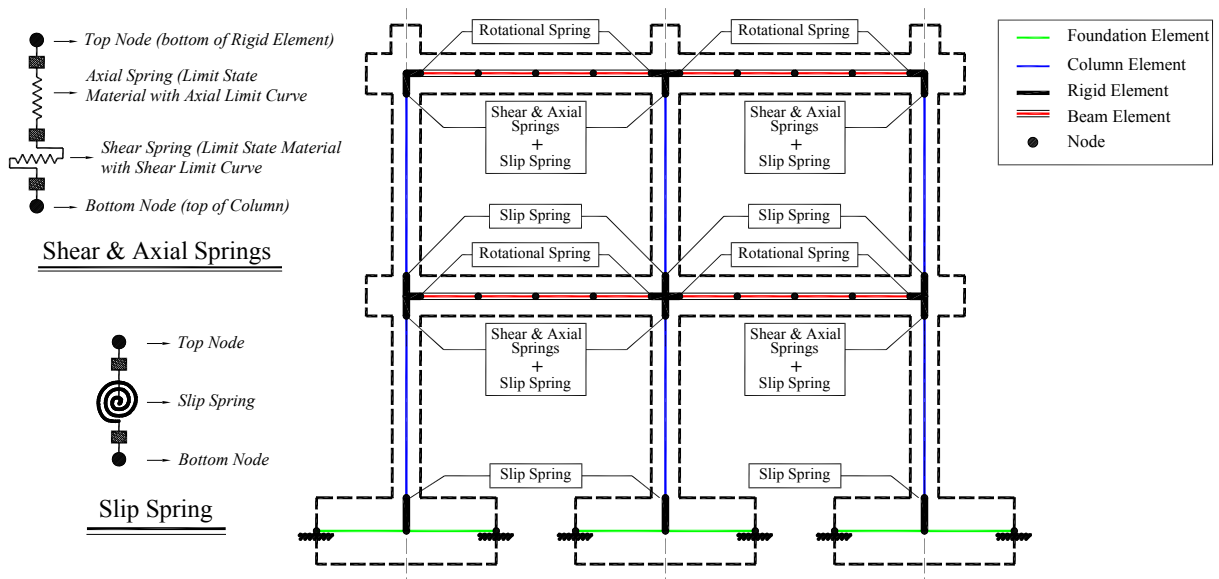


Figure 6-1. Model of shaking table specimens MCFS and HCFS.

6.2.1 Footing and Beam Elements

Considering the heavy reinforcement and substantial dimensions of the footings, they were modeled as elastic members. The force transducers and their connections to the table and footings were designed with a high stiffness such that they could be considered to provide a fixed-end condition to each end of the footing element. However, to observe the effect of modeling the force transducers (load cells) on flexibility of the system, results from two

models, with and without elastic members for load cells, were compared. The results were similar with high precision, and therefore load cells were not included in the models presented in this chapter.

The beams did not exhibit a significant degree of nonlinearity during testing; therefore, for computational efficiency, they were modeled as elastic with lumped plasticity rotational springs at the face of the joints to account for possible yielding of longitudinal reinforcement and deformations due to bar slip. The bi-linear idealization of the moment-curvature relationships for the positive and negative bending directions is shown in Figure 6-2. Cross-section analysis program XTRACT (Imbsen, 2002) was employed to obtain the moment-curvature relationships for the beams, using a tri-linear model for steel bars with strain hardening and Mander's model (Mander et al., 1988) for concrete. Based on the results of the moment curvature analysis, yield moments were estimated at 97.9 kN-m and 55.4 kN-m for first- and second-story beams, respectively. The effective flexural stiffness for the beam, EI_{flex} , was estimated from moment-curvature analysis as $0.4EI_{gross}$, where E is the concrete modulus of elasticity and I_{gross} is the gross section moment of inertia. The asymmetric beam section resulted in different yield moments and effective stiffnesses in the positive and negative bending directions. However, due to the similar top and bottom reinforcement the effective flexural stiffnesses in the positive and negative directions of bending were relatively close. The stiffnesses in the two bending directions were averaged to determine EI_{flex} . Beam discretization had little effect on the computed overall response of the frame; therefore, beams were discretized into four elastic sub-elements. The connecting nodes were used to apply masses from the gravity load on the beams.

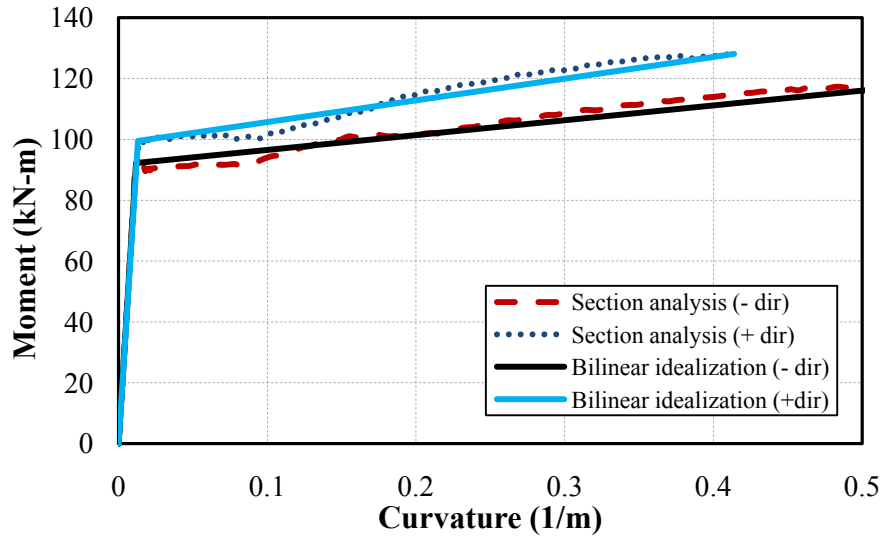


Figure 6-2. Moment-curvature relationship for first-story beams.

6.2.2 Joint Elements

As described in Chapter 3 and 4, joints in specimens MCFS and HCFS were well-confined by transverse beam stubs and additional hoops in the joints. Therefore the joints of these two specimens were modeled using rigid elements (see Figure 6-1). Tests [(Bonacci and Pantazopoulou, 1993), (Lowe and Altoontash, 2003)] have shown that even joints with confinement from transverse reinforcement, can undergo appreciable deformations, especially when structures are pushed to higher drifts (i.e 4.0% drift ratio). However, these observations were based on results from cyclic testing of 2D beam-column joints with two exposed faces. A study by Kitayama et al. (1991) shows that transverse beams significantly increase the joint shear strength. The increase is partially attributed to the confinement by the longitudinal reinforcement in the transverse beams. Considering the transverse beams in specimens MCFS and HCFS that provided confinement on all faces of the joints and negligible joint deformations observed during testing these specimens (see Chapter 4, Section 4.4), rigid elements were selected for modeling the joints of these two frames.

In contrast to specimens MCFS and HCFS, first-story joints in specimens MUF and MUFS were designed and constructed without hoops and a transverse beam on only one side to observe joint damage during testing (see Chapter 3, Section 3.2). Therefore, joints were modeled differently for these two specimens, where the joint shear deformation was modeled using a rotational spring model (scissors model) with a degrading hysteresis (Alath and Kunnath, 1995). Considering the scissors model, the free body forces for the joint panel are shown in Figure 6-3, where M_b^L and M_b^R are the beam moments, while V_b^L and V_b^R are beam shear at the joint face (superscripts L and R refer to left and right, respectively). M_c^T and M_c^B are column moments, V_c is column shear, and P^T and P^B are the axial loads from the connecting columns (superscripts T and B refer to top and bottom columns, respectively).

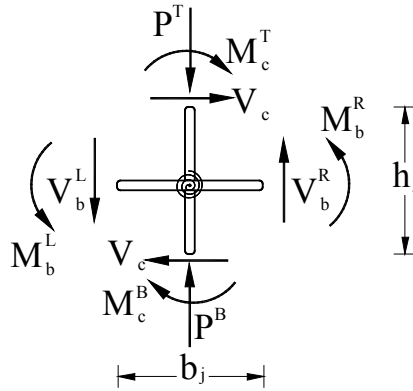


Figure 6-3. The free-body diagram of the scissors model (Alath and Kunnath, 1995)

Based on the study by Alath and Kunnath (1995), the moment at the rotational spring can be expressed in terms of the joint shear stress and sectional dimensions as follows:

From the free-body diagram shown in Figure 6-3, the joint shear can be obtained as:

$$V_j = \frac{M_b^L}{jd} + \frac{M_b^R}{jd} - V_c = (V_b^L + V_b^R) \left[\frac{L_b - b_j}{2jd} - \frac{L_b}{2L_c} \right] \quad (6.1)$$

where b_j is the width of the joint panel, L_b is the total length of the left and right beams, jd is the internal moment arm in the beam, and L_c is the total length of the top and bottom columns. Then, the joint shear stress, τ_j , is calculated as:

$$\tau_j = \frac{V_j}{A_j} \quad (6.2)$$

where A_j is the area of the joint. The moment at the rotational spring (Figure 6-3) can be obtained from the shear forces in the beams:

$$M_j = (V_b^L + V_b^R) \frac{L_b}{2} \quad (6.3)$$

Finally, from Equations 6.1 to 6.3, the moment at the rotational spring can be expressed as:

$$M_j = \tau_{jh} A_{jh} \frac{1}{\frac{1 - b_j/L_b}{jd} - \frac{1}{L_c}} \quad (6.4)$$

The relative rotation of the two rigid links, shown in Figure 6-3, represents the deformation of the joint panel, and therefore, the rotation of the spring, θ_j , is equal to the joint shear strain, γ_j , assuming flexural deformations in the joint are negligible:

$$\theta_j = \gamma_j \quad (6.5)$$

Equations 6.4 and 6.5 were used to convert the joint shear stress-strain relationship into the $M-\theta$ relationship for the scissors model. Such constitutive relationship for the panel zone was implemented in the analytical model by defining a backbone curve and hysteresis rule for the cyclic response. Based on experimental test results in the literature (see Chapter2, Section 2.4), a degrading backbone with highly pinched hysteretic behaviour was expected for beam-column joints. Therefore, *Pinching4* material, available in OpenSees with a multi-linear envelope and tri-linear cyclic path, was used to define the joint rotational spring. A complete

description of *Pinching4* material can be found in the study by Lowes et al. (2003). Data from a collection of joint tests (Celik and Ellingwood, 2008) were used in defining the backbone of the panel zone for the beam-column joints of specimens MUF and MUFS.

6.2.3 Column Elements

All columns were modeled using force-based fibre beam-column elements with five integration points and two zero-length elements located at the top and bottom of the beam-column elements. A zero-length element is defined by two nodes at the same location. The nodes are connected by multiple material objects to represent the force-deformation relationship for the element. The top zero-length elements for the columns included shear and axial springs whose behaviour were defined by LimitState material models described in Chapter 2. The limit curve for the shear spring was defined using the empirical drift capacity model from Section 2.3.1 (Equation 2.1), and the limit curve for the axial spring was defined by the axial failure model from Section 2.3.2 (Equation 2.2). The initial slope for the shear spring (the slope of the pre-failure backbone from Figure 2-5) was chosen as 2.6 MN/m based on the shear stiffness of the uncracked column (GA_v/L , where effective shear area, A_v , is approximated by $(5/6)A_g$, L is the length of the column, and $G=E/(2(1+\nu))$ is the modulus of rigidity in which E is the modulus of elasticity ($E= 4700\sqrt{f'_c}$) and ν is the Poisson ratio for concrete. The initial slope for the axial spring (the slope of the pre-failure backbone from Figure 2-6) was selected as 100 times stiffer than the axial stiffness of the column to ensure that no additional axial flexibility was introduced into the model. Rigid shear and axial springs, with negligible deformations, were incorporated in the zero-length elements at the base of the columns.

Position of shear and axial limit curves significantly influences the response of a test frame estimated by the analytical model. As discussed in Chapter 5 (Section 5.5.6), higher axial load on a column forces the drift ratios at shear and axial failure to be closer together. Figure 6-4 compares the gap between the drifts at the point of shear failure and the axial limit curve, calculated using the above-mentioned models for specimen MCFS and a one-story shaking table test specimen with lower axial load that was tested in 2005 (Wu et al., 2009). Details of the one-story test specimen (2005 Test), specifications of its columns, which were relatively similar to specimen MCFS, and results from modeling the test frame can be seen in the study by Yavari et al. (2009). It is observed that while the gap between the calculated drifts at shear and axial failure was large for the one-story specimen (2005 Test), such drifts became very close for specimen MCFS. Therefore, the analyses for the specimens with non-ductile columns (specimens MCFS, HCFS, and MUFS) are very sensitive to the position of shear and axial limits curves. As will be discussed later in this chapter, limit curves were slightly shifted for these specimens in order to simulate the observed behaviour of the columns.

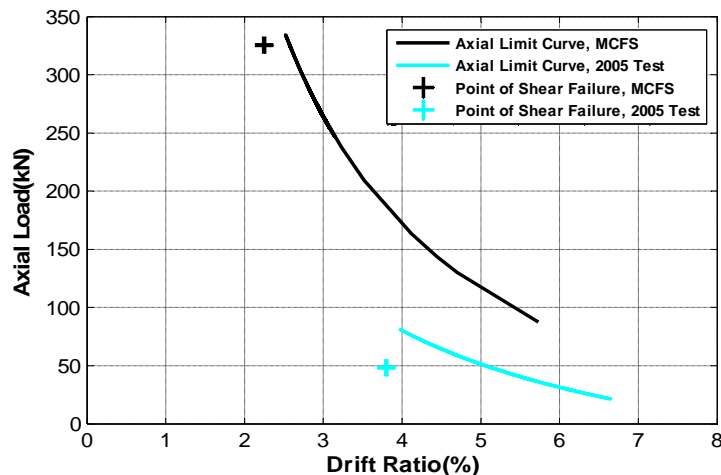


Figure 6-4. Comparison of drifts at onset of shear and axial failure, specimen MCFS and 2005 Test

Section forces (moment and axial load) at integration points of the beam-column elements were determined in OpenSEES by interpolation of the element end forces and integration of the resulting section deformations (curvatures and axial strains) over the length of the element to determine the element end deformations (rotations and axial lengthening). By capturing the moment-axial load interaction, the fibre elements are able to model the axial lengthening of the columns resulting from lateral displacements. A complete description of nonlinear fibre beam-column elements can be found in the study by Spacone et al. (1996a, 1996b). For the development of the specific force-based nonlinear beam-column element available in OpenSEES, and used for analyses here, refer to the study by de Souza (2000).

The column cross-section was subdivided into concrete and steel fibres at each section. The concrete model “Concrete01” from OpenSEES, with a compressive strength equal to the test day cylinder strength, was used to define the response of concrete fibres for all frames. The assumed constitutive relationships for concrete and steel longitudinal reinforcement used in the column models for specimen MCFS are shown in Figure 6-5, where the tensile capacity of concrete was ignored. Similar constitutive relationships for concrete and steel, but with different maximum strengths were considered for the other three specimens. Figure 6-5a demonstrates the stress-strain relationship for the cover concrete with spalling. As demonstrated in Chapter 4, minor spalling was observed at the ends of the columns during Test1. Study by Yavari et al. (2009) shows that ignoring the limited spalling of cover concrete in the analytical model eliminates the localization of curvature at the ends of force-based nonlinear beam-column elements, leading to a better simulation of their behaviour by the OpenSEES analytical model. Therefore, spalling of the cover concrete was ignored (Figure 6-5b). It should be noted that such stress-strain relationship was used to overcome the

unrealistic localization of flexural deformations at the column element ends and was not intended to represent the actual constitutive model for unconfined concrete. Although columns in the specimens (except MUF) were not well-confined, the light transverse reinforcement resulted in a slightly higher concrete strength in the core concrete compared to the concrete cylinder tests. The concrete constitutive relationship used for the confined core of all the columns was obtained according to the model by Mander et al. (1988). Figure 6-5c shows the stress-strain relationship used for the concrete core of non-ductile columns in specimens MCFS.

The reinforcing steel material for the columns was modeled using a hysteretic material with tri-linear backbone (Figure 6-5d). Amongst the available steel models in OpenSEES, Clough-type hysteretic steel model provided a better estimate of the measured response of the whole column, and therefore, this material model was used for the analyses presented in this chapter.

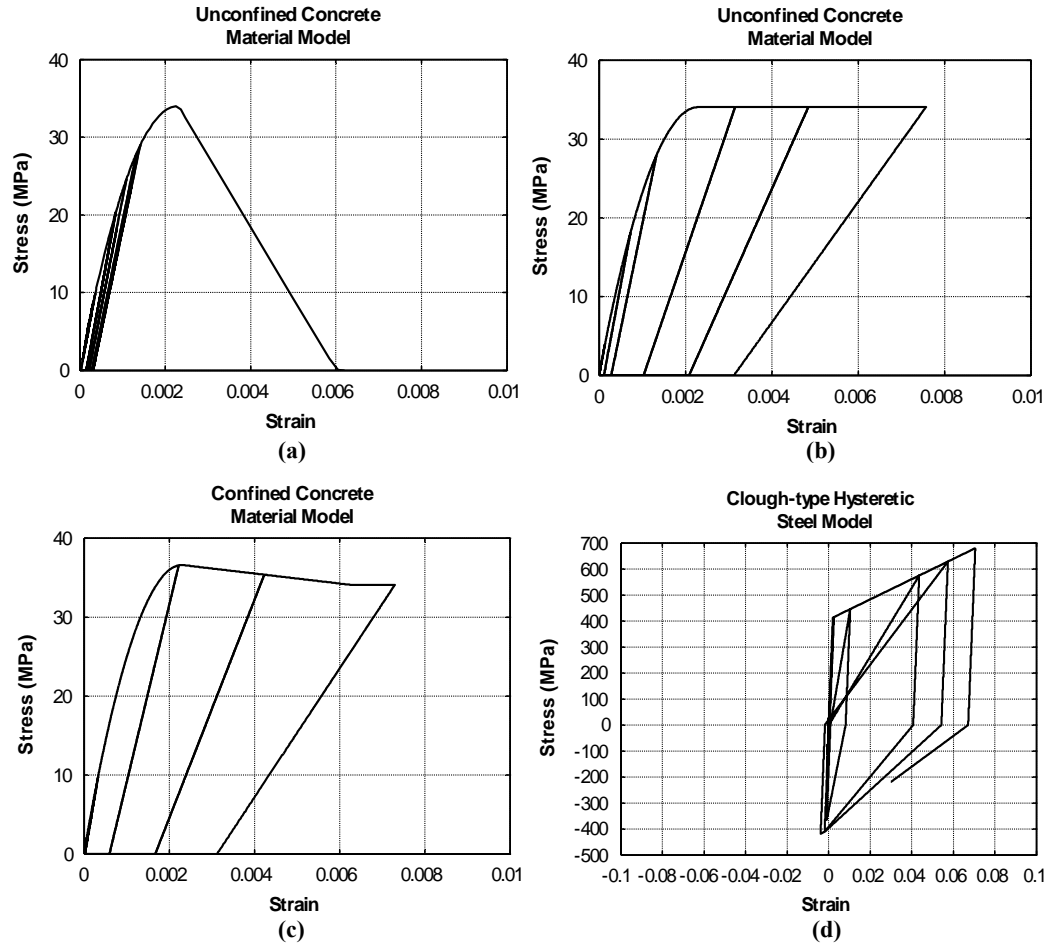


Figure 6-5. Stress-strain relationships used in modeling; a) unconfined cover concrete with spalling; b) unconfined cover concrete, spalling ignored; c) confined concrete; d) Clough-type hysteretic steel model for column longitudinal reinforcement

6.2.4 Modeling of Bar-slip for Beams and Columns

To account for the flexibility due to slip of the longitudinal reinforcing bars, elastic rotational slip springs, with rotational stiffness recommended by Elwood and Eberhard (2009), were included in zero-length elements at both ends of columns and beams. The bond stresses developed in the joints and footings were assumed to be identical in this analytical model. Elwood and Eberhard suggested that the rotational stiffness of the slip spring, K_{slip} , can be

determined by assuming a constant bond stress of u along the longitudinal reinforcement within the joint and footing and calculating the rotation at the end of the element due to elongation of the bars within the joint or footing:

$$K_{slip} = \frac{8u}{d_b f_s} EI_{flex} \quad (6.6)$$

where d_b is the nominal diameter of the longitudinal reinforcement, EI_{flex} is effective flexural rigidity obtained from the moment-curvature analysis of the column section, and the stress in the longitudinal reinforcement (f_s) can be taken as equal to the yield stress (f_y) for columns with low axial loads. Studies by Melek et al. (2003), and Sezen and Setzler (2008) suggested an average bond stress of $0.95\sqrt{f'_c}$ (in MPa units) for columns, while Sozen and Moehle (1990) calculated a mean average bond strength of $0.83\sqrt{f'_c}$ (in MPa units) from testing 35 beams under monotonic loading. The aforementioned bond stresses were considered for the columns and beams, respectively, in the current study to obtain the rotational stiffness for slip springs using Equation (6.3).

6.2.5 Load Model

The dead loads were applied at beam and column nodes as shown in Figure 6-1 based on the measured weight of the lead packets and attached steel components and the calculated weight of the beams and columns. The mass matrix included lumped masses for horizontal and vertical degrees of freedom at the beam nodes. This allowed for applying the mass of the inertial-mass-wagons (see Chapter 3) to the top node of center column in horizontal direction without influencing the mass matrix in vertical direction. Frame self-weight masses were distributed across all nodes in the model according to the tributary mass of each node. To

avoid numerical convergence issues related to massless nodes, negligible mass was assigned to those nodes.

Both horizontal and vertical components of the pre-stress forces applied to the columns by the hydraulic jacks were applied to the top nodes of second-story columns. The components of the pre-stress force were determined using the recorded pre-stress force from the top load cells and the measured relative displacement at the top level of the frames. As discussed earlier, the pre-stress force on the columns varied during the tests; therefore, the force components were applied as a time-variant force series during each test.

6.2.6 Other Modeling Parameters

By using mass-proportional damping, the equivalent viscous damping was set at 3% of critical for the measured fundamental mode of vibration for frames MCFS, HCFS, and MUFS. Stiffness-proportional damping could not be used in the model for these specimens due to unrealistically large damping forces at the node connecting the springs to the beam-column element. Study by Elwood and Moehle (2008) showed that such excessive damping forces were resulted from the large velocity caused by the sudden change in response at shear and axial failure of the zero-length springs. Since no mass was modeled at this node, the increase in velocity did not influence the mass-proportional damping forces. Stiffness-proportional damping, which reduces the influence of higher modes, was not a significant concern for the modeling of the specimens because the first mode was the dominant response for the specimens due to the large inertial-mass concentrated at the top of the specimens.

Since shear and axial springs were not included in the model for specimen MUF, damping for the specimen was modeled with constant coefficients for stiffness and mass proportional Rayleigh damping, given a damping ratio of 3% of critical at the first and second

“initial” elastic modes of vibration of the structure ($T_1=0.29$ sec, $T_2=0.07$ sec). Since the first mode was dominant for the specimen, no significant difference in the results was observed by changing the Rayleigh to mass-proportional damping. P-delta effects were included in the column-element formulation to account for nonlinear geometric effects, which may be significant at anticipated maximum drift levels.

In order to eliminate the influence of shaking table parameters on the input motion, the recorded table motions during the tests were used for the analyses. Similar to the experimental tests, the analytical models were subjected to the sequential table motions to include the residual deformations from each preceding test.

6.3 Assessment of Analytical Models

This section will evaluate the ability of the analytical models described in Section 6.2 to reproduce the observed response of the specimens as described in Chapter 4. While Section 6.3.1 discusses the results from static pushover analysis of specimen MCFS, Sections 6.3.2 through 6.3.5 compare the data from the experimental tests with the results from corresponding analyses for the four specimens. Lateral and vertical behaviour of the frames and their structural components subjected to the sequence of table motions (see Table 3-3) are studied here. The models were subjected to the table motion from the Half-Yield Test, followed by table motions from Test1 and Test2 (and Test3 for specimen MUF). However, since the table motion from Half-Yield Test did not have a significant impact on the frame behaviour, only results from Test1 and Test2 are presented in the following sections.

6.3.1 Static Pushover Analysis

Static nonlinear analyses are widely used by practicing engineers to evaluate the capacity of structures subjected to ground motions. Static monotonic analysis (pushover) for specimen MCFS is presented in this section to demonstrate the response of the columns under a simplified loading condition. The analysis was performed by linearly increasing horizontal displacements imposed to the stories at beam levels. The pattern along the height of the specimen was based on the first mode of the frame obtained from the test data and an anticipated maximum second floor displacement of 150 mm (or a frame drift of 4.8%).

Figure 6-6 compares the hysteretic response of first-story columns of specimen MCFS during Test1 with the response of the columns from the nonlinear static analysis described above. The thick straight line shows the shear limit curve calculated for the dynamic time-history analysis (see Section 6.3.2). As discussed in Chapter 3 (Section 3.4.2.2), axial load varied during the test and the monotonic response shown in Figure 6-6 was calculated using the initial axial load on the columns. It is observed that all the columns, particularly column B1, were able to survive slightly larger drift demands before initiation of shear strength degradation. By changing the axial load on the columns to the maximum axial load recorded during Test1, it is observed that the onset of shear strength degradation is in excellent agreement with the limit curves obtained during the dynamic time-history analysis (Figure 6-7). Therefore, the maximum recorded axial load was used for obtaining the results discussed below.

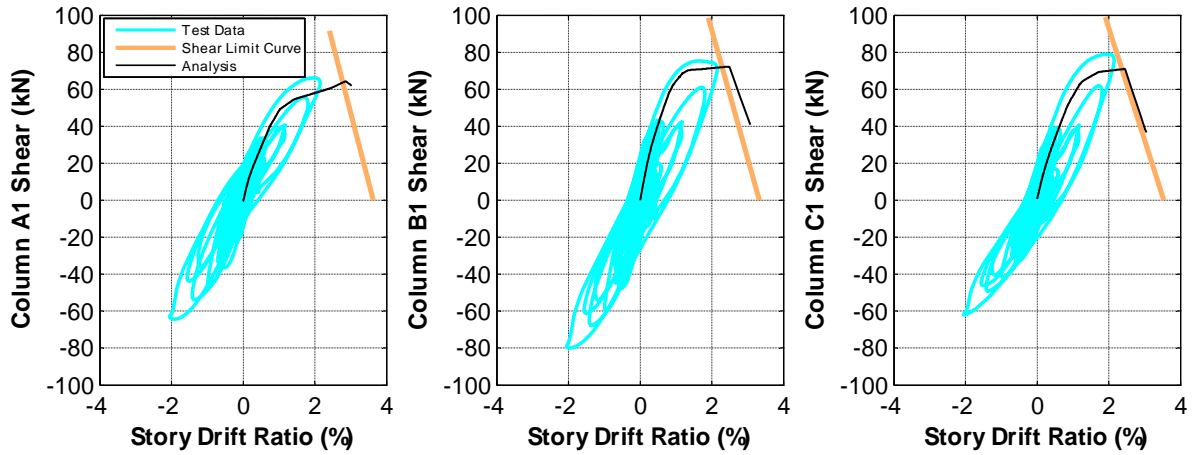


Figure 6-6. Shear response of first-story columns of specimen MCFS, monotonic analysis under initial axial load

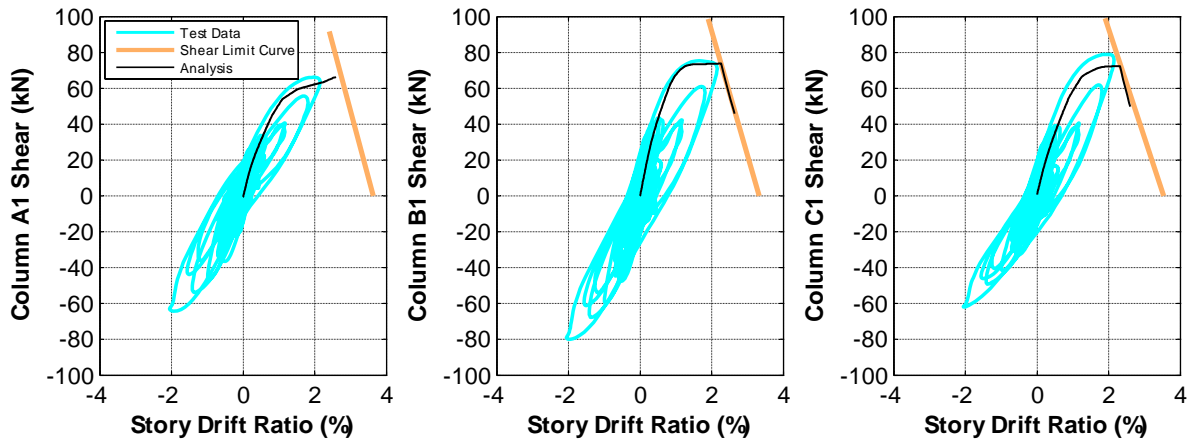


Figure 6-7. Shear response of first-story columns of specimen MCFS, monotonic analysis under peak axial load

Figure 6-8 compares the base shear hysteretic response of specimen MCFS with the overall behaviour estimated by nonlinear static (pushover) analysis for Test1 and Test2. Since the pushover shear backbone was obtained assuming undamaged members, it is observed that the backbone stiffness was higher than the stiffness obtained for the specimen in Test2, where damage from Test1 lowered the lateral stiffness of the frame. However, the analytical model was able to capture the base shear degradation reasonably well. The analysis was terminated due to non-convergence issue after the axial failure of column B1 was detected.

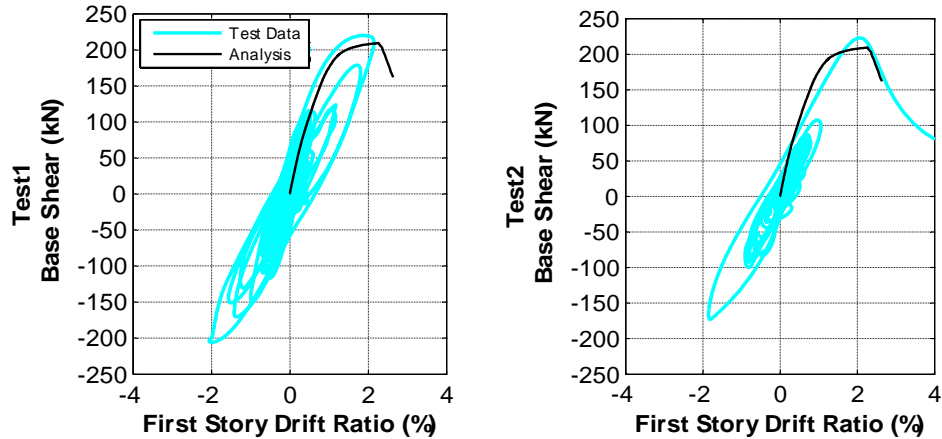


Figure 6-8. Base shear response of specimen MCFS, monotonic analysis, Test1 and Test2

Drift of a column caused by lateral load can be decomposed into the displacement components due to flexure, shear and bar slip (Priestley et al., 1996, Lehman and Moehle, 1998, Berry and Eberhard, 2007).

$$\Delta = \Delta_{slip} + \Delta_{flex} + \Delta_{shear} \quad (6.7)$$

Shear response of column B1 was plotted versus slip, flexural, and shear components of the column drift in Figure 6-9, demonstrating the behaviour of the non-ductile column model used in the analyses presented in this chapter. While the slip component of drift was extracted from the linear slip springs attached to the top and bottom of the column, the flexural component was based on the horizontal displacement of the column nonlinear fibre element. The shear component was based on the displacement of the shear spring in the zero-length element at the top of the column element. It is observed that, before the onset of shear failure, the total response of the column was dominated by the flexural displacement. Reaching the drift at onset of shear failure, the shear spring strength was degraded and forced the fibre element to unload, which resulted in less flexural displacement and higher shear displacements.

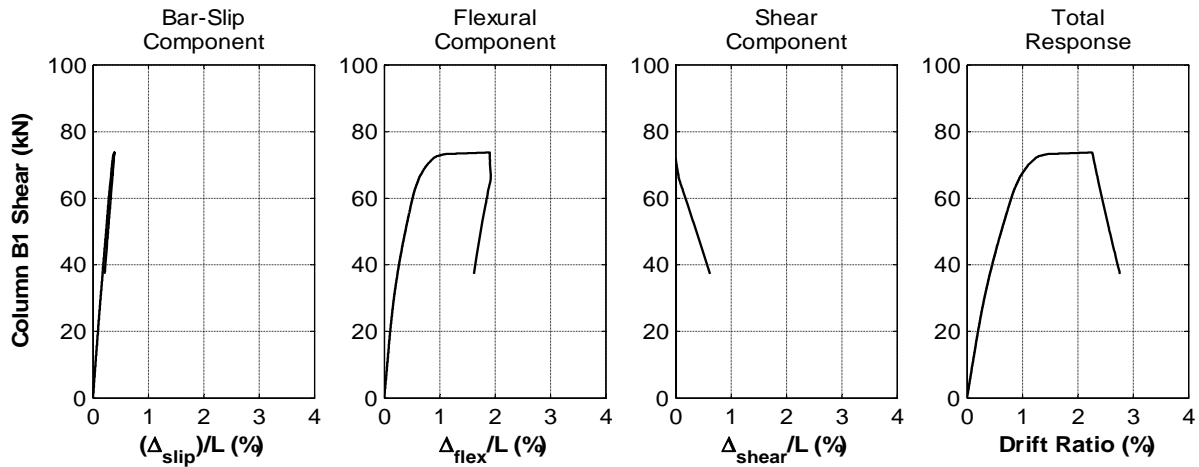


Figure 6-9. Components of drift ratio for column B1, monotonic analysis

As discussed in Chapter 3, it was of interest to investigate the influence of frame flexibility on redistribution of load in the columns and their deformations. While such complex interaction is dependent on several parameters, a simple approach was taken here to estimate the contribution of beam flexibility and rotation of the joints in lateral displacement of first-story columns of the specimens. In order to eliminate the effect of frame damage, the displacement corresponding to the point of $0.75V_{max}$ was selected. This is the point at which the effective stiffnesses of the columns were calculated. At first, drift at $0.75V_{max}$, denoted as Δ_{total} , was recorded for the columns of the model described earlier for specimen MCFS, where the beams had the stiffness similar to that observed during the experiment. In the next step, properties of the beams altered to make them rigid and the drift at $0.75V_{max}$, denoted as Δ_{column} , was recorded for the columns. The difference between the lateral displacements obtained from the two models demonstrates the contribution of the flexibility of the connecting elements in column lateral deformation.

Figure 6-10 demonstrates the deformation of the two frame models with; a) flexible beams, and; b) rigid beams. Table 6-1 compares the drift ratios of first-story columns from the two models at $0.75V_{max}$. It is observed that the contribution of frame flexibility in deformation

of column B1 was minor and therefore, considering story lateral displacement instead of column displacement for obtaining the column effective stiffness can be a reasonable assumption. Table 6-2 compares the lateral displacements of first-story columns of the analytical model for specimen MUFS, showing a slightly higher contribution of frame flexibility due to minor deformation of unconfined joints at the point of $0.75V_{max}$.

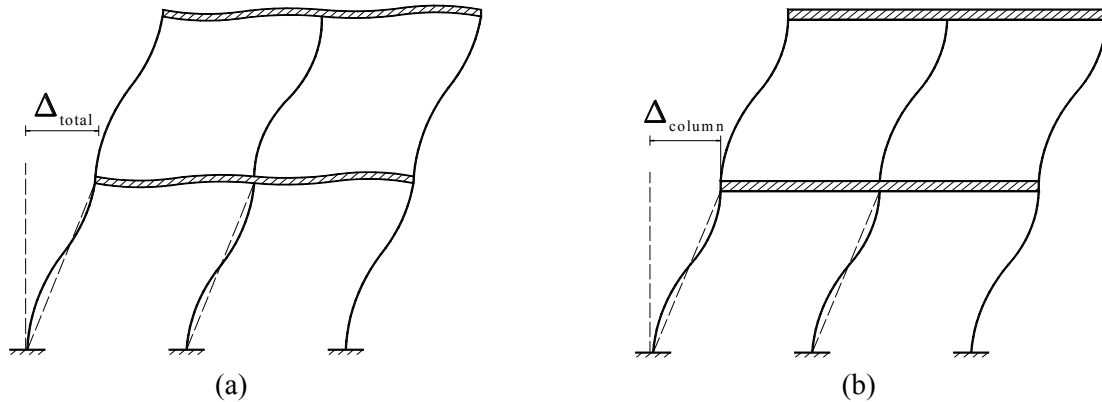


Figure 6-10. Lateral deformation of frame with; a) flexible beams; b) rigid beams

Table 6-1. Influence of joint rotation on lateral displacement of first story at $0.75V_{max}$, specimen MCFS

| At point of $0.75V_{max}$ | Column A1 | Column B1 | Column C1 |
|--|-----------|-----------|-----------|
| Δ_{total} (mm) | 13.2 | 9.8 | 12.4 |
| Δ_{column} (mm) | 11.5 | 9.5 | 10.8 |
| Contribution of frame flexibility in column lateral displacement (%) | 12.9 | 3.1 | 12.9 |

Table 6-2. Influence of joint rotation on lateral displacement of first story at $0.75V_{max}$, specimen MUFS

| At point of $0.75V_{max}$ | Column A1 | Column B1 | Column C1 |
|--|-----------|-----------|-----------|
| Δ_{total} (mm) | 13.4 | 9.9 | 12.6 |
| Δ_{column} (mm) | 11.5 | 9.5 | 10.8 |
| Contribution of frame flexibility in column lateral displacement (%) | 14.1 | 4.2 | 14.3 |

6.3.2 Analytical Model of Specimen MCFS

The initial natural period of the analytical model was obtained as 0.29 seconds which shows an excellent match with the natural period obtained from the White-Noise test (see Section 4.3). In order to compare the results from the analytical model with the experimental test results for Test1 and Test2, Figure 6-11 through Figure 6-21 plot story and frame drift ratios, base and column shears, first-story column axial loads, shear hysteretic behaviour of the columns, and axial load hysteretic behaviour of first-story columns.

6.3.2.1 Comparison of Results for Test1

Figure 6-11 compares the drift ratios from Test1 and the analysis. It is observed that the analytical model adequately captured the drift ratio phasing up to 35 seconds. Despite the slight over-shooting in some cycles, the model was also able to capture the drift ratio amplitudes reasonably well, until 34.25 sec. After the peak drift ratio was reached at that time, the results from analysis and the test data did not show a good match. Figure 6-11 also demonstrates a significant underestimation of the peak second-story drift ratio by the analytical model. Consequently, the ratio of first to second-story drift demands was overestimated in the analysis, resulting in concentration of drift in the first story during Test2 (Section 6.3.2.2). It is also observed that the analytical model underestimated the drift ratios for the first and second stories after the peak drift was reached.

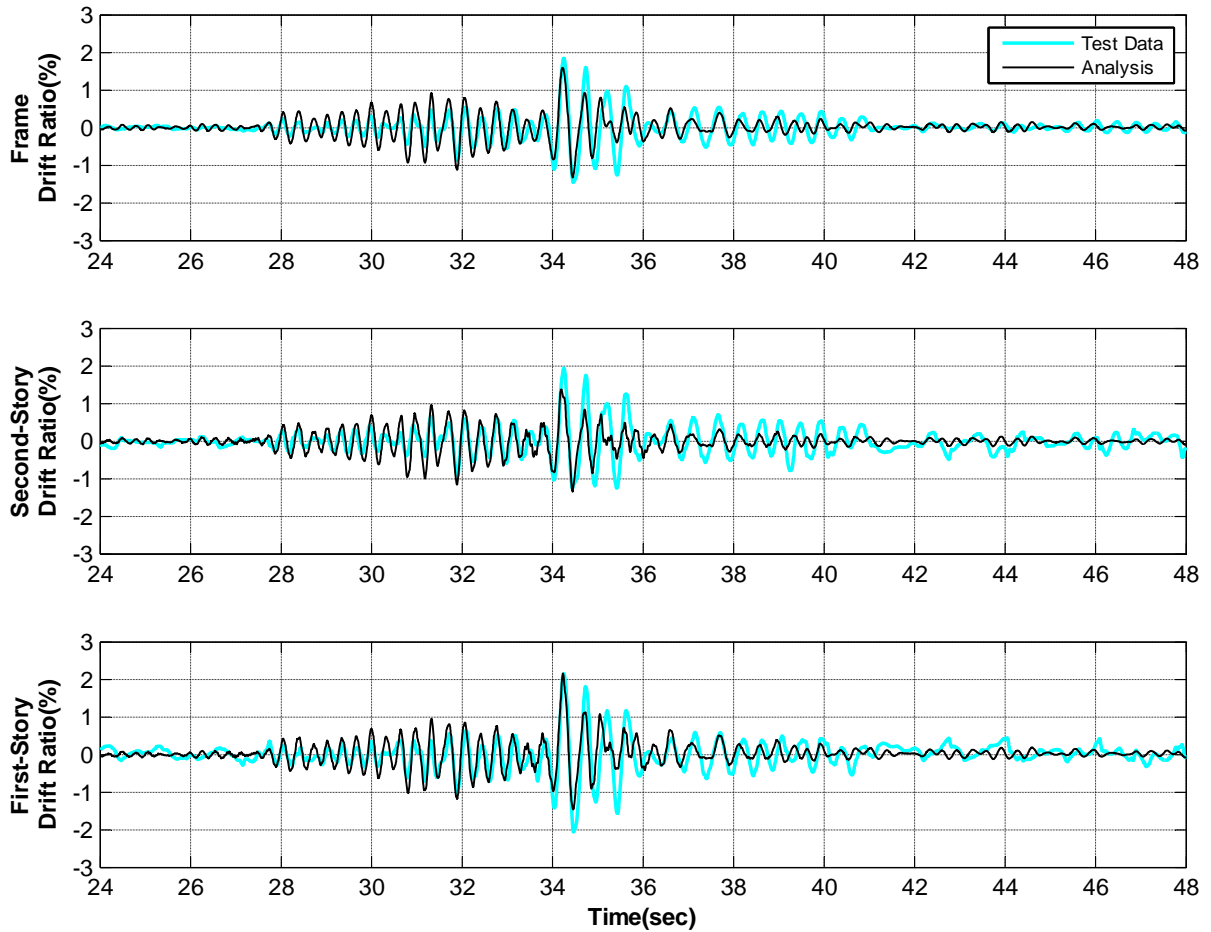


Figure 6-11. Story and frame drift ratio histories (specimen MCFS, Test1)

Figure 6-12 compares shear response histories from the test and analysis for first-story columns, second story, and the frame base shear, showing a very good agreement between the analytical and experimental results. The peak base shear was underestimated by only 6%, while a maximum under-estimation of peak shear of 12% was observed for the column B1. However, similar to the drift ratio histories (Figure 6-11), the results start to diverge after 35 seconds.

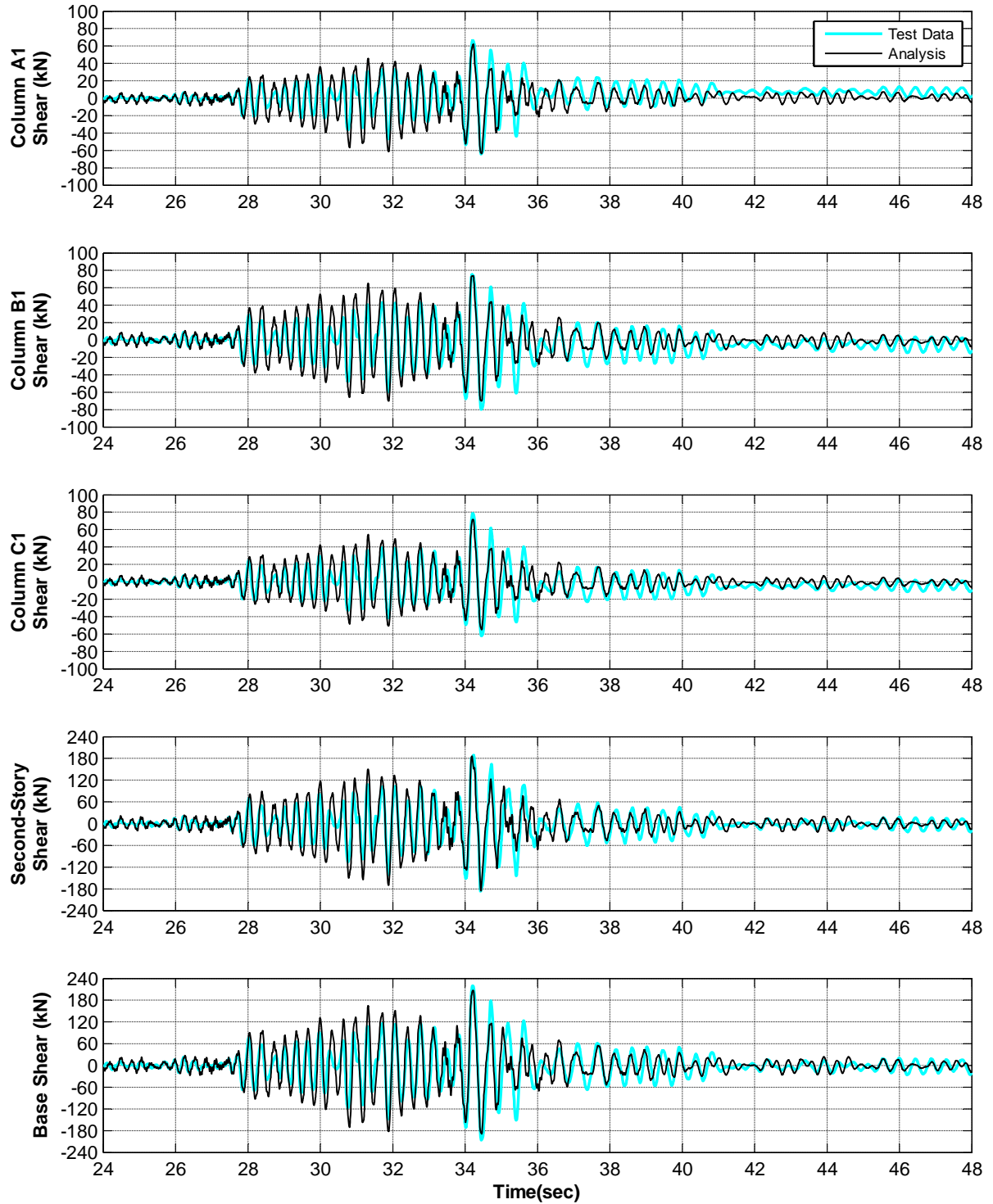


Figure 6-12. First-story columns, second-story shear and frame base shear histories (specimen MCFS, Test1)

Excellent agreement between analysis and experiment was obtained for first-story and second-story lateral stiffnesses (Figure 6-13). However, such agreement was obtained by shifting the shear and axial limit curve by 0.01% drift ratio (see Section 6.2.3). While the original shear limit underestimated the drift at shear failure causing false detection of shear failure in Test1, shifting the curve by such a small drift ratio allowed for adequate estimation of the hysteretic response of the columns (Figure 6-13).

The analytical model adequately represented both the initial stiffness as well as softening for higher amplitude loading for first-story columns. While the yield strength was well-estimated for column B1, it is observed that the model underestimated the yield strength for columns A1 and C1. Although the analytical model demonstrates a very good match for the second story initial stiffness, softening in response of second-story columns could not be captured very well.

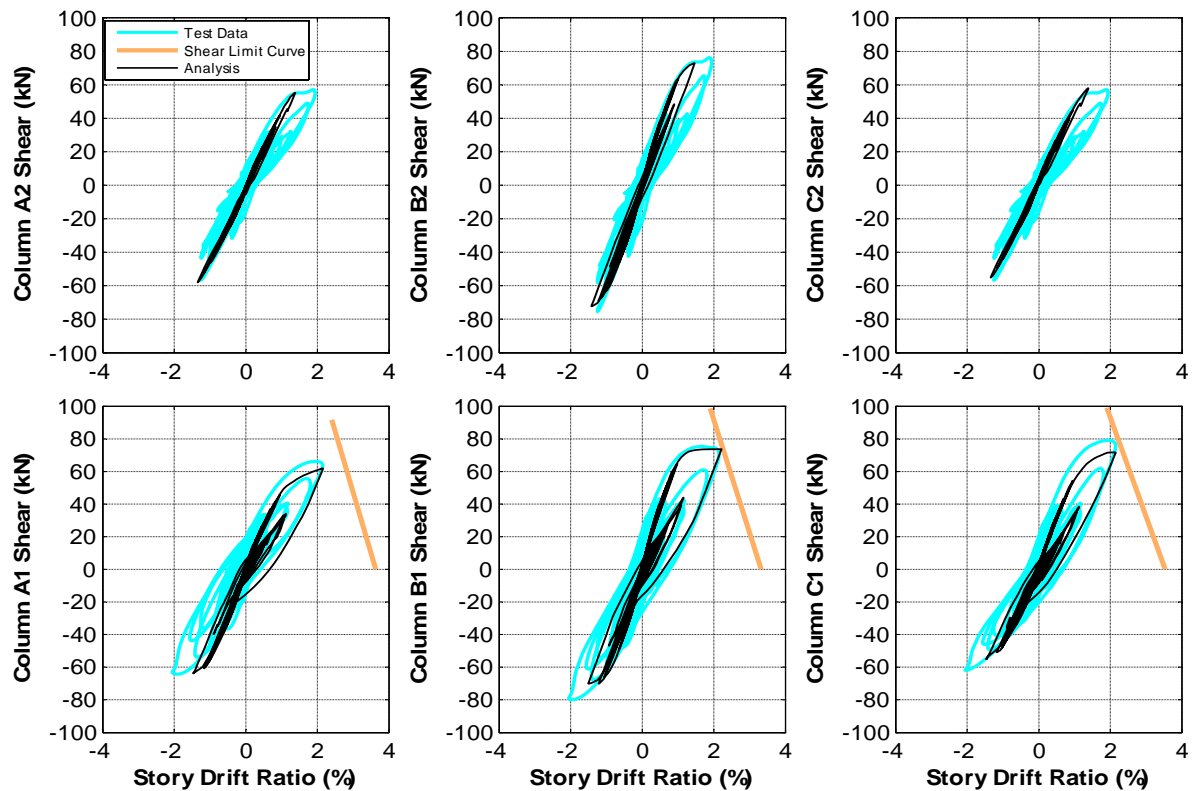


Figure 6-13. Shear hysteretic response of the columns (specimen MCFS, Test1)

Figure 6-14 and Figure 6-15 show a very good agreement between analysis and experiment for the first-story column axial loads. It should be noted that the vertical and horizontal components of the applied axial load on columns were considered in the analysis which contributed to the satisfactory match of the results from the test and analysis. Due to overturning, axial load in the columns varied during the test. Figure 6-16 demonstrates the variation in axial load in the columns due to overturning which was obtained as the difference between the axial load at the base of first-story columns and the applied axial load due to pre-stressing the columns. As expected, the effect of overturning was more significant for the exterior columns. The maximum difference was observed for column C1 at 34.25 seconds, where the peak drift ratio was recorded for first-story columns of specimen MCFS.

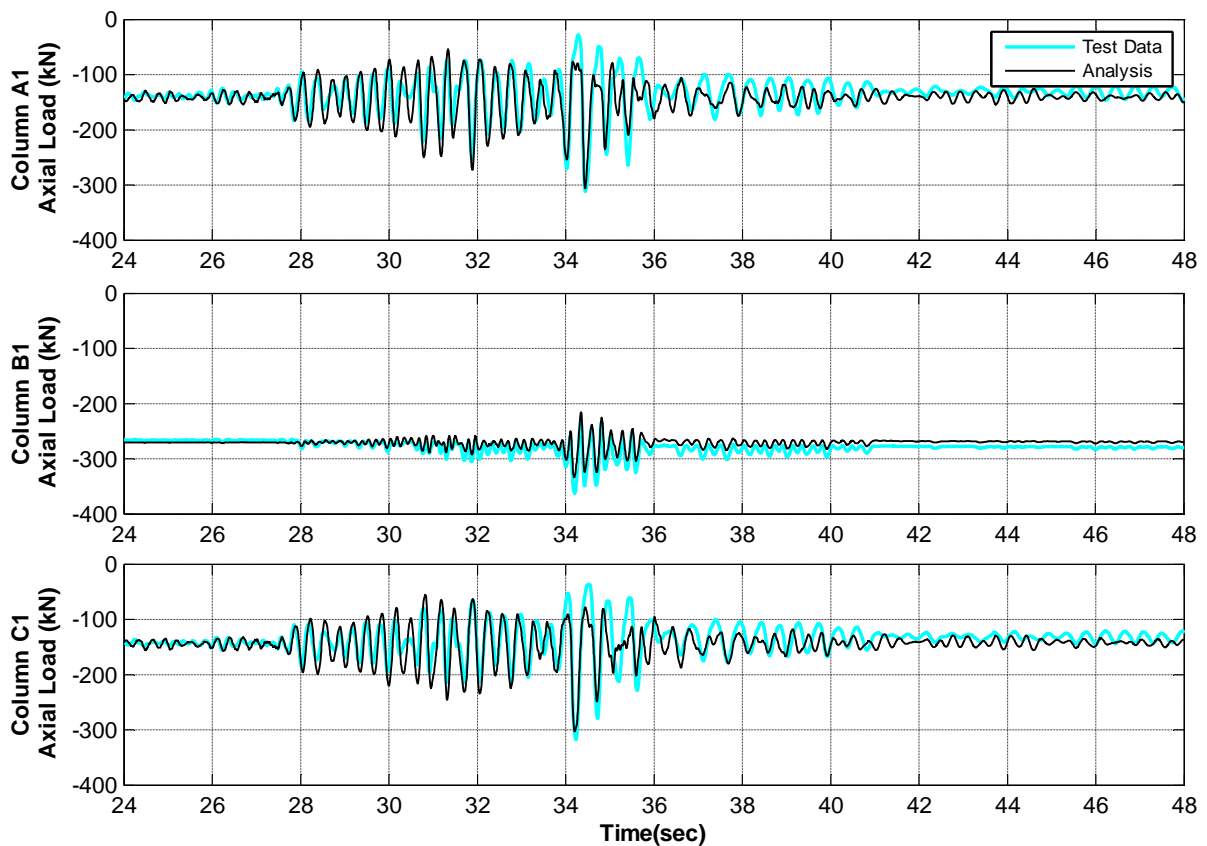


Figure 6-14. Axial load history response of first-story columns (specimen MCFS, Test1)

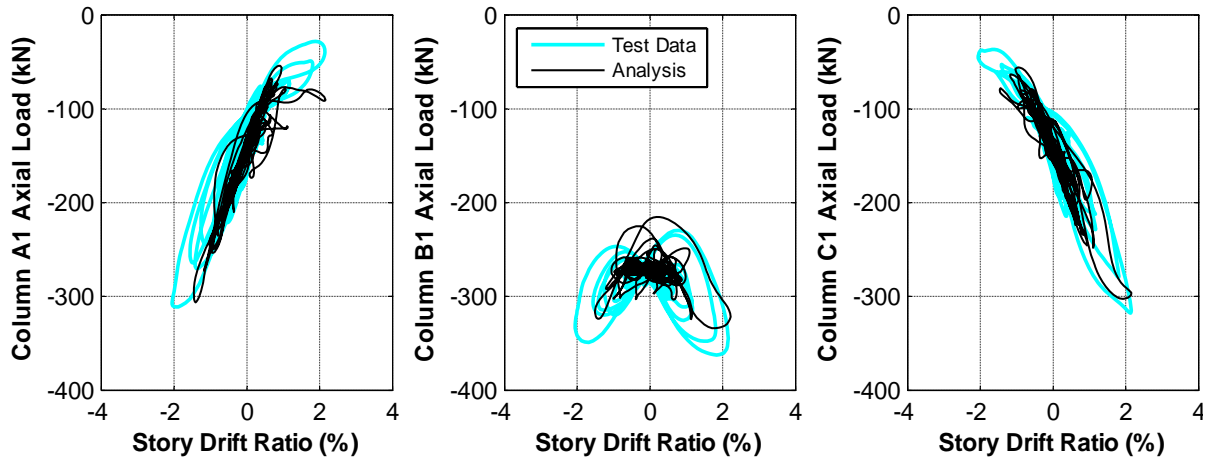


Figure 6-15. Axial load hysteretic response of first-story columns (specimen MCFS, Test1)

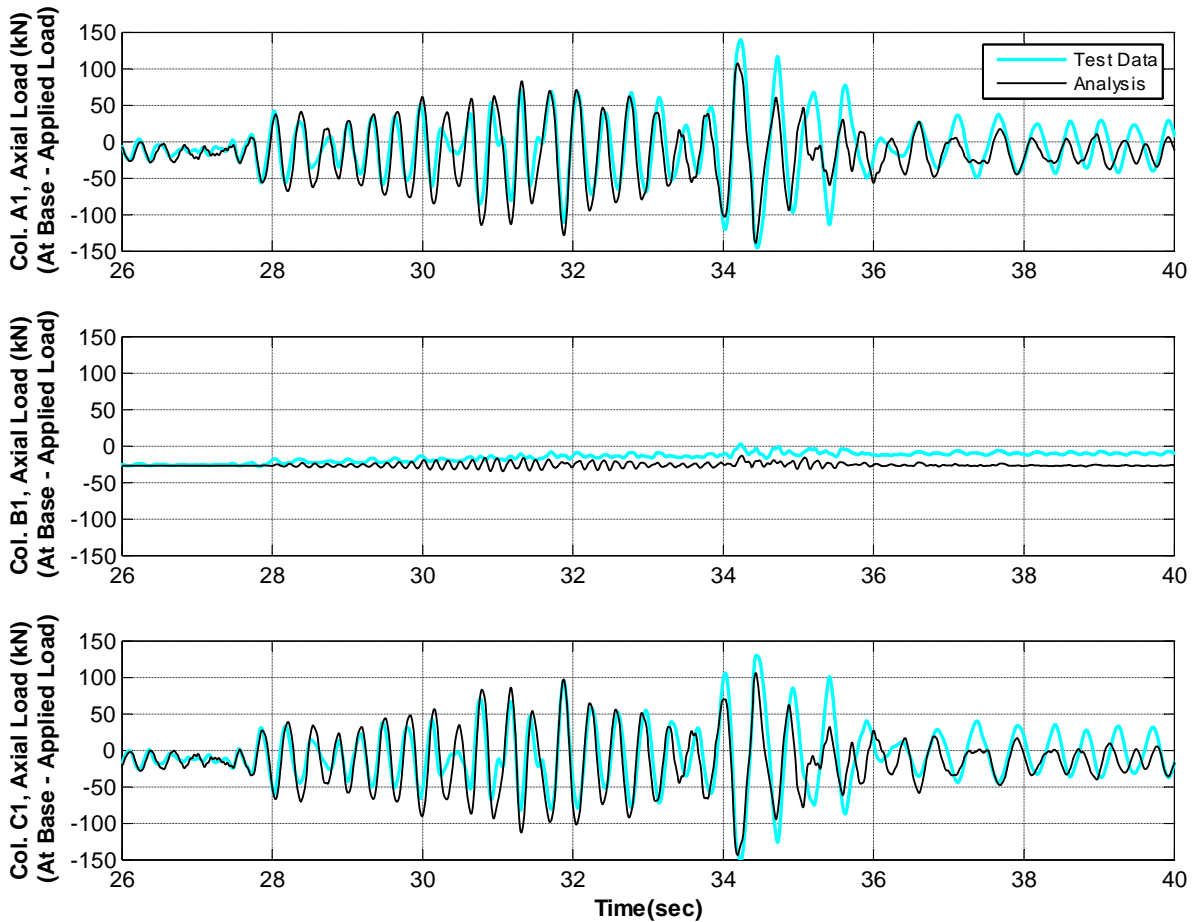


Figure 6-16. Variation of axial load on first-story columns due to overturning (specimen MCFS, Test1)

6.3.2.2 Comparison of Results for Test2

Figure 6-17 through Figure 6-21 compare analytical and experimental model results for representative response quantities. Excluding the drift ratio response between 29 and 30.5 seconds, Figure 6-17 demonstrates a very good agreement between results from Test2 and the analysis. The analytical model was also able to capture the concentration of drifts in the first story and the cycle in which the frame collapsed. Similar observations are achieved by comparing the shear responses (Figure 6-18 and Figure 6-19).

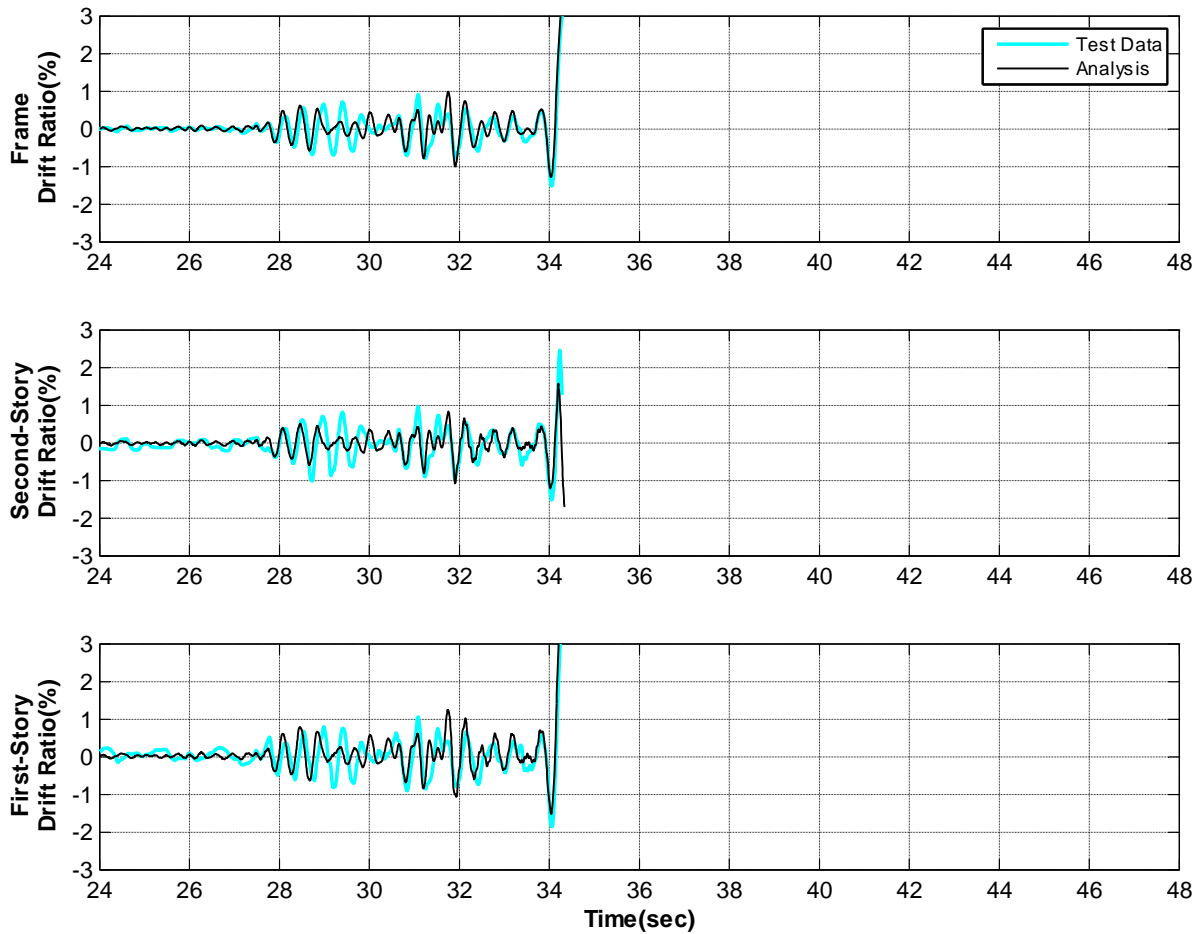


Figure 6-17. Story and frame drift ratio histories (specimen MCFS, Test2)

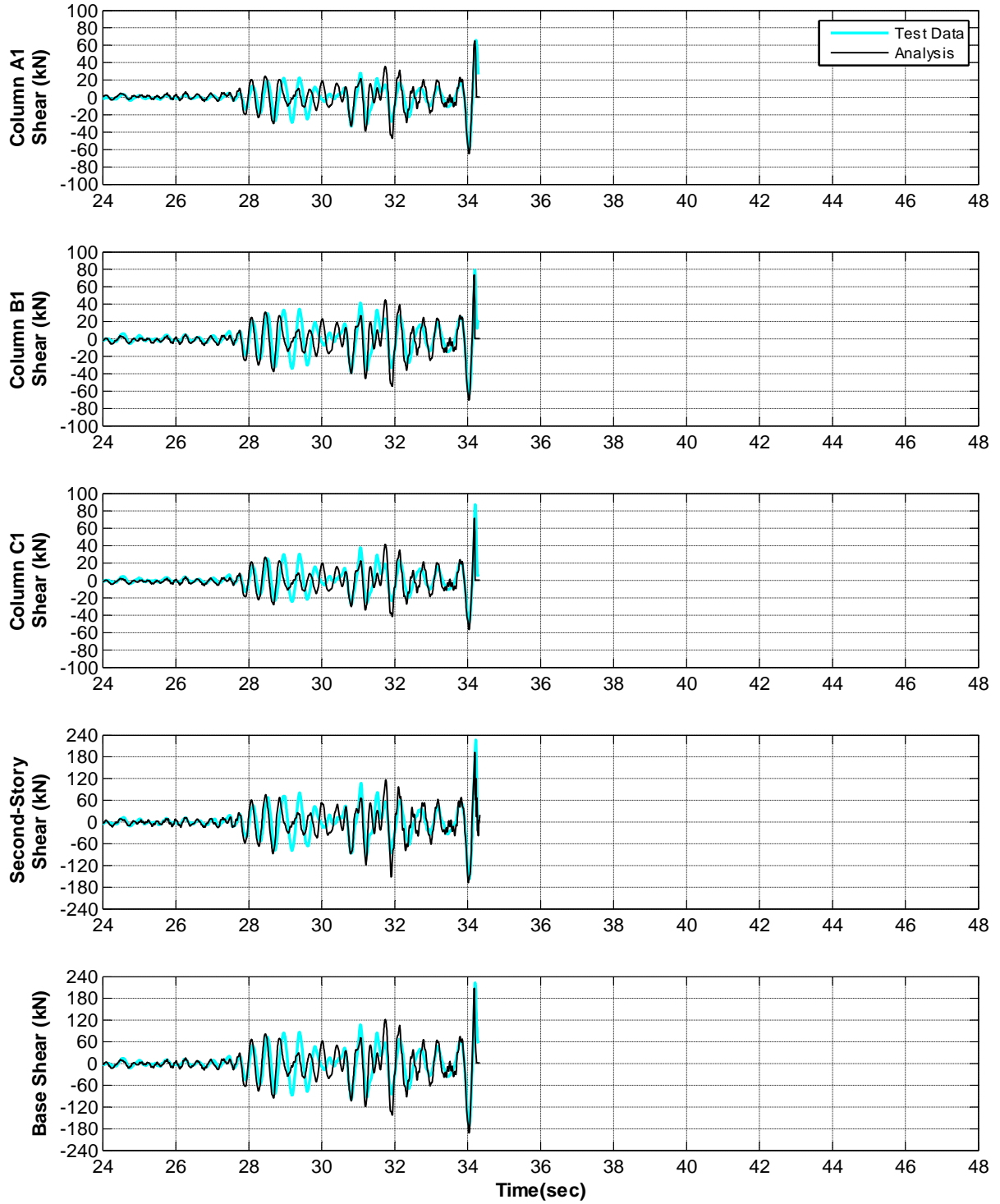


Figure 6-18. First-story columns and frame base shear histories (specimen MCFS, Test2)

Comparison of shear hysteretic response of the columns (Figure 6-19) illustrates that not only did the analytical model adequately capture the stiffness of the columns, but the onset of shear strength degradation of first-story columns was also well-estimated using the shear limit curve described in Section 2.3.1 with the slight shift mentioned earlier in Section 6.3.2.1. It is observed in the test data that softening of stiffness of the first-story columns increased the drift ratio demand in the negative direction relative to the analysis results (see red circles in Figure 6-19). The underestimation of drift demands in the negative direction appears to have contributed to lower shear demands and an overestimation of drift at shear failure in the positive direction in the next cycle (0.3% and 0.2% for columns B1 and C1, respectively) since the shear limit-curve allows for larger drift capacities at lower shear demands. Consequently, the strength degradation happened in smaller drift ratio in the following cycle. Such behaviour was not captured in the analysis and therefore, strength peaks were recorded with 0.3% and 0.2% larger drift ratios for columns B1 and C1, respectively. As shown in Figure 6-20, the axial loads in columns B1 and C1 were underestimated at the point of peak shear by the analysis which can also be another source for under-estimation of peak shear for these columns.

The axial load hysteretic responses of the analytical and experimental models are compared in Figure 6-21 showing that the onset of axial failure was detected in the analysis at lower axial loads and larger drift ratios compared with the test results for both columns B1 and C1. Employing the axial limit curve model described in Chapter 2, the analytical results indicate axial failure of column B1 started at a drift ratio of 2.7% and axial load of 348 kN. However, the test data shows that the rapid loss of the column axial load capacity commenced at 1.9% drift ratio and axial load of 377 kN. Column C1 was predicted to fail at a drift ratio of

3.1% and axial load of 288 kN, while the test results demonstrate that the column started to lose axial capacity at 2.3% drift ratio and axial load of 353 kN. During testing, gravity load redistribution led to axial load failure of column A1 after failure of columns B1 and C1. Therefore, it is observed that the failure mode detected by the analytical model was in agreement with the observed failure mode for specimen MCFS (i.e. shear and axial failure of all first-story columns, see Section 4.4).

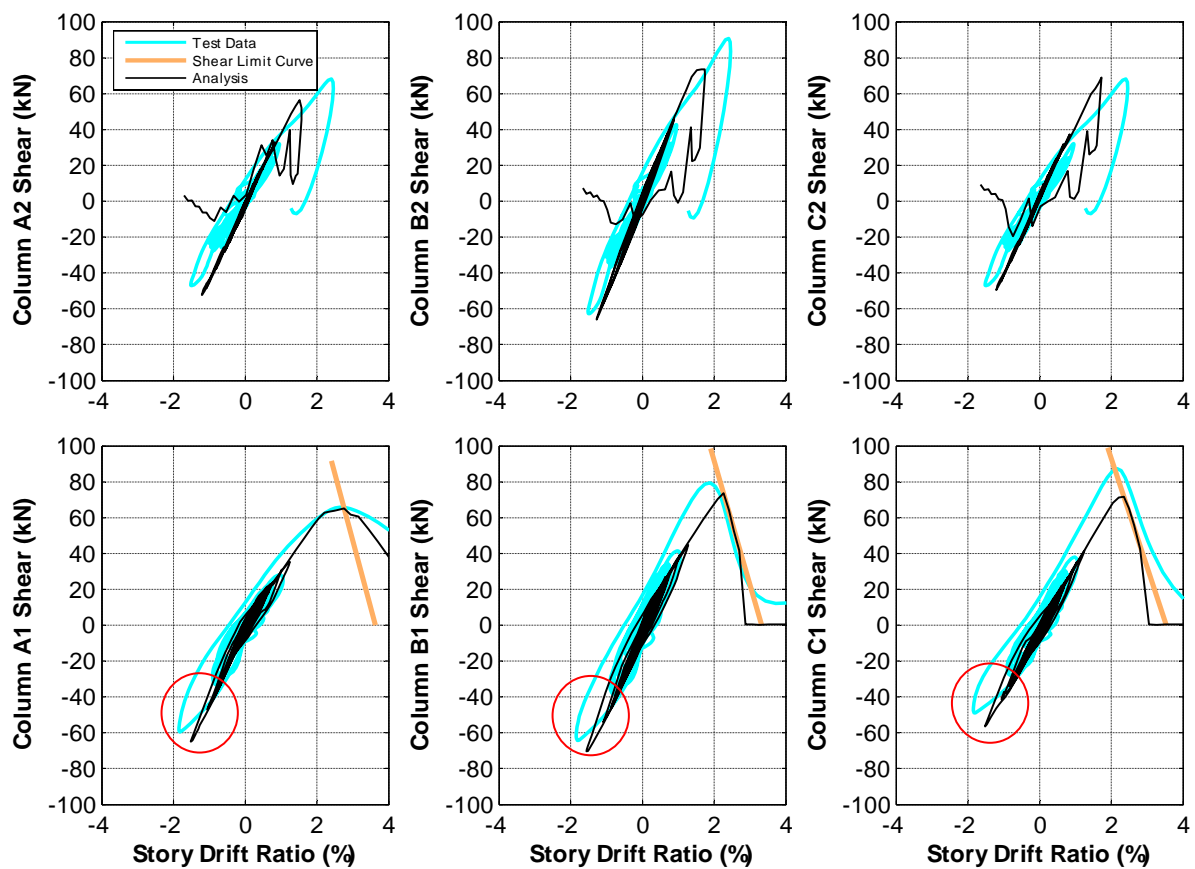


Figure 6-19. Shear hysteretic response of the columns (specimen MCFS, Test2)

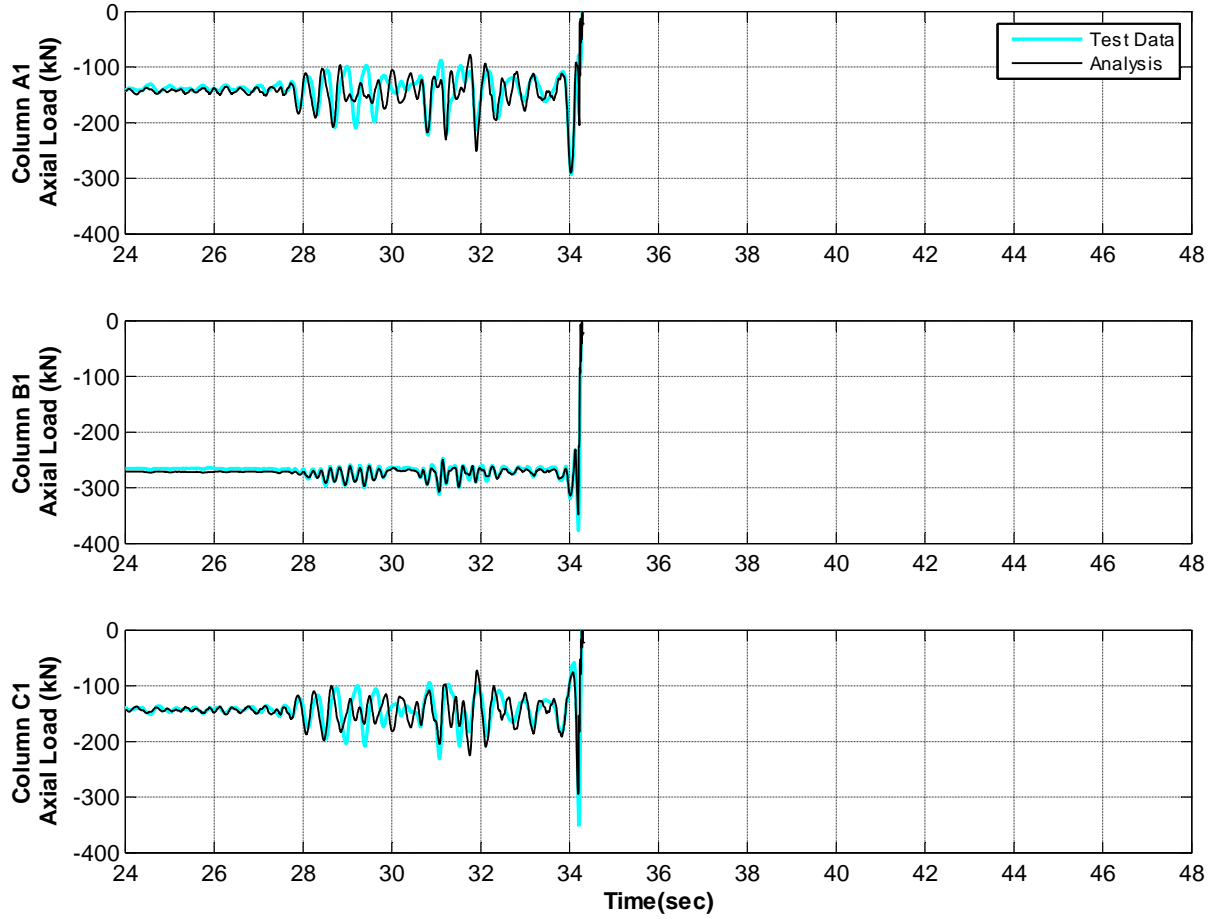


Figure 6-20. Axial load history response of first-story columns (specimen MCFS, Test2)

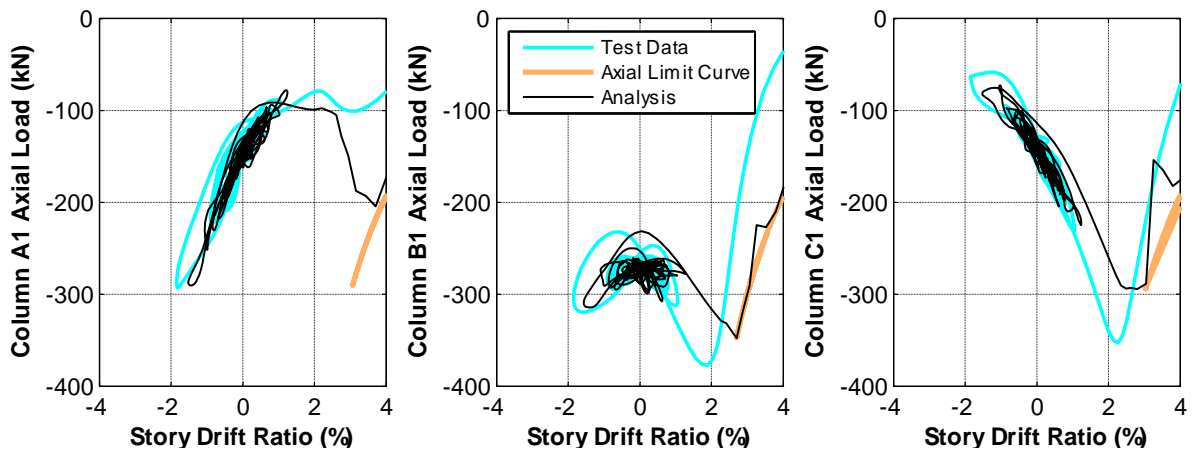


Figure 6-21. Axial load hysteretic response of first-story columns (specimen MCFS, Test2)

6.3.3 Analytical Model of Specimen HCFS

As discussed in Chapter 3, the only difference between specimens MCFS and HCFS was the axial load on the columns. Nevertheless, it affected the behaviour of the frames and their failure modes during the shaking table test. This section presents the behaviour of specimen HCFS, simulated by the analytical model. Comparison of the results from this section and Section 6.3.2 reveals the ability of the analytical model to capture the influence of axial load on behaviour of the studied frame.

The initial natural period of the analytical model was obtained as 0.29 seconds which is in good agreement with the natural period obtained from the White-Noise test (see Section 4.3).

6.3.3.1 Comparison of Results for Test1

Figure 6-22 compares the drift ratios from the experimental test and the analysis. Test results show that while the second-story drift ratio of specimen HCFS peaked at 1.9% at 34.2 seconds in the positive direction, the first story peak drift ratio was 2.5% at 34.5 seconds in the negative direction. However, it is observed that the analytical model could not capture these peak drift ratios and underestimated them by 25% and 28%, respectively. Figure 6-22 shows that the analytical model adequately captured the drift ratio phasing throughout the test, an improvement over MCFS where a good match was limited to first 35 seconds. The model was also able to capture the drift ratio amplitudes reasonably well until the peak drift (just past 34 seconds), while analytical model of MCFS over-estimated the drift ratios in some cycles between 30 and 32 seconds.

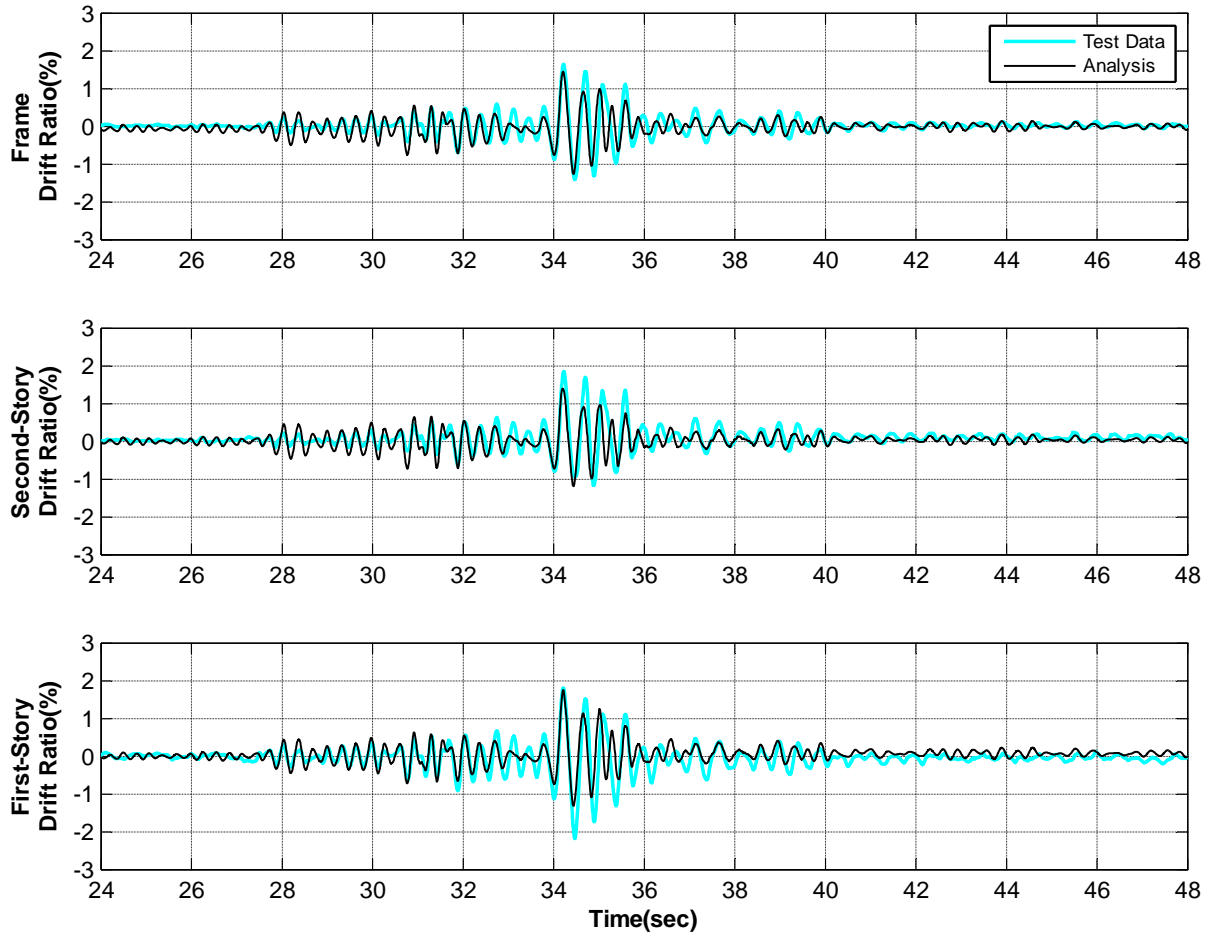


Figure 6-22. Story and frame drift ratio histories (specimen HCFS, Test1)

Figure 6-23 generally demonstrates a good agreement between analytical and experimental test results for the shear response histories for first-story columns, second story, and the frame base shear. However, it is observed that the model could not adequately estimate the shear demand between 33 and 33.8 seconds. Furthermore, experimental test results show higher shear values for column B1 in the positive direction after 34 seconds. While a positive residual shear force can be observed in the test results for column B1, negative residual shear forces were measured for columns A1 and C1 to maintain equilibrium. Such residual shear forces and redistribution of shear was not observed in the analysis. Comparison of Figure 6-12

and Figure 6-23 demonstrates that the analytical model for specimen HCFS was able to simulate the shear phasing better than the model for specimen MCFS.

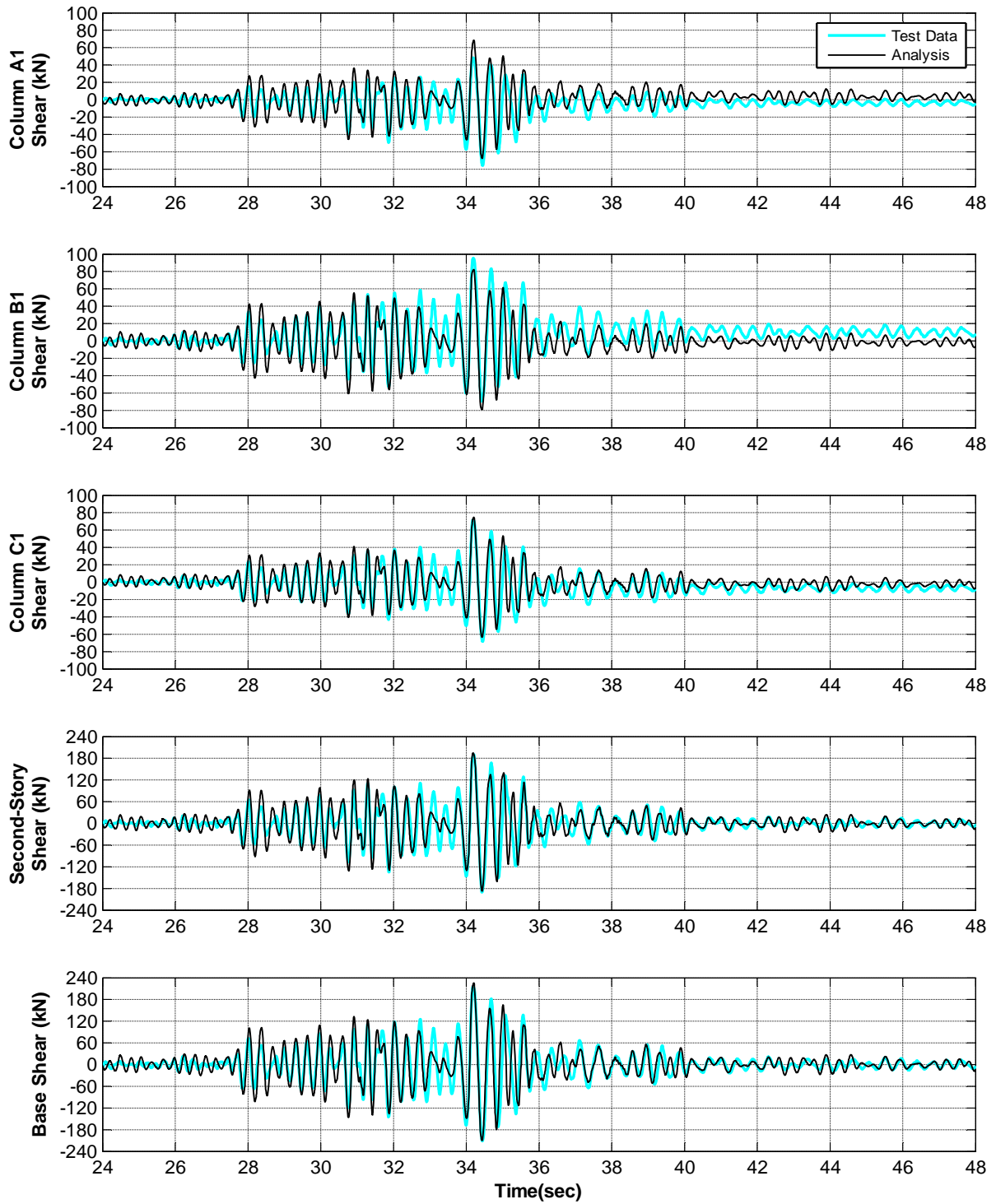


Figure 6-23. First-story columns and frame base shear histories (specimen HCFS, Test1)

Similar to the analytical model for specimen MCFS, the limit curves had to be shifted to simulate higher drift capacities to achieve a good match between the analysis and the test data. Shear hysteretic behaviour of column B1 from the analysis using the original limit curves is compared with that from the analysis with shifting the limit curves by 0.3% drift ratio in Figure 6-24. It is observed that the analytical model with the original limit curves detected the shear failure for column B1 at 1.7% drift ratio (Figure 6-24a), whereas shifting the limits curves led to much better agreement of the results from the analysis and test data.

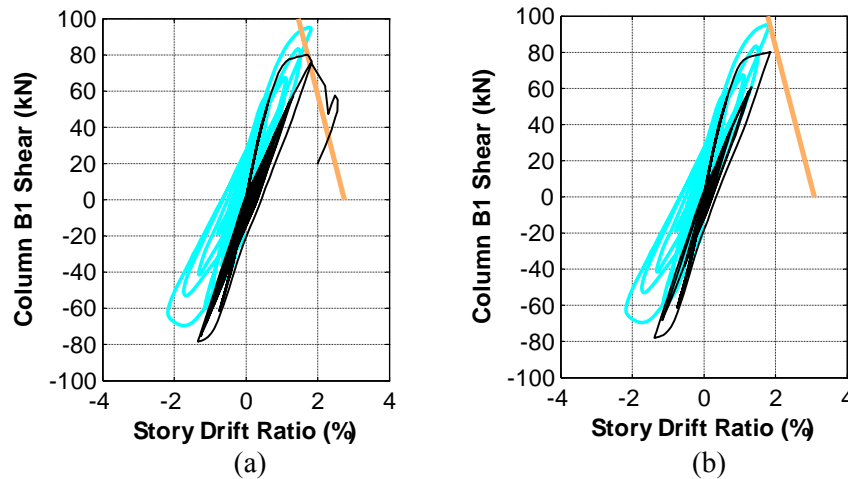


Figure 6-24. Comparison of shear hysteretic behaviour of column B1; a) limit curves were not shifted; b) limit curves were shifted by 0.3%

Figure 6-25 compares the shear hysteretic response of all the columns from the test data with the results from the analysis with shifted limit curves. It is observed that the initial stiffnesses of the stories were adequately captured by the analytical model. Softening of stiffness of column B1 in specimen HCFS was not as substantial as specimen MCFS (see Figure 6-13), and the analytical model was able to capture such difference.

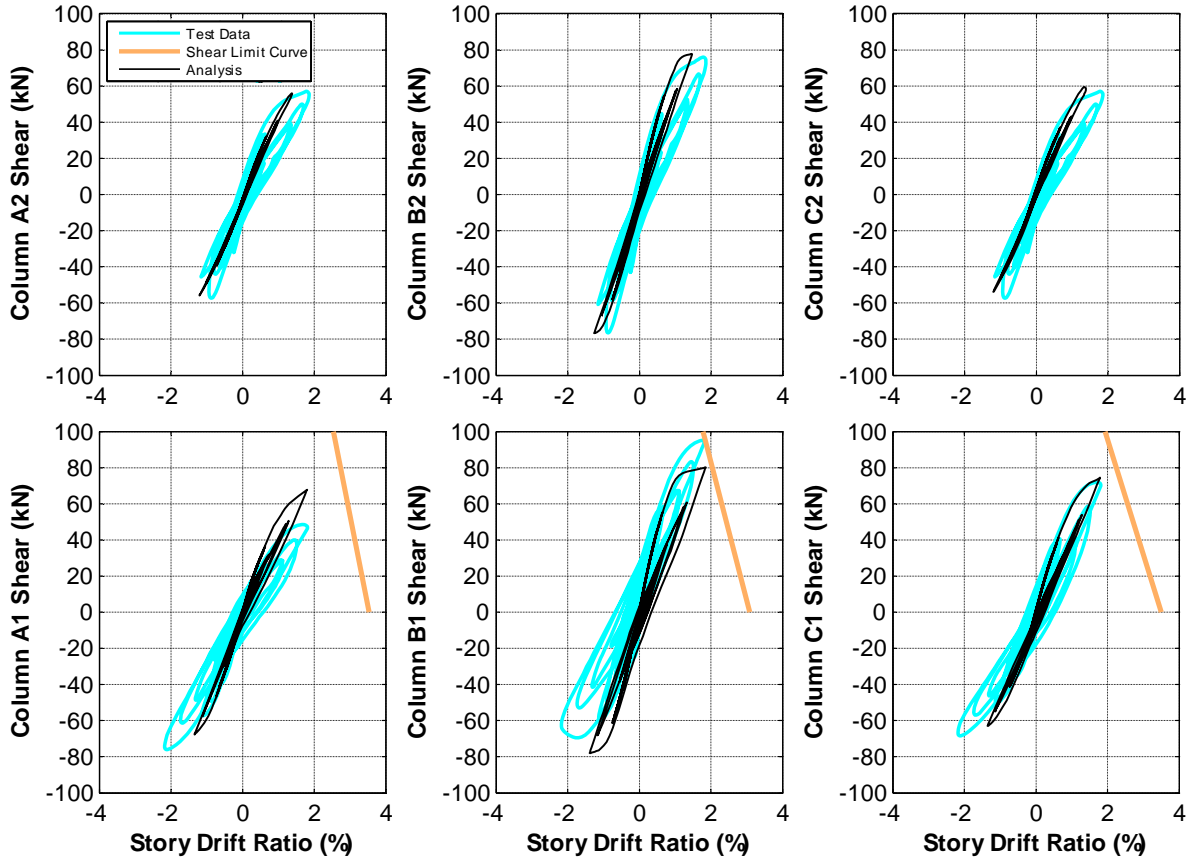


Figure 6-25. Shear hysteretic response of the columns (specimen HCFS, Test1)

Figure 6-26 and Figure 6-27 show a very good agreement between analysis and experiment for first-story columns axial loads. A divergence from the test data was observed only from 32.8 to 33.8 seconds. It is observed that the analytical model for specimen HCFS could capture the axial behaviour of the columns better than the model for specimen MCFS. This can be due to the influence of higher applied axial loads on the columns. Total axial load in the columns were generated by the applied load and the internal load due to overturning moment and the axial deformation of the columns resulted from lateral movement. The applied loads on the columns of specimen HCFS were almost twice those for specimen MCFS and according to Figure 6-28, the axial load due to overturning was about 7% higher for the exterior columns of specimen HCFS. Therefore, shortening and growth of the columns

resulted from later movement had lower impact on the total axial loads in the columns of this specimen.

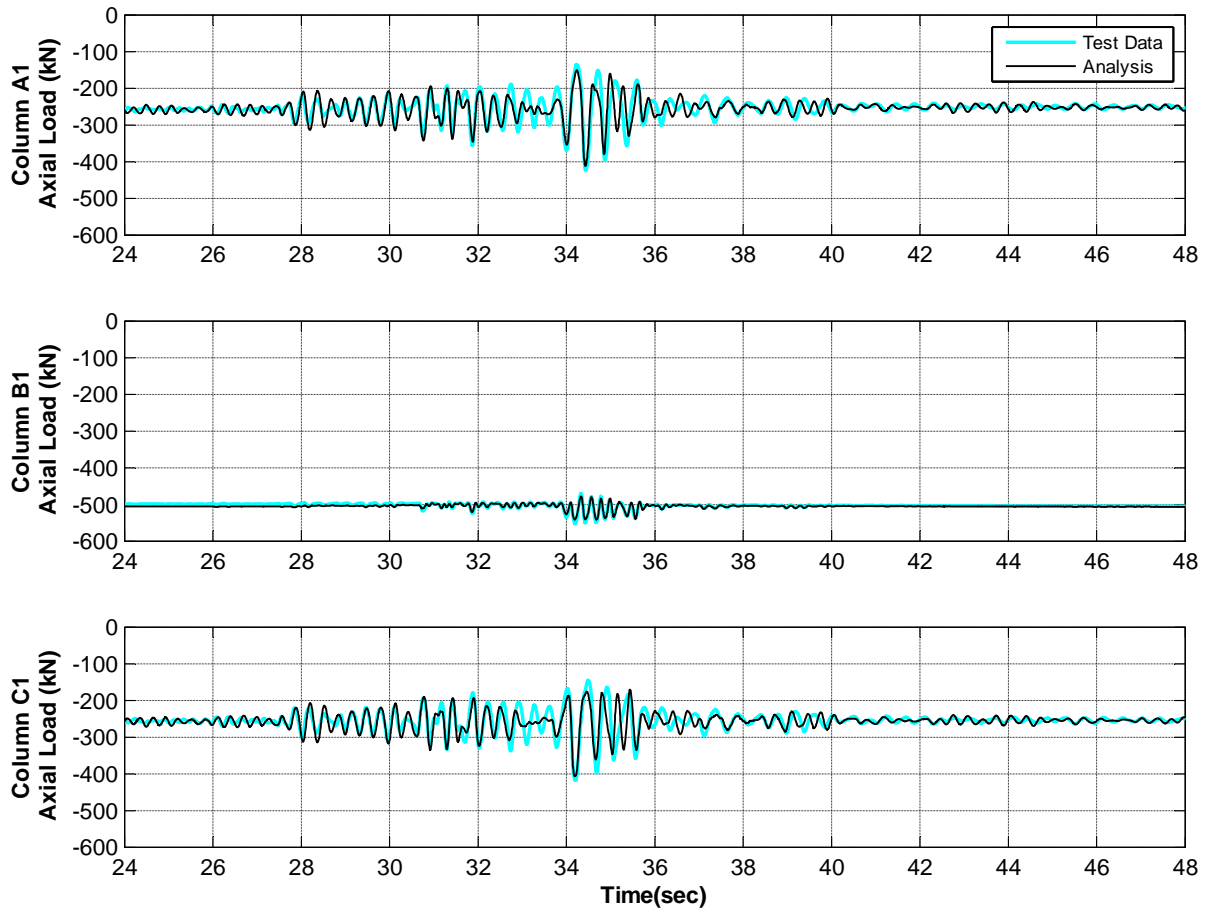


Figure 6-26. Axial load history response of first-story columns (specimen HCFS, Test1)

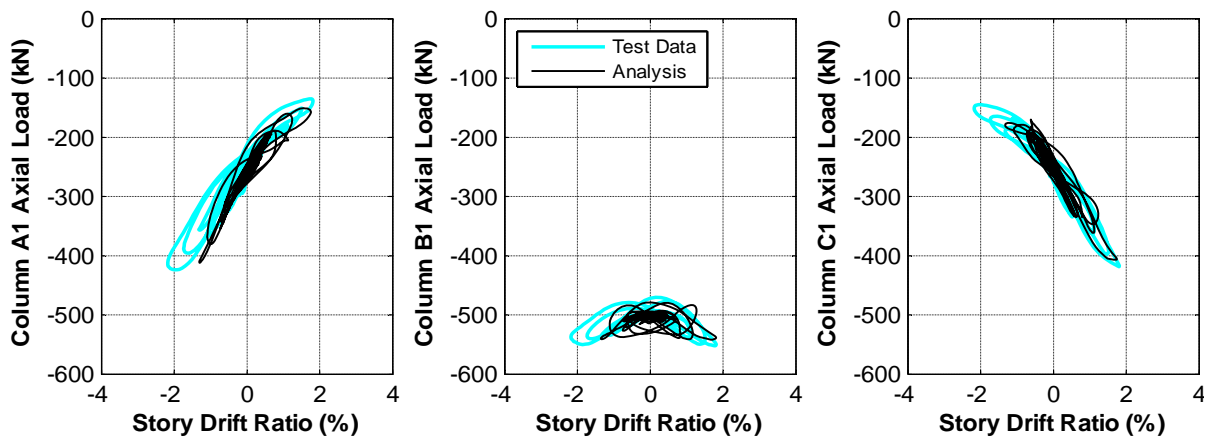


Figure 6-27. Axial load hysteretic response of first-story columns (specimen HCFS, Test1)

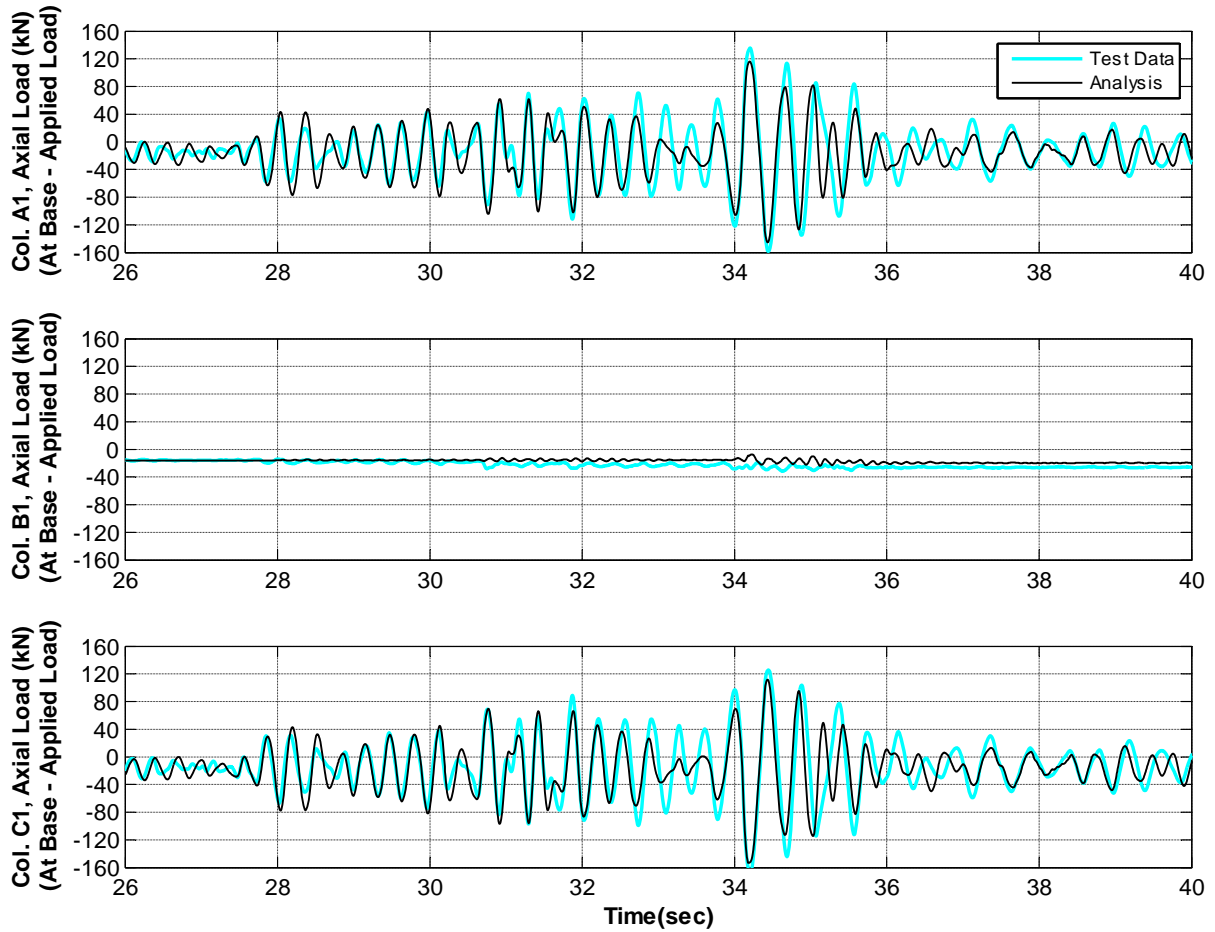


Figure 6-28. Variation of axial load on first-story columns due to overturning (specimen HCFS, Test1)

6.3.3.2 Comparison of Results for Test2

Results from analysis and recorded data from Test2 for representative response quantities are compared in Figure 6-29 through Figure 6-33. The limit curves used in simulating Test1 resulted in detecting failure of columns B1 and C1 in smaller drift ratios than those observed in the tests. As discussed in Chapter 2 (Section 2.3), the limit curves for shear and axial failures were defined based on the results from previous experimental tests. However, Elwood (2002) demonstrated that standard deviations of 0.9% and 0.5% should be considered for the shear and axial limit curves, respectively. Therefore, several analyses were carried out in this

study to obtain the best match with the test data by shifting the limit curves to larger drifts by 0.3% to 0.9%. The best agreement of the results was obtained where the limit curves were shifted by 0.8%. Figure 6-29 through Figure 6-33 demonstrate the results from such analysis.

Although the drift ratios were not captured as accurately as for Test1, still a good agreement between results is observed, particularly near the peak drift demands around 34 seconds. The model was also able to capture the concentration of drift demands in the first story for the large pulse at 34.2 seconds. This is the pulse that caused shear failure of columns B1 and C1, followed by axial failure of column B1. Comparison of shear responses (Figure 6-30 and Figure 6-31) demonstrates that the analytical model was able to estimate the maximum recorded shear relatively well. The peak base shear was under-estimated by only 2% percent, while the largest difference of 18% was observed in the results for column A1.

Shear hysteretic response of the columns are compared in Figure 6-31, illustrating that the analytical model estimated the stiffness of the columns very well. The onset of shear degradation was also adequately captured for columns B1 and C1. Similar to the experimental test data, results from the analytical model detected the failure of column B1 and C1 in shear, while no major shear degradation was recorded for column A1.

In contrast with the experimental test, the analytical model did not detect the total shear strength loss for column B1. Furthermore, the analytical model predicted a sharp degradation of shear strength for column C1 which was not observed during the test. Shear hysteretic response of second-story columns, predicted by the analytical model, were in relatively good agreement with the results from the shaking table test. As discussed in Section 4.5, column A2 failed due to excessive local deformation at the top after axial failure of column B1. Failure of column A2 occurred in a very low drift, which was mostly influenced by the column end

rotation. Since the analytical model used here was based on total column drift, it was not able to detect the failure of column A2 at such low drift ratio. Analytical models based on mechanics of the column element can capture the observed failure mode better than the model employed in this section. Development of such models should be considered in future work.

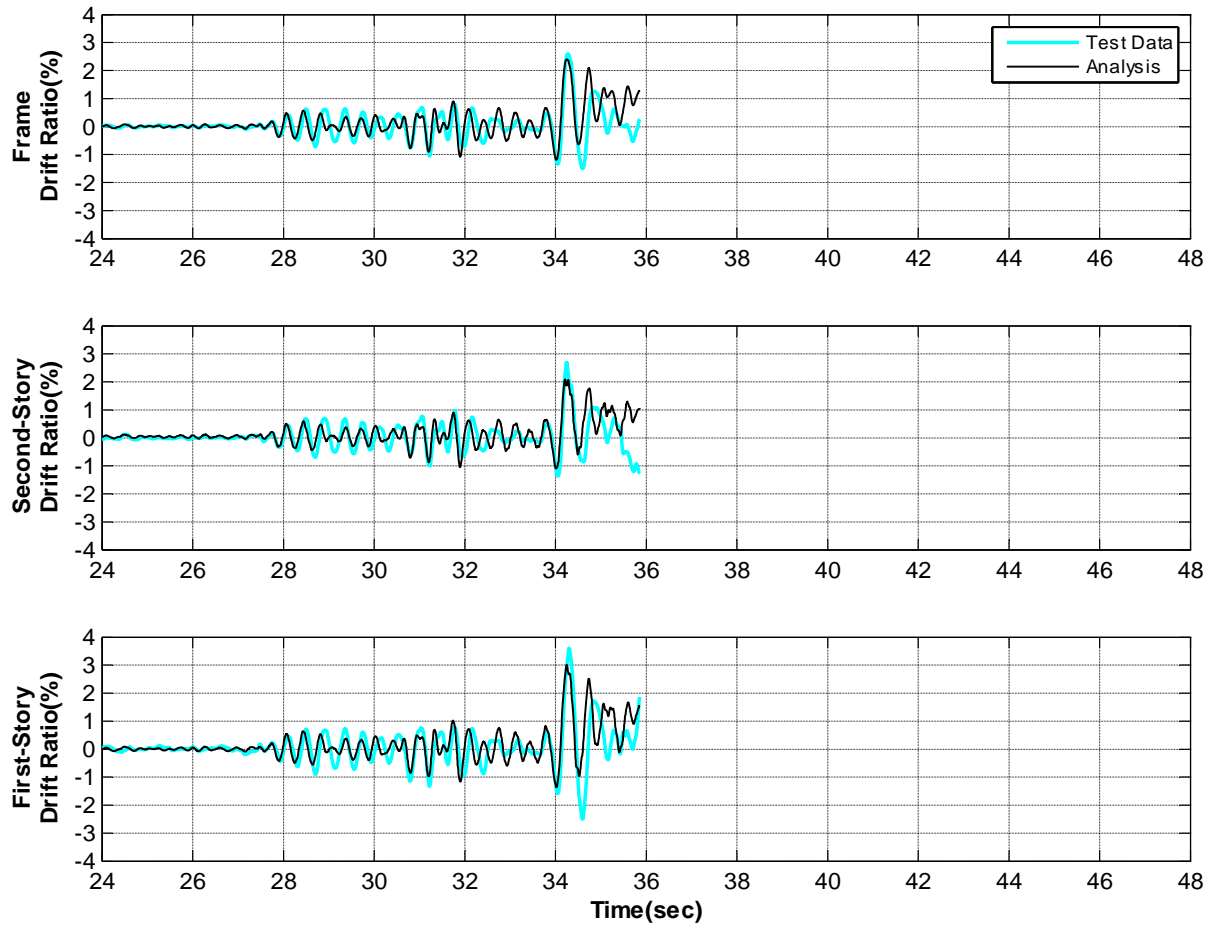


Figure 6-29. Story and frame drift ratio histories (specimen HCFS, Test2)

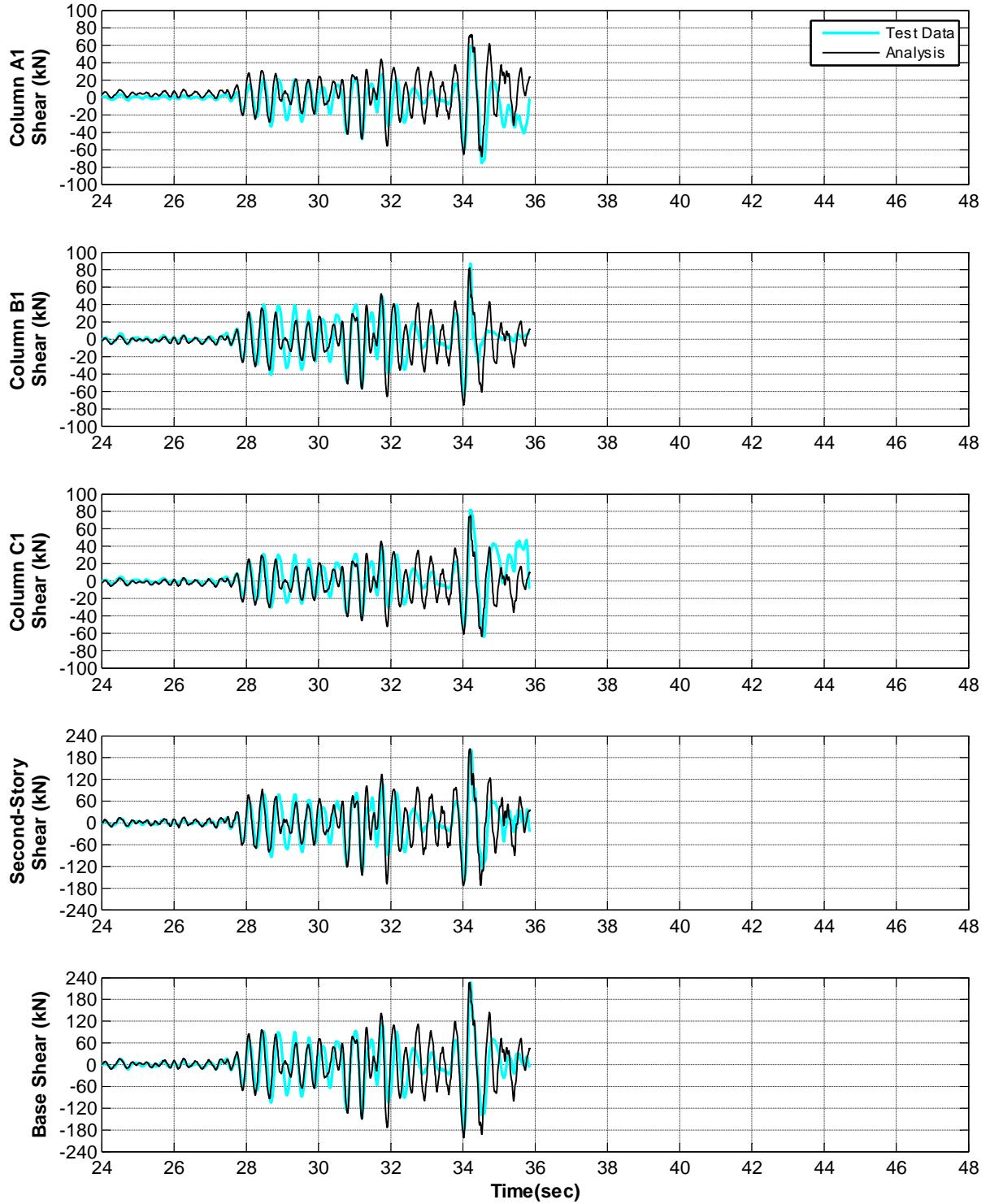


Figure 6-30. First-story columns and frame base shear histories (specimen HCFS, Test2)

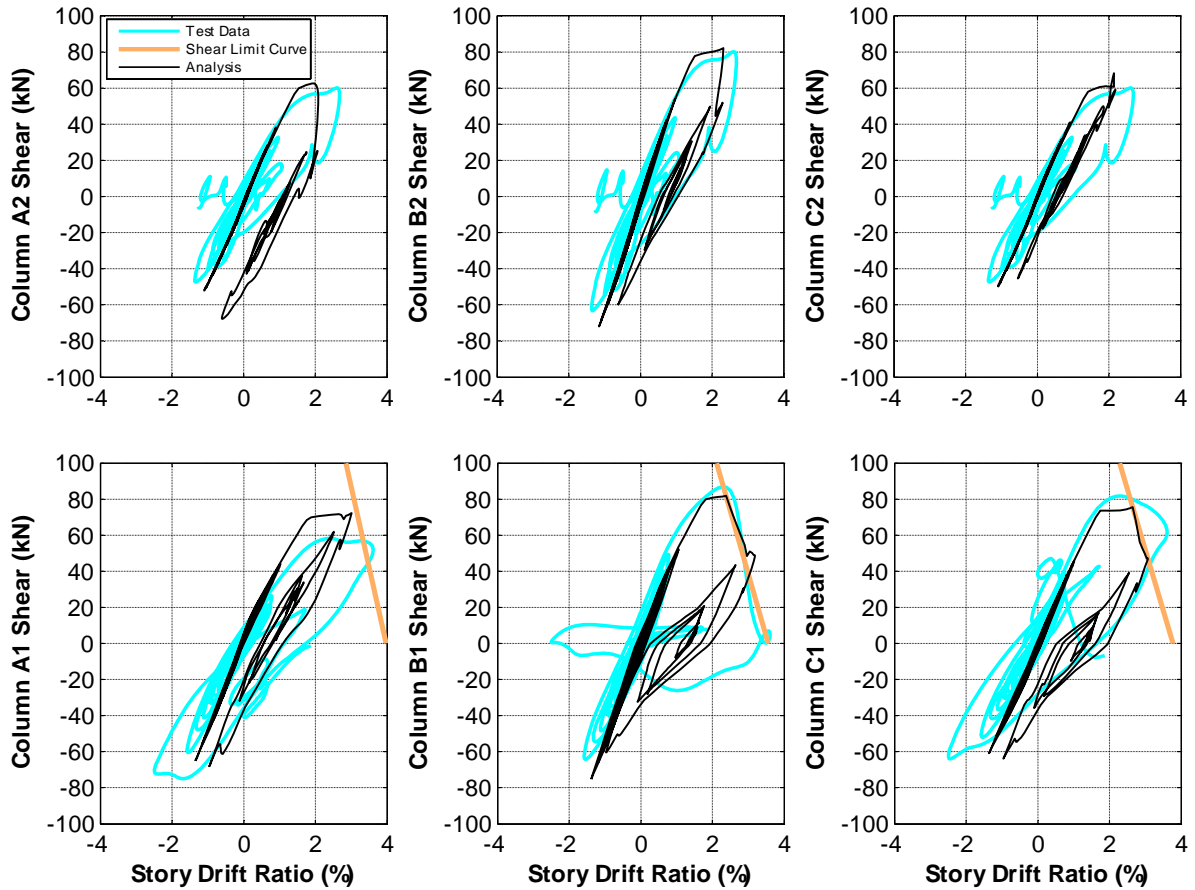


Figure 6-31. Shear hysteretic response of the columns (specimen HCFS, Test2)

Axial load history response of first-story columns is shown in Figure 6-32. It is observed that the model was able to simulate the rapid loss of axial load in the columns at the right time. Comparison of axial load hysteretic responses of the analytical and experimental models (Figure 6-33) shows that the onset of axial failure was captured at a smaller axial load but equal drift ratio for column B1. Employing the axial limit curve model described in Chapter 2, the analysis results suggested that the axial failure of column B1 started at a drift ratio of 2.6% and axial load of 537 kN. The test data shows that the rapid loss of the column axial capacity was also commenced at 2.6% drift but with axial load of 577 kN.

Onset of axial failure for column C1 was not as obvious as column B1. Axial failure of column C1 occurred in a very small drift ratio (0.33%) due to load redistribution from columns A and B, leading to collapse of the frame (see Section 4.5). As discussed in Chapter 2, the axial limit curve model was not intended to be used for the drift ratios lower than 1%. Therefore, the model was not able to capture the actual drift ratio for axial failure of column C1. According to the analysis results, column C1 experienced maximum axial load of 443 kN at a drift ratio of 2.9%, at which point axial failure was initiated as the response hit the axial limit curve. The same peak axial load, but at a drift ratio of 2.5%, was recorded during the shaking table test. While analytical model detected the axial failure of column C1 at 2.9% drift ratio, Figure 6-32 demonstrates that the column was able to maintain the axial load until time 35.76 seconds of the test when failure of columns A and B forced the collapse of column C1. This suggests that the detection of axial failure of column C1 by the analytical model at 2.9% drift ratio (34.22 sec) was not accurate. As mentioned in Chapter 5 (see Section 5.5.6), the analytical model for columns with high axial load becomes very sensitive to the drift ratios at onset of shear and axial failure. Furthermore, it was discovered in Section 5.6 that the story drift ratio may not be a good measurement of demand on a column and can be replaced by chord rotation of the column. Figure 6-33 demonstrates the validity of such arguments for column C1. Future research should revise the limit curve model using column plastic hinge or chord rotation demands instead of story drift ratio.

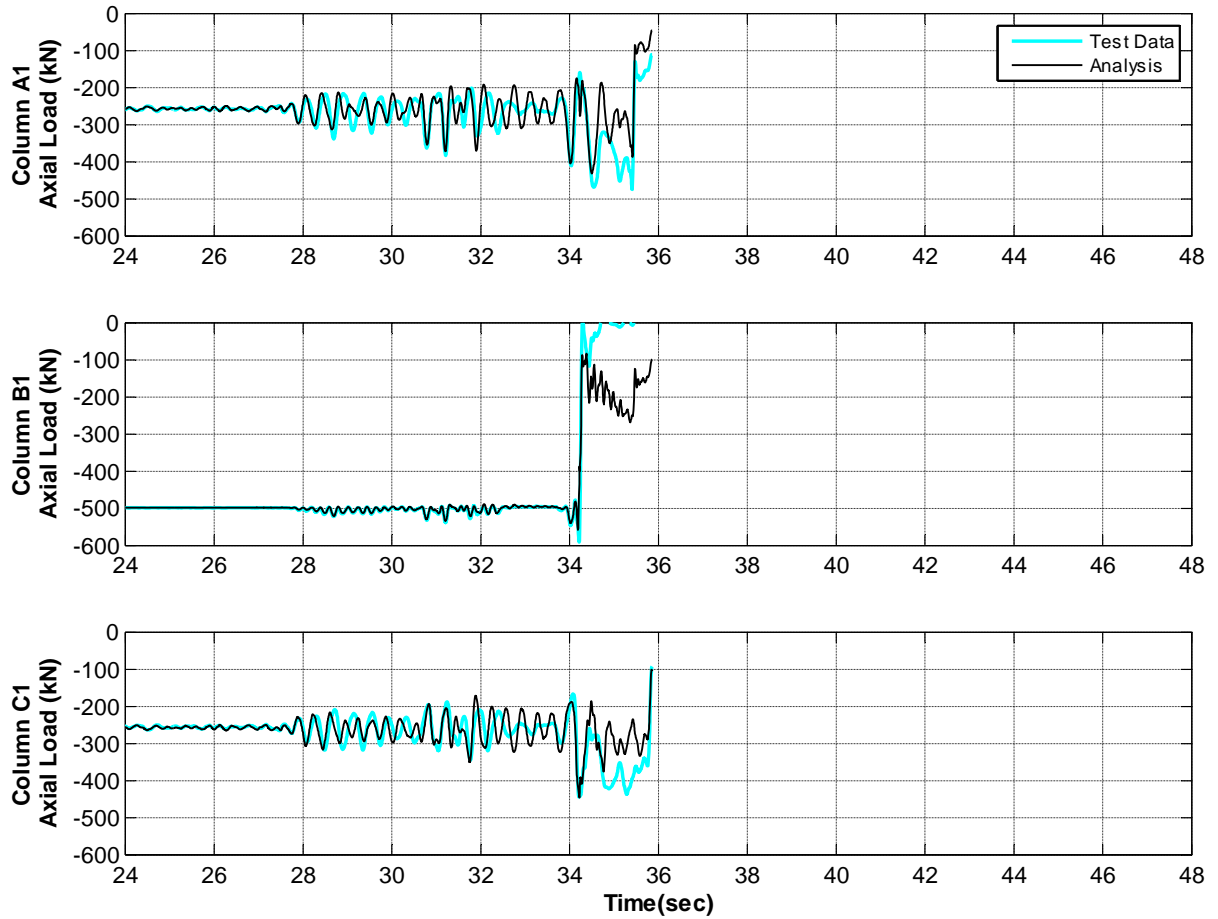


Figure 6-32. Axial load history response of first-story columns (specimen HCFS, Test2)

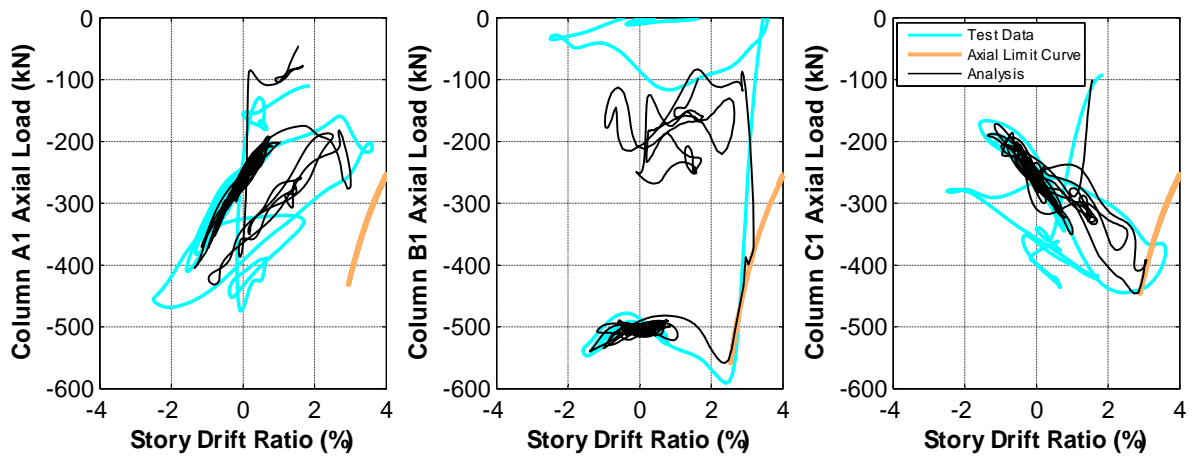


Figure 6-33. Axial load hysteretic response of first-story columns (specimen HCFS, Test2)

6.3.4 Analytical Model of Specimen MUF

As discussed in Chapters 3 and 4, column reinforcement for specimen MUF was designed such that the failure would be initiated in the joints while the columns remain ductile during the test. Such behaviour was simulated in the analytical model by removing the shear and axial springs in the zero-length elements, while the effect of column confinement was considered by adjusting the material properties for concrete fibres in the column core. To account for the flexibility due to the joint deformations, the rigid joint elements used in analytical model for specimen MCFS and HCFS were replaced by rotational springs using zero-length elements at connecting nodes of beams and columns. The properties of the springs were based on the scissors model (Alath and Kunnath, 1995) described in Section 6.2.2, where the shear stress-strain behaviour of the joint was changed to a moment-rotation relationship using the geometry of the joint panel and connected beam and columns (Equations 6.4 and 6.5).

The initial natural period of the analytical model was obtained as 0.28 seconds which is relatively close to the natural period obtained from the White-Noise test (see Section 4.3). Figure 6-34 through Figure 6-43 plot story and frame drift ratios, frame base shear, column shear, hysteresis of the columns, and axial load history records and hysteretic response of first-story columns, for Test1 and Test2.

6.3.4.1 Comparison of Results for Test1

Figure 6-34 compares the drift ratios from the experimental test and the analysis and shows the excellent capturing of drift ratios by the analytical model. Although the model slightly underestimated the amplitudes in some cycles, it was able to adequately detect the drift

ratios during most of the test. It is observed that the peak drift ratio in first story was underestimated by only 2%, while the frame peak drift was captured with a difference of 9%.

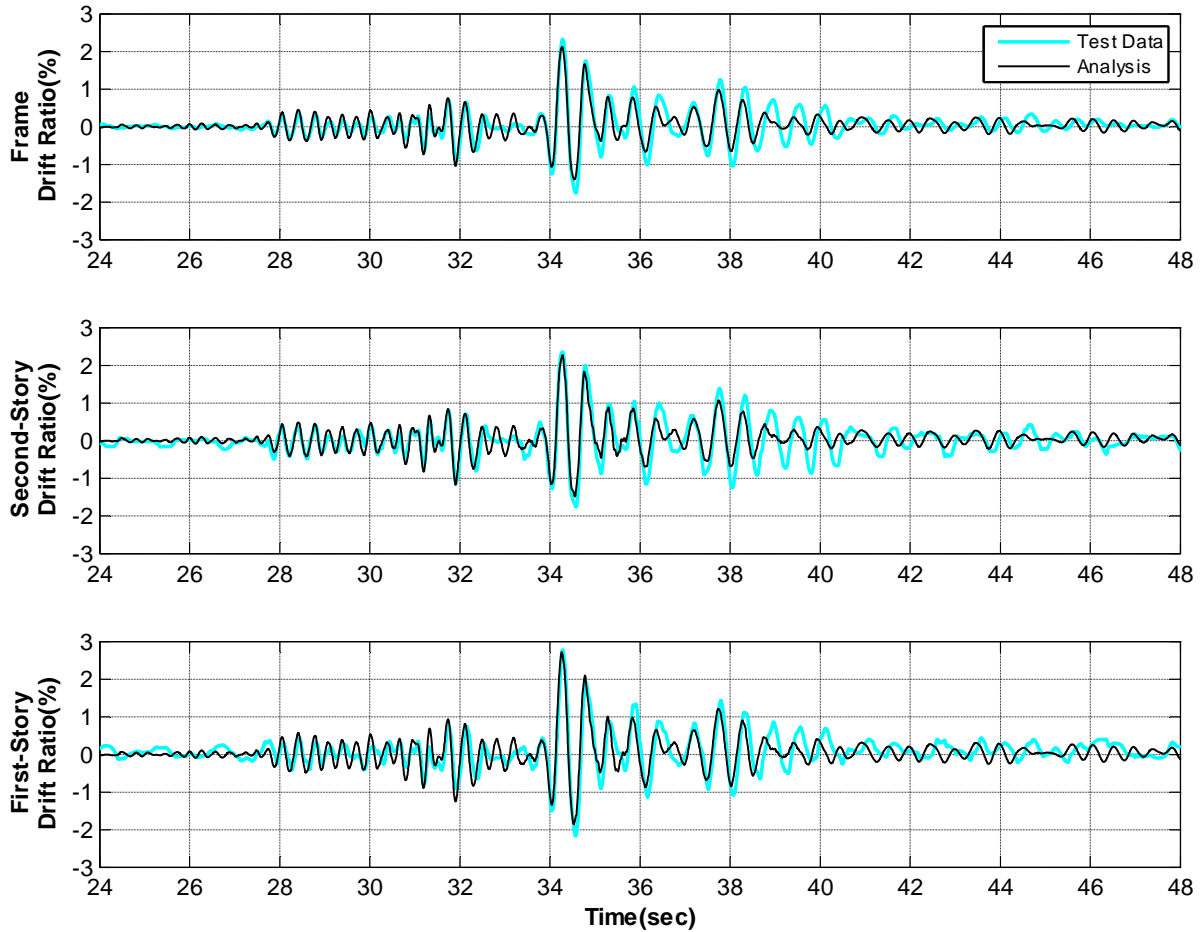


Figure 6-34. Story and frame drift ratio histories (specimen MUF, Test1)

Figure 6-35 compares shear response histories from the test and analysis for first-story columns, second story, and the frame base shear, showing a good agreement between analytical and experimental results. However, it is observed that for the time interval between 32.8 and 33.8 seconds, amplitudes were over-predicted. Maximum underestimation of 19 kN (12%) was observed for column B1 shear at 34.23 seconds.

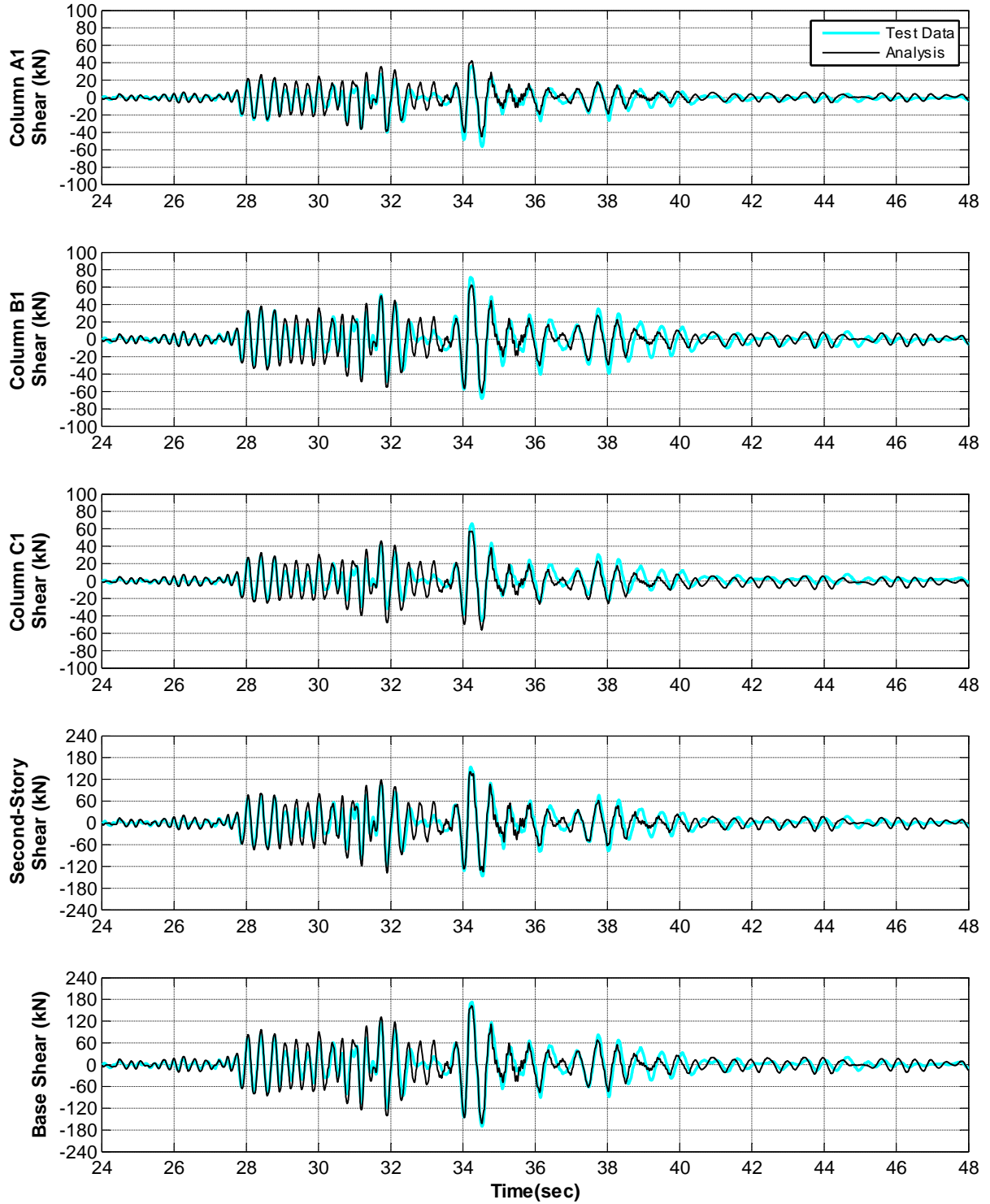


Figure 6-35. First-story columns and frame base shear histories (specimen MUF, Test1)

As discussed in Section 6.2.2, joint shear deformations were simulated by rotational springs at the joint panel zone (scissors model) and were accounted for in the story drift ratios.

In the first attempt to simulate the behaviour of the specimen, it was observed that the analytical model over-estimated the maximum shear strength of column A1 by about 40%. On the other hand, maximum shear strength was underestimated for columns B1 and C1. As discussed in Section 4.6, the bend in the beam bars was not in the right location in joint A1 and the joint yielded earlier, which limited developing shear in column A1 in the positive direction and forced the other columns to resist the shear demand. In contrast, the implemented joint model was the same for the exterior first-story joints and therefore, such early yielding at the panel zone of joint A1 could not be detected and shear in column A1 was estimated close to shear in column C1. It should be noted that the joints were modeled as lumped hinges and consequently, influence of tension and compression from overturning on the joint strength could not be captured. In a further attempt, the properties of the rotational hinge at joint A1 were altered by lowering the $M-\theta$ backbone for the rotational spring by 40%, which resulted in better compatibility of the maximum shear strength of the column with the test data. Such refinement also led to much better estimation of shear redistribution in first-story columns of the analytical model. Figure 6-36 compares the shear hysteretic response of the columns from the refined model with the test data. Excellent agreement between analysis and experiment was obtained for first- and second-story lateral stiffnesses. The analytical model adequately represented both the initial stiffness as well as softening which occurred later in the test. Figure 6-36 also demonstrates that the pinching in shear hysteretic response of the columns was reasonably well-captured by the analytical model.

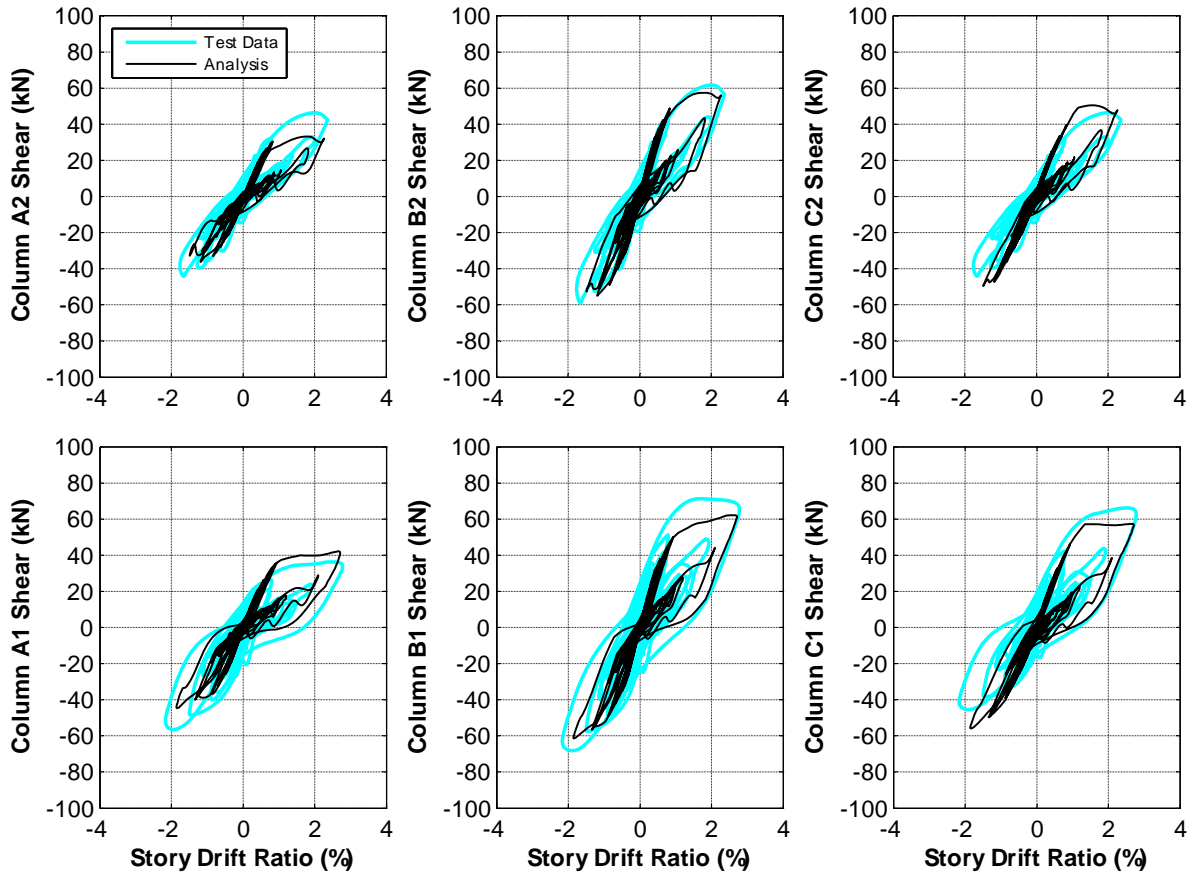


Figure 6-36. Shear hysteretic response of the columns (specimen MUF, Test1)

Figure 6-37 compares the axial load history response from the analysis and the test data for first-story columns, while Figure 6-38 compares the axial load hysteretic response from the analytical model and recorded data from the test. Despite the good agreement of the results until 32 seconds, the analytical model could not capture the decrease in axial load of column B1 that was recorded during the test. Although, the model detected the axial load in the exterior columns reasonably well, some of the peaks were under-estimated, particularly after 34 seconds.

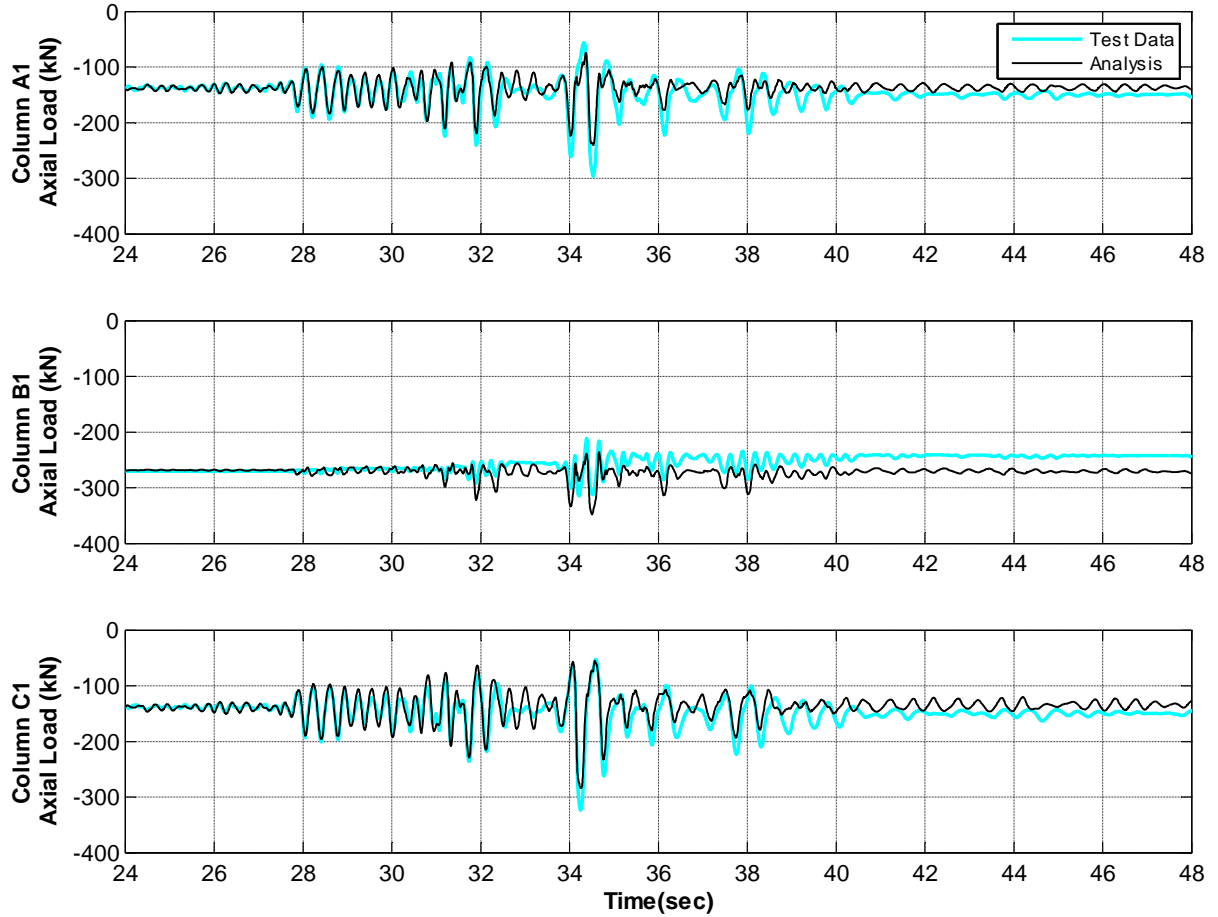


Figure 6-37. Axial load history response of first-story columns (specimen MUF, Test1)

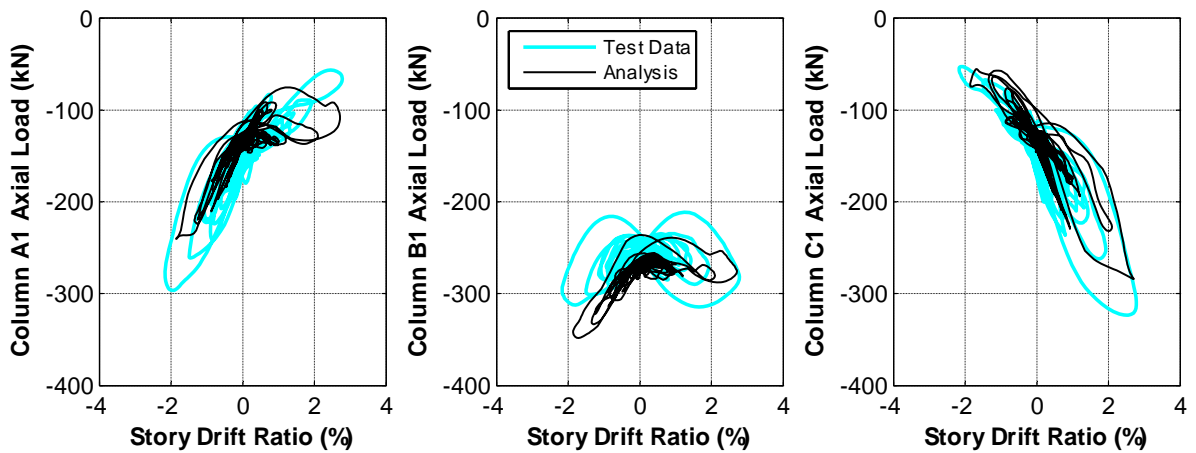


Figure 6-38. Axial load hysteretic response of first-story columns (specimen MUF, Test1)

6.3.4.2 Comparison of Results for Test2

Figure 6-39 through Figure 6-43 compare the results from analytical and experimental models for Test2. The refined analytical model described in previous section was also used to simulate the behaviour of the element during Test2. Figure 6-39 demonstrates that the analytical model captured the amplitudes and phasing very well. Similar observations were obtained by comparing the shear responses (Figure 6-40 and Figure 6-41). While the analytical model over-estimated the frame peak drift ratio by 5%, the peak shear for column B1 was under-estimated by 12%. As discussed in previous section, joint A1 failed in shear earlier than the other joints due to improper position of bend bar from the connecting beam and by accommodating most of the lateral deformation, did not allow shear to be properly developed in column A1, and therefore, shear was redistributed to columns B1 and C1. Such redistribution was also observed for Test2 and captured by the model (Figure 6-41).

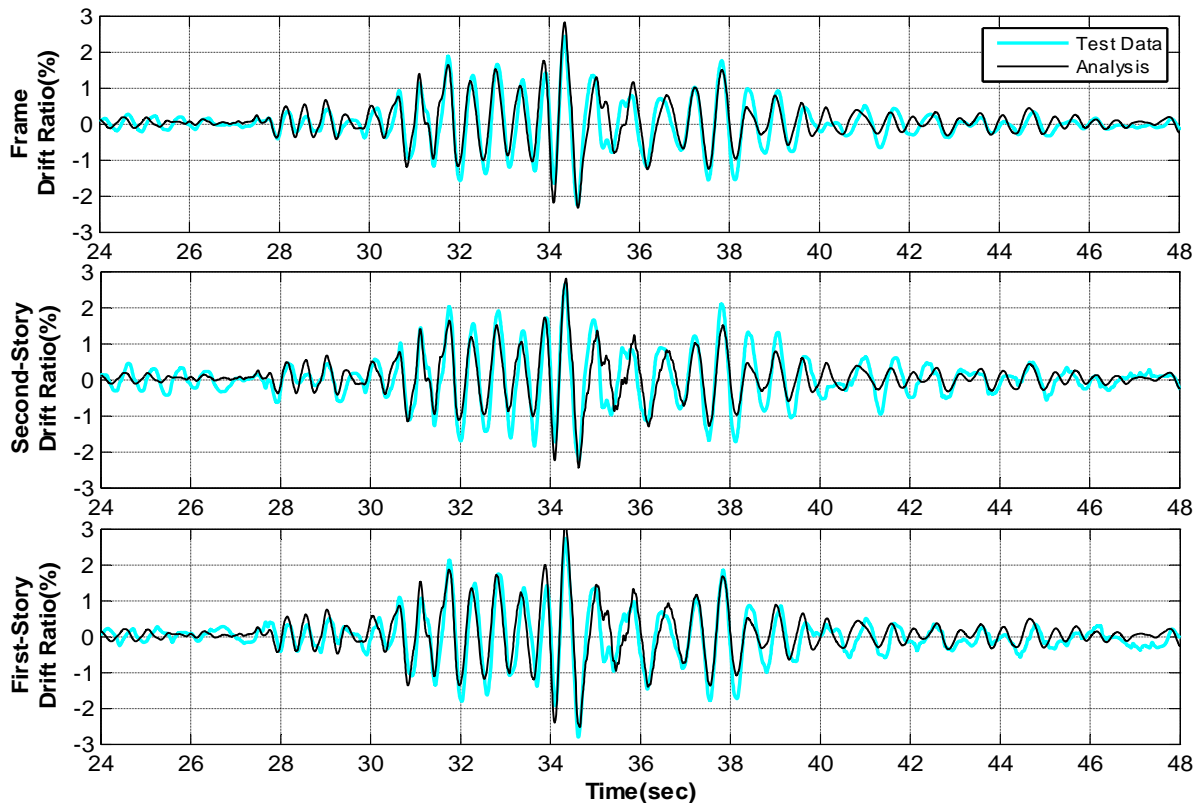


Figure 6-39. Story and frame drift ratio histories (specimen MUF, Test2)

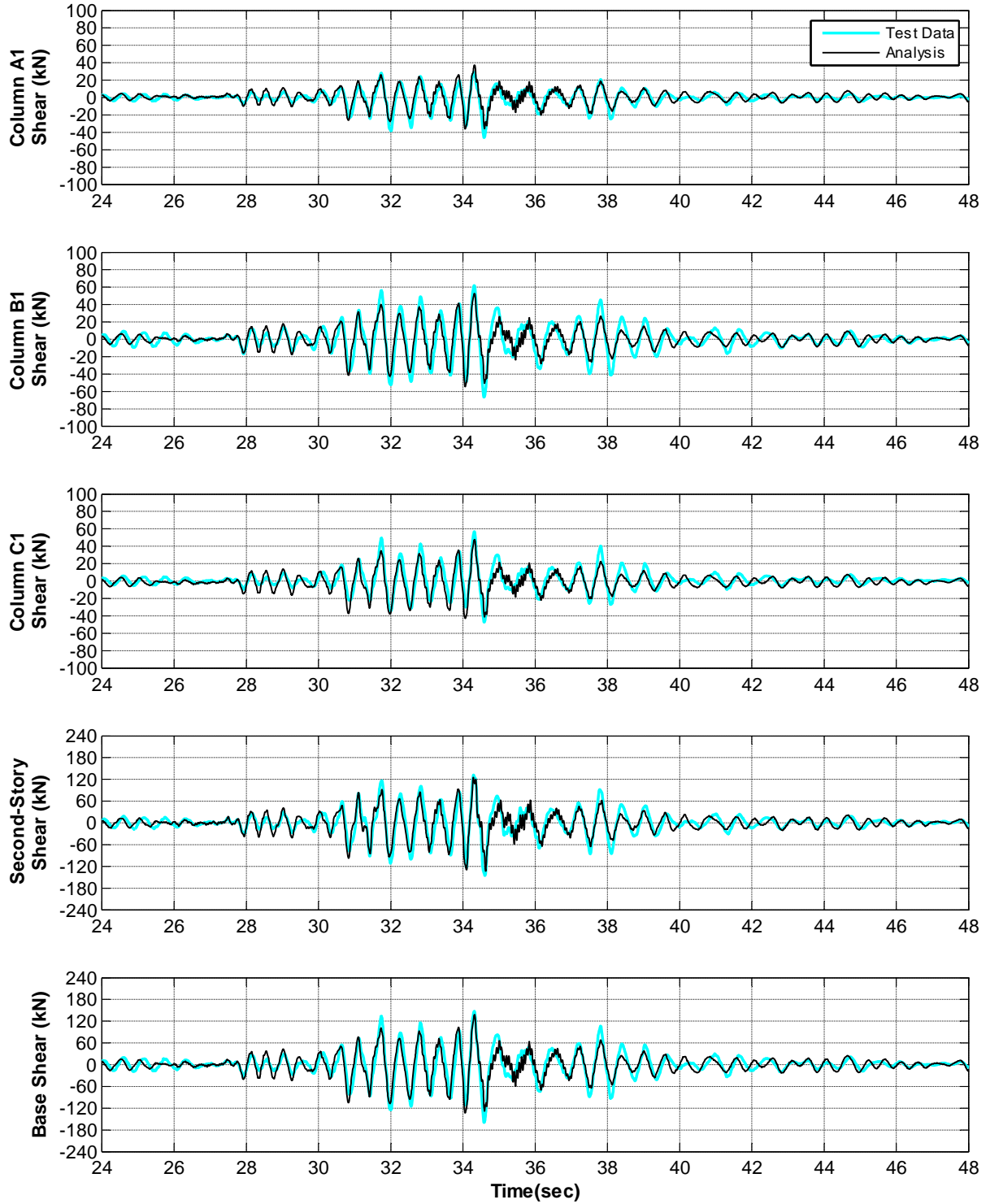


Figure 6-40. First-story columns and frame base shear histories (specimen MUF, Test2)

Figure 6-41 illustrates that the shear hysteretic response of the columns and the stiffnesses of the columns were adequately captured by the analytical model. However, it is observed that the stiffness of columns B1, C1, and A2 were smaller than those observed during the shaking table test.

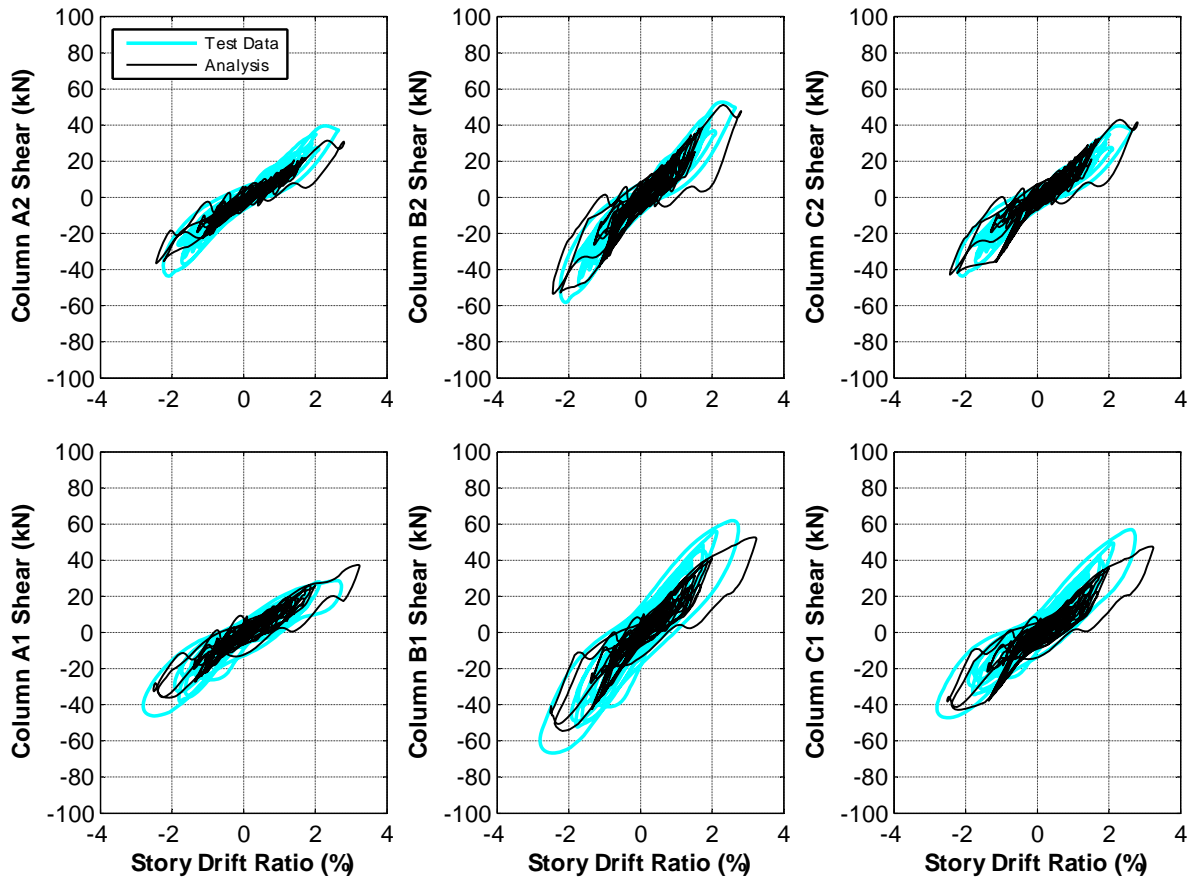


Figure 6-41. Shear hysteretic response of the columns (specimen MUF, Test2)

Comparison of the axial load responses from the analytical and experimental models in Figure 6-42 and Figure 6-43 shows that despite the underestimation of the peaks, the model was able to capture the axial behaviour of the columns reasonably well. The largest difference between the peak axial load from the experimental test and the analysis was observed for column A1 at time 34.6 seconds, where the axial load was under-estimated by 18%.

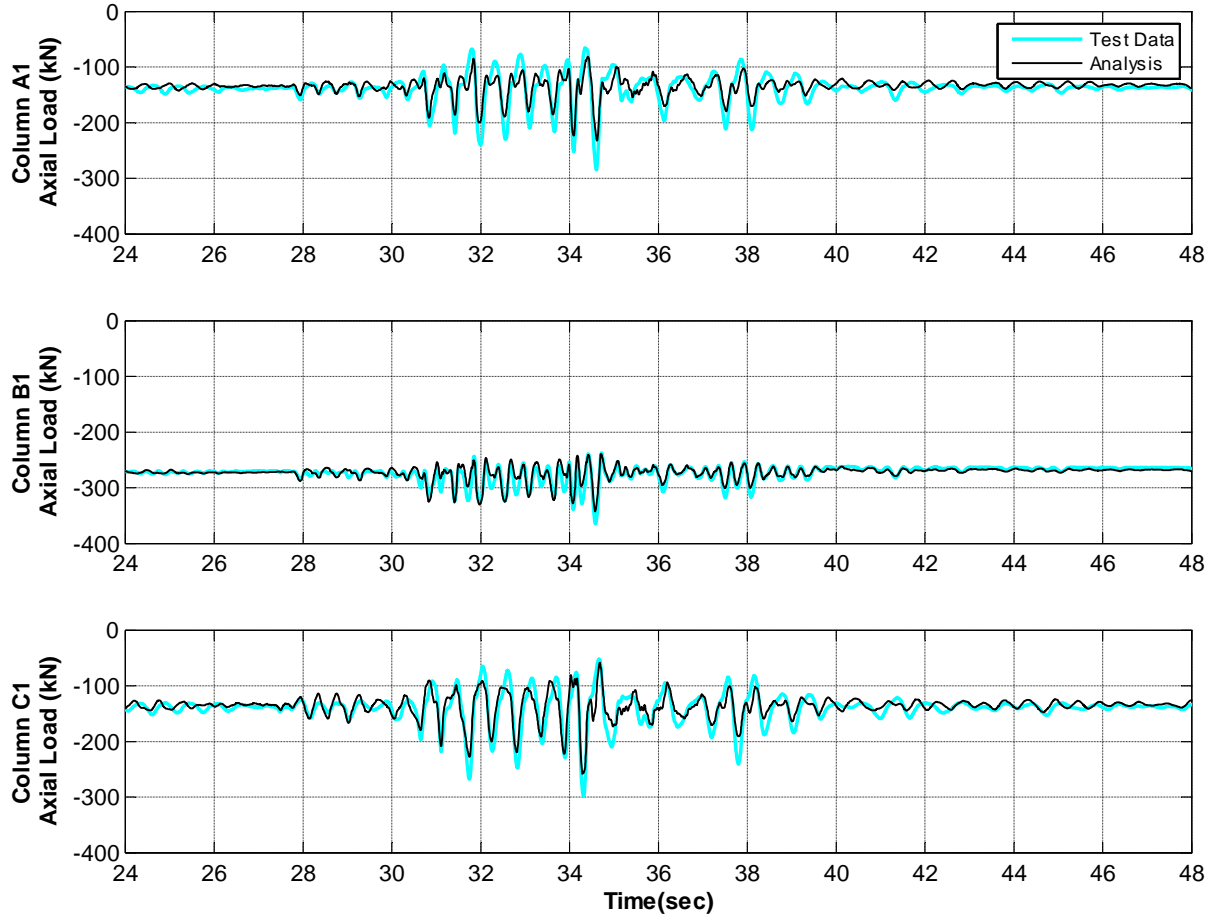


Figure 6-42. Axial load history response of first-story columns (specimen MUF, Test2)

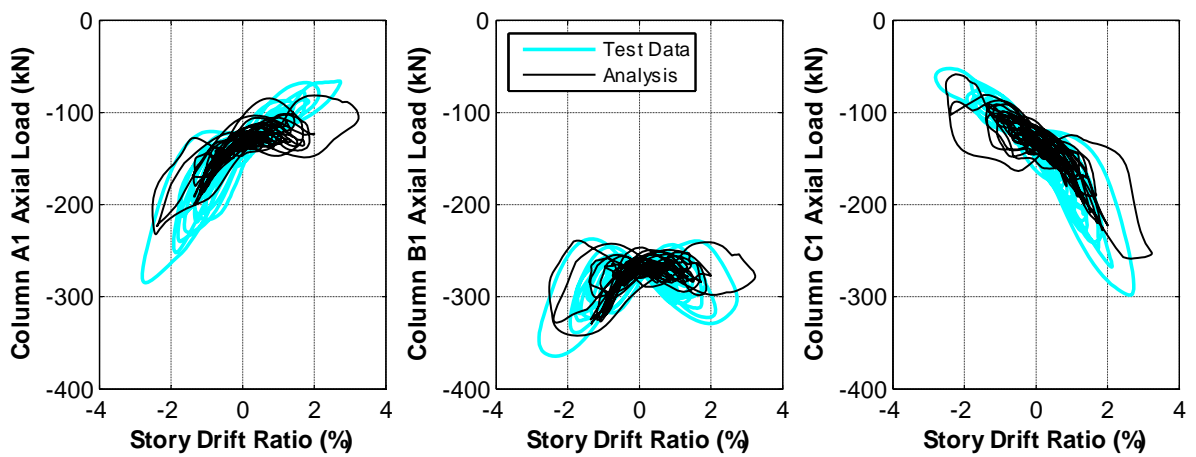


Figure 6-43. Axial load hysteretic response of first-story columns (specimen MUF, Test2)

6.3.5 Analytical Model of Specimen MUFS

The analytical model for specimen MUFS was a combination of the model for specimen MCFS and MUF. While the axial and shear springs were considered for the columns in the zero-length elements, the rotational springs were also included at the beam-column joints. Due to light transverse reinforcement of the columns and in contrast with the analytical model for specimen MUF, concrete confinement for the columns in the model for specimen MUFS was not considered. The initial natural period of the analytical model was obtained as 0.28 seconds which is very similar to the natural period obtained from the White-Noise test (see Section 4.3). Comparing the results from the analytical model with the experimental test data, Figure 6-44 through Figure 6-52 plot the story and frame drift ratios, base shear and columns shear, shear hysteretic behaviour of the columns, and first-story columns axial load history records and hysteresis for Test1 and Test2.

6.3.5.1 Comparison of Results for Test1

Figure 6-44 compares the drift ratios from the experimental test and the analysis. It is observed that despite the slight underestimation of drift in some cycles, the analytical model adequately captured the drift ratio amplitudes and phasing throughout the test.

Figure 6-45 compares shear response histories from the test and analysis for first-story columns, second story, and the frame base shear. Satisfactory agreement between test data and analysis results is observed for the base shear and second-story shear. However, overshooting of shear demand is seen for the time interval between 32.8 and 33.8 seconds. It is observed that while shear in the exterior first-story columns were adequately estimated by the analytical model, a maximum deviation of 32% from the test result was observed for column B1 at 34.5

seconds. It is also observed that the analytical model could not capture the residual shear in the columns after 39 seconds.

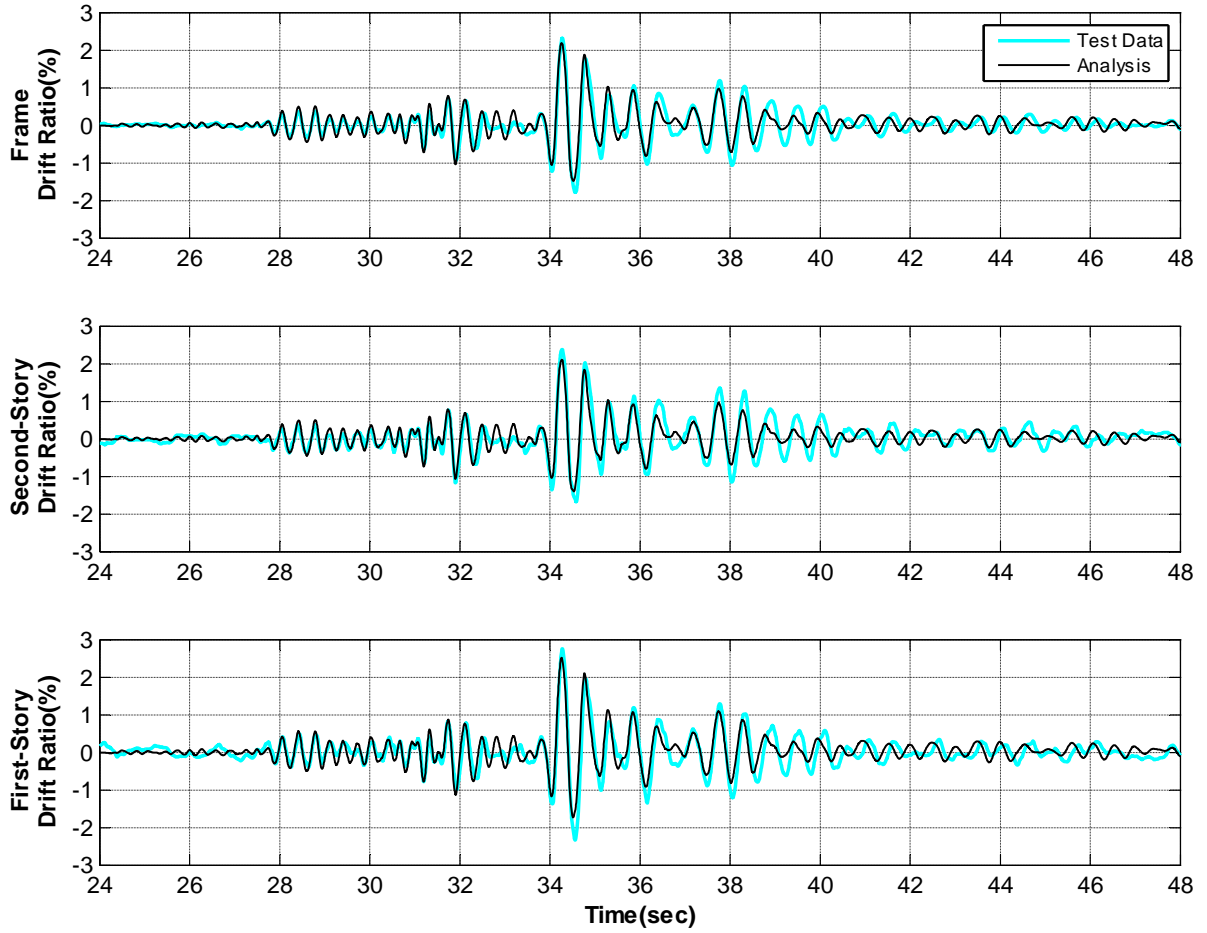


Figure 6-44. Story and frame drift ratio histories (specimen MUFS, Test1)

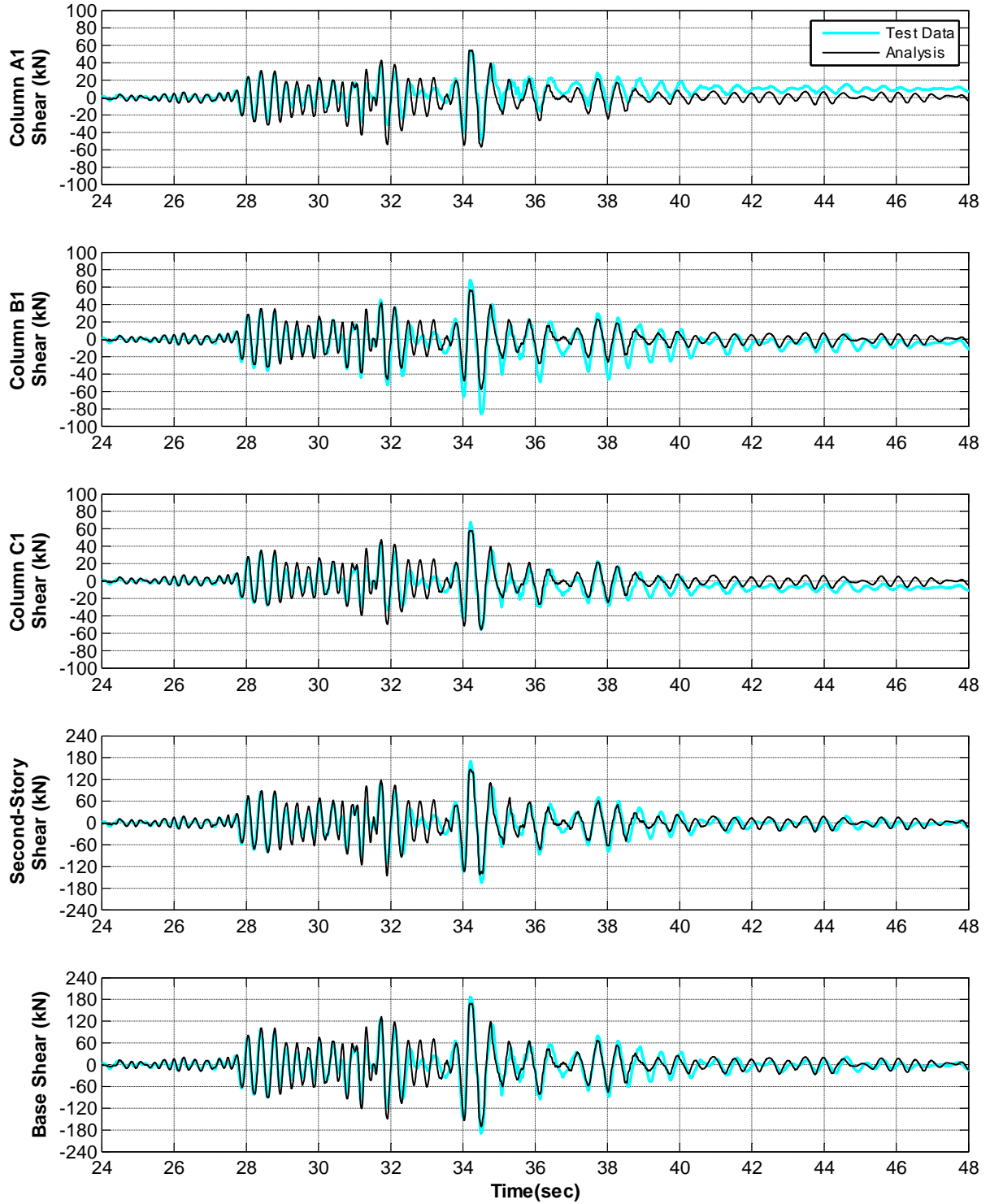


Figure 6-45. First-story columns and frame base shear histories (specimen MUFS, Test1)

Figure 6-46 demonstrates the good agreement between analysis and experiment for the first-story and second-story lateral stiffness. The analytical model adequately represented both the initial stiffness as well as softening for higher amplitude loading. Similar to the results for specimen MUF, it is observed that the pinching of the hysteresis was also well-captured for specimen MUFS. However, as discussed for Figure 6-45, the peak shear for column B1 was noticeably underestimated in the negative direction. It was demonstrated in Section 4.7 that the exterior first-story joints, particularly joint A1, were damaged more than joint B1. Consequently, in the negative direction, where overturning would typically result in higher demands on joint and column A1, shear must be redistributed to column B1 due to the prior failure of joint A1. However, such redistribution could not be simulated by the analytical model, because the joints behaviour was modeled by lumped rotational springs and could not capture the effect of tension and compression. Figure 6-46 also shows that the analytical model was not able to detect the modest shear degradation observed in the test data. It is not clear if the degradation is due to shear damage in the joints or the columns.

Figure 6-47 and Figure 6-48 show that despite the match of axial load phasing throughout the test, the analytical model was not able to capture the axial load amplitudes very well. This is particularly seen for column B1 where the captured axial load started to diverge from the test results after 31 seconds.

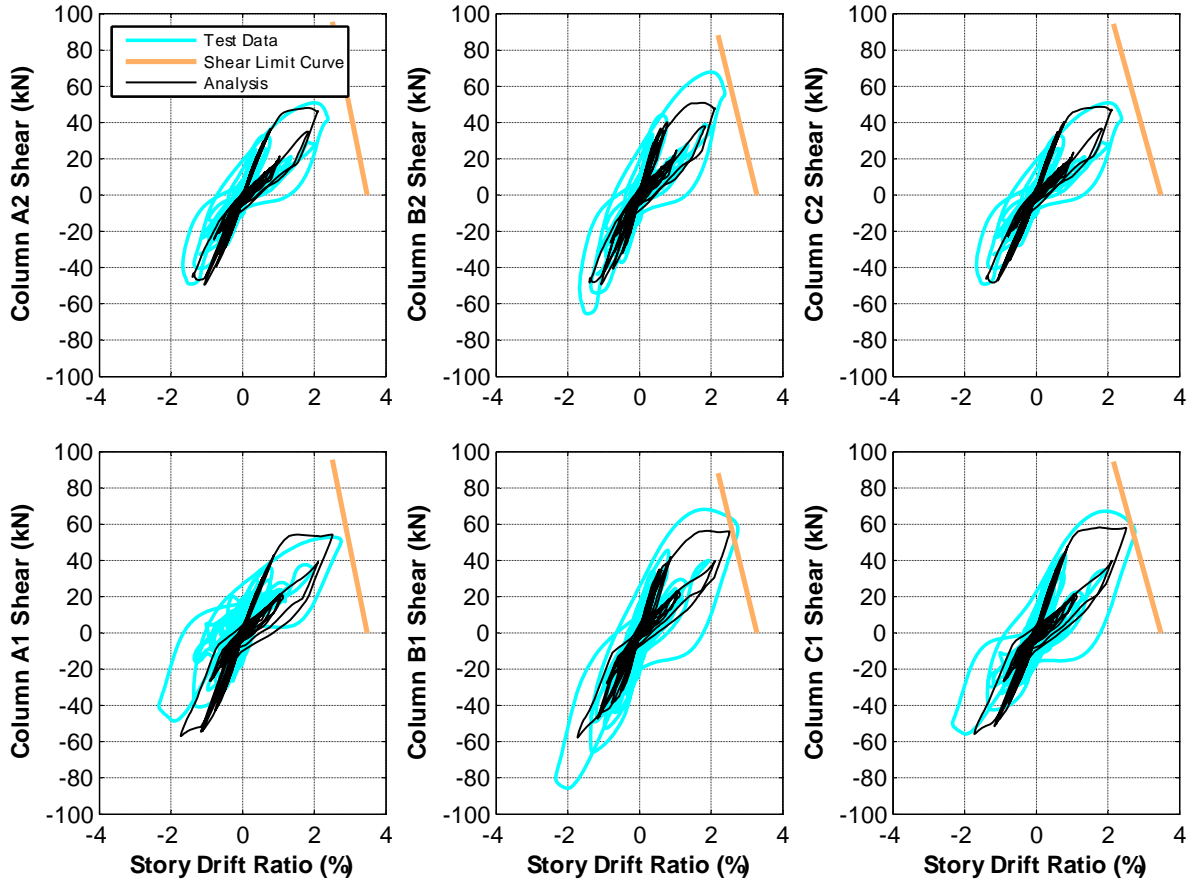


Figure 6-46. Shear hysteretic response of the columns (specimen MUFS, Test1)

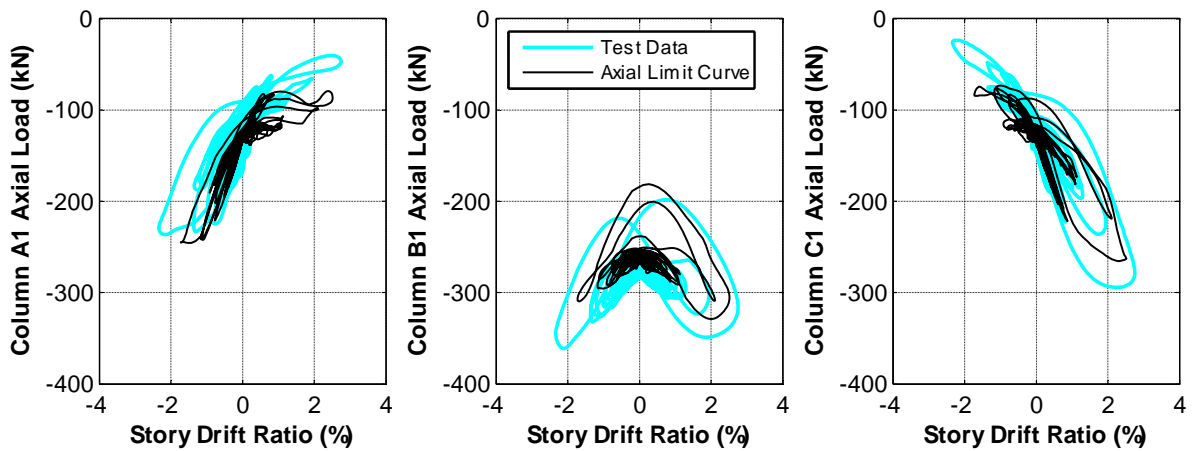


Figure 6-47. Axial load hysteretic response of first-story columns (specimen MUFS, Test1)

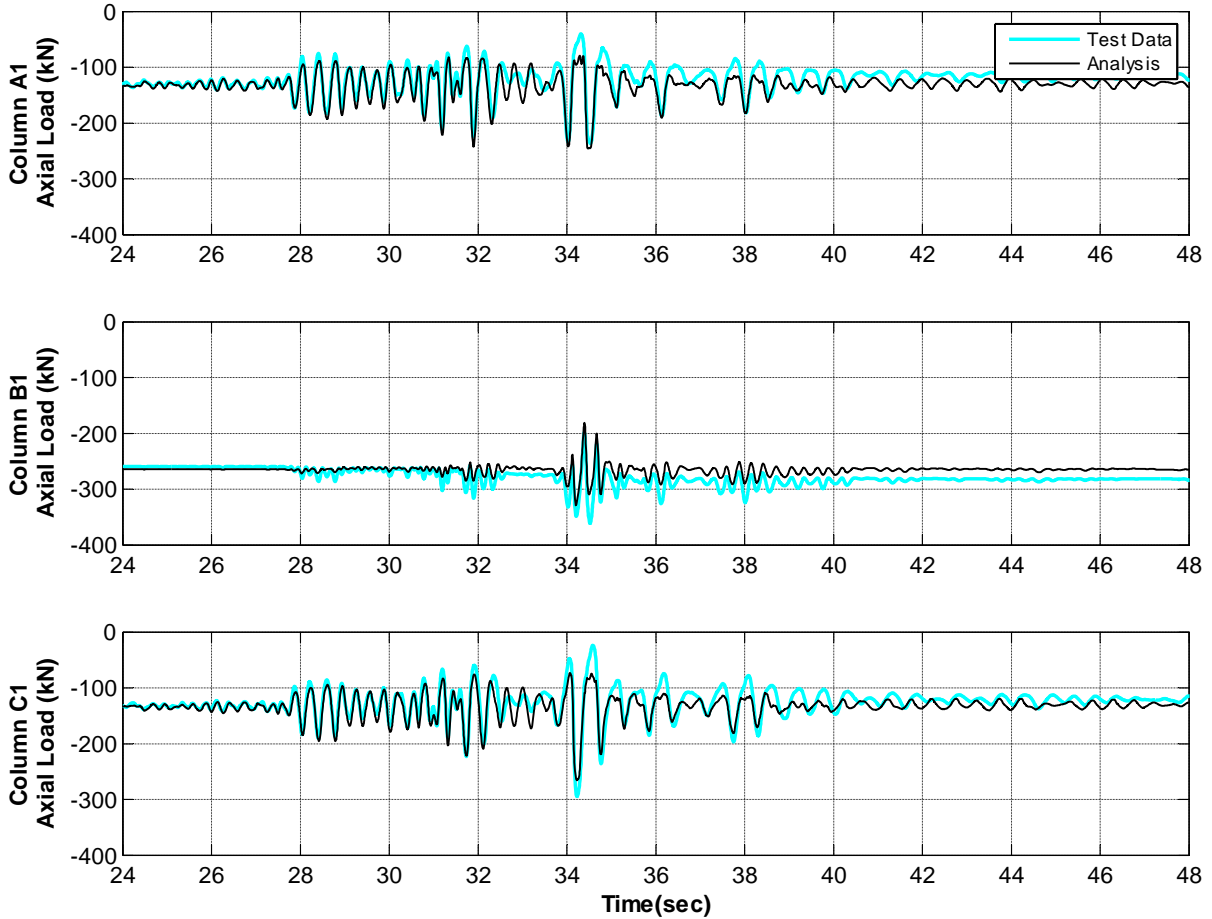


Figure 6-48. Axial load history response of first-story columns (specimen MUFS, Test1)

6.3.5.2 Comparison of Results for Test2

Figure 6-49 through Figure 6-52 compare analytical and experimental model results for representative response quantities. As discussed in Chapter 4, specimen MUFS experienced collapse due to failure of second-story columns. It was explained in Section 4.7 that the undamaged top portion of first-story joints restrained by the 70 mm slab provided a partially-fixed condition for the base of second-story columns while, the rigid and well-confined joints at second-story level provided a nearly fixed-end condition at the top of the columns in the second floor. In contrast, damage to first-story joints, below the slabs, and propagation of

cracks into the top end of first-story columns reduced the end-moment at the top of these columns. Consequently, first-story columns responded in nearly single curvature, while double-curvature response and higher local deformations at the ends of second-story columns resulted in failure of columns B2 and C2. The predictive shear and axial failure models, employed in this study, are drift-based and therefore, do not account for the localized rotation at the column ends. Consequently, the analytical model detected the collapse of the frame due to failure of first-story columns at about 34.3 seconds. Shifting the limit curves even by 0.9% drift ratio (the standard deviation for shear limit curve (Elwood, 2002)) did not improve the results and therefore, results shown here are based on the original limit curves. Despite the poor prediction of location and time steps of shear and axial failure, Figure 6-49 shows a very good agreement between drift ratios from the experimental test and the analysis up to 34.3 seconds. Furthermore, the analytical model was able to adequately capture the column shear responses (Figure 6-50).

Comparison of the shear hysteretic response of the columns in Figure 6-51 illustrates that the analytical model captured the stiffness of the columns reasonably well. However, it is observed that the drift ratios for columns B2 and C2 were smaller than the capacity drift ratios suggested by the shear limit curves. Although the onset of shear degradation was adequately detected for the first-story columns, sharp shear degradation was observed in the test data for second-story columns which was not captured by the analytical model. Hitting the shear limit curves defined for the columns in the first story, caused sudden drop in their shear strength and localization of damage at this story level. Therefore, failure of columns in the second story could not be captured and the model predicted the collapse of the frame due to failure of first-story columns of the specimen.

Figure 6-53 demonstrates a reasonable agreement between the axial load recorded during the test and the analysis results; however, the model could not precisely capture the peaks. A maximum difference of 13% between the peak axial loads from the experimental and analytical models is obtained for column C1. As shown in Figure 6-52, the analytical model predicted the axial failure of columns B1 and C1, while axial failures occurred in B2 and C2 during the shaking table tests.

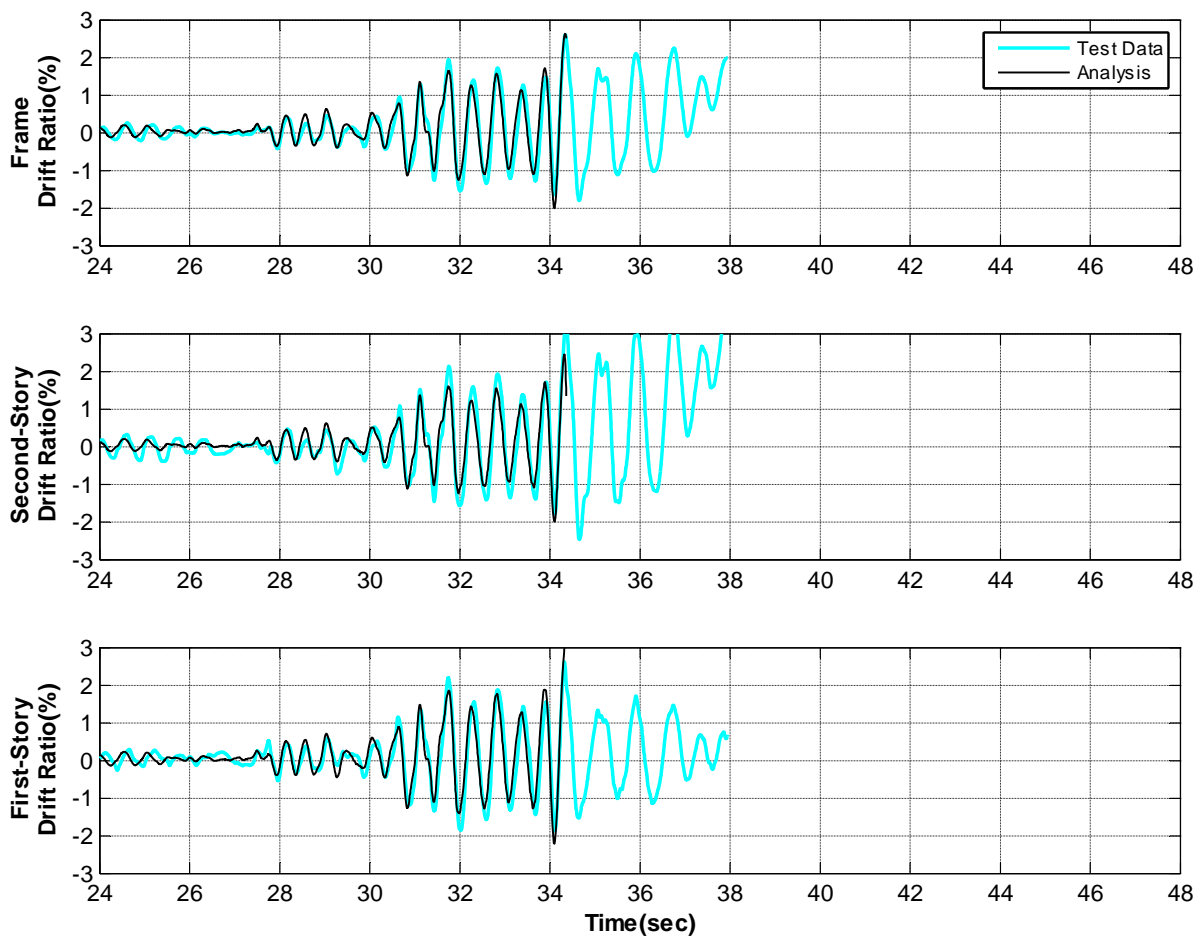


Figure 6-49. Story and frame drift ratio histories (specimen MUFS, Test2)

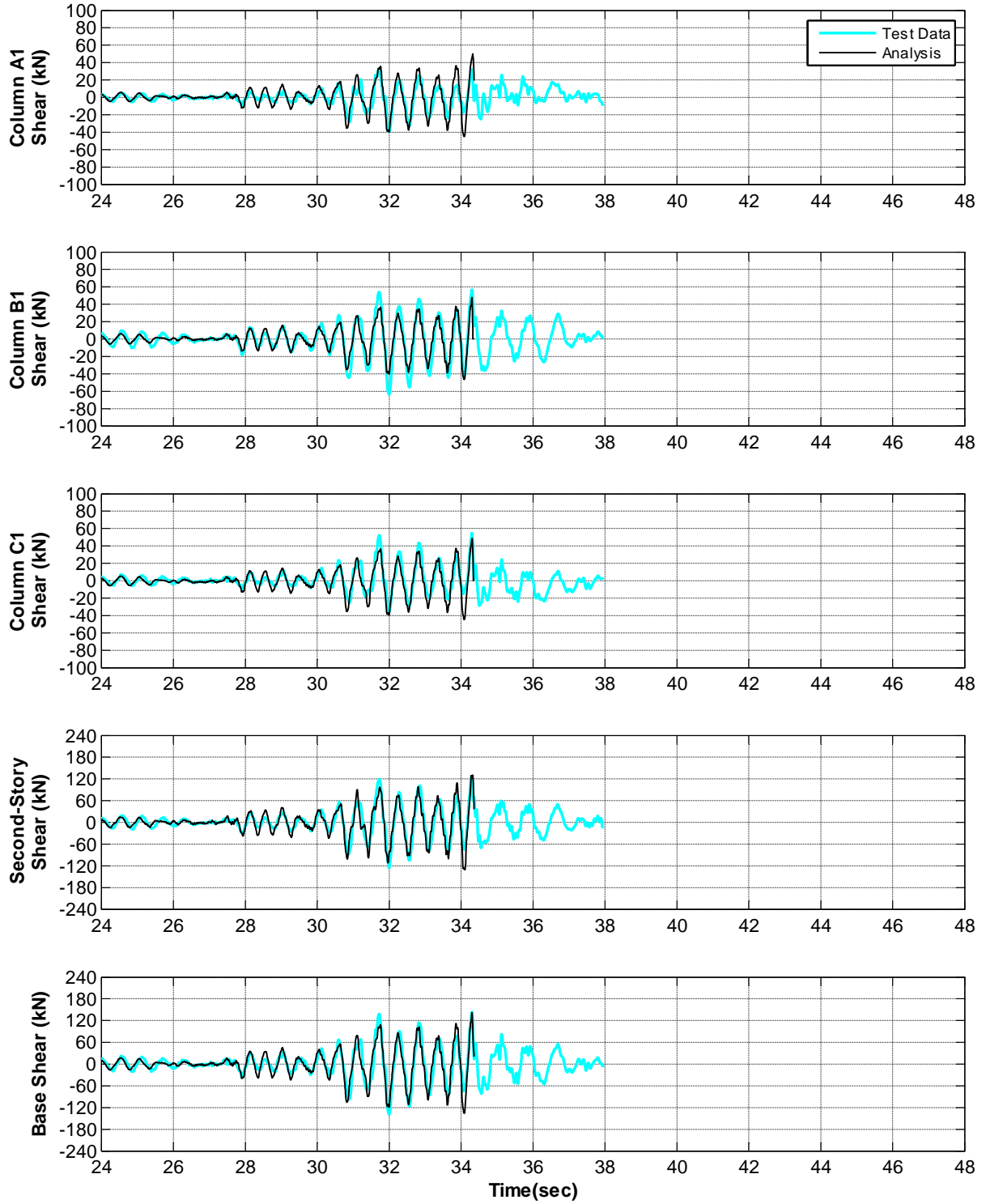


Figure 6-50. First-story columns and frame base shear histories (specimen MUFS, Test2)

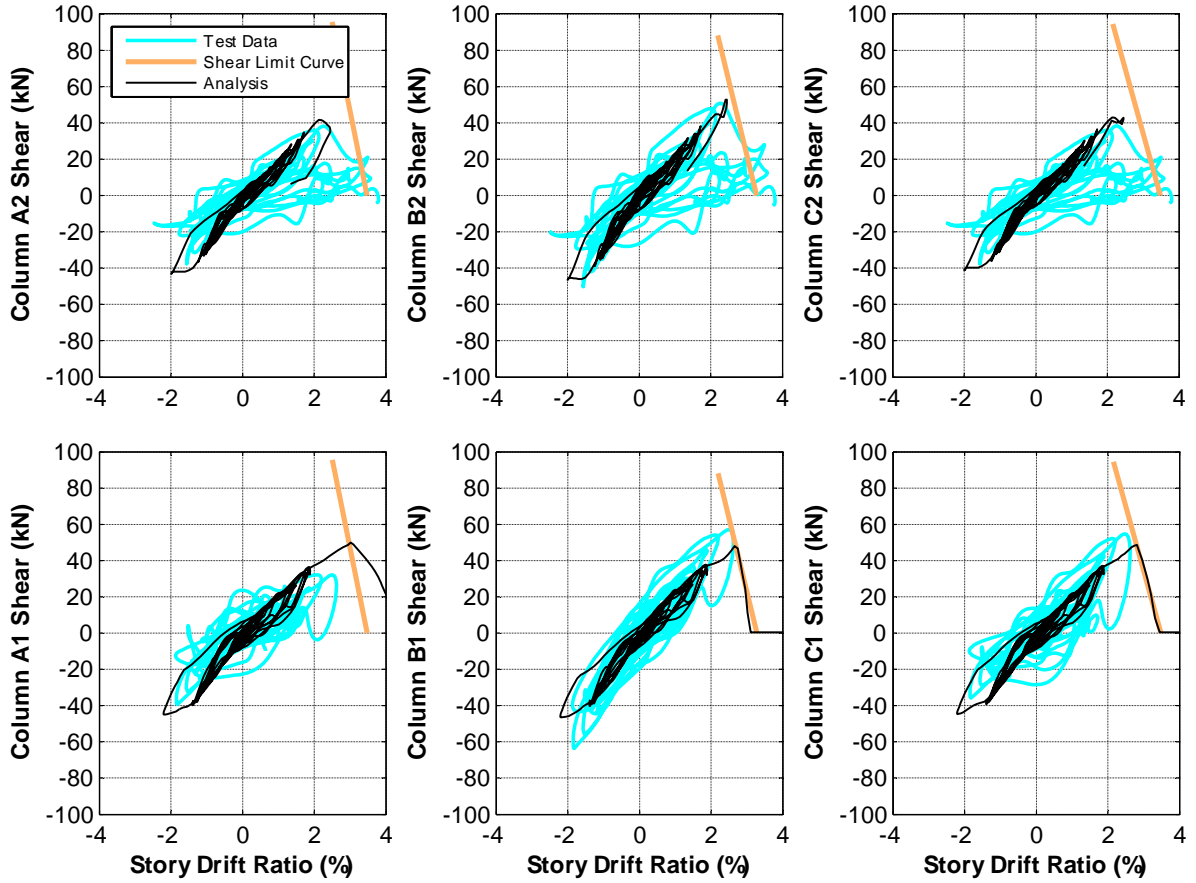


Figure 6-51. Shear hysteretic response of the columns (specimen MUFS, Test2)

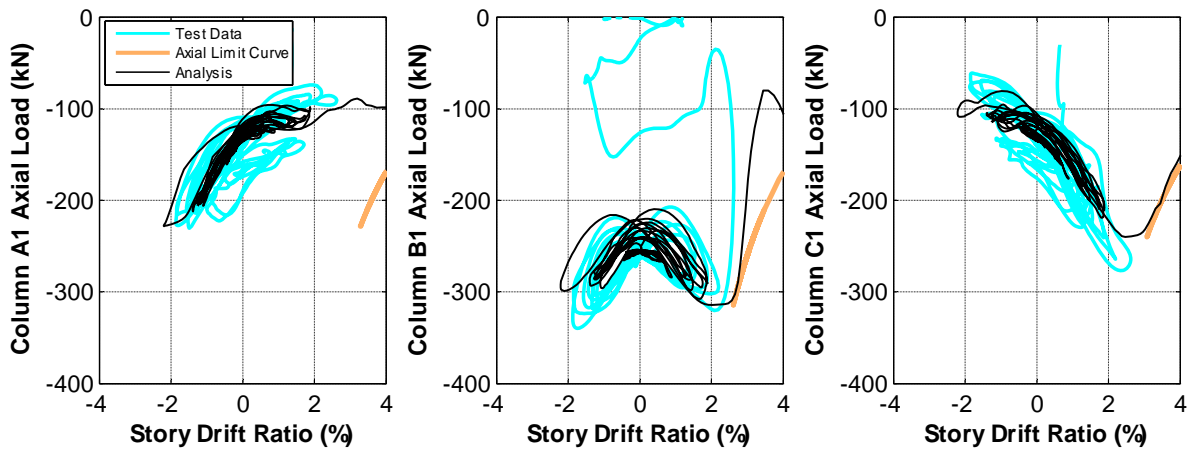


Figure 6-52. Axial load hysteretic response of first-story columns (specimen MUFS, Test2)

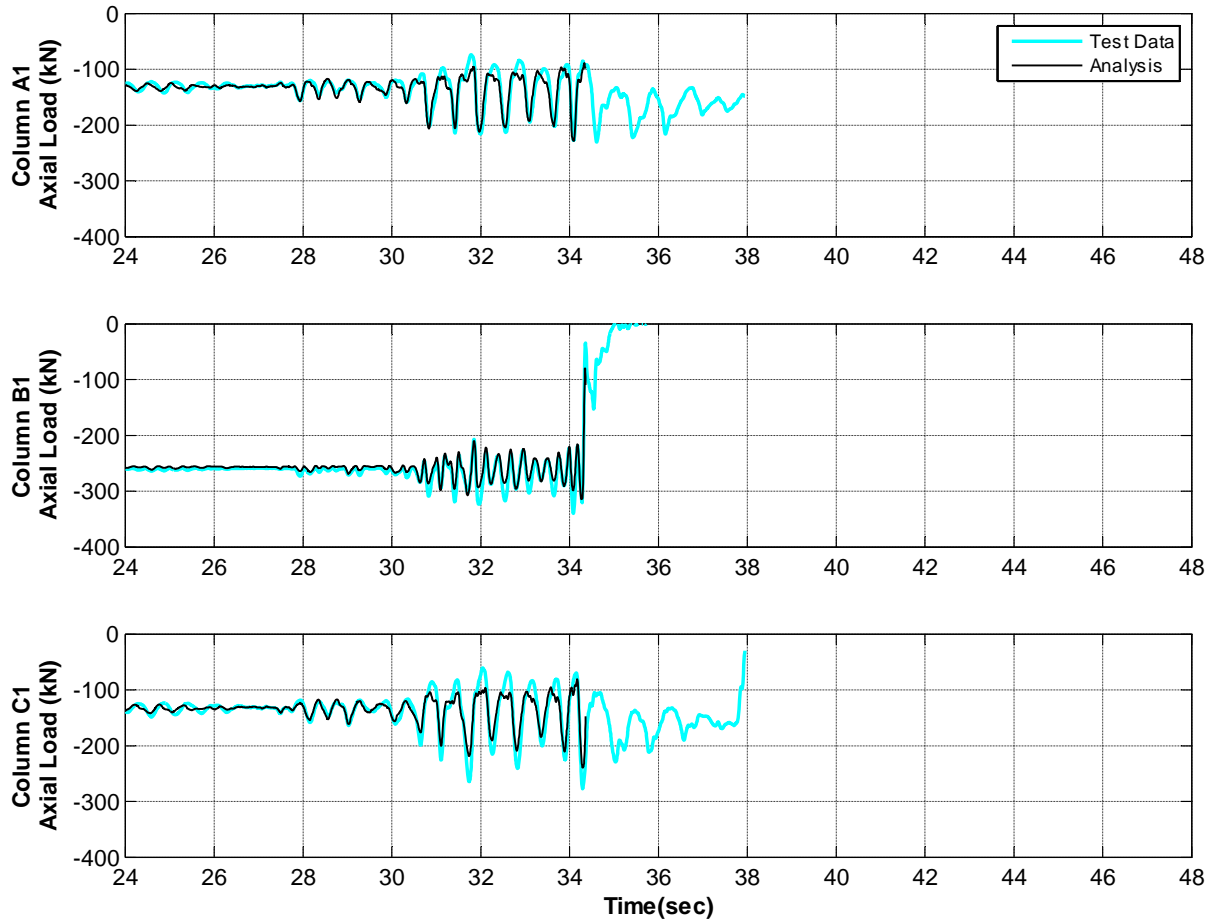


Figure 6-53. Axial load history response of first-story columns (specimen MUFS, Test2)

CHAPTER 7. SIMPLIFIED MODELING METHODS

7.1 Introduction

Although the results of the analyses, shown in previous chapter, were in reasonable agreement with the data from the shaking table tests, the procedure is very complex for practical purposes and requires special nonlinear models not available in commercial programs. In order to observe the impact of simplification in modeling on accuracy of the results, a few analyses using common simplified models were carried out and are reported in this chapter. The analytical model for specimen MCFS was selected for the course of this study. As described in Section 6.2, the columns of the specimen were modeled using fibre beam-column elements. End-springs were used at the ends of the elements to simulate bar-slip and shear and axial failure of the columns, while the joints were considered to be confined. The simplified analytical models discussed here include frames with: 1) elastic columns (no end-spring was considered for the columns of this model (Section 7.2)); 2) nonlinear columns with no end-spring (Section 7.3); 3) nonlinear columns without shear and axial springs (only bar-slip springs were considered in this model (Section 7.4)).

Analytical models with elastic column elements and lumped rotational hinges at the ends are commonly used in engineering practice. Different shear capacity backbones for such models, including the recommended backbone from ASCE-41, are evaluated in Section 7.5, and a refinement to the current backbone from ASCE-41 is proposed in Section 7.6. Results from the analyses using ASCE-41 and the proposed backbones are discussed in Section 7.7. All the models studied in this chapter are based on the specifications of specimen MCFS and will be subjected to lateral and vertical demands from testing that specimen.

7.2 Analytical Model with Elastic Elements and no End-springs

Simulating the behaviour of a frame using elastic members is the simplest type of modeling. Such model may not faithfully represent the observed nonlinear behaviour of the elements, but would be of interest for designers using drifts from an elastic analysis assuming the “equal displacement rule”. Using ASCE-41 recommendations (Equation 5.1), the effective stiffness, EI_{eff} , was assumed to be $0.3EI_g$ and $0.4EI_g$ for the exterior and center columns, respectively. Since the effect of bar-slip was already accounted for in such effective stiffnesses, no end-springs were considered for the columns and beams.

As shown in Section 6.3.2, the drift ratio from the original nonlinear-inelastic model was in good agreement with the test data for specimen MCFS during Test1 (see Figure 6-11). Figure 7-1 compares the frame drift ratios from the nonlinear-inelastic analysis (the original analysis) with the results from the linear-elastic analysis. It is observed that while the drift ratios from the linear-elastic and nonlinear-inelastic analyses did not match very well throughout the test, the peak drift ratio from the elastic analysis was only 6% lower than inelastic analysis. It should be noted that the peak first-story drift ratio from the elastic analysis was 28% lower than the one from nonlinear-inelastic analysis, indicating that the elastic

analysis adequately captured the overall frame drift but not the deformation of the frame. It is obvious that the other key parameters of the frame elements, including degrading stiffness and strength, could not be measured correctly by the linear-elastic analysis and for the sake of brevity, were not shown here.

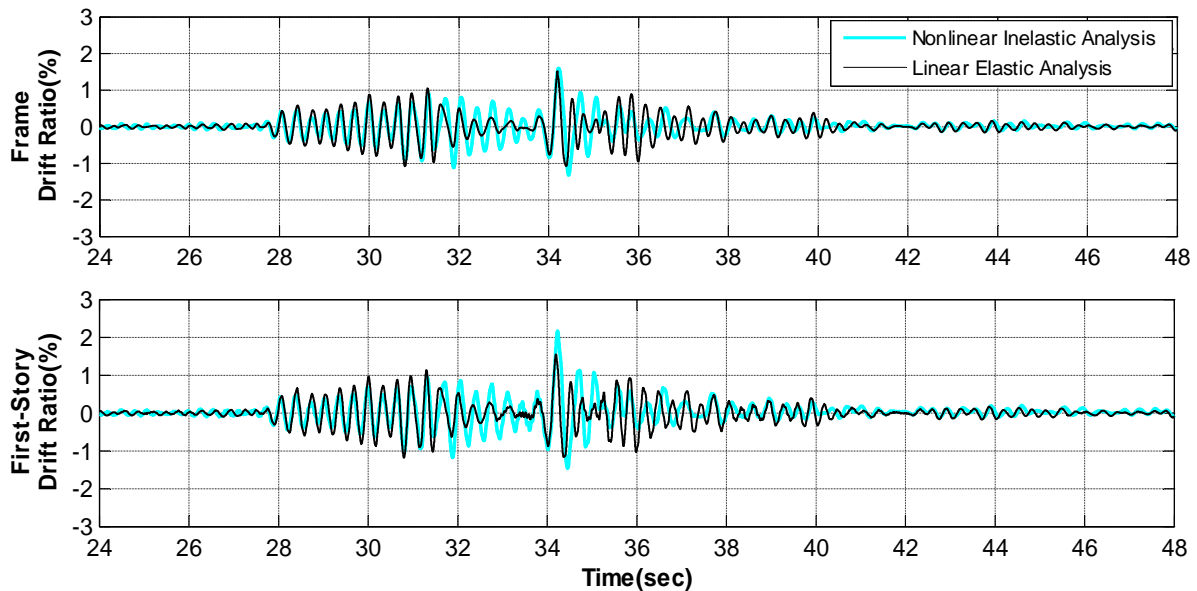


Figure 7-1. Comparison of drifts from nonlinear-inelastic and linear-elastic analyses, Test1

7.3 Analytical Model with Nonlinear Column Elements and no End-springs

Most of the available commercial engineering programs do not have the ability to detect the shear and axial failure of columns which may significantly influence the estimated capacity of reinforced concrete frames. In order to observe the effects of eliminating the end springs on overall behaviour of the specimens, the analytical model for specimen MCFS (described in Section 6.2) was modified such that the shear, axial, and slip end-springs were replaced by rigid elements.

It was observed that by eliminating the end-springs, the stiffness of the system considerably increased and the calculated natural period of the frames decreased from 0.29 to 0.22 seconds. Since the end-springs are in series with the elastic column members, elimination of the springs, particularly slip-spring, resulted in a stiffer response and smaller drift demands for the frame. Figure 7-2 confirms that the estimated peak drift ratios from the model described here are significantly smaller than the results from the shaking table test for both stories. In contrast, the results from the original analysis matched with test data (Figure 6-11) reasonably well.

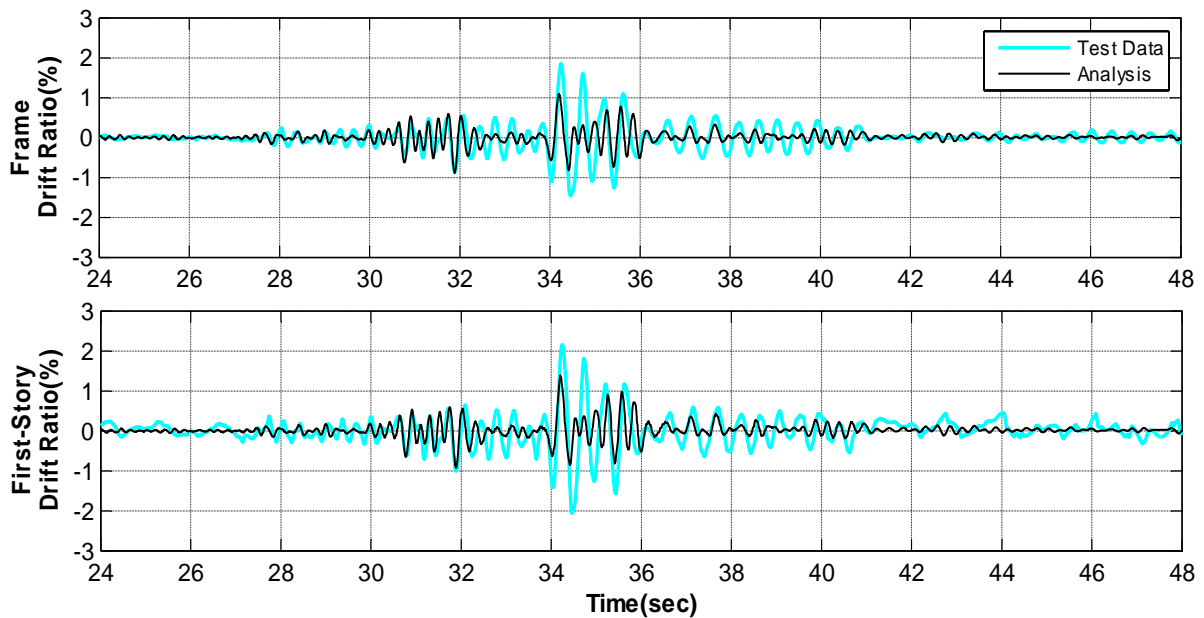


Figure 7-2. First-story and frame drift ratio histories for the model with nonlinear columns and no end-springs (specimen MCFS, Test1)

Figure 7-3 and Figure 7-4 compare the shear hysteretic response of the analytical model with the data from Test1 and Test2, respectively. The model slightly underestimated the peak shear for the columns in Test1 (with maximum difference of 15% for column B1 in the negative direction); however, the overall hysteresis loops were not well-matched (Figure 7-3).

Since the analytical model did not include the shear spring, it was not able to capture the significant strength degradation for columns B1 and C1 after 2% drift ratio in Test2 (Figure 7-4). While Figure 7-3 (Test1) demonstrates that such analytical models, capturing only the flexural behaviour of columns, tend to under-estimate the drift demands, Figure 7-4 (Test2) reveals that models not capturing shear failure will overestimate the drift capacity of non-ductile columns (in particular for columns B1 and C1) and must be used with caution for evaluation of frames with shear-critical columns.

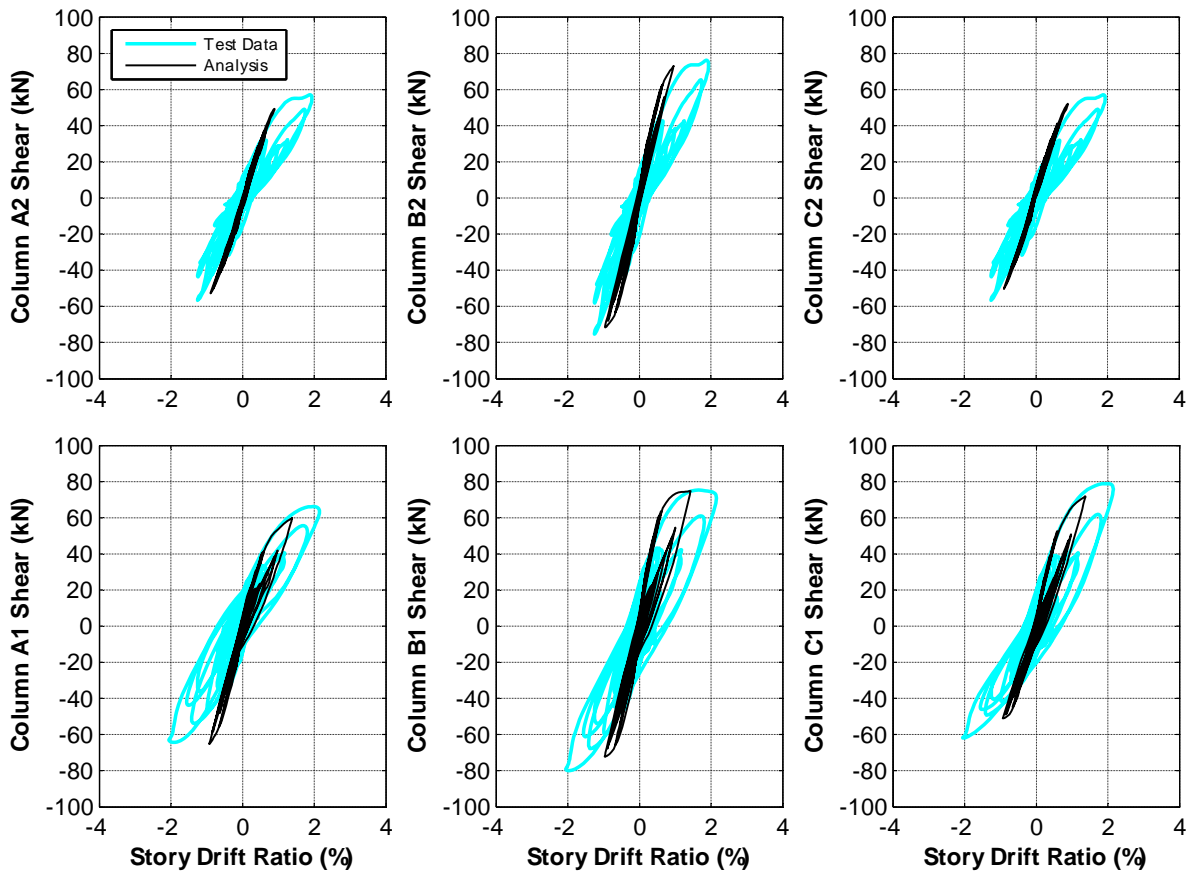


Figure 7-3. Shear hysteretic response of the columns with no end-springs (specimen MCFS, Test1)

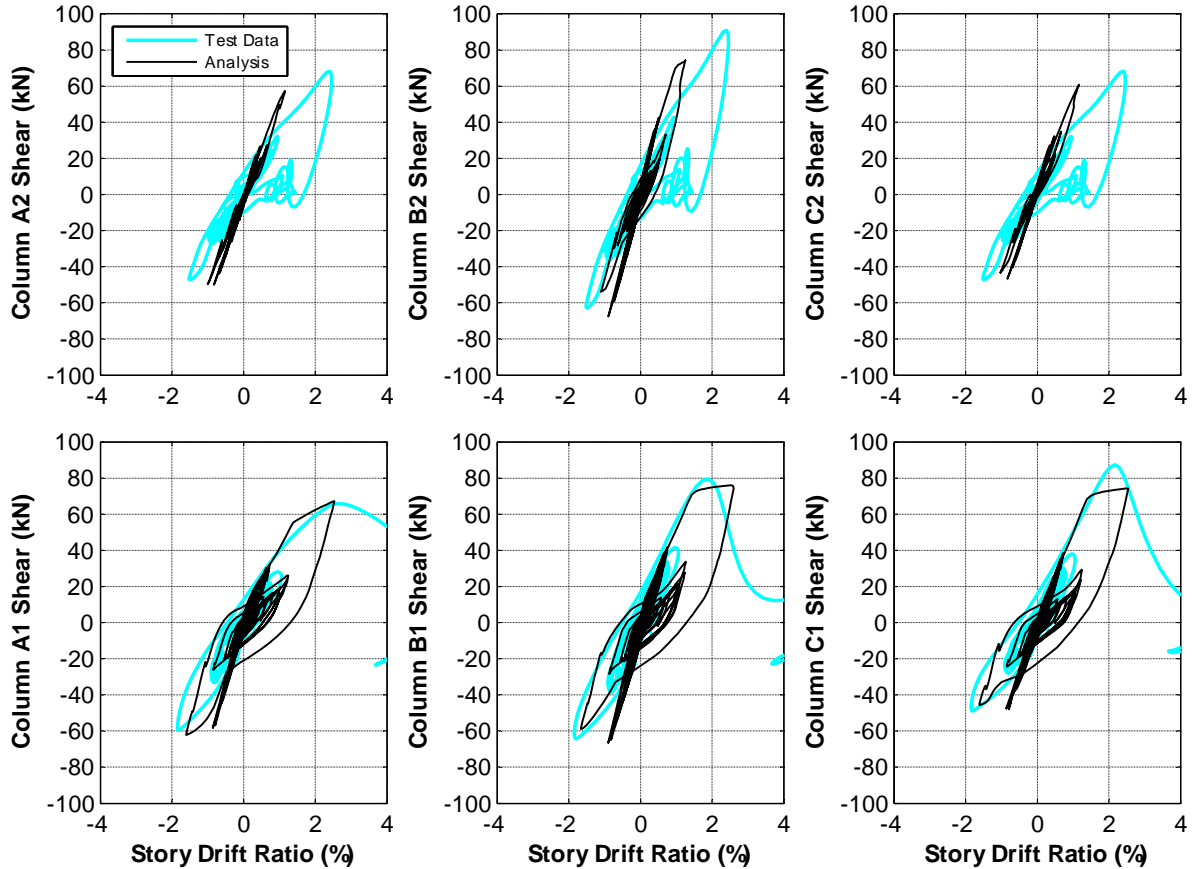


Figure 7-4. Shear hysteretic response of the columns with no end-springs (specimen MCFS, Test2)

7.4 Analytical Model with Nonlinear Column Elements and Only Bar-slip End-spring

Assessment of the analytical model with inelastic columns and no end-spring was carried out in the previous section. It was observed that the behaviour of the columns was stiffer than the tested columns and the peak drifts from the analysis for Test1 were significantly smaller than the test results. As discussed in Section 6.3.1, lateral deformation of a column can be considered as the combination of drifts resulting from shear, flexure, and bar-slip. Bar-slip can be observed early in the response and will influence the initial stiffness of the frame. Therefore, it is important to include the effect of bar-slip in the analysis, even for the

models where shear failure is not expected for the columns. In this section, results using an analytical model with inelastic columns (fibre section) and bar-slip springs at both ends are compared with the test data.

Figure 7-5 compares the drift ratios from the analysis and results from Test1. It is observed that adding the bar-slip springs significantly improved the ability of the model in capturing the drift ratio histories and peaks for the frame and its first story (compare with Figure 7-2).

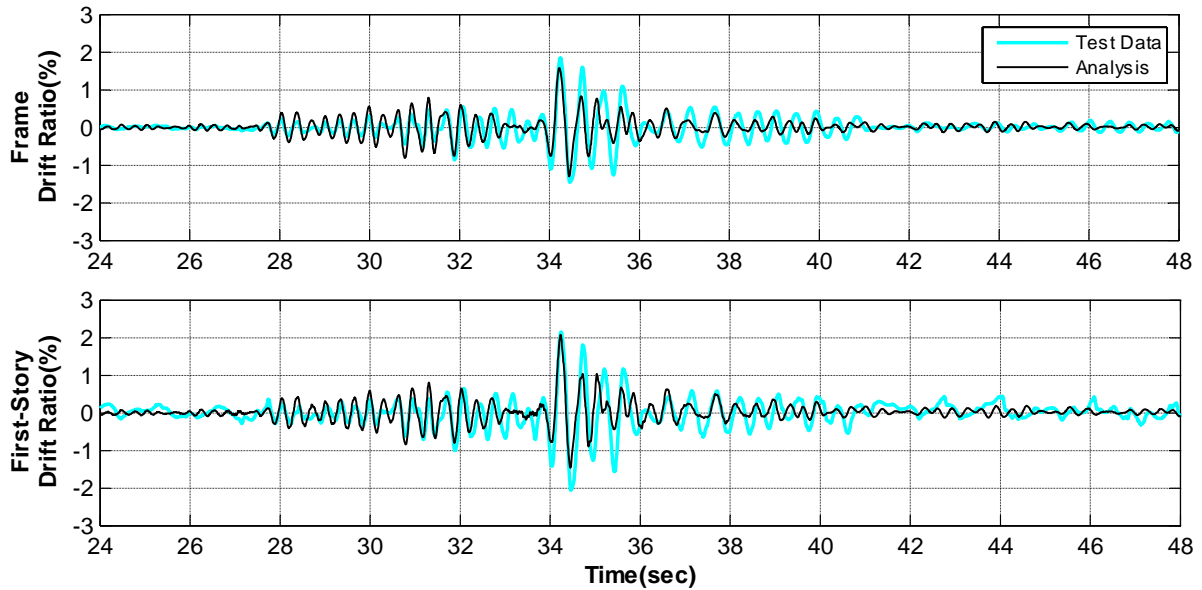


Figure 7-5. First-story and frame drift ratio histories for the model with inelastic columns and only bar-slip springs (specimen MCFS, Test1)

Figure 7-6 and Figure 7-7 compare the shear hysteretic response of the analytical model with the data from Test1 and Test2, respectively. Comparison of Figure 7-3 and Figure 7-6 demonstrates a much better agreement between the column hysteretic responses for Test1. It is also observed that the lateral stiffnesses of the columns were closer to those obtained from the test data. Although the overall behaviour of the columns estimated by the analysis for Test2

did not match the test data (Figure 7-7) since shear and axial failure were not considered in the model, it is observed that the lateral stiffnesses of the columns obtained from the analysis were very similar to those from the test, particularly for columns B1 and C1. It is also observed that despite not considering shear and axial failure, the drift demands were reasonably well estimated for these columns and a post-analysis comparison with drift capacity models would indicate that all first-story columns would be expected to have experienced shear and axial failure.

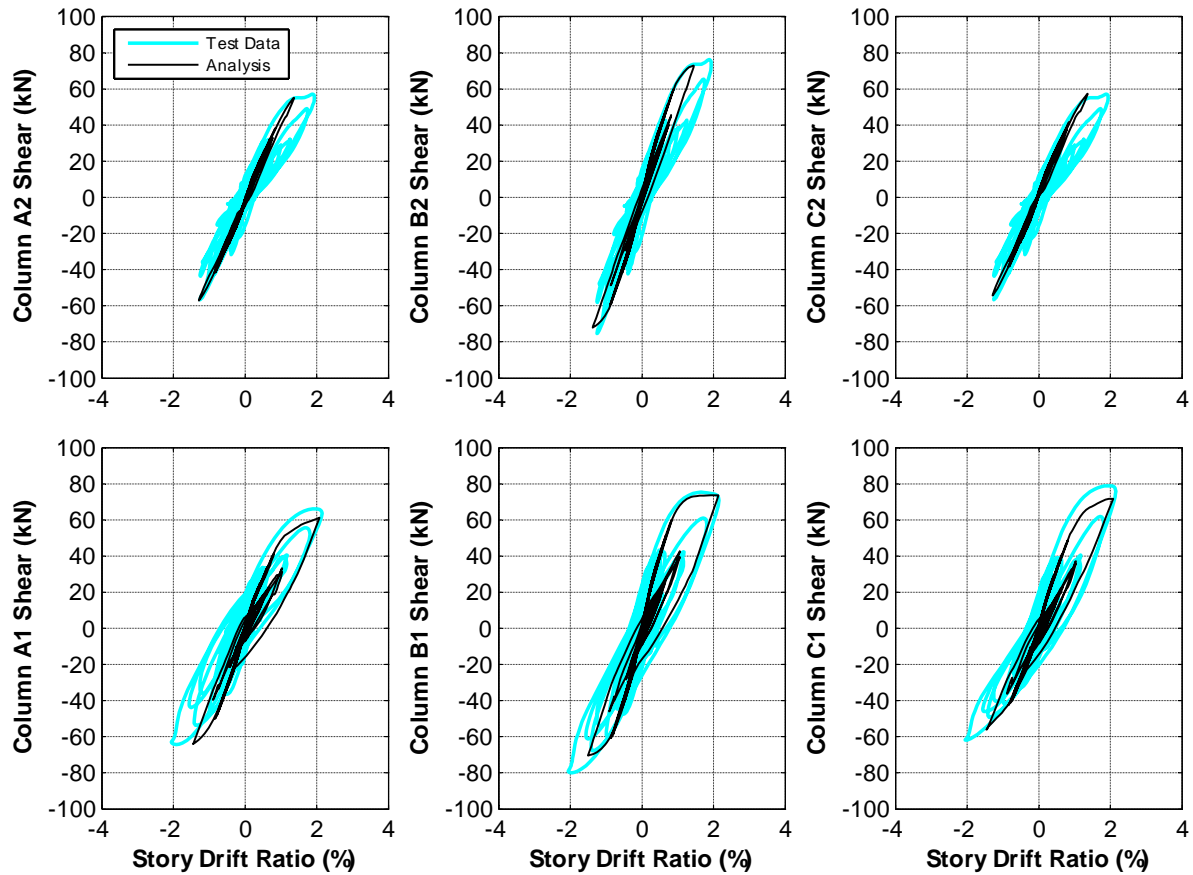


Figure 7-6. Shear hysteretic response of the columns with only bar-slip springs (specimen MCFS, Test1)

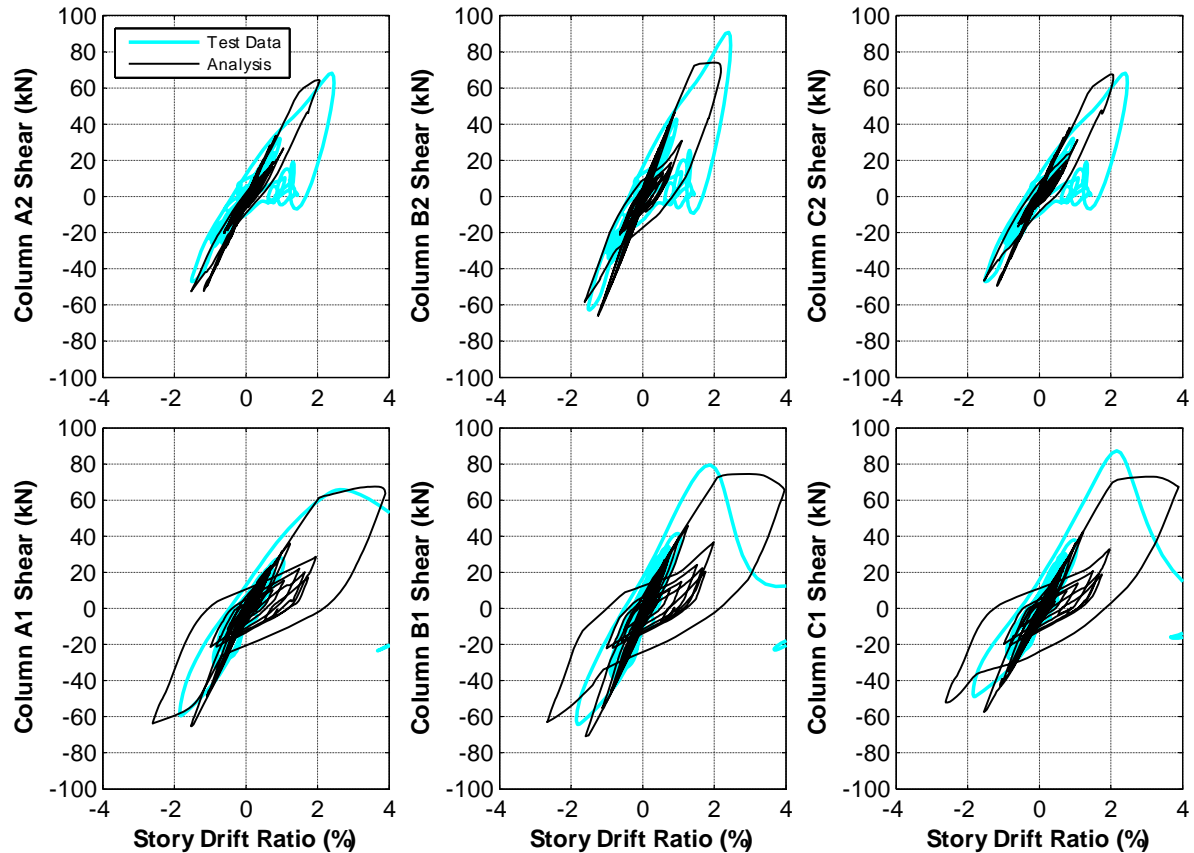


Figure 7-7. Shear hysteretic response of the columns with only bar-slip springs (specimen MCFS, Test2)

7.5 Evaluation of Capacity Backbone for Shear Hysteretic Response of Columns

In order to expedite the modeling of reinforced concrete frames, nonlinear columns are commonly replaced by elastic columns with lumped plasticity at the two ends (i.e. at the face of the beam-column joints). Such approach is easier and allows for easy calculation of plastic rotation demands and accepted by guidelines such as ASCE-41; however, stiffness of the columns and properties of the end-hinges must be carefully selected. Alternatives for effective stiffness of the elastic columns and modeling parameters for the end rotational hinges are studied and backbones using such alternatives are compared in this section. Figure 7-8 demonstrates the generalized components of force-deformation relations for modeling,

suggested by ASCE-41. While study on effective stiffness of columns (branch AB) is carried out in Section 7.5.1, modeling parameters for the other branches of the backbone are evaluated in Section 7.5.2. It should be noted that the elastic portion of Figure 7-8 (branch AB) is obtained from the elastic column element and the hinges are considered to be rigid before point B. Due to modeling limitations, branches CD and DE were replaced by the dashed line between point C and projection of point E. This approach is recommended in the commentary of ASCE-41 Supplement 1 (C6.3.1.2.2).

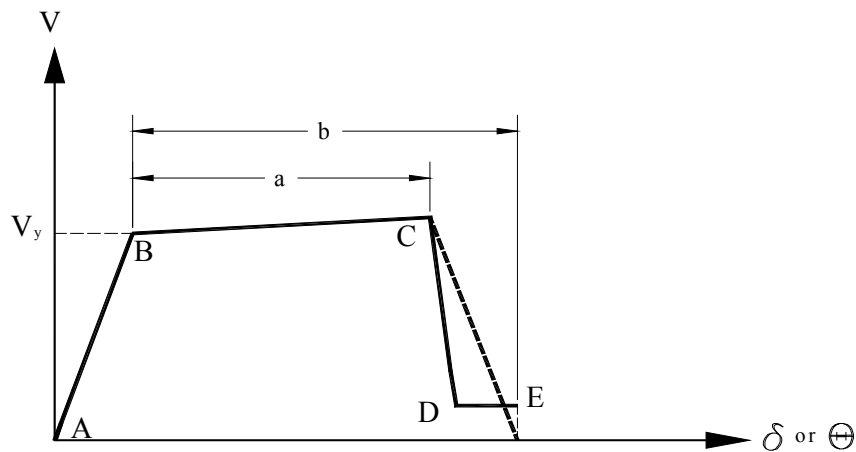


Figure 7-8. Generalized components of force-deformation relations, ASCE-41

7.5.1 Effective Stiffness of Elastic Columns

As discussed in Section 5.5.2, effective stiffness of a reinforced concrete element is generally expressed as a fraction of the elastic stiffness calculated using gross-section properties and represents the nonlinear stiffness relationship for the member. ASCE-41(2008) suggests using Equation 5.1 for the effective stiffness of an elastic column. Employing the same database as ASCE-41, Elwood and Eberhard (2009), recommended Equation 5.2. Comparison of Equations 5.1 and 5.2 demonstrates that ASCE-41 recommends a higher effective stiffness for columns with low axial loads, however, both equations result in increasing effective stiffness

ratios (EI_{eff} / EI_g) for increasing axial loads. Since the axial loads in the columns of upper stories of a frame are normally lower, this means that the effective stiffness should be reduced for the columns in upper stories of the frame. Such results can be acceptable when all the columns along the height of a frame experience similar level of demand. Nevertheless, observations of damage after earthquakes illustrate that the columns in higher stories experience less demand and damage. Therefore, for elastic models it may be appropriate to increase the effective stiffness for columns of upper stories to be closer to EI_g for assessment purposes. This also may resolve the issue noted in Section 7.2 that the elastic models can capture the overall roof displacement but not the drift profile. In order to examine the validity of the aforementioned argument, six models based on the analytical model of specimen MCFS are studied here, where the nonlinear columns were replaced by elastic columns with different effective stiffnesses (Table 7-1). No end-springs were considered for the six analytical models. While model 1 considered same effective stiffness of $0.3EI_g$, effective stiffness of $0.5EI_g$ was assumed for all columns of model 2, an approach suggested by ACI-318 (2008). Since the axial loads on the columns were mainly due to pre-stressing, the column axial load remained almost equal for the two stories. Therefore, the effective stiffnesses of second-story columns in models 3 and 5 were considered to be equal to the effective stiffnesses of the corresponding first-story columns. The effective stiffness of the columns in the second story of models 4 and 6 were increased using the following ratio:

$$EI_{eff_2} = \frac{V_2/\Delta_2}{V_1/\Delta_1} EI_{eff_1} \quad (7.1)$$

where V_1 and V_2 are the simultaneously recorded shear in the first and second stories, before cracking of any column during the test, while Δ_1 and Δ_2 are the corresponding drift ratios. Using data from Test1, Equation 7.1 results in the stiffness of the second story columns being

taken as 24% greater than the first story columns. Table 7-1 and Figure 7-9 compare the calculated peak story drifts for these models with the test data, demonstrating that model 6 captured the story drift demands much better than the other models. While model 5 (Equation 5.2) was the only model that overestimated the story drifts, comparison of the results from analyses using models 5 and 6 shows that increasing the effective stiffness of columns in higher stories results in much better predication of story drift ratios and the distribution of drifts up the height of the frame. It should be noted that increasing the effective stiffness of second-story columns (model 4) did not refine the outcome of the model with stiffnesses from Equation 5.1 (model 3), because the stiffnesses of the columns were already overestimated by the ASCE-41 suggested equation.

Table 7-1. Peak story drifts for models with different column effective stiffnesses (Specimen MCFS, Test1)

| | Calculated Natural Period (sec) | Effective Stiffness Col. B1 (Center) | Effective Stiffness Col. A1 (Exterior) | Peak 1 st -story Drift (%) | Error in 1 st -story Drift (%) | Peak 2 nd -story Drift (%) | Error in 2 nd -story Drift (%) |
|---|---------------------------------|--------------------------------------|--|---------------------------------------|---|---------------------------------------|---|
| Test Data Specimen MCFS | 0.285 | 0.38EI _g | 0.25EI _g | 2.15 | - | 1.89 | - |
| Model 1 EI _{eff} =0.3EI _g for all columns | 0.333 | 0.30EI _g | 0.30EI _g | 1.57 | 27 | 1.53 | 19 |
| Model 2 EI _{eff} =0.5EI _g for all columns | 0.272 | 0.50EI _g | 0.50EI _g | 1.72 | 20 | 1.63 | 14 |
| Model 3 Equation 5.1 | 0.315 | 0.40EI _g | 0.30EI _g | 1.58 | 27 | 1.49 | 21 |
| Model 4 Model3 + increased EI _{eff2} | 0.302 | 0.40EI _g | 0.30EI _g | 1.60 | 26 | 1.39 | 26 |
| Model 5 Equation 5.2 | 0.351 | 0.32EI _g | 0.23EI _g | 2.67 | 24 | 2.53 | 34 |
| Model 6 Model5 + increased EI _{eff2} | 0.337 | 0.32EI _g | 0.23EI _g | 2.03 | 6 | 1.68 | 11 |

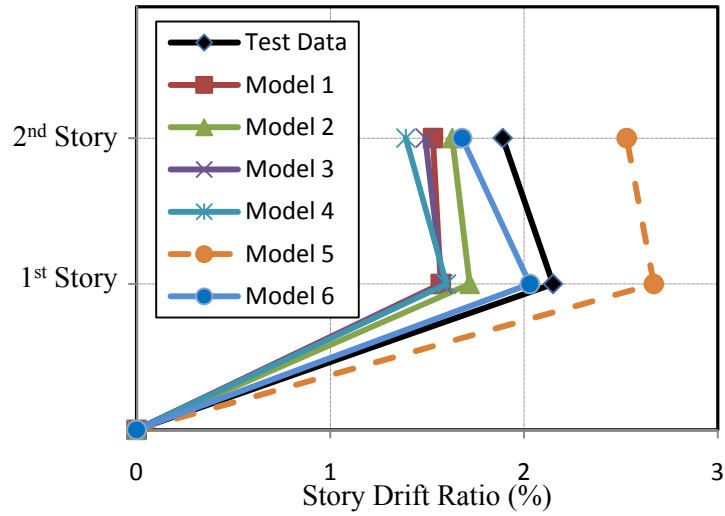


Figure 7-9. Comparison of peak story drifts from models with different column effective stiffnesses (specimen MCFS)

Figure 7-10 and Figure 7-11 compares elastic-perfectly-plastic backbones with the shear hysteretic behaviour of the columns of specimen MCFS during Test1 using the effective stiffnesses from model 3 (ASCE-41 recommendation) and model 6, respectively. Comparison of shear backbones from the two models with the hysteretic response of the columns shows a better fit for the backbone from model 6.

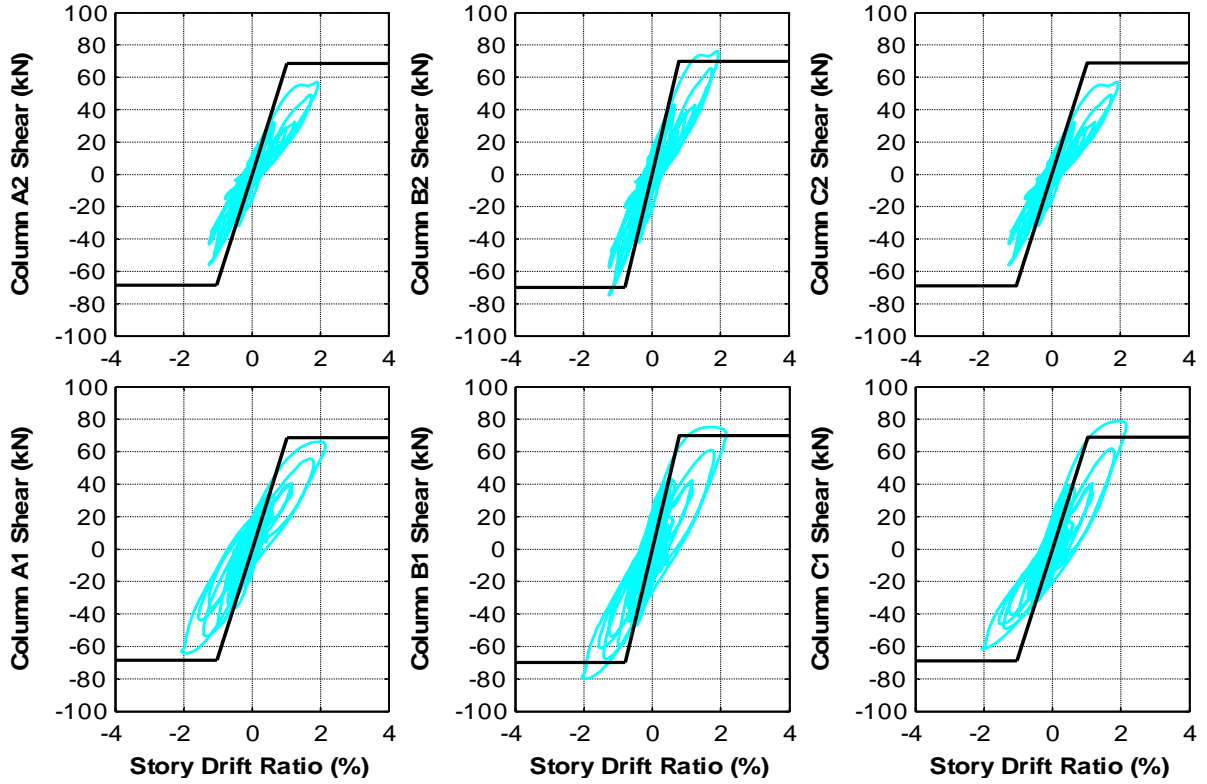


Figure 7-10. Bilinear shear backbone for columns using effective stiffness from Model 3 (ASCE 41), (specimen MCFS, Test1)

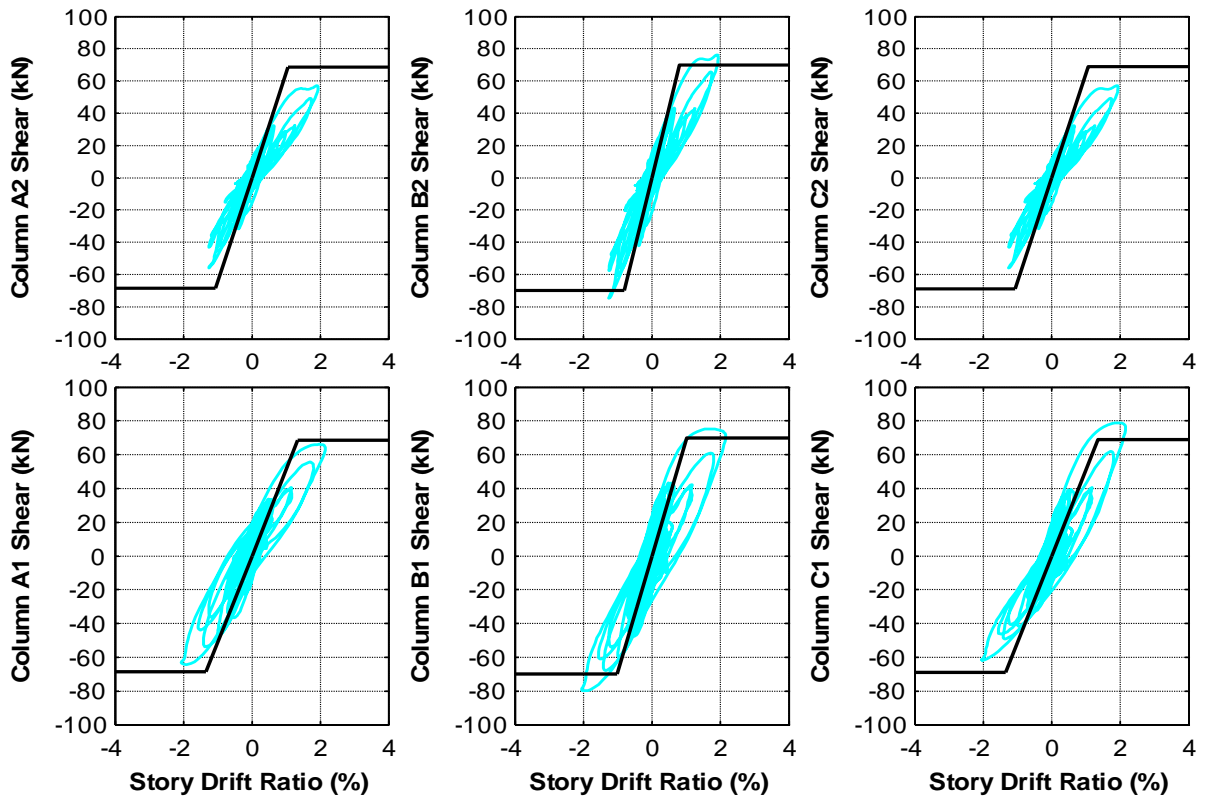


Figure 7-11. Bilinear shear backbone for columns using effective stiffness from model 6, (specimen MCFS, Test1)

This brief study shows that not only the section properties and applied axial load are important in obtaining a column effective stiffness, but the influence of other parameters such as location in the building and ductility demand must also be considered in determining the appropriate effective stiffness values. Further studies are required to select the optimum coefficients accounting for such parameters; however, a rational approach would be to use the fundamental mode shape of the building to obtain the coefficient for increasing the effective stiffness of columns in higher stories. The only drawback of such approach is the iterative procedure, where an initial effective stiffness should be assumed in order to obtain the fundamental mode shape of the frame. Since the frame studied here had only two stories, investigation on suitability of such a coefficient for multi-story frames was not possible but should be examined in future work.

7.5.2 Modeling Parameters for End Rotational Hinges

In analytical models with elastic column elements, yielding as well as strength degradation due to failure must be defined as lumped plasticity in hinges at the ends of the column element (branches after point B in Figure 7-8). Based on shear strength, V_n , plastic shear demand, V_p , and the transverse reinforcement detailing of a column, ASCE-41 (2008) suggests three possible failure conditions:

- *Condition i:* Flexure failure
- *Condition ii:* Flexure-shear failure
- *Condition iii:* Shear failure

For each condition, modeling parameters including plastic rotation angles for the end-hinges and residual strength ratios are obtained based on shear stress, axial load, and transverse reinforcement ratio of the column (See Table 6-8 of ASCE-41 (2008), Appendix Section B.5).

The modeling parameters given in ASCE-41 were based on the observations from cyclic tests of single columns (Elwood et al., 2007), while testing the frame specimens studied in this research provides the opportunity to examine the suitability of ASCE-41 recommended parameters for capturing the dynamic frame response. The analytical model for specimen MCFS with elastic columns and end rotational hinges was used for this purpose. Although the effective stiffness from model 6 discussed in the previous section was in better agreement with the test data, the effective stiffness suggested by ASCE-41 was selected to comply with all the recommendations from the guideline. Employing Equation 5.1, the effective stiffnesses of $0.3EI_g$ and $0.4EI_g$ were obtained for the exterior and interior columns, respectively.

Backbones for the column end-hinges were selected based on Table 6-8 of ASCE-41, where the columns with closed hoops with 90° hooks and $V_p/V_n \leq 1.0$ are categorized as *Condition ii* and columns with same hoop type but with $V_p/V_n > 1.0$ are grouped as *Condition iii*. For the above-mentioned table, ASCE-41 emphasises that the plastic rotation angles must be calculated using the maximum expected axial loads due to gravity and earthquake loads; however, it is silent about the axial load that must be used for selecting the column condition. If the direction of shaking is not taken into account, by considering the maximum expected axial loads due to gravity and earthquake loads (recommended in the footnote of Table 6-8 of ASCE-41 for calculating the plastic rotation angles, Appendix Section B.5), columns of the studied frame are categorized under *Condition ii*. However, the axial loads in the exterior columns significantly varied in different directions of shaking due to overturning. For instance, column C1 of specimen MCFS experienced a maximum axial load of 37.9 kN ($0.03A_gf'_c$) in the negative direction of Test1, whereas the maximum axial load of 317.6 kN ($0.23A_gf'_c$) was recorded in the positive direction of the test (see Figure 6-14). Considering such a large

difference in peak axial loads in the positive and negative directions, the category for column condition will be different for the two directions. ASCE-41 recommends using the minimum appropriate numerical values where more than one of the conditions occurs for a column. Consequently, the column classification may result in *Condition iii*.

Since the maximum and minimum axial load on the columns for the positive and negative cycles during the tests were available, effects of changing the modeling parameters in different directions were also studied for all the columns by comparing the shear hysteretic behaviour of the analytical model with the following three different backbones:

1) backbone A: *Condition ii* with similar backbones for the two opposite directions of shaking. Column axial load was defined as the maximum axial load due to gravity and earthquake.

2) backbone B: *Condition ii* with different backbones for the two opposite directions of shaking. Column axial load was obtained based on the peak recorded axial load in each direction, while the condition for columns remains as *Condition ii* for both directions.

3) backbone C: *Condition iii* with similar backbones for the two opposite directions of shaking.

Figure 7-12 and Figure 7-13 compare backbone A with hysteretic response of the MCFS columns during Test1 and Test2. It is observed that backbone A is in reasonable agreement with the shear hysteretic response of the columns. However, based on the recorded drift demands, the backbone predicts that column B1 will experience severe shear strength degradation in Test1 (Figure 7-12), while it overestimates the shear strength in columns A2 and C2. Figure 7-13 shows that the backbone underestimates the peak shear strength of columns on axis B and column C1 in Test2, while it predicts that the strength degradation of

these columns would be initiated at smaller drift ratios. Such underestimation of drift capacity resulted from using the parameters for *Condition ii* in ASCE-41 defined to represent a probability of failure of 15% based on static test data (Elwood et al., 2007). This high level of conservatism in defining the parameters for *Condition ii* columns in ASCE-41 were due to the possible degradation of axial capacity with the development of a shear-failure plane.

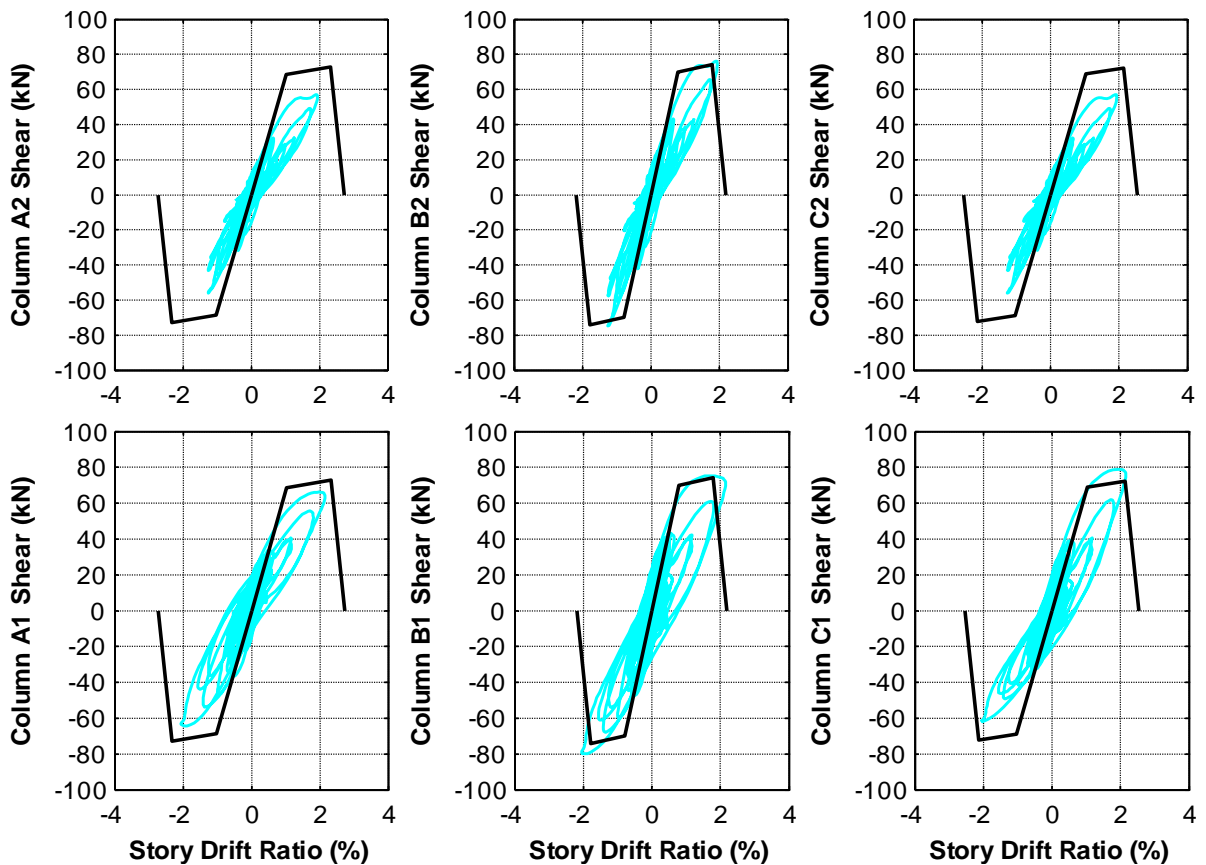


Figure 7-12. Calculated backbone A (specimen MCFS, Test1)

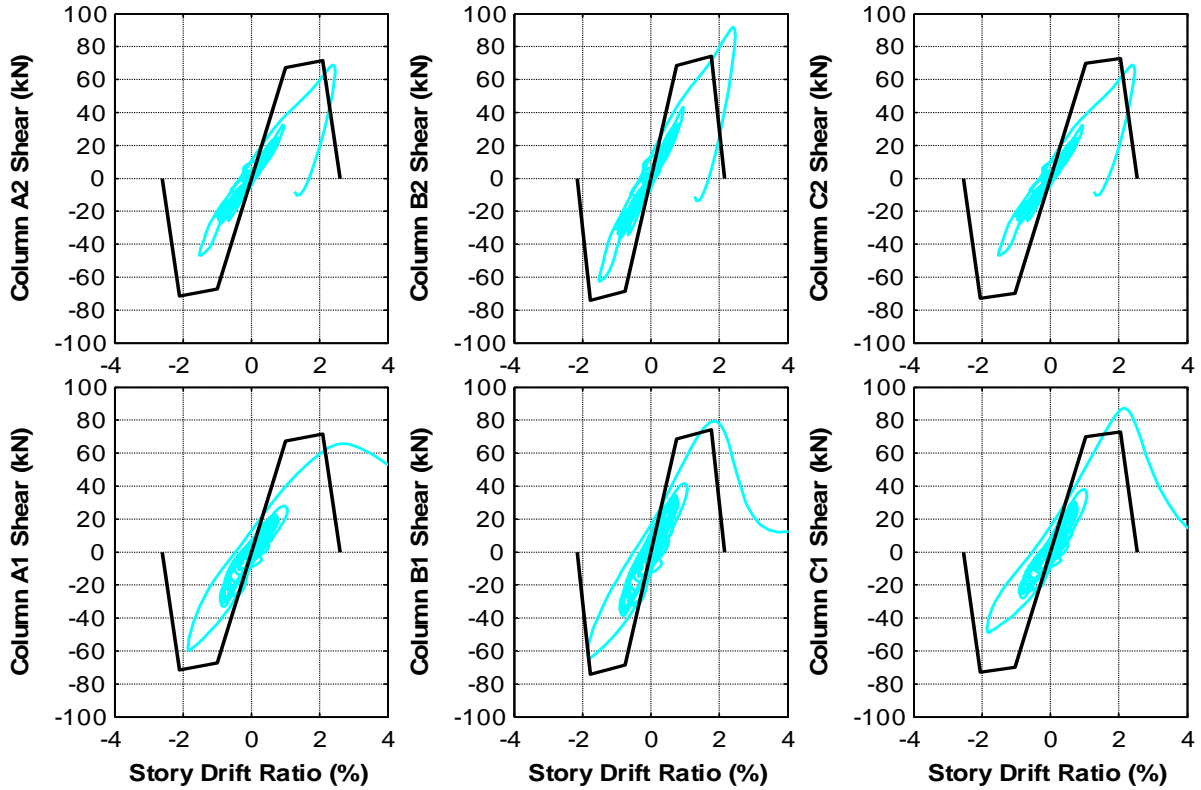


Figure 7-13. Calculated backbone A (specimen MCFS, Test2)

Shear hysteretic response of the columns during Test1 and Test2 are compared with backbone B in Figure 7-14 and Figure 7-15, respectively. Although outcomes from backbones A and B are relatively similar, comparison of Figure 7-12 and Figure 7-14 illustrates that Backbone A is in better agreement with the test data for the exterior column A1, whereas backbone B underestimates the shear strength of the column by 20% in the positive direction. On the other hand, backbone B has a better match with test data for column A2. Since fluctuation in axial load on column B was not significant during the test, both backbones similarly detect the failure of column B1 in Test1. Although comparison of Figure 7-13 and Figure 7-15 shows that backbone B provides a better match for the shear hysteretic behaviour of column C1 in the negative direction of Test2, both models underestimate the shear strength

of columns on axis B and column C1 in the positive direction, while predicting the failure of the columns at smaller drift ratios during the test.

Comparison of backbone C and test data demonstrates that by choosing *Condition iii* for the columns of specimen MCFS, their capacities are considerably underestimated (Figure 7-16). Backbone C not only predicts the collapse of the frame in Test1, it suggests that all the columns lose their shear strength instantly after the yield point. Nevertheless, the observed shear hysteresis of the columns during the test suggests that they experienced flexural yielding before strength degradation. Since backbone C was not realistic for Test1, comparison of the backbone with shear hysteresis from Test2 is not shown here.

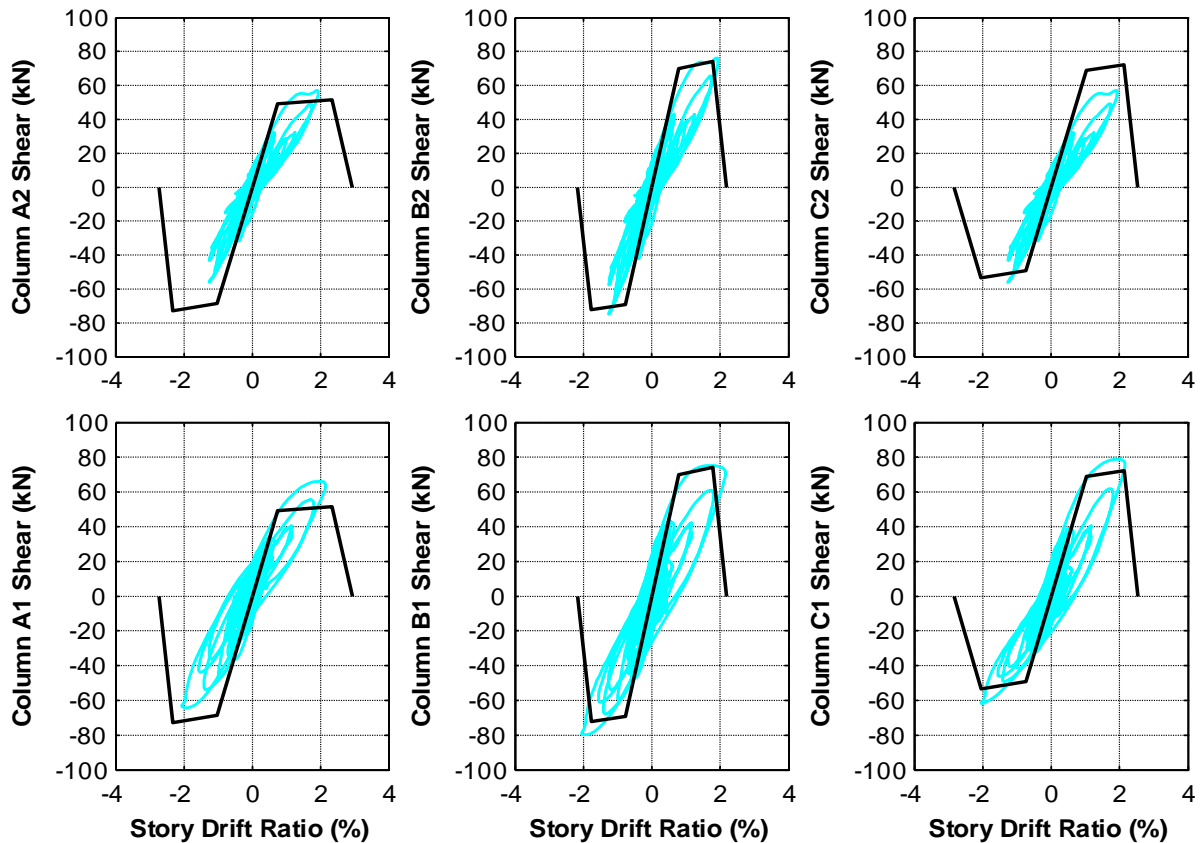


Figure 7-14. Calculated backbone B (specimen MCFS, Test1)

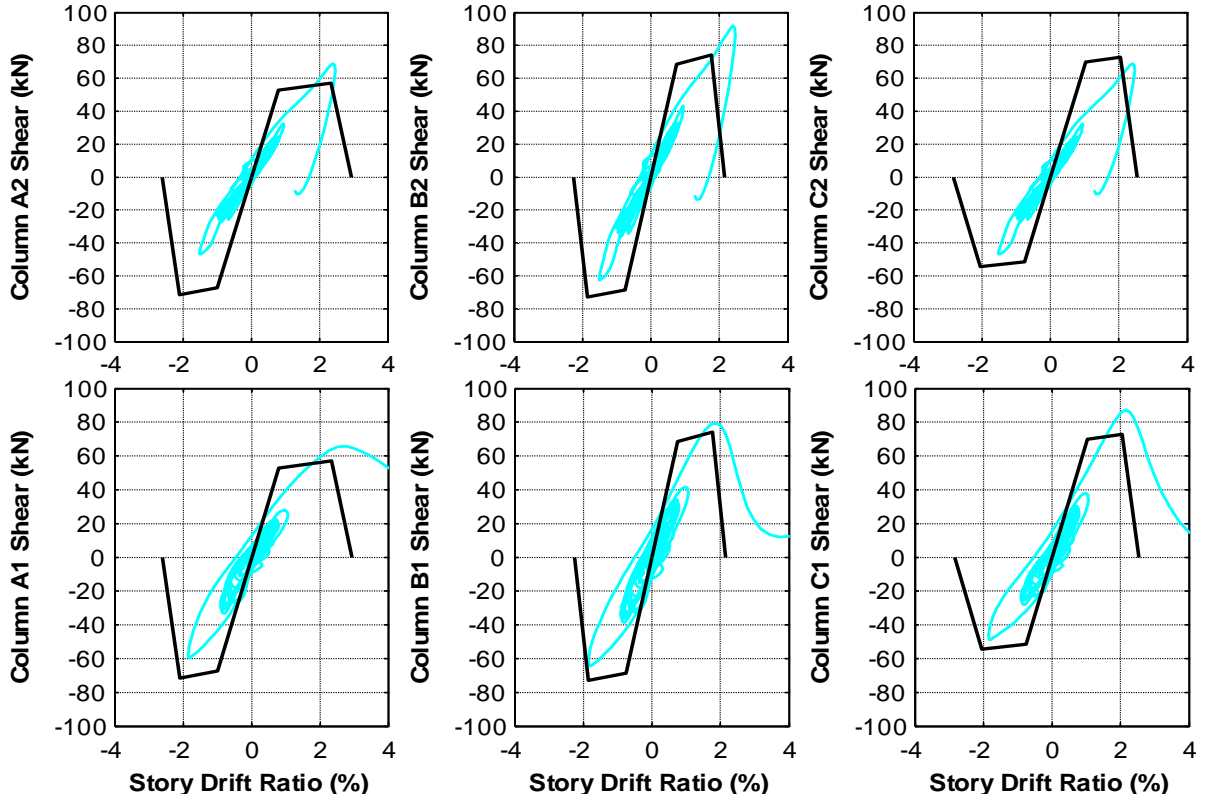


Figure 7-15. Calculated backbone B (specimen MCFS, Test2)

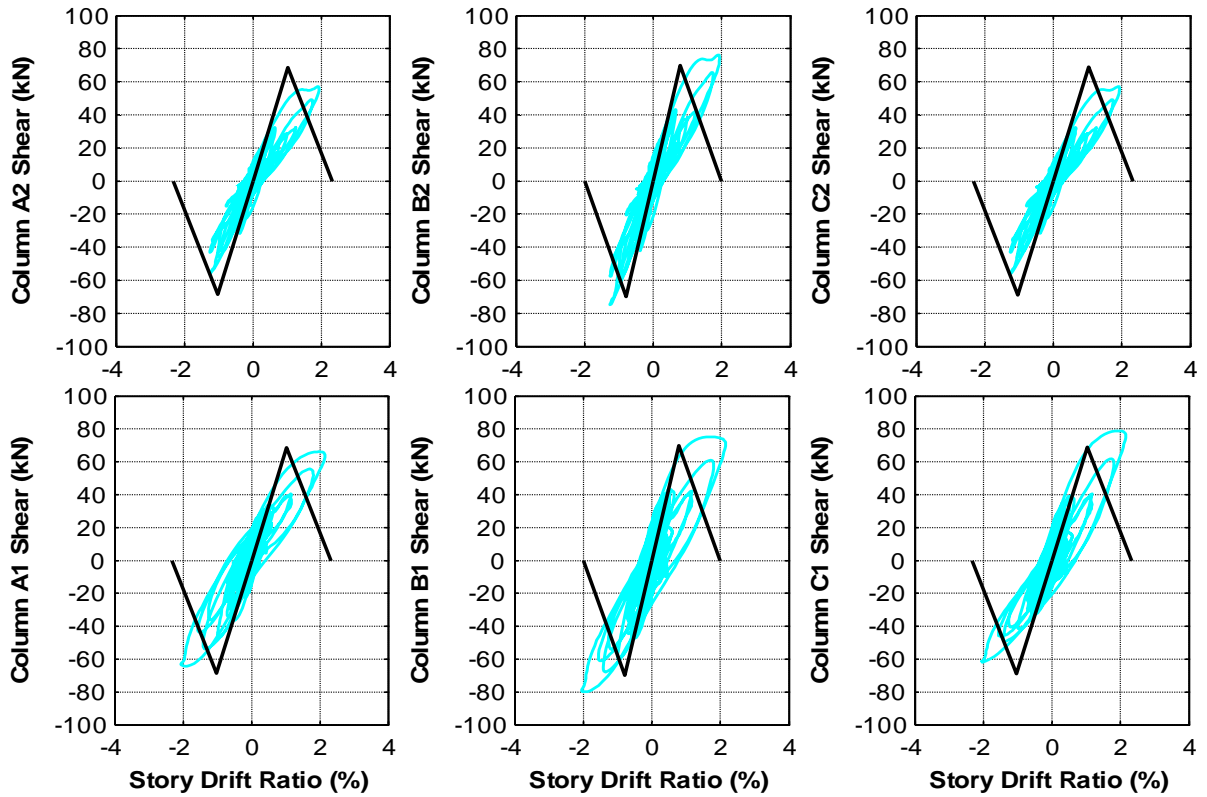


Figure 7-16. Calculated backbone C (specimen MCFS, Test1)

By comparing the results from the three backbones, it is observed that the parameters for *Condition iii* (backbone C) are very conservative, whereas using different modeling parameters for each direction of shaking (backbone B) provides more realistic results. However, calculating so many parameters required for backbone B is time consuming, particularly for frames with several columns. Furthermore, direction of shaking is unknown in a real earthquake and directions for tension and compression may not be very obvious for the interior columns of a multi-story and multi-bay frame. Consequently, the worst scenario must be taken into account during the evaluation process of exciting buildings. Comparison of backbones A and B with the test results demonstrates that using backbone A resulted in relatively well-predicted strength and drift capacities of the columns, and the simple procedure to obtain the backbone will be more practical for evaluation purposes.

As discussed earlier, ASCE-41 recommends using the minimum appropriate numerical values where more than one of the conditions occurs for a column, where such numerical values are related to the axial load in the columns. Exterior columns in a frame may experience significant difference in axial load in the opposite directions of shaking due to overturning effect which may lead to classifying such columns in *Condition iii*. As shown above, such classification is very conservative. While ASCE-41(2008) is currently silent about the axial load that must be used for selecting the column condition, it is proposed here to emphasize in ASCE-41 that the maximum expected axial loads due to gravity and earthquake loads must be used for choosing the condition for columns. Such refinement to the guideline will result in more realistic condition for columns (*Condition ii* and model A, for the example discussed above).

7.6 Proposed Shear Capacity Backbone

Based on the findings from previous sections, a shear capacity backbone is proposed in this section. While model 6 (Section 7.5.1) provided the best effective stiffnesses for the columns, plastic rotation angles of the end-hinges can be obtained using the parameters from backbone A (Section 7.5.2). Calculated backbone using such a combination is shown in Figure 7-17 and Figure 7-18 for Test1 and Test2, respectively. Although shear strength of exterior second-story columns were overestimated for Test1 (Figure 7-17), it is observed that the proposed backbone fitted the shear hysteresis of the other columns reasonably well. Figure 7-18 reveals that the slope of the strength degradation in the backbone was steeper than the actual shear degradation of columns during Test2. This suggests that the modeling parameter for end-hinge rotation angle at zero-shear strength (i.e. “b-value” recommended by ASCE-41, see Figure 7-8) is somewhat conservative. Considering the fact that the discussed analytical models are mostly used for predicting the shear and drift of frames at onset of shear and axial failure, the proposed model suggests a practical and reasonably accurate backbone for evaluation purposes. Nevertheless, further studies are required to confirm the suitability of the proposed backbone and refine the parameters to fit better with the experimental data.

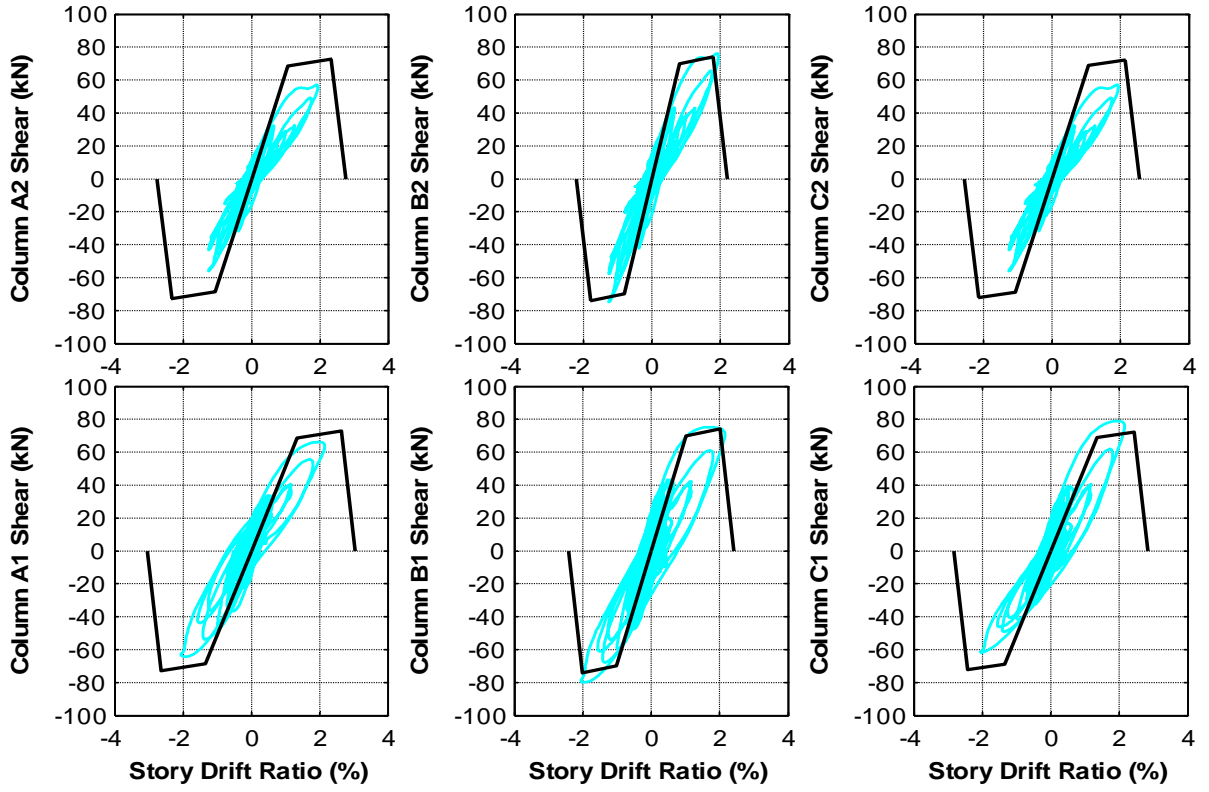


Figure 7-17. Calculate backbone using proposed model (specimen MCFS, Test1)

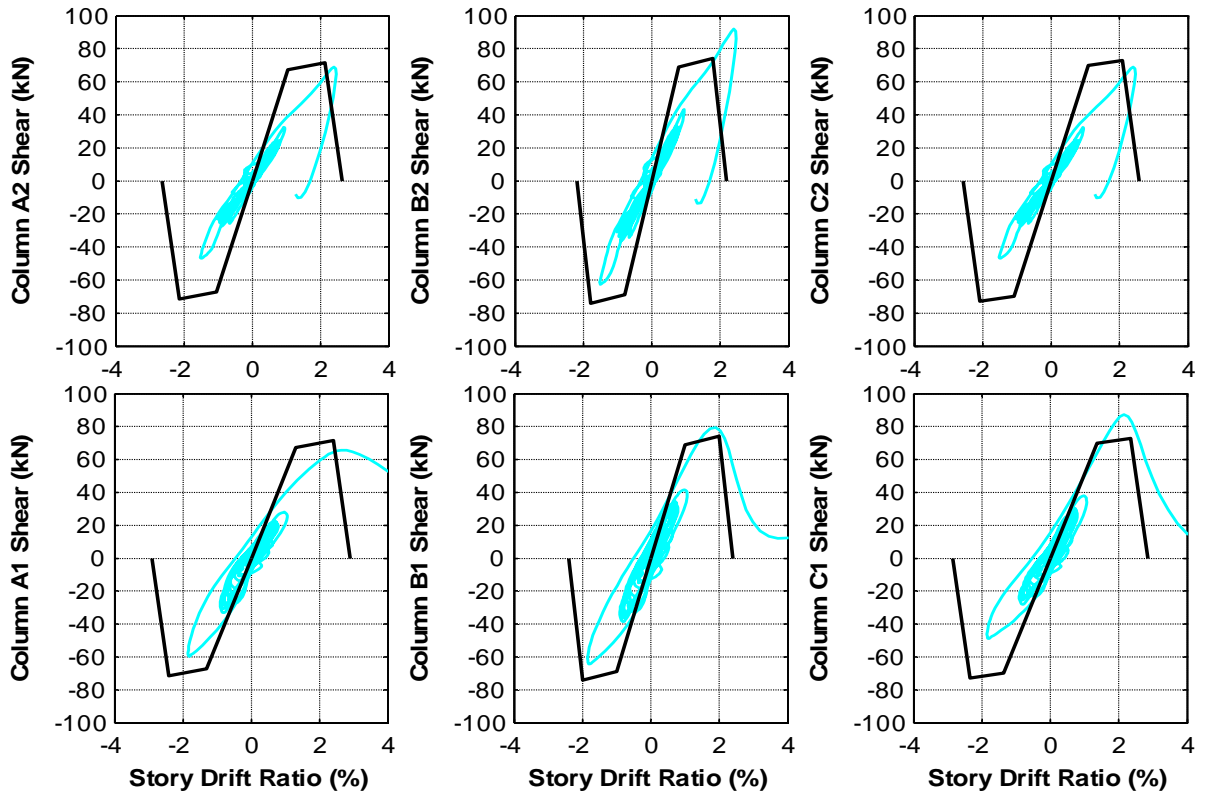


Figure 7-18. Calculate backbone using proposed model (specimen MCFS, Test2)

7.7 Evaluation of Analytical Models with Elastic Columns and End Rotational Hinges

Although a shear backbone demonstrates the overall shear response of an element, the actual demand on the member during an earthquake can only be obtained by studying the shear hysteretic response of the element from dynamic analysis. In this section, dynamic analyses are carried out for specimen MCFS using the analytical models with elastic columns and plastic rotational hinges at the ends. While Section 7.7.1 demonstrates the results from the model using ASCE-41 shear backbone, results from the model using the proposed backbone are compared with the test data in Section 7.7.2.

7.7.1 Analytical Model with ASCE-41 Backbone

The analytical model described in Section 6.2 was modified by replacing the fibre-section columns with elastic members and plastic hinges at the ends. Effective stiffnesses of the columns were calculated using model 3 (see Section 7.5.1). Since the effect of bar-slip was considered in the model for effective stiffness of the columns, no bar-slip rotational spring was defined at the ends of the columns. Properties of the plastic end-hinges were defined such that the shear backbone for the columns followed backbone A described in Section 7.5.2.

While Figure 7-19 compares the data from Test1 with the shear hysteretic response of the analytical model using backbone A for the columns, Figure 7-20 demonstrates the behaviour of the analytical model for Test2. As discussed in Section 7.5.1, using ASCE-41 effective stiffnesses resulted in higher estimation of stiffness for the columns of the analytical model for both tests. Therefore, the shear hysteretic response of the columns from the analytical model did not match the test data very well. It is also observed that the shear failure of first-story columns of specimen MCFS were estimated at noticeably lower drift ratios.

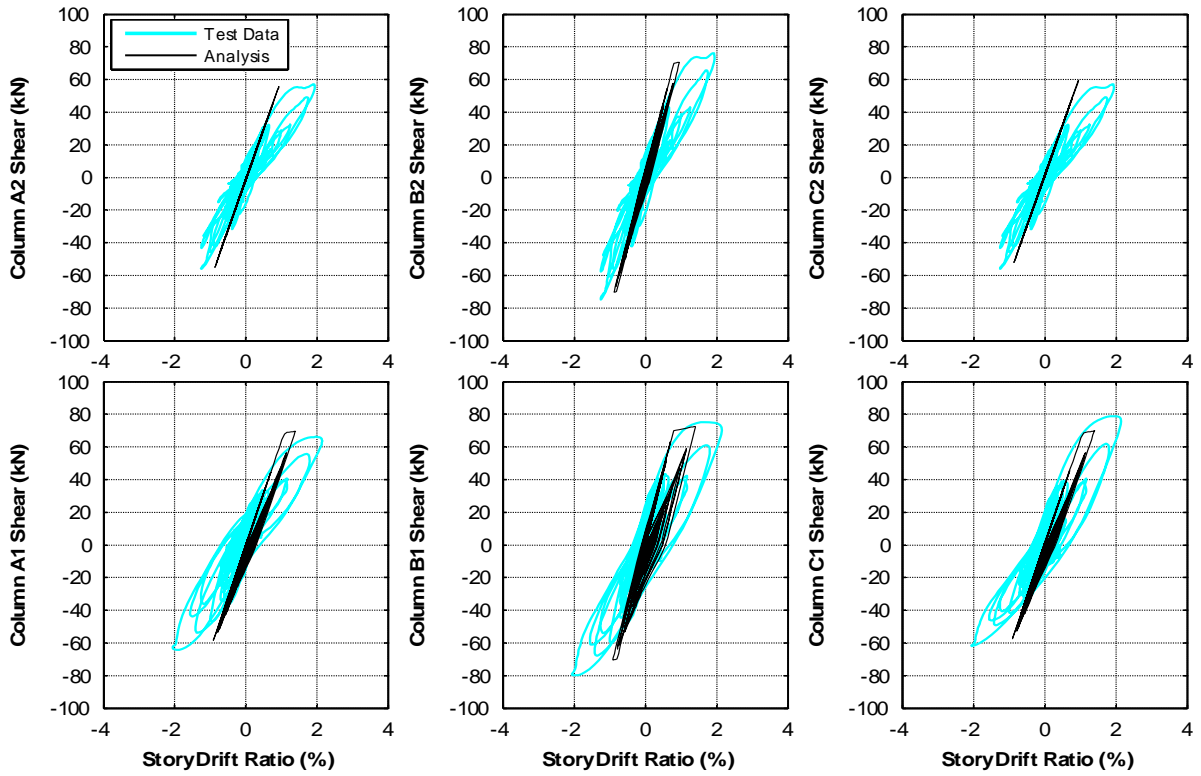


Figure 7-19. Shear hysteretic response of analytical model using elastic columns with end lumped-plasticity, ASCE-41 backbone (specimen MCFS, Test1)

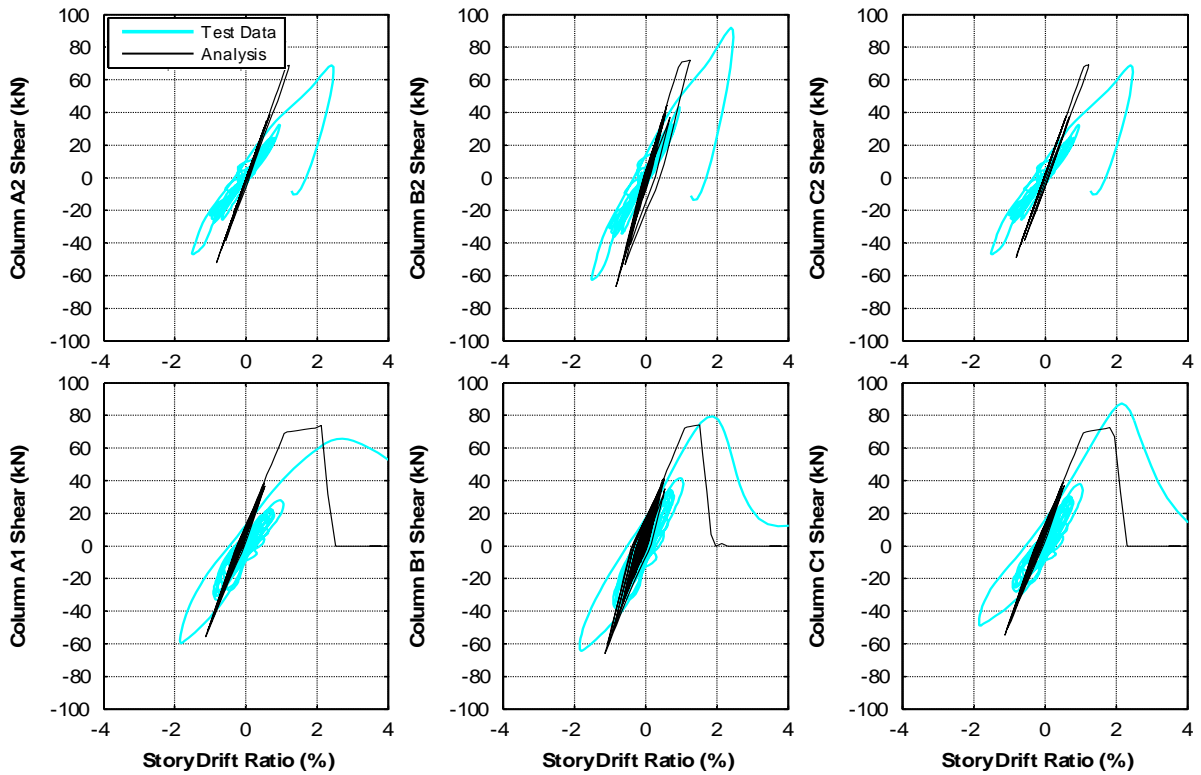


Figure 7-20. Shear hysteretic response of analytical model using elastic columns with end lumped-plasticity, ASCE-41 backbone (specimen MCFS, Test2)

7.7.2 Analytical Model with Proposed Backbone

In order to evaluate the performance of the proposed backbone, nonlinear dynamic analyses for the tests were carried out here and shear hysteretic response of the columns from the analyses are compared with the data from Test1 and Test2 in Figure 7-21 and Figure 7-22, respectively. It is observed that the proposed model adequately captured the overall behaviour of first-story columns (Figure 7-21) and their effective stiffnesses. Yielding and maximum drifts from the analyses were also well-matched with the test results. Although the model was not able to capture the yielding of the second-story exterior columns, the elastic stiffnesses obtained for these columns are in agreement with the test data. Figure 7-22 demonstrates that the proposed model predicted the column drifts at onset of shear strength degradation relatively well. However, it is observed that the columns peak shear strengths for column B1 and C1 were underestimated, while the peak shear in column A1 was overestimated by the proposed model. As shown in Figure 7-21, the analytical model detected shear strength degradation for column B1 around 2% drift ratio in the positive direction of Test1. Such strength degradation contributed in lowering shear strength estimated for column B1 during Test2. It should be noted that even the most complex model with fibre sections and shear and axial limit curves (Section 6.3.2) was not able to precisely capture the peak shear strength for column B1 during Test2 (Figure 6-19). It is also observed that the effective stiffnesses for the second-story columns of the analytical model are greater than those for the actual columns. This can be explained by the observations from the Test1, where the proposed model was not able to capture the softening of stiffness for second-story columns. Therefore, the effective stiffness of these columns remained unchanged during the analysis for Test2.

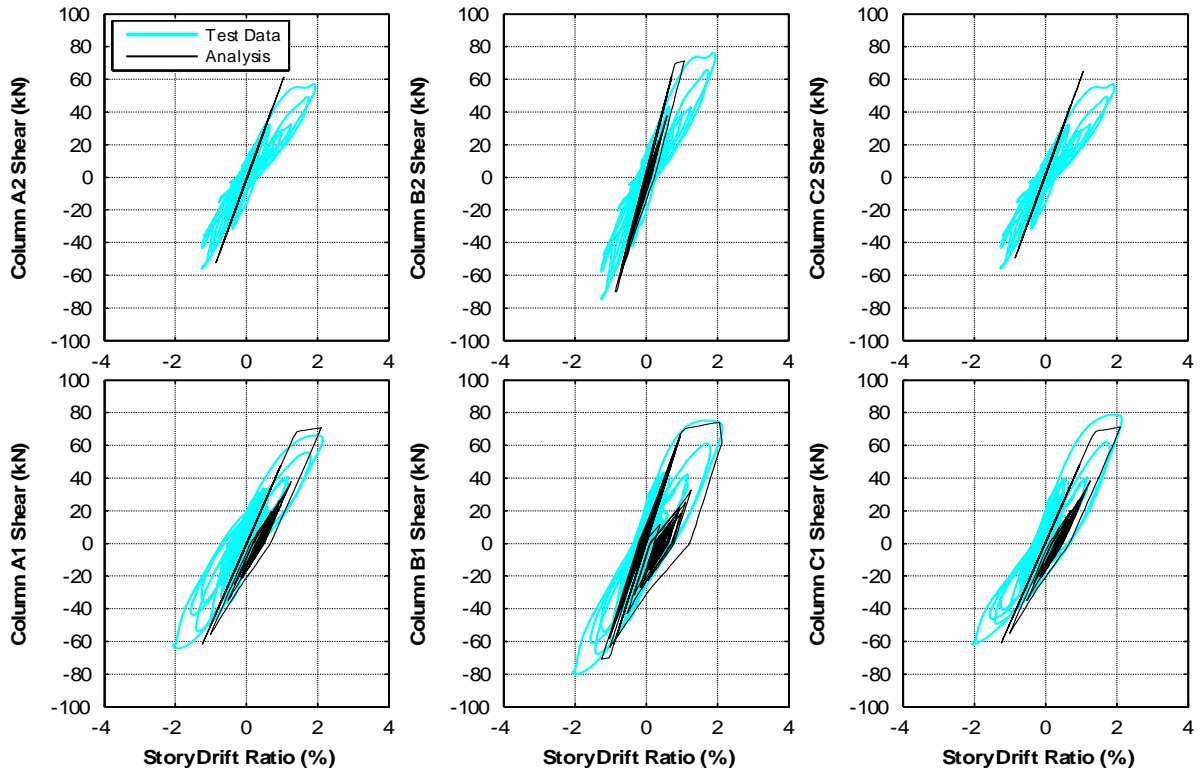


Figure 7-21. Shear hysteretic response of proposed model using elastic columns with end lumped-plasticity (specimen MCFS, Test1)

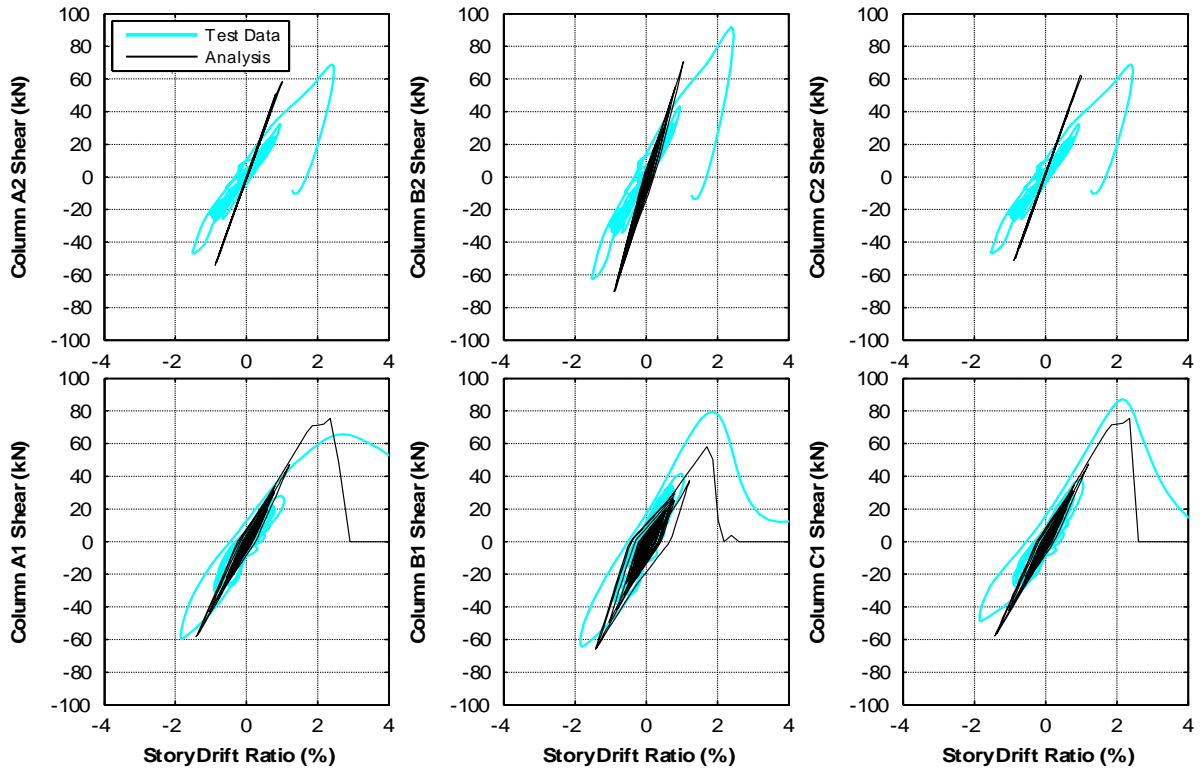


Figure 7-22. Shear hysteretic response of proposed model using elastic columns with end lumped-plasticity (specimen MCFS, Test2)

Comparison of results shown in the current and previous sections confirms that ASCE-41 recommended equation for effective stiffness of columns (Equation 5.1) results in higher effective stiffness for columns, and must be modified to account for the location of column ductility demand. It is also observed that the plastic rotation angles in Table 6-8 of ASCE-41 for end-hinges were properly defined for columns with *Condition ii*. However, the values recommended for *Condition iii* are very conservative and should not be employed for a column with limited flexural behaviour, even though the column falls into that category due to its axial load condition.

CHAPTER 8. CONCLUSIONS AND FUTURE WORK

8.1 Summary

Dynamic behaviour of non-seismically detailed reinforced concrete frames up to the point of collapse was investigated, both experimentally and analytically, in this study. Several unexplored factors influencing collapse of existing reinforced concrete frames, such as high axial load in non-ductile columns and dynamic impact of upper stories were considered in the research. Furthermore, influence of unconfined joints on overall response of non-ductile frames and distribution of lateral demand to the structural elements was investigated in this work.

Considering the very limited number of dynamic collapse tests and lack of sufficient data, the shaking table tests in this study were designed to provide data on degradation of shear and axial load strength of non-ductile reinforced concrete columns and unconfined joints, and to observe consequential redistribution of shear and axial loads to the rest of the frame system. Such benchmark test data can be used for critical validation and improvement of models used for the assessment of existing reinforced concrete frames.

The experimental part of this study included the construction and dynamic testing to collapse of four planar reinforced concrete frames with two bays and two stories. Figure 8-1 describes the four shaking table specimens. Details of design, construction and test setup for the tests were described in Chapter 3.

| | |
|---|---|
| <p>Specimen MCFS: <u>M</u>oderate Axial Load <u>C</u>onfined Joints <u>F</u>lexure-<u>S</u>hear Columns</p> | <p>Specimen HCFS: <u>H</u>igh Axial Load <u>C</u>onfined Joints <u>F</u>lexure-<u>S</u>hear Columns</p> |
| <p>Specimen MUFS: <u>M</u>oderate Axial Load <u>U</u>nconfined Joints <u>F</u>lexure-<u>S</u>hear Columns</p> | <p>Specimen MUF: <u>M</u>oderate Axial Load <u>U</u>nconfined Joints <u>F</u>lexure Columns</p> |

Figure 8-1. Shaking table tests

All the specimens were subjected to a scaled horizontal component from a ground motion recorded during the 1999 Chi-Chi earthquake in Taiwan. The input motion for the shaking table was scaled to different amplitudes and the specimens were subjected to a series of such input motions up to the point of collapse. The main dynamic tests imparted on the specimens included a half-yield level dynamic test and two high intensity dynamic tests with peak input amplitudes of approximately 1.1g and 1.35g, denoted as Test1 and Test2, respectively. While none of the specimens suffered from shear or axial failure of columns during Test1, all specimens with non-ductile columns collapsed when subjected to the 1.35g input motion (Test2). The intensity of input motion was increased to 1.62g for an additional test (Test3) on specimen MUF with ductile columns and non-ductile joints; however, the specimen did not collapse even during this high intensity shaking. Failure modes were

different for the specimens, where a combination of column shear and axial failures, formation of plastic hinges, and joint failures caused collapse of the specimens.

In the analytical part of this study, the behaviour of the specimens was simulated employing OpenSEES software (2009). Available analytical models for simulating the behaviour of unconfined joints and models for predicting shear and axial failure of non-ductile columns were evaluated by comparing the results from the analyses with the data obtained from the experimental phase of this research. While results from such detailed analytical models were compared with test data, simplified models which can be easily used by engineers for assessment of existing reinforced concrete buildings were evaluated and refinement to the current rehabilitation standard (ASCE-41, 2008) was proposed.

8.2 Original Contributions from the Research

While the experimental phase of this research took place at the National Center for Research on Earthquake Engineering (NCREE) in Taiwan, the author was responsible for the conceptual and detailed design of the specimens and lateral supporting frame, test setup and design, instrumentation, data processing, and the comprehensive and simplified analyses discussed in this dissertation.

As discussed in Chapters 1 and 2, very few shaking table tests have been performed on reinforced concrete frames up to the point of collapse. Even those rare dynamic collapse tests have mostly focused on the performance of one specific component (columns) and only considered relatively low gravity loads (Elwood, 2002, Ghannoum, 2007, Wu et al., 2009). All the previously tested specimens included ductile columns to allow for gravity load redistribution, which could affect the overall response of the specimen.

Not only were the above-mentioned limitations overcome in the current study, but several other issues were also investigated through the experimental and analytical research described in this dissertation. The original research contributions from this study include the followings:

- Testing four specimens with similar lateral demands and geometries, but different detailing of columns and beam-column joints provided the opportunity to assess the effects of variation in element specifications on behaviour of structural elements and collapse prediction of concrete frames.
- The comprehensive data on collapse performance of non-ductile concrete frames, collected during the tests, is valuable for verification of current linear and nonlinear models and future model development for non-ductile concrete components.
- The unique test setup (see Chapter 3 for details) provided the possibility to study several unexplored issues. The pre-stressing axial load system allowed for high column axial load up to $0.4A_gf'_c$. The inertial-mass system designed for this study enabled the simulation of the upper stories and their influence on overall behaviour of the frame. Including supplementary support beams in the lateral supporting system allowed the specimens to experience complete collapse while ensuring safety and protection of the shaking table equipments.
- Several observations from the experimental tests provide a better understanding of the behaviour of structural elements of non-ductile reinforced concrete frames. For instance:

- Despite the expectation of failure of columns at lower drifts for specimens with high axial load, test data for specimen HCFS demonstrates that higher axial load on the columns of a frame can result in a lower beam to column strength ratio, leading to larger beam deformations and changes in the distribution of deformations in the frame. This may also in turn change the failure mode of the frame.
 - As the axial load on a column increases, drifts at onset of shear and axial failure of the column become closer to each other. Furthermore, the rate at which axial load resistance is lost beyond the point of axial failure is faster for columns with higher axial load.
 - Based on observations from the experimental tests described in this work, likelihood of collapse of a frame due to failure of unconfined joints is lower than collapse due to failure of non-ductile columns.
- Limitations, weaknesses, and strengths of existing analytical models for predicting the behaviour of non-ductile reinforced concrete frames were investigated in detail. While existing failure models for non-ductile columns provide a reasonable estimation of points shear and axial failure, they are drift-based and should be refined to account for the rotation at the column ends.
 - Refinement to provision from the current rehabilitation guideline (ASCE, 2008) on effective stiffness of columns in multi-story frames was proposed in this work.
 - A simplified analytical model that can be adopted in engineering practice for assessing columns of existing reinforced concrete buildings was proposed in this study.

8.3 Conclusions

8.3.1 Results from Experimental Tests

Results from the shaking table tests indicated that the behaviour of the specimens were dependent on the axial stress on the columns. Axial load in column B1 of specimen HCFS at the point of shear failure was 1.6 times the axial load in the corresponding column of specimen MCFS. Test data demonstrated that the gap between drift ratios at shear and axial failure of column B1 of specimen MCFS was larger than the corresponding column of specimen HCFS. On the other hand, it was observed that the shortening after axial failure of the column from specimen HCFS was faster than specimen MCFS. This caused different damage patterns and collapse modes for specimens MCFS and HCFS. Unlike specimen MCFS, specimen HCFS suffered from damage in both levels.

Most of the joint sub-assemblages tested in literature (e.g. Clyde et al., 2000, and Walker, 2001) were designed with strong columns and weak beams which is typical of new design. Consequently, it has been commonly assumed that the joint demands are related to beam strength. However, experimental test results for specimens MUF and MUFS with unconfined joints demonstrated that inclined cracks in the joints extended into the columns rather than the beams due to the weak-column-strong-beam mechanism typical of older concrete frames. This observation illustrates that the joint demands in older buildings are more related to column strength than the beam strength. It was also experimentally demonstrated that transverse beams can provide additional confinement to beam-column joints by restraining the development of shear cracks on the confined face of the panel zone.

Opening and closing of cracks at first-story joints during testing of MUF and MUFS resulted in localization of shear deformation at the joints. Therefore, these unconfined joints

did not allow shear to be fully developed in first-story columns by accommodating much of the deformation demands and reducing the moment at the top of the columns.

It was observed that the undamaged top portion of the joint, due to confinement provided by the relatively deep slab, can provide a partially-fixed condition for the base of upper-story columns. When combined with the fully confined joints in the second story, this resulted in stiffer end conditions for the second-story columns of specimen MUFS compared with the first-story columns, contributing to the shear and axial failure of the second-story columns and collapse of the frame.

8.3.2 Results from Analytical Studies

Comparison of the test data with analytical models indicated that the yield displacement, stiffness, and flexural strength of the columns could be adequately estimated, if bar-slip springs are added to fibre section models. Although the drift-capacity models described in Chapter 2 (Equations 2.1, and 2.2), provided a reasonable estimate of the column drifts at onset of shear and axial failure, they must be used cautiously for columns with higher axial load. For such columns, the drifts at onset of shear and axial failure become very close, and therefore, the models must precisely predict the onsets of shear and axial failure, otherwise, the behaviour of the column, and the overall building frame, may not be captured correctly.

Satisfactory results from simulating the behaviour of unconfined joints in specimens MUF and MUFS by using scissors model (Alath and Kunnath, 1995) demonstrated that such a simple model can be employed to account for the nonlinear shear deformations in the joint and the impact on the frame response.

Although sophisticated modeling for capturing column shear and axial failures may result in satisfactory estimation of behaviour of the structural elements and the overall building

frame, simplified modeling is more appealing in engineering practice. Therefore, simplified analytical models with elastic column elements and lumped rotational hinges at the ends were evaluated. A refined shear backbone for simplified modeling was introduced. While the model for effective stiffness of columns was refined, the modeling parameters suggested by ASCE-41 for end hinges to define the other branches of shear backbone were examined and recommendations on selecting such parameters were proposed in this study.

In ASCE-41 a column must be classified in one of three conditions dependent on the anticipated failure mode. ASCE-41 recommends using the minimum plastic rotation limits where more than one of the conditions occurs for a column. The plastic rotation limits are related to the axial load in the columns. Exterior columns in a frame may experience significant difference in axial load in opposite directions of shaking due to overturning effects which may lead to classifying such columns as shear critical (*Condition iii*). This study showed that such classification is very conservative. While ASCE-41(2008) is currently silent about the axial load that must be used for selecting the column condition, it was proposed in this study that the maximum expected axial loads due to gravity and earthquake loads must be used for choosing the condition for columns. Such refinement to the guideline will result in more realistic plastic rotation limits for columns.

The recommended equation by ASCE-41 for effective stiffness of columns results in increasing effective stiffness ratios (EI_{eff}/EI_g) for increasing axial loads. Since the axial loads in the columns of upper stories of a frame are normally lower, this means that the effective stiffness should be reduced for those columns. Such results can be acceptable when all the columns along the height of a frame experience similar level of demand. However, observations of damage after earthquakes illustrate that the columns in higher stories

experience less demand and damage. Therefore, for elastic models, it may be appropriate to increase the effective stiffness for columns of upper stories to achieve a better estimate of the displacement profile for the building frame. A model is proposed in this thesis based on the results of the shaking table tests.

Being easy to measure and calculate, story drift ratio has been commonly used by engineers for design or assessment of columns in a frame as an indicator of lateral demand on the structure. Therefore, it was vastly employed in the course of the current research. However, story drift ratio includes deformations in all connecting components, such as joints and beams, in addition to the deformations in the columns. Consequently, an alternative approach is to employ column chord rotation instead of drift ratio. It was shown in this study that chord rotation can be a better measurement of demand on a column than drift ratio, particularly for the columns with lower axial load or columns connected to unconfined joints.

8.4 Future Research

Several topics requiring further study were identified during the course of this research:

1. It was observed in this study that the likelihood of collapse of a frame due to failure of unconfined joints is lower than failure of non-ductile columns. Further experimental and analytical studies are required to generalize this hypothesis for multi-story frames.
2. As concluded from this study, plastic hinge rotation of columns and chord rotation can provide a better measurement of lateral demand on the columns compared with drift ratio. While additional test data on column end rotation is required, capacity models should be updated to be based on rotation rather than drift. Further

investigations are required on effects of axial load on chord rotation and relations between chord rotation and shear and axial failure of non-ductile columns.

3. Since the behaviour of frames near the point of collapse are complicated and dynamic tests up to that point are limited, further test data are required to better understand mechanisms that control shear and axial failures in non-ductile columns and refine the models for the drift at shear and axial failure of such columns. Particular attention needs to be given to columns with high axial load.
4. Experimental and analytical studies are required to investigate the contribution of out-of-plane frames to the capacity of a building for resisting collapse. The redistribution of forces within a 3D building frame system should also be examined.
5. The drift capacity models should be extended to account for the effects of bidirectional bending and shear.
6. Further dynamic tests should be performed on column and frame systems with a wide range of ground motions to improve quantification of earthquake demands and to investigate the influence of the type of ground motion on the shear and axial load failure of columns, and the response of the building frames prior to collapse.
7. In order to accurately predict the point of shear and axial load failure of columns, nonlinear analytical models should be improved to achieve a better prediction of the drift demands.

8. Analytical models for non-ductile reinforced concrete columns should be developed and implemented in OpenSees based on the mechanics instead of the empirical drift capacity models.
9. Further studies are required to quantify the influence of ductility demand on effective stiffness of columns in a building frame and obtain an appropriate coefficient for increasing the effective stiffness of columns in higher stories.
10. The proposed backbone for ASCE-41 should be compared with additional experimental data to confirm its applicability.

REFERENCES

- ACI 2008. Building Code Requirements for Structural Concrete *ACI 318-08*. Farmington Hills, USA: American Concrete Institute
- ALATH, S. & KUNNATH, S. K. 1995. Modeling Inelastic Shear Deformation in RC Beam-Column Joints. Proceedings of the 10th Conference on Engineering Mechanics. Part 2 (of 2), Boulder, CO. 21-24.
- ALIRE, D. A. 2002. *Seismic Evaluation of Existing Unconfined Reinforced Concrete Beam-Column Joints*. MSCE, University of Washington.
- ALTOONTASH, A. 2004. *Simulation and Damage Models for Performance Assessment of Reinforced Concrete Beam-Column Joints*. PhD, Stanford University.
- ARTEMIS 2010. ARTeMIS Extractor Pro. 5.0 (Trial Version) ed.: Structural Vibration Solutions
- ASCE 2008. Seismic Rehabilitation of Existing Buildings. *ASCE/SEI 41, Supplement 1*. Reston, VA: American Society of Civil Engineers.
- ASCHHEIM, M. & MOEHLE, J. P. 1992. Shear Strength and Deformability of RC Bridge Columns Subjected to Inelastic Displacements. *UCB/EERC 92/04, University of California, Berkeley*.

- BERES, A., PESSIKI, S. P., WHITE, R. N. & GERGERLY, P. 1996. Implications of Experiments on the Seismic Behavior of Gravity Load Designed RC Beam-to-Column Connections. *Earthquake Spectra (EERI)* 12, 185-198.
- BERES, A., WHITE, R. & GERGELY, P. 1992. Seismic Behavior of Reinforced Concrete Frame Structures with Non-Ductile Details: Part I-Summary of Experimental Findings of Full Scale Beam-Column Joint Tests. *Technical Report NCEER*, 92.
- BERRY, M. P. & EBERHARD, M. O. 2007. Performance Modeling Strategies for Modern Reinforced Concrete Columns. *Pacific Earthquake Engineering Research Center Report*. Berkeley, CA: University of California, Berkeley.
- BIDDAH, A. & GHOBARAH, A. 1999. Modeling of Shear Deformation and Bond Slip in Reinforced Concrete Joints. *Structural Engineering and Mechanics*, 7, 413.
- BONACCI, J. & PANTAZOPOULOU, S. 1992. Consideration of Questions about Beam-Column Joints. *ACI Structural Journal*, 89, 27-36.
- BONACCI, J. & PANTAZOPOULOU, S. 1993. Parametric Investigation of Joint Mechanics. *ACI Structural Journal*, 90 (1), 61-71.
- CALVI, G. M., MAGENES, G. & PAMPANIN, S. 2002. Experimental Test on a Three Storey RC Frame Designed for Gravity Only. *In: Proceedings of the Twelfth European Conference on Earthquake Engineering*, London, UK.
- CELIK, O. C. & ELLINGWOOD, B. R. 2008. Modeling Beam-Column Joints in Fragility Assessment of Gravity Load Designed Reinforced Concrete Frames. *Journal of Earthquake Engineering*, 12, 357-381.
- CHEUNG, P., PAULAY, T. & PARK, R. 1991. Mechanisms of Slab Contributions in Beam-Column Sub-assemblages. *Design of beam-column joints for seismic resistance*, ACI SP-123, 259-289.

- CLYDE, C., PANTELIDES, C. & REAVELEY, L. 2000. Performance-Based Evaluation of Exterior Reinforced Concrete Building Joints for Seismic Excitation. *Pacific Earthquake Engineering Research Report*. Berkeley, CA: University of California, Berkeley.
- COMARTIN, C. 1995. Guam Earthquake of August 8, 1993 Reconnaissance Report. *Earthquake Spectra*.
- DE SOUZA, R. M. 2000. *Force-based Finite Element for Large Displacement Inelastic Analysis of Frames*. Ph.D. Dissertation, University of California, Berkeley.
- DOANGÜN, A. 2004. Performance of Reinforced Concrete Buildings During the May 1, 2003 Bingöl Earthquake in Turkey. *Engineering Structures*, 26, 841-856.
- EHSANI, M. & WIGHT, J. K. 1985. Exterior Reinforced Concrete Beam-to-Column Connections Subjected to Earthquake-Type Loading. *Journal of the American Concrete Institute*, 82, 492-499.
- ELMORSI, M., KIANOUSH, M. & TSO, W. 2000. Modeling Bond-Slip Deformations in Reinforced Concrete Beam-Column Joints. *Canadian Journal of Civil Engineering*, 27, 490-505.
- ELWOOD, K. 2002. *Shake Table Tests and Analytical Studies on the Gravity Load Collapse of Reinforced Concrete Frames*. PhD, University of California, Berkeley.
- ELWOOD, K., EERI, M., MATAMOROS, A., WALLACE, J., LEHMAN, D., HEINTZ, J., MITCHELL, A., MOORE, M., VALLEY, M. & LOWES, L. 2007. Update to ASCE/SEI 41 Concrete Provisions. *Earthquake Spectra*, 23, 493.
- ELWOOD, K. J. & EBERHARD, M. O. 2009. Effective Stiffness of Reinforced Concrete Columns. *ACI Structural Journal*, 106 (4), 476-484.

- ELWOOD, K. J. & MOEHLE, J. P. 2005. Drift Capacity of Reinforced Concrete Columns with Light Transverse Reinforcement. *Earthquake Spectra*, 21, 71-89.
- ELWOOD, K. J. & MOEHLE, J. P. 2008. Dynamic Collapse Analysis for a Reinforced Concrete Frame Sustaining Shear and Axial Failures. *Earthquake Engineering & Structural Dynamics*, 37, 991-1012.
- FLEURY, F., REYNOUARD, J. & MERABET, O. 2000. Multicomponent Model of Reinforced Concrete Joints for Cyclic Loading. *Journal of Engineering Mechanics*, 126, 804.
- FRENCH, C. & MOEHLE, J. 1991. Effect of Floor Slab on Behavior of Slab-Beam-Column Connections. *Design of Beam-Column Joints for Seismic Resistance, SP-123, American Concrete Institute, Farmington Hills, Mich, 225-258.*
- GHANNOUM, W. M. 2007. *Experimental and Analytical Dynamic Collapse Study of a Reinforced Concrete Frame with Light Transverse Reinforcement*. PhD, University of California, Berkeley.
- GILBERTSEN, N. & MOEHLE, J. 1980. Experimental Study of Small-Scale R/C Columns Subjected to Axial and Shear Force Reversals. *Civil Engineering Studies SRS-481*.
- HALL, J. 1995. Northridge Earthquake of January 17, 1994 Reconnaissance Report. *Earthquake Spectra*, 11, 1.
- HOFFMANN, G., KUNNATH, S., REINHORN, A. & MANDER, J. 1992. Gravity-Load-Designed Reinforced Concrete Buildings: Seismic Evaluation of Existing Construction and Detailing Strategies for Improved Seismic Resistance. *Technical Report NCEER*, 92.
- IMBSEN, C. C. 2002. XTRACT Software, Cross-Section Analysis Program for Structural Engineers. 2.6.2 ed.: Imbsen and associates, Inc.

- KATO, D. & OHNISHI, K. 2002. Axial Load Carrying Capacity of R/C Columns Under Lateral Load Reversals. *Third US-Japan Workshop on Performance Based Earthquake Engineering Methodology for Reinforced Concrete Building Structures, Seattle, WA, PEER Report*. Berkeley: Pacific Earthquake Engineering Research Center.
- KITAYAMA, K., OTANI, S. & AOYAMA, H. 1991. Development of Design Criteria for RC Interior Beam-Column Joints. *Design of Beam-Column Joints for Seismic Resistance*, ACI SP-123, 97-123.
- KREGER, M. E. & LINBECK, L. 1986. Behavior of Reinforced Concrete Columns Subjected to Lateral and Axial Load Reversal. *Proceeding of Third U.S. National Conference on Earthquake Engineering*
- LAM, S., WU, B., WONG, Y., WANG, Z., LIU, Z. & LI, C. 2003. Drift Capacity of Rectangular Reinforced Concrete Columns with Low Lateral Confinement and High-Axial Load. *Journal of Structural Engineering*, 129, 733.
- LEE W.H.K., S. T. C., KUO K.W., CHEN, K.C., WU, C.F. CWB 2001. Free-field Strong-motion Data from the 921 Chi-Chi Earthquake. Taipei, Taiwan: Seismological Observation Center, Central Weather Bureau, .
- LEHMAN, D. E. & MOEHLE, J. P. 1998. Seismic Performance of Well-Confined Concrete Bridge Columns. *Pacific Earthquake Engineering Research Center Report, University of California, Berkeley, PEER-1998/01*, 316.
- LEJANO, B., SHIRAI, N., ADACHI, H., ONO, A. & AMITU, S. 1992. Deformation Properties and Shear Resistance Mechanism of Reinforced Concrete Column with High and Fluctuating Axial Force. *In: Earthquake Engineering, Tenth World Conference, Balkema, Rotterdam*. Taylor & Francis, 3007-3012.

- LOWES, L., MITRA, N. & ALTOONTASH, A. 2003. A Beam-Column Joint Model for Simulating the Earthquake Response of Reinforced Concrete Frames. *University of California, Berkeley*.
- LOWES, L. N. & ALTOONTASH, A. 2003. Modeling Reinforced-Concrete Beam-Column Joints Subjected to Cyclic Loading. *Journal of Structural Engineering*, 129 (12), 1686-1697.
- LYNN, A. C. 2001. *Seismic Evaluation of Existing Reinforced Concrete Building Columns*. Ph.D. dissertation, University of California, Berkeley.
- MANDER, J. B., PRIESTLEY, M. J. N. & PARK, R. 1988. Theoretical Stress-Strain Model for Confined Concrete. *Journal of Structural Engineering*, 114 (8), 1804-1826.
- MATHWORKS 2007. Matlab, The Language of Technical Computing. 7.4 ed.
- MATTHEWS, T. W. 2007. *Explosive Testing to Assess Dynamic Load Redistribution in a Reinforced Concrete Frame Building*. MASC, The University of British Columbia.
- MATTOCK, A. 1988. Discussion. *Prestressed Concrete Institute Journal*, 33, 165-166.
- MATTOCK, A. & HAWKINS, N. 1972. Shear Transfer in Reinforced Concrete-Recent Research. *Pre-stressed Concrete Institute Journal*, 17, 55-75.
- MELEK, M., WALLACE, J. W. & CONTE, J. P. 2003. Experimental Assessment of Columns with Short Lap Splices Subjected to Cyclic Loads. *Pacific Earthquake Engineering Research Center Report, PEER*. Berkeley, CA: University of California, Berkeley.
- MINOWA, C., OGAWA, N., HAYASHIDA, T., KOGOMA, I. & OKADA, T. 1995. Dynamic and Static Collapse Tests of Reinforced Concrete Columns. *Nuclear Engineering and Design*, 156, 269-276.

- MITCHELL, D., DEVAL, R., SAATCIOGLU, M., SIMPSON, R., TINAWI, R. & TREMBLAY, R. 1995. Damage to Concrete Structures Due to the 1994 Northridge Earthquake. *Canadian Journal of Civil Engineering*, 22, 361-377.
- MOEHLE, J. & MAHIN, S. 1991. Observations on the Behaviour of Reinforced Concrete Buildings During Earthquakes, ACI Publication SP-127. *Earthquake-Resistant Concrete Structures: Inelastic Response and Design-Ghosh, SK (ed.)*.
- MOI 2009. Building Technical Regulations. Taipei, Taiwan: Construction and Planning Agency, Ministry of the Interior.
- MOSTAFAEI, H. & KABEYASAWA, T. 2007. Axial-Shear-Flexure Interaction Approach for Reinforced Concrete Columns. *ACI Structural Journal*, 104.
- OHUE, M., MORIMOTO, H., FUJII, S. & MORITA, S. 1985. The Behavior of R.C. Short Columns Failing in Splitting Bond-Shear Under Dynamic Lateral Loading. *Transactions of the Japan Concrete Institute*, 7, 293-300.
- OPENSEES. 2009. *Open System for Earthquake Engineering Simulation*. [Online]. Pacific Earthquake Engineering Research Center, university of California Available: <http://www.opensees.berkeley.edu>.
- OTANI, S. 1999. RC Building Damage Statistics and SDF Response with Design Seismic Forces. *Earthquake Spectra*, 15, 485-501.
- OUSALEM, H., KABEYASAWA, T. & TASAI, A. Year. Evaluation of Ultimate Deformation Capacity at Axial Load Collapse of Reinforced Concrete Columns. *In: 13th World Conference on Earthquake Engineering, 2004 Vancouver, B.C., Canada*.
- PAMPANIN, S., CALVI, G. & MORATTI, M. 2002. Seismic Behavior of RC Beam-column Joints Designed for Gravity Only. *In: Twelfth European Conference on Earthquake Engineering, London, UK*.

- PANTELIDES, C., HANSEN, J., NADAULD, J. & REAVELEY, L. 2002. Assessment of Reinforced Concrete Building Exterior Joints with Substandard Details. *PEERC Report*, 18, 1-013.
- PARK, R. 2002. A Summary of Results of Simulated Seismic Load Tests on Reinforced Concrete Beam-Column Joints, Beams and Columns with Substandard Reinforcing Details. *Journal of Earthquake Engineering*, 6, 147-174.
- PESSIKI, S. P., CONLEY, C. H., GERGELY, P. & WHITE, R. N. 1990. Seismic Behavior of Lightly Reinforced Concrete Column and Beam-Column Joint Details. *Technical Report NCEER-90-0014, National Center for Earthquake Engineering Research, State University of New York at Buffalo, Buffalo, NY.*
- PINHO, R. & ELNASHAI, A. S. 2000. Dynamic Collapse Testing of a Full-Scale Four Storey RC Frame. *ISSET Journal of Earthquake Technology*, 37, 143-164.
- PINTO, A., VARUM, H. & MOLINA, J. 2002. Experimental Assessment and Retrofit of Full-Scale Models of Existing RC Frames. *In: Twelfth European Conference on Earthquake Engineering*, London, UK.
- PRIESTLEY, M., CALVI, G. & KOWALSKY, M. 2007. *Displacement-Based Seismic Design of Structures*, Pavia, Italy, IUSS Press.
- PRIESTLEY, M. J. N., RANZO, G., BENZONI, G. & KOWALSKY, M. J. 1996. Yield Displacement of Circular Bridge Columns. *Caltrans Seismic Research Workshop, California Department of Transportation, Sacramento, CA*, 12.
- PRIESTLEY, M. J. N., VERMA, R. & XIAO, Y. 1994. Seismic Shear Strength of Reinforced Concrete Columns. *Journal of Structural Engineering*, 120, 2310-2329.

- PUJOL, S., RAMIREZ, J. A., AND SOZEN, M. A. 1999. Drift Capacity of Reinforced Concrete Columns Subjected to Cyclic Shear Reversals. *American Concrete Institute, Farmington Hills, Michigan*, SP-187, 255-274.
- SEZEN, H. 2002. *Seismic Behavior and Modeling of Reinforced Concrete Building Columns*. PhD, University of California, Berkeley.
- SEZEN, H., ELWOOD, K., WHITTAKER, A., MOSALAM, K., WALLACE, J. & STANTON, J. 2000. Structural Engineering Reconnaissance of the August 17, 1999 Earthquake: Kocaeli (Izmit), Turkey. *University of California, Berkeley*.
- SEZEN, H. & MOEHLE, J. 2004. Shear strength model for lightly reinforced concrete columns. *Journal of Structural Engineering*, 130, 1692.
- SEZEN, H. & SETZLER, E. J. 2008. Reinforcement Slip in Reinforced Concrete Columns. *ACI Structural Journal*, 105 (3), 280-288.
- SHIN, M. & LAFAVE, J. M. 2004. Modeling of Cyclic Joint Shear Deformation Contributions in RC Beam-Column Connections to Overall Frame Behavior. *Structural Engineering and Mechanics*, 18, 645-669.
- SHIN, Y. B. 2007. *Dynamic Response of Ductile and Non-Ductile Reinforced Concrete Columns*. PhD, University of California, Berkeley.
- SOZEN, M. A. & MOEHLE, J. P. 1990. Development and Lap-Splice Lengths for Deformed Reinforcing Bars in Concrete. *Report to the Portland Cement Association and Concrete Reinforcing Steel Institute*.
- SPACONE, E., FILIPPOU, F. C. & TAUCER, F. F. 1996a. Fiber Beam-Column Model for Nonlinear Analysis of R/C Frames: Part I. Formulation. *Earthquake Engineering & Structural Dynamics*, 25 (7), 711-725.

- SPACONE, E., FILIPPOU, F. C. & TAUCER, F. F. 1996b. Fiber Beam-Column Model for Nonlinear Analysis of R/C Frames: Part II. Application. *Earthquake Engineering & Structural Dynamics*, 25 (7), 727-742.
- TASAI, A. 2000. Residual Axial Capacity of Reinforced Concrete Columns during Shear Deterioration. *In: Second US-Japan Workshop on Performance-Based Earthquake Engineering Methodology for Reinforced Concrete Building Structures*, Sapporo, Japan. Pacific Earthquake Engineering Research Center, University of California, PEER, 257-267.
- THERMOU, G. E. & PANTAZOPOULOU, S. J. 2011. Assessment Indices for the Seismic Vulnerability of Existing R.C. Buildings. *Earthquake Engineering & Structural Dynamics*, 40 , 293-313.
- TOWNSEND, W. H. & HANSON, R. D. 1977. Reinforced Concrete Connection Hysteresis Loops. *ACI Publication SP53-13. Reinforced Concrete Structures in Seismic Zones.* , 351-370.
- UMEMURA, H. & ENDO, T. 1970. Report by Umemura Lab. Also in "A List of Past Experimental Results of Reinforced Concrete Columns" by Masaya H., Building Research Institute, Ministry of Construction. Japan. *Tokyo University*.
- WALKER, S. 2001. *Seismic Performance of Existing Reinforced Concrete Beam-Column Joints*. MSCE, University of Washington.
- WATANABE, F. & ICHINOSE, T. 1992. *Strength and Ductility of RC Members Subjected to Combined Bending and Shear*, New York, Elsevier Applied Science.
- WIGHT, J. K. & SOZEN, M. A. 1973. Shear Strength Decay in Reinforced Concrete Columns Subjected to Large Deflection Reversals. *Structural Research Series No. 403*, University of Illinois, Urbana.

- WU, C. L., KUO, W. W., YANG, Y. S., HWANG, S. J., ELWOOD, K. J., LOH, C. H. & MOEHLE, J. P. 2009. Collapse of a Non-Ductile Concrete Frame: Shaking Table Tests. *Earthquake Engineering & Structural Dynamics*, 38, 205-224.
- YAVARI, S., ELWOOD, K. J. & WU, C. L. 2009. Collapse of a non-ductile concrete frame: Evaluation of analytical models. *Earthquake Engineering & Structural Dynamics*, 38, 225-241.
- YOSHIMURA, M. & NAKAMURA, T. 2002. Intermediate-Story Collapse of Concrete Buildings. *In: Third U.S.-Japan Workshop on Performance-Based Earthquake Engineering Methodology for Reinforced Concrete Building Structures*, Seattle, Washington. PEER, Pacific Earthquake Engineering Research Center, University of California at Berkeley., 107-118.
- YOSHIMURA, M. & YAMANAKA, N. 2000. Ultimate Limit State of RC Columns. *In: Second U.S.-Japan Workshop on Performance-Based Earthquake Engineering Methodology for Reinforced Concrete Building Structures*, September 11-13, Sapporo, Japan. PEER, Pacific Earthquake Engineering Research Center, University of California at Berkeley., 313-326.
- YOUSSEF, M. & GHOBARAH, A. 2001. Modeling of RC Beam-Column Joints and Structural Walls. *Journal of Earthquake Engineering*, 5, 93-111.

APPENDICES

Appendix A. Specimen Drawings and Material Properties

A.1 As-built Specimen Drawings and Specifications

Four shaking table test specimens with similar geometry, but different specifications, were constructed conforming to the plans shown in Figure A-1 through Figure A-8. The reinforcement met the following specifications:

- All reinforcement, with the exception of the column ties, complied with Taiwanese standards with specifications very similar to ASTM A706 for grade 60.
- Plain reinforcing 5mm smooth bar was used for the column transverse reinforcement.
- All stirrup hooks within the footings and beams were 135° bend plus 6 bar diameters extension.
- The column tie hooks were 90° bend. The tie spacing in columns of specimen MUF was 1/3 of the columns in other specimens to provide proper confinement.
- The concrete clear cover over the transverse reinforcement in the columns was 17 mm.
- Normal-weight concrete was cast in four stages: footing, first story, second story, and top column stubs. The construction joints were located at the base of the columns.

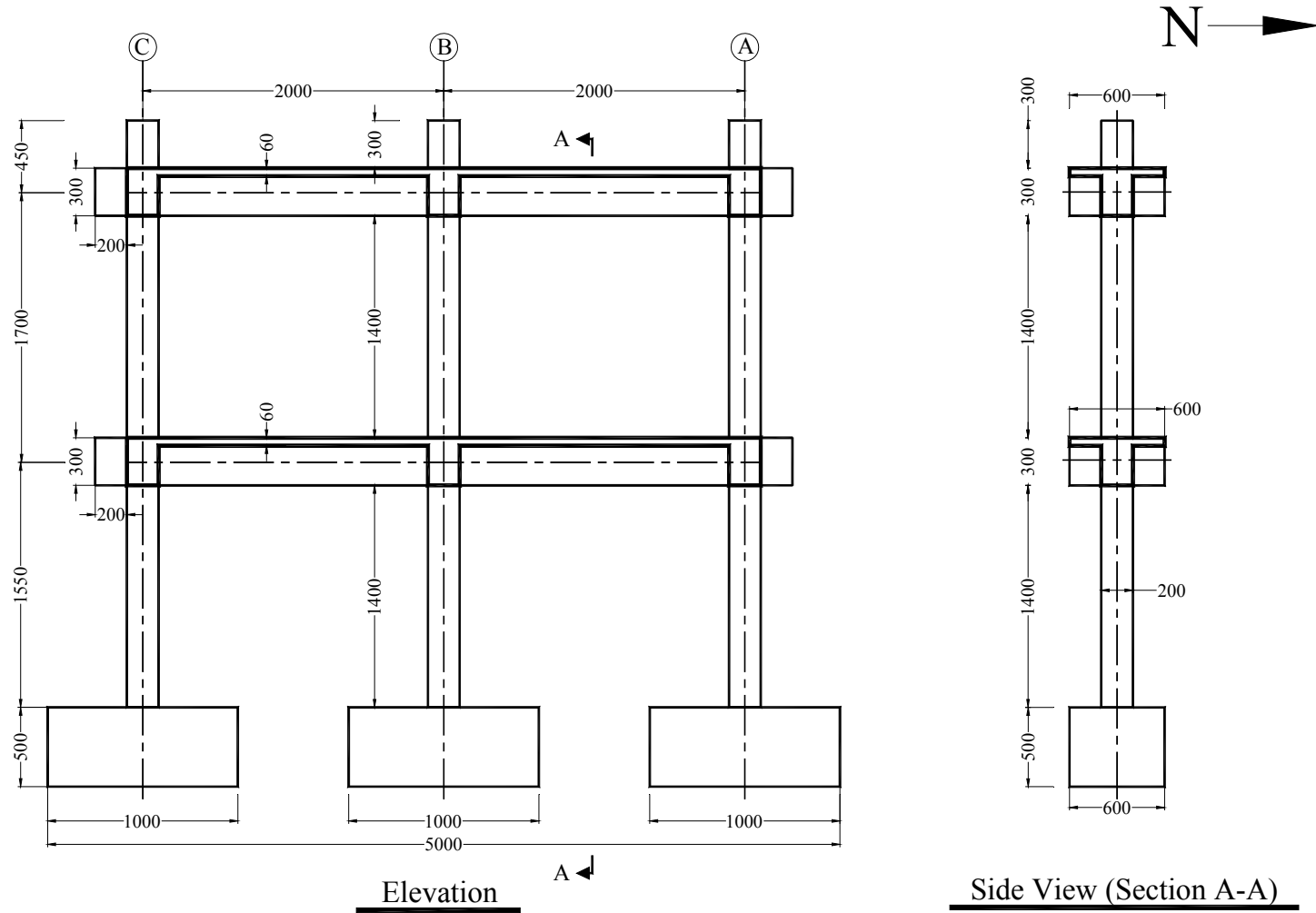


Figure A-1. Specimens MCFS and HCFS

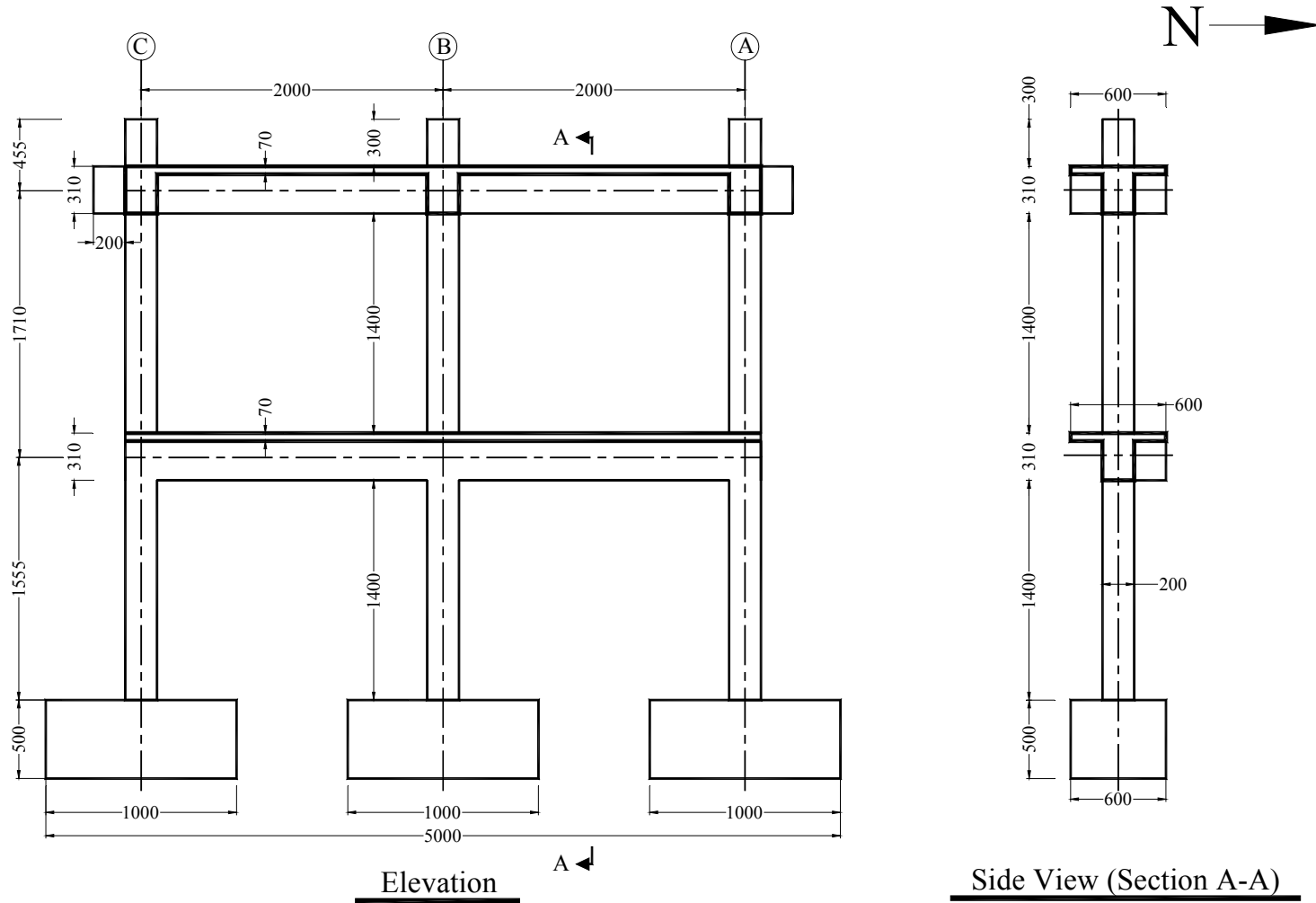


Figure A-2. Specimens MUF and MUFS

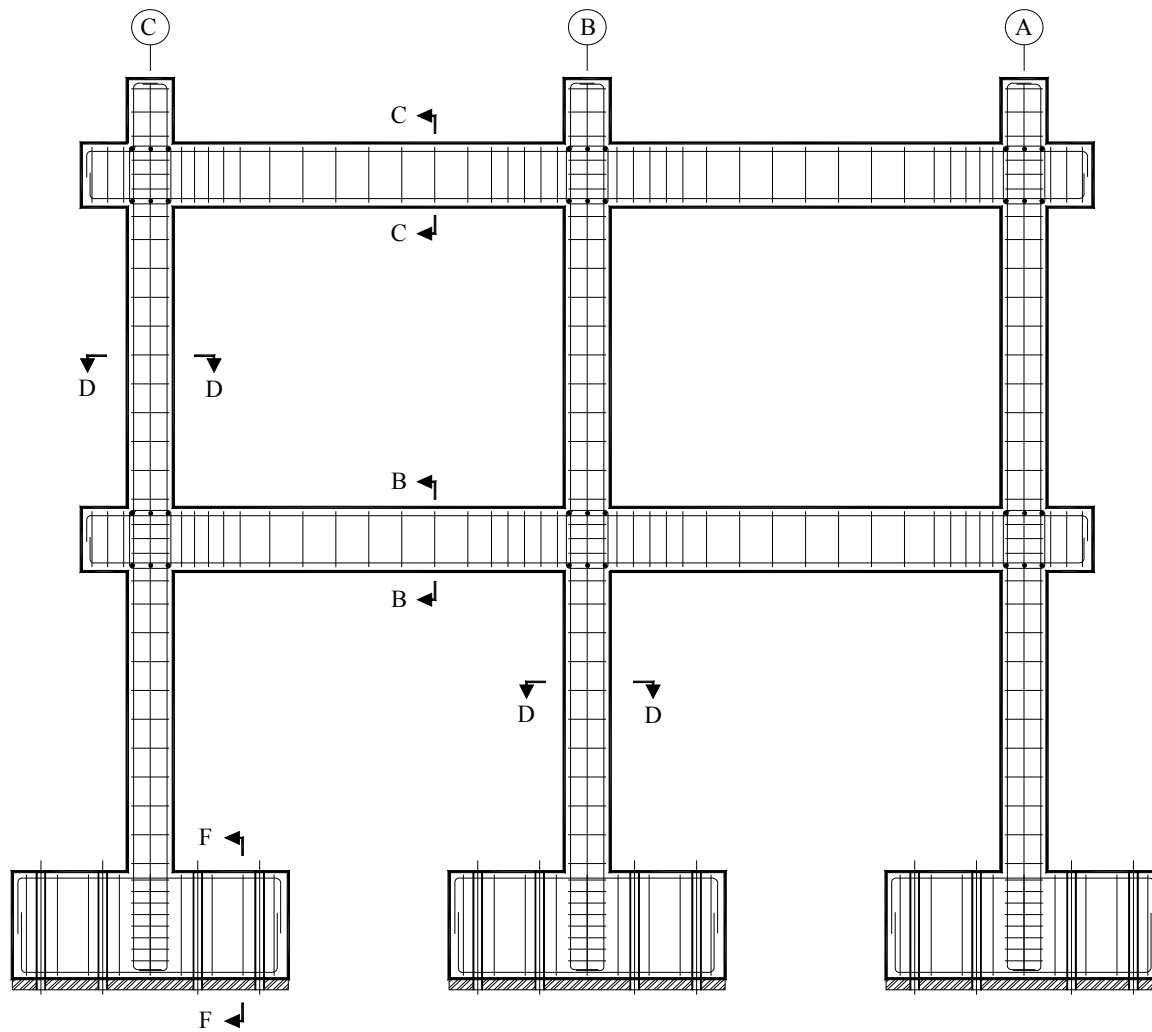


Figure A-3. Reinforcement layout (elevation), specimens MCFS and HCFS.

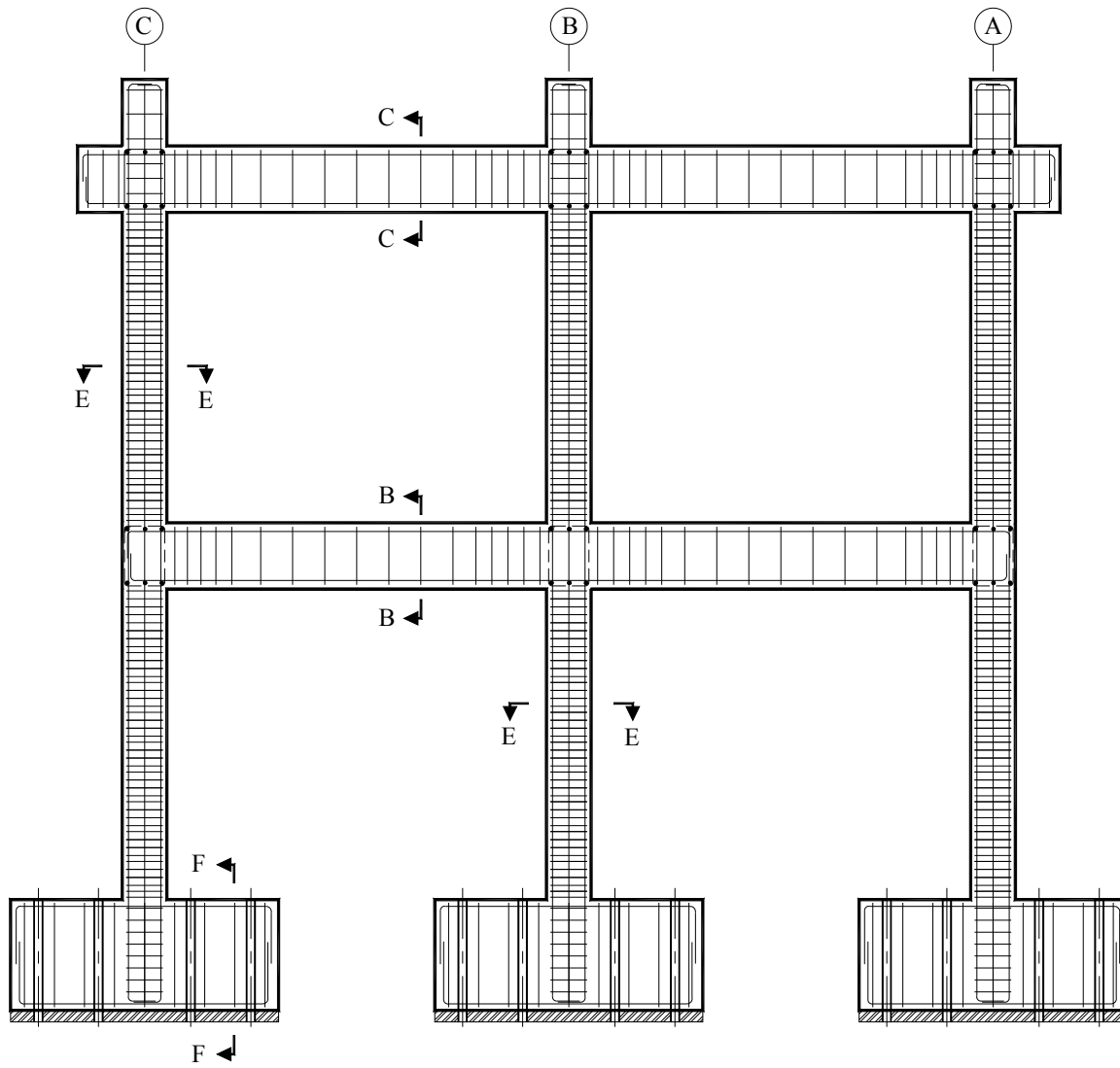


Figure A-4. Reinforcement layout (elevation), specimens MUF.

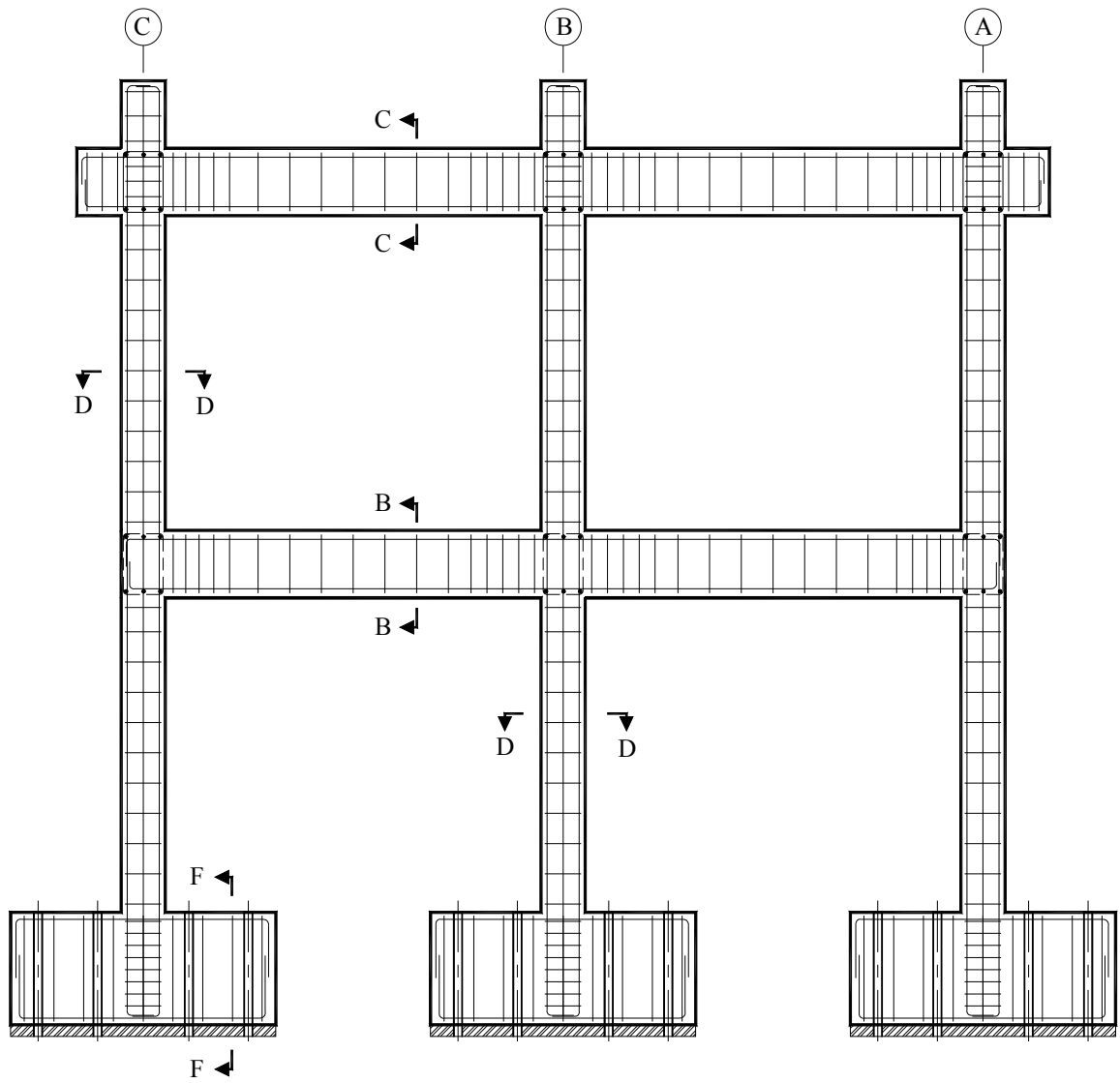
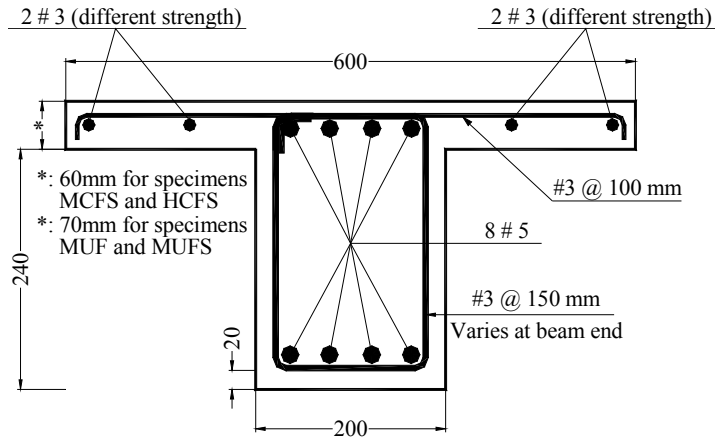
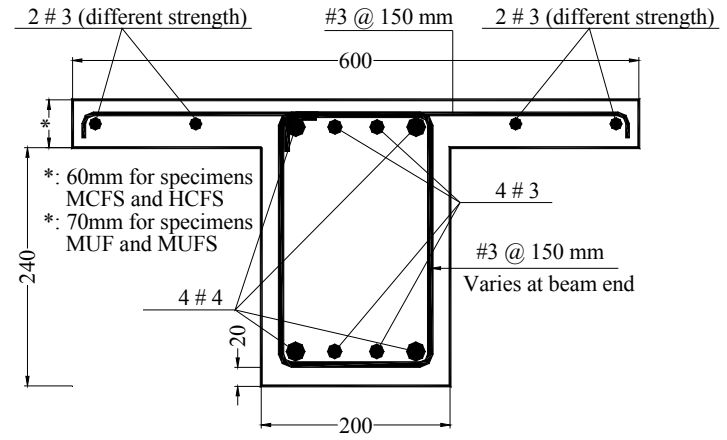


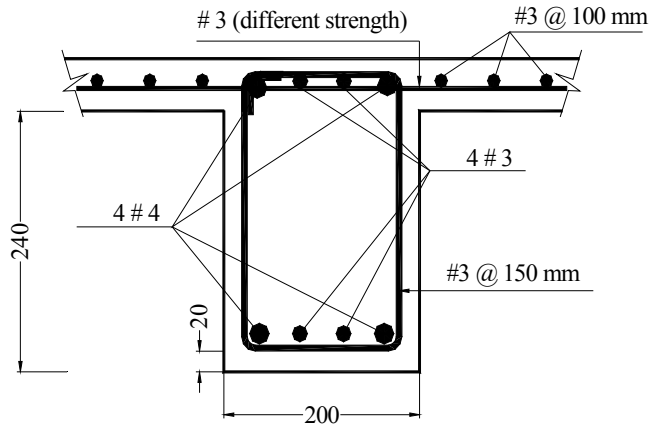
Figure A-5. Reinforcement layout (elevation), specimen MUFS



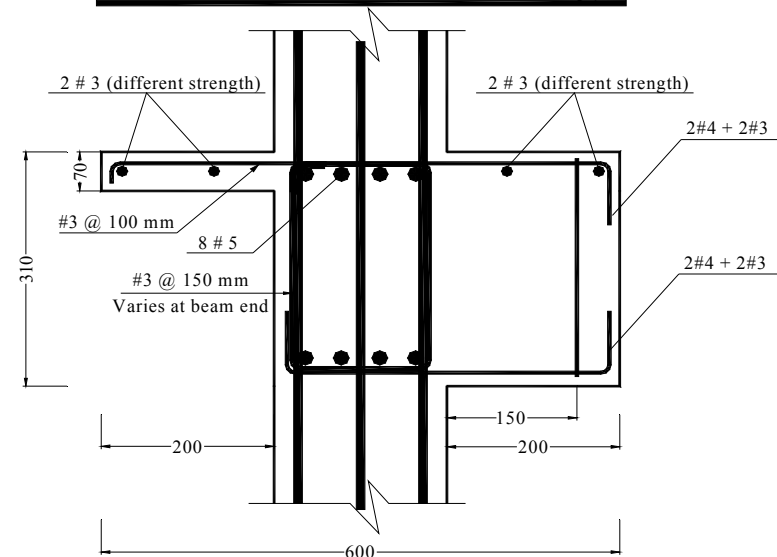
Beam Section B-B (First Story)



Beam Section C-C (Second Story)

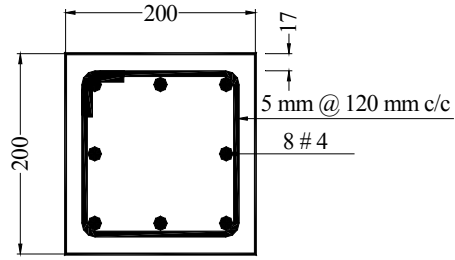


Transverse Beam Section, at Middle Column

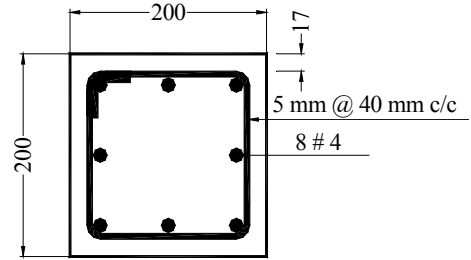


Transverse Beam Section (at First-Story Joints)

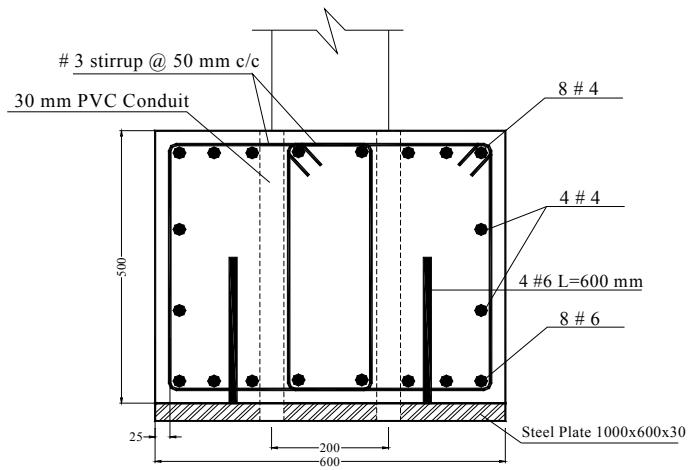
Figure A-6. Reinforcement details of longitudinal and transverse beam



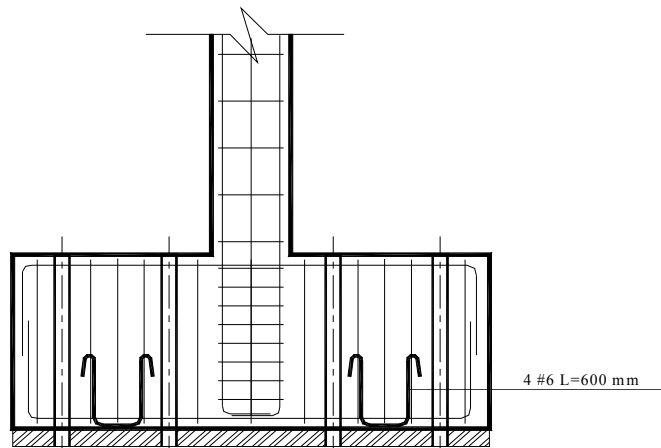
Column Section D-D



Column Section E-E

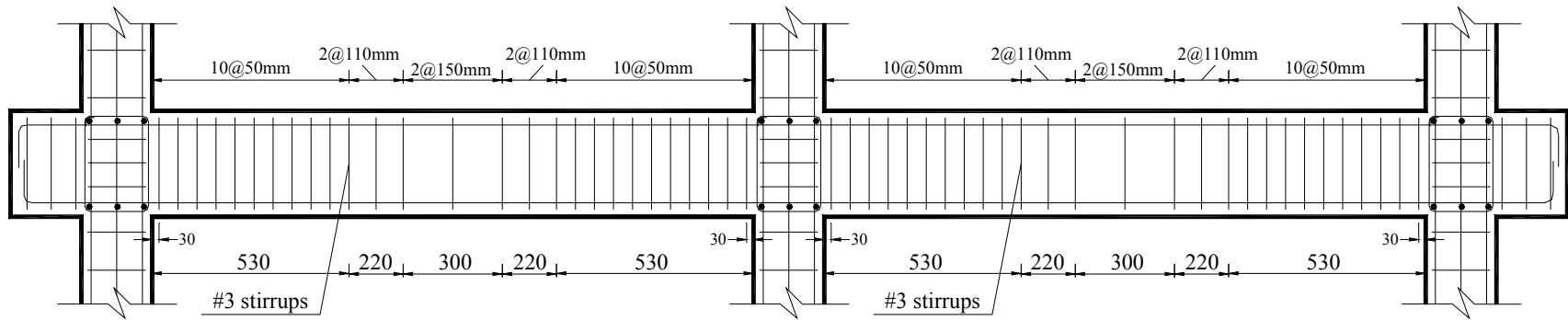


Footing Side Section F-F

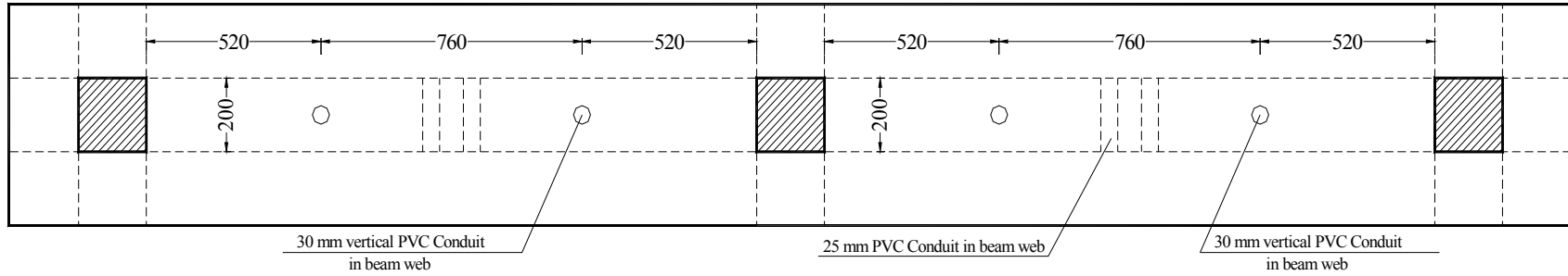


**Embedded bars connecting
bottom steel plate to footing**

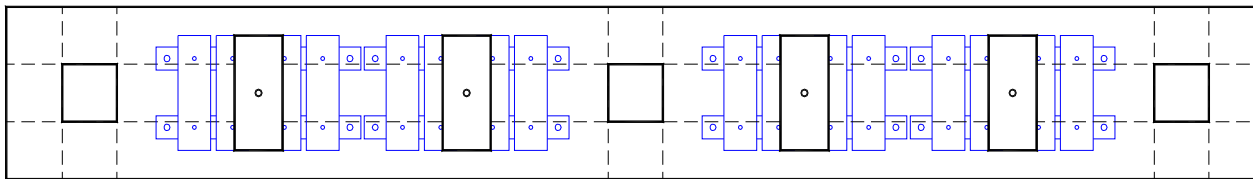
Figure A-7. Reinforcement details of columns and footings



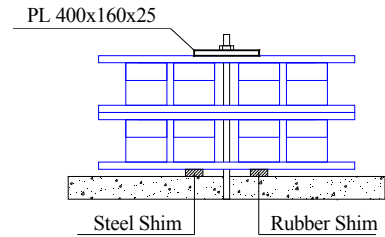
Stirrups in Beams



Location of Sleeves in Slabs for Weights on First Floor Beams



Orientation of Lead Packets on Beams



Connection of Weights to Beams

Figure A-8. Beam stirrups, layout of weights on beams, and detail of connection of weights to beams

A.2 Material Properties

A.2.1 Concrete Properties

At the time of casting, 150mm diameter by 300mm-high standard cylinders were cast according to ASTM C31 requirements and were kept in the same environment as the test specimens. Concrete was poured at four levels of footing, first story, second story, and top column stubs. Six cylinders were prepared at each stage for the specimens. Three cylinders were tested 28 days after casting, and the rest were tested shortly after the day of the shaking table tests. Table A-1 summarizes the average results from the cylinder tests used for the analytical models. Table A-2 demonstrates the cylinder test results for different stories of specimens MCFS and HCFS, while Table A-3 shows the results for stories of specimens MUF and MUFS. Figure A-9 to Figure A-11 demonstrate the stress-strain relationship for cylinders for specimens MUF and MUFS. These plots are for the cylinders tested 15 days after testing specimen MUFS and 32 days after testing specimen MUF. Similar plots were obtained for specimens MCFS and HCFS; however, they were not shown here for the sake of brevity.

Table A-1. Average concrete compressive strengths for columns

| Specimen | 28-Day Mean Strength (MPa) | Shaking Table Test Day Strength (MPa) |
|-----------------|-----------------------------------|--|
| MCFS | 31.0 | 34.0 |
| HCFS | 31.0 | 34.4 |
| MUF | 30.2 | 35.8 |
| MUFS | 30.2 | 36.5 |

Table A-2. Concrete compressive strength test results for specimens MCFS and HCFS

| Location | f'_c (28-day) | | | f'_c (Cylinder Test-day)* | | |
|--------------------------------|-----------------|---------|------|-----------------------------|---------|------|
| | Cylinder | Average | Cov. | Cylinder | Average | Cov. |
| | MPa | MPa | % | MPa | MPa | % |
| Footing | 31.8 | 32.7 | 2.9 | 35.4 | 38.9 | 9.9 |
| | 32.6 | | | 38.2 | | |
| | 33.6 | | | 43.1 | | |
| First-story beams and columns | 29.4 | 31.1 | 5.5 | 40.7 | 37.7 | 10.3 |
| | 32.8 | | | 39.1 | | |
| | 31.0 | | | 33.3 | | |
| Second-story beams and columns | 30.8 | 30.8 | 1.8 | 37.7 | 34.3 | 14.1 |
| | 31.4 | | | 28.7 | | |
| | 30.3 | | | 36.4 | | |

* Cylinder Test-day was 19 days after testing specimen MCFS and 14 days after testing specimen HCFS

Table A-3. Concrete compressive strength test results for specimens MUF and MUFS

| Location | f'_c (28-day) | | | f'_c (Cylinder Test-day)* | | |
|--------------------------------|-----------------|---------|------|-----------------------------|---------|------|
| | Cylinder | Average | Cov. | Cylinder | Average | Cov. |
| | MPa | MPa | % | MPa | MPa | % |
| Footing | 31.0 | 30.8 | 4.8 | 35.3 | 36.8 | 3.6 |
| | 32.1 | | | 37.6 | | |
| | 29.2 | | | 37.6 | | |
| First-story beams and columns | 30.6 | 30.7 | 1.3 | 37.7 | 38.4 | 1.8 |
| | 31.2 | | | 38.5 | | |
| | 30.4 | | | 39.0 | | |
| Second-story beams and columns | 29.5 | 29.6 | 0.2 | 32.9 | 35.8 | 10.1 |
| | 29.6 | | | 34.6 | | |
| | 29.6 | | | 39.8 | | |

* Cylinder Test-day was 32 days after testing specimen MUF and 15 days after testing specimen MUFS

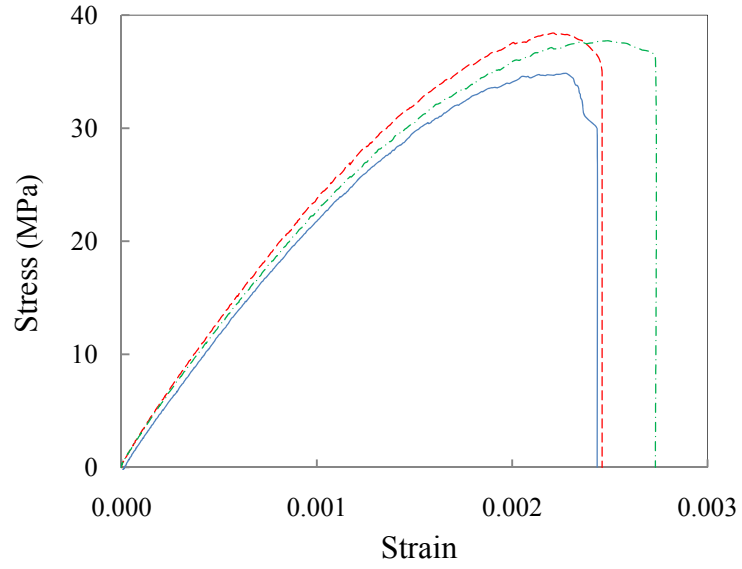


Figure A-9. Concrete stress-strain plots for three cylinders from footing concrete, specimens MUF and MUFS

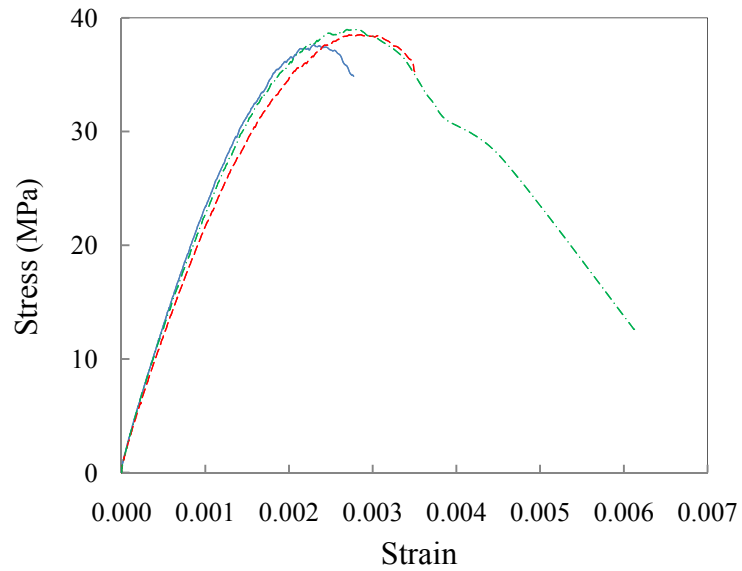


Figure A-10. Concrete stress-strain plots for three cylinders from first-story concrete, specimens MUF and MUFS

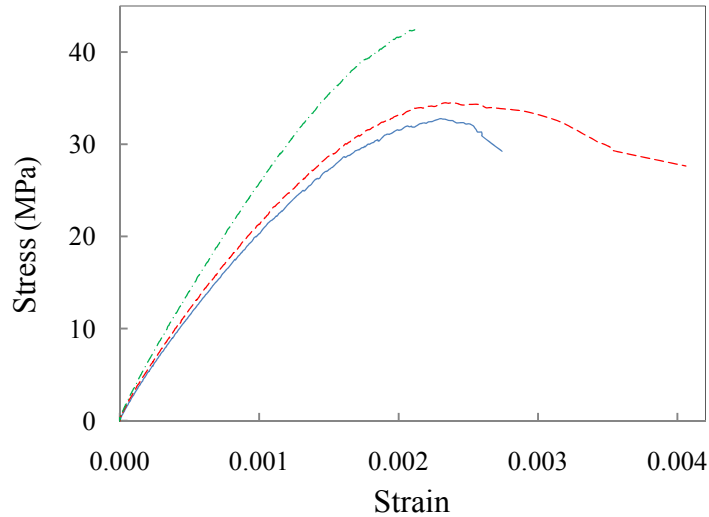


Figure A-11. Concrete stress-strain plots for three cylinders from second-story concrete, specimens MUF and MUFS

A.2.2 Reinforcing Steel Properties

For each size of reinforcement used in the test specimens, three steel coupons were tested according to ASTM A370. The results for rebar used in the columns of the four specimens are summarized in Table A-4. The yield stress, f_y , was taken from the plateau just after first yield, and the yield strain, ϵ_y , was taken as the strain at the peak at first yield. The stress at starting point of strain-hardening was taken as f_y , while the strain at such point, ϵ_{sh} , was taken as the strain at the point where the stress starts to increase. The ultimate stress, f_u , was assumed as the maximum stress recorded during the coupon test; while the ultimate strain, ϵ_u , reported in Table A-4 was taken as the maximum strain recorded during the coupon test (note that f_u and ϵ_u do not occur at the same time during coupon test results shown in Figure A-13 and Figure A-16). The modulus of elasticity, E_s , was determined by calculating a linear fit to the data for strains below 0.002. Table A-5 demonstrates the steel properties used in other structural elements of specimens MCFS and HCFS, while properties of reinforcement in the structural elements of specimens MUF and MUFS are shown in Table A-6.

Table A-4. Averages from column reinforcing steel coupon tests

| Specimen | No. of Tests | f_y (MPa) | f_u (MPa) | ϵ_y | ϵ_h | ϵ_u | E_s (MPa) |
|----------|--------------|----------------|----------------|--------------|--------------|--------------|----------------|
| MCFS | 3* | 439.0 | 685.0 | 0.0022 | 0.019 | 0.279 | 199860 |
| HCFS | 3* | 439.0 | 685.0 | 0.0022 | 0.019 | 0.279 | 199860 |
| MUF | 3 | 467.0 | 702 | 0.0023 | 0.006 | 0.293 | 204824 |
| MUFS | 3 | 467.0 | 702 | 0.0023 | 0.006 | 0.293 | 204824 |

*. Results from one coupon test were ignored (see Figure A-13 and Figure A-14)

Table A-5. Reinforcing steel properties for specimens MCFS, HCFS

| Location | Purpose | Type | f_y (MPa) | f_u (MPa) |
|----------------------------|---------------|------------|----------------|----------------|
| Footing | stirrup | #3 | 452.2 | 640.4 |
| | long. | #4 | 437.0 | 637.5 |
| | long. | #6 | 445.6 | 637.5 |
| 1 st story beam | long. | #5 | 439.8 | 666.9 |
| | stirrup | #3 | 452.2 | 640.4 |
| 2 nd story beam | long. | #4 | 437.0 | 637.5 |
| | long. stirrup | #3 | 452.2 | 640.4 |
| Slab | long. | #3 | 274.6 | 384.4 |
| | stirrup | #3 | 452.2 | 640.4 |
| Joint | stirrup | ϕ 0.5 | 469.0 | 480.0 |

Table A-6. Reinforcing steel properties for specimens MUF, MUFS

| Location | Purpose | Type | f_y (MPa) | f_u (MPa) |
|----------------------------|---------------|------|----------------|----------------|
| Footing | stirrup | #3 | 456.6 | 652.2 |
| | long. | #4 | 449.3 | 647.3 |
| | long. | #6 | 473.7 | 657.1 |
| 1 st story beam | long. | #5 | 446.5 | 637.5 |
| | stirrup | #3 | 456.6 | 652.2 |
| 2 nd story beam | long. | #4 | 449.3 | 647.3 |
| | long. stirrup | #3 | 456.6 | 652.2 |
| Slab | long. | #3 | 358.7 | 474.0 |
| | stirrup | #3 | 456.6 | 652.2 |
| Joint | stirrup | none | - | - |

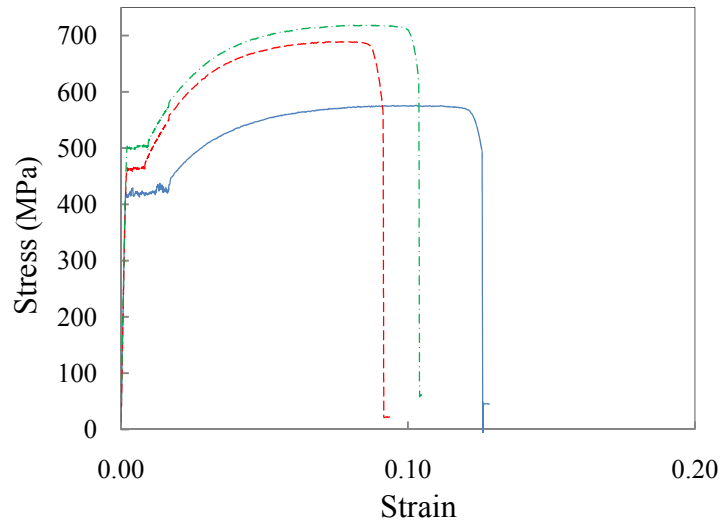


Figure A-12. Reinforcing steel stress-strain plots for rebar #3, specimens MCFS and HCFS

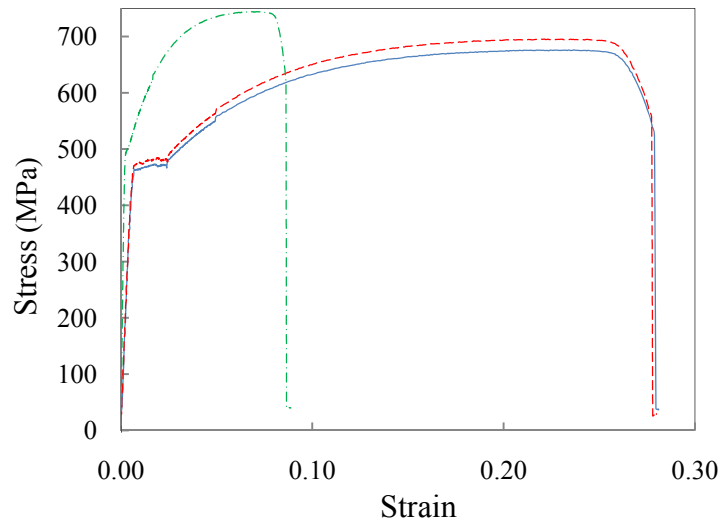


Figure A-13. Reinforcing steel stress-strain plots for rebar #4, specimens MCFS and HCFS (dash-dotted curve ignored)

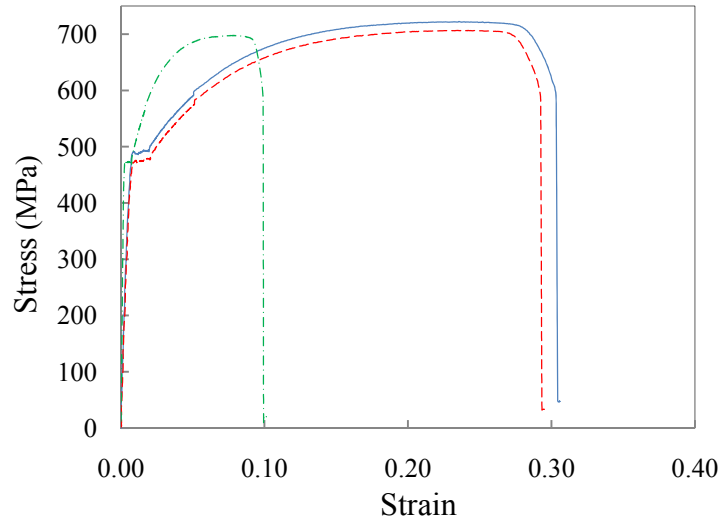


Figure A-14. Reinforcing steel stress-strain plots for rebar #5, specimens MCFS and HCFS (dash-dotted curve ignored)

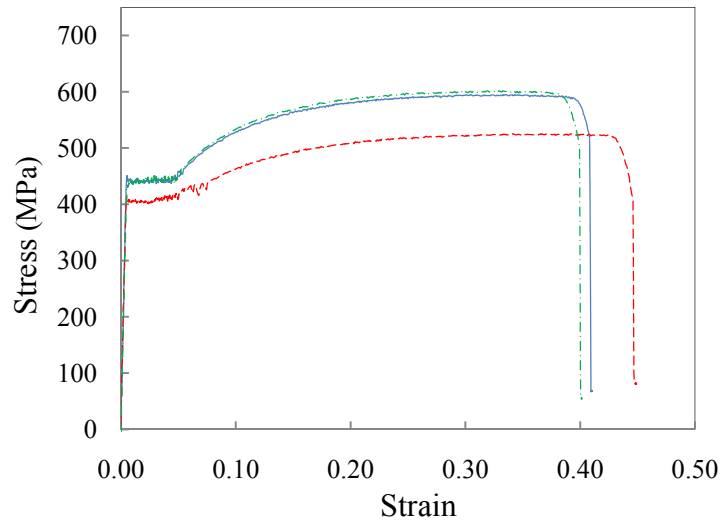


Figure A-15. Reinforcing steel stress-strain plots for rebar #3, specimens MUF and MUFS

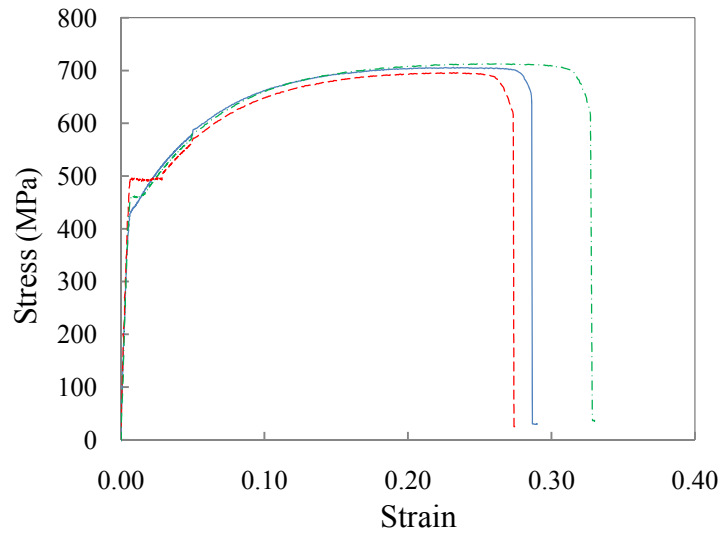


Figure A-16. Reinforcing steel stress-strain plots for rebar #4, specimens MUF and MUFS

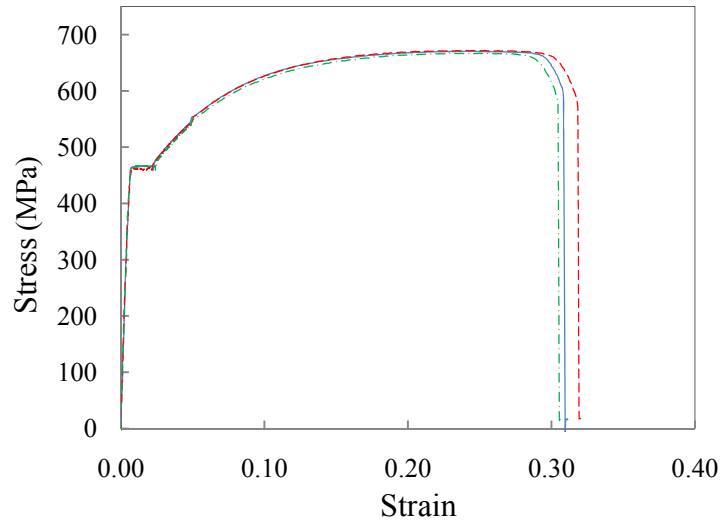


Figure A-17. Reinforcing steel stress-strain plots for rebar #5, specimens MUF and MUFS

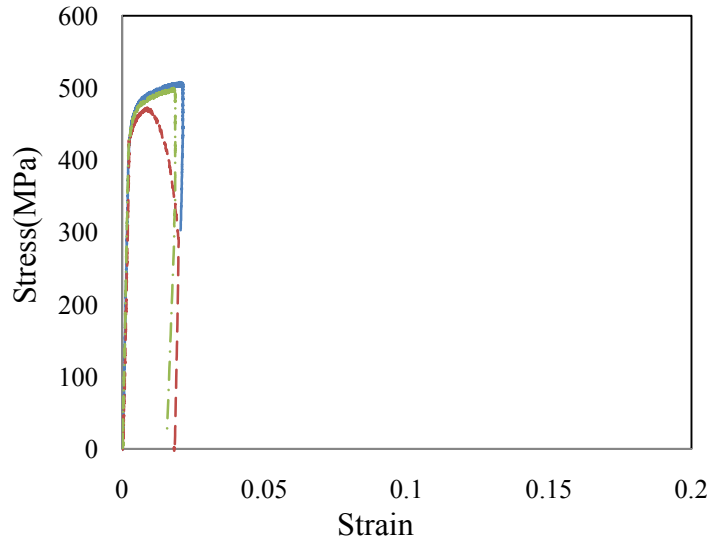


Figure A-18. Reinforcing steel stress-strain plots for transverse rebar 5mm, all specimens

Appendix B. Instrumentation, Procedures, and Data Reduction

B.1 Introduction

The experimental setup, discussed in Chapter 3, was designed to observe collapse behaviour of four frames with similar geometry, but with different detailing and applied load. While Section B.2 demonstrates the breakdown of inertial-mass weights and gravity load on the beams for each frame, details of instrumentation for each specimen are shown in Section B.3. The procedures used to reduce the recorded data to the results presented in Chapters 4 and 5 will be discussed in Section B.4. Finally, Section B.5 demonstrates the modeling parameters defined in ASCE-41 for non-ductile columns.

B.2 Breakdown of Weights Connected to Specimens

As discussed in Section 3.4.2.1, gravity load on the beams was considered by means of lead packets connected to the beams (see Figure A-8 for details). Inertial-mass wagons were also connected to the specimens at the top point of second-story center column. Breakdown of the weights connected to the specimens is shown in Table B-1. Due to limitations caused by the connections of inertial-mass wagons to the specimen, the layout of the lead weights on

second-story beams was different from the first story. Steel plates were attached to the sides of the beams to compensate the difference between the weight of lead packets and original designed loads. Therefore, the total weight connected to the second story must be considered as the combination of the weight from lead packets and the steel plates. Total weight of each specimen is also shown in Table B-1.

Table B-1. Weight of inertial-Mass wagons, connections, lead packet stacks on the beams, and specimen

| | MCFS | HCFS | MUF | MUFS |
|--|-------|-------|-------|-------|
| Inertial-Mass Wagon, North (kN) | 50.4 | 49.8 | 50.8 | 49.8 |
| Inertial-Mass Wagon, South (kN) | 51.1 | 51.1 | 51.1 | 51.1 |
| Connection of Inertial-Mass Wagons to Specimen (kN) | 3.6 | 3.6 | 3.6 | 3.6 |
| First-Story Lead Weight (kN) | 19.7 | 19.7 | 19.7 | 19.7 |
| Second-Story Lead Weight (kN) | 7.8 | 7.8 | 7.8 | 7.8 |
| Second-Story Steel Weight (kN) | 10.8 | 10.8 | 10.8 | 10.8 |
| Specimen Weight (kN) | 96.09 | 96.08 | 96.98 | 96.99 |

B.3 Instrumentation

The instrumentation can be grouped into the following categories:

- 1) Force transducers (or load cells) that measure shear and axial forces at the base of test frames footings,
- 2) Accelerometers to measure the acceleration at each story and the inertial-mass wagon,

- 3) Displacement transducers to measure the global displacements of the specimen, vertical displacement of columns, and deformation of exterior first-story joints,
- 4) Strain gages to measure the strain in the reinforcement.

Table B-2 to Table B-5 list the instruments used for the specimens.

Table B-2. Instrumentation list for specimen MCFS

| Channel # | Category | Description | Name |
|-----------|--------------------|------------------------------------|----------|
| 1 | Accelerometer | Footing B Horizontal | AC FBH |
| 2 | Accelerometer | Footing B Vertical | AC FBV |
| 3 | Accelerometer | A1 Horizontal | AC A1H |
| 4 | Accelerometer | A1 Transverse | AC A1T |
| 5 | Accelerometer | A1 Vertical | AC A1V |
| 6 | Accelerometer | B1 Horizontal | AC B1H |
| 7 | Accelerometer | B1 Vertical | AC B1V |
| 8 | Accelerometer | C1 Horizontal | AC C1H |
| 9 | Accelerometer | C1 Transverse | AC C1T |
| 10 | Accelerometer | C1 Vertical | AC C1V |
| 11 | Accelerometer | A2 Horizontal | AC A2H |
| 12 | Accelerometer | A2 Vertical | AC A2V |
| 13 | Accelerometer | B2 Horizontal | AC B2H |
| 14 | Accelerometer | B2 Transverse | AC B2T |
| 15 | Accelerometer | B2 Vertical | AC B2V |
| 16 | Accelerometer | C2 Horizontal | AC C2H |
| 17 | Accelerometer | C2 Vertical Left | AC C2V |
| 18 | Accelerometer | First Floor Mass Horizontal North | AC FFMHN |
| 19 | Accelerometer | Second Floor Mass Horizontal North | AC SFMHN |
| 20 | Accelerometer | Inertia Mass Horizontal North | AC IMHN |
| 78 | Accelerometer | Inertial-Mass Horizontal South | AC IMHS |
| 21 | Local Displacement | Column B1 Bottom Slip North | LD B1BSN |
| 22 | Local Displacement | Column B1 Bottom Slip South | LD B1BSS |
| 80 | Local Displacement | Column B1 Bottom Vertical North | LD B1BVN |
| 81 | Local Displacement | Column B1 Bottom Vertical South | LD B1BVS |
| 82 | Local Displacement | Column B1 Bottom Horizontal | LD B1BH |
| 83 | Local Displacement | Column B1 Bottom Diagonal | LD B1BD |
| 84 | Local Displacement | Column B1 Top Vertical North | LD B1TVN |
| 85 | Local Displacement | Column B1 Top Vertical South | LD B1TVS |
| 86 | Local Displacement | Column B1 Top Horizontal | LD B1TH |
| 87 | Local Displacement | Column B1 Top Diagonal | LD B1TD |
| 88 | Local Displacement | Column B1 Top Slip North | LD B1TSN |
| 89 | Local Displacement | Column B1 Top Slip South | LD B1TSS |
| 90 | Local Displacement | Joint C1 Vertical North | LD JC1VN |
| 91 | Local Displacement | Joint C1 Vertical South | LD JC1VS |
| 92 | Local Displacement | Joint C1 Horizontal Top | LD JC1HT |
| 93 | Local Displacement | Joint C1 Horizontal Bottom | LD JC1HB |

| Channel # | Category | Description | Name |
|-----------|---------------------|---|------------|
| 94 | Local Displacement | Joint C1 Diagonal Top North | LD JC1DTN |
| 95 | Local Displacement | Joint C1 Diagonal Top South | LD JC1DTS |
| 23 | Global Displacement | Column A1 Vertical North | GD A1VN |
| 24 | Global Displacement | Column A1 Vertical South | GD A1VS |
| 25 | Global Displacement | Column A1 Horizontal Transverse | GD A1HT |
| 26 | Global Displacement | Column A1 Horizontal Longitudinal | GD A1HL |
| 27 | Global Displacement | Column A1 Horizontal Longitudinal Top | GD A1HLT |
| 28 | Global Displacement | Column B1 Vertical North | GD B1VN |
| 29 | Global Displacement | Column B1 Vertical South | GD B1VS |
| 30 | Global Displacement | Column C1 Vertical North | GD C1VN |
| 31 | Global Displacement | Column C1 Vertical South | GD C1VS |
| 32 | Global Displacement | Column C1 Horizontal Transverse | GD C1HT |
| 33 | Global Displacement | Column A2 Vertical | GD A2V |
| 34 | Global Displacement | Column A2 Horizontal Longitudinal | GD A2HL |
| 35 | Global Displacement | Column B2 Vertical | GD B2V |
| 36 | Global Displacement | Column B2 Horizontal Transverse | GD B2HT |
| 37 | Global Displacement | Column C2 Vertical | GD C2V |
| 38 | Global Displacement | Diagonal B1 Bottom A1 Top | GD DB1BA1T |
| 39 | Global Displacement | Diagonal B1 Bottom C1 Top | GD DB1BC1T |
| 40 | Global Displacement | Diagonal Middle Beam B2 Top | GD DMBB2T |
| 41 | Global Displacement | Diagonal Middle Beam C2 Top | GD DMBC2T |
| 42 | Global Displacement | Diagonal Middle Beam Steel Beam Top | GD DMBSBT |
| 43 | Global Displacement | Longitudinal North Mass First Floor Top | GD LNMFST |
| 44 | Global Displacement | Longitudinal North Mass Second FL Top | GD LNMSFT |
| 45 | Global Displacement | Longitudinal North Inertial-Mass Top | GD LNIMT |
| 46 | Global Displacement | Transverse North Inertial-Mass Top | GD TNIMT |
| 47 | Global Displacement | Footing B1 Vertical Left | GD FB1VL |
| 96 | Global Displacement | Beam A1B1 Horizontal Longitudinal | GD A1B1HL |
| 97 | Global Displacement | Beam B1C1 Horizontal Longitudinal | GD B1C1HL |
| 98 | Global Displacement | Beam A2B2 Horizontal Longitudinal | GD A2B2HL |
| 99 | Global Displacement | Beam B2C2 Horizontal Longitudinal | GD B2C2HL |
| 100 | Global Displacement | Temposonic Mass Car Left | GD TEMPML |
| 48 | Force Transducer | Column A Axial North | FT CAAN |
| 49 | Force Transducer | Column A In-Plane Shear North | FT CAIPSN |
| 50 | Force Transducer | Column A Out-Of-Plane Shear North | FT CAOPSN |
| 51 | Force Transducer | Column A Axial South | FT CAAS |
| 52 | Force Transducer | Column A In-Plane Shear South | FT CAIPSS |
| 53 | Force Transducer | Column A Out-Of-Plane Shear South | FT CAOPSS |
| 54 | Force Transducer | Column B Axial North | FT CBAN |
| 55 | Force Transducer | Column B In-Plane Shear North | FT CBIPSN |
| 56 | Force Transducer | Column B Out-Of-Plane Shear North | FT CBOPSN |
| 57 | Force Transducer | Column B Axial South | FT CBAS |
| 58 | Force Transducer | Column B In-Plane Shear South | FT CBIPSS |
| 59 | Force Transducer | Column B Out-Of-Plane Shear South | FT CBOPSS |
| 60 | Force Transducer | Column C Axial North | FT CCAN |
| 61 | Force Transducer | Column C In-Plane Shear North | FT CCIPSN |
| 62 | Force Transducer | Column C Out-Of-Plane Shear North | FT CCOPSN |
| 63 | Force Transducer | Column C Axial South | FT CCAS |

| Channel # | Category | Description | Name |
|-----------|------------------|-----------------------------------|------------|
| 64 | Force Transducer | Column C In-Plane Shear South | FT CCI PSS |
| 65 | Force Transducer | Column C Out-Of-Plane Shear South | FT CCOPSS |
| 66 | Force Transducer | Column A Top Hinge | FT CATH |
| 67 | Force Transducer | Column B Top Hinge | FT CBTH |
| 68 | Force Transducer | Column C Top Hinge | FT CCTH |

Table B-3. Instrumentation list for specimen HCFS

| Channel # | Category | Description | Name |
|-----------|--------------------|------------------------------------|----------|
| 1 | Accelerometer | Footing B Horizontal | AC FBH |
| 2 | Accelerometer | Footing B Vertical | AC FBV |
| 3 | Accelerometer | A1 Horizontal | AC A1H |
| 4 | Accelerometer | A1 Transverse | AC A1T |
| 5 | Accelerometer | A1 Vertical | AC A1V |
| 6 | Accelerometer | B1 Horizontal | AC B1H |
| 7 | Accelerometer | B1 Vertical | AC B1V |
| 8 | Accelerometer | C1 Horizontal | AC C1H |
| 9 | Accelerometer | C1 Transverse | AC C1T |
| 10 | Accelerometer | C1 Vertical | AC C1V |
| 11 | Accelerometer | A2 Horizontal | AC A2H |
| 12 | Accelerometer | A2 Vertical | AC A2V |
| 13 | Accelerometer | B2 Horizontal | AC B2H |
| 14 | Accelerometer | B2 Transverse | AC B2T |
| 15 | Accelerometer | B2 Vertical | AC B2V |
| 16 | Accelerometer | C2 Horizontal | AC C2H |
| 17 | Accelerometer | C2 Vertical Left | AC C2V |
| 18 | Accelerometer | First Floor Mass Horizontal North | AC FFMHN |
| 19 | Accelerometer | Second Floor Mass Horizontal North | AC SFMHN |
| 20 | Accelerometer | Inertia Mass Horizontal North | AC IMHN |
| 78 | Accelerometer | Inertial-Mass Horizontal South | AC IMHS |
| 21 | Local Displacement | Column B1 Bottom Slip North | LD B1BSN |
| 22 | Local Displacement | Column B1 Bottom Slip South | LD B1BSS |
| 80 | Local Displacement | Column B1 Bottom Vertical North | LD B1BVN |
| 81 | Local Displacement | Column B1 Bottom Vertical South | LD B1BVS |
| 82 | Local Displacement | Column B1 Bottom Horizontal | LD B1BH |
| 83 | Local Displacement | Column B1 Bottom Diagonal | LD B1BD |
| 84 | Local Displacement | Column B1 Top Vertical North | LD B1TVN |
| 85 | Local Displacement | Column B1 Top Vertical South | LD B1TVS |
| 86 | Local Displacement | Column B1 Top Horizontal | LD B1TH |
| 87 | Local Displacement | Column B1 Top Diagonal | LD B1TD |
| 88 | Local Displacement | Column B1 Top Slip North | LD B1TSN |
| 89 | Local Displacement | Column B1 Top Slip South | LD B1TSS |
| 90 | Local Displacement | Joint C1 Vertical North | LD JC1VN |
| 91 | Local Displacement | Joint C1 Vertical South | LD JC1VS |
| 92 | Local Displacement | Joint C1 Horizontal Top | LD JC1HT |
| 93 | Local Displacement | Joint C1 Horizontal Bottom | LD JC1HB |

| Channel # | Category | Description | Name |
|-----------|---------------------|---|------------|
| 94 | Local Displacement | Joint C1 Diagonal Top North | LD JC1DTN |
| 95 | Local Displacement | Joint C1 Diagonal Top South | LD JC1DTS |
| 23 | Global Displacement | Column A1 Vertical North | GD A1VN |
| 24 | Global Displacement | Column A1 Vertical South | GD A1VS |
| 25 | Global Displacement | Column A1 Horizontal Transverse | GD A1HT |
| 26 | Global Displacement | Column A1 Horizontal Longitudinal | GD A1HL |
| 27 | Global Displacement | Column A1 Horizontal Longitudinal Top | GD A1HLT |
| 28 | Global Displacement | Column B1 Vertical North | GD B1VN |
| 29 | Global Displacement | Column B1 Vertical South | GD B1VS |
| 30 | Global Displacement | Column C1 Vertical North | GD C1VN |
| 31 | Global Displacement | Column C1 Vertical South | GD C1VS |
| 32 | Global Displacement | Column C1 Horizontal Transverse | GD C1HT |
| 33 | Global Displacement | Column A2 Vertical | GD A2V |
| 34 | Global Displacement | Column A2 Horizontal Longitudinal | GD A2HL |
| 35 | Global Displacement | Column B2 Vertical | GD B2V |
| 36 | Global Displacement | Column B2 Horizontal Transverse | GD B2HT |
| 37 | Global Displacement | Column C2 Vertical | GD C2V |
| 38 | Global Displacement | Diagonal B1 Bottom A1 Top | GD DB1BA1T |
| 39 | Global Displacement | Diagonal B1 Bottom C1 Top | GD DB1BC1T |
| 40 | Global Displacement | Diagonal Middle Beam B2 Top | GD DMBB2T |
| 41 | Global Displacement | Diagonal Middle Beam C2 Top | GD DMBC2T |
| 42 | Global Displacement | Diagonal Middle Beam Steel Beam Top | GD DMBSBT |
| 43 | Global Displacement | Longitudinal North Mass First Floor Top | GD LNMFFT |
| 44 | Global Displacement | Longitudinal North Mass Second FL Top | GD LNMSFT |
| 45 | Global Displacement | Longitudinal North Inertia- Mass Top | GD LNIMT |
| 46 | Global Displacement | Transverse North Inertial-Mass Top | GD TNIMT |
| 47 | Global Displacement | Footing B1 Vertical Left | GD FB1VL |
| 96 | Global Displacement | Beam A1B1 Horizontal Longitudinal | GD A1B1HL |
| 97 | Global Displacement | Beam B1C1 Horizontal Longitudinal | GD B1C1HL |
| 98 | Global Displacement | Beam A2B2 Horizontal Longitudinal | GD A2B2HL |
| 99 | Global Displacement | Beam B2C2 Horizontal Longitudinal | GD B2C2HL |
| 100 | Global Displacement | Temposonic Mass Car Left | GD TEMPML |
| 48 | Force Transducer | Column A Axial North | FT CAAN |
| 49 | Force Transducer | Column A In-Plane Shear North | FT CAIPSN |
| 50 | Force Transducer | Column A Out-Of-Plane Shear North | FT CAOPSN |
| 51 | Force Transducer | Column A Axial South | FT CAAS |
| 52 | Force Transducer | Column A In-Plane Shear South | FT CAIPSS |
| 53 | Force Transducer | Column A Out-Of-Plane Shear South | FT CAOPSS |
| 54 | Force Transducer | Column B Axial North | FT CBAN |
| 55 | Force Transducer | Column B In-Plane Shear North | FT CBIPSN |
| 56 | Force Transducer | Column B Out-Of-Plane Shear North | FT CBOPSN |
| 57 | Force Transducer | Column B Axial South | FT CBAS |
| 58 | Force Transducer | Column B In-Plane Shear South | FT CBIPSS |
| 59 | Force Transducer | Column B Out-Of-Plane Shear South | FT CBOPSS |
| 60 | Force Transducer | Column C Axial North | FT CCAN |
| 61 | Force Transducer | Column C In-Plane Shear North | FT CCIPSN |
| 62 | Force Transducer | Column C Out-Of-Plane Shear North | FT CCOPSN |
| 63 | Force Transducer | Column C Axial South | FT CCAS |

| Channel # | Category | Description | Name |
|-----------|------------------|-----------------------------------|-----------|
| 64 | Force Transducer | Column C In-Plane Shear South | FT CCISS |
| 65 | Force Transducer | Column C Out-Of-Plane Shear South | FT CCOPSS |
| 66 | Force Transducer | Column A Top Hinge | FT CATH |
| 67 | Force Transducer | Column B Top Hinge | FT CBTH |
| 68 | Force Transducer | Column C Top Hinge | FT CCTH |

Table B-4. Instrumentation list for specimen MUF

| Channel # | Category | Description | Name |
|-----------|--------------------|------------------------------------|----------|
| 1 | Accelerometer | Footing B Horizontal | AC FBH |
| 2 | Accelerometer | Footing B Vertical | AC FBV |
| 3 | Accelerometer | A1 Horizontal | AC A1H |
| 4 | Accelerometer | A1 Transverse | AC A1T |
| 5 | Accelerometer | A1 Vertical | AC A1V |
| 6 | Accelerometer | B1 Horizontal | AC B1H |
| 7 | Accelerometer | B1 Vertical | AC B1V |
| 8 | Accelerometer | C1 Horizontal | AC C1H |
| 9 | Accelerometer | C1 Transverse | AC C1T |
| 10 | Accelerometer | C1 Vertical | AC C1V |
| 11 | Accelerometer | A2 Horizontal | AC A2H |
| 12 | Accelerometer | A2 Vertical | AC A2V |
| 13 | Accelerometer | B2 Horizontal | AC B2H |
| 14 | Accelerometer | B2 Transverse | AC B2T |
| 15 | Accelerometer | B2 Vertical | AC B2V |
| 16 | Accelerometer | C2 Horizontal | AC C2H |
| 17 | Accelerometer | C2 Vertical Left | AC C2V |
| 18 | Accelerometer | First Floor Mass Horizontal North | AC FFMHN |
| 19 | Accelerometer | Second Floor Mass Horizontal North | AC SFMHN |
| 20 | Accelerometer | Inertia Mass Horizontal North | AC IMHN |
| 78 | Accelerometer | Inertial-Mass Horizontal South | AC IMHS |
| 21 | Local Displacement | Column B1 Bottom Slip North | LD B1BSN |
| 22 | Local Displacement | Column B1 Bottom Slip South | LD B1BSS |
| 80 | Local Displacement | Column B1 Bottom Vertical North | LD B1BVN |
| 81 | Local Displacement | Column B1 Bottom Vertical South | LD B1BVS |
| 82 | Local Displacement | Column B1 Bottom Horizontal | LD B1BH |
| 83 | Local Displacement | Column B1 Bottom Diagonal | LD B1BD |
| 84 | Local Displacement | Column B1 Top Vertical North | LD B1TVN |
| 85 | Local Displacement | Column B1 Top Vertical South | LD B1TVS |
| 86 | Local Displacement | Column B1 Top Horizontal | LD B1TH |
| 87 | Local Displacement | Column B1 Top Diagonal | LD B1TD |
| 88 | Local Displacement | Joint A1 Diagonal East | LD JA1DE |
| 89 | Local Displacement | Joint C1 Diagonal East | LD JC1DE |
| 90 | Local Displacement | Joint C1 Vertical North | LD JC1VN |
| 91 | Local Displacement | Joint C1 Vertical South | LD JC1VS |
| 92 | Local Displacement | Joint C1 Horizontal Top | LD JC1HT |
| 93 | Local Displacement | Joint C1 Horizontal Bottom | LD JC1HB |

| Channel # | Category | Description | Name |
|-----------|---------------------|---|------------|
| 94 | Local Displacement | Joint C1 Diagonal Top North | LD JC1DTN |
| 95 | Local Displacement | Joint C1 Diagonal Top South | LD JC1DTS |
| 23 | Global Displacement | Column A1 Vertical North | GD A1VN |
| 24 | Global Displacement | Column A1 Vertical South | GD A1VS |
| 25 | Global Displacement | Column A1 Horizontal Transverse | GD A1HT |
| 26 | Global Displacement | Column A1 Horizontal Longitudinal | GD A1HL |
| 27 | Global Displacement | Column A1 Horizontal Longitudinal Top | GD A1HLT |
| 28 | Global Displacement | Column B1 Vertical North | GD B1VN |
| 29 | Global Displacement | Column B1 Vertical South | GD B1VS |
| 30 | Global Displacement | Column C1 Vertical North | GD C1VN |
| 31 | Global Displacement | Column C1 Vertical South | GD C1VS |
| 32 | Global Displacement | Column C1 Horizontal Transverse | GD C1HT |
| 33 | Global Displacement | Column A2 Vertical | GD A2V |
| 34 | Global Displacement | Column A2 Horizontal Longitudinal | GD A2HL |
| 35 | Global Displacement | Column B2 Vertical | GD B2V |
| 36 | Global Displacement | Column B2 Horizontal Transverse | GD B2HT |
| 37 | Global Displacement | Column C2 Vertical | GD C2V |
| 38 | Global Displacement | Diagonal B1 Bottom A1 Top | GD DB1BA1T |
| 39 | Global Displacement | Diagonal B1 Bottom C1 Top | GD DB1BC1T |
| 40 | Global Displacement | Diagonal Middle Beam B2 Top | GD DMBB2T |
| 41 | Global Displacement | Diagonal Middle Beam C2 Top | GD DMBC2T |
| 42 | Global Displacement | Diagonal Middle Beam Steel Beam Top | GD DMBSBT |
| 43 | Global Displacement | Longitudinal North Mass First Floor Top | GD LNMFFT |
| 44 | Global Displacement | Longitudinal North Mass Second FL Top | GD LNMSFT |
| 45 | Global Displacement | Longitudinal North Inertial-Mass Top | GD LNIMT |
| 46 | Global Displacement | Transverse North Inertial-Mass Top | GD TNIMT |
| 47 | Global Displacement | Footing B1 Vertical Left | GD FB1VL |
| 96 | Global Displacement | Beam A1B1 Horizontal Longitudinal | GD A1B1HL |
| 97 | Global Displacement | Beam B1C1 Horizontal Longitudinal | GD B1C1HL |
| 98 | Global Displacement | Beam A2B2 Horizontal Longitudinal | GD A2B2HL |
| 99 | Global Displacement | Beam B2C2 Horizontal Longitudinal | GD B2C2HL |
| 100 | Global Displacement | Temposonic Mass Car Left | GD TEMPML |
| 48 | Force Transducer | Column A Axial North | FT CAAN |
| 49 | Force Transducer | Column A In-Plane Shear North | FT CAIPSN |
| 50 | Force Transducer | Column A Out-Of-Plane Shear North | FT CAOPSN |
| 51 | Force Transducer | Column A Axial South | FT CAAS |
| 52 | Force Transducer | Column A In-Plane Shear South | FT CAIPSS |
| 53 | Force Transducer | Column A Out-Of-Plane Shear South | FT CAOPSS |
| 54 | Force Transducer | Column B Axial North | FT CBAN |
| 55 | Force Transducer | Column B In-Plane Shear North | FT CBIPSN |
| 56 | Force Transducer | Column B Out-Of-Plane Shear North | FT CBOPSN |
| 57 | Force Transducer | Column B Axial South | FT CBAS |
| 58 | Force Transducer | Column B In-Plane Shear South | FT CBIPSS |
| 59 | Force Transducer | Column B Out-Of-Plane Shear South | FT CBOPSS |
| 60 | Force Transducer | Column C Axial North | FT CCAN |
| 61 | Force Transducer | Column C In-Plane Shear North | FT CCIPSN |
| 62 | Force Transducer | Column C Out-Of-Plane Shear North | FT CCOPSN |
| 63 | Force Transducer | Column C Axial South | FT CCAS |

| Channel # | Category | Description | Name |
|-----------|------------------|-----------------------------------|------------|
| 64 | Force Transducer | Column C In-Plane Shear South | FT CCI PSS |
| 65 | Force Transducer | Column C Out-Of-Plane Shear South | FT CCOPSS |
| 66 | Force Transducer | Column A Top Hinge | FT CATH |
| 67 | Force Transducer | Column B Top Hinge | FT CBTH |
| 68 | Force Transducer | Column C Top Hinge | FT CCTH |

Table B-5. Instrumentation list for specimen MUFS

| Channel # | Category | Description | Name |
|-----------|--------------------|------------------------------------|----------|
| 1 | Accelerometer | Footing B Horizontal | AC FBH |
| 2 | Accelerometer | Footing B Vertical | AC FBV |
| 3 | Accelerometer | A1 Horizontal | AC A1H |
| 4 | Accelerometer | A1 Transverse | AC A1T |
| 5 | Accelerometer | A1 Vertical | AC A1V |
| 6 | Accelerometer | B1 Horizontal | AC B1H |
| 7 | Accelerometer | B1 Vertical | AC B1V |
| 8 | Accelerometer | C1 Horizontal | AC C1H |
| 9 | Accelerometer | C1 Transverse | AC C1T |
| 10 | Accelerometer | C1 Vertical | AC C1V |
| 11 | Accelerometer | A2 Horizontal | AC A2H |
| 12 | Accelerometer | A2 Vertical | AC A2V |
| 13 | Accelerometer | B2 Horizontal | AC B2H |
| 14 | Accelerometer | B2 Transverse | AC B2T |
| 15 | Accelerometer | B2 Vertical | AC B2V |
| 16 | Accelerometer | C2 Horizontal | AC C2H |
| 17 | Accelerometer | C2 Vertical Left | AC C2V |
| 18 | Accelerometer | First Floor Mass Horizontal North | AC FFMHN |
| 19 | Accelerometer | Second Floor Mass Horizontal North | AC SFMHN |
| 20 | Accelerometer | Inertia Mass Horizontal North | AC IMHN |
| 78 | Accelerometer | Inertial-Mass Horizontal South | AC IMHS |
| 21 | Local Displacement | Column B1 Bottom Slip North | LD B1BSN |
| 22 | Local Displacement | Column B1 Bottom Slip South | LD B1BSS |
| 80 | Local Displacement | Column B1 Bottom Vertical North | LD B1BVN |
| 81 | Local Displacement | Column B1 Bottom Vertical South | LD B1BVS |
| 82 | Local Displacement | Column B1 Bottom Horizontal | LD B1BH |
| 83 | Local Displacement | Column B1 Bottom Diagonal | LD B1BD |
| 84 | Local Displacement | Column B1 Top Vertical North | LD B1TVN |
| 85 | Local Displacement | Column B1 Top Vertical South | LD B1TVS |
| 86 | Local Displacement | Column B1 Top Horizontal | LD B1TH |
| 87 | Local Displacement | Column B1 Top Diagonal | LD B1TD |
| 88 | Local Displacement | Joint A1 Diagonal East | LD JA1DE |
| 89 | Local Displacement | Joint C1 Diagonal East | LD JC1DE |
| 90 | Local Displacement | Joint C1 Vertical North | LD JC1VN |
| 91 | Local Displacement | Joint C1 Vertical South | LD JC1VS |
| 92 | Local Displacement | Joint C1 Horizontal Top | LD JC1HT |
| 93 | Local Displacement | Joint C1 Horizontal Bottom | LD JC1HB |

| Channel # | Category | Description | Name |
|-----------|---------------------|---|------------|
| 94 | Local Displacement | Joint C1 Diagonal Top North | LD JC1DTN |
| 95 | Local Displacement | Joint C1 Diagonal Top South | LD JC1DTS |
| 23 | Global Displacement | Column A1 Vertical North | GD A1VN |
| 24 | Global Displacement | Column A1 Vertical South | GD A1VS |
| 25 | Global Displacement | Column A1 Horizontal Transverse | GD A1HT |
| 26 | Global Displacement | Column A1 Horizontal Longitudinal | GD A1HL |
| 27 | Global Displacement | Column A1 Horizontal Longitudinal Top | GD A1HLT |
| 28 | Global Displacement | Column B1 Vertical North | GD B1VN |
| 29 | Global Displacement | Column B1 Vertical South | GD B1VS |
| 30 | Global Displacement | Column C1 Vertical North | GD C1VN |
| 31 | Global Displacement | Column C1 Vertical South | GD C1VS |
| 32 | Global Displacement | Column C1 Horizontal Transverse | GD C1HT |
| 33 | Global Displacement | Column A2 Vertical | GD A2V |
| 34 | Global Displacement | Column A2 Horizontal Longitudinal | GD A2HL |
| 35 | Global Displacement | Column B2 Vertical | GD B2V |
| 36 | Global Displacement | Column B2 Horizontal Transverse | GD B2HT |
| 37 | Global Displacement | Column C2 Vertical | GD C2V |
| 38 | Global Displacement | Diagonal B1 Bottom A1 Top | GD DB1BA1T |
| 39 | Global Displacement | Diagonal B1 Bottom C1 Top | GD DB1BC1T |
| 40 | Global Displacement | Diagonal Middle Beam B2 Top | GD DMBB2T |
| 41 | Global Displacement | Diagonal Middle Beam C2 Top | GD DMBC2T |
| 42 | Global Displacement | Diagonal Middle Beam Steel Beam Top | GD DMBSBT |
| 43 | Global Displacement | Longitudinal North Mass First Floor Top | GD LNMFFT |
| 44 | Global Displacement | Longitudinal North Mass Second FL Top | GD LNMSFT |
| 45 | Global Displacement | Longitudinal North Inertial-Mass Top | GD LNIMT |
| 46 | Global Displacement | Transverse North Inertial-Mass Top | GD TNIMT |
| 47 | Global Displacement | Footing B1 Vertical Left | GD FB1VL |
| 96 | Global Displacement | Beam A1B1 Horizontal Longitudinal | GD A1B1HL |
| 97 | Global Displacement | Beam B1C1 Horizontal Longitudinal | GD B1C1HL |
| 98 | Global Displacement | Beam A2B2 Horizontal Longitudinal | GD A2B2HL |
| 99 | Global Displacement | Beam B2C2 Horizontal Longitudinal | GD B2C2HL |
| 100 | Global Displacement | Temposonic Mass Car Left | GD TEMPML |
| 48 | Force Transducer | Column A Axial North | FT CAAN |
| 49 | Force Transducer | Column A In-Plane Shear North | FT CAIPSN |
| 50 | Force Transducer | Column A Out-Of-Plane Shear North | FT CAOPSN |
| 51 | Force Transducer | Column A Axial South | FT CAAS |
| 52 | Force Transducer | Column A In-Plane Shear South | FT CAIPSS |
| 53 | Force Transducer | Column A Out-Of-Plane Shear South | FT CAOPSS |
| 54 | Force Transducer | Column B Axial North | FT CBAN |
| 55 | Force Transducer | Column B In-Plane Shear North | FT CBIPSN |
| 56 | Force Transducer | Column B Out-Of-Plane Shear North | FT CBOPSN |
| 57 | Force Transducer | Column B Axial South | FT CBAS |
| 58 | Force Transducer | Column B In-Plane Shear South | FT CBIPSS |
| 59 | Force Transducer | Column B Out-Of-Plane Shear South | FT CBOPSS |
| 60 | Force Transducer | Column C Axial North | FT CCAN |
| 61 | Force Transducer | Column C In-Plane Shear North | FT CCIPSN |
| 62 | Force Transducer | Column C Out-Of-Plane Shear North | FT CCOPSN |
| 63 | Force Transducer | Column C Axial South | FT CCAS |

| Channel # | Category | Description | Name |
|-----------|------------------|-----------------------------------|------------|
| 64 | Force Transducer | Column C In-Plane Shear South | FT CCI PSS |
| 65 | Force Transducer | Column C Out-Of-Plane Shear South | FT CCOPSS |
| 66 | Force Transducer | Column A Top Hinge | FT CATH |
| 67 | Force Transducer | Column B Top Hinge | FT CBTH |
| 68 | Force Transducer | Column C Top Hinge | FT CCTH |

B.3.1 Force Transducers

Force transducers (load cells) were used in pairs under each of footings to monitor the redistribution of shear and axial load during testing. Each force transducer was capable of measuring orthogonal shears and axial load. Due to significant shear and axial loads expected to be induced during the tests, load cells with high capacity (1000 kN for axial load and 500 kN for shear) were fabricated. Each load cell with the external diameter of 200mm and height of 250mm was connected to 300x300x25 mm end plates. Figure B-1 demonstrates the connection of load cells to the table and footings.



Figure B-1. Connection of load cells to footings and shaking table

B.3.2 Accelerometers

Accelerometers with a sensitivity of $100\text{Hz} \pm 0.5\%$ were mounted on the west side of the specimen at the footing on axis B (vertical and longitudinal directions), joints at each story

level (vertical, longitudinal and transverse directions), and on inertial-mass wagons. Figure B-2 demonstrates the location and name of the accelerometers used for the shaking table tests.

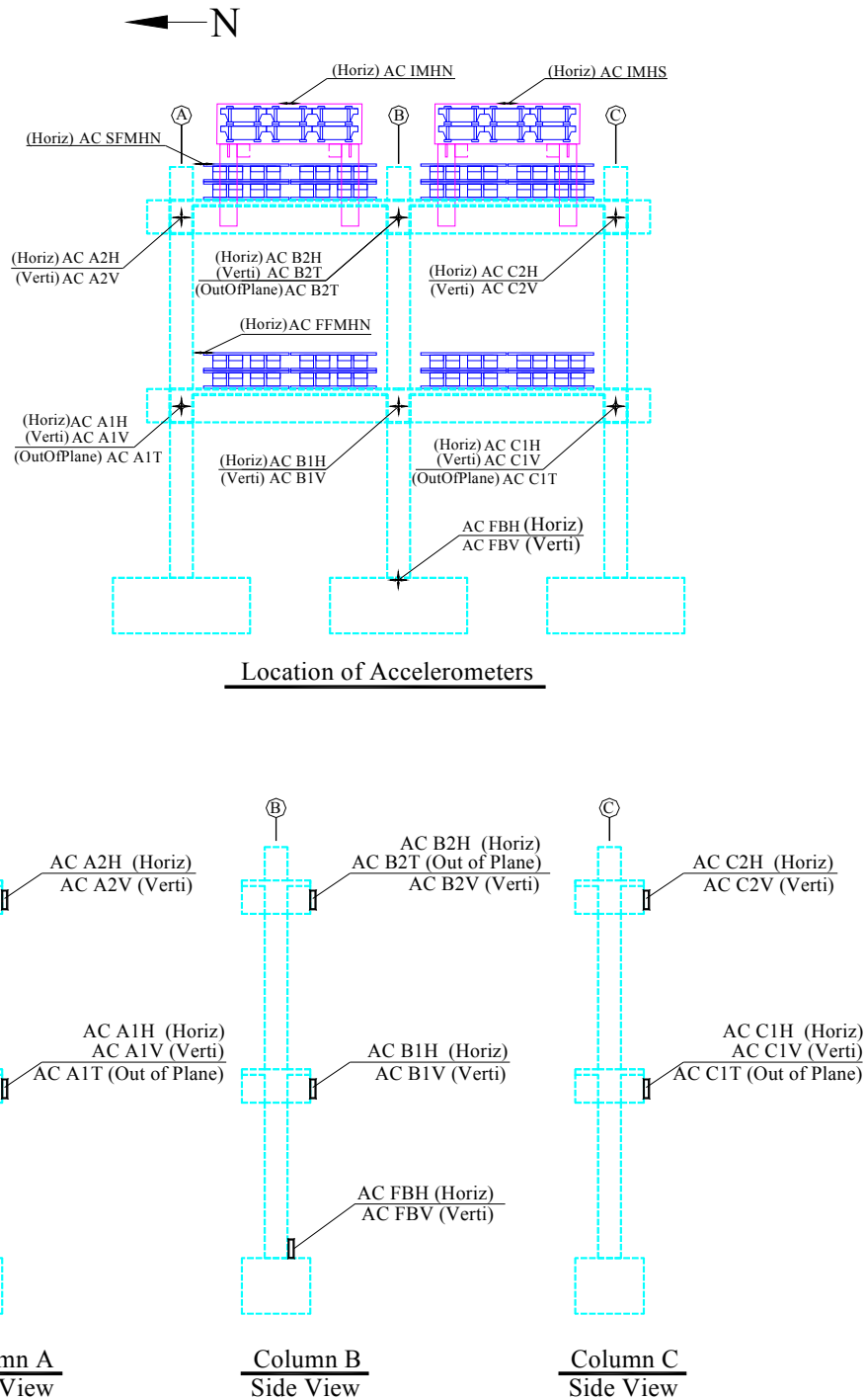


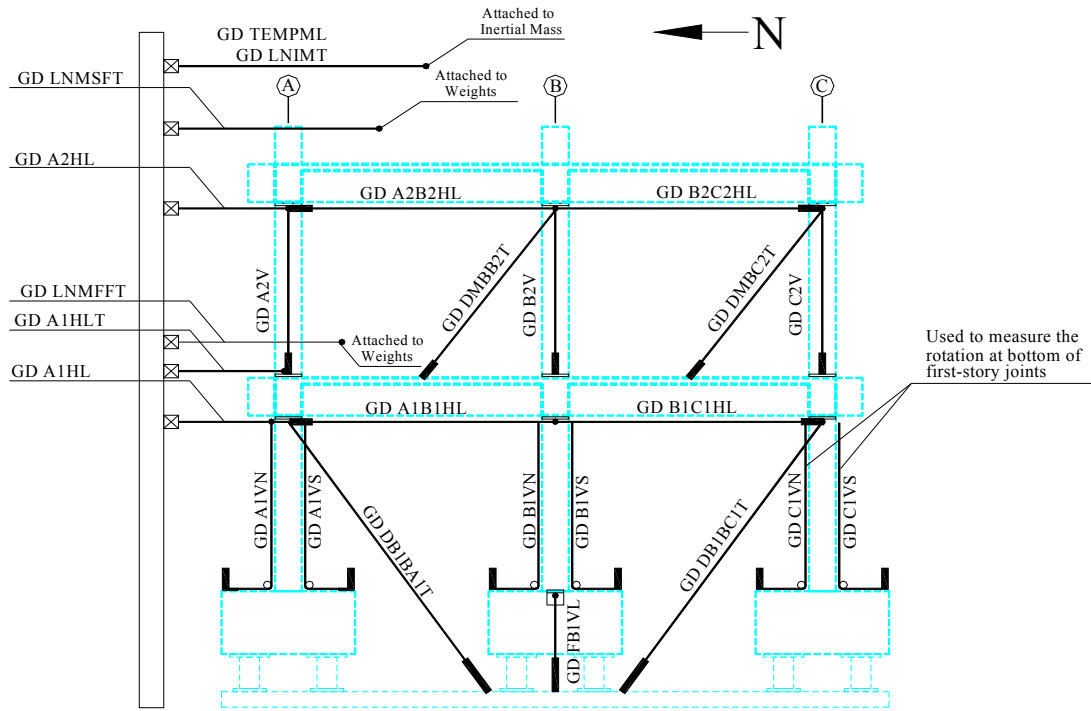
Figure B-2. Location and name of accelerometers

B.3.3 Displacement Measuring Instruments

There were three groups of displacement transducers (DTs) attached to the test frame: 1) DTs attached to the frame at story levels to measure global horizontal displacement of the frame; 2) DTs used for measuring the vertical displacement of the columns; 3) DTs attached to the frame joints for monitoring relative joint deformations. Figure B-3 and Figure B-4 demonstrate the location and name of the displacement transducers used for all the specimens. DTs included *string-pot* and *Novotechnik* potentiometers. With a measurement range up to 1000mm and linearity of $\pm 0.15\%$, string-pots were used for measuring the global deformation of the specimens and vertical displacement of columns. On the other hand, Novotechniks with a measurement range of 100mm and linearity of $\pm 0.075\%$ were used for local instrumentation of members such as the exterior joints. Six Novotechnik potentiometers were mounted on the confined face of joint C1 of all the specimens, while additional potentiometers were mounted on the open face of the exterior joints A1 and C1 in specimens MUF and MUFS to measure the shear deformations. Figure B-5 and Figure B-6 demonstrate the location and name of the instruments used to measure the local deformation of exterior first-story joints and column B1. All DTs were listed and described for each specimen in Table B-2 through Table B-5.

B.3.4 Strain Gages

A total of 40 strain gages were placed on longitudinal and transverse reinforcing bars of columns, beams, and joints. Figure B-7 to Figure B-10 show detailed locations of these strain gages. Many of the gages were damaged during construction and did not provide output during the tests, therefore, only the strain gages whose readings were recorded during the tests were shown in above-mentioned figures.



Elevation View of Displacement Measuring Instruments

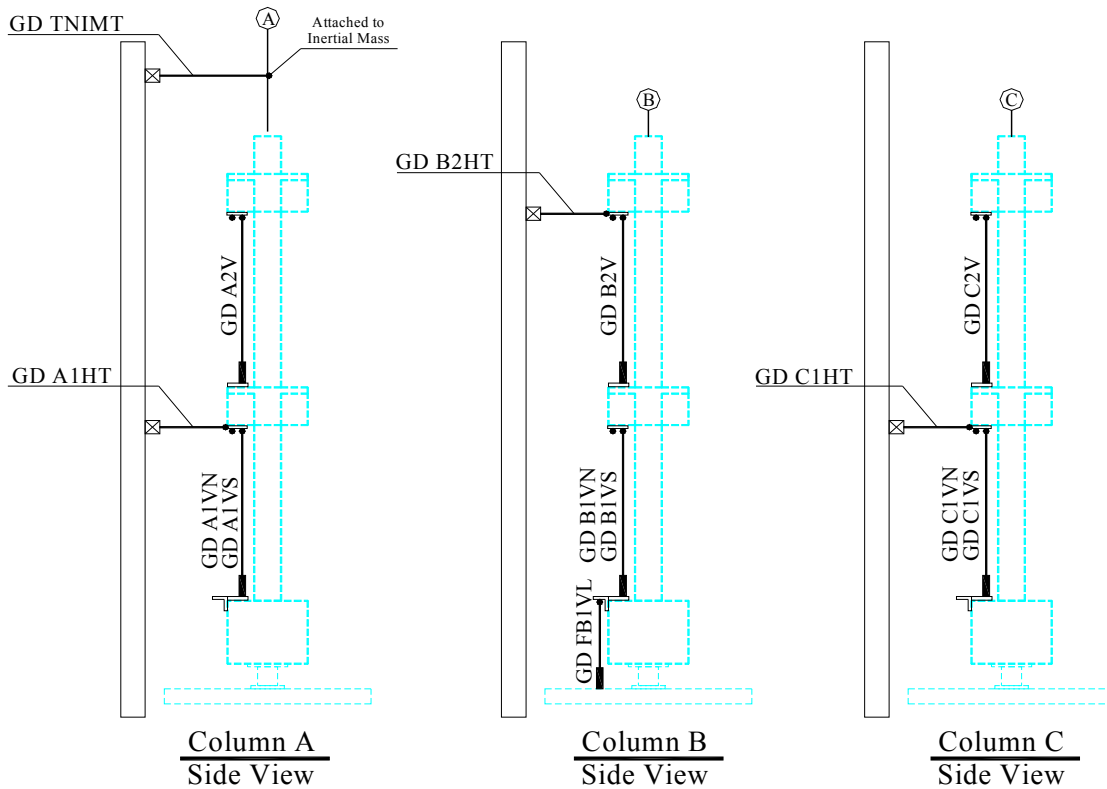
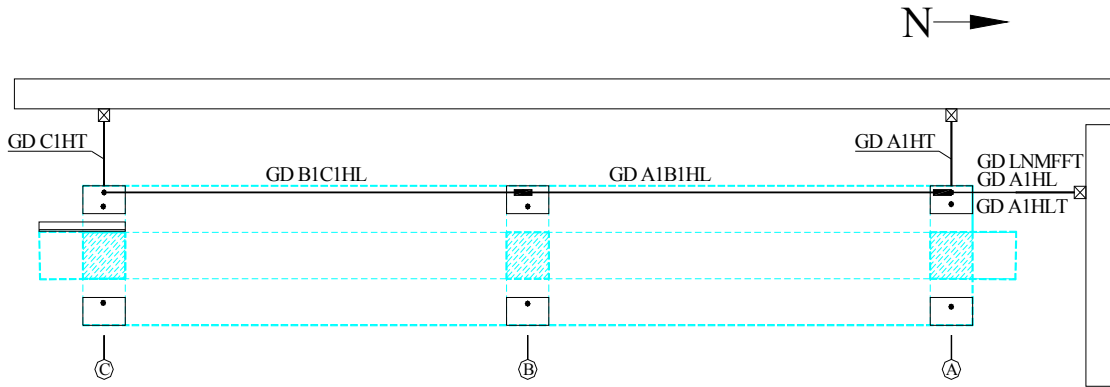
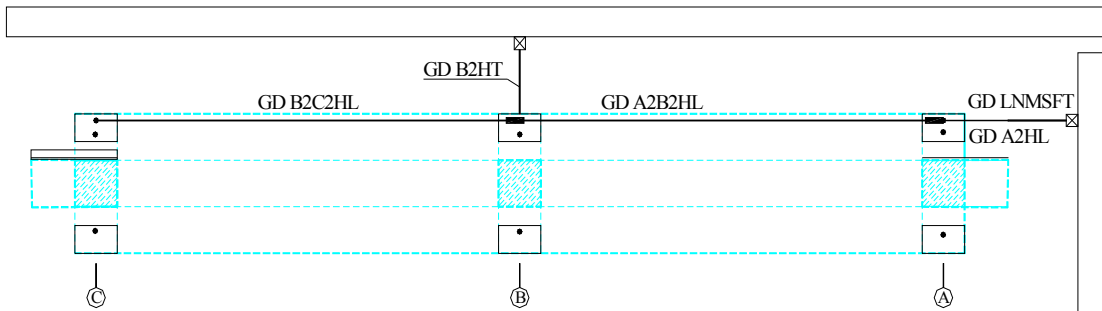


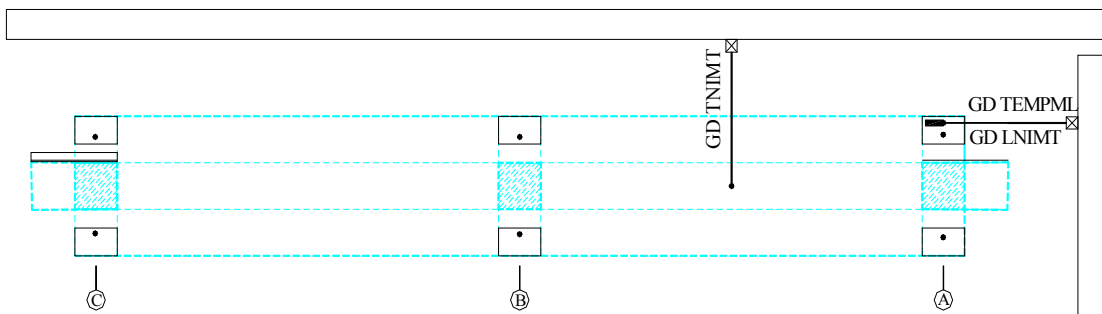
Figure B-3. Elevation and side views of displacement measuring instruments



First-Story Plan View of Disp. Measuring Instruments



Second-Story Plan View of Disp. Measuring Instruments



Top Plan View of Disp. Measuring Instruments

Figure B-4. Plan view of displacement measuring instruments

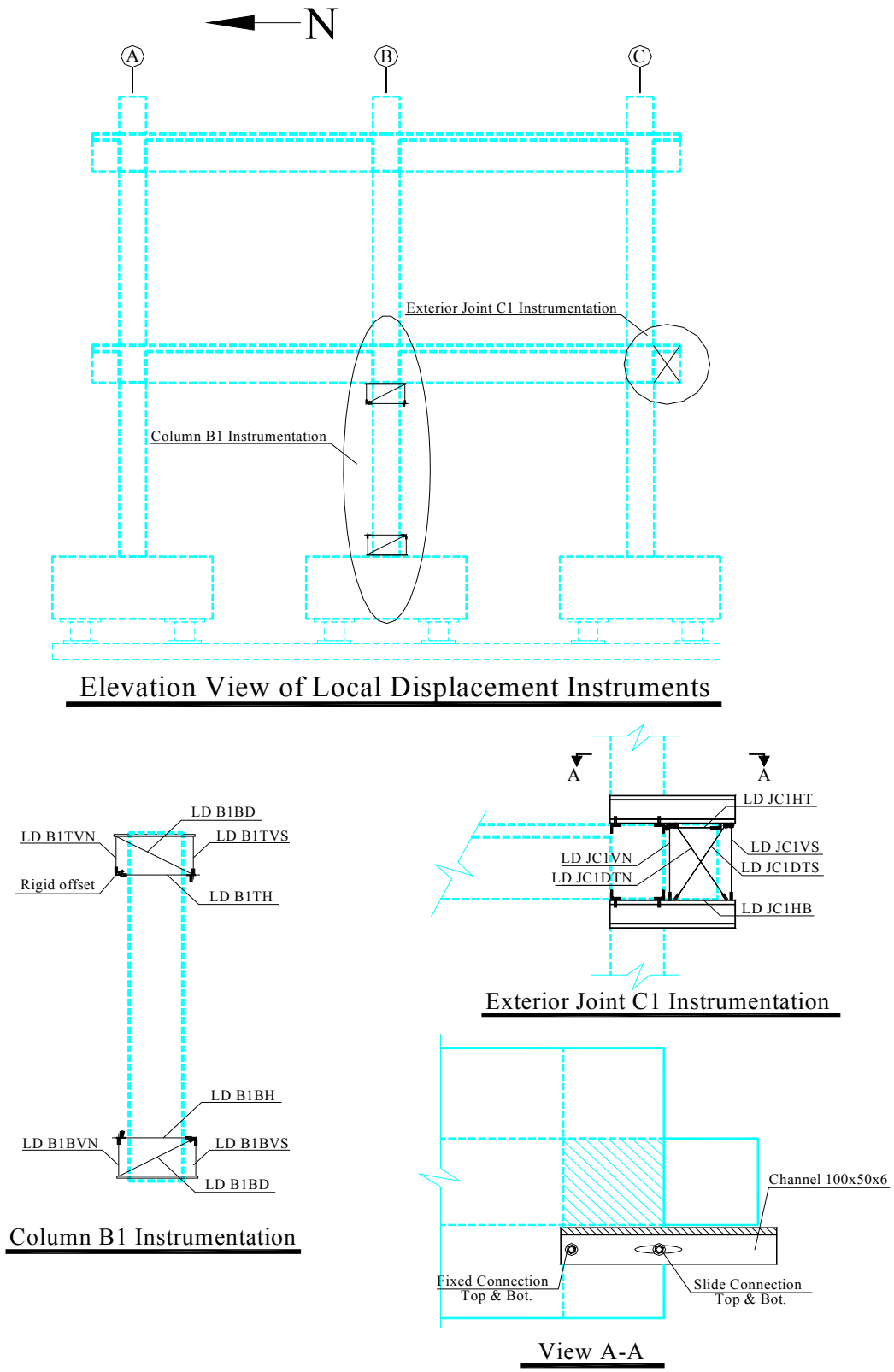
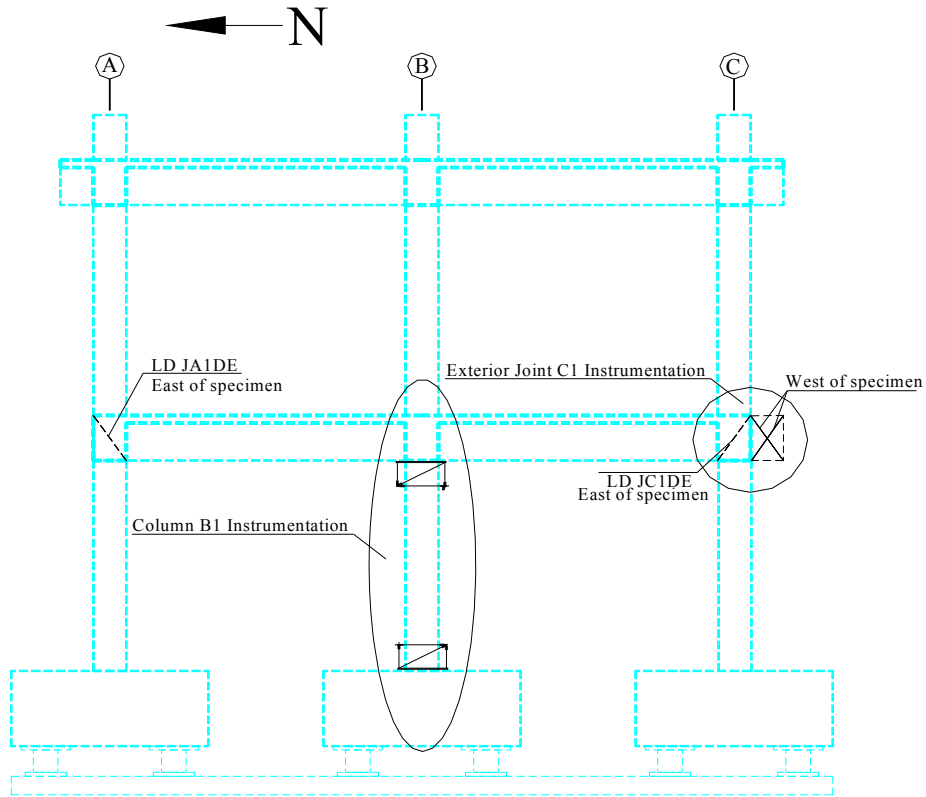
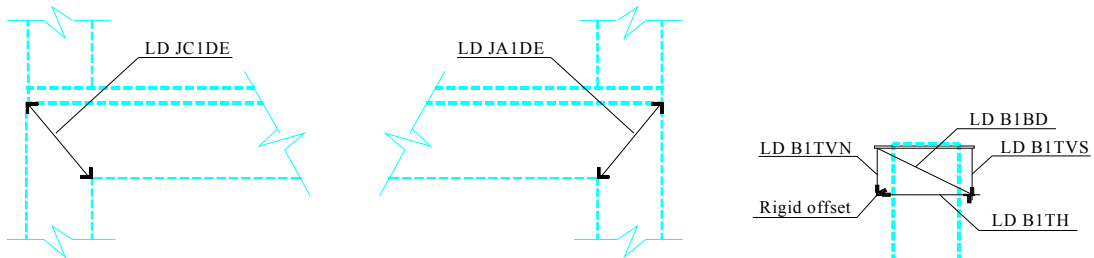


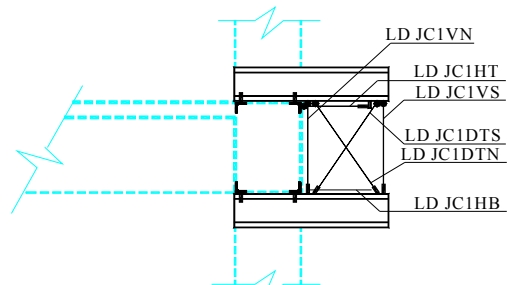
Figure B-5. Layout of local instrumentation for column B1 and Joint C1, specimens MCFS and HCFS



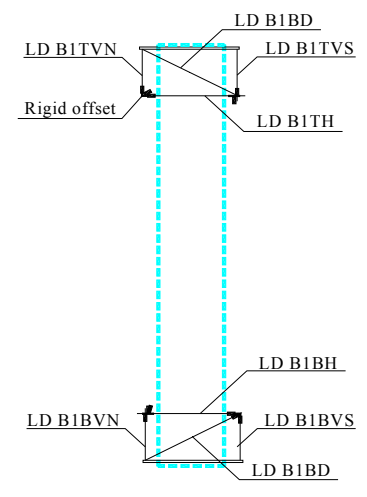
Elevation View of Local Displacement Instruments



Exterior Joints Instrumentation (East Side)

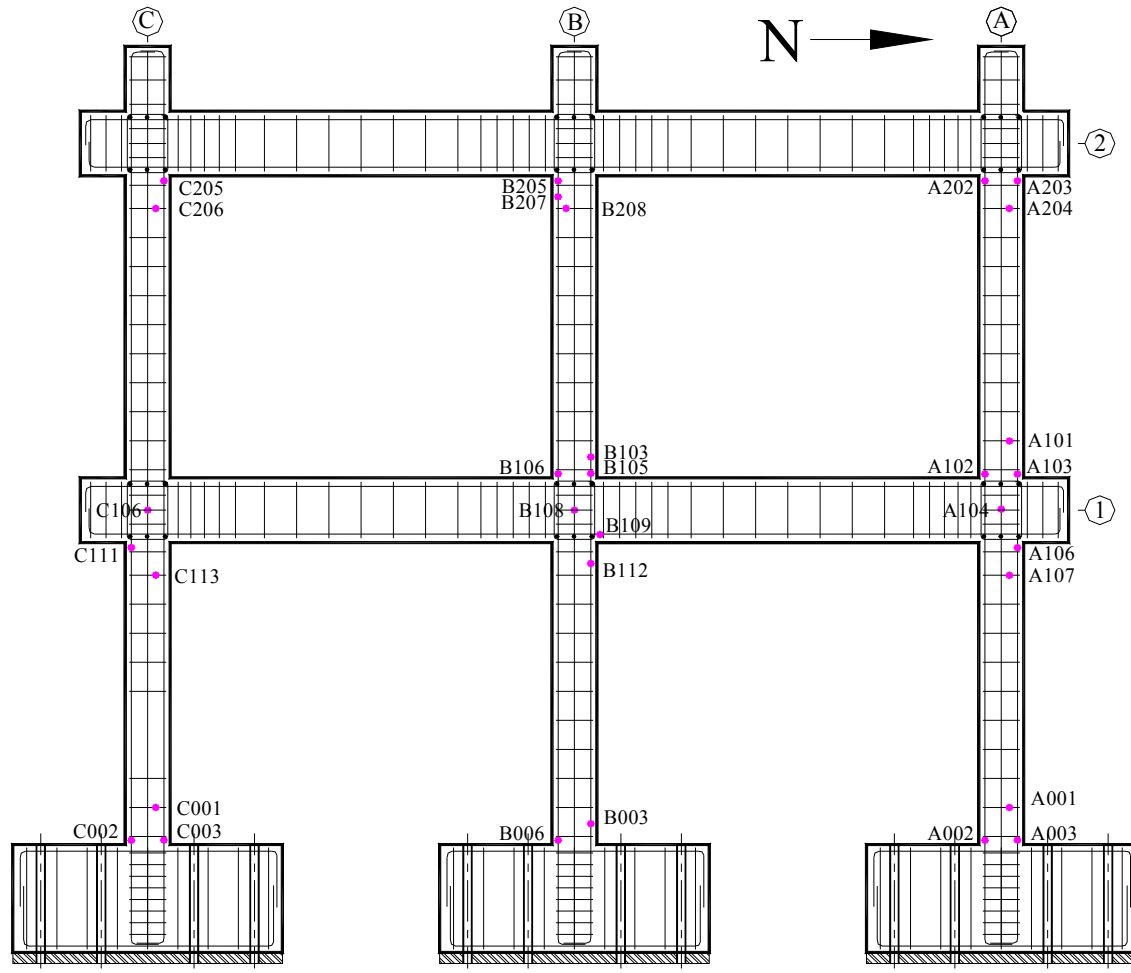


Exterior Joint C1 Instrumentation (West Side)



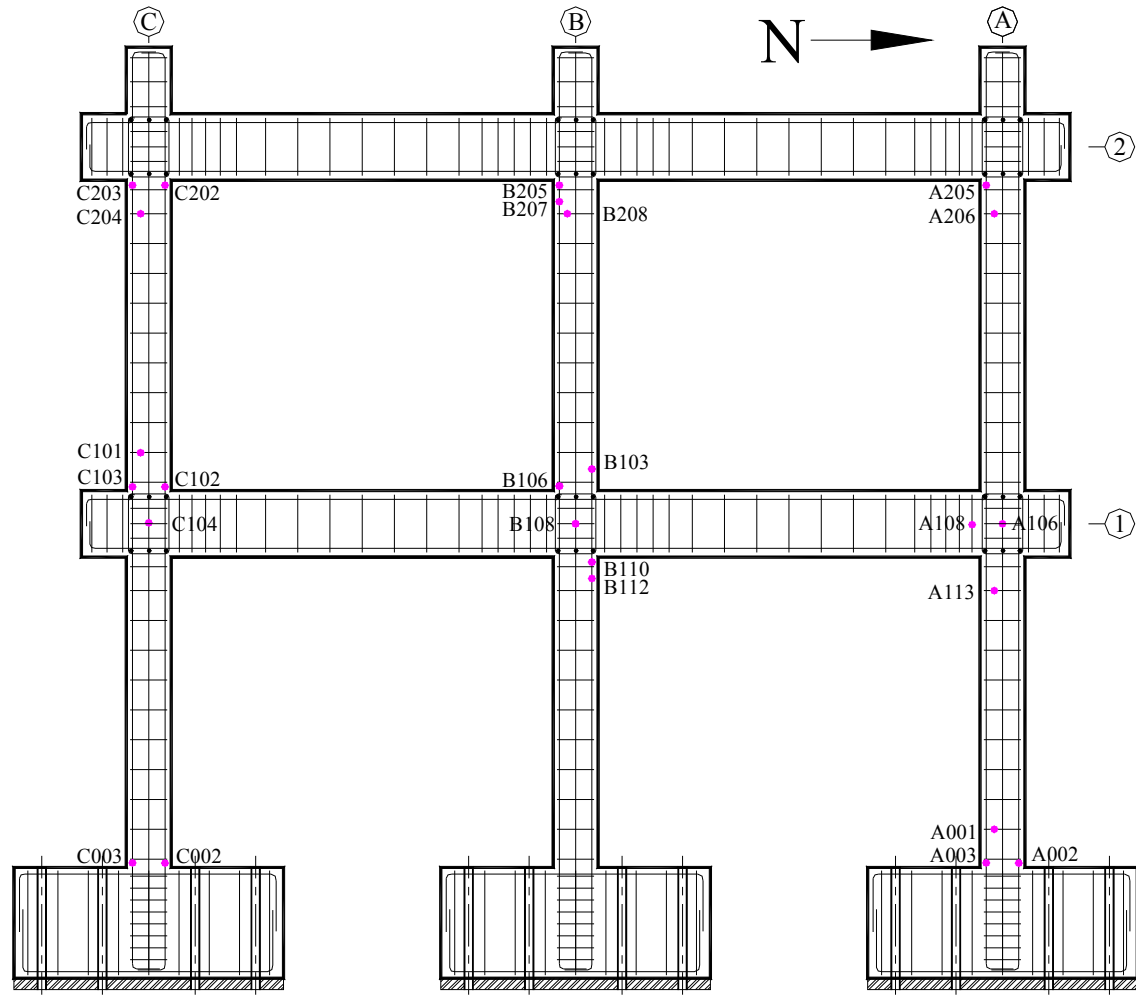
Column B1 Instrumentation

Figure B-6. Layout of local instrumentation for column B1 and Joint C1, specimens MUF and MUFS



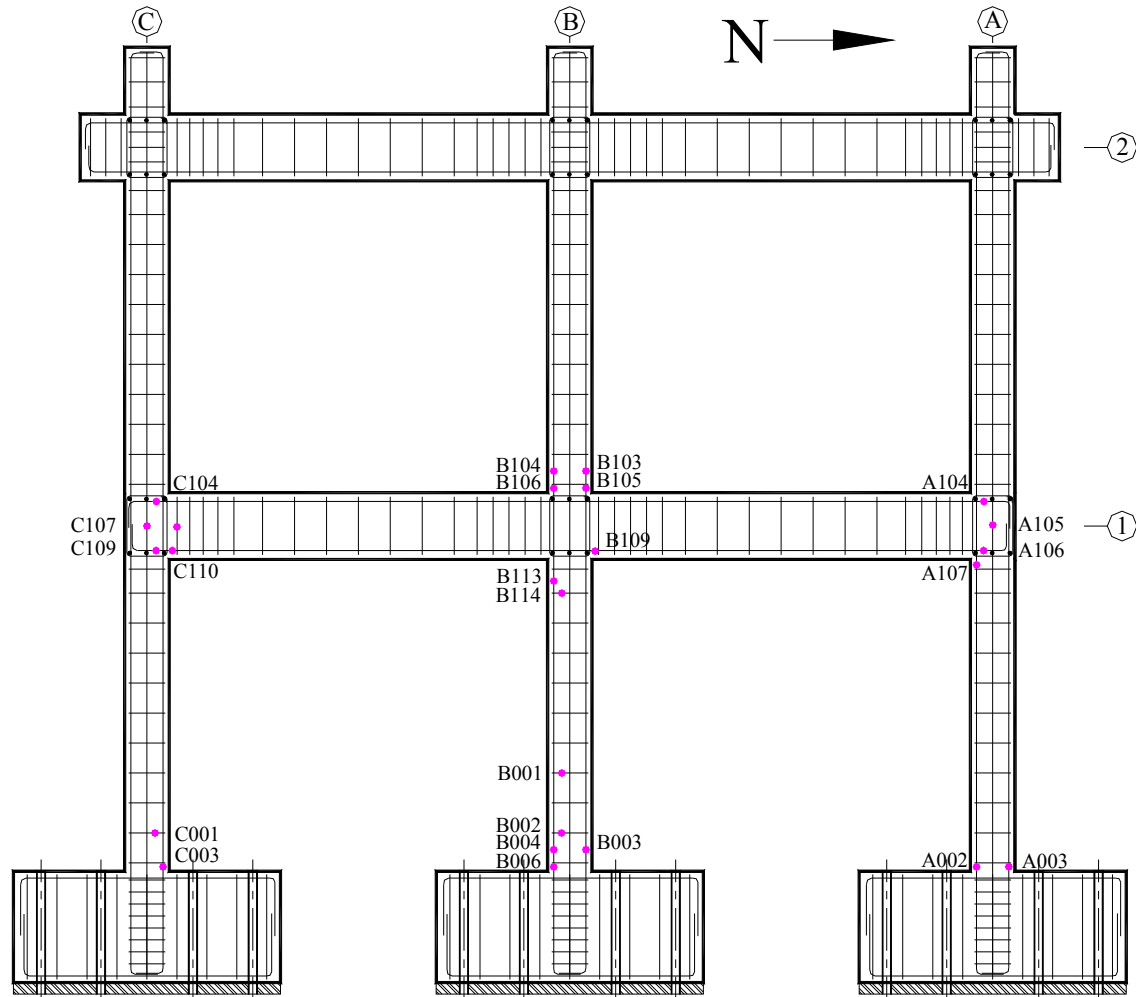
Number of gages: [Column A: 12
Column B: 11
Column C: 8

Figure B-7. Location of strain gages, specimen MCFS



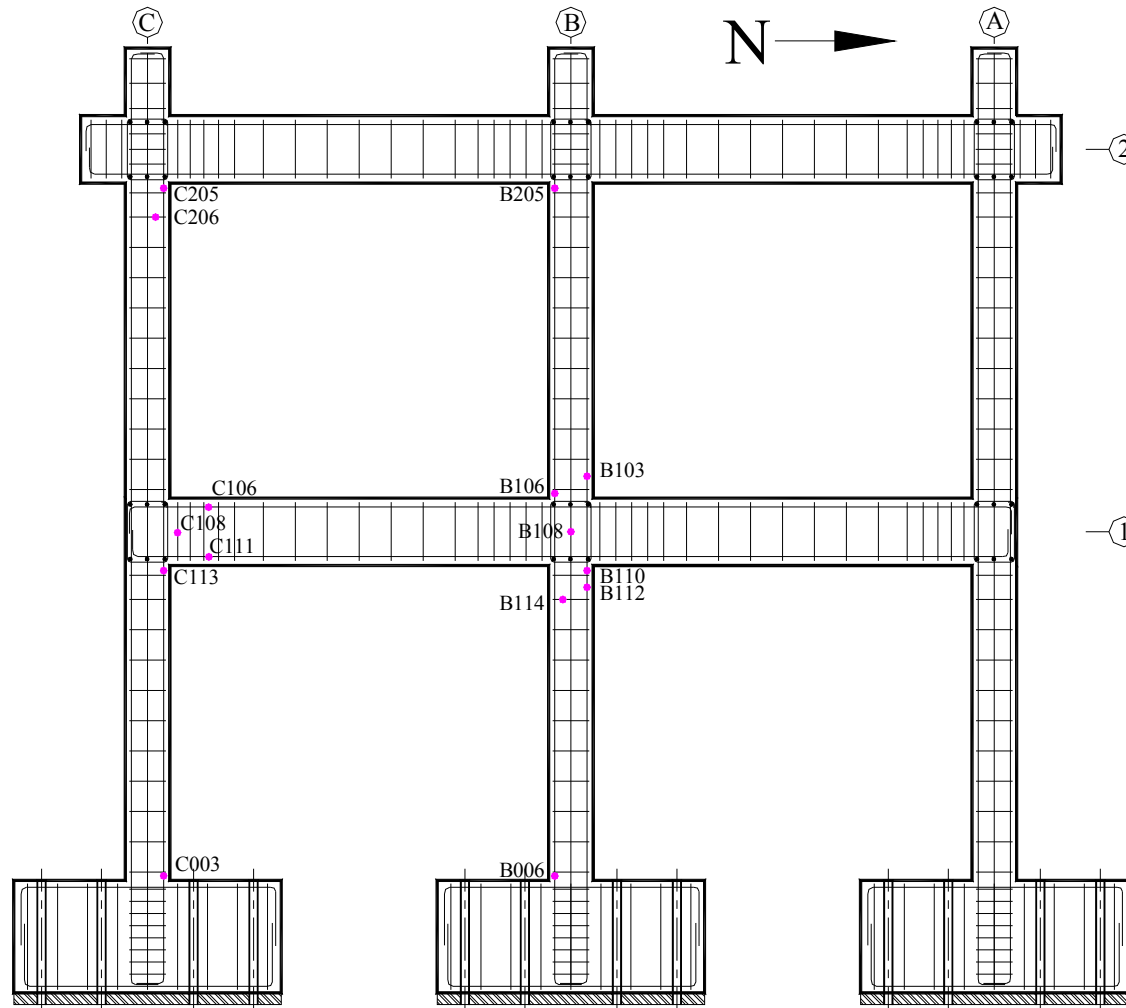
Number of gages: { Column A: 8
Column B: 8
Column C: 9

Figure B-8. Location of strain gages, specimen HCFS



Number of gages: — Column A: 6
 — Column B: 12
 — Column C: 6

Figure B-9. Location of strain gages, specimen MUF



Number of gages: — Column A: 0
 — Column B: 8
 — Column C: 7

Figure B-10. Location of strain gages, specimen MUFS

B.4 Data Reduction

This section summarizes the procedures used to reduce the recorded data to the results presented in Chapters 4 and 5. Frequency filtering was applied to all instrument channels to eliminate high frequency noise content of instrumentation outputs. The built-in Matlab 7.4 (MathWorks, 2007) filtering function “filtfilt” was used with a Butterworth 8th order band-pass filter design. More information on the command can be found in the software help of Matlab 7.4 (MathWorks, 2007).

In order to compare the results from the sequential shaking table tests of each specimen, as well as the results from testing different specimens (Chapters 4 and 5), data must be synchronized. As discussed in Chapter 3, the four specimens were subjected to the same input table motion. Therefore, the longitudinal acceleration recorded at table-level was selected to synchronize the rest of the recorded data for different tests. Time steps at five peaks were compared and matched to provide the best possible synchronization of data. As the same input motion, but with different amplitudes were used for the sequential testing of each specimen, similar procedure was taken to synchronize the data from sequential testing of each specimen.

The longitudinal displacements were recorded by several instruments including diagonal displacement transducers (see Figure B-3 and Figure B-4). The results from the instruments measuring horizontal displacement were compared with the horizontal component from the output from the diagonal instruments to confirm the accuracy of data. The corrected vertical displacements from the north and south sides of first-story columns were averaged to get the vertical displacements for such columns shown in Chapter 4.

The base shear for each of the specimens was determined by summing the shear values recorded by the force transducers. While shear for each of the columns in the first story was

obtained by summing the shear recorded from the load cells under the columns, it was not possible to directly measure the shear for second-story columns. Therefore, the shear in such columns was considered as a portion of the total shear calculated for the second story of the specimen. In the first step, second-story shear was obtained by subtracting the lateral force in the first story (first-story mass \times first-story acceleration) from the base shear. Then, at each time-step, the ratio of column shear to the base shear was obtained for each of first-story columns and multiplied by the shear in the second story to estimate the shear in the corresponding column in the second story. Although this method seemed to estimate shear in second-story column reasonably well, the results became improperly large at small base shear values (before 25 and after 35 seconds). Ignoring the large peaks, Figure B-11 demonstrates that the ratio of column shear to base shear tended to remain near 0.3 for the exterior columns and 0.4 for the middle one. Similar ratios were observed for all the specimens. Therefore, such coefficients were used to estimate shear in second-story columns.

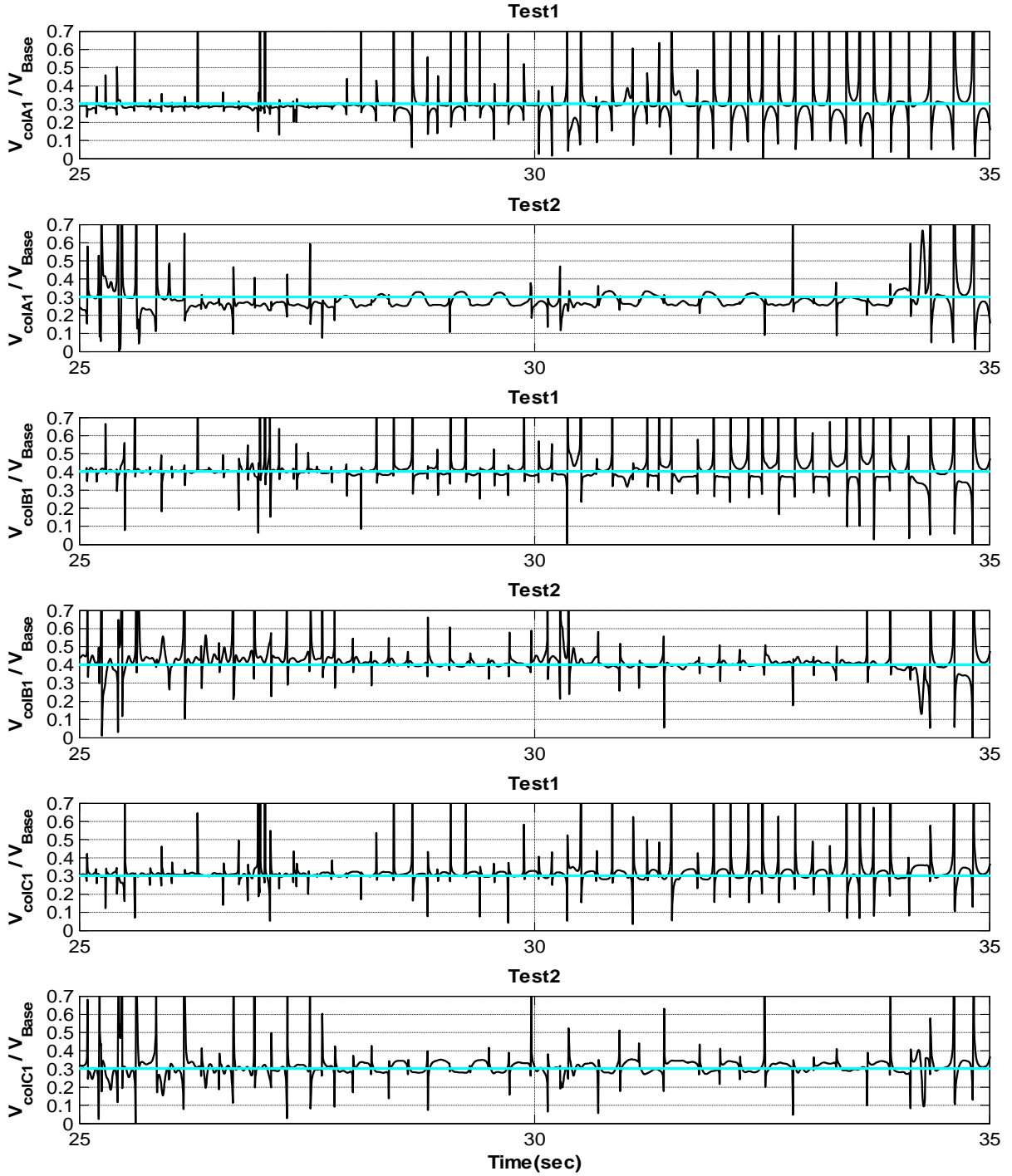


Figure B-11. Ratio of column shear to base shear for first-story columns of specimen MCFS

Moments, shears, and axial forces for first-story columns of each specimen were calculated using shear, and axial load readings of load cells. Figure C-17 shows a typical first-

story column, load cell layout, and a schematic representation of forces. From basic equilibrium, the following equations were obtained that relate column forces to load cell readings (see Figure B-12 for illustration of terms):

Column Axial Loads: (Units: kN)

$$A_b = A_1 + A_2 - M_f \times g$$

$$A_t = A_b - W_{col}$$

where A_b is axial load at the base of column (this is the axial load presented in all figures), A_t is axial load at the top of column, A_1 and A_2 are the load cell axial load readings, M_f is the mass of footing, and W_{col} is the weight of column.

Shear Forces at Column Base and Top (Units: kN)

$$V_b = V_1 + V_2 - M_f \times Acc_f$$

$$V_t = V_b - M_{col}/2 \times Acc_f - M_{col}/2 \times Acc_{1st}$$

where V_b is column shear at the base (this is the shear presented in all figures), V_1 and V_2 are the load cell shear readings, V_t is shear at the column top, M_{col} is the column mass, Acc_f is the footing acceleration (acceleration recorded at footing B₀ was used for all), and Acc_{1st} is first-story horizontal acceleration (average of acceleration recorded at Joints A1, B1, and C1 was used for all).

Moments at Column Base and Top (Units: kN-m)

$$M_b = -(V_1 + V_2) \times 0.65 + (A_1 - A_2) \times 0.6/2 + M_f \times Acc_f \times 0.5/2$$

$$M_t = V_b \times 1.4 - M_b - A_b \times \Delta - M_{col}/2 \times Acc_f \times (3/4 \times 1.4) - M_{col}/2 \times Acc_{1st} \times (1/4 \times 1.4)$$

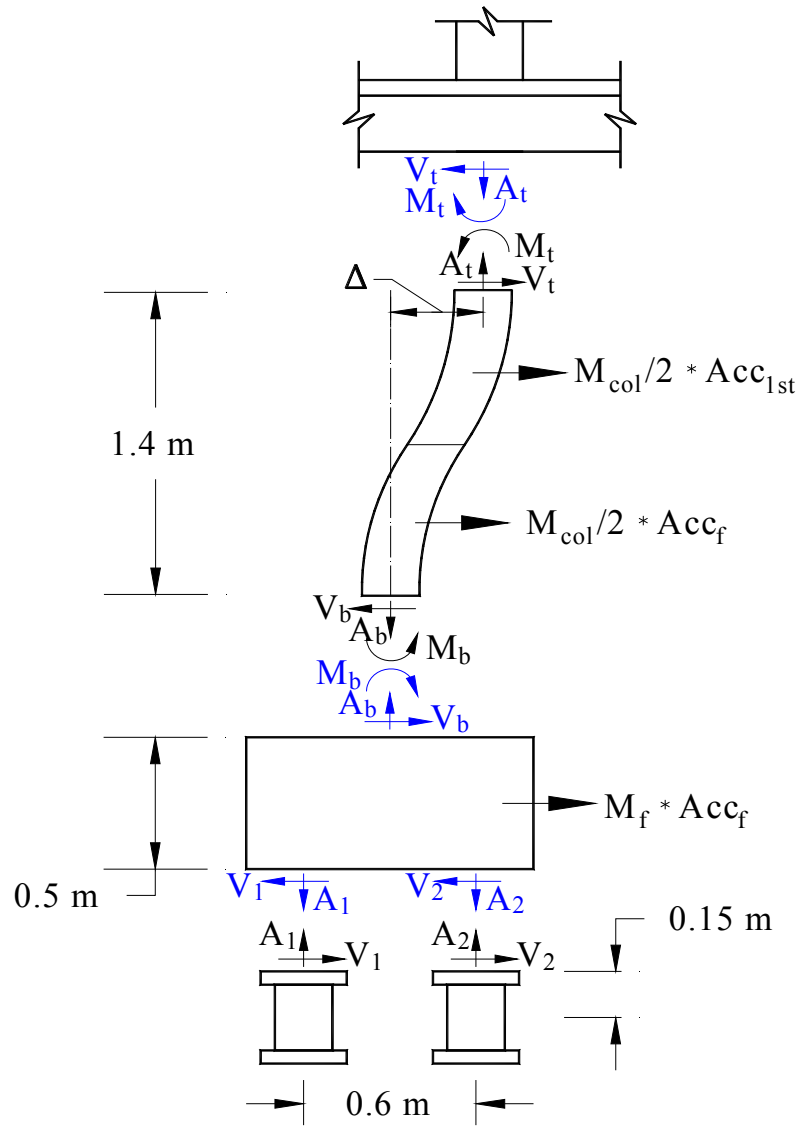


Figure B-12. Free-body diagram for first-story columns

B.5 Condition Assessment and Modeling Parameters for Existing Reinforced Concrete Columns Recommended by ASCE-41

Considering the capability of existing reinforced concrete columns to sustain limited plastic deformation due to flexural yielding prior to shear failure, ASCE-41 Supplement-1 (2008), classified such columns into three categories based on the nominal shear strength, V_n , the plastic shear demand on the column, V_p , and the transverse reinforcement detailing as shown in Table B-6.

Table B-6. Classification of columns for determination of modeling parameters (ASCE-41, 2008)

| | Transverse Reinforcement Details | | |
|------------------------------|--|-----------------------------|--|
| | ACI conforming details with 135° hooks | Closed hoops with 90° hooks | Other (including lap spliced transverse reinforcement) |
| $V_p/(V_n/k) \leq 0.6$ | Condition i | Condition ii | Condition ii |
| $1.0 \geq V_p/(V_n/k) > 0.6$ | Condition ii | Condition ii | Condition iii |
| $V_p/(V_n/k) > 1.0$ | Condition iii | Condition iii | Condition iii |

Note: k represents a modifier based on ductility demand, defined in ASCE-41.

The conditions in Table B-6 approximately correspond to the following failure modes:

- *Condition i*: Flexure failure
- *Condition ii*: Flexure-shear failure
- *Condition iii*: Shear failure

For each of these conditions, the modeling parameters for nonlinear analysis can be obtained using Table B-7 (Table 6-8 from ASCE-41, 2008). Plastic rotation angles a and b , required for obtaining M- θ relations for a column, was shown in Chapter 7 (Figure 7-8). Subsequently, shear backbone for the column can be calculated using the M- θ relations.

Table B-7. Modeling parameters and numerical acceptance criteria for nonlinear procedures for reinforced concrete columns (Table 6-8 of ASCE-41)

| Conditions | Modeling Parameters [‡] | | | Acceptance Criteria ^{‡,§} | | | | | | |
|--|----------------------------------|-------------------------------|-------------------------|------------------------------------|----------------|-------|-------|-------|-------|-------|
| | Plastic Rotations Angle, radians | | Residual Strength Ratio | Plastic Rotations Angle, radians | | | | | | |
| | | | | Performance Level | | | | | | |
| | a | b | c | IO | Component Type | | | | | |
| Primary | | | | | Secondary | | | | | |
| | | | | LS | CP | LS | CP | | | |
| Condition i. * | | | | | | | | | | |
| $\frac{P}{A_g f'_c}$ † | $\rho = \frac{A_v}{b_w s}$ | | | | | | | | | |
| ≤ 0.1 | ≥ 0.006 | | 0.035 | 0.060 | 0.2 | 0.005 | 0.026 | 0.035 | 0.045 | 0.060 |
| ≥ 0.6 | ≥ 0.006 | | 0.010 | 0.010 | 0.0 | 0.003 | 0.008 | 0.009 | 0.009 | 0.010 |
| ≤ 0.1 | = 0.002 | | 0.027 | 0.034 | 0.2 | 0.005 | 0.020 | 0.027 | 0.027 | 0.034 |
| ≥ 0.6 | = 0.002 | | 0.005 | 0.005 | 0.0 | 0.002 | 0.003 | 0.004 | 0.004 | 0.005 |
| Condition ii. * | | | | | | | | | | |
| $\frac{P}{A_g f'_c}$ † | $\rho = \frac{A_v}{b_w s}$ | $\frac{V}{b_w d \sqrt{f'_c}}$ | | | | | | | | |
| ≤ 0.1 | ≥ 0.006 | ≤ 3 (0.25) | 0.032 | 0.060 | 0.2 | 0.005 | 0.024 | 0.032 | 0.045 | 0.060 |
| ≤ 0.1 | ≥ 0.006 | ≥ 6 (0.5) | 0.025 | 0.060 | 0.2 | 0.005 | 0.019 | 0.025 | 0.045 | 0.060 |
| ≥ 0.6 | ≥ 0.006 | ≤ 3 (0.25) | 0.010 | 0.010 | 0.2 | 0.003 | 0.008 | 0.009 | 0.009 | 0.010 |
| ≥ 0.6 | ≥ 0.006 | ≥ 6 (0.5) | 0.008 | 0.008 | 0.2 | 0.003 | 0.006 | 0.007 | 0.007 | 0.008 |
| ≤ 0.1 | ≤ 0.0005 | ≤ 3 (0.25) | 0.012 | 0.012 | 0.0 | 0.005 | 0.009 | 0.010 | 0.010 | 0.012 |
| ≤ 0.1 | ≤ 0.0005 | ≥ 6 (0.5) | 0.006 | 0.006 | 0.0 | 0.004 | 0.005 | 0.005 | 0.005 | 0.006 |
| ≥ 0.6 | ≤ 0.0005 | ≤ 3 (0.25) | 0.004 | 0.004 | 0.0 | 0.002 | 0.003 | 0.003 | 0.003 | 0.004 |
| ≥ 0.6 | ≤ 0.0005 | ≥ 6 (0.5) | 0.0 | 0.0 | 0.0 | 0.0 | 0.0 | 0.0 | 0.0 | 0.0 |
| Condition iii. * | | | | | | | | | | |
| $\frac{P}{A_g f'_c}$ † | $\rho = \frac{A_v}{b_w s}$ | | | | | | | | | |
| ≤ 0.1 | ≥ 0.006 | | 0.0 | 0.060 | 0.0 | 0.0 | 0.0 | 0.0 | 0.045 | 0.060 |
| ≥ 0.6 | ≥ 0.006 | | 0.0 | 0.008 | 0.0 | 0.0 | 0.0 | 0.0 | 0.007 | 0.008 |
| ≤ 0.1 | ≤ 0.0005 | | 0.0 | 0.006 | 0.0 | 0.0 | 0.0 | 0.0 | 0.005 | 0.006 |
| ≥ 0.6 | ≤ 0.0005 | | 0.0 | 0.0 | 0.0 | 0.0 | 0.0 | 0.0 | 0.0 | 0.0 |
| Condition iv. Columns controlled by inadequate development or splicing along the clear height * | | | | | | | | | | |
| $\frac{P}{A_g f'_c}$ † | $\rho = \frac{A_v}{b_w s}$ | | | | | | | | | |
| ≤ 0.1 | ≥ 0.006 | | 0.0 | 0.060 | 0.4 | 0.0 | 0.0 | 0.0 | 0.045 | 0.060 |
| ≥ 0.6 | ≥ 0.006 | | 0.0 | 0.008 | 0.4 | 0.0 | 0.0 | 0.0 | 0.007 | 0.008 |
| ≤ 0.1 | ≤ 0.0005 | | 0.0 | 0.006 | 0.2 | 0.0 | 0.0 | 0.0 | 0.005 | 0.006 |
| 0.6 | ≤ 0.0005 | | 0.0 | 0.0 | 0.0 | 0.0 | 0.0 | 0.0 | 0.0 | 0.0 |

* Refer to Section 6.4.2.2.2 of ASCE-41 for definition of conditions i, ii, and iii. Columns are considered to be controlled by inadequate development or splices where the calculated steel stress at the splice exceeds the steel stress specified by Eq. (6-2) of ASCE-41. Where more than one of the conditions i, ii, iii, and iv occurs for a given component, use the minimum appropriate numerical value from the table.

† Where $P > 0.7A_g f'_c$, the plastic rotation angles should be taken as zero for all performance levels unless the column has transverse reinforcement consisting of hoops with 135 degree hooks spaced at $\leq d/3$ and the strength provided by the hoops (V_s) is at least three-fourths of the design shear. Axial load P shall be based on the maximum expected axial loads due to gravity and earthquake loads.

‡ Values between those listed in the table should be determined by linear interpolation.

§ Primary and secondary component demands should be within secondary component acceptance criteria where the full backbone curve is explicitly modeled including strength degradation and residual strength in accordance with Section 3.4.3.2 of ASCE-41.

|| V is the design shear force from NSP or NDP. f'_c in psi units (MPa in parentheses).

Appendix C. Results of Test3 for Specimen MUF

As discussed in Chapters 3 and 4, specimen MUF was the only specimen that did not collapse during Test2. Therefore, the intensity of the input table motion was increased up to the table limits (Test3). Specimen did not collapse even under such table demands. Results from Test3 for specimen MUF are shown in this section.

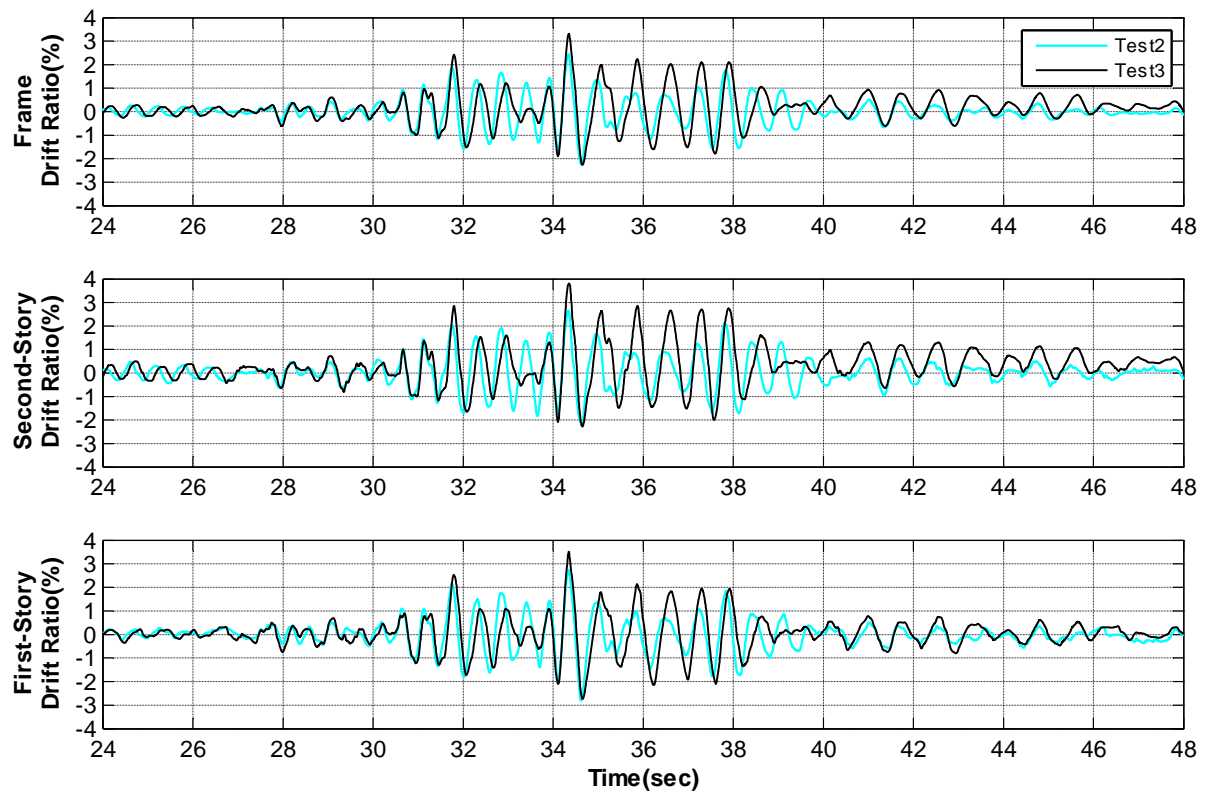


Figure C-1. Story-level drift response history for specimen MUF, Test2 and Test3

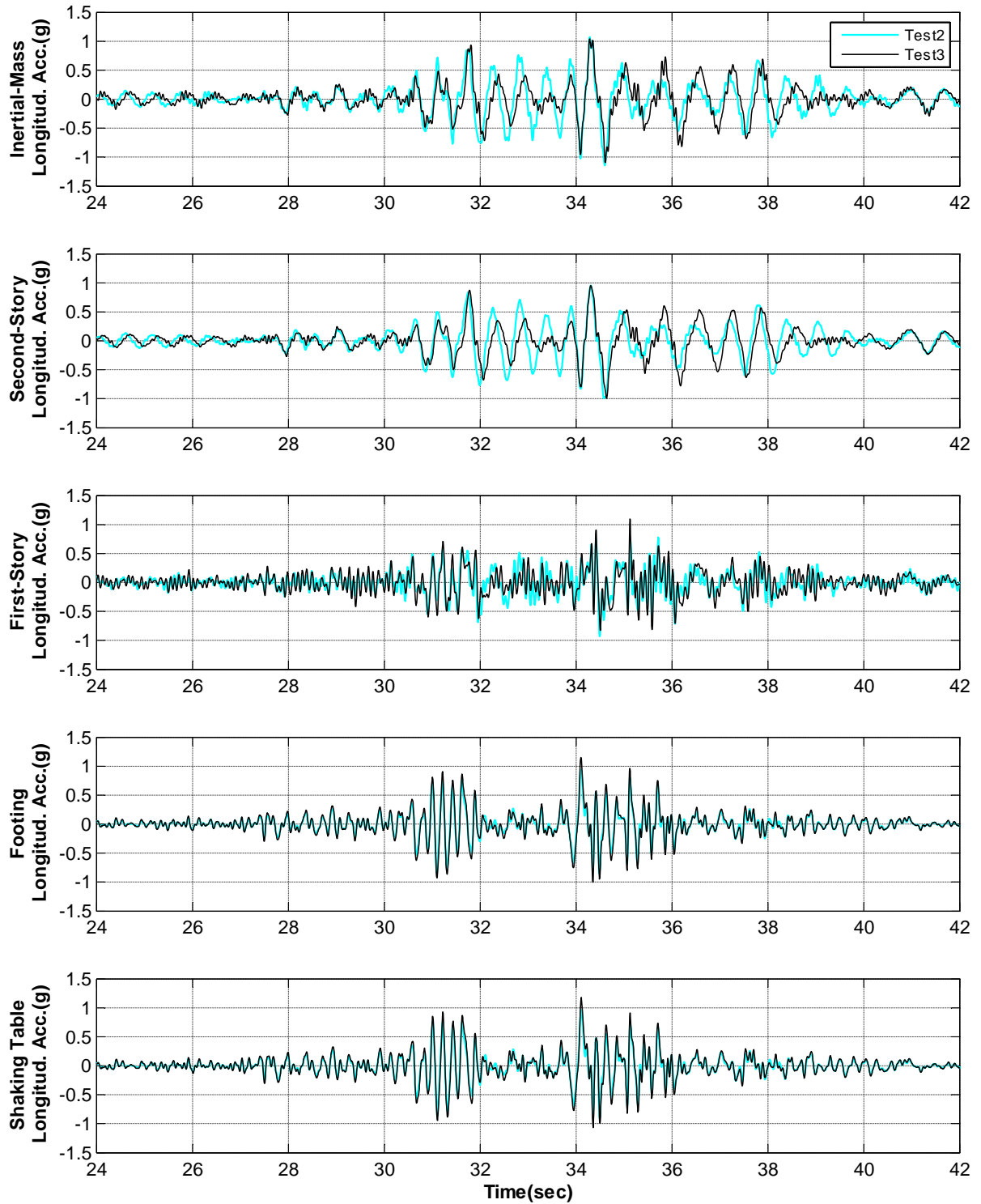


Figure C-2. Story-level acceleration records for specimen MUF, Test2 and Test3

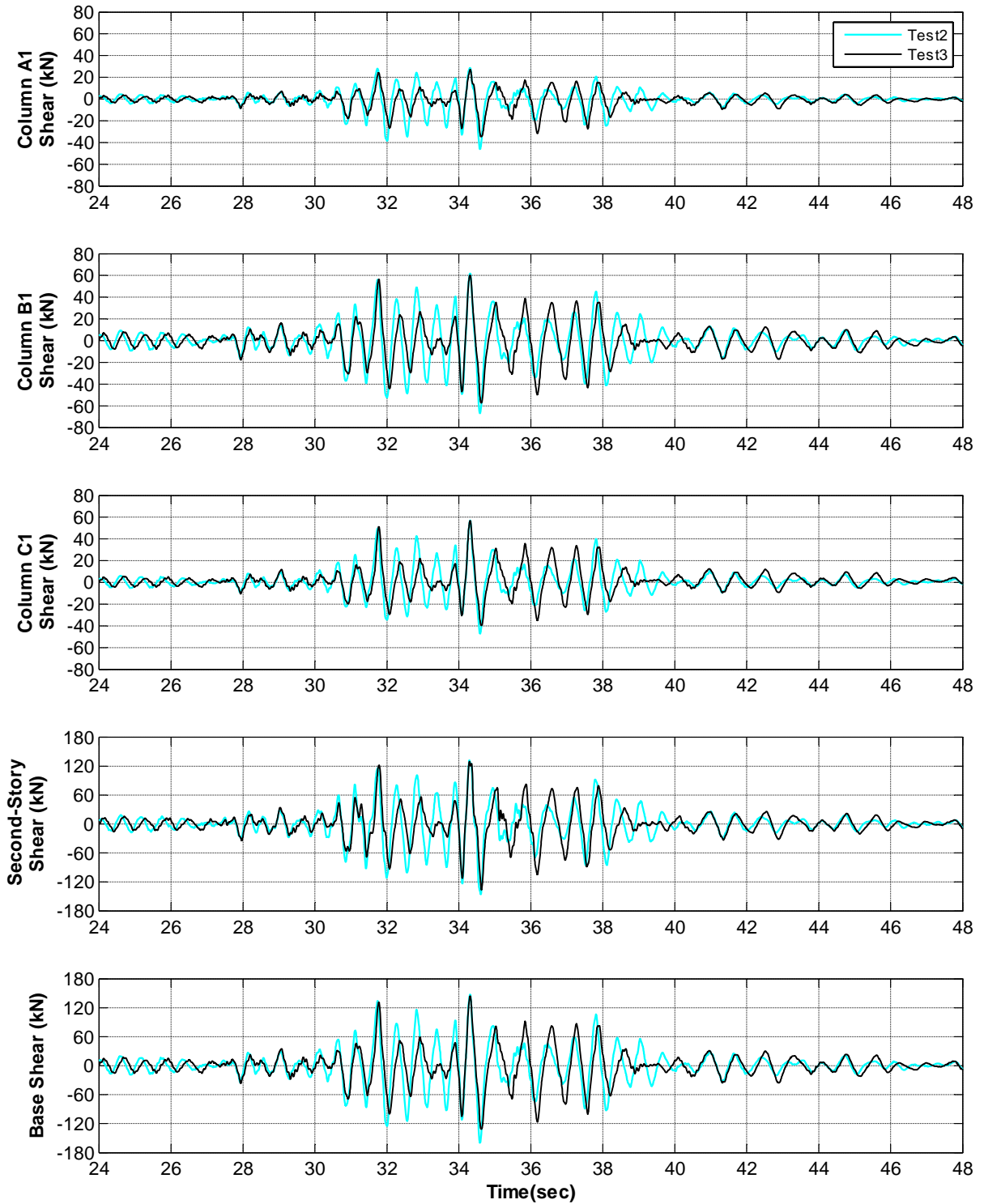


Figure C-3. First-story columns and frame base shear histories for specimen MUF, Test2 and Test3

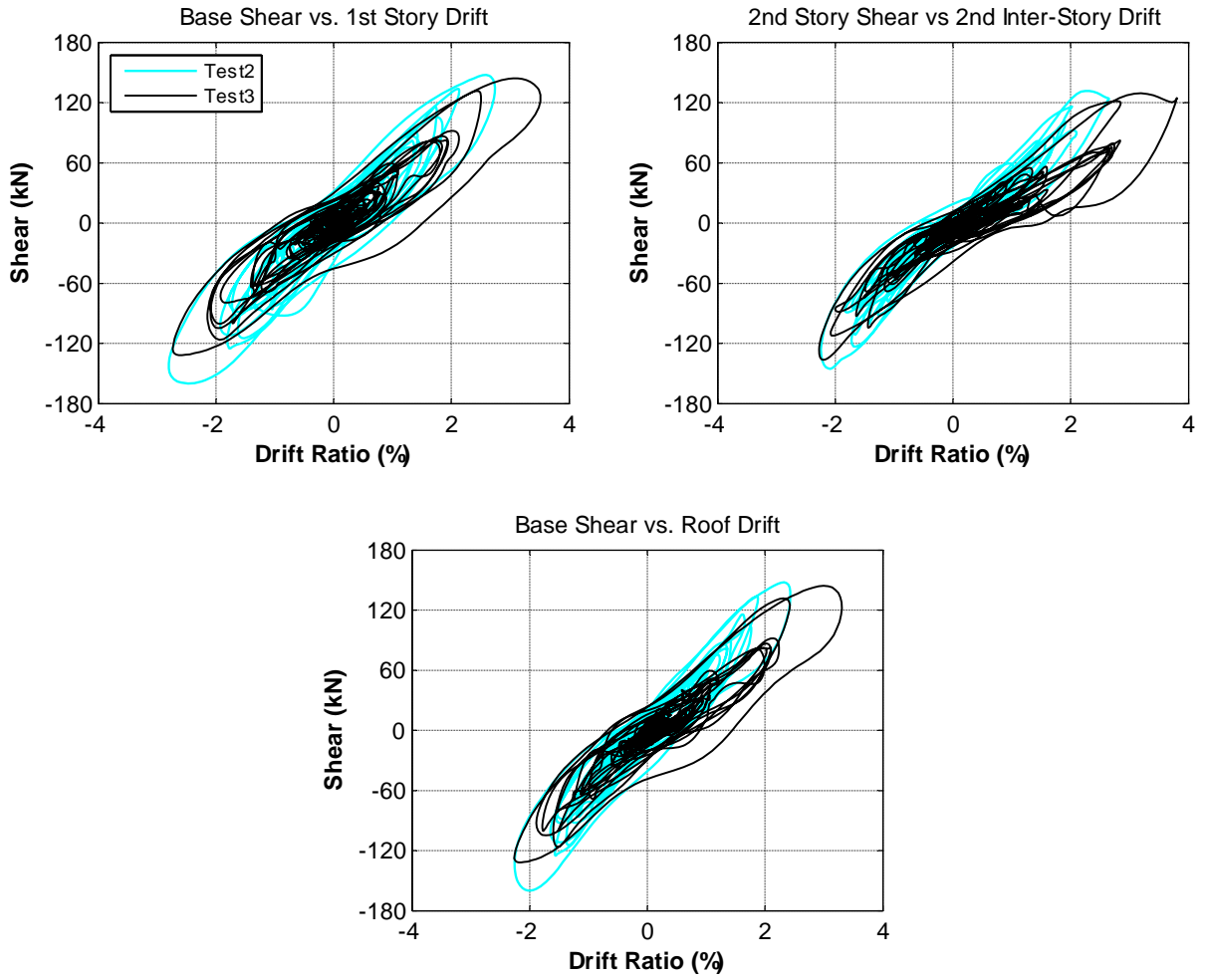


Figure C-4. Story-level shear hysteretic response of specimen MUF, Test2 and Test3

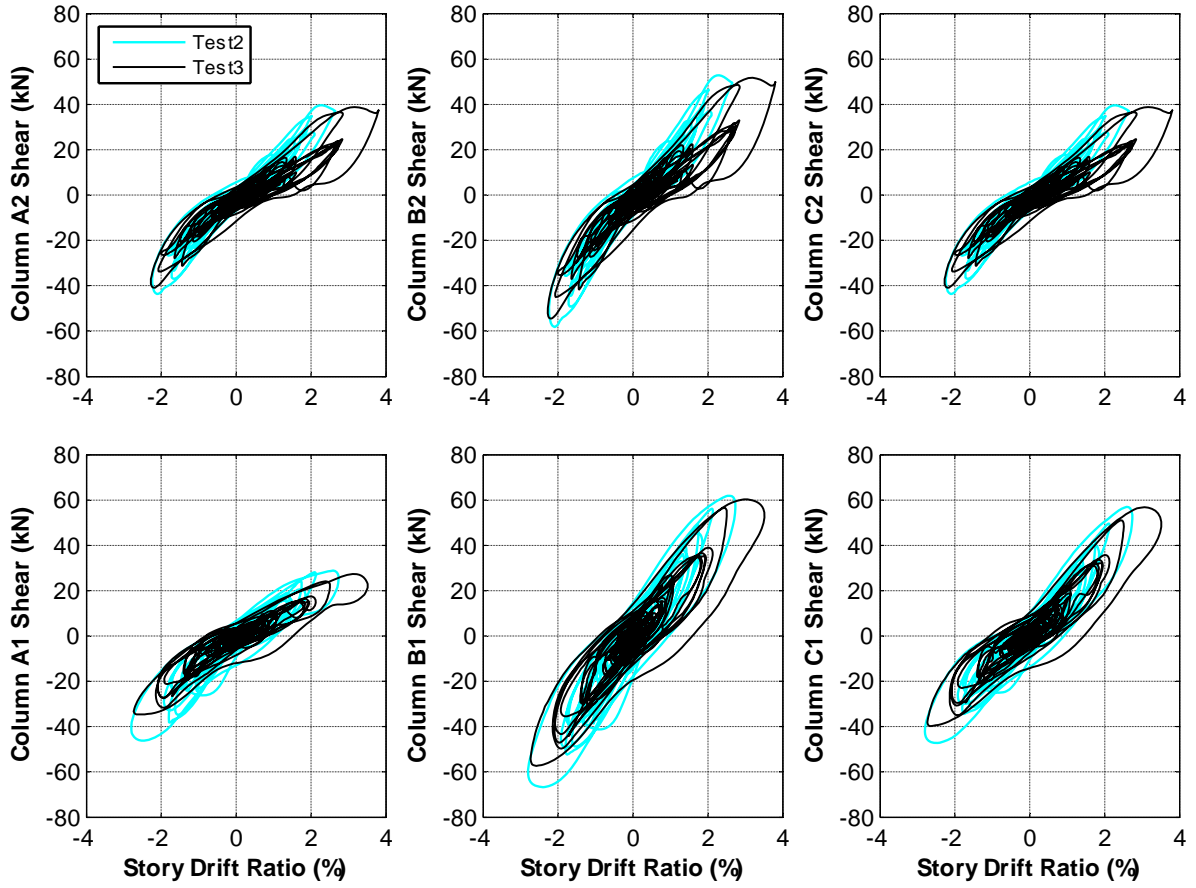


Figure C-5. Shear hysteretic response of specimen MUF columns, Test2 and Test3

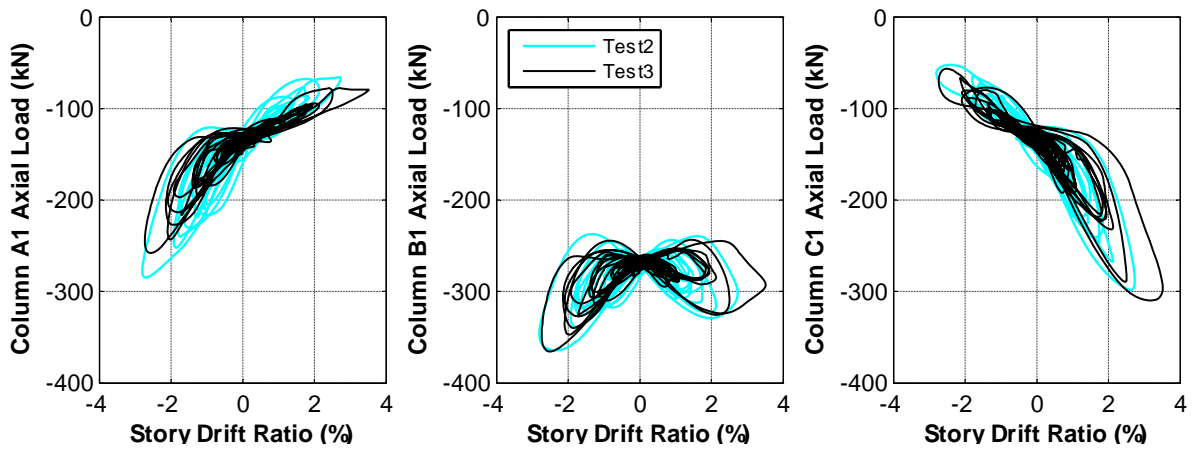


Figure C-6. Axial load hysteretic response of first-story columns of specimen MUF, Test2 and Test3

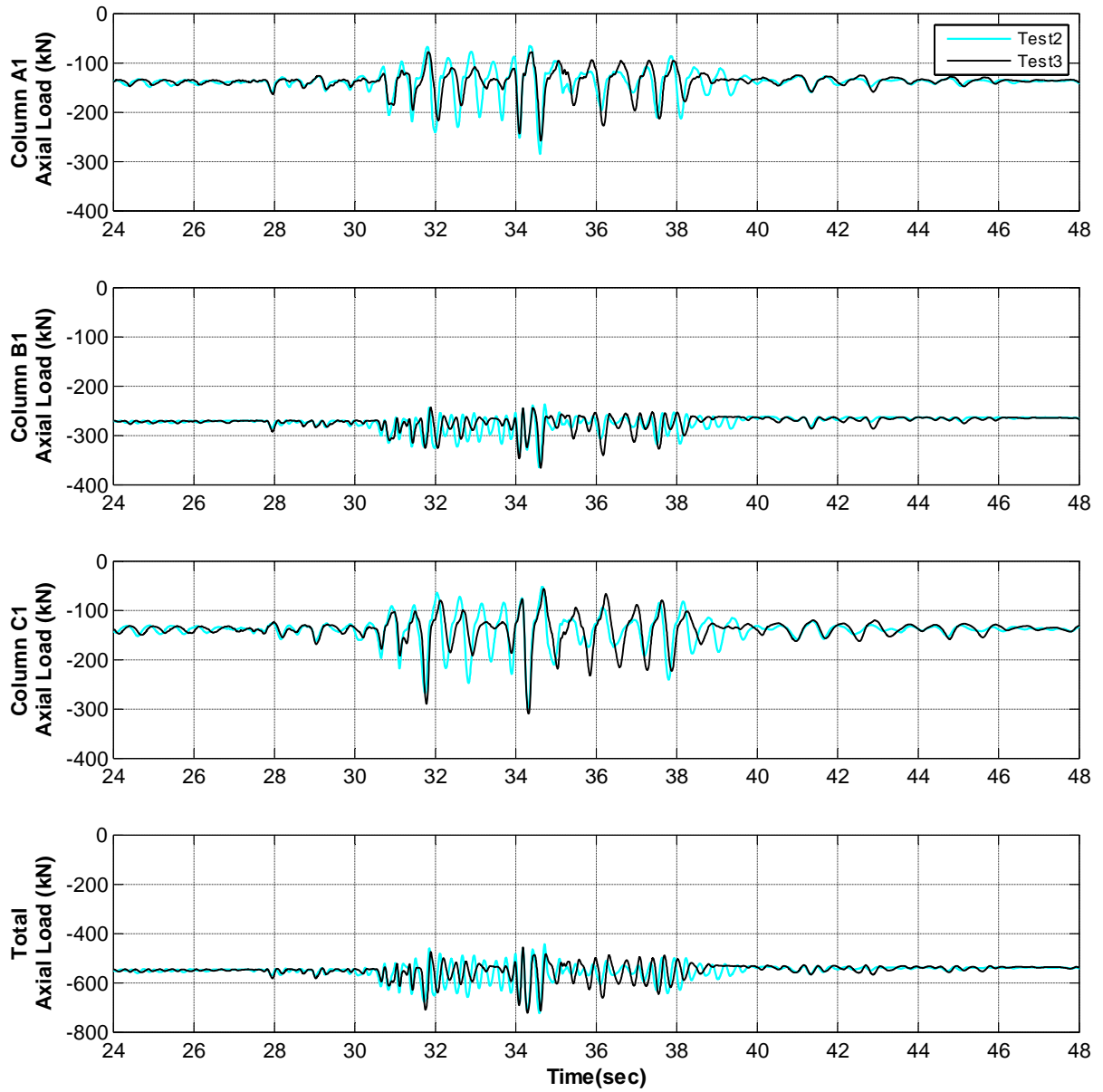


Figure C-7. Axial load response history of first-story columns of specimen MUF, Test2 and Test3

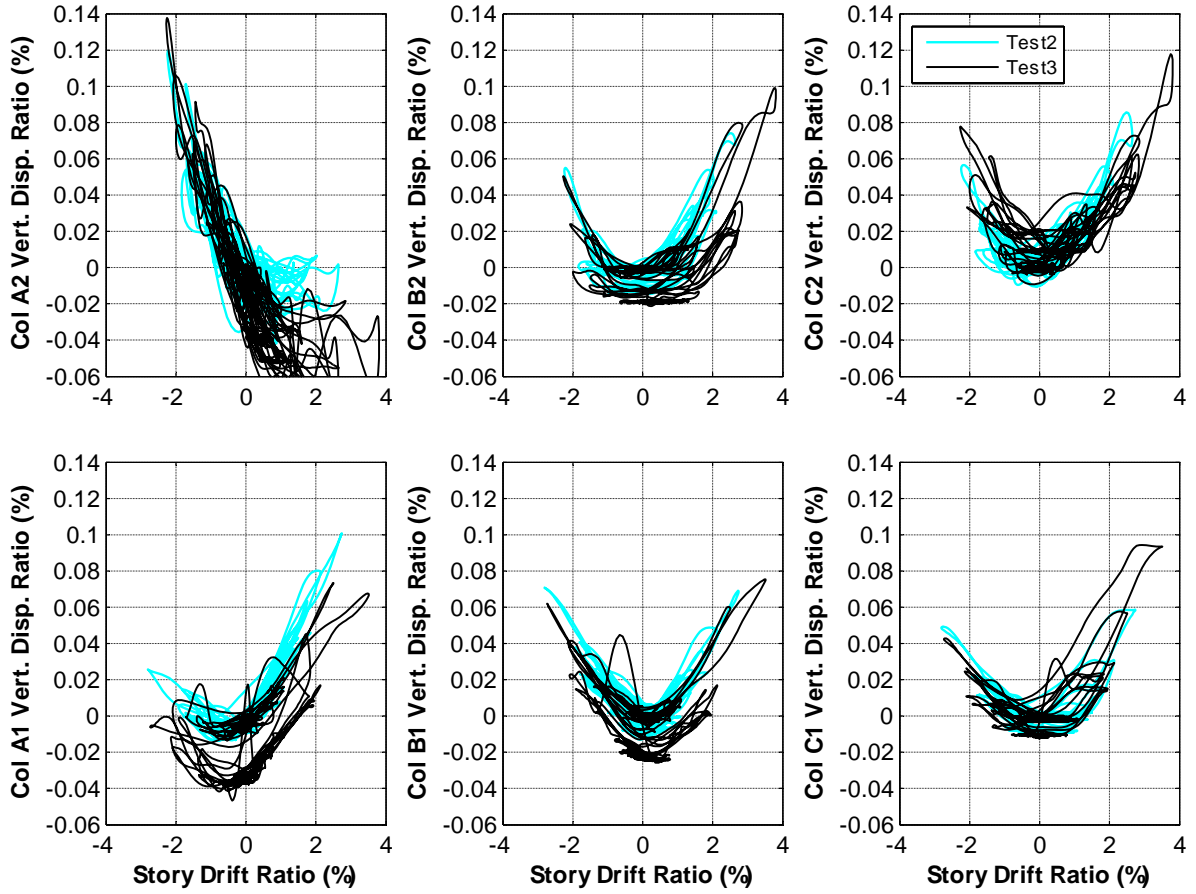


Figure C-8. Vertical displacement of specimen MUF columns, Test2 and Test3

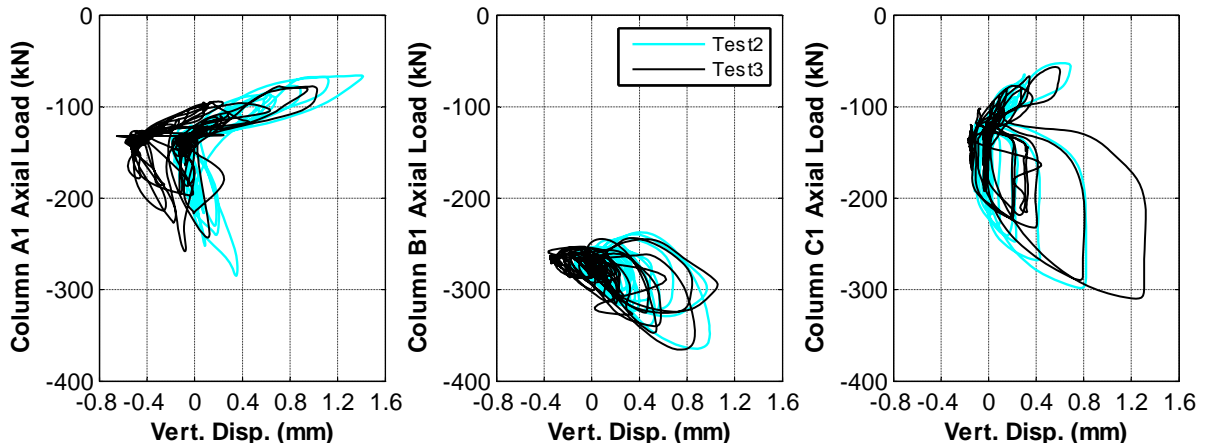


Figure C-9. Variation of axial load of specimen MUF columns with vertical displacement ratio, Test2 and Test3

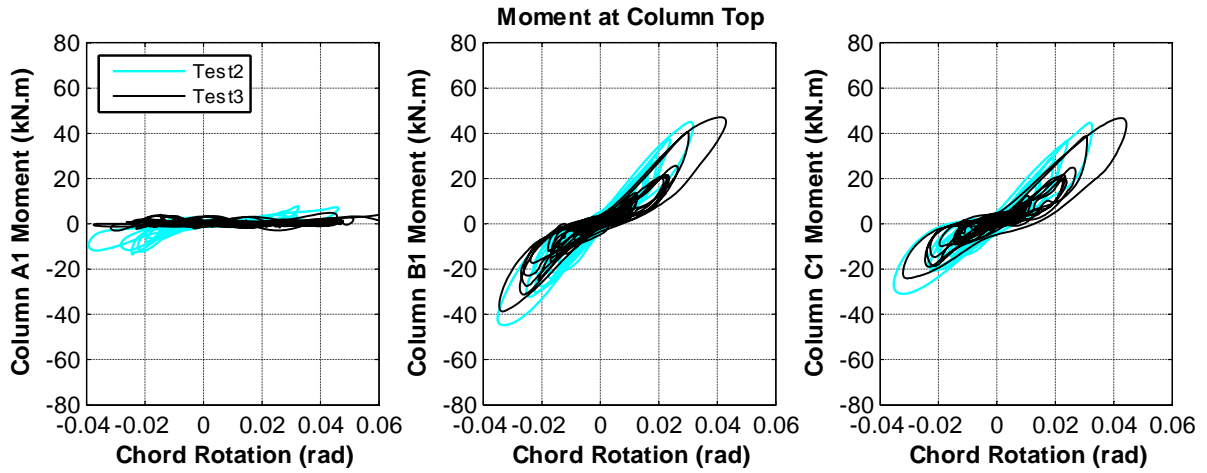


Figure C-10. Moment-chord rotation relationship at top of first-story columns of specimen MUF, Test2 and Test3

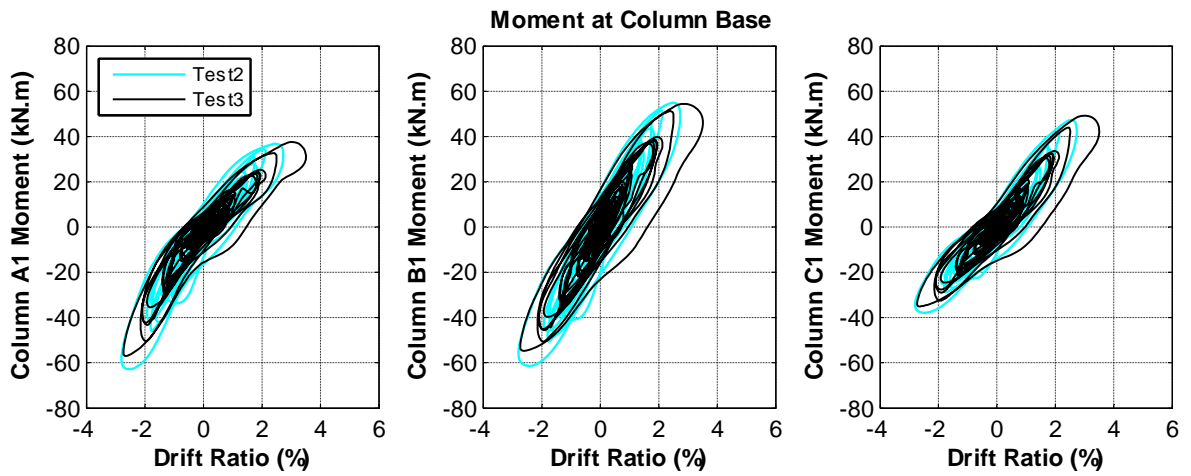


Figure C-11. Moment hysteretic response of first-story columns of specimen MUF, Test2 and Test3

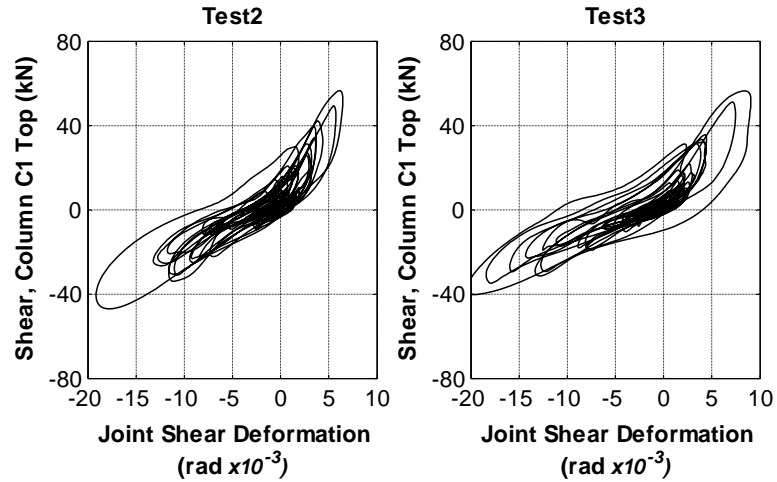


Figure C-12. Relation between shear force and shear deformation of joint C1 of specimen MUF, recorded at unconfined face of the joint, Test2 and Test3

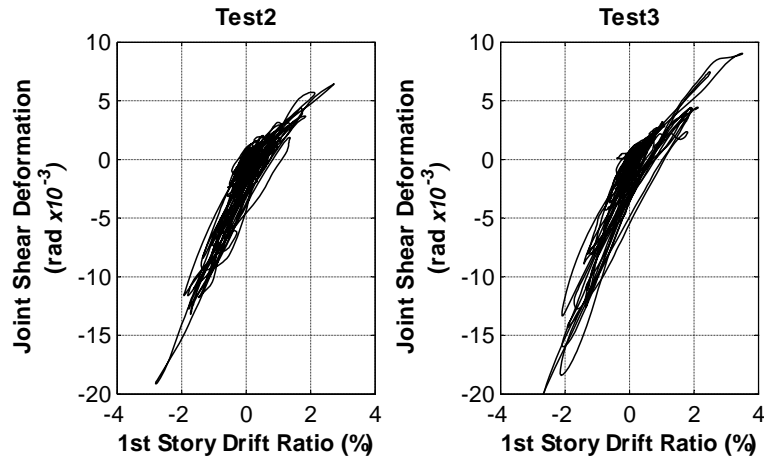


Figure C-13. Relation between shear deformation at joint C1, recorded at unconfined face and first-story drift of specimen MUF, Test2 and Test3